NATIONAL AERONAUTICS AND SPACE ADMINISTRATION

Technical Report No. 32-77

Design Parameters for Ballistic Interplanetary Trajectories Part II. One-Way Transfers to Mercury and Jupiter

V. C. Clarke, Jr.
W. E. Bollman
P. H. Feitis
R. Y. Roth

JET PROPULSION LABORATORY
CALIFORNIA INSTITUTE OF TECHNOLOGY
PASADENA, CALIFORNIA

January 15, 1966

NATIONAL AERONAUTICS AND SPACE ADMINISTRATION

Technical Report No. 32-77

Design Parameters for Ballistic Interplanetary Trajectories Part II. One-Way Transfers to Mercury and Jupiter

V. C. Clarke, Jr.
W. E. Bollman
P. H. Feitis
R. Y. Roth

T. W. Hamilton, *Manager*
Systems Analysis Section

JET PROPULSION LABORATORY
CALIFORNIA INSTITUTE OF TECHNOLOGY
PASADENA, CALIFORNIA

January 15, 1966

Prepared Under Contract No. NAS 7-100
National Aeronautics & Space Administration

CONTENTS

I. Introduction. Analytical Model for Interplanetary Trajectories . . . 1

A. Heliocentric Motion . . . 1

1. Determination of Planar Orientation . . . 1
2. In-Plane Relations . . . 2
3. Lambert's Theorem . . . 2

B. Launch–Planet Escape Hyperbola . . . 3

1. Assumptions . . . 3
2. Size and Shape of Escape Hyperbola . . . 3

C. Calculation of Differential Corrections . . . 4

II. Detailed Equations for Trajectory Computations . . . 7

A. Heliocentric Phase . . . 7

1. Determination of Position at Launch and Arrival . . . 7
2. Application of Lambert's Theorem . . . 8
3. Calculation of Velocity Vectors for Probe and Planet . . . 11
4. Calculation of Various Trajectory Parameters . . . 11

B. The Planetocentric-Conic Trajectories . . . 13

C. Differential Corrections . . . 16

III. Discussion and Explanation of Results . . . 19

A. Introduction . . . 19

1. Trajectory Computations . . . 19
2. Trajectory Analysis . . . 19

B. Classification of Trajectories . . . 19

1. Type I and Type II . . . 19
2. Class I and Class II . . . 29
3. Minimum-Energy Trajectories . . . 29

C. Mission Payload . . . 33

D. Launch Period . . . 33

E. General Characteristics of Trajectories . . . 34

1. Geocentric Parameters . . . 34
2. Heliocentric Parameters . . . 34
3. Planetocentric Parameters . . . 38

F. Discussion of Earth–Mercury and Earth–Jupiter Trajectory Parameters . . . 38

1. Declination of the Geocentric Asymptote Φ_* . . . 38
2. Angle Between the Sun–Earth Vector and the Outgoing Geocentric Asymptote ξ_L . . . 38
3. Celestial Latitude of the Geocentric Asymptote γ_L . . . 39
4. True Anomaly at Launch and Arrival and Heliocentric Transfer Angle . . . 39
5. Aphelion and Perihelion of the Transfer Orbit . . . 39
6. Time of Flight . . . 39

CONTENTS (Cont'd)

7. Communication Distance 40
8. Inclination of the Heliocentric Transfer Plane i and Celestial Latitude at Arrival β_p 40
9. Asymptotic Approach Speed V_{h_p} 41
10. Angle Between the Incoming Asymptote and the Arrival Planet's Orbital Plane γ_p 41
11. Angle Between the Arrival Planet–Sun Vector and the Incoming Asymptote ξ_p 41
12. Right Ascension Θ_p and Declination Φ_p of the Incoming Planet-Centered Asymptote 41
13. Angle Between the Planet–Earth Vector and the Incoming Asymptote ζ_E 41
14. Angle Between the Planet–Canopus Vector and the Incoming Asymptote ζ_c 43

G. Procedures for Utilization of Graphs in Design of Planetary Trajectories 43

IV. Mercury 1967: Trajectory-Parameter Graphs 47

V. Mercury 1968: Trajectory-Parameter Graphs 80

VI. Jupiter 1968–69: Trajectory-Parameter Graphs 113

VII. Jupiter 1969–70: Trajectory-Parameter Graphs 150

VIII. Jupiter 1970–71: Trajectory-Parameter Graphs 182

IX. Jupiter 1972: Trajectory-Parameter Graphs 217

X. Jupiter 1973: Trajectory-Parameter Graphs 251

Nomenclature 288

References 289

TABLES

2–1. Mean planet elements 12

3–1. Characteristics of minimum-energy transfer 31

3–2. Mercury Type I and II transfer characteristics 35

3–3. Type I Jupiter transfer characteristics 36

3–4. Type II Jupiter transfer characteristics 37

FIGURES

1–1. Heliocentric-transfer geometry 2

1–2. In-plane–transfer geometry 2

1–3. Determination of hyperbolic-excess velocity vector 3

1–4. Vehicle flight plane 5

1–5. Impact parameter 6

1–6. The R, S, T target coordinate system 6

2–1. Geometrical configuration of heliocentric conic: (a) central angle less than 180 deg; (b) central angle greater than 180 deg . . . 9

2–2. Trajectory-plane–launch-site geometry 14

2–3. Trajectory-plane geometry 14

2–4. Ascent-trajectory geometry 15

2–5. Powered trajectory modified by coasting 15

2–6. Relation between longitude, right ascension, and time in equatorial plane 16

3–1. Mercury 1964–1968: Minimum injection energy vs launch date, Type I 20

3–2. Mercury 1968–1972: Minimum injection energy vs launch date, Type I 21

3–3. Mercury 1972–1976: Minimum injection energy vs launch date, Type I 22

3–4. Mercury 1964–1968: Minimum injection energy vs launch date, Type II 23

3–5. Mercury 1968–1972: Minimum injection energy vs launch date, Type II 24

3–6. Mercury 1972–1976: Minimum injection energy vs launch date, Type II 25

3–7. Jupiter 1969–1973: Minimum injection energy vs launch date, Type I 26

3–8. Jupiter 1969–1973. Minimum injection energy vs launch date, Type II 27

3–9. Junipter 1968–1969: Time of flight vs launch date 28

3–10. Jupiter 1968–1969: Minimum injection energy vs launch date . . 30

3–11. Typical payload capability curves for *Atlas/Centaur*, *Saturn 1B*, and *Saturn 5* launch vehicles 33

3–12. Permissible regions of the declination of the geocentric asymptote Φ_∞ for Cape Kennedy launchings 38

3–13. Inclination of the heliocentric orbital plane to ecliptic vs heliocentric central angle 40

FIGURES (Cont'd)

3–14. Crescent orientations for typical trajectories to Mercury and Jupiter as observed from approaching spacecraft 42

3–15. Near-Jupiter geometry for typical trajectories, viewed from above ecliptic plane: (a) Type I trajectory, encountering Jupiter before aphelion; (b) Type I–II trajectory, encountering Jupiter after aphelion 43

3–16. Near-Mercury geometry for typical trajectories, viewed from above ecliptic plane: (a) Type I trajectory, encountering Mercury before perihelion; (b) Type II trajectory, encountering Mercury after perihelion 44

3–17. Steps for construction of arrival date loci 46

4–1. Mercury 1967: Minimum injection energy vs launch date . . . 49

4–2. Mercury 1967: Time of flight vs launch date 50

4–3. Mercury 1967: Heliocentric central angle vs launch date . . . 51

4–4. Mercury 1967: Earth-Mercury communication distance vs launch date 52

4–5(I). Mercury 1967: Declination of the geocentric asymptote vs launch date, Type I 53

4–5(II). Mercury 1967: Declination of the geocentric asymptote vs launch date, Type II 54

4–6(I). Mercury 1967: Right ascension of the geometric asymptote vs launch date, Type I 55

4–6(II). Mercury 1967: Right ascension of the geocentric asymptote vs launch date, Type II 56

4–7(I). Mercury 1967: Angle between outgoing geocentric asymptote and launch planet's orbital plane vs launch date, Type I . . . 57

4–7(II). Mercury 1967: Angle between outgoing geocentric asymptote and launch planet's orbital plane vs launch date, Type II . . . 58

4–8(I). Mercury 1967: Angle between Sun–Earth vector and outgoing geocentric asymptote vs launch date, Type I 59

4–8(II). Mercury 1967: Angle between Sun–Earth vector and outgoing geocentric asymptote vs launch date, Type II 60

4–9(I). Mercury 1967: True anomaly in transfer ellipse at launch time vs launch date, Type I 61

4–9(II). Mercury 1967: True anomaly in transfer ellipse at launch time vs launch date, Type II 62

4–10. Mercury 1967: True anomaly in transfer ellipse at arrival time vs launch date 63

4–11(I). Mercury 1967: Perihelion of transfer orbit vs launch date, Type I . 64

4–11(II). Mercury 1967: Perihelion of transfer orbit vs launch date, Type II . 65

FIGURES (Cont'd)

4–12(I). Mercury 1967: Aphelion of transfer orbit vs launch date, Type I . 66

4–12(II). Mercury 1967: Aphelion of transfer orbit vs launch date, Type II . 67

4–13(I). Mercury 1967: Inclination of the heliocentric transfer plane vs launch date, Type I 68

4–13(II). Mercury 1967: Inclination of the heliocentric transfer plane vs launch date, Type II 69

4–14. Mercury 1967: Celestial latitude at arrival time vs launch date . . 70

4–15(I). Mercury 1967: Asymptotic speed with rescept to Mercury vs launch date, Type I 71

4–15(II). Mercury 1967: Asymptotic speed with respect to Mercury vs launch date, Type II 72

4–16(I). Mercury 1967: Angle between incoming hermiocentric asymptote and arrival planet's orbital plane vs launch date, Type I 73

4–16(II). Mercury 1967: Angle between incoming hermiocentric asymptote and arrival planet's orbital plane vs launch date, Type II 74

4–17. Mercury 1967: Angle between Mercury–Sun vector and incoming hermiocentric asymptote vs launch date 75

4–18(I). Mercury 1967: Declination of the hermiocentric asymptote vs launch date, Type I 76

4–18(II). Mercury 1967: Declination of the hermiocentric asymptote vs launch date, Type II 77

4–19(I). Mercury 1967: Right ascension of hermiocentric asymptote vs launch date, Type I 78

4–19(II). Mercury 1967: Right ascension of hermiocentric asymptote vs launch date, Type II 79

5–1. Mercury 1968: Minimum injection energy vs launch date . . . 82

5–2. Mercury 1968: Time of flight vs launch date 83

5–3. Mercury 1968: Heliocentric central angle vs launch date . . . 84

5–4. Mercury 1968: Earth–Mercury communication distance vs launch date 85

5–5(I). Mercury 1968: Declination of the geocentric asymptote vs launch date, Type I 86

5–5(II). Mercury 1968: Declination of the geocentric asymptote vs launch date, Type II 87

5–6(I). Mercury 1968: Right ascension of the geocentric asymptote vs launch date, Type I 88

FIGURES (Cont'd)

5–6(II). Mercury 1968: Right ascension of the geocentric asymptote vs launch date, Type II 89

5–7(I). Mercury 1968: Angle between outgoing geocentric asymptote and launch planet's orbital plane vs launch date, Type I 90

5–7(II). Mercury 1968: Angle between outgoing geocentric asymptote and launch planet's orbital plane vs launch date, Type II 91

5–8(I). Mercury 1968: Angle between Sun–Earth vector and outgoing geocentric asymptote vs launch date, Type I 92

5–8(II). Mercury 1968: Angle between Sun–Earth vector and outgoing geocentric asymptote vs launch date, Type II 93

5–9(I). Mercury 1968: True anomaly in transfer ellipse at launch time vs launch date, Type I 94

5–9(II). Mercury 1968: True anomaly in transfer ellipse at launch time vs launch date, Type II 95

5–10. Mercury 1968: True anomaly in transfer ellipse at launch time vs launch date 96

5–11(I). Mercury 1968: Perihelion of transfer orbit vs launch date, Type I 97

5–11(II). Mercury 1968: Perihelion of transfer orbit vs launch date, Type II 98

5–12(I). Mercury 1968: Apehelion of transfer orbit vs launch date, Type I 99

5–12(II). Mercury 1968: Aphelion of transfer orbit vs launch date, Type II 100

5–13(I). Mercury 1968: Inclination of the heliocentric transfer plane vs launch date, Type I 101

5–13(II). Mercury 1968: Inclination of the heliocentric transfer plane vs launch date, Type II 102

5–14. Mercury 1968: Celestial latitude at arrival time vs launch date . 103

5–15(I). Mercury 1968: Asymptotic speed with respect to Mercury vs launch date, Type I 104

5–15(II). Mercury 1968: Asymptotic speed with respect to Mercury vs launch date, Type II 105

5–16(I). Mercury 1968: Angle between the incoming hermiocentric asymptote and arrival planet's orbital plane vs launch date, Type I 106

5–16(II). Mercury 1968: Angle between the incoming hermiocentric asymptote and arrival planet's obital plane vs launch date, Type II 107

FIGURES (Cont'd)

5–17. Mercury 1968: Angle between Mercury–Sun vector and incoming hermiocentric asymptote vs launch date, Type I 108

5–18(I). Mercury 1968: Declination of the hermiocentric asymptote vs launch date, Type I 109

5–18(II). Mercury 1968: Declination of the hermiocentric asymptote vs launch date, Type II 110

5–19(I). Mercury 1968: Right ascension of the hermiocentric asymptote vs launch date, Type I 111

5–19(II). Mercury 1968: Right ascension of the hermiocentric asymptote vs launch date, Type II 112

6–1. Jupiter 68–69: Minimum injection energy vs launch date . . . 115

6–2. Jupiter 68–69: Time of flight vs launch date 116

6–3. Jupiter 68–69: Heliocentric central angle vs launch date . . . 117

6–4(I). Jupiter 68–69: Earth–Jupiter communication distance vs launch date, Type I 118

6–4(II). Jupiter 68–69: Earth–Jupiter communication distance vs launch date, Type II 119

6–5(I). Jupiter 68–69: Declination of the geocentric asymptote vs launch date, Type I 120

6–5(II). Jupiter 68–69: Declination of the geocentric asymptote vs launch date, Type II 121

6–6(I). Jupiter 68–69: Right ascension of the geocentric asymptote vs launch date, Type I 122

6–6(II). Jupiter 68–69: Right ascension of the geocentric asymptote vs launch date, Type II 123

6–7(I). Jupiter 68–69: Angle between the outgoing geocentric asymptote and launch planet's orbital plane vs launch date, Type I 124

6–7(II). Jupiter 68–69: Angle between the outgoing geocentric asymptote and launch planet's orbital plane vs launch date, Type II 125

6–8(I). Jupiter 68–69: Angle between Sun–Earth vector and the outgoing geocentric asymptote vs launch date, Type I 126

6–8(II). Jupiter 68–69: Angle between Sun–Earth vector and the outgoing geocentric asymptote vs launch date, Type II 127

6–9(I). Jupiter 68–69: True anomaly in transfer ellipse at launch time vs launch date, Type I 128

6–9(II). Jupiter 68–69: True anomaly in transfer ellipse at launch time vs launch date, Type II 129

FIGURES (Cont'd)

6–10. Jupiter 68–69: True anomaly in transfer ellipse at arrival time vs launch date . . . 130

6–11(I). Jupiter 68–69: Perihelion of transfer orbit vs launch date, Type I . . . 131

6–11(II). Jupiter 68–69: Perihelion of transfer orbit vs launch date, Type II . . . 132

6–12(I). Jupiter 68–69: Aphelion of transfer orbit vs launch date, Type I . . . 133

6–12(II). Jupiter 68–69: Aphelion of transfer orbit vs launch date, Type II . . . 134

6–13(I). Jupiter 68–69: Inclination of the heliocentric transfer plane vs launch date, Type I . . . 135

6–13(II). Jupiter 68–69: Inclination of the heliocentric transfer plane vs launch date, Type II . . . 136

6–14. Jupiter 68–69: Celestial latitude at arrival time vs launch date . . . 137

6–15(I). Jupiter 68–69: Asymptotic speed with respect to Jupiter vs launch date, Type I . . . 138

6–15(II). Jupiter 68–69: Asymptotic speed with respect to Jupiter vs launch date, Type II . . . 139

6–16. Jupiter 68–69: Angle between incoming zeocentric asymptote and arrival planet's orbital plane vs launch date . . . 140

6–17. Jupiter 68–69: Angle between Jupiter–Sun vector and incoming zeocentric asymptote vs launch date . . . 141

6–18(I). Jupiter 68–69: Declination of the zeocentric asymptote vs launch date, Type I . . . 142

6–18(II). Jupiter 68–69: Declination of the zeocentric asymptote vs launch date, Type II . . . 143

6–19(I). Jupiter 68–69: Right ascension of zeocentric asymptote vs launch date, Type I . . . 144

6–19(II). Jupiter 68–69: Right ascension of zeocentric asymptote vs launch date, Type II . . . 145

6–20(I). Jupiter 68–69: Angle between Planet–Earth vector and incoming asymptote vs launch date, Type I . . . 146

6–20(II). Jupiter 68–69: Angle between Planet–Earth vector and incoming asymptote vs launch date, Type II . . . 147

6–21(I). Jupiter 68–69: Angle between the planet–Canopus vector and incoming asymptote vs launch date, Type I . . . 148

6–21(II). Jupiter 68–69: Angle between the planet–Canopus vector and incoming asymptote vs launch date, Type II . . . 149

FIGURES (Cont'd)

7–1. Jupiter 69–70: Minimum injection energy vs launch date . . . 152

7–2. Jupiter 69–70: Time of flight vs launch date 153

7–3. Jupiter 69–70: Heliocentric central angle vs launch date . . . 154

7–4(I). Jupiter 69–70: Earth–Jupiter communication distance vs launch date, Type I 155

7–4(II). Jupiter 69–70: Earth–Jupiter communication distance vs launch date, Type II 156

7–5(I). Jupiter 69–70: Declination of the geocentric asymptote vs launch date, Type I 157

7–5(II). Jupiter 69–70: Declination of the geocentric asymptote vs launch date, Type II 158

7–6(I). Jupiter 69–70: Right ascension of the geocentric asymptote vs launch date, Type I 159

7–6(II). Jupiter 69–70: Right ascension of the geocentric asymptote vs launch date, Type II 160

7–7(I). Jupiter 69–70: Angle between outgoing geocentric asymptote and launch planet's orbital plane vs launch date, Type I . . . 161

7–7(II). Jupiter 69–70: Angle between outgoing geocentric asymptote and launch planet's orbital plane vs launch date, Type II . . . 162

7–8. Jupiter 69–70: Angle between Sun–Earth vector and outgoing geocentric asymptote vs launch date 163

7–9. Jupiter 69–70: True anomaly in transfer ellipse at launch time vs launch date 164

7–10. Jupiter 69–70: True anomaly in transfer ellipse at arrival time vs launch date 165

7–11(I). Jupiter 69–70: Perihelion of transfer orbit vs launch date, Type I 166

7–11(II). Jupiter 69–70: Perihelion of transfer orbit vs launch date, Type II 167

7–12(I). Jupiter 69–70: Aphelion of transfer orbit vs launch date, Type I 168

7–12(II). Jupiter 69–70: Aphelion of transfer orbit vs launch date, Type II 169

7–13(I). Jupiter 69–70: Inclination of the heliocentric transfer plane vs launch date, Type I 170

7–13(II). Jupiter 69–70: Inclination of the heliocentric transfer plane vs launch date, Type II 171

7–14. Jupiter 69–10: Celestial latitude at arrival time vs launch date . . 172

FIGURES (Cont'd)

7–15(I). Jupiter 69–70: Asymptotic speed with respect to Jupiter vs launch date, Type I . . . 173

7–15(II). Jupiter 69–70: Asymptotic speed with respect to Jupiter vs launch date, Type II . . . 174

7–16(I). Jupiter 69–70: Angle between incoming zeocentric asymptote and arrival planet's orbital plane vs launch date, Type I . . . 175

7–16(II). Jupiter 69–70: Angle between incoming zeocentric asymptote and arrival planet's orbital plane vs launch date, Type II . . . 176

7–17. Jupiter 69–70: Angle between Jupiter–Sun vector and incoming zeocentric asymptote vs launch date . . . 177

7–18(I). Jupiter 69–70: Declination of the zeocentric asymptote vs launch date, Type I . . . 178

7–18(II). Jupiter 69–70: Declination of the zeocentric asymptote vs launch date, Type II . . . 179

7–19(I). Jupiter 69–70: Right ascension of the zeocentric asymptote vs launch date, Type I . . . 180

7–19(II). Jupiter 69–70: Right ascension of the zeocentric asymptote vs launch date, Type II . . . 181

8–1. Jupiter 70–71: Minimum injection energy vs launch date . . . 184

8–2. Jupiter 70–71: Time of flight vs launch date . . . 185

8–3. Jupiter 70–71: Heliocentric central angle vs launch date . . . 186

8–4(I). Jupiter 70–71: Earth–Jupiter communication distance vs launch date, Type I . . . 187

8–4(II). Jupiter 70–71: Earth–Jupiter communication distance vs launch date, Type II . . . 188

8–5(I). Jupiter 70–71: Declination of the geocentric asymptote vs launch date, Type I . . . 189

8–5(II). Jupiter 70–71: Declination of the geocentric asymptote vs launch date, Type II . . . 190

8–6. Jupiter 70–71: Right ascension of the geocentric asymptote vs launch date . . . 191

8–7. Jupiter 70–71: Angle between outgoing geocentric asymptote and launch planet's orbital plane vs launch date . . . 192

8–8(I). Jupiter 70–71: Angle between Sun–Earth vector and outgoing geocentric asymptote vs launch date, Type I . . . 193

8–8(II). Jupiter 70–71: Angle between Sun–Earth vector and outgoing geocentric asymptote vs launch date, Type II . . . 194

8–9(I). Jupiter 70–71: True anomaly in transfer ellipse at launch time vs launch date, Type I . . . 195

FIGURES (Cont'd)

8–9(II). Jupiter 70–71: True Anomaly in transfer ellipse at launch time vs launch date, Type II 196

8–10. Jupiter 70–71: True anomaly in transfer ellipse at arrival time vs launch date 197

8–11(I). Jupiter 70–71: Perihelion of transfer orbit vs launch date, Type I 198

8–11(II). Jupiter 70–71: Perihelion of transfer orbit vs launch date, Type II 199

8–12(I). Jupiter 70–71: Aphelion of transfer orbit vs launch date, Type I 200

8–12(II). Jupiter 70–71: Aphelion of transfer orbit vs launch date, Type II 201

8–13(I). Jupiter 70–71: Inclination of the heliocentric transfer plane vs launch date, Type I 202

8–13(II). Jupiter 70–71: Inclination of the heliocentric transfer plane vs launch date, Type II 203

8–14. Jupiter 70–71: Celestial latitude at arrival time vs launch date . . 204

8–15(I). Jupiter 70–71: Asymptotic speed with respect to Jupiter vs launch date, Type I 205

8–15(II). Jupiter 70–71: Asymptotic speed with respect to Jupiter vs launch date, Type II 206

8–16. Jupiter 70–71: Angle between incoming zeocentric asymptote and arrival planet's orbital plane vs launch date 207

8–17. Jupiter 70–71: Angle between Jupiter–Sun vector and incoming zeocentric asymptote vs launch date 208

8–18(I). Jupiter 70–71: Declination of zeocentric asymptote vs launch date, Type I 209

8–18(II). Jupiter 70–71: Declination of zeocentric asymptote vs launch date, Type II 210

8–19(I). Jupiter 70–71: Right ascension of zeocentric asymptote vs launch date, Type I 211

8–19(II). Jupiter 70–71: Right ascension of zeocentric asymptote vs launch date, Type II 212

8–20(I). Jupiter 70–71: Angle between planet–Earth vector and incoming asymptote vs launch date, Type I 213

8–20(II). Jupiter 70–71: Angle between planet–Earth vector and incoming asymptote vs launch date, Type II 214

8–21(I). Jupiter 70–71: Angle between planet–Canopus vector and incoming asymptote vs launch date, Type I 215

FIGURES (Cont'd)

8–21(II). Jupiter 70–71: Angle between planet–Canopus vector and incoming asymptote vs launch date, Type II 216

9–1. Jupiter 1972: Minimum injection energy vs launch date 219

9–2. Jupiter 1972: Time of flight vs launch date 220

9–3. Jupiter 1972: Heliocentric central angle vs launch date 221

9–4(I). Jupiter 1972: Earth–Jupiter communication distance vs launch date, Type I 222

9–4(II). Jupiter 1972: Earth–Jupiter communication distance vs launch date, Type II 223

9–5. Jupiter 1972: Declination of the geocentric asymptote vs launch date 224

9–6. Jupiter 1972: Right ascension of geocentric asymptote vs launch date 225

9–7. Jupiter 1972: Angle between outgoing geocentric asymptote and launch planet's orbital plane vs launch date 226

9–8(I). Jupiter 1972: Angle between Sun–Earth vector and outgoing geocentric asymptote vs launch date, Type I 227

9–8(II). Jupiter 1972: Angle between Sun–Earth vector and outgoing geocentric asymptote vs launch date, Type II 228

9–9(I). Jupiter 1972: True anomaly in transfer ellipse at launch time vs launch date, Type I 229

9–9(II). Jupiter 1972: True anomaly in transfer ellipse at launch time vs launch date, Type II 230

9–10. Jupiter 1972: True anomaly in transfer ellipse at arrival time vs launch date 231

9–11(I). Jupiter 1972: Perihelion of transfer orbit vs launch date, Type I 232

9–11(II). Jupiter 1972: Perihelion of transfer orbit vs launch date, Type II 233

9–12(I). Jupiter 1972: Aphelion of transfer orbit vs launch date, Type I . . 234

9–12(II). Jupiter 1972: Aphelion of transfer orbit vs launch date, Type II . 235

9–13(I). Jupiter 1972: Inclination of the heliocentric transfer plane vs launch date, Type I 236

9–13(II). Jupiter 1972: Inclination of the heliocentric transfer plane vs launch date, Type II 237

9–14(I). Jupiter 1972: Celestial latitude at arrival time vs launch date, Type I 238

FIGURES (Cont'd)

9–14(II). Jupiter 1972: Celestial latitude at arrival time vs launch date, Type II 239

9–15(I). Jupiter 1972: Asymptotic speed with respect to Jupiter vs launch date, Type I 240

9–15(II). Jupiter 1972: Asymptotic speed with respect to Jupiter vs launch date, Type II 241

9–16. Jupiter 1972: Angle between incoming zeocentric asymptote and arrival planet's orbital plane vs launch date 242

9–17. Jupiter 1972: Angle between Jupiter–Sun vector and incoming zeocentric asymptote vs launch date 243

9–18. Jupiter 1972: Declination of zeocentric asymptote vs launch date 244

9–19(I). Jupiter 1972: Right ascension of zeocentric asymptote vs launch date, Type I 245

9–19(II). Jupiter 1972: Right ascension of zeocentric asymptote vs launch date, Type II 246

9–20(I). Jupiter 1972: Angle between planet–Earth vector and incoming asymptote vs launch date, Type I 247

9–20(II). Jupiter 1972: Angle between planet–Earth vector and incoming asymptote vs launch date, Type II 248

9–21(I). Jupiter 1972: Angle between planet–Canopus vector and incoming asymptote vs launch date, Type I 249

9–21(II). Jupiter 1972: Angle between planet–Canopus vector and incoming asymptote vs launch date, Type II 250

10–1. Jupiter 1973: Minimum injection energy vs launch date 253

10–2(I). Jupiter 1973: Time of flight vs launch date, Type I 254

10–2(II). Jupiter 1973: Time of flight vs launch date, Type II 255

10–3. Jupiter 1973: Heliocentric central angle vs launch date 256

10–4(I). Jupiter 1973: Earth–Jupiter communication distance vs launch date, Type I 257

10–4(II). Jupiter 1973: Earth–Jupiter communication distance vs launch date, Type II 258

10–5(I). Jupiter 1973: Declination of geocentric asymptote vs launch date, Type I 259

10–5(II). Jupiter 1973: Declination of geocentric asymptote vs launch date, Type II 260

10–6(I). Jupiter 1973: Right ascension of geocentric asymptote vs launch date, Type I 261

FIGURES (Cont'd)

10–6(II). Jupiter 1973: Right ascension of geocentric asymptote vs launch date, Type II 262

10–7. Jupiter 1973: Angle between outgoing geocentric asymptote and launch planet's orbital plane vs launch date 263

10–8(I). Jupiter 1973: Angle between Sun–Earth vector and outgoing geocentric asymptote vs launch date, Type I 264

10–8(II). Jupiter 1973: Angle between Sun–Earth vector and outgoing geocentric asymptote vs launch date, Type II 265

10–9(I). Jupiter 1973: True anomaly in transfer ellipse at launch time vs launch date, Type I 266

10–9(II). Jupiter 1973: True anomaly in transfer ellipse at launch time vs launch date, Type II 267

10–10. Jupiter 1973: True anomaly in transfer ellipse at arrival time vs launch date 268

10–11(I). Jupiter 1973: Perihelion of transfer orbit vs launch date, Type I 269

10–11(II). Jupiter 1973: Perihelion of transfer orbit vs launch date, Type II 270

10–12(I). Jupiter 1973: Aphelion of transfer orbit vs launch date, Type I 271

10–12(II). Jupiter 1973: Aphelion of transfer orbit vs launch date, Type II 272

10–13(I). Jupiter 1973: Inclination of the heliocentric transfer plane vs launch date, Type I 273

10:13(II). Jupiter 1973: Inclination of the heliocentric transfer plane vs launch date, Type II 274

10–14(I). Jupiter 1973: Celestial latitude at arrival time vs launch date, Type I 275

10–14(II). Jupiter 1973: Celestial latitude at arrival time vs launch date, Type II 276

10–15(I). Jupiter 1973: Asymptotic speed with respect to Jupiter vs launch date, Type I 277

10–15(II). Jupiter 1973: Asymptotic speed with respect to Jupiter vs launch date, Type II 278

10–16. Jupiter 1973: Angle between incoming zeocentric asymptote and arrival planet's orbital plane vs launch date 279

10–17. Jupiter 1973: Angle between Jupiter–Sun vector and incoming zeocentric asymptote vs launch date 280

FIGURES (Cont'd)

10–18. Jupiter 1973: Declination of zeocentric asymptote vs launch date 281

10–19(I). Jupiter 1973: Right ascension of zeocentric asymptote vs launch date, Type I 282

10–19(II). Jupiter 1973: Right ascension of zeocentric asymptote vs launch date, Type II 283

10–20(I). Jupiter 1973: Angle between planet–Earth vector and incoming asymptote vs launch date, Type I 284

10–20(II). Jupiter 1973: Angle between planet–Earth vector and incoming asymptote vs launch date, Type II 285

10–21(I). Jupiter 1973: Angle between planet–Canopus vector and incoming asymptote vs launch date, Type I 286

10–21(II). Jupiter 1973: Angle between planet–Canopus vector and incoming asymptote vs launch date, Type II 287

FOREWORD

This report presents, in graphical form, the results of studies of the characteristics of ballistic interplanetary trajectories to Mercury (launch dates: 1967–1968) and Jupiter (launch dates: 1968–1973). Also included are a description of the physical model, the development of the equations of the model, and a discussion of the properties of the trajectories.

ABSTRACT

16591

The general characteristics of ballistic interplanetary trajectories are discussed, and detailed equations are developed for the analytical model. Extensive data are presented in graphical form for trajectories to Mercury (launch dates: 1967–1968) and Jupiter (launch dates: 1968–1973). These graphs include: (1) curves of *vis viva* geocentric energy vs launch date for minimum-energy trajectories and (2) curves of 19–21 different trajectory parameters vs launch date for various *vis viva* geocentric energies. The trajectories were computed on the IBM 7090 digital computer by numerical evaluation of the analytical model, after which specific parameters of interest were automatically plotted, carefully checked, and analyzed. Procedures are outlined for use of these data by the trajectory engineer in the design and analysis of interplanetary trajectories.

Author

I. INTRODUCTION. ANALYTICAL MODEL FOR INTERPLANETARY TRAJECTORIES

The analytical model used in the generation of Mercury and Jupiter trajectory parameters consists of three distinct phases of two-body motion: (1) an escape hyperbola near the launch planet, (2) elliptical[1] motion under the attraction of the Sun, and (3) terminal hyperbolic motion near the target planet.

A. Heliocentric Motion

Solution of the heliocentric elliptic motion is obtained first under the following assumptions:

(1) The launch and target planets move in orbits about the Sun as given in the national ephemerides. Their velocity components are obtained by using two-body conic formulas, mean orbital elements, and their tabular positions, as listed in the ephemerides.

(2) The launch and target planets are massless. Thus, the only force acting on the probe is that of the Sun.

(3) The position of the probe at launch into the heliocentric orbit is the center of the massless launch planet. Its position at arrival on the heliocentric orbit is the center of the massless target planet.

Thus, for solution of the heliocentric phase of motion, the attractions of the launch and target planets are temporarily disregarded. The primary result to be obtained from the solution of the heliocentric-transfer problem is determination of the hyperbolic-excess velocity vector relative to the launch planet.

1. Determination of Planar Orientation

Since the launch and arrival positions of the probe are assumed to be the centers of the launch and target planets, they can immediately be determined, given the launch and arrival[2] times, by consulting the ephemeris. Further, the orientation of the heliocentric transfer plane can immediately be found. Let $\mathbf{R}_L$ be the Sun–launch-planet position vector at launch time T_L, and let $\mathbf{R}_p$ be the Sun–target-planet position vector at arrival time T_a (Fig. 1–1). Planar orientation is then found from the unit normal $\mathbf{W}$ to the plane, as follows:

$$\mathbf{W} = \frac{\mathbf{R}_L \times \mathbf{R}_p}{R_L R_p \sin \Psi} \qquad (1\text{–}1)$$

where the angle Ψ is defined below. The inclination i to

[1]Hyperbolic heliocentric motion is not considered herein.

[2]Or, for convenience, the launch date and flight time can be specified.

the ecliptic plane[3] can be found by

$$\cos i = \mathbf{W} \cdot \mathbf{K}' \qquad (1\text{–}2)$$

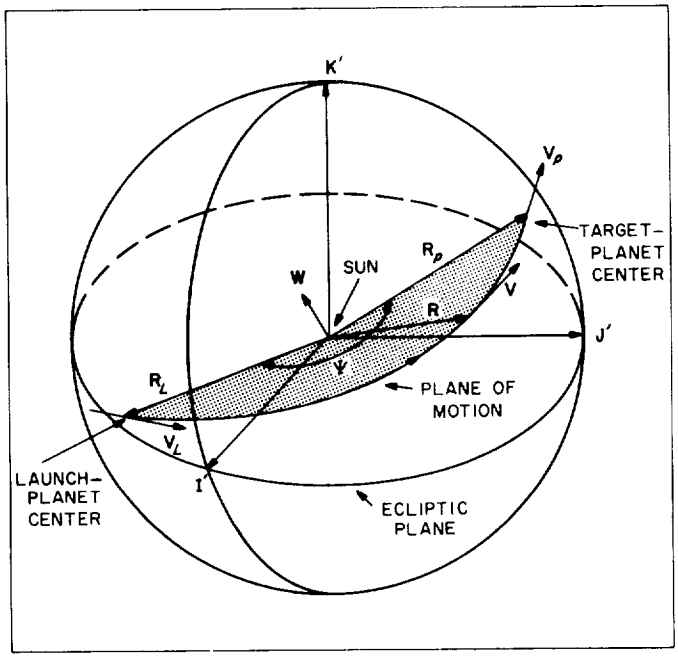

Fig. 1–1. Heliocentric-transfer geometry

where $\mathbf{K}'$ is a unit vector pointing in the direction of the ecliptic north pole.

2. In-Plane Relations

The heliocentric central angle Ψ (Fig. 1–1) is also readily determined by utilizing the positions of the launch and target planets. This angle may be obtained from

$$\cos \Psi = \frac{\mathbf{R}_L \cdot \mathbf{R}_p}{|\mathbf{R}_L|\,|\mathbf{R}_p|} \qquad (1\text{–}3)$$

$$\sin \Psi = \text{sgn}\,[(\mathbf{R}_L \times \mathbf{R}_p) \cdot \mathbf{K}']\,(1 - \cos^2 \Psi)^{1/2} \qquad (1\text{–}4)$$

The velocity vector $\mathbf{V}$ of the spacecraft anywhere along its path may be obtained from

$$\mathbf{V} = \frac{V}{R}[(\mathbf{W} \times \mathbf{R}) \cos \Gamma + \mathbf{R} \sin \Gamma] \qquad (1\text{–}5)$$

Here, $\mathbf{R}$ is the heliocentric position vector, $R = |\mathbf{R}|$, and V is the heliocentric speed, obtained from

$$V = \sqrt{(GM_S)\left(\frac{2}{R} - \frac{1}{a}\right)} \qquad (1\text{–}6)$$

and the path angle Γ is found from

$$\sin \Gamma = \left[\sqrt{\frac{R}{(1 - e^2)\,(2a - R)}}\right] e \sin v \qquad (1\text{–}7)$$

In Eqs. 1–6 and 1–7, GM_S is the universal gravitational constant times the mass of the Sun ($=2.959122083 \times 10^{-4}$ au^3/day^2); a and e are the semimajor axis and eccentricity of the transfer ellipse, respectively; and v is the true anomaly of the probe, given by

$$\cos v = \frac{a(1 - e^2) - R}{eR} \qquad (1\text{–}8)$$

Now, there are two unknowns in Eqs. 1–5 to 1–8 which prevent their immediate evaluation: the semimajor axis a and the eccentricity e. The determination of these quantities is the main problem. Battin (Ref. 1) has shown that the eccentricity is actually a function of the semimajor axis. Thus, it is first necessary to determine a. The semimajor axis is related to the time of flight T_F by Lambert's Theorem, which states: *The transfer time between any two points on an ellipse is a function of the sum of the distances of each point from the focus, the distance between the points, and the semimajor axis of the ellipse.* Functionally, the theorem is stated as

$$T_F = T_F\,(R_L + R_p, C, a) \qquad (1\text{–}9)$$

where the distance C between the launch planet at launch time and the target planet at arrival time, as shown in Fig. 1–2, is obtained from

$$C = |\mathbf{R}_p - \mathbf{R}_L| \qquad (1\text{–}10)$$

Since the time of flight T_F and the launch and arrival positions R_L and R_p are known, only the semimajor axis remains to be found by iterative solution of Eq. 1–9. After the semimajor axis a is obtained, the heliocentric velocities of the probe at launch and arrival times $\mathbf{V}_L$

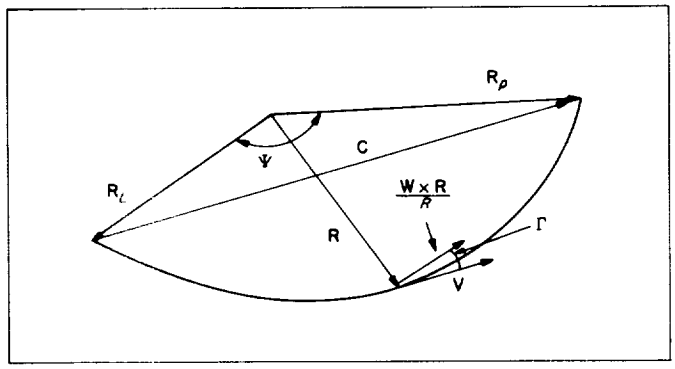

Fig. 1–2. In-plane–transfer geometry

[3]In this Report, the interest is only in transfers which have the same rotational motion about the Sun as do the planets: thus, $0 \leq i \leq \pi/2$.

and $\mathbf{V}_p$ may be evaluated from Eq. 1–5 under the conditions $R = R_L$ and $R = R_p$. The path angles Γ_L, Γ_p and true anomalies v_L, v_p at launch and arrival times[4] may also be evaluated from Eqs. 1–7 and 1–8 under the same conditions.

Finally, the desired end result, the hyperbolic-excess velocity $\mathbf{V}_{hL}$ relative to the launch planet, may be found (Fig. 1–3) by

$$\mathbf{V}_{hL} = \mathbf{V}_L - \mathbf{V}_1 \qquad (1\text{–}11)$$

where $\mathbf{V}_1$ is the velocity of the launch planet at launch time.

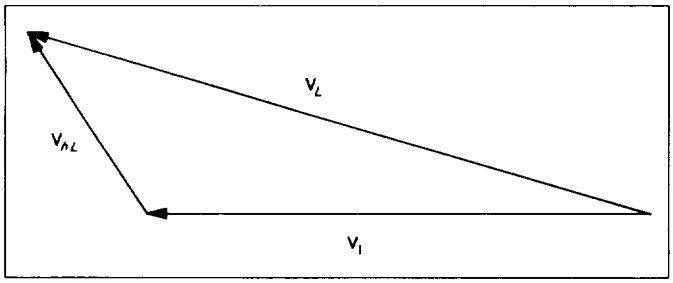

Fig. 1–3. Determination of hyperbolic-excess velocity vector

B. Launch-Planet Escape Hyperbola

The key result from the solution of heliocentric transfer is the hyperbolic-excess velocity vector $\mathbf{V}_{hL}$ at launch. The reason for the importance of this vector is that it tells the direction in which the probe must be traveling relative to the launch planet when on the point of leaving the planet's gravitational influence. There are an infinite number of escape trajectories (all hyperbolas) which can have the same hyperbolic-excess velocity vector. However, only a portion of these are practical for use when related to existing launch sites and boost-vehicle constraints. For example, it would be ridiculously costly in payload—and impractical—to shoot a vehicle straight up. Criteria for selection of a family of feasible escape trajectories are given below.

1. Assumptions

The solution of the escape phase of motion is obtained under the following assumptions: (1) The probe is acted on only by the gravitational force of the launch planet, and (2) the oblateness effects of the launch planet are neglected.

[4]The details of quadrant choice for these angles are found in Ref. 3.

The direction of the asymptote of the escape hyperbola is found by normalizing the hyperbolic-excess vector $\mathbf{V}_{hL}$. The injection energy C_3 of the escape hyperbola[5] is found by squaring the hyperbolic-excess speed, or

$$C_3 = V_{hL}^2 \qquad (1\text{–}12)$$

Thus, in contrast to the heliocentric problem, the launch planet is now "massy," whereas the influence of the Sun is neglected. However, the hyperbolic-excess velocity vectors found by solving the heliocentric problem are used as a starting point to solve the escape problem.

2. Size and Shape of Escape Hyperbola

As previously stated, only some of the infinite number of escape trajectories are practical. Two of the practical aspects of a set of trajectories are the sizes and shapes of the hyperbolas.

Size is basically determined by the energy C_3, which, in turn, is a function of boost-vehicle capability. For boost vehicles in use at this writing (or shortly to be available), values of energy less than or equal to 25 km^2/sec^2 are considered reasonable. The larger the value of energy that the booster is required to deliver, the smaller the payload and launch period over which the vehicle may be fired.

The shape of the hyperbola is determined by its eccentricity, which is a function of both the energy and the perifocal distance, according to

$$e = 1 + \frac{R_p C_3}{GM} \qquad (1\text{–}13)$$

where R_p is the perifocal distance and GM is the universal gravitational constant times the mass of the launch planet. From Eq. 1–13, it can be seen that, for a fixed perifocal distance, the eccentricity increases linearly with the energy. The value of perifocal distance is not arbitrary, but depends strongly on the boost-vehicle trajectory. It has been shown (Ref. 2) that, in the great majority of cases, it is necessary and desirable to use a circular parking orbit as part of the preinjection phase of the escape trajectory. It is, further, an interesting fact that the altitude of the parking orbit determines the perifocal distance. If h is the parking-orbit altitude and R_0 is the launch planet's radius, then, to an extremely close degree of approximation,

$$R_p = R_0 + h \qquad (1\text{–}14)$$

[5]C_3 is actually twice the total energy per unit mass; i.e., the *vis viva* integral.

or the perifocal distance is equal to the launch-planet-centered radius of the parking orbit. In Ref. 2, it also has been shown that the lowest possible parking orbit (80–100 nm) allows greatest payload capability. Thus, using 100 nm for the parking-orbit altitude, a practical value of perifocal distance is 6560 km. The perifocal distance will vary only slightly about this value for other parking-orbit altitudes, or even for direct-ascent-type preinjection trajectories. Therefore, *both* the size and shape are essentially determined by the energy alone, which is found from Eq. 1-12.

Given the size and shape of the escape hyperbola, its planar orientation must be determined. This can be done by considering two vectors: (1) the direction of the hyperbolic-excess vector, denoted by a unit vector **S**, and (2) a unit vector $\mathbf{R}_L^1$ directed from the center of the launch planet to the launch site. The vehicle's flight plane will essentially be determined by these two vectors, as shown in Fig. 1-4. A unit normal **W** to the launch-planet-centered flight plane is determined by

$$\mathbf{W} = \frac{\mathbf{R}_L^1 \times \mathbf{S}}{|\mathbf{R}_L^1 \times \mathbf{S}|} \qquad (1\text{–}15)$$

with the constraint that the Z component of **W** is always positive.

Since $\mathbf{R}_L^1$ is a function of time, according to the rotation rate of the launch planet, the planar orientation must continually change. In effect, this says that the launch azimuth is a continuous function of launch time.

A detailed description of the geometrical aspects of the launch-planet ascent trajectory is not given here, but may be found in Ref. 2.

C. Calculation of Differential Corrections

The calculation of differential corrections for interplanetary trajectories may be accomplished in several ways and depends on the choice of independent and dependent variables. In this Report, a numerical differencing scheme is used. Basically, the independent variables—the injection energy C_3, declination Φ_S, and right ascension Θ_S of the outgoing asymptote **S** of the escape hyperbola—are varied, one at a time, to produce variations in the dependent variables—the components of the impact parameter **B** and the time-of-flight T_F.

The impact parameter **B** is defined as a vector originating at the center of the target planet and directed perpendicular to the incoming asymptote of the target-centered approach hyperbola (Fig. 1-5). The impact parameter **B** is resolved into two components which lie in a plane normal to the incoming asymptote **S**. The orientations of the reference axes in this plane are arbitrary, but one is usually selected to lie in a fixed plane. Thus, define a unit vector **T**, lying in the *ecliptic* plane, according to

$$\mathbf{T} = \frac{\mathbf{S} \times \mathbf{K}'}{|\mathbf{S} \times \mathbf{K}'|} \qquad (1\text{–}16)$$

where **K′** is a unit vector normal to the ecliptic plane. The remaining axis is then given by a unit vector **R**, defined by

$$\mathbf{R} = \mathbf{S} \times \mathbf{T} \qquad (1\text{–}17)$$

Figure 1-6 illustrates the orientation of the **R**, **S**, **T** target coordinates.

The impact parameter **B** lies in the **R–T** plane and has miss components $\mathbf{B} \cdot \mathbf{T}$ and $\mathbf{B} \cdot \mathbf{R}$. The condition $\mathbf{B} \cdot \mathbf{T} = \mathbf{B} \cdot \mathbf{R} = 0$ denotes vertical impact on the target. Thus, $\mathbf{B} \cdot \mathbf{T}$, $\mathbf{B} \cdot \mathbf{R}$, and T_F are the three target dependent variables. If Q_i represents a set of generalized independent variables, such as injection position and velocity or other convenient variables, then the partial derivatives $\partial \mathbf{B} \cdot \mathbf{T}/\partial Q_i$, $\partial \mathbf{B} \cdot \mathbf{R}/\partial Q_i$, $\partial T_F/\partial Q_i$ are first-order differential corrections or error coefficients relating miss at the target and flight-time errors to the independent variables.

A convenient set of independent variables for interplanetary trajectories is the *vis viva* injection energy C_3, the declination Φ_S, and the right ascension Θ_S of the asymptote of the escape hyperbola. These variables essentially describe the launch hyperbolic-excess velocity vector $\mathbf{V}_{hL}$.

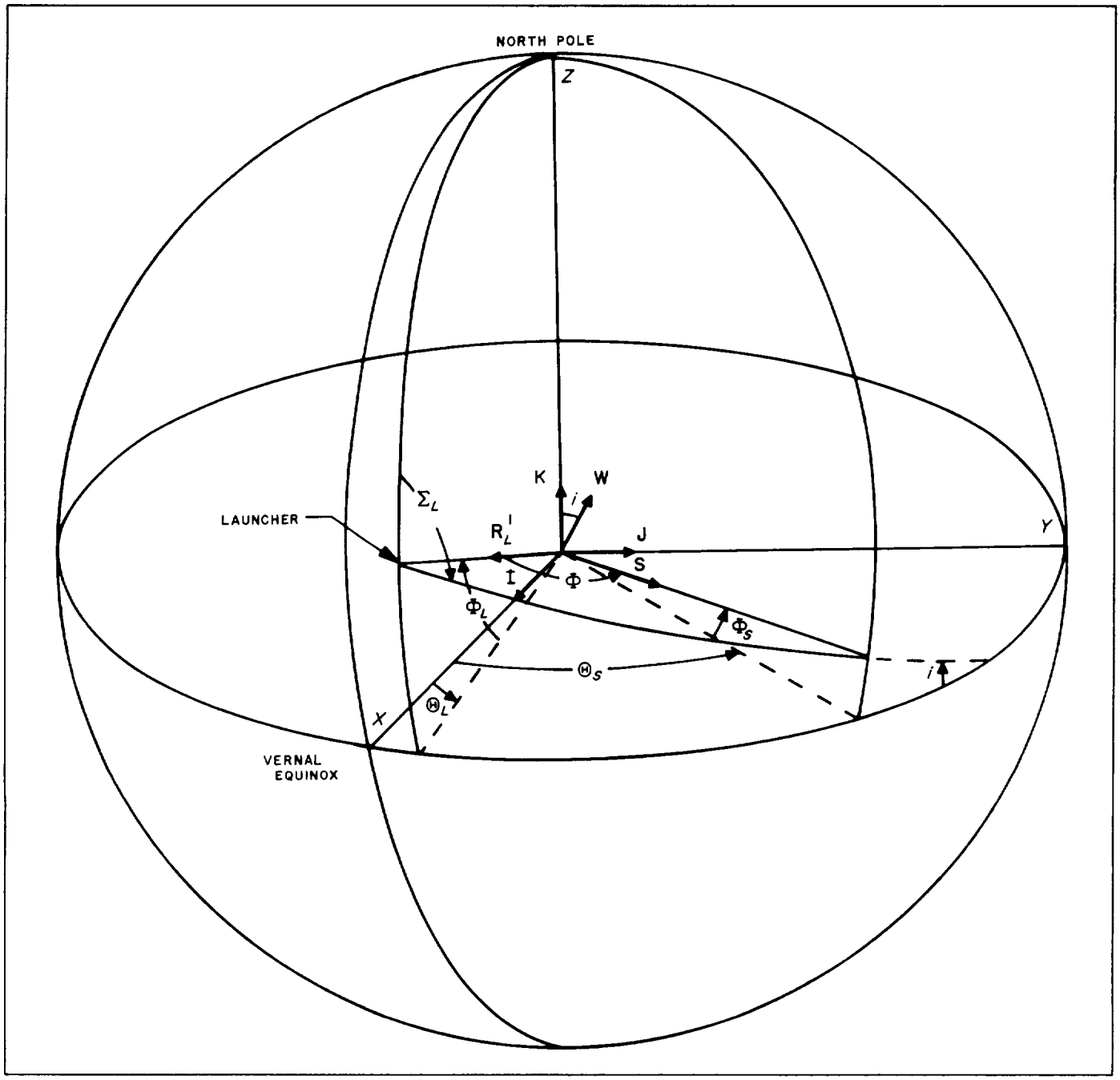

Fig. 1–4. Vehicle flight plane

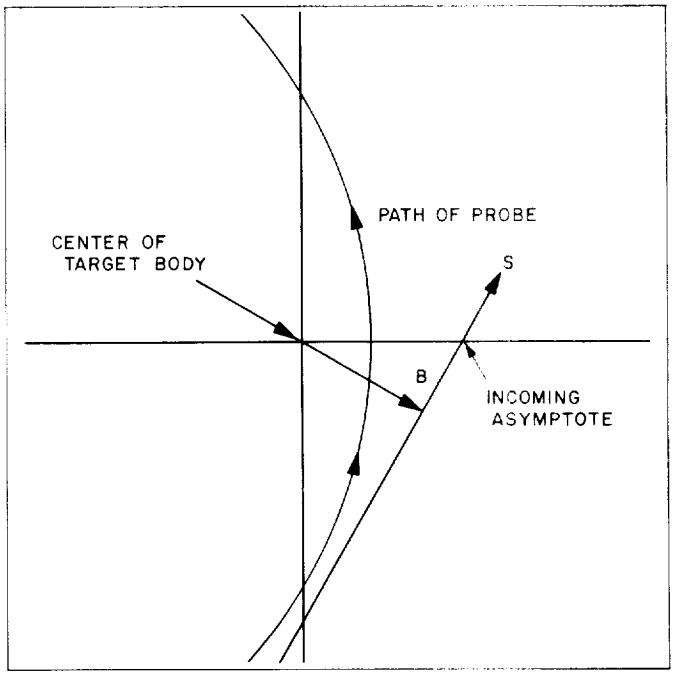

Fig. 1–5. Impact parameter

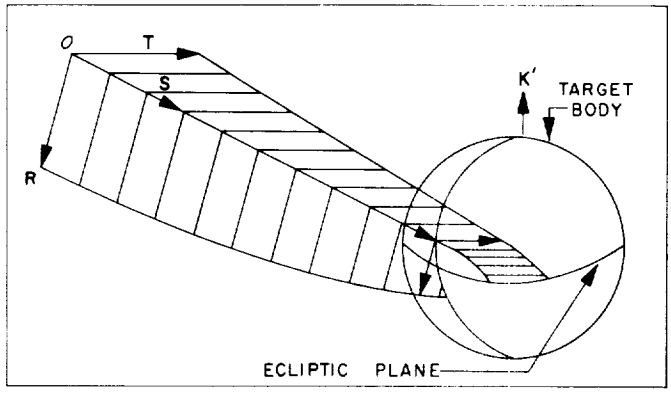

Fig. 1–6. The R, S, T target coordinate system

II. DETAILED EQUATIONS FOR TRAJECTORY COMPUTATIONS

In Section I, a summary was given of the physical model used to generate the parameters of Mercury and Jupiter trajectories. The purpose of this Section is to present, in full detail, the equations of the Jet Propulsion Laboratory's Heliocentric Conic Trajectory Program[6], including the equations of Lambert's Theorem[7], which were developed for this investigation. The equations were coded for the Laboratory's IBM 7090 digital computer.

This program has proved very useful over the past few years in studying and analyzing interplanetary trajectories. Some of the results of these studies are presented graphically in Sections III to X of this Report. The program has been devised for calculation of trajectories from any planet in the solar system to any other planet. In addition, by adding the appropriate orbital elements, trajectories to comets or to any body of known motion may be computed.

The Heliocentric Conic Trajectory Program is divided into four major sections:

(1) The heliocentric phase, in which basic computations are made for a unique conic trajectory, of given flight time, that passes through the center of two massless planets rotating around the Sun, as defined in the national ephemerides.

(2) The near-launch-planet phase, in which a launch-planet–centered conic is fitted to the heliocentric conic for a given launch azimuth and launch site.

(3) The near-target-planet phase, in which the parameters of the planetocentric conic at the target are calculated.

(4) Computation of partial derivatives which relate miss and time-of-flight errors at the target to variations in the hyperbolic-excess velocity vector of the escape hyperbola near the launch planet.

[6]Coded by W. J. Scholey and R. Y. Roth of the JPL Computer Applications and Data Systems Section.

[7]Developed by E. Dobies, formerly of JPL, and coded by C. A. Seafeldt, of the JPL Computer Applications and Data Systems Section.

A. Heliocentric Phase

1. Determination of Position at Launch and Arrival

For any given time, the positions of the planets can be obtained from the ephemerides, referenced to a given coordinate system and epoch. For the present purposes, the heliocentric ephemerides of the planets, referenced to the mean equator and equinox of 1950.0, were selected.

From these ephemerides, one may find the position vector $\mathbf{R}'_L$ of the launch planet at launch time T_L, the position vector $\mathbf{R}'_p$ of the target planet at arrival time T_a, and the position vector $\mathbf{R}'_{L,1}$ of the launch planet at arrival time. For practical and computational purposes, it is convenient to transform these coordinates to a heliocentric ecliptic, mean-of-*launch*-date system. Thus, two rotation matrices must be computed. First, a rotation is made from heliocentric equatorial coordinates, mean of 1950.0, to heliocentric equatorial, mean of *launch* date. This is accomplished by means of the matrix A, whose elements are given below (as obtained from Ref. 3):

$$\left.\begin{aligned}
a_{11} &= 1 - 0.00029697T^2 - 0.00000013T^3 \\
a_{12} &= -a_{21} = -0.02234988T - 0.00000676T^2 + 0.00000221T^3 \\
a_{13} &= -a_{31} = -0.00971711T + 0.00000207T^2 + 0.00000096T^3 \\
a_{22} &= 1 - 0.00024976T^2 - 0.00000015T^3 \\
a_{23} &= a_{32} = -0.00010859T^2 - 0.00000003T^3 \\
a_{33} &= 1 - 0.00004721T^2 + 0.00000002T^3
\end{aligned}\right\} \qquad (2\text{–}1)$$

where T is the number of Julian Centuries of 36,525 days past the epoch 1950.0.

The second rotation transforms the coordinates from heliocentric equatorial, mean of launch date, to heliocentric ecliptic, mean of launch date. This is accomplished by means of the matrix E:

$$E = \begin{bmatrix} 1 & 0 & 0 \\ 0 & \cos\epsilon & \sin\epsilon \\ 0 & -\sin\epsilon & \cos\epsilon \end{bmatrix} \qquad (2\text{–}2)$$

where ϵ is the mean obliquity of the ecliptic on the launch date and sin ϵ and cos ϵ are approximated by the following equations from Ref. 4:

$$\left.\begin{aligned}\sin\epsilon &= \sin\epsilon_0 + P(T)\cos\epsilon_0 - \frac{1}{2}P^2(T)\sin\epsilon_0\\ \cos\epsilon &= \cos\epsilon_0 - P(T)\sin\epsilon_0 - \frac{1}{2}P^2(T)\cos\epsilon_0\end{aligned}\right\} \quad (2\text{–}3)$$

where

$$P(T) = -0.0002271111T - 0.0000000286T^2 + 0.00000000878T^3 \quad (2\text{–}4)$$

and ϵ_0 is the mean obliquity of the ecliptic for 1950.0.

Now, in general, the components of the position vectors $\mathbf{R}_L$, $\mathbf{R}_{LA}$, and $\mathbf{R}_p$ are found in mean-equinox, ecliptic-of-launch-date coordinates by

$$\left.\begin{matrix}\mathbf{R}_L\\ \mathbf{R}_{LA}\\ \mathbf{R}_p\end{matrix}\right\} = EA \left\{\begin{matrix}\mathbf{R}'_L\\ \mathbf{R}'_{LA}\\ \mathbf{R}'_p\end{matrix}\right. \quad (2\text{–}5)$$

The unit vectors $\mathbf{R}_L^1$, $\mathbf{R}_p^1$ may then be found:

$$\mathbf{R}_L^1 = \frac{\mathbf{R}_L}{R_L} \qquad \mathbf{R}_p^1 = \frac{\mathbf{R}_p}{R_p} \quad (2\text{–}6)$$

where

$$R_L = |\mathbf{R}_L| \text{ and } R_p = |\mathbf{R}_p| \quad (2\text{–}7)$$

The heliocentric central angle Ψ, i. e., the angle between $\mathbf{R}_L$ and $\mathbf{R}_p$, is computed from

$$\left.\begin{aligned}\cos\Psi &= \frac{\mathbf{R}_L\cdot\mathbf{R}_p}{R_L R_p}\\ \sin\Psi &= \text{sgn}\,[(\mathbf{R}_L\times\mathbf{R}_p)\cdot\mathbf{K}'](1-\cos^2\Psi)^{1/2}\end{aligned}\right\} \quad (2\text{–}8)$$

where $\mathbf{K}'$ is the unit vector normal to the ecliptic plane in the direction of the ecliptic north pole.

The unit vector $\mathbf{W}$ normal to the probe's orbit plane, is found from the vector equation

$$\mathbf{W} = \frac{\mathbf{R}_L\times\mathbf{R}_p}{R_L R_p \sin\Psi} \quad (2\text{–}9)$$

Subsequently, the inclination of the orbit to the ecliptic plane i may be found from

$$\cos i = \mathbf{W}\cdot\mathbf{K}' \quad (2\text{–}10)$$

where $0 \leq i \leq \pi/2$ are the only cases of interest to this program.

Essentially, calculation of the $\mathbf{W}$ vector determines the planar orientation of the transfer conic.

2. Application of Lambert's Theorem

As shown in Section I, the semimajor axis a may be found, given the flight time T_F, $\mathbf{R}_L$, and $\mathbf{R}_p$. One uses Lambert's Theorem, which states:

> *The transfer time between any two points on an ellipse is a function of the sum of the distances of each point from the focus, the distance between the points, and the semimajor axis of the ellipse.*

Or, functionally,

$$T_F = T_F(R_L + R_p, C, a) \quad (2\text{–}11)$$

where C is the chord distance from $\mathbf{R}_L$ to $\mathbf{R}_p$, or

$$C = |\mathbf{R}_p - \mathbf{R}_L| \quad (2\text{–}12)$$

Now, since T_F, $\mathbf{R}_L$, $\mathbf{R}_p$, and C are known, Lambert's Theorem can be used to solve for a by an iterative process described below.

First, the transfer time T_m of the minimum-heliocentric-energy trajectory is computed from Eqs. 2–13 to 2–22.

The minimum semimajor axis a_m for an ellipse can be found from

$$a_m = (R_L + R_p + C)/4 \quad (2\text{–}13)$$

and e_m, the eccentricity of the orbit with a minimum semimajor axis, is expressed by

$$e_m = \sqrt{1 - \frac{p_m}{a_m}} \quad (2\text{–}14)$$

where p_m is the semilatus rectum obtained by

$$p_m = \frac{2(2a_m - R_L)(2a_m - R_p)}{C} \quad (2\text{–}15)$$

The true anomaly at launch v_{Lm} is found from Eqs. 2–16 and 2–17. First, compute the angle ϕ:

$$\cos\phi = \frac{R_L - a_m(1-e_m^2)}{e_m R_L} \qquad 0 \leq \phi \leq \pi \quad (2\text{–}16)$$

where ϕ is an angle from the aphelion to R_L.

It can then be shown from the geometry of the minimum-energy ellipse (Fig. 2–1) that

$$\left.\begin{aligned}v_{Lm} &= \pi - \phi \quad 0 < \Psi < \pi\\ v_{Lm} &= \pi + \phi \quad \pi < \Psi < 2\pi\end{aligned}\right\} \quad (2\text{–}17)$$

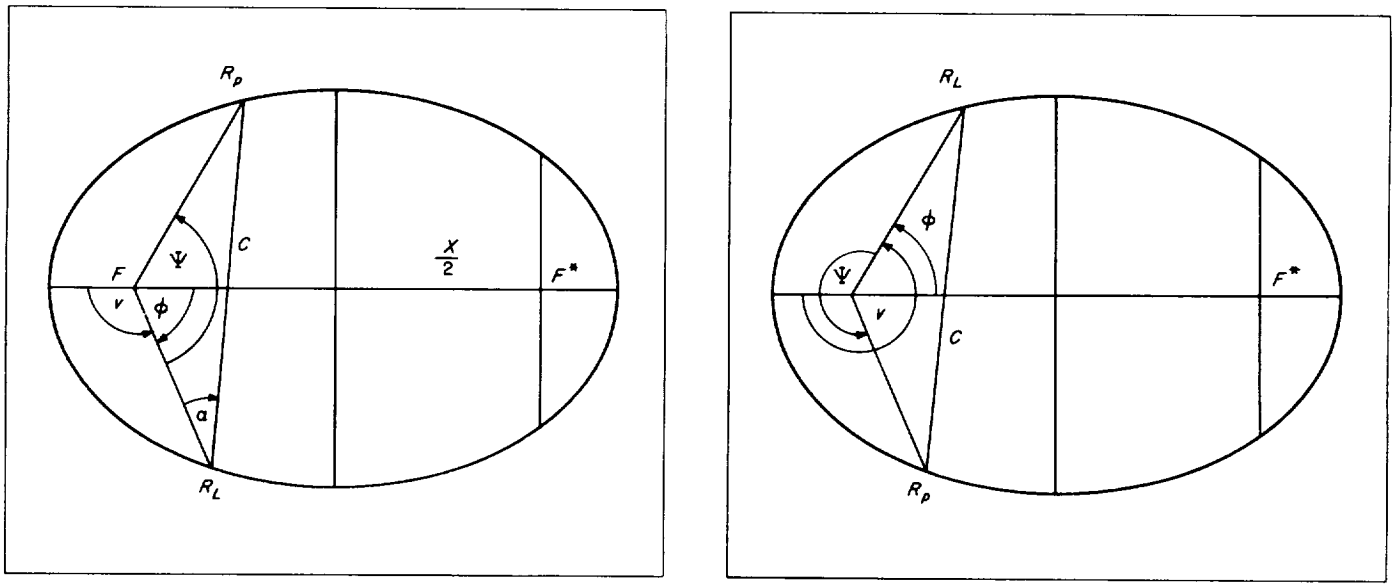

(a) Central angle less than 180 deg

(b) Central angle greater than 180 deg

Fig. 2–1. Geometrical configuration of heliocentric conic

The true anomaly at arrival on the minimum-energy ellipse υ_{pm} can be found from

$$\upsilon_{pm} = \upsilon_{Lm} + \Psi \tag{2–18}$$

Now, the mean anomaly M_{Lm} at launch in the ellipse can be found from

$$M_{Lm} = E_{Lm} - e_m \sin E_{Lm} \tag{2–19}$$

where E_{Lm}, the eccentric anomaly, is given by the equations

$$\left.\begin{aligned} \cos E_{Lm} &= \frac{e_m + \cos \upsilon_{Lm}}{1 + e_m \cos \upsilon_{Lm}} \\ \text{and} \\ \sin E_{Lm} &= \frac{\sqrt{1 - e_m^2} \sin \upsilon_{Lm}}{1 + e_m \cos \upsilon_{Lm}} \end{aligned}\right\} \quad 0 \leq E_{Lm} \leq 2\pi \tag{2–20}$$

The mean anomaly at arrival M_{pm} can be obtained in a similar manner. Then, the mean-anomaly difference is

$$\Delta M_m = M_{pm} - M_{Lm} \tag{2–21}$$

By use of this difference, T_m, the time for a minimum-energy trajectory from launch to target, can be found from the equation

$$T_m = \frac{a_m^{3/2} \Delta M_m}{2\pi} \tag{2–22}$$

where the units are years and astronomical units (au).

Next, the semimajor axis a, corresponding to the given flight time T_F, is obtained. At this point, there can be two types of trajectories, $T_F > T_m$ or $T_F < T_m$.

For $T_F > T_M$, let $a_{i+1} = (i + 1)a_m$, until $T_F(a_{i+1}) > T_F$

For $T_F < T_M$, let $a_{i+1} = (i + 1)a_m$, until $T_F(a_{i+1}) < T_F$

where $i = 1, 2, \ldots n$, and $a_1 = a_m$. Note that $T_F(a_i)$ is the time of flight corresponding to a_i, and is calculated from Eqs. 2–24 to 2–29 and 2–19 to 2–22; here, however, the subscript i is used in place of m. When $T(a_i) < T_F < T(a_{i+1})$, then $a_i < a < a_{i+1}$, and a slope-intercept method is used to obtain an approximation on a. Using a_{i+1} for a first estimate on a_j, and using

$$a_j = a_{j-1} - \Delta a \left[\frac{T_F - T(a_{j-1})}{T(a_i) - T_F}\right]$$

$$\Delta a = (a_{j-1} - a_i) \tag{2–23}$$

subscript $j = 1, 2, \ldots n$

for subsequent estimates, the value of a_j is used for a to calculate α and β.

$$\left.\begin{aligned} \beta &= \cos^{-1}\left[\frac{C^2 + R_L^2 - R_p^2 - 4a(R_p - R_L)}{2C(2a - R_L)}\right] \\ \alpha &= \cos^{-1}\left[\frac{R_L - R_p \cos \Psi}{C}\right] \end{aligned}\right\} \begin{aligned} 0 < \beta < \pi \\ 0 < \alpha < \pi \end{aligned} \tag{2–24}$$

Now, the linear eccentricity X can be found from

$$X^2 = 4a^2 - 2R_L(2a - R_L)\left[1 + \cos(|\alpha - \beta|)\right] \quad (2\text{–}25a)$$

$$X^2 = 4a^2 - 2R_L(2a - R_L)\left[1 + \cos(|\alpha + \beta|)\right] \quad (2\text{–}25b)$$

Equation 2–25a is used if $T_F > T_m$, and $\Psi > \pi$; or if $T_F < T_m$, and $\Psi < \pi$. However, Eq. 2–25b applies if $T_F > T_m$, and $\Psi < \pi$; or if $T_F < T_m$, and $\Psi > \pi$.

Then, the true anomaly at launch is found from

$v_L =$

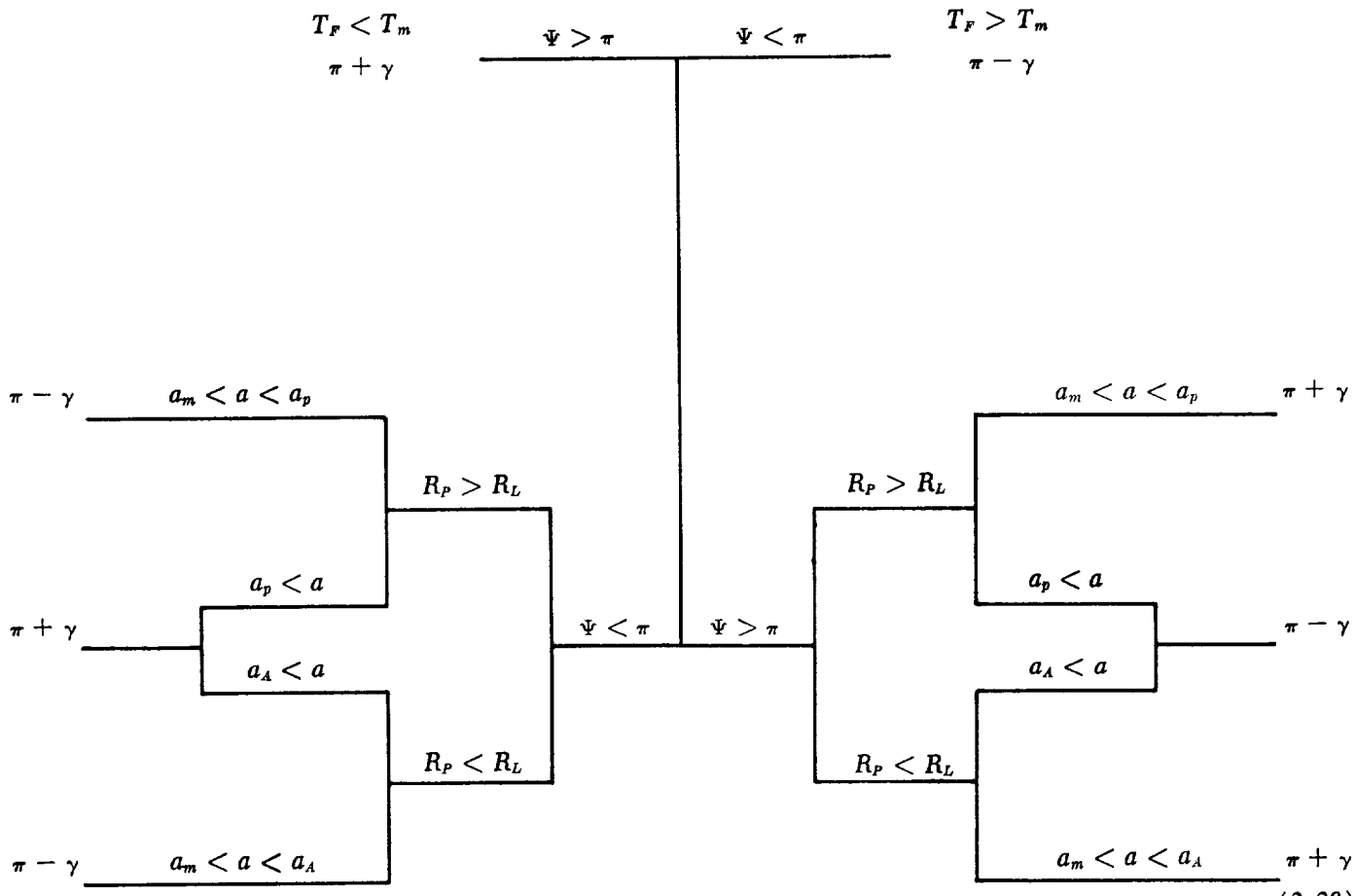

(2–26)

and γ is found from

$$\cos\gamma = \frac{X^2 + 4a\,R_L - 4a^2}{2\,X\,R_L} \quad (2\text{–}27)$$

$$\left.\begin{aligned} a_A &= \frac{R_p}{1 + \dfrac{R_p - R_L}{R_p - R_L\cos\Psi}} \\ a_p &= \frac{R_L}{1 + \dfrac{R_L - R_p}{R_L - R_p\cos\Psi}} \end{aligned}\right\} \quad R_p > R_L \quad (2\text{–}28)$$

Also, a_A and a_p, the semimajor-axis limits, are found from

If $R_L > R_p$, a_A and a_p are interchanged. The true anomaly at arrival v_p is found from

$$v_p = v_L + \Psi \qquad 0 < v_p < 2\pi$$

and the eccentricity e is found from

$$e = \frac{X}{2a} \tag{2-29}$$

Then, $T(a_j)$ is recalculated using Eqs. 2–19 to 2–22.

When $|T_F - T(a_j)| < \epsilon$, a predetermined convergence criterion, the conic is considered to be the one desired, and $a(= a_n)$, e, v_L, v_p are the parameters of the heliocentric transfer orbit.

At this point, the transfer orbit is completely determined. Other key quantities are calculated as shown in the following paragraphs.

3. Calculation of Velocity Vectors for Probe and Planet

The heliocentric velocity of the probe $\mathbf{V}$ (with the subscript L for launch time or p for arrival time), can be calculated by using the equation

$$\mathbf{V} = \frac{V}{R}[(\mathbf{W} \times \mathbf{R}) \cos \Gamma + \mathbf{R} \sin \Gamma] \tag{2-30}$$

where

$$V = \sqrt{(GM_S)\left(\frac{2}{R} - \frac{1}{a}\right)} \tag{2-31}$$

The path angle Γ can be found by the expression

$$\sin \Gamma = \left[\sqrt{\frac{R}{(1 - e^2)(2a - R)}}\right] e \sin v \tag{2-32}$$

where

$$0 \leq \Gamma \leq \frac{\pi}{2} \quad \text{if} \quad 0 \leq v \leq \pi$$

$$-\frac{\pi}{2} \leq \Gamma \leq 0 \quad \text{if} \quad \pi \leq v \leq 2\pi$$

The velocity vectors $\mathbf{V}_1$ and $\mathbf{V}_2$ of the launch and target planets, respectively, are found in a similar manner. In this calculation, however, the semimajor axis a, the path angle Γ, and the eccentricity of the orbit e all refer to the respective planet's orbit around the Sun. The true anomaly v of the planet in its orbit at any time can be found from Eqs. 2–33 to 2–36.

The unit vector $\mathbf{W}$ normal to the planet's orbit plane is given by

$$\mathbf{W} = \sin \Omega \sin i, \cos \Omega \sin i, \cos i \tag{2-33}$$

where i is the inclination of the planet's orbital plane to the ecliptic and Ω is the longitude of the planet's ascending node.

The unit vector $\mathbf{P}$ directed toward the perihelion is expressed by

$$\left.\begin{aligned} P_X &= \cos \omega \cos \Omega - \sin \omega \sin \Omega \cos i \\ P_Y &= \cos \omega \sin \Omega + \sin \omega \cos \Omega \cos i \\ P_Z &= \sin \omega \sin i \end{aligned}\right\} \tag{2-34}$$

where ω is the argument of perihelion of the planet.

The unit vector $\mathbf{Q}$ right-handed to $\mathbf{P}$ and $\mathbf{W}$, is obtained from

$$\mathbf{Q} = \mathbf{W} \times \mathbf{P}$$

Then

$$\left.\begin{aligned} \cos v &= \mathbf{R}^1 \cdot \mathbf{P} \\ \sin v &= \mathbf{R}^1 \cdot \mathbf{Q} \end{aligned}\right\} \tag{2-35}$$

where, again, $\mathbf{R}^1$ is the Sun–planet unit vector.

Numerical values for the planet elements a, e, i, Ω, and ω (from Ref. 5) are presented in Table 2–1.

Finally, the hyperbolic-excess velocity vector at launch or arrival $\mathbf{V}_h$ can be found from

$$\mathbf{V}_h = \mathbf{V} - \mathbf{V}_{planet} \tag{2-36}$$

4. Calculation of Various Trajectory Parameters

To assist the trajectory engineer in selecting and designing interplanetary trajectories, various key trajectory parameters are computed. The formulas for these are given below.

The angle γ between the hyperbolic-excess velocity vector and the planet's orbital plane can be found at launch and arrival by

$$\sin \gamma = \frac{\mathbf{W} \cdot \mathbf{V}_h}{V_h} \qquad -\frac{\pi}{2} \leq \gamma \leq \frac{\pi}{2} \tag{2-37}$$

The right ascension Θ and the declination Φ of the asymptote (launch or arrival) can be found by use of the expressions

$$\sin \Phi = S_Z \qquad -\frac{\pi}{2} \leq \Phi \leq \frac{\pi}{2} \tag{2-38}$$

Table 2–1. Mean planet elements

Planet	Semimajor axis a, au	Eccentricity e	Inclination to ecliptic i, deg	Longitude of ascending node Ω, deg	Argument of perihelion ω, deg
Mercury	0.387098	0.205625 + 0.000020T[a]	7.003819 + 0.00175T	47.737778 + 1.18500T	28.937778 + 0.36944T
Venus	0.723331	0.006793 − 0.000050T	3.394264 + 0.00125T	76.236389 + 0.90556T	54.619305 + 0.50139T
Earth	1.000000	0.016729 − 0.000042T	0	0	102.078056 + 1.71667T
Mars	1.523679	0.093357 + 0.000094T	1.849986 − 0.000639T	49.173611 + 0.77389T	285.965000 + 1.06667T
Jupiter	5.2027	0.048417 + 0.000164T	1.305875 − 0.005694T	99.948611 + 1.01056T	273.577222 + 0.59944T
Saturn	9.546	0.055720 − 0.000345T	2.490583 − 0.003889T	113.226806 + 0.87306T	338.850694 + 1.08528T
Uranus	19.20	0.0471 + 0.0002T	0.772792 + 0.000639T	73.726528 + 0.49861T	96.129028 + 1.11250T
Neptune	30.09	0.00872 + 0.00004T	1.774486 − 0.00953T	131.230833 + 1.09889T	272.935934 − 0.43222T
Pluto	39.5	0.247	17.140000 − 0.00556T	109.633750 + 1.35806T	113.860694 + 0.03083T

[a]Measured in Julian Centuries from 1950.0

and

$$\left.\begin{aligned}\cos\Theta &= \frac{S_X}{\sqrt{S_X^2 + S_Y^2}}\\ \sin\Theta &= \frac{S_Y}{\sqrt{S_X^2 + S_Y^2}}\end{aligned}\right\} \quad 0 \le \Theta \le 2\pi \qquad (2\text{–}39)$$

where

$$\mathbf{S} = \frac{\mathbf{V}_h}{V_h} E^T = (S_X, S_Y, S_Z) \qquad (2\text{–}40)$$

Here, E is the rotation matrix given by Eq. 2–2; $\mathbf{S}$ is a unit vector in the direction of the outgoing asymptote when $\mathbf{V}_h$ is calculated at launch, and in the direction of the incoming asymptote when $\mathbf{V}_h$ is calculated at the target.

Other quantities which are of interest for the heliocentric phase are given in Eqs. 2–41 to 2–48, below.

The communication distance at arrival R_C is expressed by

$$\left.\begin{aligned}R_C &= |\mathbf{R}_C|\\ \mathbf{R}_C &= \mathbf{R}_p - \mathbf{R}_{LA}\end{aligned}\right\} \qquad (2\text{–}41)$$

The arrival (or departure) angle α is obtained from

$$\cos\alpha = \frac{\mathbf{V}_{planet} \cdot \mathbf{V}_h}{V_{planet}\, V_h} \qquad 0 \le \alpha \le \pi \qquad (2\text{–}42)$$

The angle ζ_L between the launch hyperbolic-excess velocity and the Sun–launch–planet line at launch is defined by

$$\cos\zeta_L = \frac{\mathbf{V}_{hL} \cdot \mathbf{R}_L^1}{V_{hL}} \qquad 0 \le \zeta_L \le \pi \qquad (2\text{–}43)$$

There are six other angles: ζ_p, the Sun–probe–target angle; ζ_E, the Sun–target–Earth angle; ζ_C, the probe-target–Canopus angle; η_S, the supplement of the angle between the projection of the target–Sun vector on the **R**–**T** plane and the **T** direction; η_E, the supplement of the angle between the projection of the target–Earth vector on the **R**–**T** plane and the **T** direction; η_C, the supplement of the angle between the projection of the target–Canopus vector on the **R**–**T** plane and the **T** direction. Here, **T** is a unit vector lying in the ecliptic plane, given by

$$\left.\begin{aligned}\mathbf{T} &= \frac{\mathbf{S}_p \times \mathbf{K}'}{|\mathbf{S}_p \times \mathbf{K}'|}\\ \mathbf{R} &= \mathbf{S}_p \times \mathbf{T}\end{aligned}\right\} \qquad (2\text{–}44)$$

and

$$\left.\begin{aligned}\cos\zeta_p &= -\mathbf{S}_p \cdot \mathbf{R}_p^1\\ \cos\zeta_E &= -\mathbf{S}_p \cdot \mathbf{R}_C^1\\ \cos\zeta_C &= \mathbf{S}_p \cdot \mathbf{C}\end{aligned}\right\} \quad 0 \le \zeta \le \pi \qquad (2\text{–}45)$$

where **C** is a unit vector to the star Canopus, and $\mathbf{R}_C^1$ is obtained by normalizing $\mathbf{R}_C$ from Eq. 2–41.

$$\left.\begin{aligned}
\sin\eta_S &= \frac{\mathbf{R}\cdot\mathbf{R}_p^1}{\sin\zeta_p}\\
\cos\eta_S &= \frac{\mathbf{T}\cdot\mathbf{R}_p^1}{\sin\zeta_p}\\
\sin\eta_E &= \frac{\mathbf{R}\cdot\mathbf{R}_C^1}{\sin\zeta_E}\\
\cos\eta_E &= \frac{\mathbf{T}\cdot\mathbf{R}_C^1}{\sin\zeta_E}\\
\sin\eta_C &= -\frac{\mathbf{R}\cdot\mathbf{C}}{\sin\zeta_C}\\
\cos\eta_C &= -\frac{\mathbf{T}\cdot\mathbf{C}}{\sin\zeta_C}
\end{aligned}\right\} \quad 0 \le \eta \le 2\pi \qquad (2\text{–}46)$$

The angle σ_p between the projection of the incoming asymptote on the target planet's orbital plane and the target-planet–Sun line at arrival time is defined by

$$\left.\begin{aligned}
\cos\sigma_p &= -\mathbf{R}_p^1\cdot\mathbf{S}_{pr}\\
\sin\sigma_p &= -\mathbf{S}_{pr}\cdot(\mathbf{W}_2\times\mathbf{R}_p^1)
\end{aligned}\right\} \quad -\pi \le \sigma_p \le \pi \qquad (2\text{–}47)$$

where $\mathbf{S}_{pr}$, the projection of $\mathbf{S}_p$ on the target planet's orbital plane, can be found by

$$\mathbf{S}_{pr} = \frac{\mathbf{S}_p - \mathbf{W}_2(\mathbf{S}_p\cdot\mathbf{W}_2)}{|\mathbf{S}_p - \mathbf{W}_2(\mathbf{S}_p\cdot\mathbf{W}_2)|} \qquad (2\text{–}48)$$

Here, $\mathbf{W}_2$ is a unit vector normal to the target planet's orbital plane.

B. The Planetocentric-Conic Trajectories

The trajectory near the launch planet is found by application of several conditions:

(1) The injection energy C_3 and the direction **S** of the outgoing asymptote of the escape hyperbola are obtained from the solution of the heliocentric-transfer problem as given in Section II–A above.

(2) The vehicle is launched from a given launch site, specified by its latitude and longitude, into a low-altitude circular parking orbit.

(3) After coasting in the parking orbit for a time t_c, as determined below, the final stage ignites and propels the spacecraft to the final injection energy.

(4) The parking-orbit altitude plus the launch planet's radius is equal to the perifocal distance of the escape hyperbola. This is a good practical approximation, since it is most efficient to inject the spacecraft into the escape hyperbola near the perifocus.

(5) The launch planet is assumed to be spherical in shape.

Given these conditions, the following formulae are used to compute the parameters of the near-launch-planet trajectory.

The eccentricity e of the launch-planet conic can be computed from

$$e = 1 + \frac{R_p C_3}{GM_L} \qquad (2\text{–}49)$$

where R_p is the perifocal distance of the near-launch-planet conic, and C_3 is the *vis viva* energy, defined as

$$C_3 = V_{hL}^2 \qquad (2\text{–}50)$$

and GM_L is the universal gravitational constant times the mass of the launch planet. The radius to injection R is found from

$$R = \frac{p}{1 + e\cos v} \qquad (2\text{–}51)$$

where v is the true anomaly of injection on the launch-planet escape hyperbola, and p is the semilatus rectum given by

$$p = \frac{-GM_L(1 - e^2)}{C_3} \qquad (2\text{–}52)$$

The path angle at injection Γ is found from

$$\cos\Gamma = \frac{\sqrt{p\,GM_L}}{VR} \qquad \begin{aligned} &0 \le \Gamma \le \frac{\pi}{2}, \text{ if } 0 \le v \le \pi\\ &-\frac{\pi}{2} \le \Gamma \le 0, \text{ if } \pi \le v \le 2\pi \end{aligned} \qquad (2\text{–}53)$$

where V, the injection speed, is given by

$$V = \sqrt{C_3 + \frac{2GM_L}{R}} \qquad (2\text{–}54)$$

The vector **W**, perpendicular to the plane of the conic, can be found by the solution of the two vector equations

$$\left.\begin{aligned}
\mathbf{W}\cdot\mathbf{S} &= 0 \quad & W_X S_X + W_Y S_Y + W_Z S_Z &= 0\\
\mathbf{W}\cdot\mathbf{W} &= 1 \quad & W_X^2 + W_Y^2 + W_Z^2 &= 1
\end{aligned}\right\} \qquad (2\text{–}55)$$

where

$$W_X = \frac{-(W_Y S_Y + W_Z S_Z)}{S_X} \qquad (2\text{–}56)$$

and

$$W_Y = \frac{-W_Z S_Y S_Z}{S_X^2 + S_Y^2} \pm \frac{S_X}{S_X^2 + S_Y^2}\sqrt{1 - S_Z^2 - W_Z^2} \qquad (2\text{–}57)$$

It should be recalled that **S** is a unit vector in the direction of the outgoing asymptote of the escape hyperbola. Thus, a condition is set on W_Z:

$$W_Z^2 \leq 1 - S_Z^2 \qquad (2\text{–}58)$$

From the geometry (Fig. 2–2) of the launch azimuth Σ_L and the launch latitude Φ_L, it can be shown that

$$W_Z = \cos \Phi_L \sin \Sigma_L \qquad (2\text{–}59)$$

From Eqs. 2–58 and 2–59, the W_Z^2 restrictions can be calculated as a restriction on Σ_L, since Φ_L and **S** are fixed:

$$\sin^2 \Sigma_L \leq \frac{1 - S_Z^2}{\cos^2 \Phi_L} \qquad (2\text{–}60)$$

A vector **B**, orthogonal to **S** and **W**, is calculated:

$$\mathbf{B} = \mathbf{S} \times \mathbf{W} \qquad (2\text{–}61)$$

Now, let **P** be a unit vector in the direction of the perifocus as shown in Fig. 2–3:

$$\mathbf{P} = \mathbf{S} \cos v_s + \mathbf{B} \sin v_s \qquad (2\text{–}62)$$

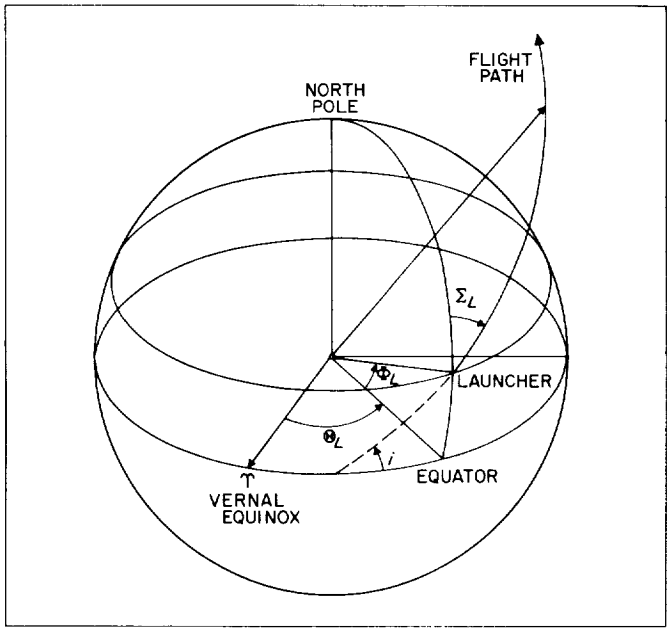

Fig. 2–2. Trajectory-plane–launch-site geometry

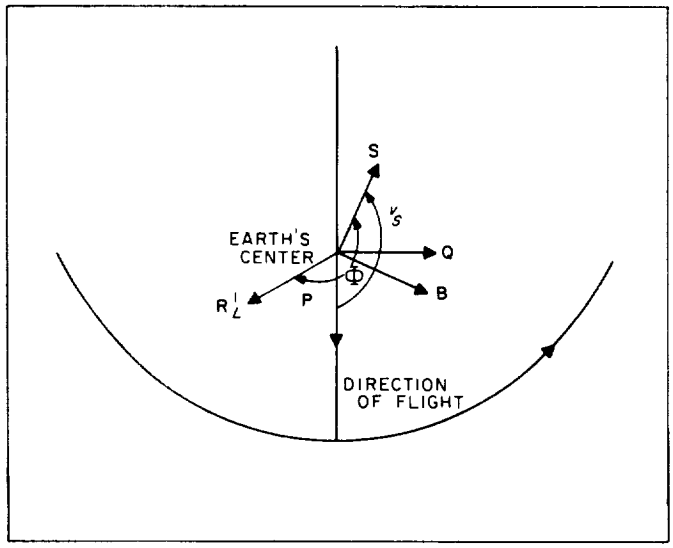

Fig. 2–3. Trajectory-plane geometry

Then **Q** is the unit vector at right angles to **P**:

$$\mathbf{Q} = \mathbf{S} \sin v_s - \mathbf{B} \cos v_s \qquad (2\text{–}63)$$

The true anomaly v_s of the outgoing asymptote **S** is given by

$$\cos v_s = -\frac{1}{e} \qquad 0 \leq v_s \leq \pi \qquad (2\text{–}64)$$

The right ascension Θ_L of the launcher can be found from

$$\left.\begin{aligned} \cos \Theta_L &= \frac{W_X \sin \Phi_L \sin \Sigma_L + W_Y \cos \Sigma_L}{W_Z^2 - 1} \\ \sin \Theta_L &= \frac{W_Y \sin \Phi_L \sin \Sigma_L - W_X \cos \Sigma_L}{W_Z^2 - 1} \end{aligned}\right\} \quad 0 \leq \Theta_L \leq 2\pi \qquad (2\text{–}65)$$

where Φ_L is the latitude of the launcher. A unit vector $\mathbf{R}_L^1$ in the direction of the launcher can be calculated in the vernal-equinox equatorial system by

$$\mathbf{R}_L^1 = \cos \Phi_L \cos \Theta_L, \cos \Phi_L \sin \Theta_L, \sin \Phi_L \qquad (2\text{–}66)$$

The angle Φ between the launcher and the perifocus of the conic is given by

$$\left.\begin{aligned} \cos \Phi &= \mathbf{R}_L^1 \cdot \mathbf{P} \\ \sin \Phi &= \mathbf{R}_L^1 \cdot \mathbf{Q} \end{aligned}\right\} \quad 0 \leq \Phi \leq 2\pi \qquad (2\text{–}67)$$

The angle between launch and injection Φ_I is defined by

$$\Phi_I = 2\pi - \Phi + v \qquad (2\text{–}68)$$

where, again, v is the true anomaly at injection into the escape hyperbola.

A unit vector $\mathbf{R}^1$ toward injection is seen in Fig. 2–4 to be

$$\mathbf{R}^1 = \mathbf{P}\cos v + \mathbf{Q}\sin v = (R_X, R_Y, R_Z) \qquad (2\text{–}69)$$

The injection latitude Φ is given by

$$\sin\Phi = R_Z \qquad -\frac{\pi}{2} \leq \Phi \leq \frac{\pi}{2} \qquad (2\text{–}70)$$

The right ascension of injection Θ can be found from

$$\left.\begin{aligned}\cos\Theta &= \frac{R_X}{\sqrt{R_X^2 + R_Y^2}} \\ \sin\Theta &= \frac{R_Y}{\sqrt{R_X^2 + R_Y^2}}\end{aligned}\right\} \qquad 0 \leq \Theta \leq 2\pi \qquad (2\text{–}71)$$

The longitude of injection θ can be calculated from

$$\theta = \Theta - \Theta_L - \omega t_b + \theta_L \qquad 0 \leq \theta \leq 2\pi \qquad (2\text{–}72)$$

where

θ_L is the longitude of the launcher
ω is the rotational rate of the earth
t_b is the time from launch to injection

Here,

$$t_b = t_1 + t_2 + \left[\Phi_I - (\Phi_1 + \Phi_2)\right] k_\phi^\cdot \qquad (2\text{–}73)$$

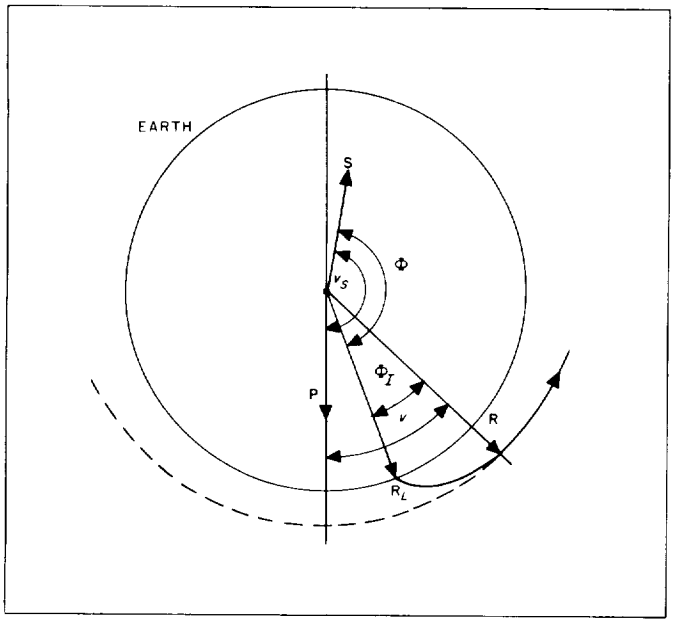

Fig. 2–4. Ascent-trajectory geometry

where

t_1 is the time of first burn (into the parking orbit)
t_2 is the time of second burn (into the escape hyperbola)
Φ_1 is the angle of first burn
Φ_2 is the angle of final burn
$k_\phi^\cdot$ is the inverse parking-orbit rate = 14.689 sec/deg for a 100-nm Earth parking orbit

The time of coast t_c is given by

$$t_c = \left[\Phi_I - (\Phi_1 + \Phi_2)\right] k_\phi^\cdot \qquad (2\text{–}74)$$

The relations stated above are illustrated in Fig. 2–5.

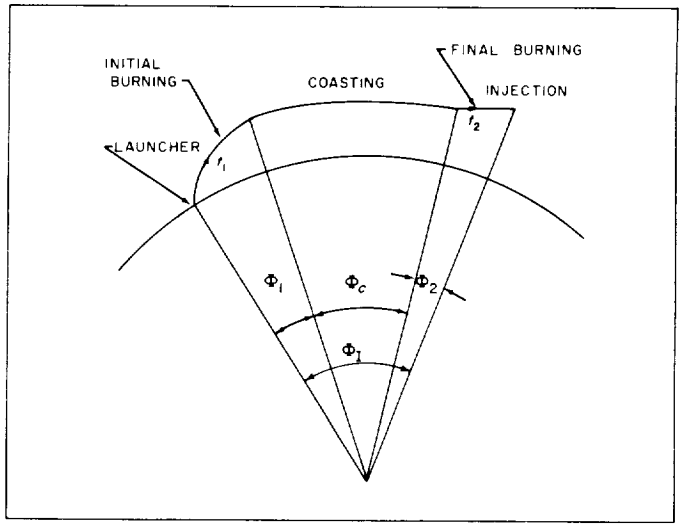

Fig. 2–5. Powered trajectory modified by coasting

The azimuth at injection Σ can be computed from

$$\cos\Sigma = \frac{S_Z - k_3\sin\Phi}{k_4\cos\Phi} \qquad 0 \leq \Sigma \leq \pi \qquad (2\text{–}75)$$

where

$$\left.\begin{aligned}k_3 &= \frac{\sqrt{e^2-1}}{e}\sin v - \frac{1}{e}\cos v \\ k_4 &= \frac{\sqrt{e^2-1}}{e}\cos v + \frac{1}{e}\sin v\end{aligned}\right\} \qquad (2\text{–}76)$$

The unit vector to final-stage ignition $\mathbf{R}_2^1$ can be found in a manner similar to that used for $\mathbf{R}$:

$$\mathbf{R}_2^1 = \mathbf{P}\cos(v - \Phi_2) + \mathbf{Q}\sin(v - \Phi_2) \qquad (2\text{–}77)$$

The latitude Φ_2 of final-stage ignition is computed from

$$\sin \Phi_2 = R_{Z2} \qquad -\frac{\pi}{2} \leq \Phi_2 \leq \frac{\pi}{2} \tag{2-78}$$

The right ascension Θ_2 of final-stage ignition is given by

$$\left.\begin{aligned} \cos \Theta_2 &= \frac{R_{X2}}{\sqrt{R_{X2}^2 + R_{Y2}^2}} \\ \sin \Theta_2 &= \frac{R_{Y2}}{\sqrt{R_{X2}^2 + R_{Y2}^2}} \end{aligned}\right\} \quad 0 \leq \Theta_2 \leq 2\pi \tag{2-79}$$

and the longitude θ_2 of final stage ignition is defined by

$$\theta_2 = \theta + \Theta_2 - \Theta + \omega t_2 \tag{2-80}$$

The angle Δv between injection and the outgoing asymptote is expressed as

$$\Delta v = v_s - v$$

The launch time T_L can be found by

$$T_L = \frac{\Theta_L - \theta_L - GHA}{\omega} \qquad 0 \leq (\Theta_L - \theta_L - GHA) \leq 2\pi \tag{2-81}$$

where GHA is the Greenwich Hour Angle at 0^h UT of the launch day as shown in Fig. 2–6, and is obtained from

$$\begin{aligned} GHA = {} & 100°.07554260 \\ & + 0°.9856473460\ T_d \qquad 0 \leq GHA \leq 2\pi \\ & + 2°.9015 \times 10^{-13}\ T_d^2 \end{aligned} \tag{2-82}$$

Here, T_d = days past 0^h January 1, 1950.

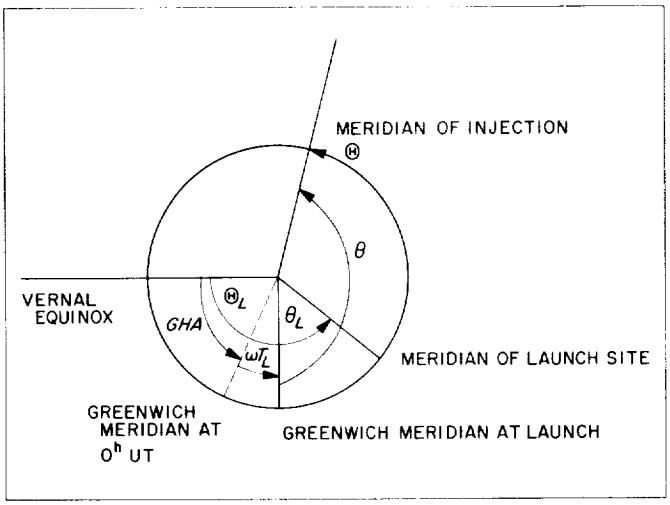

Fig. 2–6. Relation between longitude, right ascension, and time in equatorial plane

The injection time T is calculated from

$$T = T_L + t_b \tag{2-83}$$

C. Differential Corrections

As outlined in Section I–C, the calculation of differential corrections, or partial derivatives relating variations in the impact parameter **B** and flight time T_F to variations in the hyperbolic-excess velocity vector $\mathbf{V}_{hL}$ at launch, are performed by a numerical differencing technique.[8]

The basic idea in this technique is to compute a varied or perturbed trajectory and then difference it with the reference case. A small variation $\Delta\mathbf{V}_{hL}$ in the hyperbolic-excess velocity vector is equivalent to a small variation $\Delta\mathbf{V}_L$ in the launch heliocentric-velocity vector. Letting primed quantities denote variables on the perturbed trajectory, the launch heliocentric velocity on this trajectory is, then,

$$\mathbf{V}_L' = \mathbf{V}_L + \Delta\mathbf{V}_{hL} \tag{2-84}$$

where

$$\begin{aligned} \Delta\mathbf{V}_{hL} = {} & (C_3)^{1/2}\,\Delta\Phi_S[-\sin\Phi_S\cos\Theta_S, -\sin\Phi_S\sin\Theta_S, \cos\Phi_S], \\ & (C_3)^{1/2}\,\Delta\Theta_S[-\cos\Phi_S\sin\Theta_S, \cos\Phi_S\cos\Theta_S, 0], \\ & \frac{-\Delta C_3}{2(C_3)^{1/2}}[\cos\Phi_S\cos\Theta_S, \cos\Phi_S\sin\Theta_S, \sin\Phi_S] \end{aligned}$$

where $\Delta\Phi_S$, $\Delta\Theta_S$ are small angular variations (0.2 deg), and the energy variation is $\Delta C_3 = 0.005\ C_3$.

The semimajor axis a' is obtained from

$$a' = \frac{R_L}{2 - \dfrac{V_L'^2 R_L}{GM_S}} \tag{2-85}$$

The radial rate $\dot{R}_L'$ is given by

$$\dot{R}_L' = \frac{\mathbf{V}_L' \cdot \mathbf{R}_L}{R_L} \tag{2-86}$$

The semilatus rectum p' and eccentricity e' are computed from

$$p' = \frac{R_L^2\,(V_L'^2 - \dot{R}_L'^2)}{GM_S} \tag{2-87}$$

$$e' = \left(1 - \frac{p'}{a'}\right)^{1/2} \tag{2-88}$$

[8]This method was developed by William Kizner, Research Specialist, Systems Analysis Section, Jet Propulsion Laboratory.

The eccentric anomaly at launch E'_L is expressed by

$$\sin E'_L = \frac{R_L \dot{R}'_L}{e' (a' G M_S)^{1/2}}$$
$$\cos E'_L = \frac{1}{e'}\left(1 - \frac{R_L}{a'}\right) \tag{2-89}$$

The mean anomaly at launch M'_L is obtained from

$$M'_L = E'_L - e' \sin E'_L \tag{2-90}$$

The mean orbital rate n' is given by

$$n' = \frac{(GM_S)^{1/2}}{a'^{3/2}} \tag{2-91}$$

The mean anomaly at the target M'_p is stated as

$$M'_p = n' T_F + M'_L \tag{2-92}$$

The eccentric anomaly at the target E'_p is obtained from the expansion

$$E'_p = E_p + \left(\frac{1}{1 - e' \cos E_p}\right)\Delta M - \frac{1}{2}\left[\frac{e' \sin E_p}{(1 - e' \cos E_p)^3}\right]\Delta M^2 + \frac{1}{6}\left[\frac{(3 e' \sin E_p)^2 - (1 - e' \cos E_p)(e' \cos E_p)}{(1 - e' \cos E_p)^5}\right]\Delta M^3 \tag{2-93}$$

if

$$\cos E_p \geqq 0$$

However,

$$E'_p = E_p + \frac{e \cos E_p - 1 + \sqrt{(e \cos E_p - 1)^2 + (2e \sin E_p)\,\Delta M}}{e \sin E_p} \tag{2-94}$$

if

$$\cos E_p < 0$$

where

$$\Delta M = M'_p - (E_p - e' \sin E_p)$$

The true anomalies at launch and at the target, v'_L and v'_p are found from

$$\cos v'_L = \frac{p' - R_L}{e' R_L} \tag{2-95}$$

$0 < v'_L < \pi$ if $\dot{R}'_L$ is positive

$\pi < v'_L < 2\pi$ if $\dot{R}'_L$ is negative

$$\cos v'_p = \frac{\cos E'_p - e'}{1 - e' \cos E_p}$$
$$\sin v'_p = \frac{(1 - e'^2)^{1/2} \sin E'_p}{1 - e' \cos E'_p} \tag{2-96}$$

The heliocentric central angle Ψ' is given by

$$\Psi' = v'_p - v'_L \tag{2-97}$$

The angular momentum $\mathbf{h}'$ is expressed as

$$\mathbf{h}' = \mathbf{R}_L \times \mathbf{V}'_L \tag{2-98}$$

The heliocentric position vector at the target is given by

$$\mathbf{R}'_p = R'_p \left(\frac{\mathbf{R}_L}{R_L} \cos \Psi' + \frac{\mathbf{h}' \times \mathbf{R}_L}{h' R_L} \sin \Psi'\right) \tag{2-99}$$

where

$$R'_p = a' (1 - e' \cos E'_p) \tag{2-100}$$

A vector in the direction of perihelion with magnitude e' is computed from

$$\boldsymbol{\varepsilon}' = \frac{\mathbf{V}'_L \times \mathbf{h}'}{GM_S} - \frac{\mathbf{R}_L}{R_L} \tag{2-101}$$

The heliocentric velocity at the target is defined by

$$\mathbf{V}'_p = \frac{\mathbf{h}'}{p'} \times \left(\frac{\mathbf{R}'_p}{R_p} + \boldsymbol{\varepsilon}'\right) \tag{2-102}$$

The hyperbolic-excess velocity at the target is expressed by

$$\mathbf{V}'_{hp} = \mathbf{V}'_p - \mathbf{V}_2 \tag{2-103}$$

The difference between the heliocentric position vectors on the perturbed and reference trajectories is given by

$$\Delta \mathbf{R}'_p = \mathbf{R}'_p - \mathbf{R}_p \tag{2-104}$$

The impact parameter $\mathbf{B}$ is computed from

$$\mathbf{B} = -\frac{(\Delta \mathbf{R}'_p \cdot \mathbf{V}'_{hp})\,\mathbf{V}'_{hp}}{V'^2_{hp}} + \Delta \mathbf{R}'_p$$

The flight-time error is stated as

$$\Delta T_F = \frac{\Delta \mathbf{R}'_p \cdot \mathbf{V}'_{hp}}{V'^2_{hp}} \tag{2-105}$$

The partial derivatives are formed by dividing $\Delta\Theta_S$, $\Delta\Phi_S$, and ΔC_3 into the miss components $\mathbf{B} \cdot \mathbf{T}$, $\mathbf{B} \cdot \mathbf{R}$, and flight-time error ΔT_F. In addition to the component partials, the quantity $\partial B / \partial Q_i$ is defined by

$$\frac{\partial B}{\partial Q_i} = \left[\left(\frac{\partial \mathbf{B} \cdot \mathbf{T}}{\partial Q_i}\right)^2 + \left(\frac{\partial \mathbf{B} \cdot \mathbf{R}}{\partial Q_i}\right)^2\right]^{1/2} \tag{2-106}$$

The three partials, $\partial B/\partial\Theta_S$, $\partial B/\partial\Phi_S$, $\partial B/\partial C_3$, are important measures of the error sensitivity of a trajectory.

The effect of uncertainty in the knowledge of the astronomical-unit–to–kilometer conversion factor on target miss and flight time may be determined by the following formulae:

$$\frac{\partial \mathbf{B}\cdot\mathbf{T}}{\partial au} = \frac{-2C_3}{au}\frac{\partial \mathbf{B}\cdot\mathbf{T}}{\partial C_3}$$
$$\frac{\partial \mathbf{B}\cdot\mathbf{R}}{\partial au} = \frac{-2C_3}{au}\frac{\partial \mathbf{B}\cdot\mathbf{R}}{\partial C_3} \qquad (2\text{–}107)$$

whence

$$\frac{\partial B}{\partial au} = \frac{2C_3}{au}\frac{\partial B}{\partial C_3} \qquad (2\text{–}108)$$

and

$$\frac{\partial T_F}{\partial au} = \frac{-2C_3}{au}\frac{\partial T_F}{\partial C_3} \qquad (2\text{–}109)$$

where au is the astronomical-unit–to–kilometer conversion factor

The effect of solar-radiation pressure acting on the probe may also be evaluated as follows: In Eq. 2–84, let $\Delta\mathbf{V}_{hL} = 0$, but in Eqs. 2–85, 2–87, 2–89, 2–91, and 2–101, vary GM_S by adding an increment ΔGM_S. This procedure gives rise to a varied trajectory from which the impact parameter **B** and flight-time error ΔT_F may be obtained. The partials $\partial B/\partial GM_S$ and $\partial T_F/\partial GM_S$ may then be calculated. Since the acceleration caused by solar-radiation pressure acts in a direction opposite to the gravitational attraction of the Sun, radiation pressure has the effect of decreasing the Sun's gravitational attraction or decreasing GM_S. A decrease, $\Delta GM_S = -2.4 \times 10^3$ km^3/sec^2, corresponds to the solar-radiation pressure acting on a 300-kg spacecraft having a perfectly reflecting area of 3.6 m^2. Thus the miss, always being a positive number, is obtained by $\Delta B_{sp} = 2.4 \times 10^3\ \partial B/\partial GM_S$, and the corresponding flight-time error is $\Delta T_{F_{sp}} = -2.4 \times 10^3\ \partial T_F/\partial GM_S$, which is sign-sensitive.

III. DISCUSSION AND EXPLANATION OF RESULTS

A. Introduction

1. Trajectory Computations

Minimum (geocentric) energy trajectories from Earth to Mercury for the period 1964–1975 and from Earth to Jupiter for the period 1968–1973 were computed on the 7094 digital computer by numerically evaluating the analytical model explained in Sections I and II. This computation resulted in curves of C_3 (*vis viva* geocentric energy) vs launch date for these trajectories.

For each target planet, several 75-day launch intervals were analyzed in greater detail: curves of 19–21 key trajectory parameters vs launch date for various *vis viva* geocentric energies (C_3) were automatically plotted.

2. Trajectory Analysis

Careful analysis of the results shows that as many as four ballistic flight paths to the target planet exist per launch date for a given *vis viva* geocentric energy (C_3), assuming trips of less than one revolution around the Sun. A more extensive analysis might reveal more than four flight paths. Actually, feasible launchings can occur only for small time intervals (1–3 months), when the relative positions of the Earth and target planet are such that the velocity requirements for ballistic transfers can be reasonably achieved by modern boost vehicles. These intervals occur once during each synodic period of the planet. A synodic period is the time interval required for the Earth and target planet to attain successive identical relative angular relationships in heliocentric longitude, e.g., the time between Earth and target planet alignments (116 days for Mercury; 390 days for Jupiter).

Figures 3–1 to 3–6 show the minimum injection energy required for transit to Mercury vs launch date. The dates of Earth–Mercury alignment are indicated by arrows (↑). Favorable launch opportunities (i.e., relative minima in injection energy) and planet alignments occur about every 116 days. Two families of conic trajectories exist (Types I and II), and will be described in detail in Section B. After three synodic periods (348 days), Mercury and Earth again assume approximately the same space-fixed position. This condition is also reflected in Figs. 3–1 to 3–3, in which the minimum energy curve for Type I trajectories has very pronounced minima at 348-day intervals. Type II trajectories exhibit this periodic behavior also, although the curves are more complicated.

Within the time period considered, the minimum injection energy reaches an absolute minimum on November 23, 1967, for Type I trajectories, and on November 3, 1968, for Type II trajectories. Only the launch opportunities centered around these dates are discussed in detail in Sections IV and V. The results are fairly representative for all other launch opportunities.

If the synodic period of the Earth and target planet were a rational fraction of a year, and if their orbits remained unchanged, the minimum energy curves would be exactly periodic functions of time.

Figures 3–7 and 3–8 show the minimum injection energy for transits to Jupiter vs launch date for Type I and Type II trajectories. The dates of Earth–Jupiter alignment are indicated by arrows (↑).

Favorable launch opportunities, planet oppositions, and approximately the same space-fixed geometry of Earth and Jupiter occur every synodic period (390 days). For launch opportunities, the absolute minimum injection energy occurs on December 30, 1969, for Type II transfers, and on January 3, 1970, for Type I trajectories. The launch opportunities centered around these dates are discussed in detail in Section VII. In addition, because of some interesting features that were discovered, the launch opportunity extending from November 1968 to January 1969 is treated in detail in Section VI.

B. Classification of Trajectories

1. Type I and Type II

In observing the variation of any trajectory parameter vs launch date for fixed geocentric energies C_3, it is noted that two separate groups of closed contours, rather than one, are described (see Fig. 3–9). These two sets of energy contours are designated as Type I and Type II trajectories, where Type I trajectories are defined as having heliocentric-transfer angles less than 180 deg, and Type II trajectories are those having heliocentric-transfer angles greater than 180 deg. A Type I trajectory traverses less than half-way around the Sun from launch to planet encounter, whereas a Type II trajectory would traverse more than half-way, but less than one full revolution, around the Sun. For a given launch day and energy, then, Type II trajectories require greater flight times than do Type I. The existence of these two sets of energy contours can be attributed to the fact that the orbits of Earth and

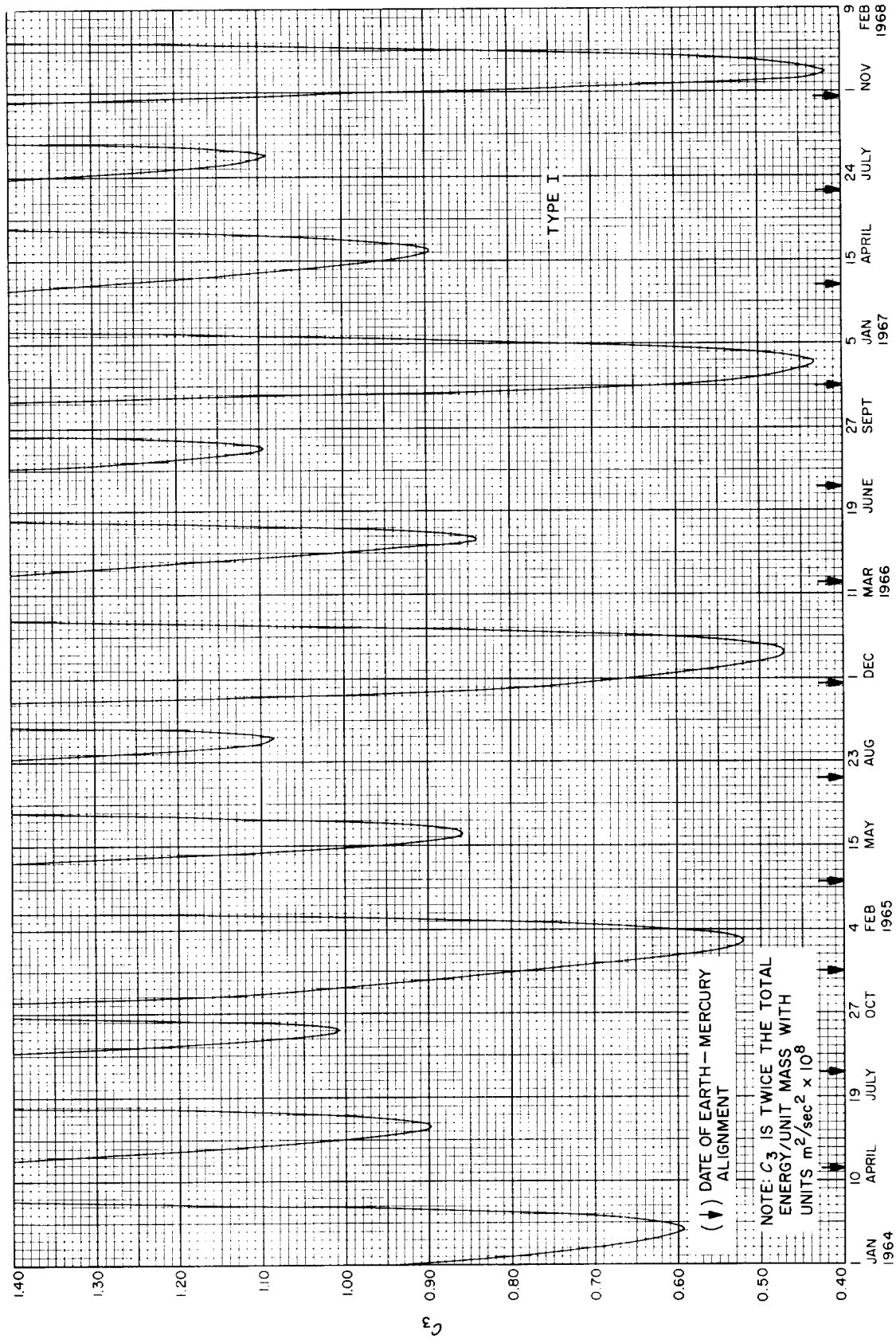

Fig. 3-1. Mercury 1964–1968: Minimum injection energy vs launch date, Type I

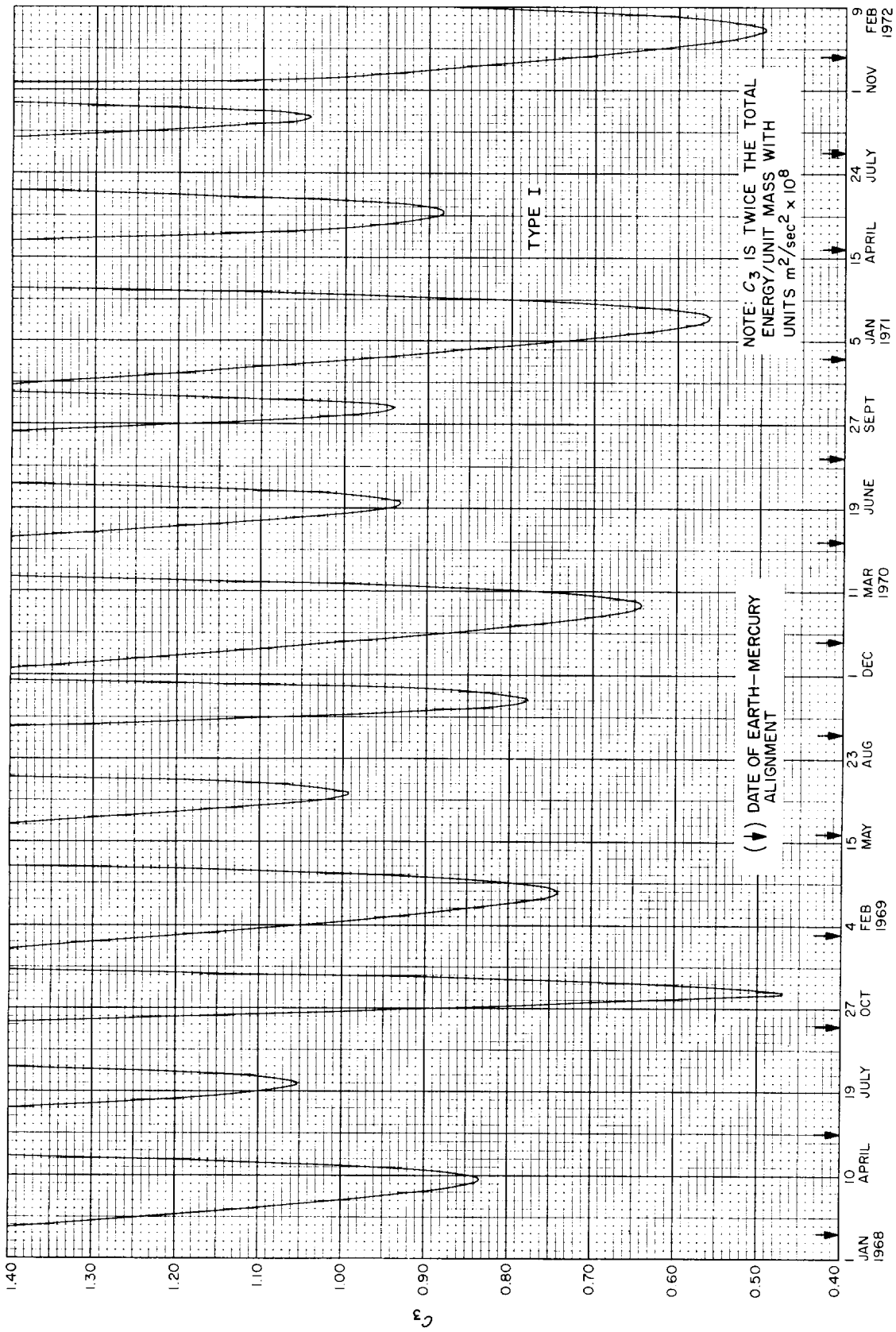

Fig. 3–2. Mercury 1968–1972: Minimum injection energy vs launch date, Type I

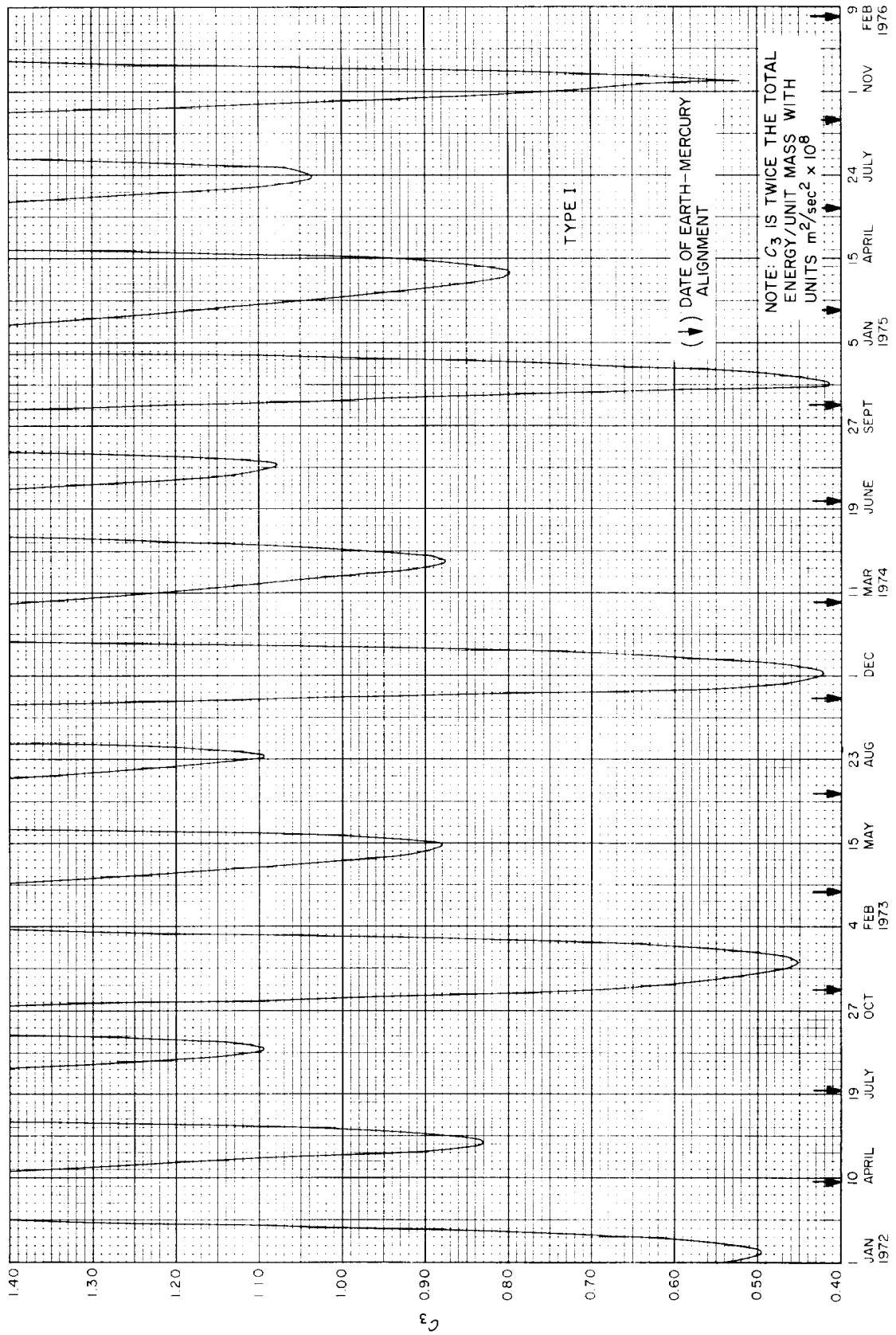

Fig. 3–3. Mercury 1972–1976: Minimum injection energy vs launch date, Type I

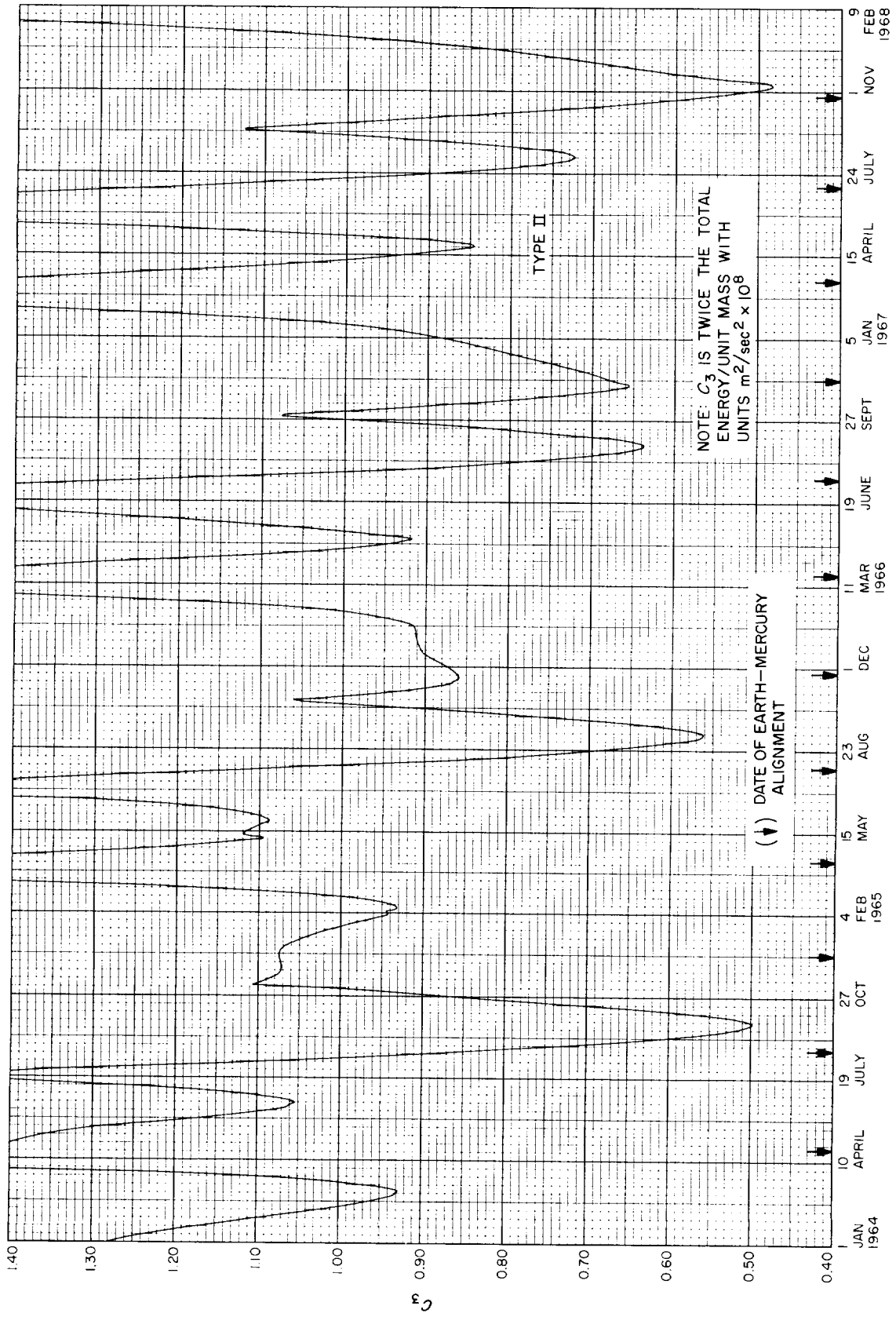

Fig. 3-4. Mercury 1964–1968: Minimum injection energy vs launch date, Type II

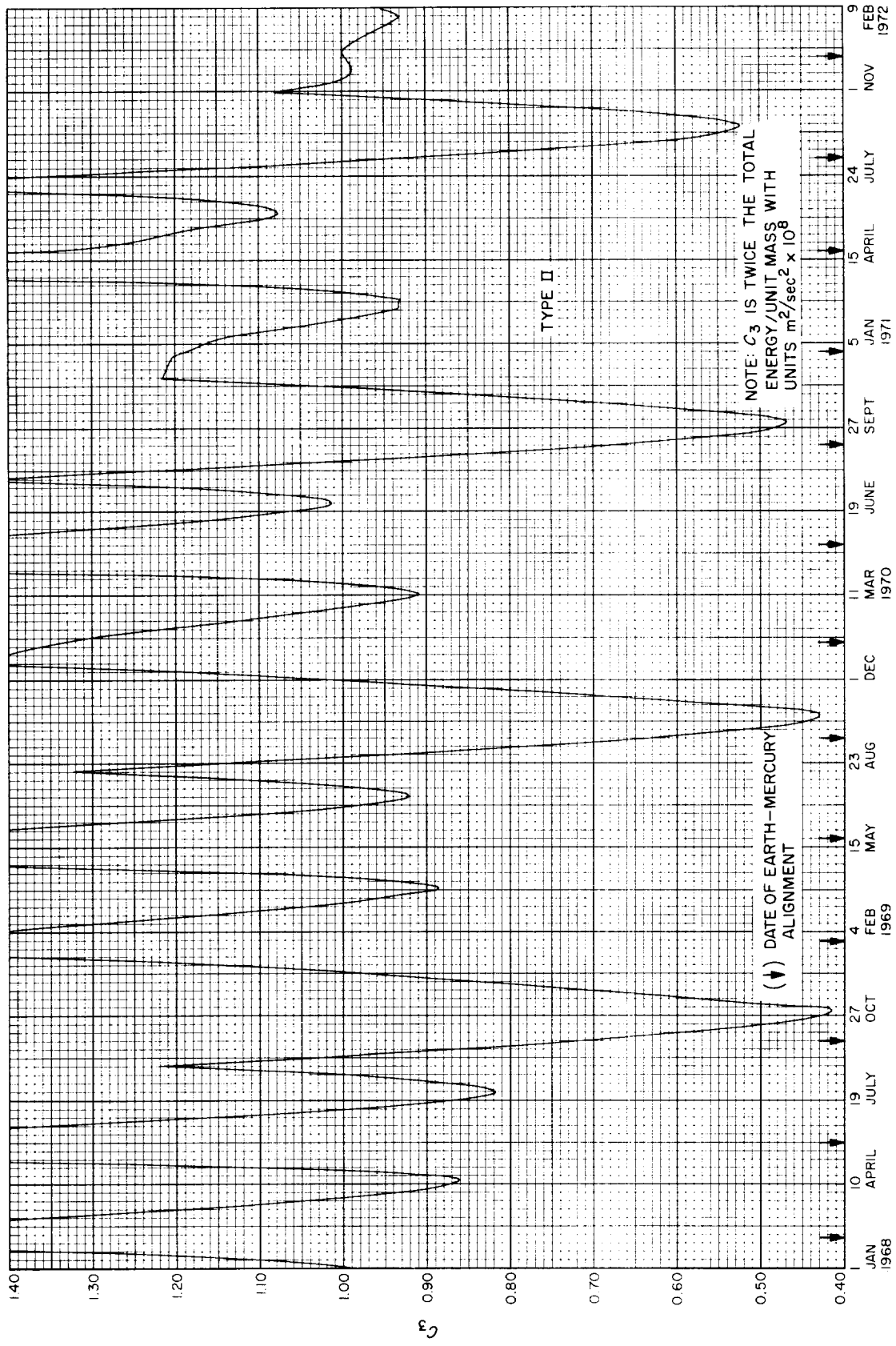

Fig. 3–5. Mercury 1968–1972: Minimum injection energy vs launch date, Type II

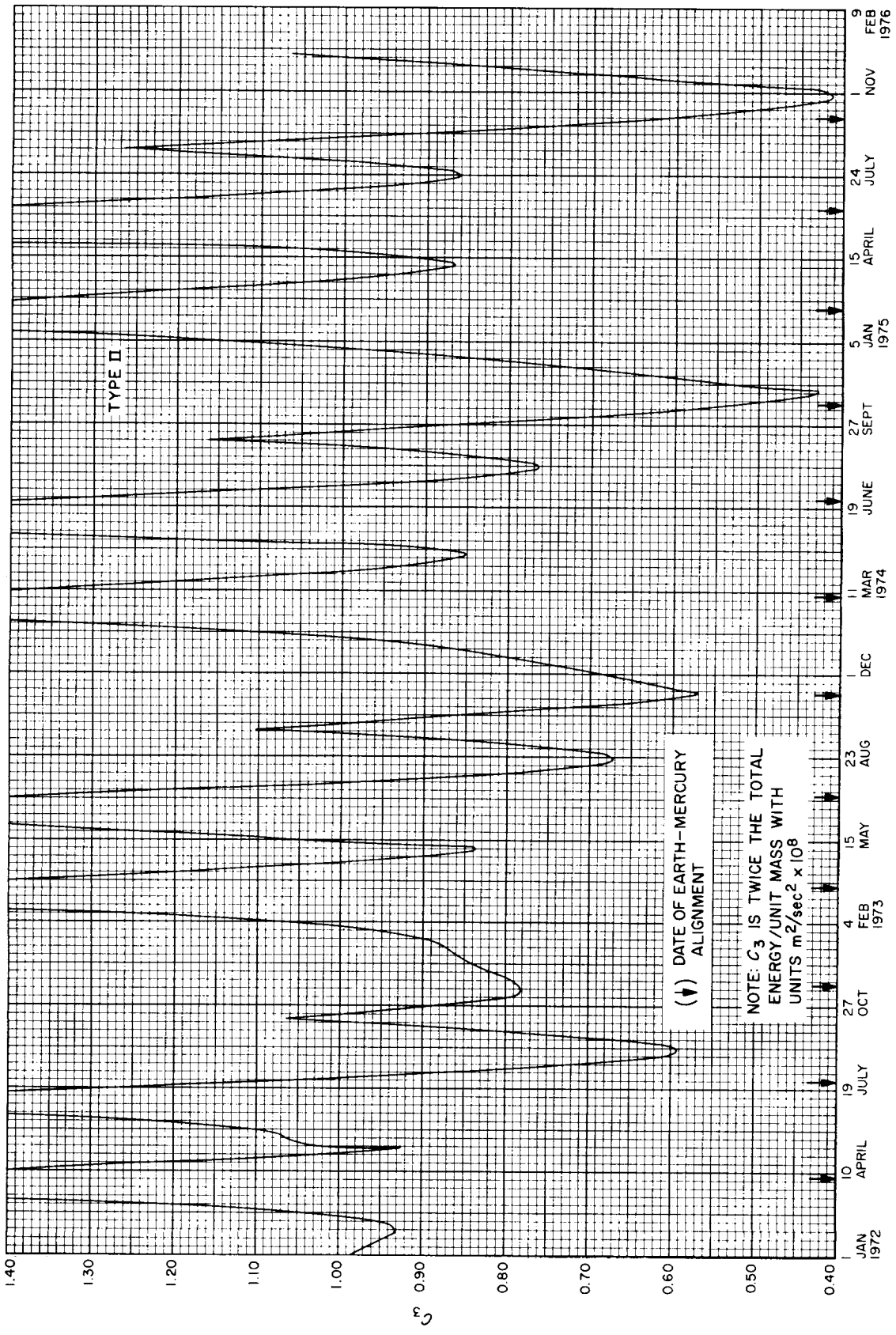

Fig. 3–6. Mercury 1972–1976: Minimum injection energy vs launch date, Type II

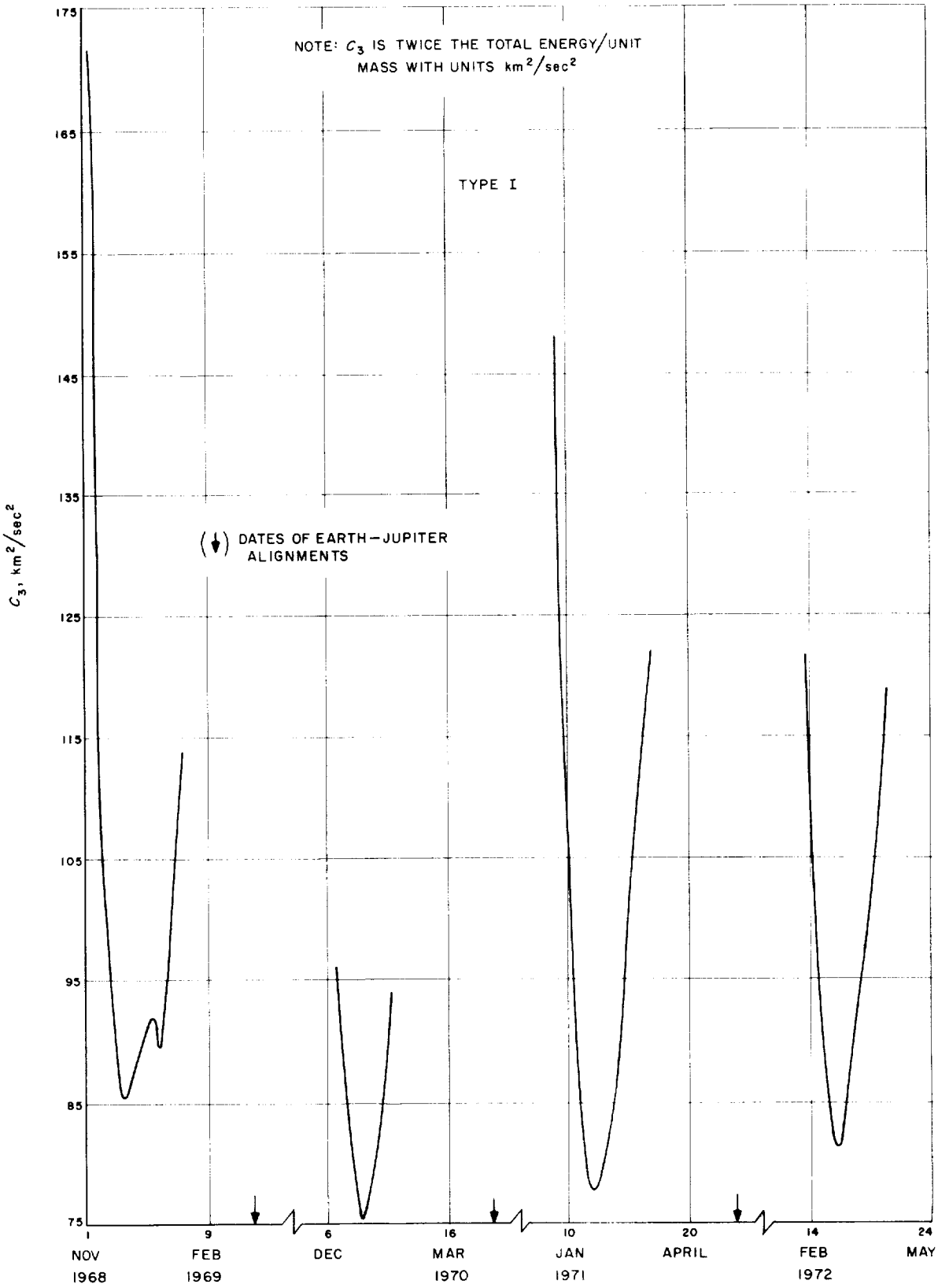

Fig. 3–7. Jupiter 1969–1973: Minimum injection energy vs launch date, Type I

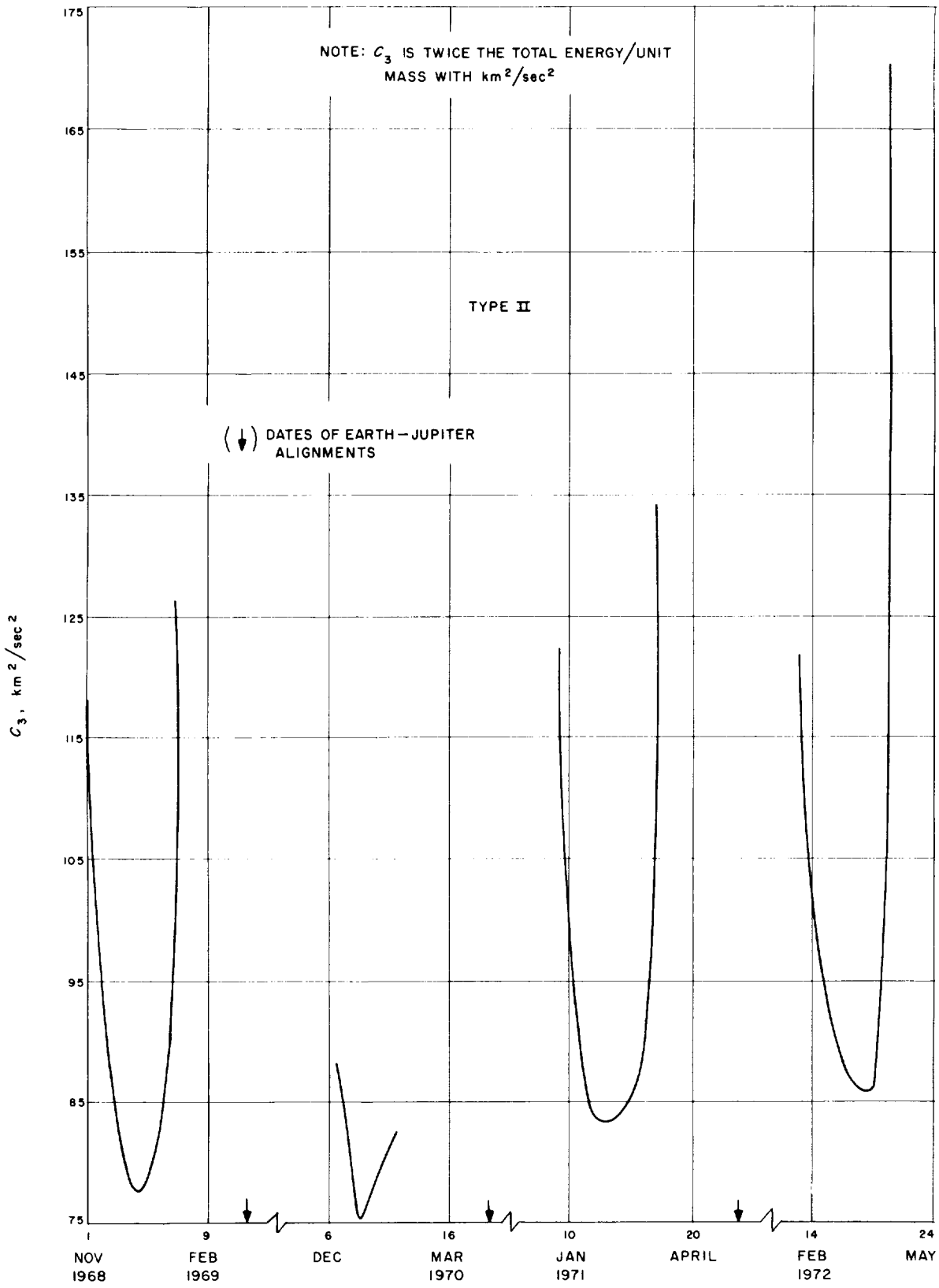

Fig. 3–8. Jupiter 1969–1973: Minimum injection energy vs launch date, Type II

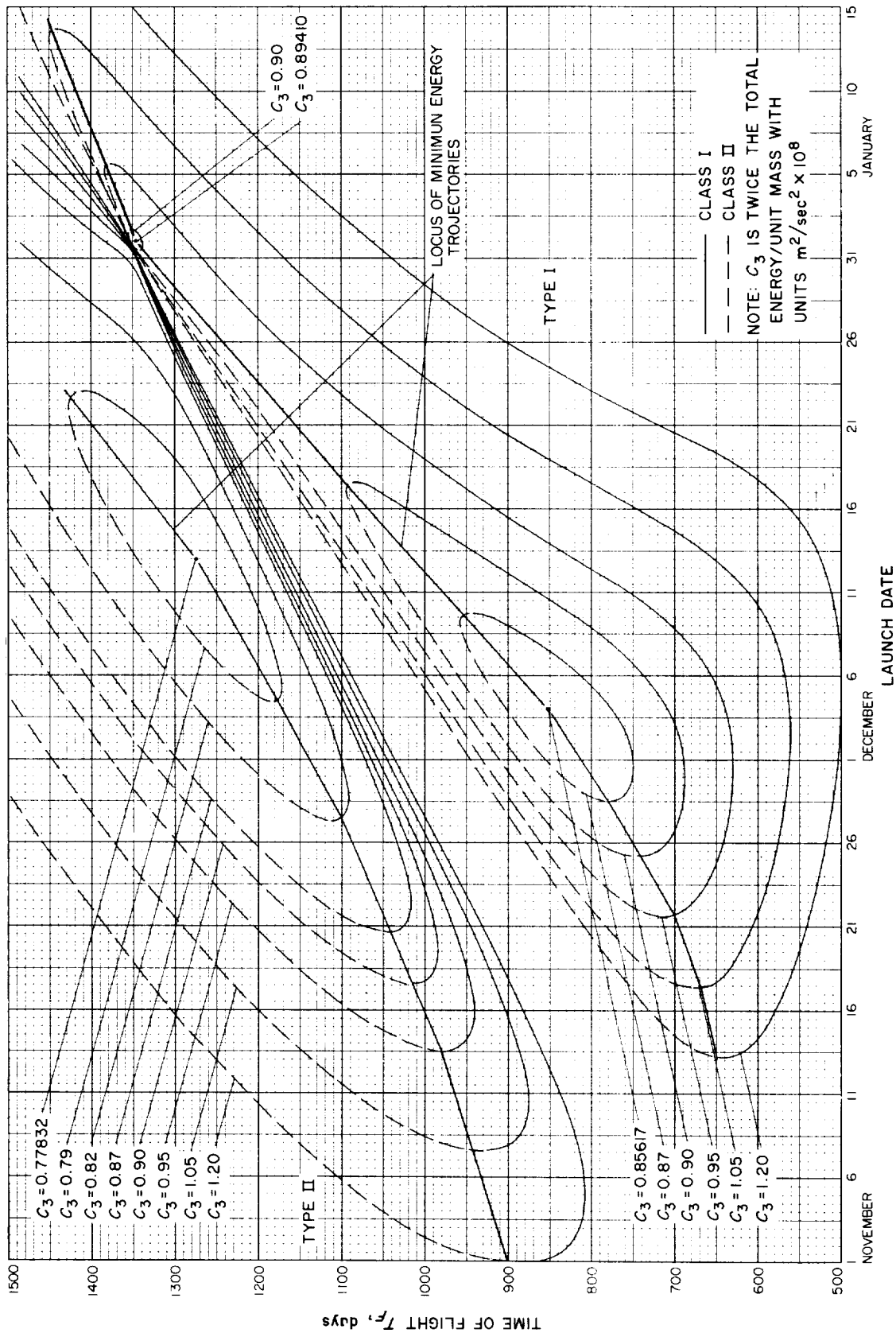

Fig. 3-9. Jupiter 1968–1969: Time of flight vs launch date

the destination planet are not coplanar. If the Earth and target planet had coplanar circular orbits, only a single group of energy contours would exist. If the orbits of Earth and the target planet were circular as well, this single group of energy contours would include the well-known Hohmann's transfer orbit. The Hohmann transfer orbit is tangential to the orbits of Earth and target planet, has a heliocentric transfer angle of 180 deg, and requires the least *vis viva* geocentric energy (C_3) among all transfer trajectories. The Hohmann minimum-energy trajectory would remain constant for each synodic period, retaining the same flight time and *vis viva* geocentric energy. The fact that the orbits of Mercury and Jupiter are slightly inclined with respect to the ecliptic (7 and 1.3 deg, respectively) strongly influences the transfer trajectories and causes the single group of trajectory contours to split into two families, thus necessitating the designation of Type I and Type II trajectories.

In Fig. 3–9 note the small family of closed contours centered around January 1, 1969. This group has been designated Type I-A. Type I-A trajectories exist for Venus also. They are not attractive because their flight times are longer for a given *vis viva* geocentric energy.

2. Class I and Class II

As Fig. 3–9 shows, two trajectories usually exist for a given type, energy, and launch date. Trajectories corresponding to the lower portions of the energy contours are designated as Class I and are connected by solid lines and correspond to shorter flight times and smaller heliocentric central angle. Trajectories corresponding to the upper part of the energy contours are designated as Class II and are connected by dashed lines and correspond to longer flight times and larger heliocentric angle. For a given launch date and geocentric energy, the Type I–Class I trajectory has the shortest flight time and the Type II–Class II trajectory has the longest flight time.

For example, Fig. 3–9 shows that for the launch date November 26, 1969, and C_3 = 120 km^2/sec^2, the Type I–Class I trajectory has a flight time of 520 days, whereas the Type II–Class II trajectory has a flight time of 1460 days. The flight time for the Type I–Class II trajectory is 880 days, and for the Type II–Class I trajectory it is 982 days.

3. Minimum Energy Trajectories

a. Minimum-energy loci. Further study of Fig. 3–9 shows that the geocentric energy C_3 has a relative minimum of C_3 = 85.617 km^2/sec^2 on December 4, 1968, where the flight time is 850 days. By moving away from this point in any direction, C_3 increases. Type I trajectories corresponding to C_3 = 87 km^2/sec^2 only exist from November 29, 1968 (flight time 780 days) to December 10, 1968 (flight time 950 days). The geocentric energy required is smaller inside the contour and larger outside it. Consequently, the minimum possible energy on November 29 and December 10, 1968, for Type I trajectories is 87 km^2/sec^2. A curve of minimum geocentric energy vs launch date may be constructed for Type I and Type II trajectories by constructing the vertical tangents to the contours of a given parameter such as launch time. By connecting these points, a locus of minimum energy (Fig. 3–9) is obtained which separates Class I and Class II trajectories within a given type.

Figure 3–10 was constructed in this way from Fig. 3–9 and shows minimum geocentric energy vs launch date from November 18, 1968, to January 7, 1969. The curve corresponding to Type II trajectories was terminated on December 28, 1968, because flight times corresponding to later launch dates are in excess of four years. Two relative minima, C_3 = 85.617 km^2/sec^2 on December 4, 1968, and C_3 = 89.410 km^2/sec^2 on January 1, 1969, exist for Type I trajectories because of the noncoplanar and noncircular nature of the orbits of the Earth and Jupiter. The relative minimum for Type II trajectories is C_3 = 77.832 km^2/sec^2 and occurs on December 13, 1968.

b. Absolute minimum-energy trajectories. The absolute minimum-energy trajectory for each type is defined as the trajectory with the least geocentric energy within each synodic period of the planet. Such trajectories are useful as first approximations of launch dates, communication distances at planet encounter, and flight times for missions within a given launch opportunity. Table 3–1 shows the characteristics of absolute minimum-energy trajectories to Mercury and Jupiter. These trajectories occur once every synodic period of the target planet, as explained in Section III.A.2. For Mercury, a sharp decrease in the absolute minimum energy occurs every third synodic period (348 days), as can be seen from Figs. 3–1 to 3–7. Table 3–1 shows that the lowest possible geocentric energy to Mercury is 41.2 km^2/sec^2 (launch date October 31, 1968, Type II); to Jupiter it is 75.3 km^2/sec^2 (launch date January 3, 1970, Type I).

Very recently Cutting and Sturms (Ref. 6) showed that it is possible to reduce the energy requirements for a Mercury mission by 70% by an encounter with Venus before arrival at Mercury. The following is a typical trajectory: Launch date August 14, 1970, injection energy 13 km^2/sec^2, arrival date at Venus, November 26, 1970,

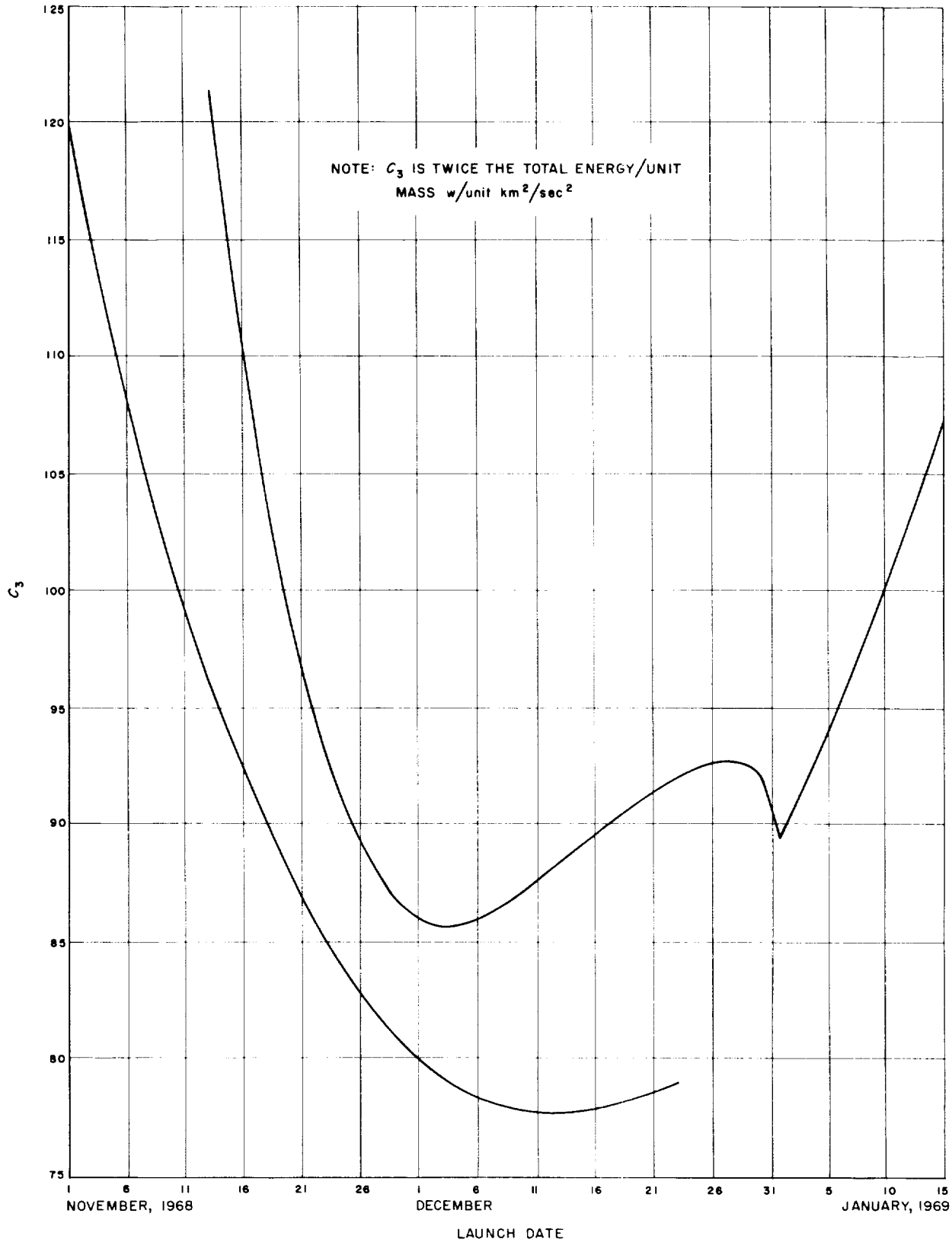

Fig. 3–10. Jupiter 1968–1969: Minimum injection energy vs launch date

Table 3-1. Characteristics of minimum-energy-transfer

Planet	Trajectory type	Launch date	Flight time, days	Geocentric injection energy,[a] $m^2/s^2 \times 10^6$	Heliocentric central angle,[b] deg	Sun-planet distance at arrival, 10^6 km	Earth-planet distance at arrival, 10^6 km	Celestial latitude of planet at arrival,[c] deg
Mercury	I	2/11/64	95	0.593	128.4	69.3	102	−4.69
	I	6/14/64	95	0.895	153.6	46.4	135	1.04
	I	10/6/64	86	1.006	142.6	53.2	126	6.70
	II	3/1/64	105	0.926	215.7	50.5	178	−3.79
	II	6/18/64	105	1.053	234.2	50.9	188	6.99
	II	9/24/64	116	0.497	221.5	66.8	176	0.70
	I	1/21/65	97	0.517	135.6	69.8	106	−3.25
	I	5/29/65	97	0.847	163.7	46.8	142	0.43
	I	9/19/65	86	1.074	139.9	50.2	125	7.04
	I	12/31/65	101	0.467	146.6	69.5	112	−2.09
	II	2/8/65	109	0.935	218.2	53.6	178	−5.52
	II	5/27/65	107	1.085	216.1	46.6	174	5.60
	II	9/10/65	115	0.561	229.8	65.7	184	1.40
	II	11/16/65	150	0.861	203.6	69.8	121	−3.32
	I	5/15/66	97	0.829	172.2	47.1	150	−0.24
	I	9/3/66	86	1.095	139.6	48.2	126	6.65
	I	12/11/66	104	0.434	156.4	68.5	119	−0.83
	II	5/6/66	107	0.893	187.0	46.7	154	0.50
	II	8/25/66	115	0.636	236.4	64.0	189	2.40
	II	11/8/66	135	0.646	184.1	67.7	115	−0.11
	I	4/26/67	92	0.897	133.7	55.1	120	−6.07
	I	8/17/67	87	1.077	139.2	46.8	126	5.66
	I	11/23/67	107	0.412	169.6	67.8	130	−0.16
	II	4/25/67	104	0.842	192.6	47.1	161	−0.20
	II	8/12/67	112	0.722	239.4	62.0	192	3.55
	II	11/7/67	123	0.470	185.7	67.8	130	−0.16
	I	4/5/68	91	0.834	122.3	61.6	108	−6.98
	I	7/28/68	90	1.039	139.9	46.1	126	4.12
	I	11/12/68	103	0.449	177.4	67.5	143	0.10
	II	4/12/68	102	0.858	199.3	47.5	168	−0.85
	II	7/28/68	110	0.822	242.8	59.6	195	4.61
	III	11/1/68	115	0.410	191.3	67.9	146	−0.24
	I	3/15/69	92	0.738	120.7	66.2	102	−6.42
	I	7/11/69	92	0.987	144.6	46.0	129	2.91
	I	11/1/69	90	0.778	153.2	60.6	131	4.15
	II	3/27/69	103	0.891	204.5	48.6	171	−2.15
	II	7/13/69	108	0.921	241.9	56.4	193	5.86
	II	10/18/69	115	0.428	203.0	67.5	159	0.10
	I	2/22/70	94	0.644	124.7	68.6	101	−5.37
	I	6/24/70	94	0.929	149.4	46.3	132	1.64
	I	10/16/70	87	0.940	145.9	55.7	127	6.05
	II	3/10/70	105	0.910	211.4	49.9	175	−3.24
	II	6/28/70	106	1.014	239.2	53.1	191	6.75
	II	10/3/70	116	0.468	215.6	67.1	171	0.38
	I	2/1/71	96	0.562	129.9	69.7	102	−3.93
	I	6/7/71	96	0.873	154.4	46.9	135	0.17
	I	9/29/71	86	1.041	139.9	51.5	124	7.00
	II	2/23/71	105	0.927	217.0	51.4	179	−4.25
	II	6/9/71	106	1.075	226.6	48.6	182	6.73
	II	9/19/71	115	0.524	223.9	66.1	179	1.10
	I	1/13/72	98	0.497	138.8	69.7	108	−2.77
	I	5/22/77	97	0.836	163.7	47.3	143	−0.46
	I	9/11/72	86	1.090	136.0	48.7	123	6.84
	I	12/22/72	102	0.451	149.8	69.0	114	−1.43
	II	1/27/72	114	0.933	221.8	55.5	177	−6.16

Table 3-1 (Cont'd)

Planet	Trajectory type	Launch date	Flight time, days	Geocentric injection energy,[a] $m^2/s^2 \times 10^6$	Heliocentric central angle,[b] deg	Sun-planet distance at arrival, 10^6 km	Earth-planet distance at arrival, 10^6 km	Celestial latitude of planet at arrival, deg
Mercury	II	5/7/72	113	0.961	184.2	46.8	147	0.30
	II	9/4/72	114	0.592	232.0	65.1	187	1.83
	II	11/12/72	146	0.782	201.7	69.7	123	−2.79
	I	5/13/73	93	0.858	173.3	47.2	154	− .29
	I	8/26/73	87	1.098	140.7	47.6	127	6.40
	I	12/3/73	105	0.423	161.3	68.1	123	−0.45
	II	5/4/73	103	0.858	188.1	46.8	158	0.46
	II	8/20/73	113	0.672	237.4	63.2	191	2.85
	II	11/8/73	129	0.555	183.6	67.7	121	−0.10
	I	4/18/74	91	0.874	128.2	57.8	115	−6.66
	I	8/9/74	88	1.067	139.9	46.4	127	5.18
	I	11/16/74	108	0.412	176.3	67.7	137	−0.09
	II	4/22/74	101	0.842	194.6	47.2	165	−0.20
	II	8/6/74	111	0.762	241.2	61.2	194	3.92
	II	11/8/74	116	0.419	184.3	67.7	137	−0.09
	I	3/27/75	92	0.798	121.4	63.9	105	−6.92
	I	7/22/75	90	1.023	139.4	46.1	126	3.54
	I	11/13/75	97	0.555	177.0	67.4	150	0.18
	II	4/5/75	103	0.873	200.6	48.1	168	−1.56
	II	7/24/75	108	0.862	243.2	58.8	196	4.92
	II	10/28/75	114	0.414	195.9	67.8	152	−0.17
Jupiter	I	1/2/70	985	0.752	178.8	779.0	742	0.00
	II	12/31/69	994	0.753	181.4	778.7	758	−0.01
	I	12/4/68	852	0.856	165.8	804.4	703	0.88
	IA	12/31/68	1349	0.884	180.4	779.2	735	0.01
	II	12/13/68	1277	0.778	191.3	784.1	636	0.18
	I	1/31/71	808	0.777	167.8	767.4	783	−0.41
	II	2/6/71	1180	0.833	194.8	750.0	816	−1.02
	I	3/6/72	744	0.812	162.0	751.6	882	−0.96
	II	3/31/72	1396	0.857	198.8	742.1	771	−1.23
	I	4/12/73	721	0.841	159.9	741.7	889	−1.29
	II	5/11/73	1404	0.839	196.3	754.4	812	−0.73

[a] Twice the total energy per unit mass, or *vis viva* integral.

[b] The angle subtended at the Sun between the Sun–Earth line at launch and the Sun–planet line at arrival time.

[c] Measured from the ecliptic.

Venus perigee altitude 2676 km, Mercury arrival date January 30, 1971, hyperbolic excess velocity at Mercury 12.3 km/sec.

For transfers to Mercury, the geocentric energy is smallest if (1) Mercury is at aphelion (66.8×10^6 km) at encounter, (2) Mercury is in the ecliptic at encounter, (3) the heliocentric central angle is 180 deg, and (4) Earth is at perihelion at launch. Owing to the large inclination ($i = 7$ deg) and eccentricity ($e = 0.2$) of Mercury's orbit, large variations in absolute minimum geocentric energy occur, as Table 3–1 shows: The trajectory (launch date, October 31, 1968) corresponding to the lowest geocentric energy ($C_3 = 41.2$ km^2/sec^2) has a heliocentric central angle of HCA = 192.3 deg, the Sun–Planet distance at arrival is SPP = 67.9×10^6 km, and the celestial latitude at arrival is LAP = 0.46 deg. The trajectory with launch date November 24, 1967, has almost the same energy (41.3 km^2/sec^2), even though the heliocentric transfer angle is smaller by 24 deg (HCA = 168.6 deg). The trajectory launched on May 15, 1966, shows the effect of arrival near Mercury perihelion (SPP = 47.6×10^6 km). The geocentric energy is nearly doubled ($C_3 = 84.8$ km^2/sec^2). It is difficult to find a trajectory in Table 3–1 which would show only the effect of reaching Mercury out of the ecliptic. However, several trajectories can be found for which arrival occurs at Mercury aphelion and when it is strongly inclined to the ecliptic. For example,

for a launch date of September 2, 1966, SPP = 47.6×10^6 km, LAP = 6.39 deg and C_3 = 109.9 km²/sec². It is interesting to note that these trajectory characteristics are almost duplicated for launch date August 26, 1973. Summarizing, it can be said that large variations in celestial latitude and Sun–Mercury distance at encounter strongly influence geocentric energy, whereas the effect of changes in heliocentric central angle is small.

It should be noted that within the time interval considered in this report (1964–1975), Mercury aphelion occurs very near the ecliptic so that trajectories with very favorable energy characteristics can be found. As Mercury's aphelion point moves away from the ecliptic, the minimum-energy requirements increase.

For Earth–Jupiter transfers, the geocentric energy will be smallest if (1) Jupiter is at perihelion (740×10^6 km) at encounter, (2) Jupiter is in the ecliptic at encounter, (3) the heliocentric central angle is 180 deg, and (4) the Earth is at aphelion (147×10^6 km) at launch.

Variations in absolute minimum geocentric energy are caused by the inclination (i = 1.3 deg) and eccentricity (e = 0.048) of Jupiter's orbit and the elliptic orbit of the Earth.

The trajectory with the smallest energy in Table 3-1 (C_3 = 75.3 km²/sec²) occurs for the launch date January 3, 1970. Arrival occurs 985 days later, when Jupiter is close to the ecliptic (LAP = 0.004 deg) but relatively far from perihelion (SPP = 778.5×10^6 km).

Further study of Table 3-1 shows that the strongest variations in geocentric energy are caused by large changes in the Sun–Jupiter distance at arrival. In order to reduce Earth-to-Jupiter flight times to two years, the geocentric energy required is C_3 = 88 km²/sec² (launch date December 1, 1968).

C. Mission Payload

The geocentric energy at launch C_3 determines the payload that can be placed on an interplanetary trajectory. Figure 3-11 shows approximate payload estimates vs C_3 for three launch-vehicle configurations: two-stage *Atlas/Centaur*, three-stage *Saturn 1B*, and three-stage *Saturn 5*. These curves are only intended to give a general idea of payload; they were obtained from the open literature (Ref. 7).

The maximum payload that can be placed on an Earth–Mercury trajectory using the *Saturn 1B* launch vehicle is 2500 lb. This payload is increased to 53,000 lb if the *Saturn 5* is used.

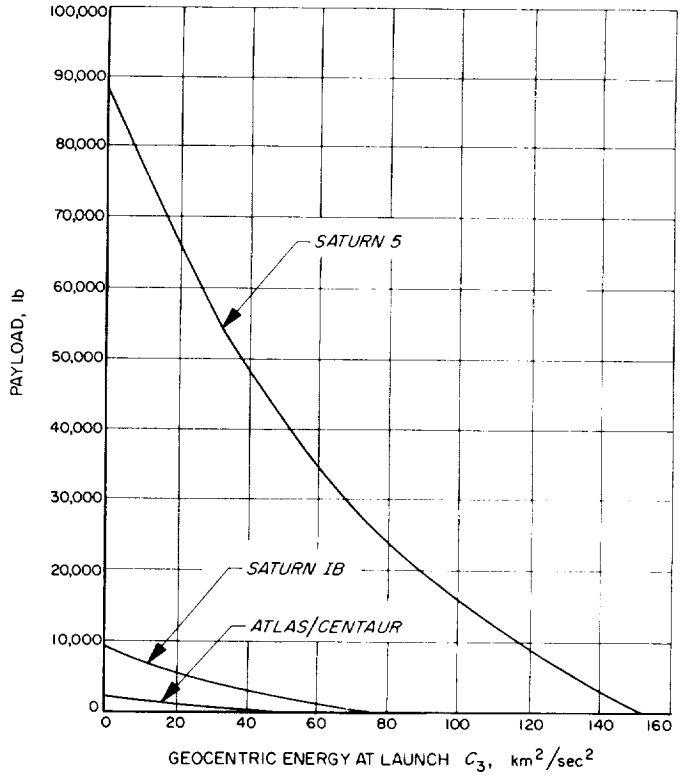

Fig. 3–11. Typical payload capability curves for *Atlas/Centaur*, *Saturn 1B*, and *Saturn 5* launch vehicles

Using the *Saturn 5* vehicle, the maximum payload that could be placed on an Earth–Jupiter trajectory is 26,000 lb.

D. Launch Period

The practical design of a mission to Mercury and Jupiter will involve the establishment of a launch period, i.e., a period of consecutive days on which launch is possible. On each day the trajectories would have to satisfy numerous constraints, such as those placed on energy, communication distance, flight time, etc. For most missions, constraints on arrival conditions would exist also.

As a first approximation, launch periods can be designed on the basis of geocentric energy, alone. Naturally, then, the minimum geocentric energy on every launch day is chosen. For each trajectory type the curves of minimum energy allow establishment of launch periods of arbitrary length centered around each of the

absolute minimum-energy launch dates given in Table 3–1. This selection has been carried out in Tables 3–2, 3–3, and 3–4 for several of the Earth–Mercury and Earth–Jupiter opportunities tabulated in Table 3–1.

For each trajectory type and class, launch periods of 15, 30, and 45 days were determined. Each launch period has a maximum geocentric energy associated with it. This maximum value is reached on the first and last day of each launch period and results in the lowest payload.

The minimum injection energy during the launch period can be found from the corresponding absolute minimum-energy trajectory in Table 3–1. It is of interest for orbiter missions since more fuel can be added to the retro tanks as the geocentric energy decreases during the launch period, resulting in closer orbits at the target planet. Table 3–2 also shows the variations, during the launch period, of the most important trajectory characteristics on which constraints are usually placed.

The Earth-to-target-planet flight times T_F will affect virtually every spacecraft subsystem. The communication distance at arrival R_C indicates the design of the communications system. The planetocentric asymptotic speed V_∞ is a measure of the speed of the spacecraft at the time of closest approach to the target and is important for both orbiter and flyby missions.

The geocentric asymptotic declination is included in Table 3–2 because it is an important parameter in determining the injection location over the Earth's surface. Acceptable values for this parameter are estimated to lie between −34 and +34 deg. Values outside this range result in severe restrictions for Cape Kennedy launchings.

As an example, note how the 45-day launch period November 21, 1968 to January 5, 1969, for Type II, Class I trajectories to Jupiter was found from the curve of minimum geocentric energy, Fig. 3–10. Starting with the launch date December 13, 1968 ($C_3 = 77.8$ km^2/sec^2), C_3 was increased until the range of launch dates was 45 days. These limits then defined the launch period and the corresponding maximum energy ($C_3 = 86.2$ km^2/sec^2) over the period.

Sometimes it happens that the curves of minimum geocentric energy corresponding to Type I and Type II trajectories intersect within the launch period for a given type. It then becomes possible to design launch periods during which both Type I and Type II trajectories would be used. The corresponding geocentric energies are lower than if either type were used alone.

E. General Characteristics of Trajectories

In order to gain further insight into the nature of Earth–Mercury and Earth–Jupiter trajectories, plots of several key trajectory variables were prepared for each of the launch opportunities. The relevant trajectory parameters can be categorized into three groups: geocentric, heliocentric, and planetocentric. Sections IV–XV show detailed plots of the following trajectory parameters, which are italicized:

1. Geocentric Parameters

During the geocentric phase, the magnitude and direction of the hyperbolic-excess velocity vector $\mathbf{V}_{hp}$, or the velocity vector of the spacecraft relative to the Earth at the time of injection into heliocentric orbit, are of principal interest.

The magnitude of $\mathbf{V}_{hp}$ is represented by the *geocentric energy at launch*, $C_3 = V_{hp}^2$. All plots of trajectory parameters show contours of constant and integral values of C_3.

The direction of $\mathbf{V}_{hp}$, also called the outgoing asymptote $\mathbf{S}$, is given relative to several coordinate systems. The *right ascension* Θ_s and *declination* Φ_s of the outgoing asymptote specify its direction relative to a geocentric equatorial coordinate system. The celestial latitude γ_L of $\mathbf{S}$ or the *angle between the geocentric asymptote and the launch planet's orbital plane* and the *angle between the Sun–Earth vector and outgoing geocentric asymptote* ζ_L specify the orientation of $\mathbf{S}$ relative to the heliocentric ecliptic coordinate system.

Obviously, the energy has a direct influence on spacecraft weight. The declination of the outgoing asymptote also severely restricts the interplanetary trajectories which are possible in a more complicated way.

2. Heliocentric Parameters

The following properties of heliocentric transfer ellipse are presented: *aphelion distance* R_a, *perihelion distance* R_p, and *inclination* i with respect to the ecliptic. The eccentricity e and semimajor axis a of the heliocentric ellipse can be found from these. Sections IV–XV show graphs of *true anomaly in the transfer ellipse at launch* V_L and *true anomaly in the transfer ellipse at arrival* V_p, as well as of their difference, the *heliocentric central angle* Ψ.

The Earth-to-target-planet *time of flight* T_F and *communication distance* R_C are of direct interest to designers of all spacecraft subsystems.

Table 3-2. Mercury transfer characteristics

Launch dates	Launch period, days	Maximum geocentric injection energy, $km^2/sec^2 \times 10^4$	Class I Trajectories								Class II Trajectories							
			Flight time, days		Communication distance, 10^6 km		Planetocentric asymptotic speed, km/sec		Declination of the geocentric asymptote, deg		Flight time, days		Communication distance, 10^6 km		Planetocentric asymptotic speed, km/sec		Declination of the geocentric asymptote, deg	
			Min	Max	Min	Max	Min	Max	Min	Max	Min	Max	Min	Max	Min	Max	Min	Max
Type I																		
11/16–12/1/67	15	0.4415	99	114	125	131	14.20	15.62	−18.0	−3.9	99	113	128	132	14.50	15.60	−26.0	−8.0
11/11–12/11/67	30	0.5685	88	115	114	133	15.60	20.15	−21.0	12.3	91	116	125	138	14.80	17.50	−39.0	12.3
11/5–12/20/67	45	0.8195	76	118	103	136	18.10	27.96	−23.0	16.0	84	119	116	144	15.10	20.07	−48.2	22.0
11/8–11/23/68	15	0.5902	91	103	127	139	13.90	16.74	−13.7	7.0	94	105	134	147	12.52	16.93	−43.8	8.0
10/31–11/30/68	30	0.7825	81	105	112	145	13.93	25.00	−23.3	9.3	87	107	123	151	13.81	18.86	−51.2	16.7
Type II																		
10/29–11/13/67	15	0.5367	119	132	127	146	12.90	15.80	−20.8	12.0	122	134	130	150	12.02	12.52	−4.5	12.0
10/23–11/22/67	30	0.5957	118	139	125	158	12.09	17.10	−25.2	18.4	122	141	130	162	12.48	15.10	−6.8	17.1
10/16–11/30/67	45	0.668	117	146	123	168	12.37	17.80	−28.7	21.9	118	148	130	172	12.76	18.31	−7.8	18.6
10/23–11/7/68	15	0.443	108	121	141	147	12.50	14.81	−27.8	−7.9	108	124	147	155	11.90	12.31	−13.8	−1.9
10/12–11/11/68	30	0.5305	106	134	137	160	12.15	16.68	−37.1	3.5	112	136	145	171	12.68	15.15	−15.0	5.6
10/4–11/18/68	45	0.6188	105	141	134	176	11.96	18.10	−44.5	10.1	115	143	143	181	12.88	18.86	−16.0	7.9

Table 3-3. Type I Jupiter transfer characteristics

Launch dates	Launch period, days	Maximum geocentric injection energy, $m^2/sec^2 \times 10^{-4}$	Class I Trajectories								Class II Trajectories							
			Flight time, days		Communication distance, 10^6 km		Planetocentric asymptotic speed, km/sec		Declination of the geocentric asymptote, deg		Flight time, days		Communication distance, 10^6 km		Planetocentric asymptotic speed, km/sec		Declination of the geocentric asymptote, deg	
			Min	Max	Min	Max	Min	Max	Min	Max	Min	Max	Min	Max	Min	Max	Min	Max
11/27–12/12/68	15	0.8782	729	990	648	949	5.62	7.74	21.9	25.5	768	998	651	900	5.61	7.20	24.8	29.7
11/24–12/24/68	30	0.9161	666	1190	651	957	5.58	8.88	20.0	25.5	735	1197	652	940	5.60	7.70	21.0	33.4
11/22/68–1/6/69	45	0.9491	632	1378	630	957	5.60	9.67	−1.0	25.5	715	1384	632	946	5.62	8.00	−10.0	35.8
12/27/69–1/11/70	15	0.7882	811	1038	632	854	5.74	6.66	−7.8	6.3	850	1044	634	882	5.74	6.40	−19.5	8.5
12/21/69–1/20/70	30	0.8622	671	1118	636	938	5.75	8.72	−11.8	7.8	760	1128	628	920	5.82	7.30	−28.0	17.8
12/15/69–1/29/70	45	0.9581		1180	632		5.78		−15.0	9.9	715	1205	628		5.90	8.00	−33.8	25.2
1/24–2/8/71	15	0.8020	714	870	637	920	6.15	7.76	−23.0	−16.2	767	899	611	885	6.03	7.20	−30.1	−22.5
1/18–2/17/71	30	0.8735	624	970	609	920	5.90	9.54	−25.0	−12.9	725	994	611	912	5.89	7.71	−39.0	−24.5
1/12–2/26/71	45	0.9788	550	1076	609	920	5.93	11.51	−28.5	11.1	688	1095	611	919	6.13	8.40	−46.5	24.5
2/28–3/4/72	15	0.8407	651	810	737	900	6.45	8.56	−36.4	−29.6	700	840	680	900	6.27	7.80	−43.0	−35.5
2/22–3/23/72	30	0.9165	574	920	600	900	6.05	10.39	−38.0	−26.5	665	944	596	899	6.03	8.50	−51.0	−37.0
2/17–4/2/72	45	1.0239	514	1048	595	900	6.05	12.30	−40.0	−24.7	635	1060	595	900	6.14	9.10	−58.1	−39.0
4/5–4/20/73	15	0.8680	629	800	765	890	6.35	8.58	−39.5	−34.1	675	826	705	891	6.21	7.80	−45.1	−39.2
3/30–4/29/73	30	0.9387	558	930	592	890	6.02	10.35	−40.5	−31.1	640	945	592	890	6.02	8.50	−51.8	−40.0
3/26–5/10/73	45	1.0285	505	1061	592	890	6.04	12.00	−41.0	−29.3	620	1076	592	892	6.11	9.02	−57.5	−40.2

Table 3-4. Type II Jupiter transfer characteristics

Launch dates	Launch period, days	Maximum geocentric injection energy, $m^2/sec^2 \times 10^4$	Class I Trajectories								Class II Trajectories							
			Flight time, days		Communication distance, 10^6 km		Planetocentric asymptotic speed, km/sec		Declination of the geocentric asymptote, deg		Flight time, days		Communication distance, 10^6 km		Planetocentric asymptotic speed, km/sec		Declination of the geocentric asymptote, deg	
			Min	Max	Min	Max	Min	Max	Min	Max	Min	Max	Min	Max	Min	Max	Min	Max
12/6–12/21/68	15	0.7860	1192	1375	630	810	5.77	6.47	−3.8	2.1	1205	1395	630	817	5.79	6.50	−2.5	2.0
11/30–12/30/68	30	0.8062	1123		630	934	5.63		−7.8	4.5	1140		630	925	5.65		−3.7	2.5
11/21/68–1/5/69	45	0.8620	1029		631	940	5.60		−14.1	9.0	1050		630	940	5.59		−5.2	
12/25/69–1/9/70	15	0.7759	955	1210	664	921	5.70	6.05	−13.7	6.2	970	1215	682	919	5.70	6.08	−8.5	1.00
12/21/69–1/20/70	30	0.8039	926	1375	612	919	5.71	6.84	−18.8	11.0	940	1392	609	919	5.71	6.86	−9.7	−0.60
1/30–2/14/71	15	0.8367	1095	1290	600	900	6.01	6.77	−4.1	−0.5	1099	1291	597	897	6.04	6.78	−5.7	−3.0
1/25–2/24/71	30	0.8462	1025		595	900	5.89	7.37	−6.0	1.9	1030		595	899	5.90	7.38	−7.4	−3.0
1/21–3/7/71	45	0.8655	959		595	900	5.90			4.8	965		595	900	5.88			−4.0
3/19–4/3/72	15	0.8625	1270		591		6.93			−3.7	1275		596		6.94			−5.0
3/7–4/6/72	30	0.8835	1123		591		6.34			0.2	1132		590		6.36			−4.0
2/24–4/9/72	45	0.9340	988		591		6.03			5.8	1000		592		6.04			−4.5
5/4–5/19/73	15	0.8412	1329	1475	630		7.18	7.73	−4.1	−1.9	1335	1480	634		7.20	7.74	−4.1	−2.5

The *celestial latitude at arrival time* β_p is referred to the ecliptic plane.

3. Planetocentric Parameters

The direction of the approach hyperbolic-excess velocity vector $\mathbf{V}_{hp}$, or velocity of the spacecraft with respect to the target planet at arrival, is described in several coordinate systems.

The *right ascension* Θ_p and *declination* Φ_p of the unit vector along $\mathbf{V}_{hp}$, also known as the approach or incoming asymptote **S**, are referred to the Earth's equatorial plane. The *angle between the incoming asymptote and the arrival planet's orbital plane* γ_p and the *angle between the target planet–Sun vector and the incoming-planet-centered asymptote* ζ_p relate the incoming asymptote direction to the orbital plane of the target planet. The *angle between the planet–Earth vector and the incoming asymptote* ζ_E defines the motion of the spacecraft relative to the Earth–planet line a few days prior to encounter. The *angle between the planet–Canopus vector and the incoming asymptote* ζ_C is of importance because Canopus will most likely be the second attitude reference for these missions, in addition to the Sun.

The magnitude of $\mathbf{V}_{hp}$, *the asymptotic speed with respect to the target planet* V_{hp}, is of great importance for orbiter, lander, and multiplanet missions.

F. Discussion of Earth–Mercury and Earth–Jupiter Trajectory Parameters[9]

1. Declination of the Geocentric Asymptote Φ_s

Equation (2–60) defined an inequality between Φ_s, Σ_L (the launch azimuth), and Φ_L (the latitude of the launch site):

$$\sin^2 \Sigma_L \leqq \frac{\cos^2 \Phi_s}{\cos^2 \Phi_L}$$

The regions within which launch from Cape Kennedy can occur are shown in Fig. 3–12 as a function of Σ_L. Usually, the launch azimuth will be restricted to lie within certain bounds established by range safety considerations (typically 90 to 114 deg).

For the two Mercury opportunities considered (1967, 1968), the declination constraint does not restrict the Type I–Class I trajectories, which have the shortest flight times. The constraint does eliminate a substantial part of the other trajectories (i.e., Type I–Class I and Type II–Class I and II). This can be seen from the corresponding plots of Φ_s vs launch date (Figs. 4–5, 5–5).

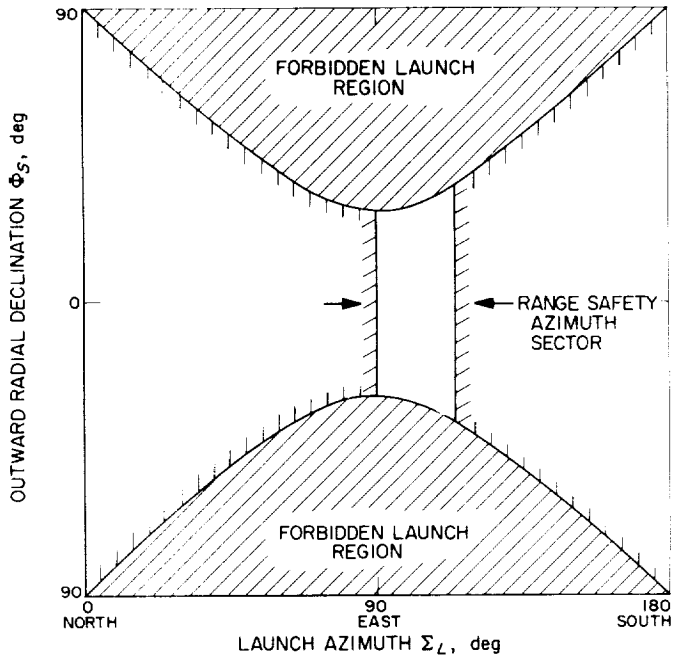

Fig. 3–12. Permissible regions of the declination of the geocentric asymptote Φ_s for Cape Kennedy launchings

For the 1968–69, 1969–70, and 1970–71 Jupiter opportunities, the declination constraint does not restrict the possible Type I–Class I trajectories (see Figs. 6–5, 7–5, 8–5). In 1972 and 1973 it becomes almost impossible to use this kind of trajectory (see Figs. 9–5, and 10–5). In fact, in 1972 and 1974 only the Type II–Class I trajectories are not affected by the declination constraint. All other trajectory types are severely restricted by the constraint.

2. Angle Between the Sun–Earth Vector and the Outgoing Geocentric Asymptote ξ_L

This quantity, which is of importance for spacecraft using the Earth and Sun as attitude references, takes on values between 80 and 130 deg for the 1967 Mercury Type I trajectories (45 to 110 deg for Type II trajectories; see Fig. 4–8). It takes on approximately the same range of values during the 1968 Mercury opportunity owing to the fact that the Earth–Sun–Mercury constellation is about the same for both opportunities. The quantity varies between 45 and 120 deg for the five Jupiter opportunities considered herein (1968–69, 1969–70, 1970–71,

[9] A detailed discussion of the influence of the trajectory parameters on trajectory design is presented in Ref. 8 (Section III.D). The following material is intended as supplementary to that presented in Ref. 8 and 9.

1972, 1973) for energies less than 120 km²/sec². In all cases, it decreases with increasing launch date.

3. Celestial Latitude of the Geocentric Asymptote γ_L

This quantity, referred to in the graphs as the angle between the outgoing geocentric asymptote and the launch planet's orbital plane, is strongly dependent on the celestial latitude at arrival time β_P. (See Ref. 1, page 35. Fig. 3–14 of Ref. 8 applies for Earth–Mercury trajectories as well as for Earth–Venus trajectories.)

For the Mercury opportunities in 1967 and 1968, the target planet is relatively close to the ecliptic at encounter, which causes γ_L to take on values on the order of 10 deg. For Jupiter, γ_L can take on values between −45 to +45 deg for the energy range considered herein. Note that the Type I–Class I trajectories, which have the shortest flight times, all lie very close to the ecliptic. The Type II–Class II trajectories, which correspond to the longest flight time, also show this characteristic.

It might be asked how γ_L can take on such high values in spite of the fact that Jupiter's inclination is only 2.5 deg. In Ref. 8, page 34, it is shown that

$$\sin \gamma_L = \frac{V_L \cos \Gamma_L \sin i}{V_{h_L}}$$

where V_L is the heliocentric velocity at launch, V_{h_L} is the hyperbolic-excess velocity at launch, Γ_L is the heliocentric path angle at launch, and i is the inclination of the trajectory. The magnification factor V_L/V_{h_L} is on the order of 4 for Earth–Jupiter trajectories.

4. True Anomaly at Launch and Arrival and Heliocentric Transfer Angle

In general, low-energy elliptic heliocentric orbits from the Earth to the inner planets (Mercury, Venus) will have aphelion distance on the order of 1 au (astronomical unit) and perihelion distances on the order of the distance between the target planet at the Sun (0.3 au for Mercury). Consequently, launch will occur near aphelion (true anomaly $V_L = 180$ deg) and arrival near perihelion (true anomaly $V_P = 0$ deg). Figures 4–9 and 5–9 show that the variation in V_L is small, 160 to 200 deg for Type I and Type II Mercury trajectories. Note that launch occurs before aphelion at the beginning of the launch period, and after aphelion at the end of the launch period, as was the case for Earth–Venus trajectories.

Employing the same reasoning, low-energy trajectories to the outer planets (Mars, Jupiter, etc.) have perihelion distances on the order of 1 au and aphelion distances on the order of the Sun–target planet distance. Figures 6–9, 7–9, 8–9, and 10–9 show that for an Earth–Jupiter trajectory, the true anomaly at launch remains within 30 deg of perihelion ($V_L = 0$ deg). Figures 6–10, 7–10, 8–10, 9–10, and 10–10 show that the Jupiter encounter can take place from about 40 deg before to 30 deg after aphelion.

Figures 4– through 10–3 show the variation in the heliocentric transfer angle Ψ, or the difference between the true anomalies at launch and encounter, for Earth–Mercury and Earth–Jupiter trajectories, respectively. Note that none of the Type I or Type II contours intersect the $\Psi = 180$ deg line.

5. Aphelion and Perihelion of the Transfer Orbit

Figures 4–12 and 5–12 show that for Earth–Mercury trajectories the aphelion distance (point farthest from the Sun) varies from 1 au by less than 10%. The perihelion distances show stronger variations (Figs. 4–11 and 5–11). As mentioned in Ref. 8, the probe passes aphelion after launch if the true anomaly at launch is less than 180 deg; it passes perihelion before arrival (i.e., passes within Mercury's orbit) if the true anomaly at arrival is positive.

For Earth–Jupiter transfer, the perihelion distance does not change drastically (Figs. 6– to 10–11). Note, however, that the aphelion distances can become as large as 2400×10^6 km, or over 3 times the Sun–Jupiter distance for geocentric energies $C_3 = 120$ km²/sec² (Figs. 6– through 10–12). The plots of true anomaly show that aphelion would take place after Jupiter encounter. Owing to the exceptionally large mass of Jupiter, it will exert a very strong perturbation on the trajectory during encounter.

6. Time of Flight

Typical Earth–Mercury flight times range from 80 to 160 days, as is shown in Figs. 4–2 and 5–2. As the launch date progresses, it is seen that flight times are shortened for both Type I and Type II trajectories. Type II trajectories offer lower energies and larger launch windows for a given energy, with only a slight penalty in flight time.

Flight times to Jupiter are on the order of 1 to 4 years (Figs. 6– through 10–2). As launch date is delayed, flight time increases substantially for a given energy.

7. Communication Distance

For Mercury trajectories, the communication distance at encounter increases as launch date is delayed, whereas flight time decreases. The communication distance can take on values between 100×10^6 km to 180×10^6 km (see Figs. 4–4 and 5–4).

The communications distances at Jupiter arrival extend from 650×10^6 km to 950×10^6 km. Since the Sun–Jupiter distance is 740×10^6 km and the Earth–Sun distance is 150×10^6 km, it is clear that if the communications distance at encounter is around 890×10^6 km, the Sun will lie very close to the Jupiter–Earth line (see Figs. 6– through 10–4).

8. Inclination of the Heliocentric Transfer Plane i and Celestial Latitude at Arrival β_p

The inclination i of the heliocentric transfer orbit to the ecliptic plane is essentially a function of two parameters, (1) the heliocentric central angle Ψ, and (2) the celestial latitude β_p of the planet at arrival, since

$$\sin i = \left| \frac{\sin \beta_p}{\sin \Psi} \right|$$

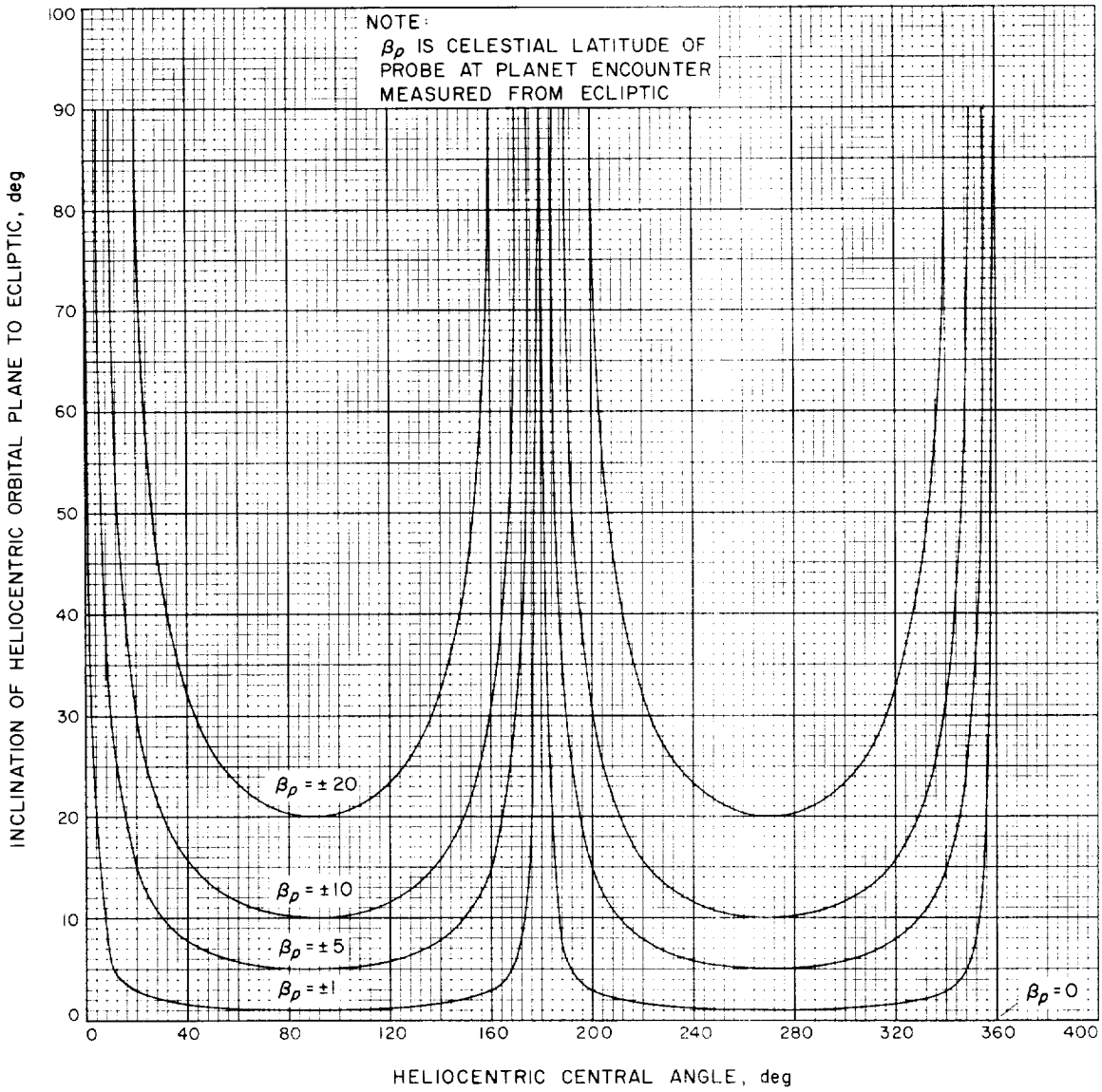

Fig. 3–13. Inclination of the heliocentric orbital plane to ecliptic vs heliocentric central angle

If the heliocentric central angle is fixed, and the absolute magnitude of the celestial latitude at arrival is increased, the inclination also increases. If the celestial latitude of the planet at arrival is zero, the inclination is equal to zero, no matter what the heliocentric central angle may be (with the exception of a central angle of 180 deg). However, as shown in Fig. 3–13, if the celestial latitude β_p of the planet at encounter is fixed at an absolute value greater than zero, and the central angle is varied, the inclination will reach its minimum value (equal to β_p) at central angles of 90 and 270 deg, or its maximum value of 90 deg at the central angles equal to β_p, $180-\beta_p$, $180+\beta_p$, and $360-\beta_p$. It is because of the fact that the inclination increases near the central angles of $180 \pm \beta_p$ that Type I–Class II and Type II–Class I trajectories come into existence. The increasing heliocentric inclination eventually results in a sharp increase in energy C_3 as the central angle approaches 180 deg $\pm\beta_p$, thereby bringing the two groups of energy contours into existence. It may now become apparent that the inclination of the heliocentric orbital plane may take on values greater than the celestial latitude of the planet at arrival because of the varying heliocentric central angle.

For the Mercury and Jupiter trajectories considered herein the inclination can be as high as 12 deg. By definition, inclination is positive, whether encounter takes place above or below the ecliptic. Figures 4–13 and 5–13 show inclination vs launch date for Mercury. Figures 6– through 10–13 show this parameter for Earth–Jupiter transfers.

9. Asymptotic Approach Speed V_{h_p}

Figures 4–15 and 5–15 show that the variation in asymptotic speed with respect to Mercury is from 12 to 24 km/sec for both Type I and Type II trajectories. Type I–Class I trajectories (shortest flight times) have higher approach speeds than Type I–Class II trajectories. It will be recalled that approach speeds to Venus were on the order of 3.75–10.7 km/sec.

Approach speeds to Jupiter lie in the range of 5.5–14 km/sec. The lowest asymptotic approach speeds are obtained using Type I–Class II or Type II–Class I trajectories, shown in Figs. 6– through 10–15.

10. Angle Between the Incoming Asymptote and the Arrival Planet's Orbital Plane γ_p

For Mercury, Type I–Class I and Type II–Class II trajectories have values of γ_p in the range -10 to $+30$ deg. This angle can become as large as 60 deg for the other trajectories, as is explained in Ref. 8, page 51. (See Figs. 4–16 and 5–16.) For Jupiter trajectories, γ_p remains on the order of 15 deg or less for all opportunities. It takes on values on the order of 5 deg for Type I–Class I and Type II–Class II trajectories. (See Figs. 6– through 10–16.)

11. Angle Between the Arrival Planet–Sun Vector and the Incoming Asymptote ξ_p

For Mercury Type I trajectories, the angle ζ_p is acute, whereas it varies between 60 and 160 deg for Type II trajectories. (See Figs. 4-17 and 5-17.) This angle is of considerable importance in the analysis of postencounter Jupiter trajectories (see Section III.F). As was shown for the Mars case in Ref. 8, page 51, ζ_p values for Type I–Class I trajectories are obtuse at the beginning of the launch windows and become acute at the end of the launch windows. The angle is smaller for the other Jupiter trajectories as is shown in Figs. 6 through 10-17.

Figure 3–14 shows the illuminated crescent orientations at arrival for various values of ζ_p. Figures 3–15a and 3–15b show near-planet geometries for Type I and Type II approach trajectories to Mercury and Jupiter, respectively.

Figures 3–16a and 3–16b show these trajectories as viewed by an observer in inertial space.

12. Right Ascension Θ_p and Declination Φ_p of the Incoming Planet-Centered Asymptote

For Mercury trajectories, Θ_p takes on values from 300 to 355 deg. Right ascension $\Theta_p = 360$ deg corresponds to the vernal equinox direction, or direction of the Sun–Earth vector at the beginning of spring. The declination Φ_p measured relative to the Earth's equator, varies from -40 to $+40$ deg.

For the Jupiter trajectories, there is a considerable variation in Θ_p for different launch opportunities: 160 to 185 deg (1968–69), 290 to 320 deg (1973). The corresponding variations in Φ_p are -8 to 22 deg (1968–69) and -36 to -8 deg (1973), respectively.

13. Angle Between the Planet–Earth Vector and the Incoming Asymptote ζ_E

Plots of this parameter are not available for the Mercury trajectories at this time. The angle ζ_E is equivalent to the Earth–probe–target-planet angle a few days before arrival. The angle $\zeta_E = 180$ deg corresponds to motion along the Earth–target-planet line, away from the Earth, during the

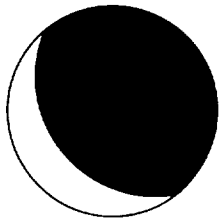

(a) MERCURY TYPE I TRAJECTORY (γ_p > 0 deg)
ENCOUNTER BEFORE PERIHELION

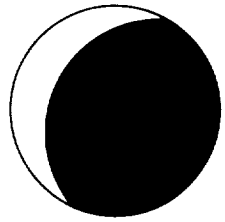

(b) MERCURY TYPE I TRAJECTORY (γ_p < 0 deg)
ENCOUNTER BEFORE PERIHELION

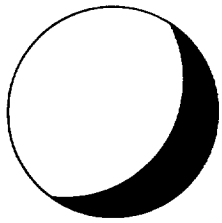

(c) MERCURY TYPE II TRAJECTORY (γ_p > 0 deg)
ENCOUNTER AFTER PERIHELION

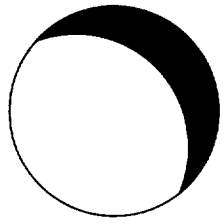

(d) MERCURY TYPE II TRAJECTORY (γ_p < 0 deg)
ENCOUNTER AFTER PERIHELION

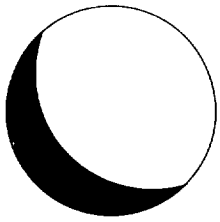

(e) JUPITER TYPE I TRAJECTORY (γ_p > 0 deg)
ENCOUNTER BEFORE APHELION

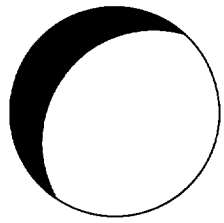

(f) JUPITER TYPE I TRAJECTORY (γ_p < 0 deg)
ENCOUNTER BEFORE APHELION

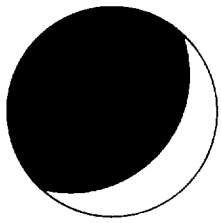

(g) JUPITER TYPE I TRAJECTORY (γ_p > 0 deg)
ENCOUNTER AFTER APHELION

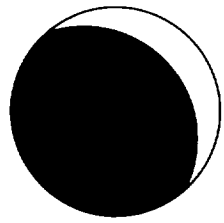

(h) JUPITER TYPE I TRAJECTORY (γ_p < 0 deg)
ENCOUNTER AFTER APHELION

Fig. 3–14. Crescent orientations for typical trajectories to Mercury and Jupiter as observed from approaching spacecraft

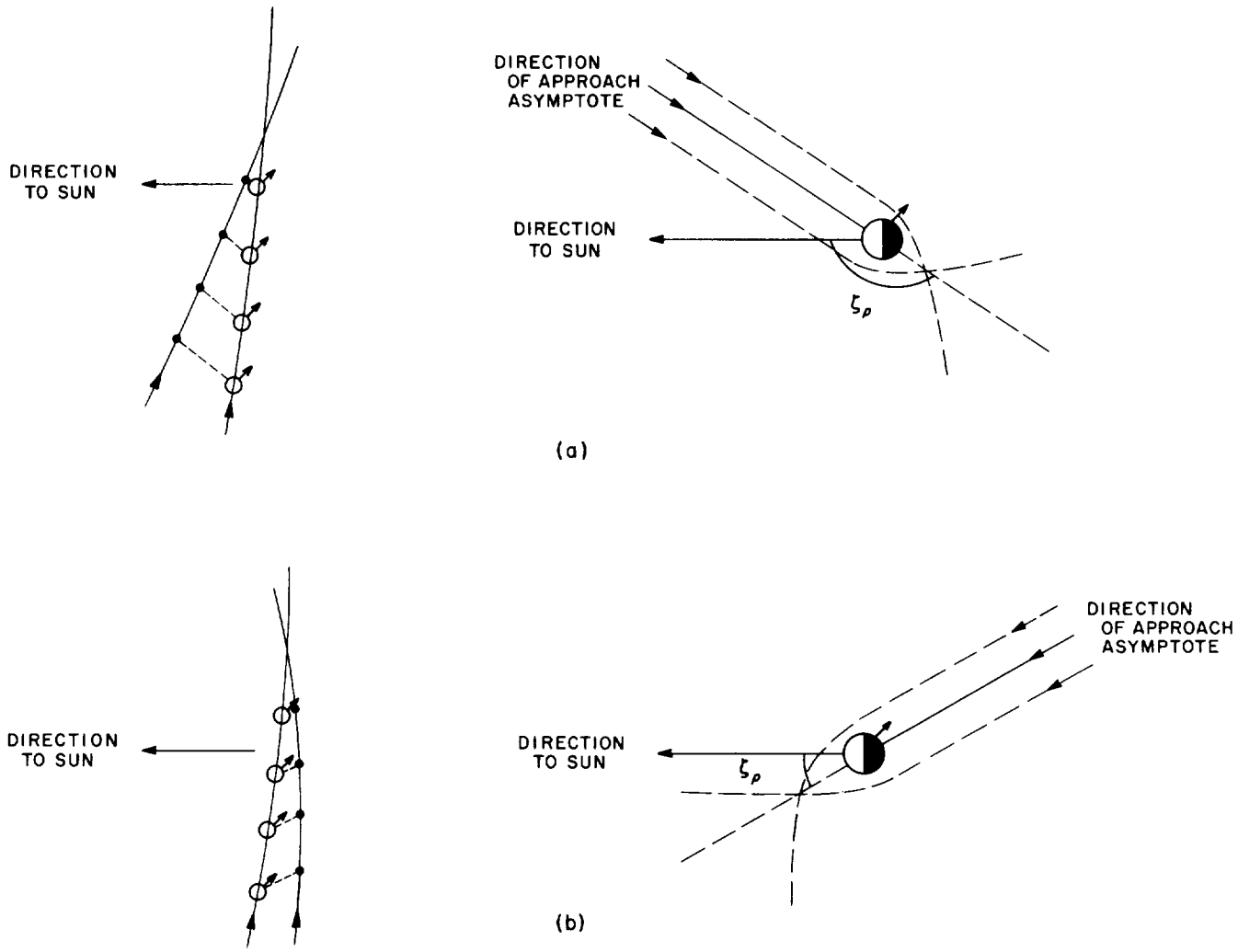

Fig. 3–15. Near-Jupiter geometry for typical trajectories, viewed from above ecliptic plane: (a) Type I trajectory, encountering Jupiter before aphelion; (b) Type I–II trajectory, encountering Jupiter after aphelion

last few days before target-planet encounter; $\zeta_E = 180$ deg means that the probe will be occulted from view of the Earth because of bending of the trajectory by the target planet. Figures 6– through 10–20 show that this parameter varies between 60 and 160 deg for Earth–Jupiter trajectories.

14. Angle Between the Planet–Canopus Vector and the Incoming Asymptote ζ_c

Plots of ζ_c are not available for Earth–Mercury transfers at this time. For Earth–Jupiter transfers, the ranges of ζ_c are 75–150 deg (1968–69), 20–50 deg (1970–71), 0–20 deg (1972), 90–118 deg (1973), respectively; $\zeta_c = 0$ deg indicates that the spacecraft will approach Jupiter along the spacecraft–Jupiter–Canopus line. (See Figs. 6– through 10–21.)

G. Procedures for Utilization of Graphs in Design of Planetary Trajectories

For a trajectory design, a source of information must be available which can be quickly scanned to determine the range of feasible trajectories for a mission. The graphs presented in Sections IV to X of this report constitute such a source. The order and procedure for actual use of these graphs by the trajectory engineer in the design and analysis of trajectories are now reviewed.

(1) Both Type I and Type II transfers should be scanned. Those trajectories should be selected for which the declination of the outgoing geocentric asymptote lies roughly between −34 and +34 deg. These are the feasible trajectories for launchings from AFETR. The algebraic value of the declina-

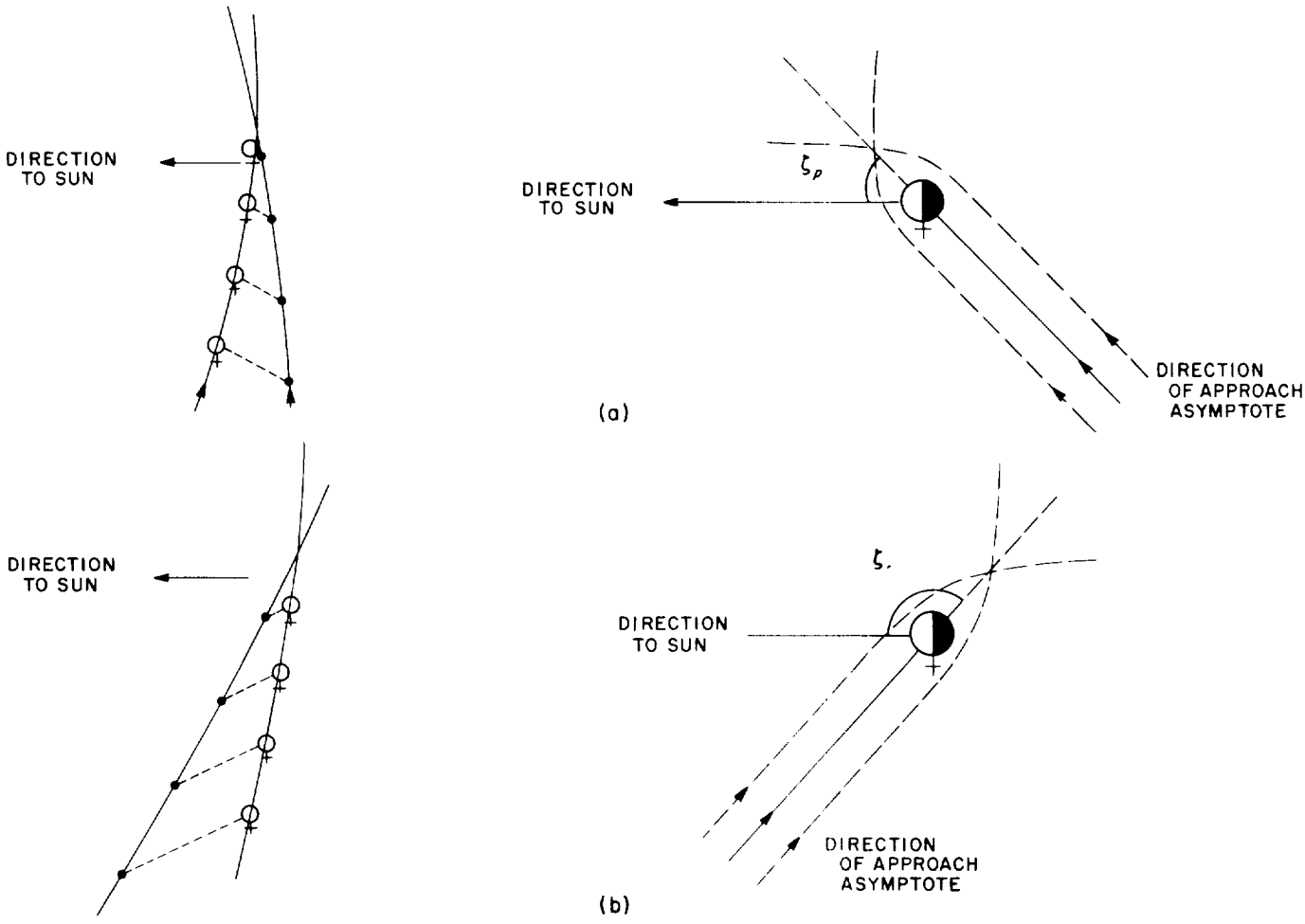

Fig. 3–16. Near-Mercury geometry for typical trajectories, viewed from above ecliptic plane: (a) Type I trajectory, encountering Mercury before perihelion; (b) Type II trajectory, encountering Mercury after perihelion

tion reveals vital information concerning the pre-injection trajectory (see Section III.E.1).

(2) For the trajectories of paragraph (1), the energy requirements (C_3) for various firing periods should be observed. If it is found that booster payload capability and the desired payload weight match the required injection energy for a given firing period (for example, 30 days) and also satisfy paragraph (1) for Type I and Type II trajectories, a decision must then be made to utilize either Type I or Type II trajectories or, perhaps, both (see Section III.D).

(3) In making the decision to utilize either the Type I or the Type II trajectory, or both, the curves of flight time and Earth–probe communication distance vs launch date are most helpful. In general, Type II trajectories have longer flight times and Earth–probe distances at encounter than do Type I. The actual differences in magnitude depend on the mission and range of injection energy. In general, the longer the flight time the greater is the sensitivity of the trajectory to injection errors.

(4) Next, the parameter ζ_L, the angle between the outgoing asymptote and the Sun–Earth vector at heliocentric injection, should be studied. It will be recalled that this is equivalent to the Earth–probe–Sun angle at a few days after launch. Since there are usually many limitations on a spacecraft which is stabilized and controlled in attitude by optical references (such as the Earth, Sun, and Canopus), the Earth–probe–Sun angle may be restricted near the Earth and, perhaps, throughout the flight. The parameter ζ_L is most helpful in trajectory design for determining the constraint near the Earth.

(5) If the value of ζ_L is less than 90 deg for Mercury trajectories, the probe is usually being injected into the heliocentric-transfer orbit before aphelion and will travel outside the Earth's orbit before "falling" in toward Mercury. To be precise, one can observe the curves of true anomaly at launch. Because of temperature-control problems, there may be a restriction on the maximum Sun–probe distance during flight. To determine this maximum distance during flight, one simply finds the aphelion distance of the probe from the graphs. If ζ_L is greater than 90 deg, then the maximum distance during flight to Mercury is essentially the Sun–probe distance at launch.

(6) If the value of ζ_L is greater than 90 deg for Jupiter trajectories, the probe is usually being injected into the heliocentric-transfer orbit before perihelion and will "fall" inside the Earth's orbit before traversing out to Jupiter. Temperature-control considerations may restrict the minimum Sun–probe distance during flight. To determine the minimum distance, simply find the perihelion of the probe's transfer orbit for the desired trajectory or range of trajectories. If ζ_L is less than 90 deg, the minimum Sun–probe distance during flight to Jupiter is the distance at launch.

(7) For a spacecraft stabilized and controlled in attitude by Sun and Earth optical references, a constraint may exist which will restrict the Earth–probe–Sun angle to a value greater than 0 deg by a few degrees or less than 180 deg by a few degrees. This immediately implies that a trajectory must be chosen that has an inclination of the heliocentric orbital plane to the ecliptic which is *greater than 0 deg*. To satisfy the above constraint, the inclination may have to be 0.25, 0.50, or even 1.0 deg, depending on the restriction and on the trajectory itself. The values of the orbital inclinations for specific trajectories can be found from the graphs in Sections IV to X.

(8) For essentially all feasible Type II trajectories to Mercury and a few of Type I, Mercury encounter for some missions will take place *after* perihelion of the transfer orbit. This means that the probe will pass closest to the Sun several days or, perhaps, several weeks before encounter, depending on the trajectory. Because of temperature-control requirements, there may be a restriction on the minimum Sun–probe distance during flight. To determine the value of this parameter, one finds the perihelion distance of the probe for the desired trajectory from the graphs. This parameter is the minimum Sun–probe distance during flight to Mercury if the true anomaly of arrival is in the first or second quadrant.

(9) For Type I trajectories to Jupiter, encounter usually takes place before aphelion of the transfer orbit. For those trajectories having true anomalies at arrival in the third or fourth quadrant, however, encounter will take place after aphelion. This means that the maximum Sun–probe distance during flight occurs before encounter. Temperature-control considerations may restrict the maximum Sun–probe distance during flight. To determine this maximum for the necessary trajectories, find the value of the aphelion distance from the graphs in Sections VI to X.

(10) For planetary missions such as landers or orbiters, it will probably become necessary to utilize trajectories for which the hyperbolic-excess speed at the planet is nearly minimum. In fact, in order to maximize the scientific-payload weight, a "tradeoff" must be made in minimizing the geocentric energy or planetocentric energy. Such trajectories will allow the heaviest payloads to be landed on the planet or injected in a desired elliptical orbit around the planet with the use of retro-maneuvers. The trajectory designer can find the values of the hyperbolic-excess speeds at the planet for various trajectories from the graphs in Sections IV to X, and can determine the feasibility of the trajectories from the procedures in paragraphs (1) to (9).

(11) For a spacecraft which is stabilized and controlled in attitude by optical references, there may be certain restrictions on the Sun–probe–planet angle as the probe approaches the planet. Such restrictions may be necessary because of approach-guidance considerations. The parameter ζ_p, the angle between the approach asymptote and the target-planet–Sun vector, is equivalent to the Sun–probe–planet angle a few days before encounter. The parameter can be most helpful in analyzing permissible trajectories near the planet.

(12) Regarding the design of trajectories near the planet, it is needless to say that, by altering the parameters in the preinjection trajectory near Earth by small increments, the probe can be made to pass on any side of the planet. However, the inclinations of the planetocentric hyperbolic orbit (or elliptical orbit, assuming that the required retro-maneuver is made

in the orbital plane of the hyperbola) to the planet's orbital plane depends on the aiming point at the planet, as well as on the parameter γ_p, the angle between the approach asymptote and the planet's orbital plane. The minimum inclination which can be attained is equal to γ_p. If γ_p is zero, the inclination of the orbit to the planet's orbital plane will range from 0 to 180 deg, depending on the aiming point. Inclinations of 0 to 90 deg imply direct motion (in the direction of the planet's orbital rotation), whereas inclinations from 90 to 180 deg imply retrograde motion (opposite to the planet's orbital rotation). If γ_p $+45$ deg, the inclination may range from 45 to 135 deg for all aiming points. If γ_p $+90$ deg, the inclination will equal 90 deg for any aiming point which is chosen at the planet. For $\gamma_p > 0$ deg, the probe will approach the planet from a path below the planet's orbital plane; for $\gamma_p < 0$ deg, the approach will be from above. In many cases, it may be desirable to design the near-planet trajectory with a prescribed inclination in mind such that the probe will pass the target body in the planet's orbital or, perhaps, equatorial plane. It is thus apparent that the parameter γ_p may or may not permit the selected pass. To find the value of γ_p for a given trajectory, observe the curve of γ_p vs launch date for the desired mission.

(13) To comprehend fully the significance of each parameter and its variation with launch date and arrival date, it may be advantageous to construct the loci of constant arrival dates on each pertinent graph in Sections IV to X. This may be done in three steps, as shown in Fig. 3–17.

(a) Construct the loci of desired arrival dates on the curves of flight time vs launch date.

(b) Mark the launch dates and geocentric energies for which intersection of the arrival loci and the various energy contours occur.

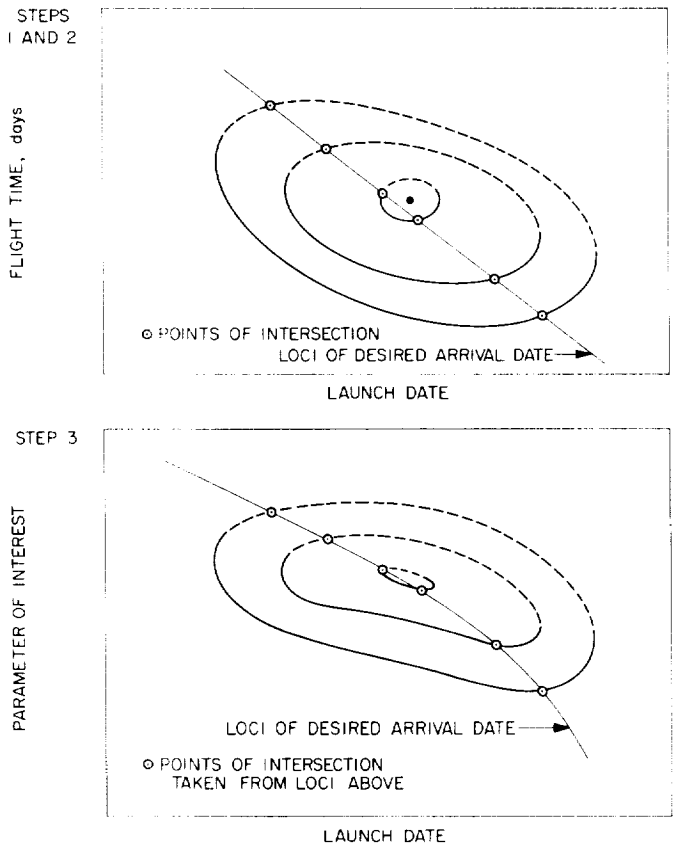

Fig. 3–17. Steps for construction of arrival date loci

(c) Take the intersection points of (b) and construct the arrival-date loci on the graph of interest.

Experience has shown that trajectory parameters tend to exhibit an invariance if the arrival date is held fixed while the launch date is varied. This fact has proved very useful in trajectory design.

IV. MERCURY 1967: TRAJECTORY PARAMETER GRAPHS

Figure

4–1. Mercury 1967: Minimum injection energy vs launch date

4–2. Mercury 1967: Time of flight vs launch date

4–3. Mercury 1967: Heliocentric central angle vs launch date

4–4. Mercury 1967: Earth-Mercury communication distance vs launch date

4–5(I). Mercury 1967: Declination of the geocentric asymptote vs launch date, Type I

4–5(II). Mercury 1967: Declination of the geocentric asymptote vs launch date, Type II

4–6(I). Mercury 1967: Right ascension of the geocentric asymptote vs launch date, Type I

4–6(II). Mercury 1967: Right ascension of the geocentric asymptote vs launch date, Type II

4–7(I). Mercury 1967: Angle between outgoing geocentric asymptote and launch planet's orbital plane vs launch date, Type I

4–7(II). Mercury 1967: Angle between outgoing geocentric asymptote and launch planet's orbital plane vs launch date, Type II

4–8(I). Mercury 1967: Angle between Sun–Earth vector and outgoing geocentric asymptote vs launch date, Type I

4–8(II). Mercury 1967: Angle between Sun–Earth vector and outgoing geocentric asymptote vs launch date, Type II

4–9(I). Mercury 1967: True anomaly in transfer ellipse at launch time vs launch date, Type I

4–9(II). Mercury 1967: True anomaly in transfer ellipse at launch time vs launch date, Type II

4–10. Mercury 1967: True anomaly in transfer ellipse at arrival time vs launch date

4–11(I). Mercury 1967: Perihelion of transfer orbit vs launch date, Type I

4–11(II). Mercury 1967: Perihelion of transfer orbit vs launch date, Type II

4–12(I). Mercury 1967: Aphelion of transfer orbit vs launch date, Type I

4–12(II). Mercury 1967: Aphelion of transfer orbit vs launch date, Type II

4–13(I). Mercury 1967: Inclination of the heliocentric transfer plane vs launch date, Type I

4–13(II). Mercury 1967: Inclination of the heliocentric transfer plane vs launch date, Type II

4–14. Mercury 1967: Celestial latitude at arrival time vs launch date

IV. MERCURY 1967: TRAJECTORY PARAMETER GRAPHS (Cont'd)

Figure

4–15(I). Mercury 1967: Asymptotic speed with respect to Mercury vs launch date, Type I

4–15(II). Mercury 1967: Asymptotic speed with respect to Mercury vs launch date, Type II

4–16(I). Mercury 1967: Angle between incoming hermiocentric asymptote and arrival planet's orbital plane vs launch date, Type I

4–16(II). Mercury 1967: Angle between incoming hermiocentric asymptote and arrival planet's orbital plane vs launch date, Type II

4–17. Mercury 1967: Angle between Mercury–Sun vector and incoming hermiocentric asymptote vs launch date

4–18(I). Mercury 1967: Declination of the hermiocentric asymptote vs launch date, Type I

4–18(II). Mercury 1967: Declination of the hermiocentric asymptote vs launch date, Type II

4–19(I). Mercury 1967: Right ascension of hermiocentric asymptote vs launch date, Type I

4–19(II). Mercury 1967: Right ascension of hermiocentric asymptote vs launch date, Type II

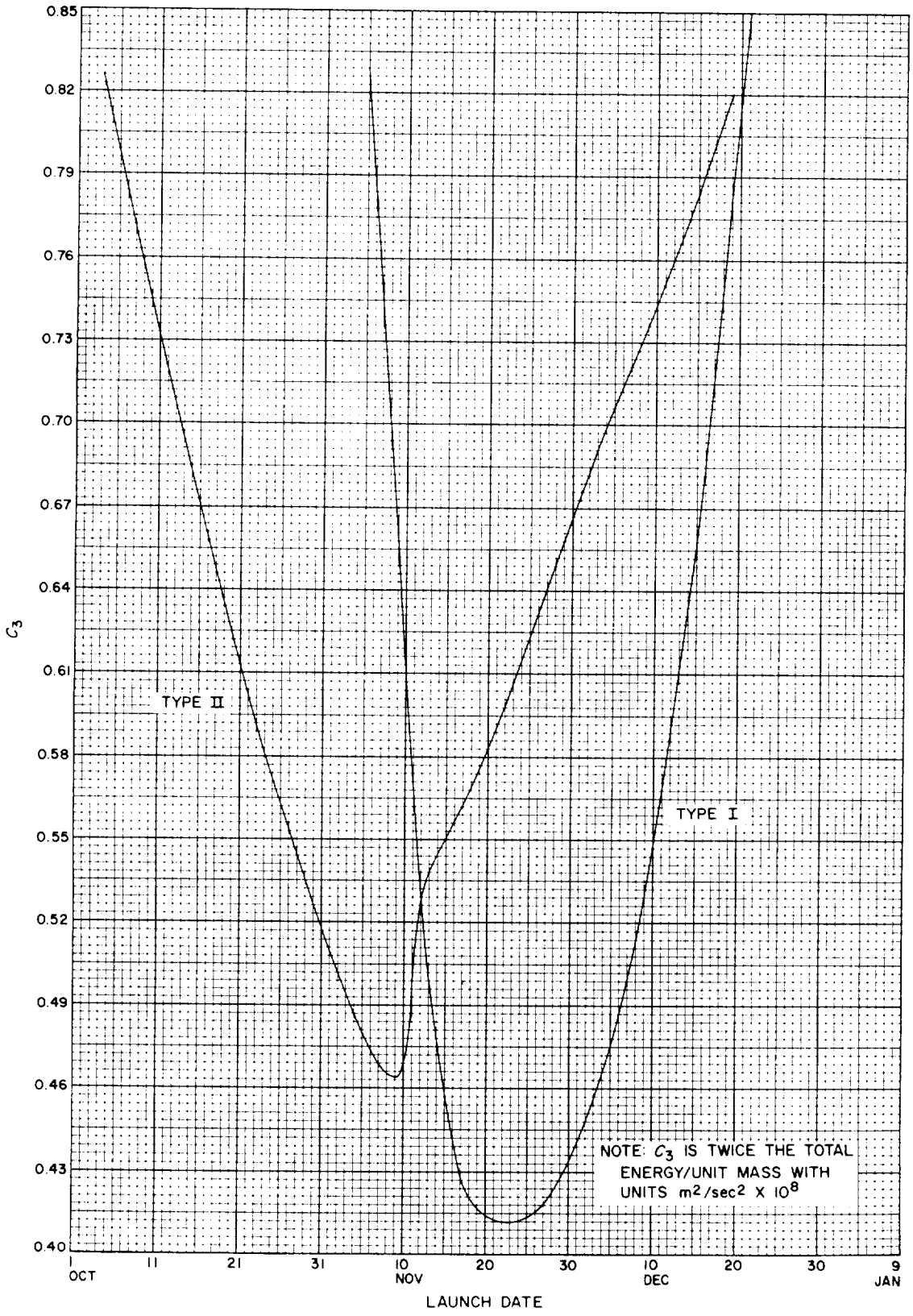

Fig. 4–1. Mercury 1967: Minimum injection energy vs launch date

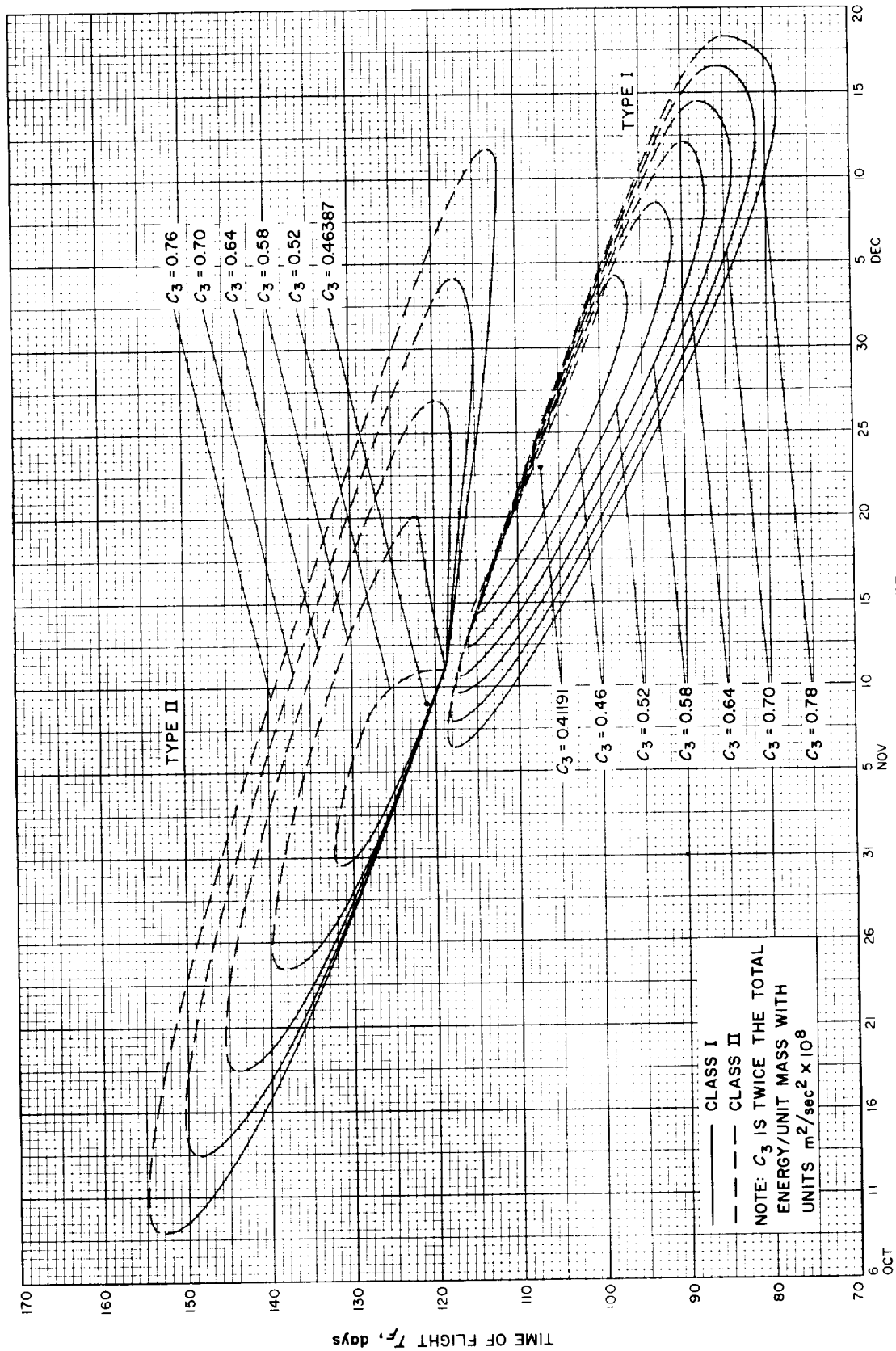

Fig. 4-2. Mercury 1967: Time of flight vs launch date

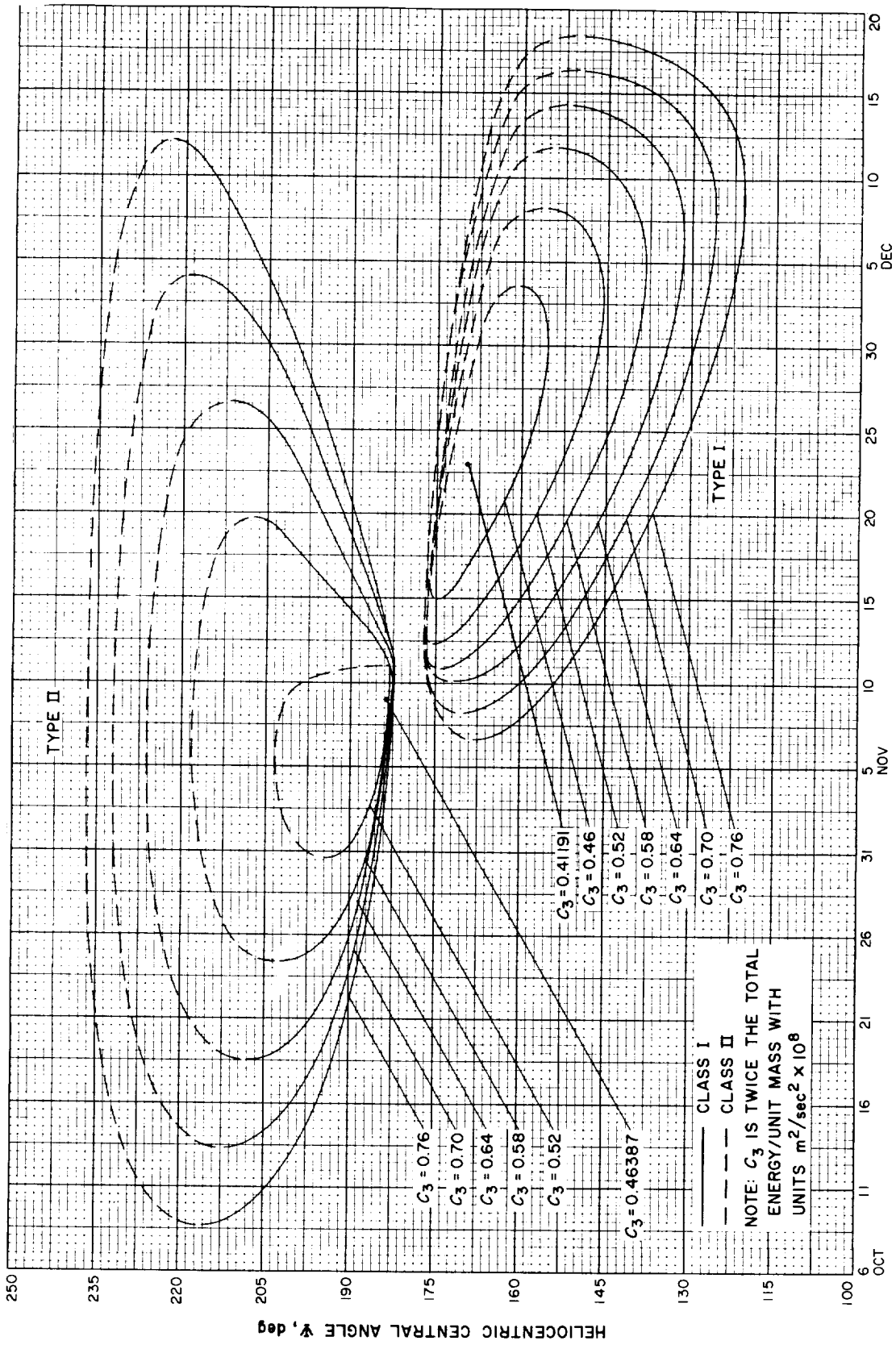

Fig. 4-3. Mercury 1967: Heliocentric central angle vs launch date

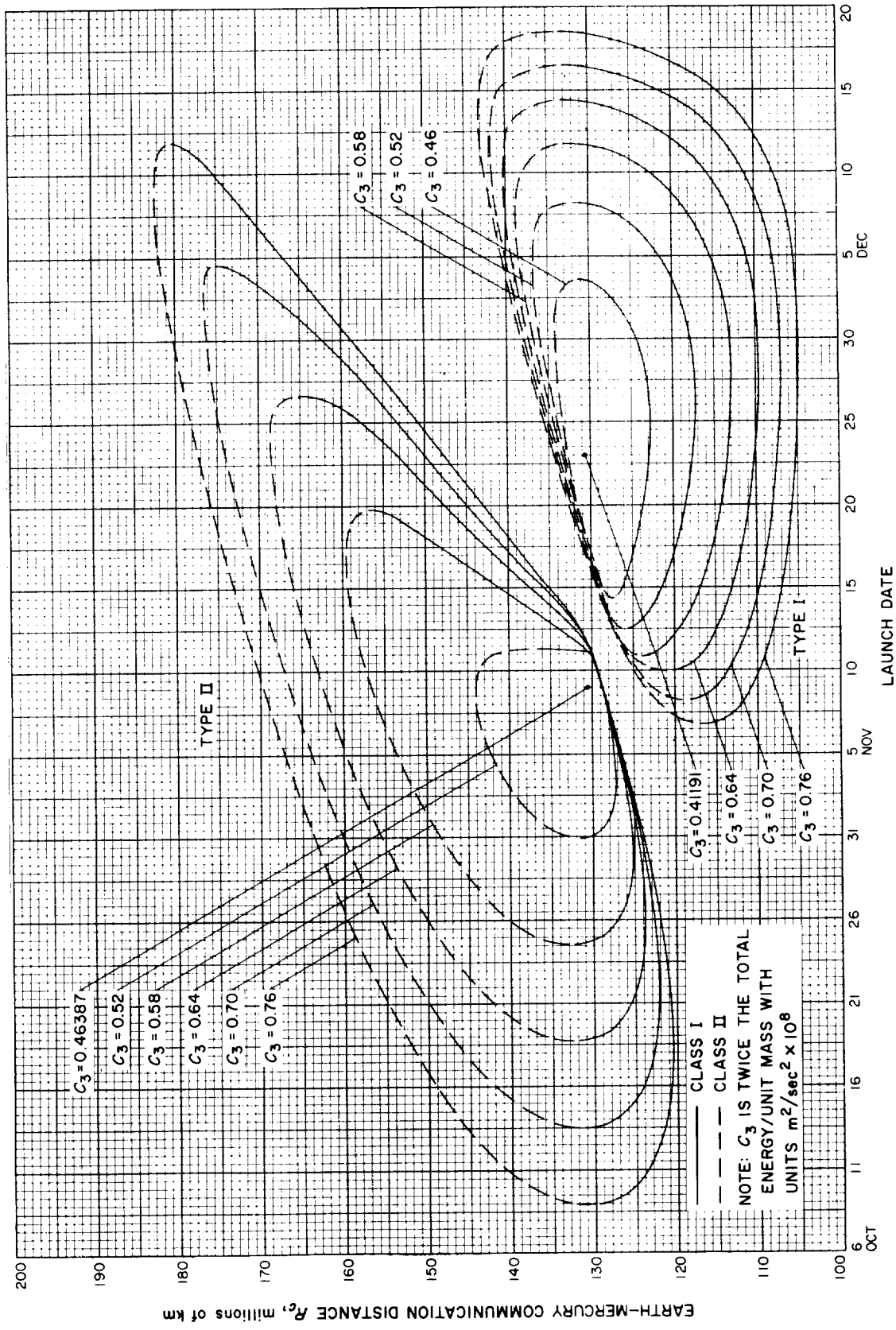

Fig. 4–4. Mercury 1967: Earth–Mercury communication distance vs launch date

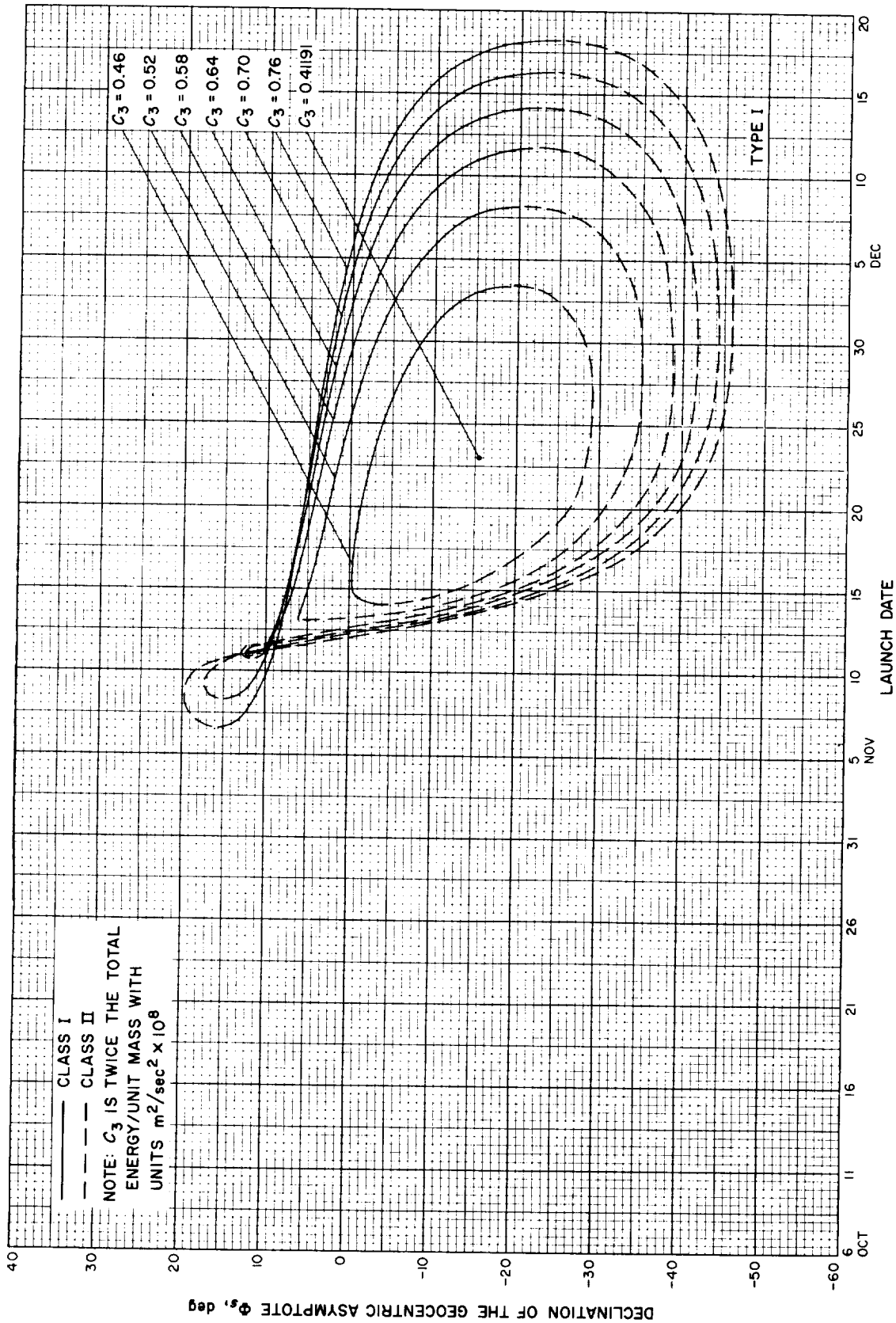

Fig. 4-5(I). Mercury 1967: Declination of the geocentric asymptote vs launch date, Type I

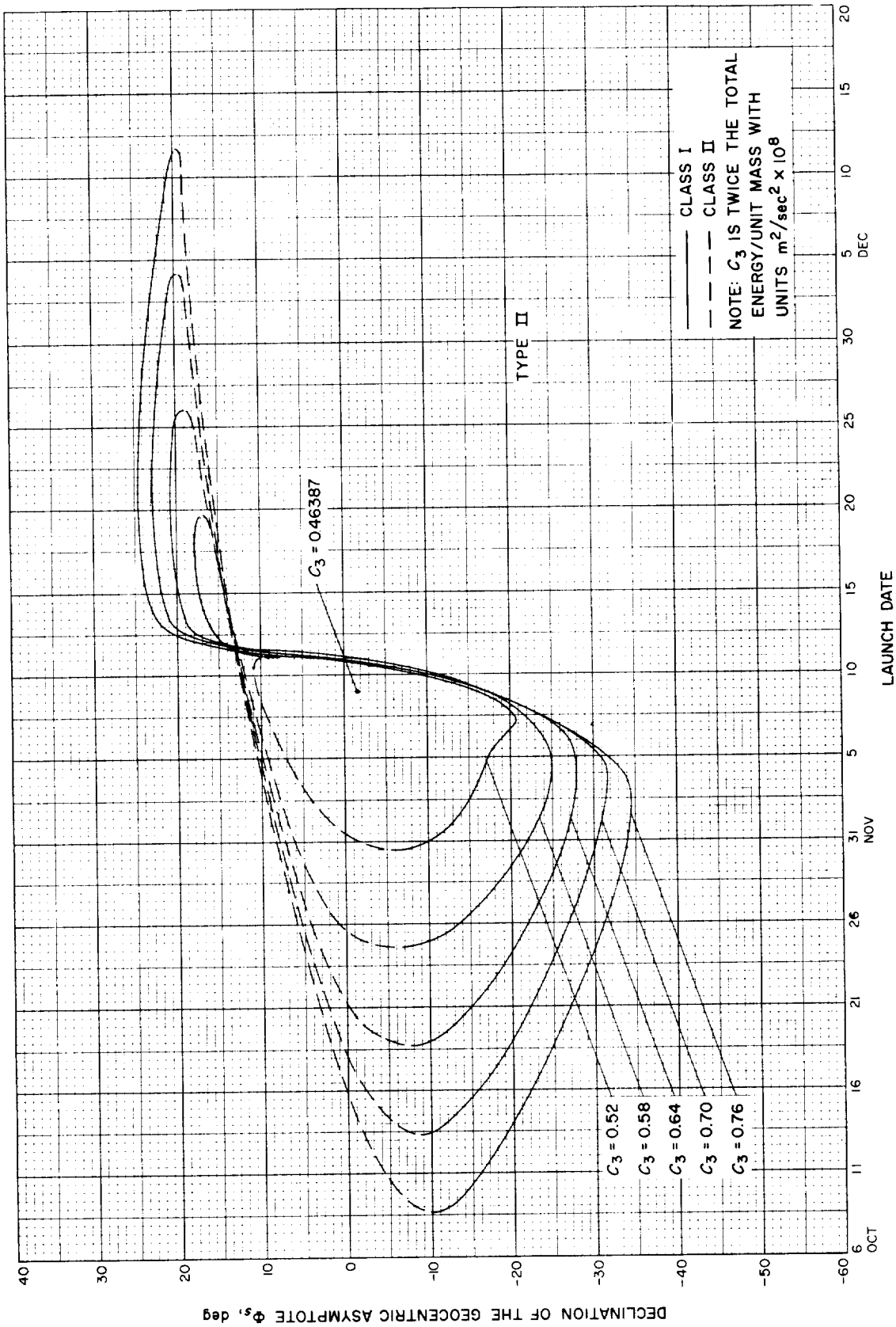

Fig. 4–5(II). Mercury 1967: Declination of the geocentric asymptote vs launch date, Type II

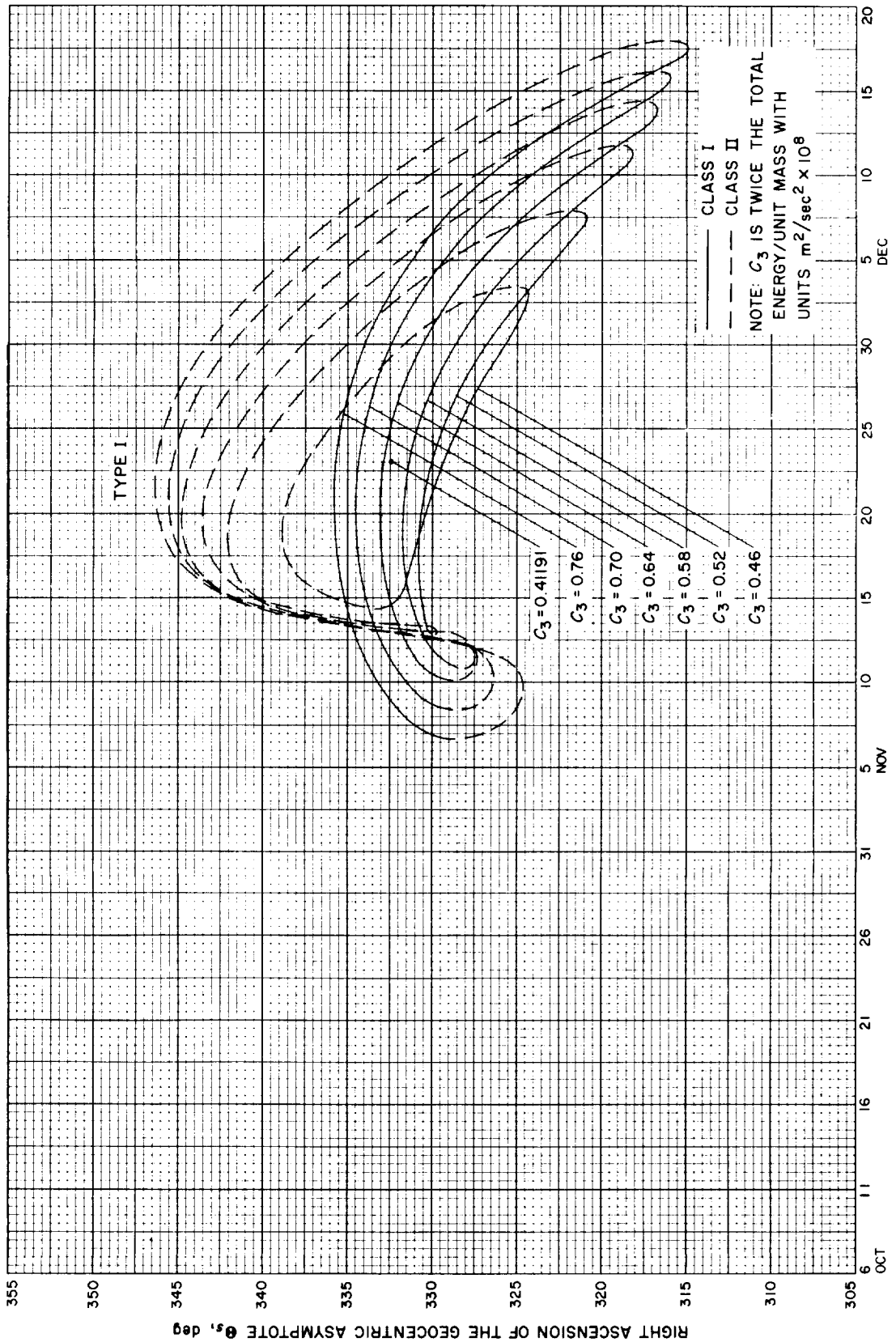

Fig. 4–6(I). Mercury 1967: Right ascension of the geocentric asymptote vs launch date, Type I

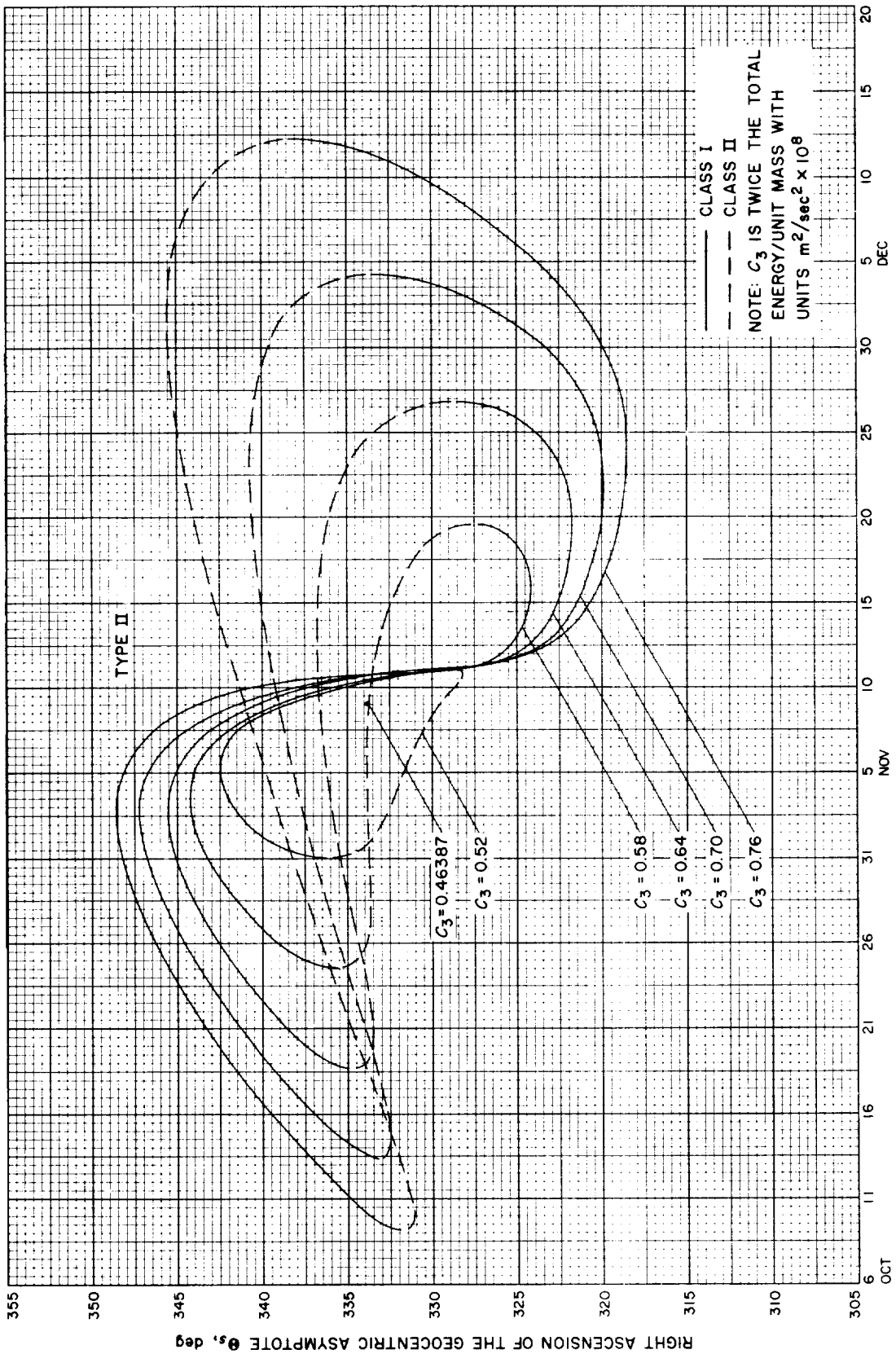

Fig. 4-6(II). Mercury 1967: Right ascension of the geocentric asymptote vs launch date, Type II

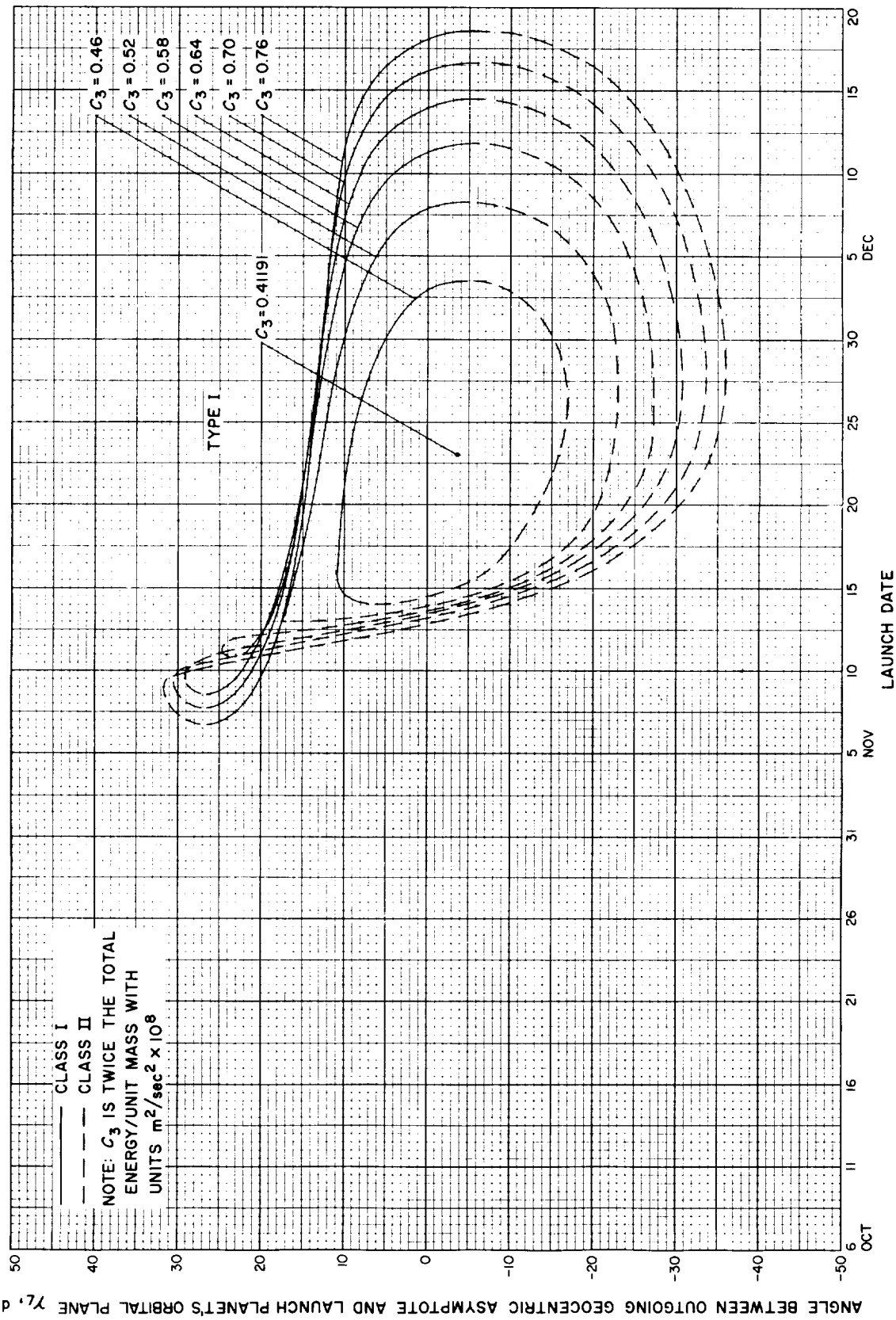

Fig. 4–7(II). Mercury 1967: Angle between outgoing geocentric asymptote and launch planet's orbital plane vs launch date, Type I

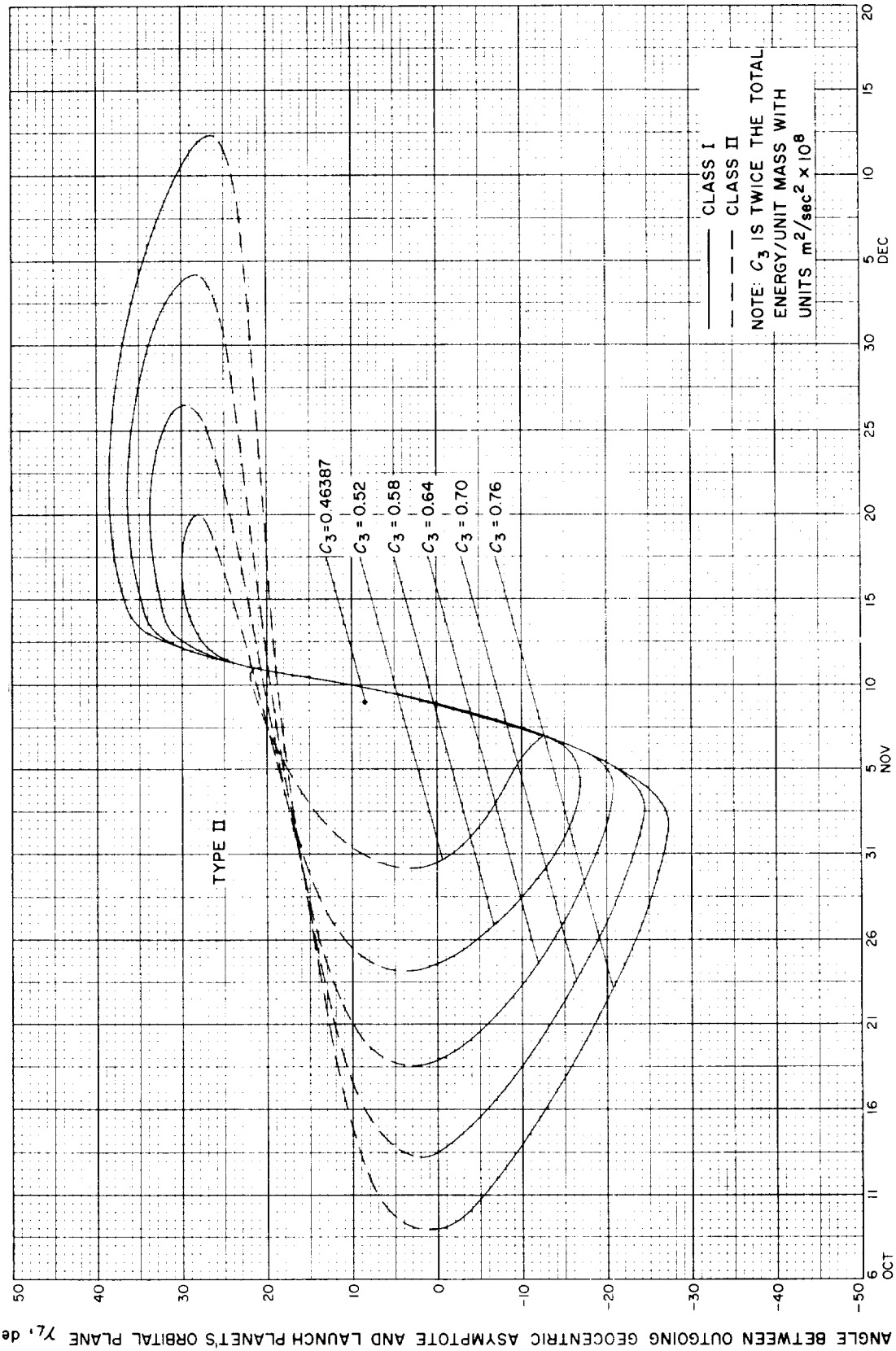

Fig. 4-7(II). Mercury 1967: Angle between outgoing geocentric asymptote and launch planet's orbital plane vs launch date, Type II

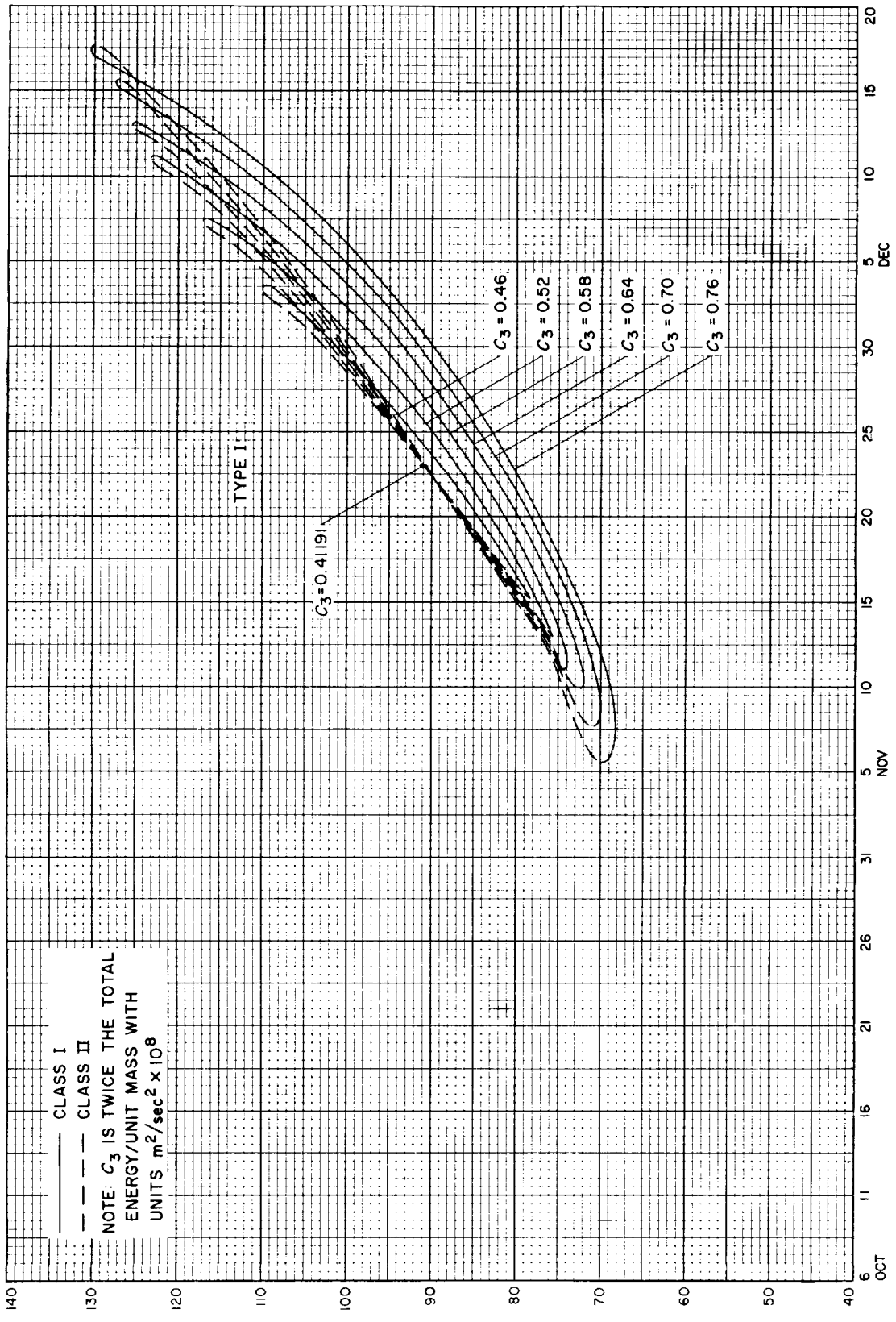

Fig. 4-8(I). Mercury 1967: Angle between Sun–Earth vector and outgoing geocentric asymptote vs launch date, Type I

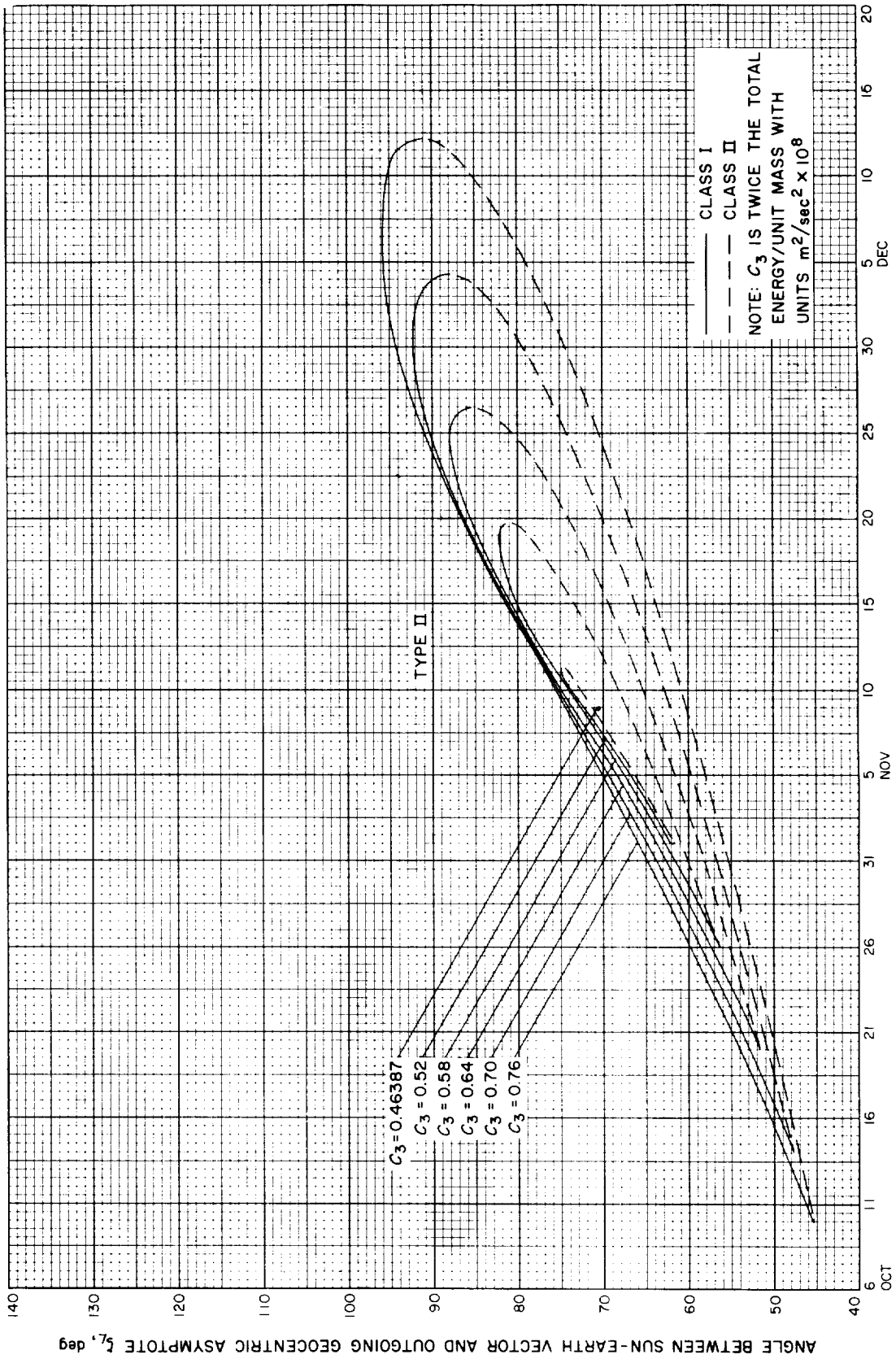

Fig. 4-8(II). Mercury 1967: Angle between Sun–Earth vector and outgoing geocentric asymptote vs launch date, Type II

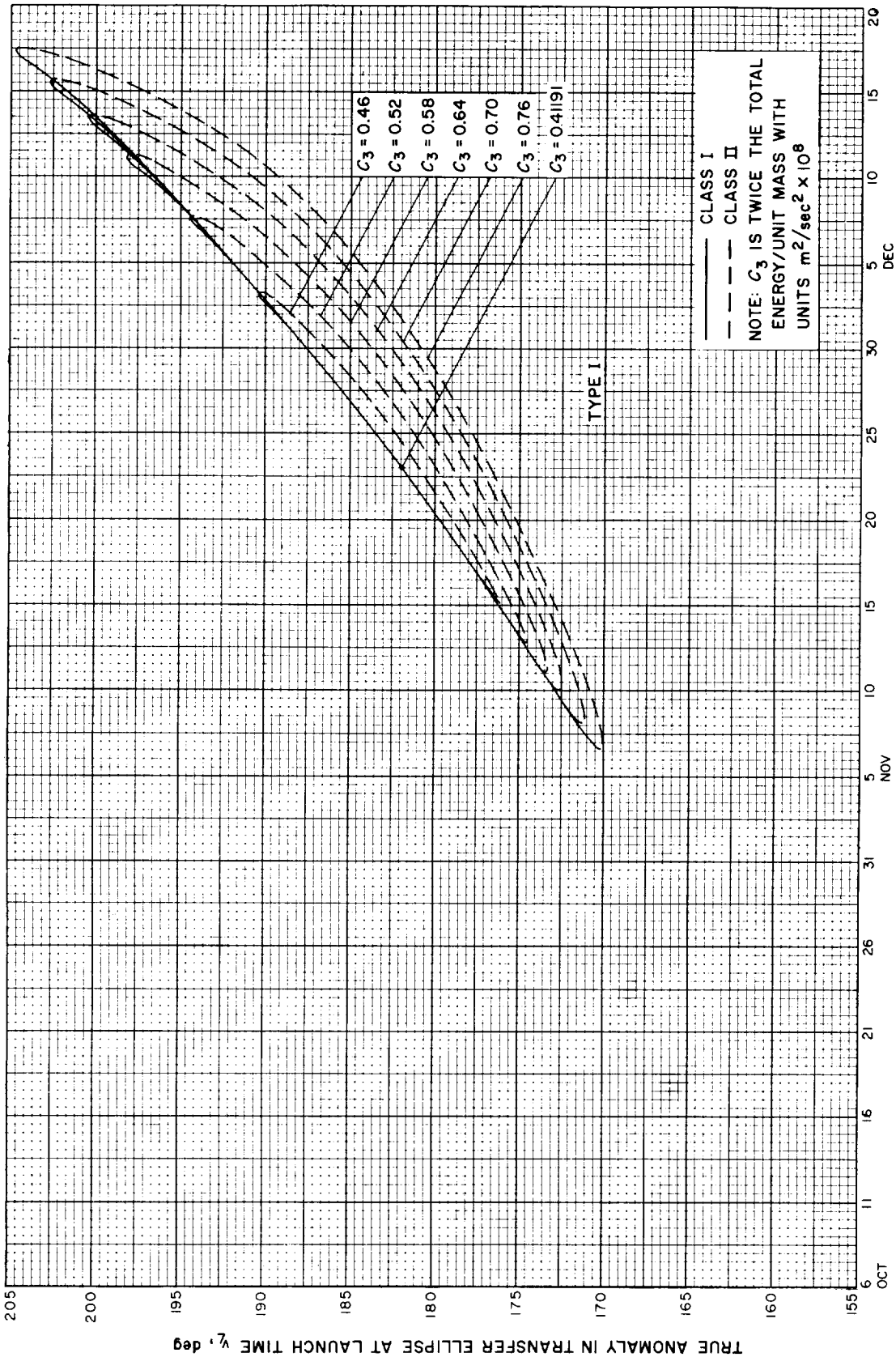

Fig. 4-9(I). Mercury 1967: True anomaly in transfer ellipse at launch time vs launch date, Type I

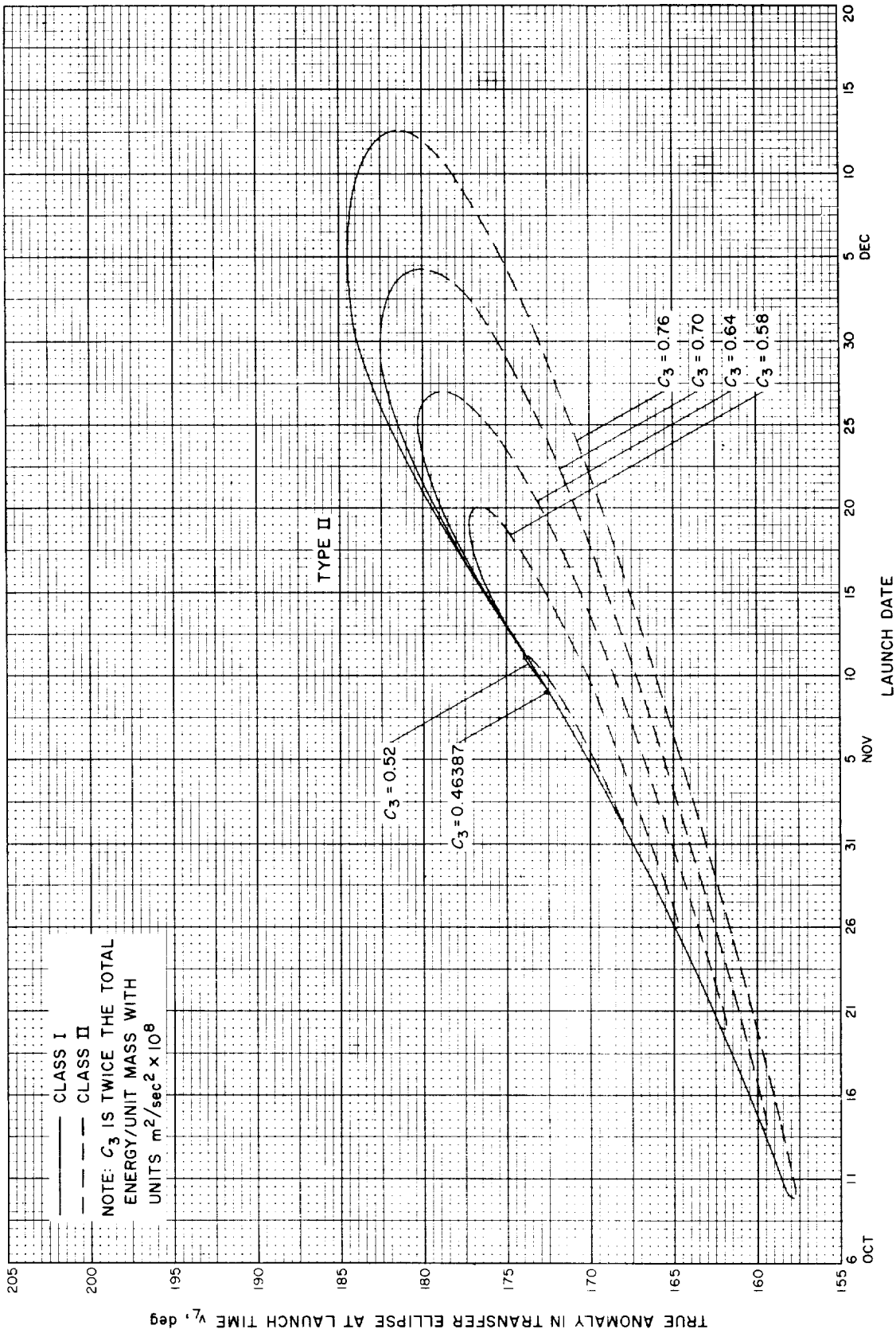

Fig. 4-9(II). Mercury 1967: True anomaly in transfer ellipse at launch time vs launch date, Type II

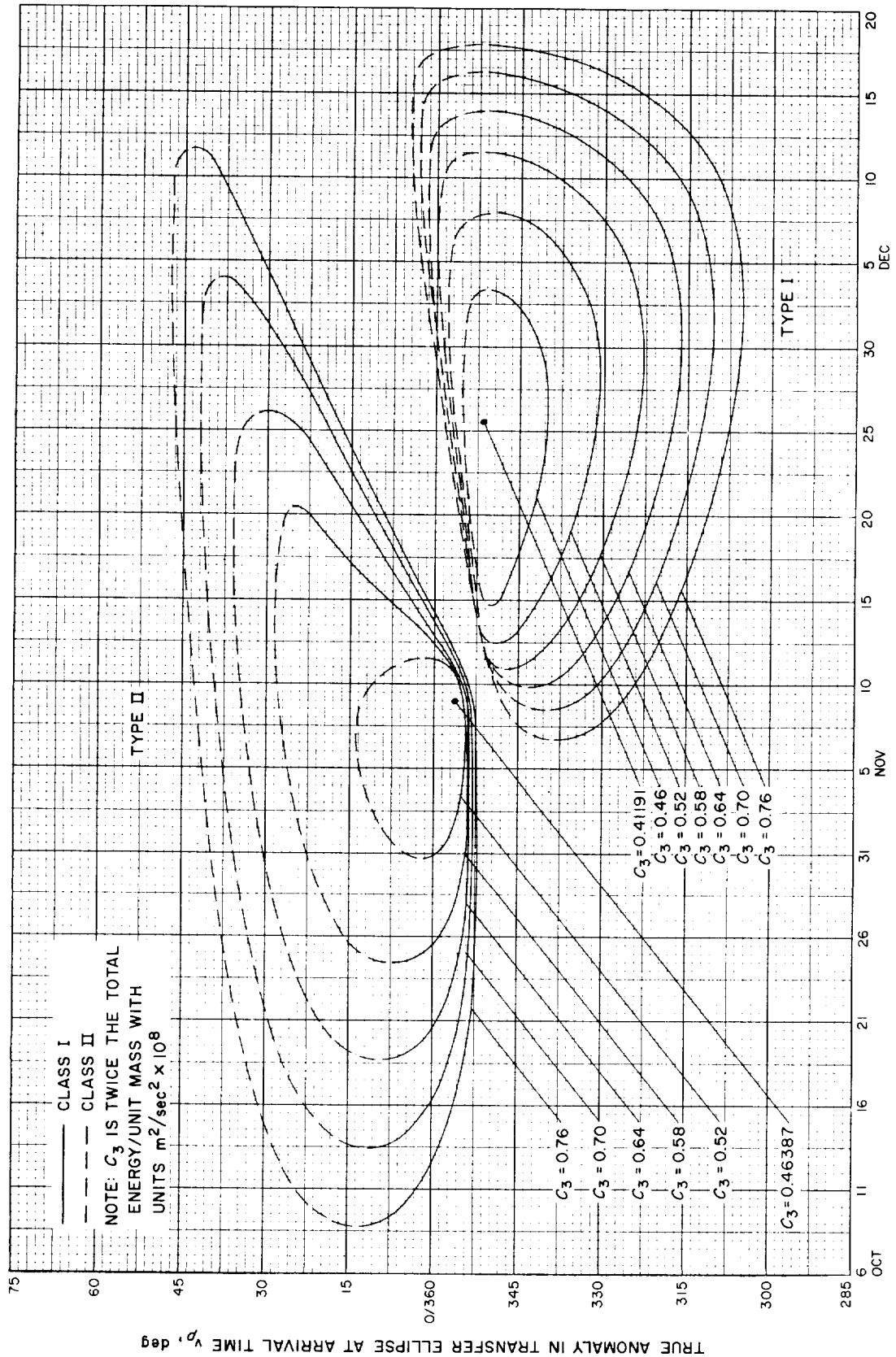

Fig. 4–10. Mercury 1967: True anomaly in transfer ellipse at arrival time vs launch date

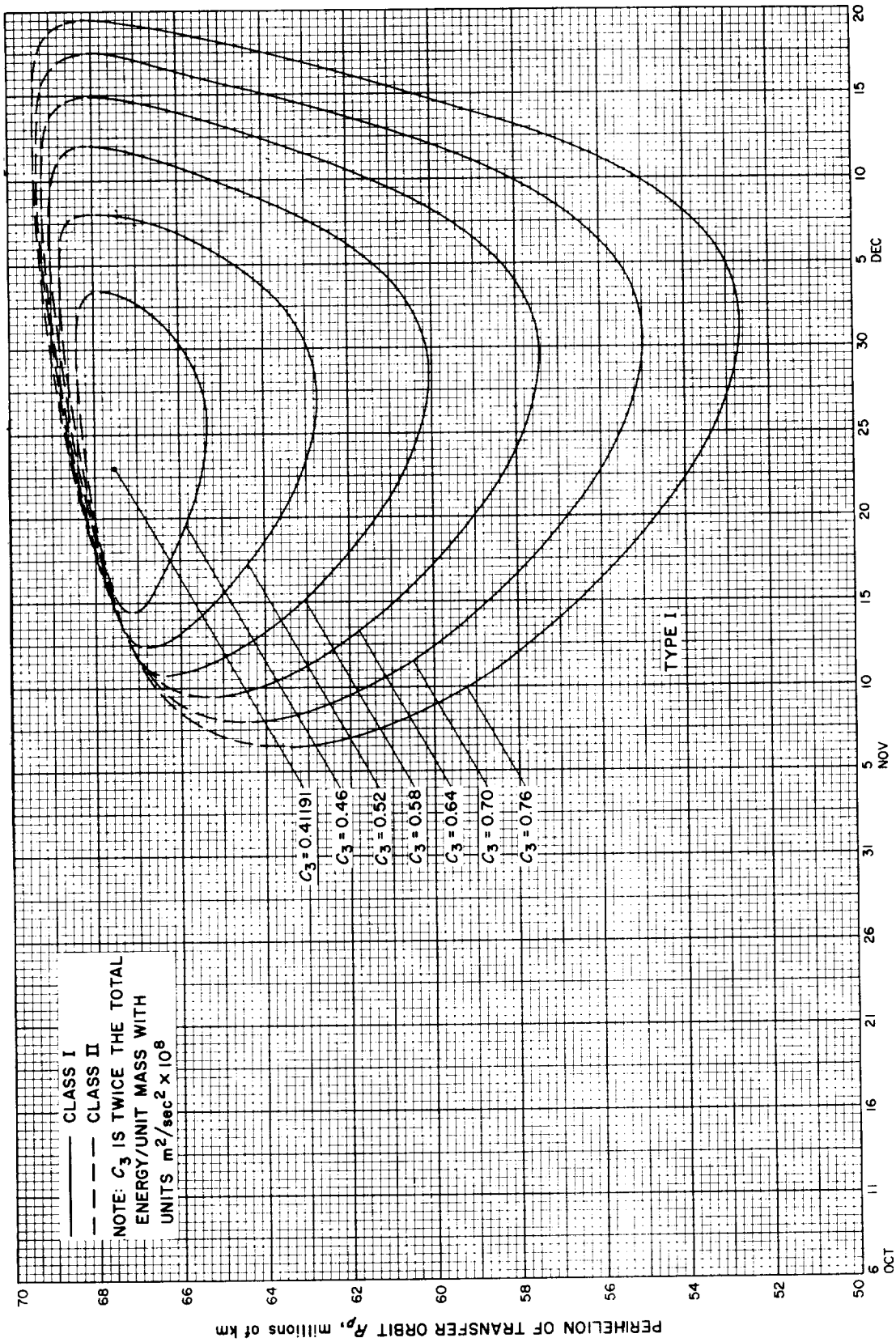

Fig. 4-11(I). Mercury 1967: Perihelion of transfer orbit vs launch date, Type I

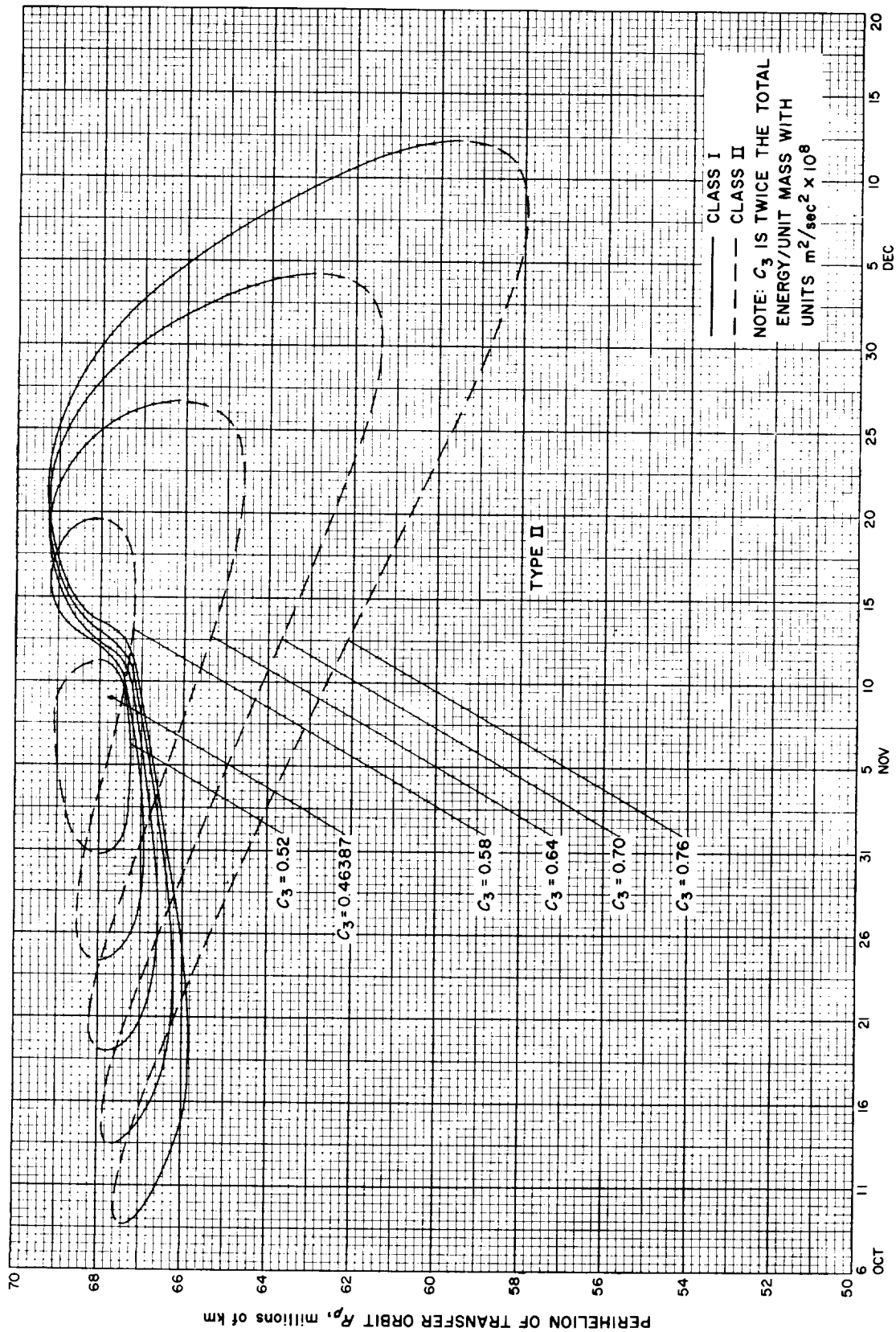

Fig. 4-11(II). Mercury 1967: Perihelion of transfer orbit vs launch date, Type II

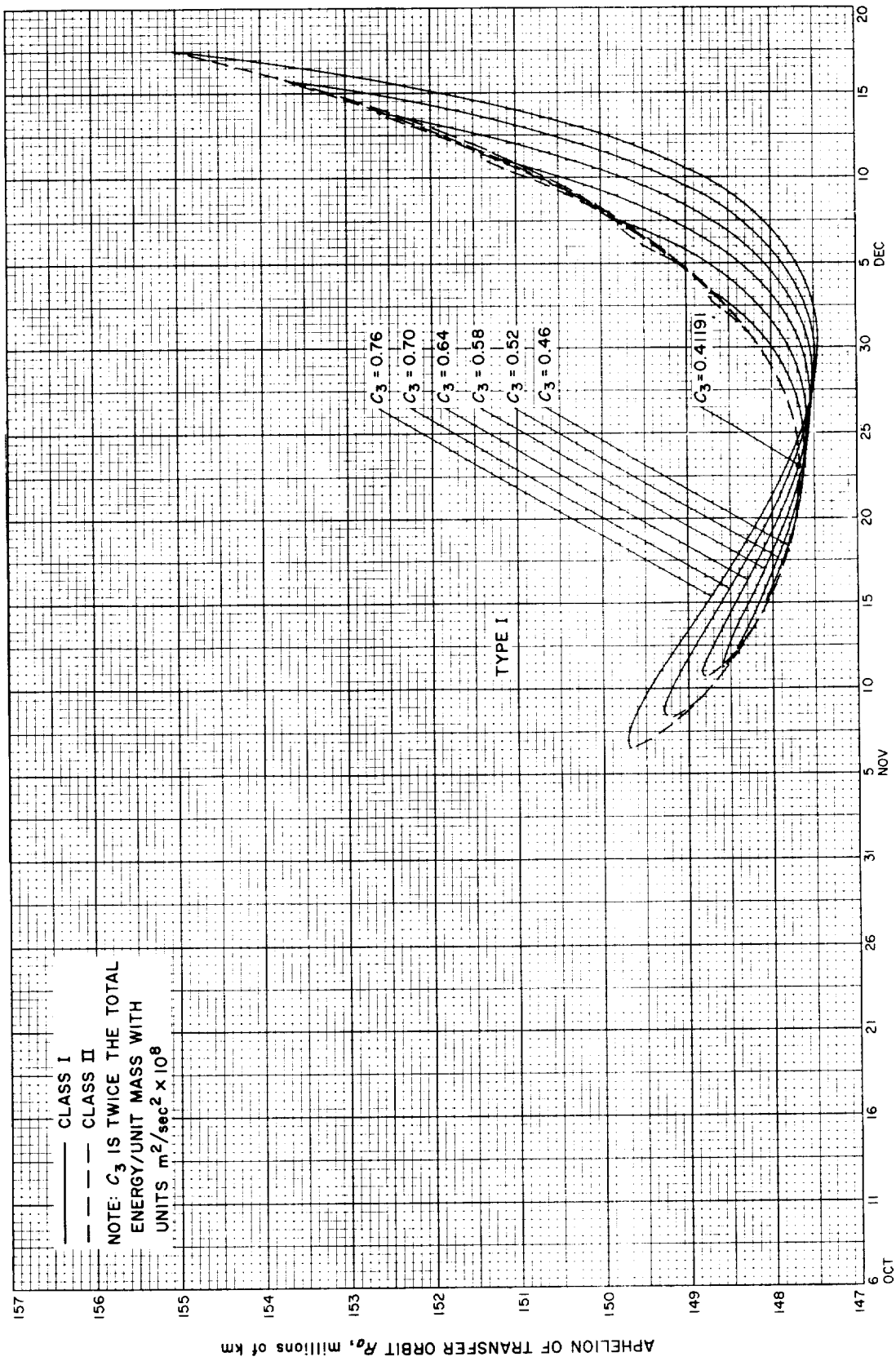

Fig. 4-12(I). Mercury 1967: Aphelion of transfer orbit vs launch date, Type I

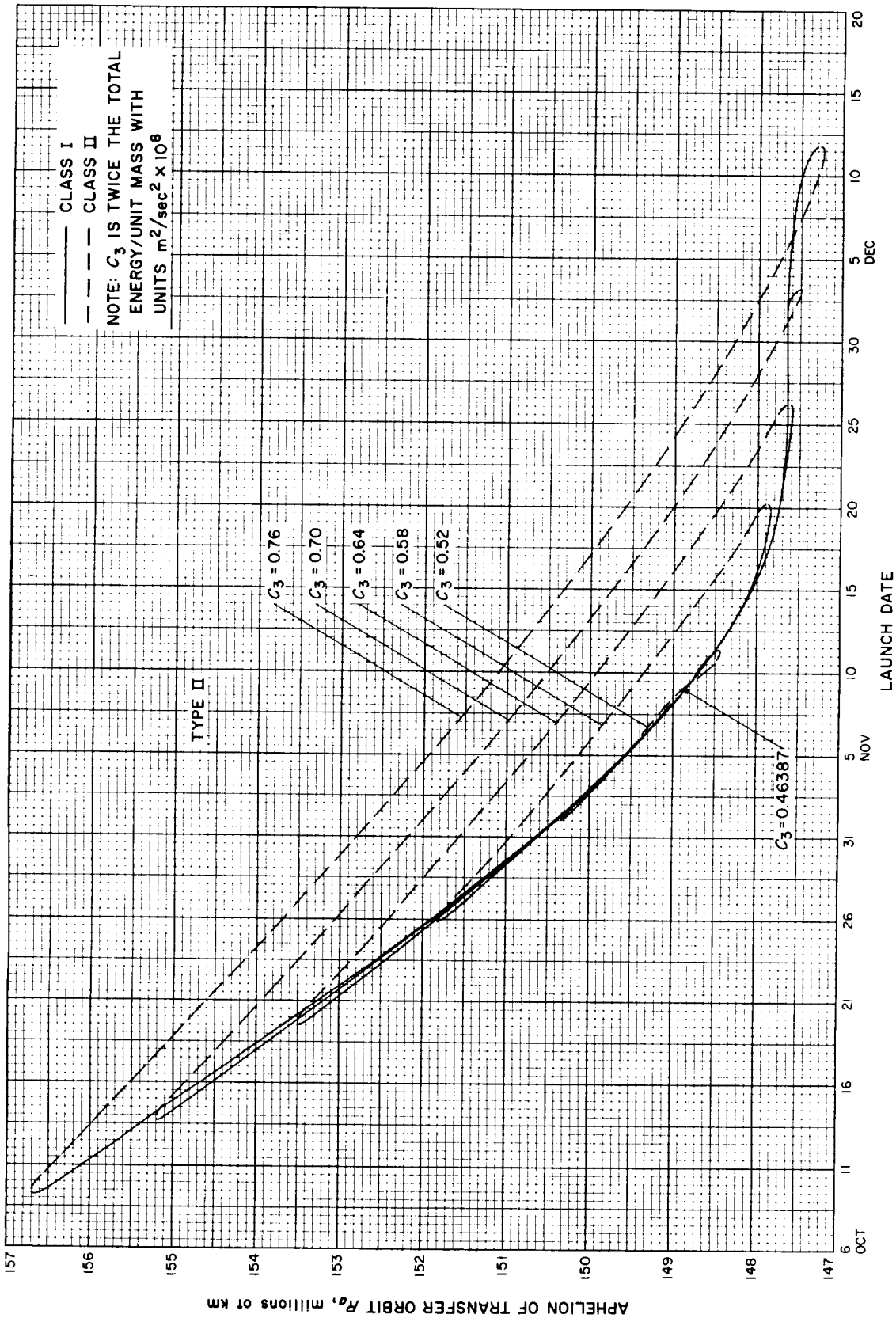

Fig. 4-12(II). Mercury 1967: Aphelion of transfer orbit vs launch date, Type II

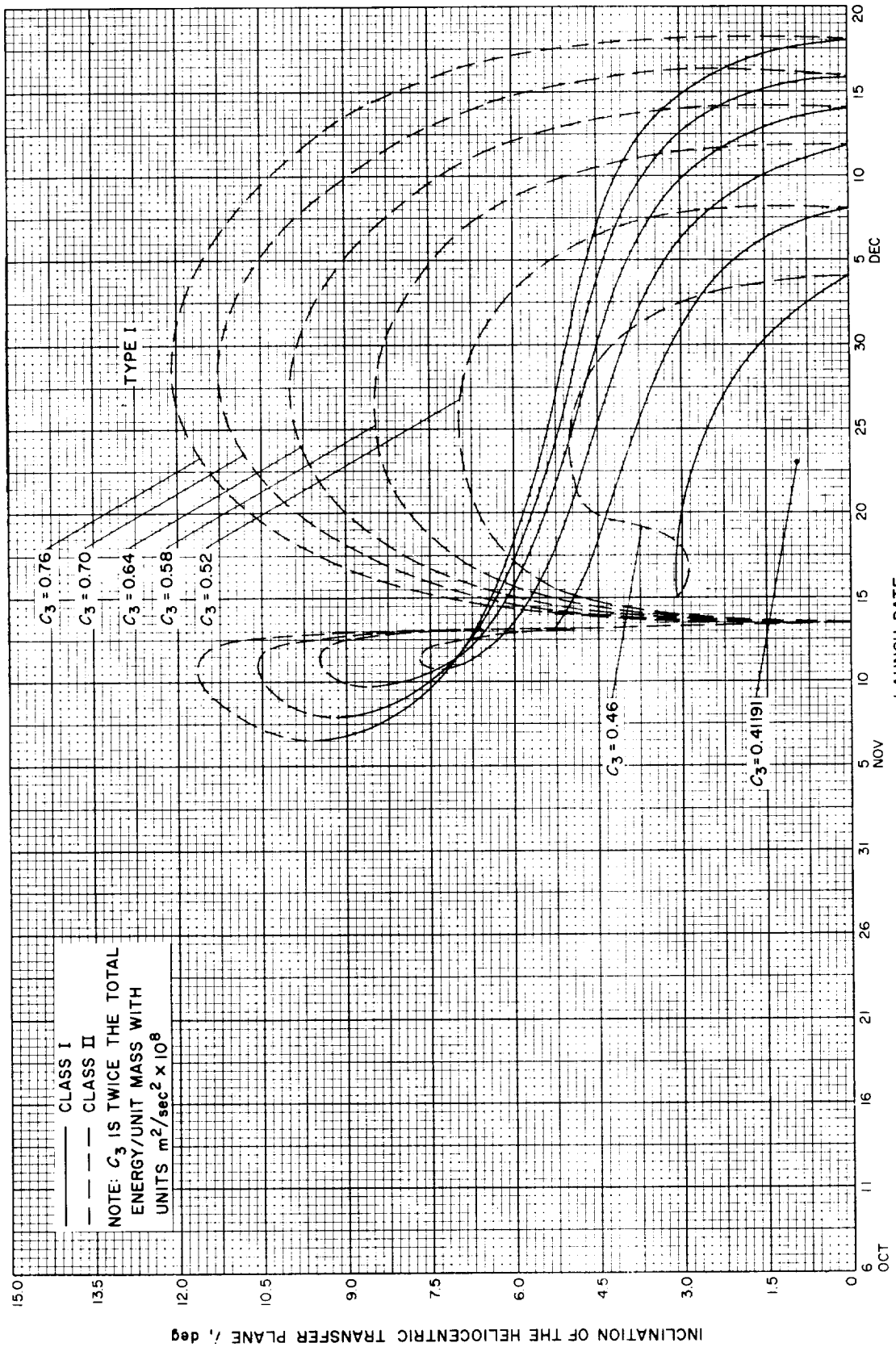

Fig. 4-13(I). Mercury 1967: Inclination of the heliocentric transfer plane vs launch date, Type I

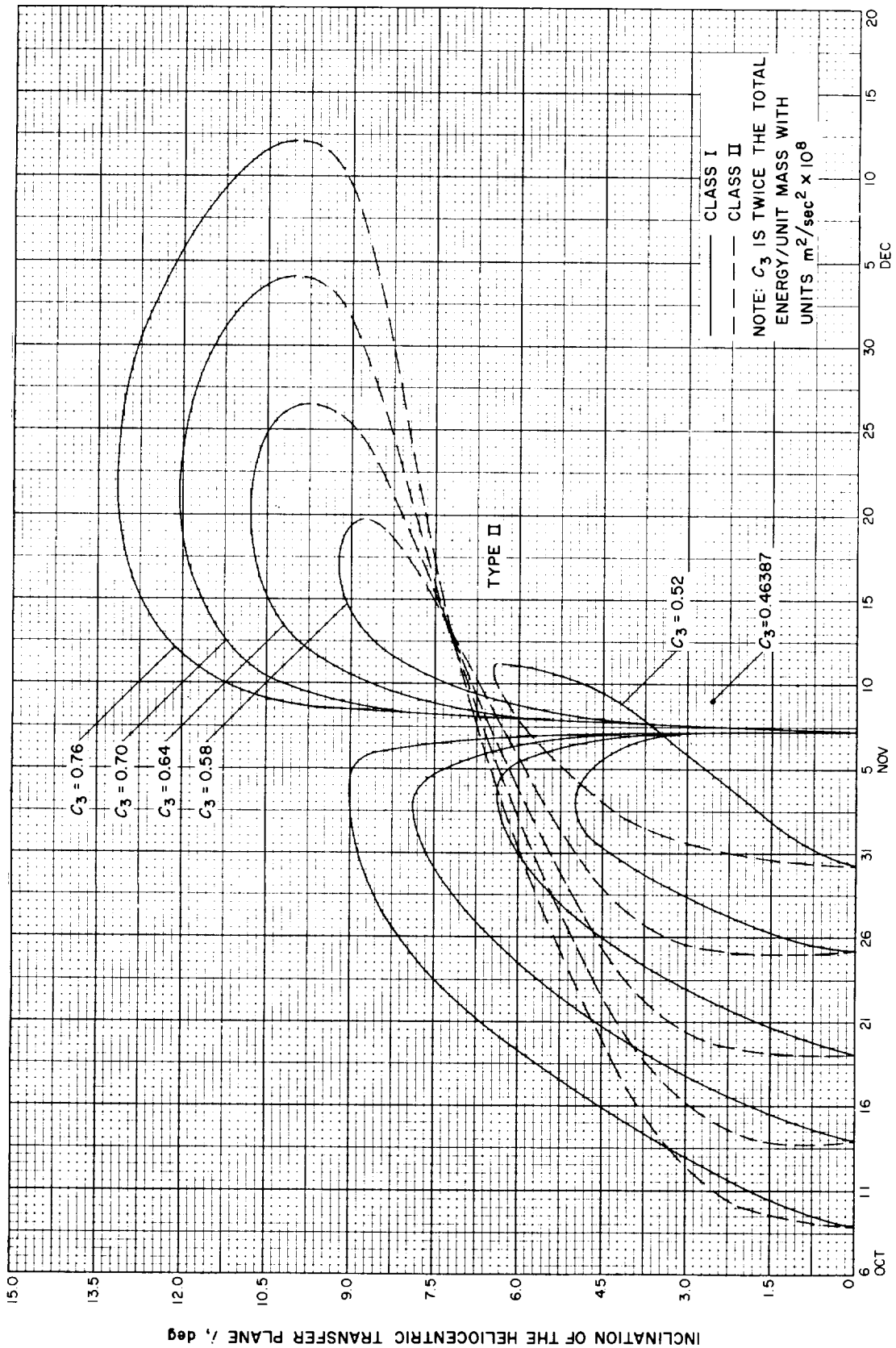

Fig. 4–13(II). Mercury 1967: Inclination of the heliocentric transfer plane vs launch date, Type II

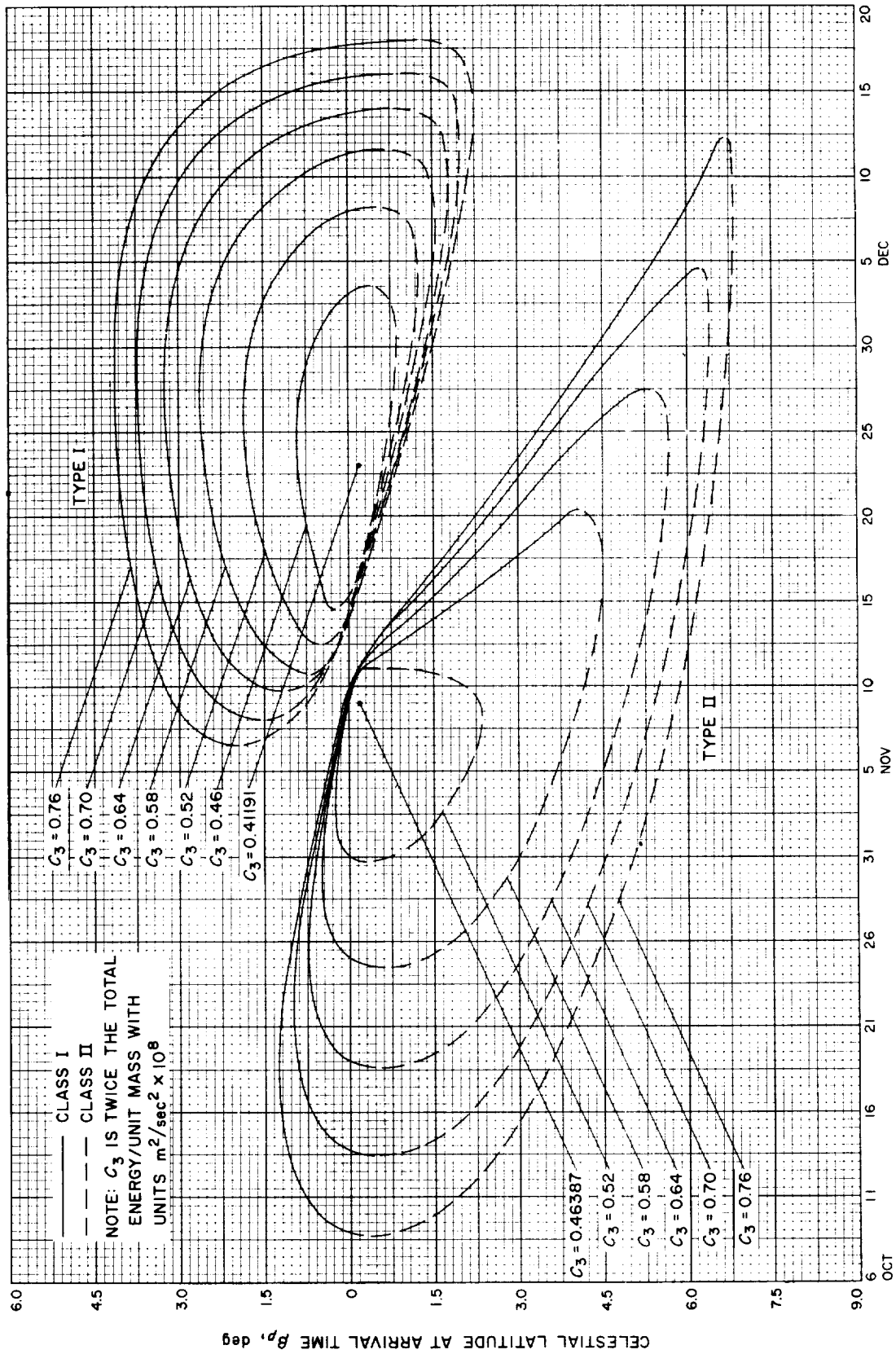

Fig. 4-14. Mercury 1967: Celestial latitude at arrival time vs launch date

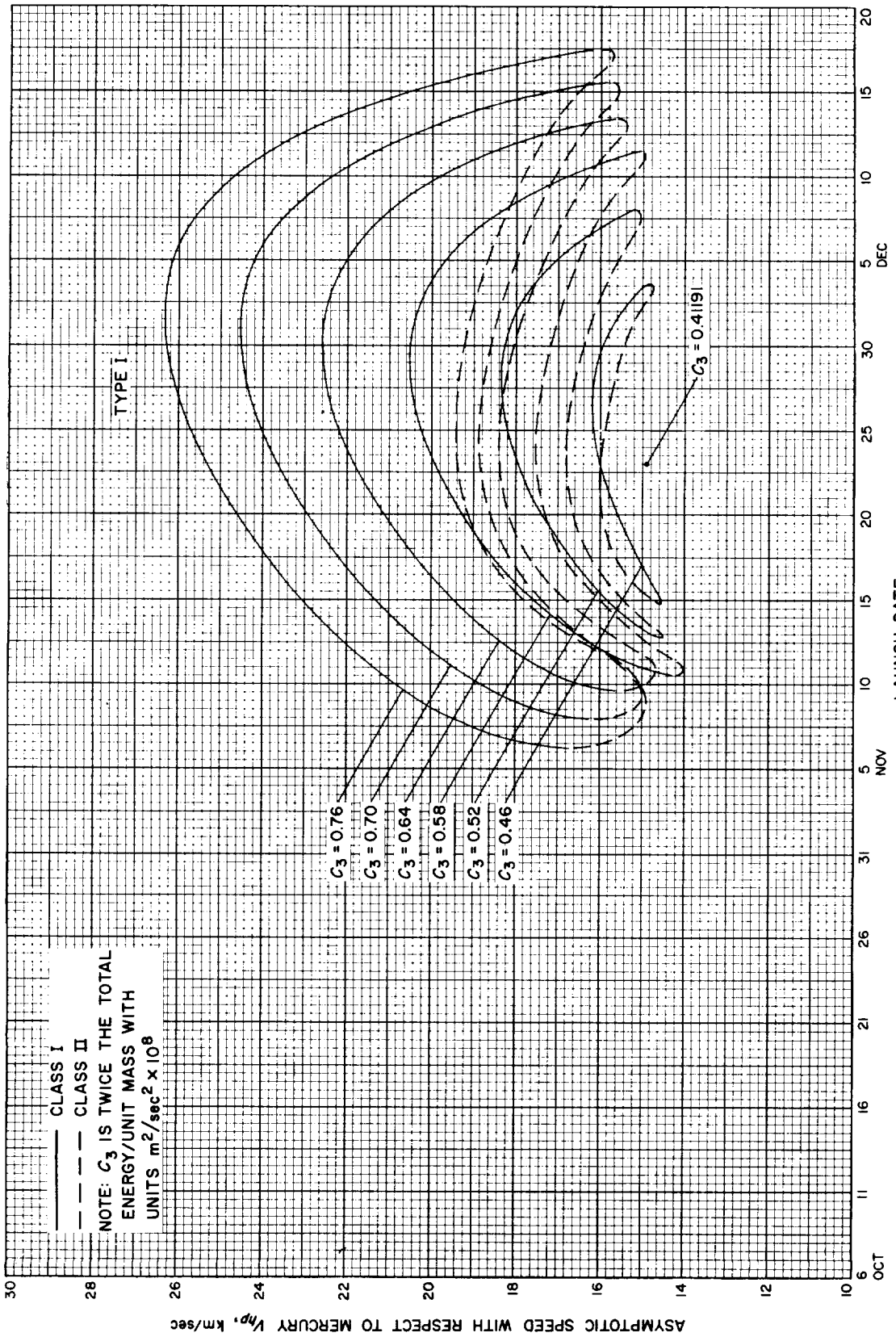

Fig. 4-15(I). Mercury 1967: Asymptotic speed with respect to Mercury vs launch date, Type I

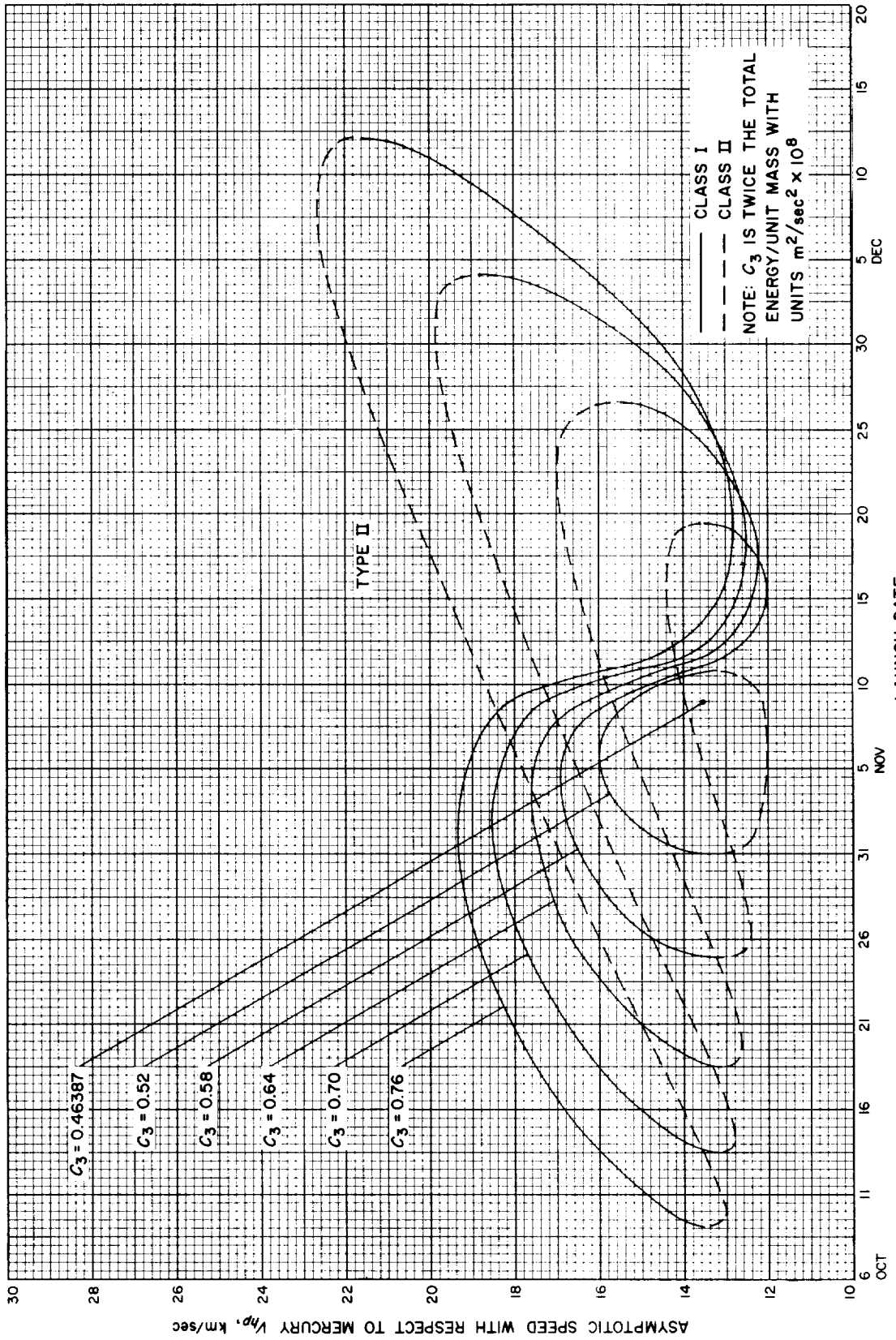

Fig. 4–15(II). Mercury 1967: Asymptotic speed with respect to Mercury vs launch date, Type II

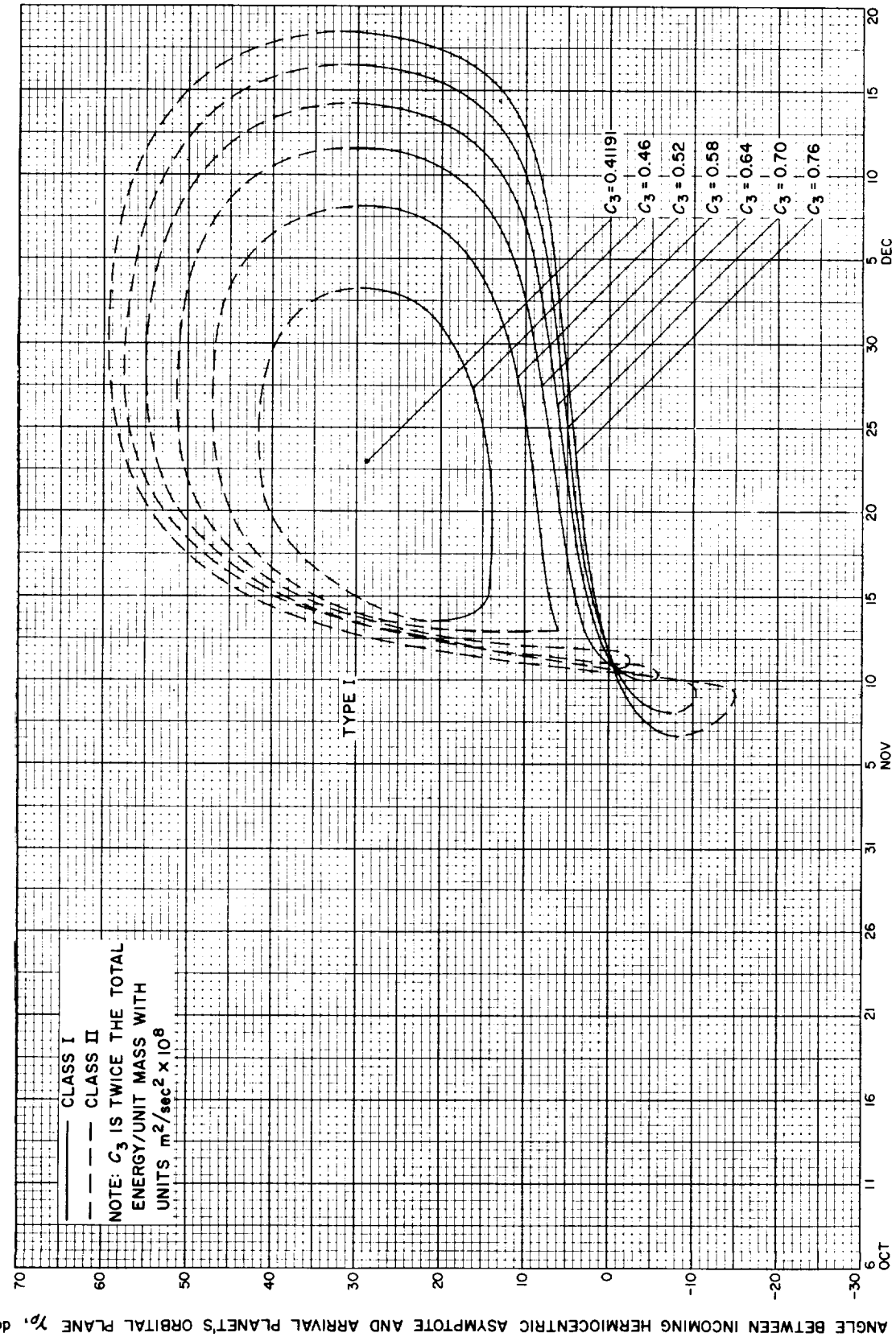

Fig. 4-16(I). Mercury 1967: Angle between incoming hermiocentric asymptote and arrival planet's orbital plane vs launch date, Type I

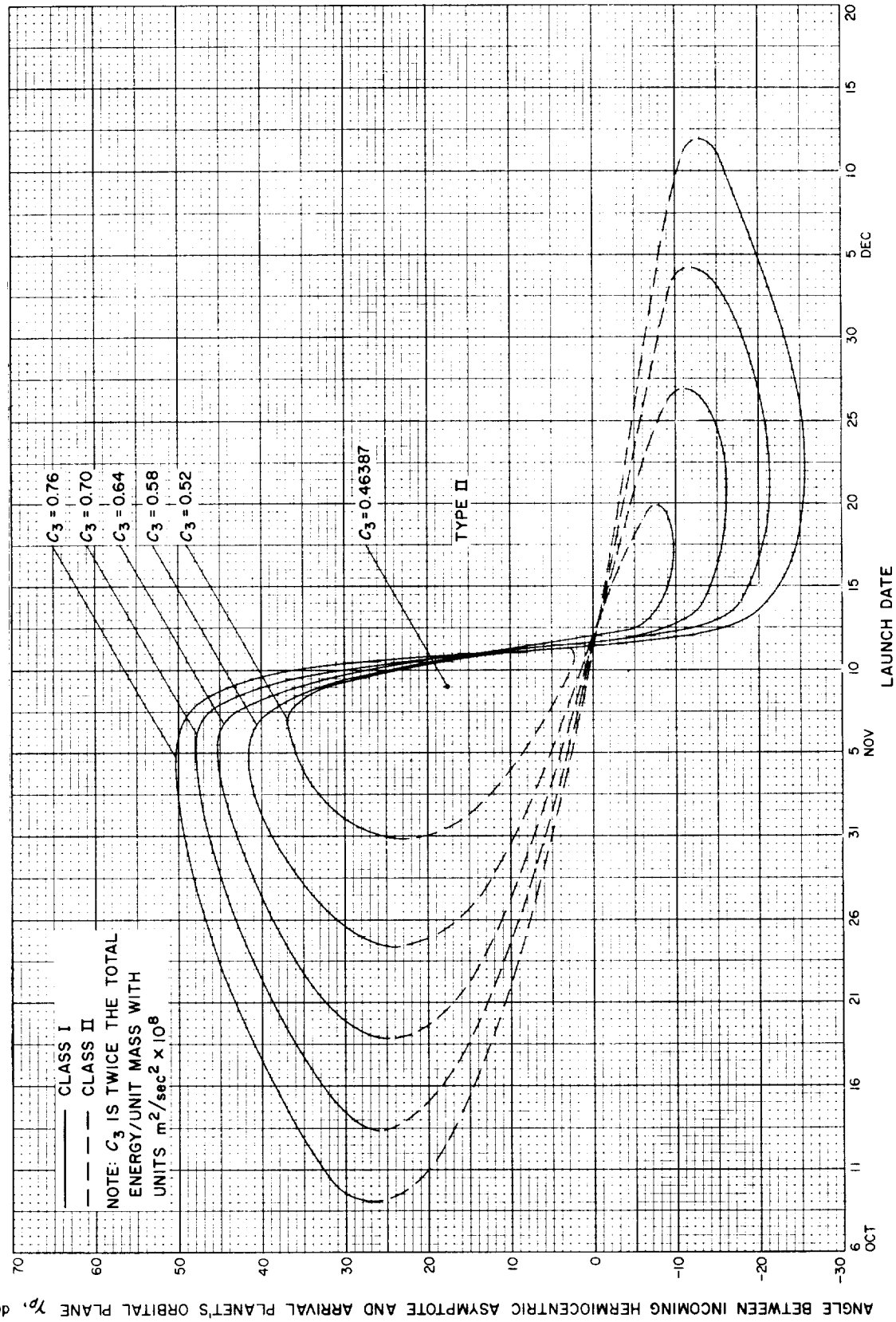

Fig. 4–16(II). Mercury 1967: Angle between incoming hermiocentric asymptote and arrival planet's orbital plane vs launch date, Type II

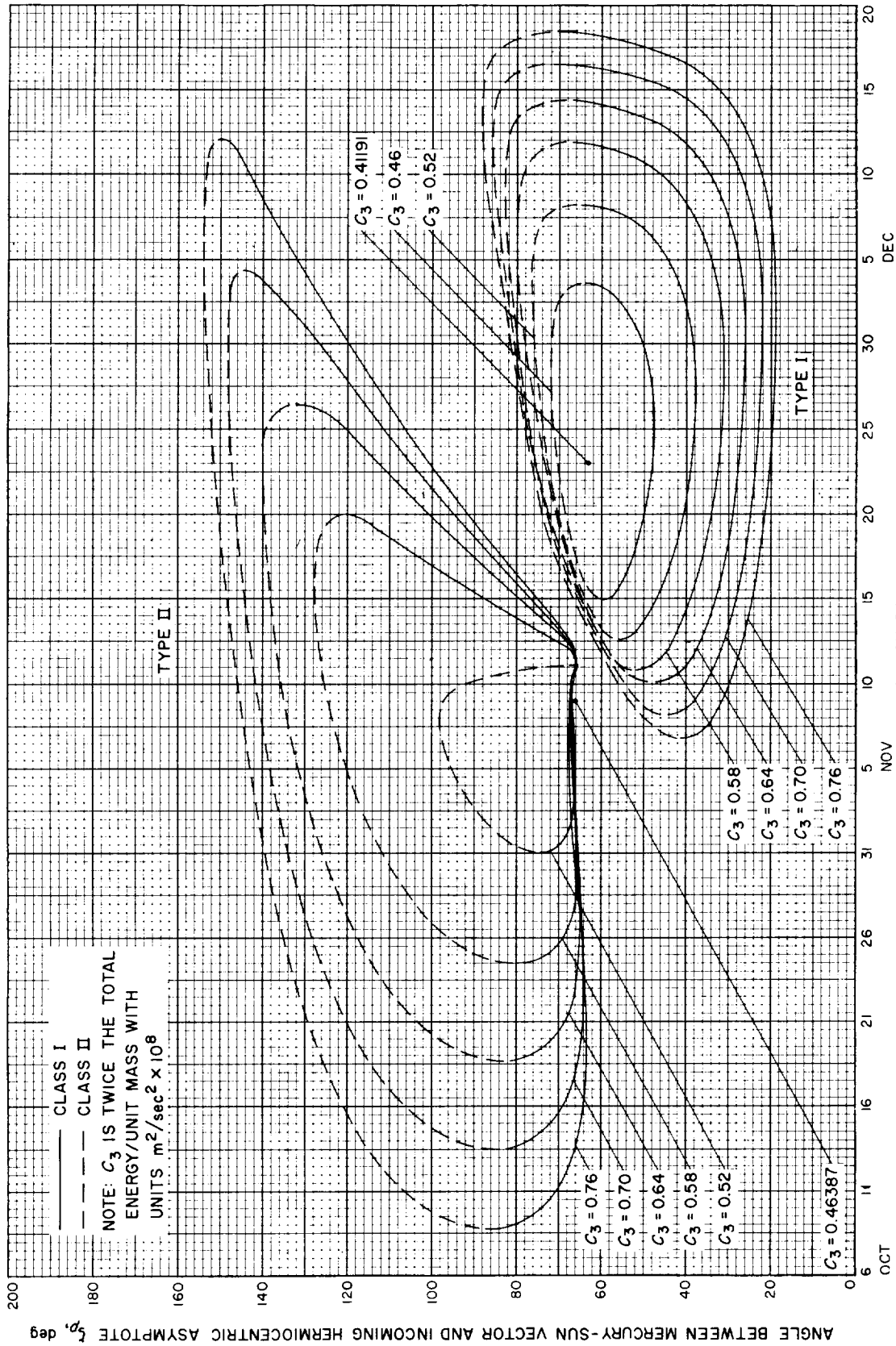

Fig. 4–17. Mercury 1967: Angle between Mercury–Sun vector and incoming hermiocentric asymptote vs launch date

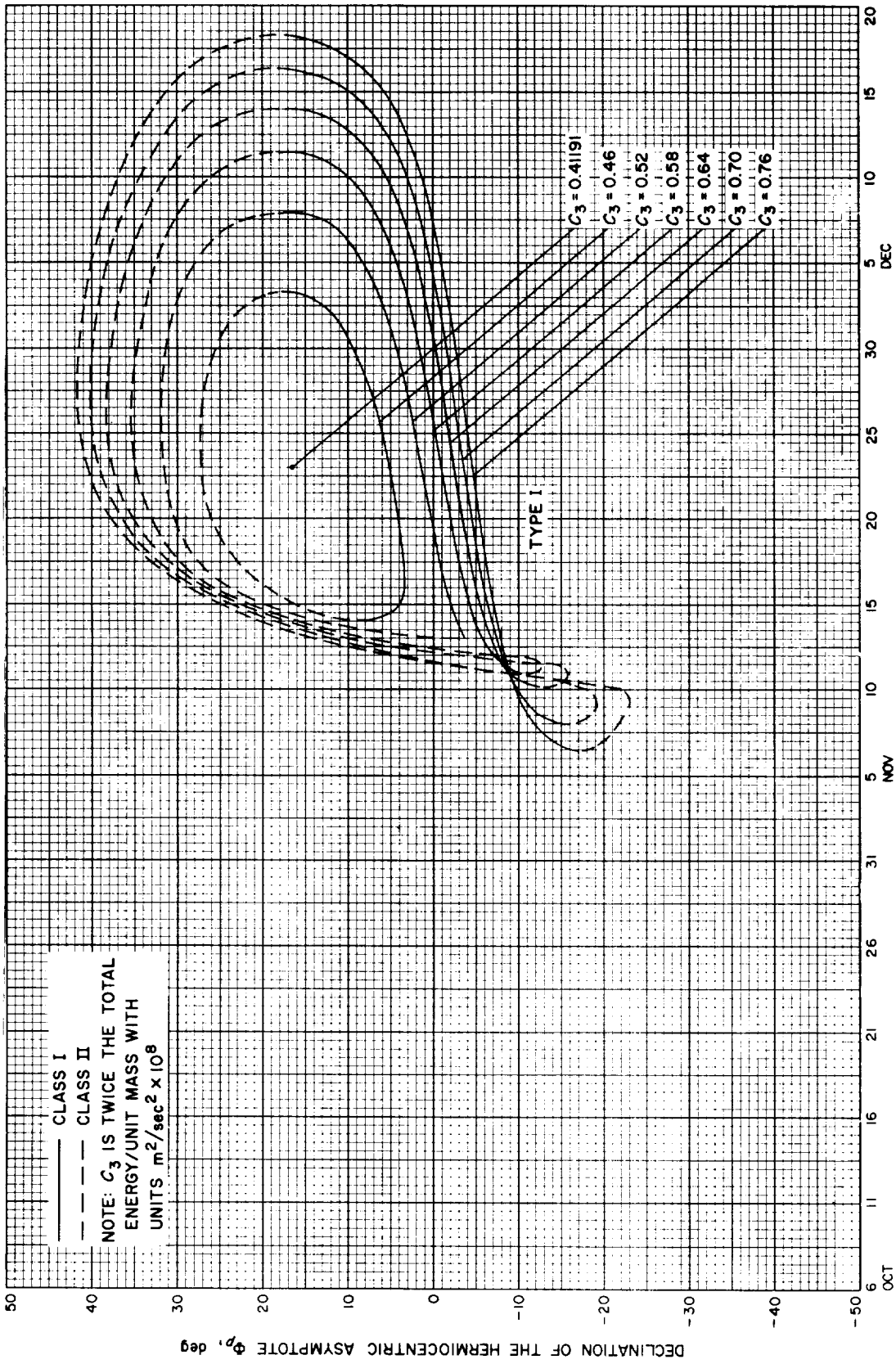

Fig. 4–18(I). Mercury 1967: Declination of the hermiocentric asymptote vs launch date, Type I

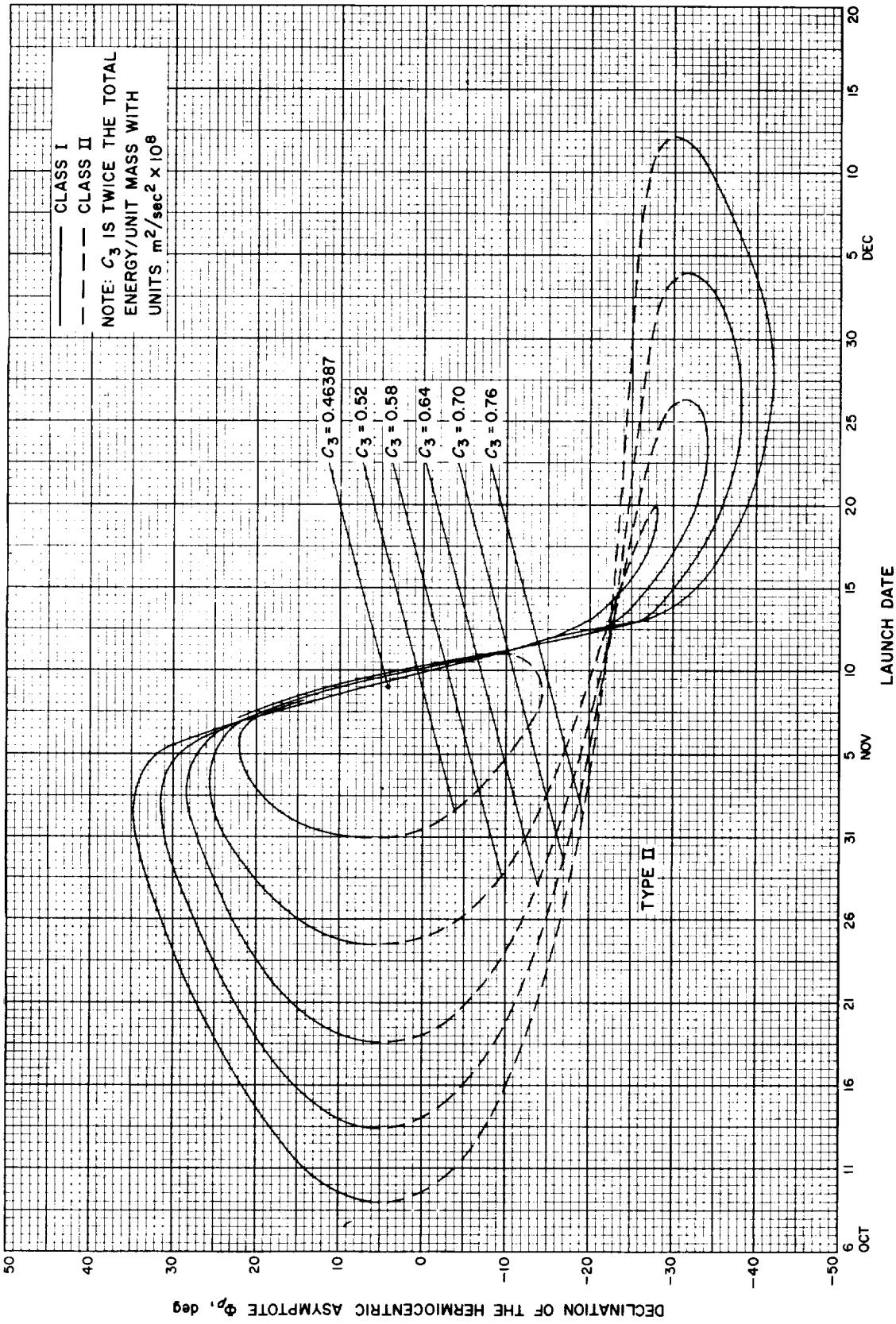

Fig. 4-18(II). Mercury 1967: Declination of the hermiocentric asymptote vs launch date, Type II

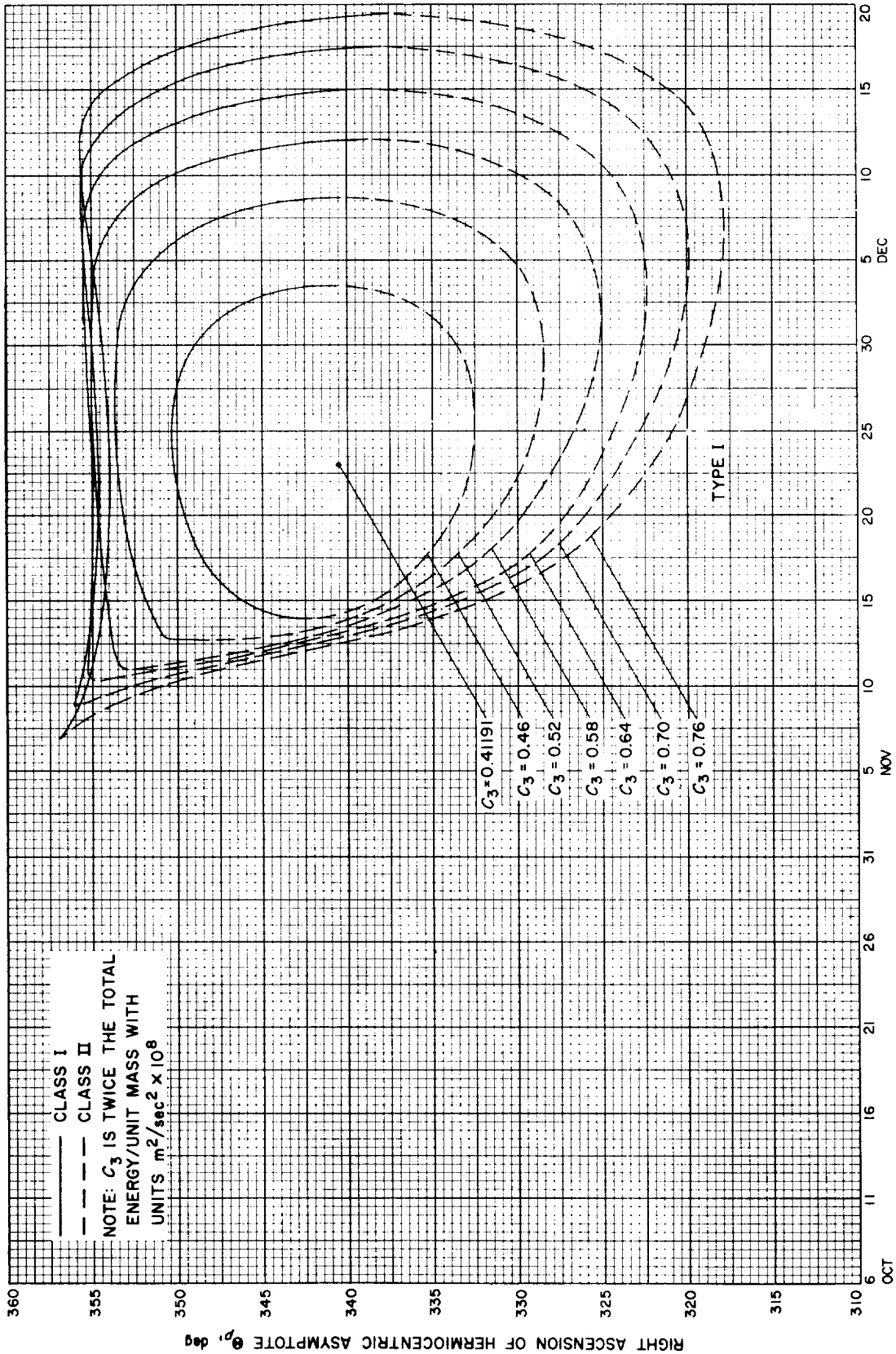

Fig. 4–19(I). Mercury 1967: Right ascension of hermiocentric asymptote vs launch date, Type I

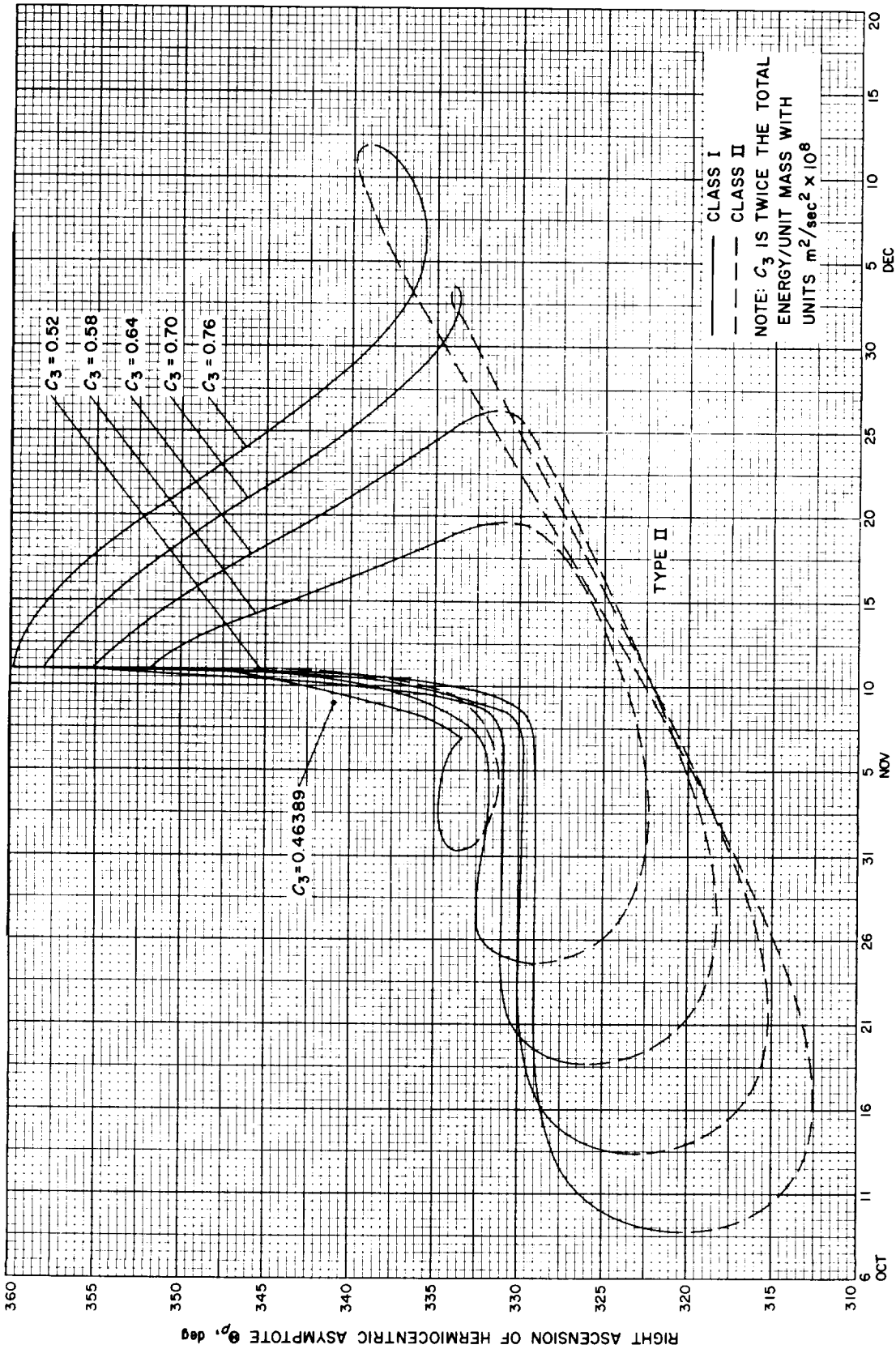

Fig. 4-19(II). Mercury 1967: Right ascension of hermiocentric asymptote vs launch date, Type II

V. MERCURY 1968: TRAJECTORY PARAMETER GRAPHS

Figure

5–1. Mercury 1968: Minimum injection energy vs launch date

5–2. Mercury 1968: Time of flight vs launch date

5–3. Mercury 1968: Heliocentric central angle vs launch date

5–4. Mercury 1968: Earth–Mercury communication distance vs launch date

5–5(I). Mercury 1968: Declination of the geocentric asymptote vs launch date, Type I

5–5(II). Mercury 1968: Declination of the geocentric asymptote vs launch date, Type II

5–6(I). Mercury 1968: Right ascension of the geocentric asymptote vs launch date, Type I

5–6(II). Mercury 1968: Right ascension of the geocentric asymptote vs launch date, Type II

5–7(I). Mercury 1968: Angle between outgoing geocentric asymptote and launch planet's orbital plane vs launch date, Type I

5–7(II). Mercury 1968: Angle between outgoing geocentric asymptote and launch planet's orbital plane vs launch date, Type II

5–8(I). Mercury 1968: Angle between Sun–Earth vector and outgoing geocentric asymptote vs launch date, Type I

5–8(II). Mercury 1968: Angle between Sun–Earth vector and outgoing geocentric asymptote vs launch date, Type II

5–9(I). Mercury 1968: True anomaly in transfer ellipse at launch time vs launch date, Type I

5–9(II). Mercury 1968: True anomaly in transfer ellipse at launch time vs launch date, Type II

5–10. Mercury 1968: True anomaly in transfer ellipse at launch time vs launch date

5–11(I). Mercury 1968: Perihelion of transfer orbit vs launch date, Type I

5–11(II). Mercury 1968: Perihelion of transfer orbit vs launch date, Type II

5–12(I). Mercury 1968: Aphelion of transfer orbit vs launch date, Type I

5–12(II). Mercury 1968: Aphelion of transfer orbit vs launch date, Type II

5–13(I). Mercury 1968: Inclination of the heliocentric transfer plane vs launch date, Type I

V. MERCURY 1968: TRAJECTORY PARAMETER GRAPHS (Cont'd)

Figure

5–13(II). Mercury 1968: Inclination of the heliocentric transfer plane vs launch date, Type II

5–14. Mercury 1968: Celestial latitude at arrival time vs launch date

5–15(I). Mercury 1968: Asymptotic speed with respect to Mercury vs launch date, Type I

5–15(II). Mercury 1968: Asymptotic speed with respect to Mercury vs launch date, Type II

5–16(I). Mercury 1968: Angle between the incoming hermiocentric asymptote and arrival planet's orbital plane vs launch date, Type I

5–16(II). Mercury 1968: Angle between the incoming hermiocentric asymptote and arrival planet's orbital plane vs launch date, Type II

5–17. Mercury 1968: Angle between Mercury–Sun vector and incoming hermiocentric asymptote vs launch date, Type I

5–18(I). Mercury 1968: Declination of the hermiocentric asymptote vs launch date, Type I

5–18(II). Mercury 1968: Declination of the hermiocentric asymptote vs launch date, Type II

5–19(I). Mercury 1968: Right ascension of the hermiocentric asymptote vs launch date, Type I

5–19(II). Mercury 1968: Right ascension of the hermiocentric asymptote vs launch date, Type II

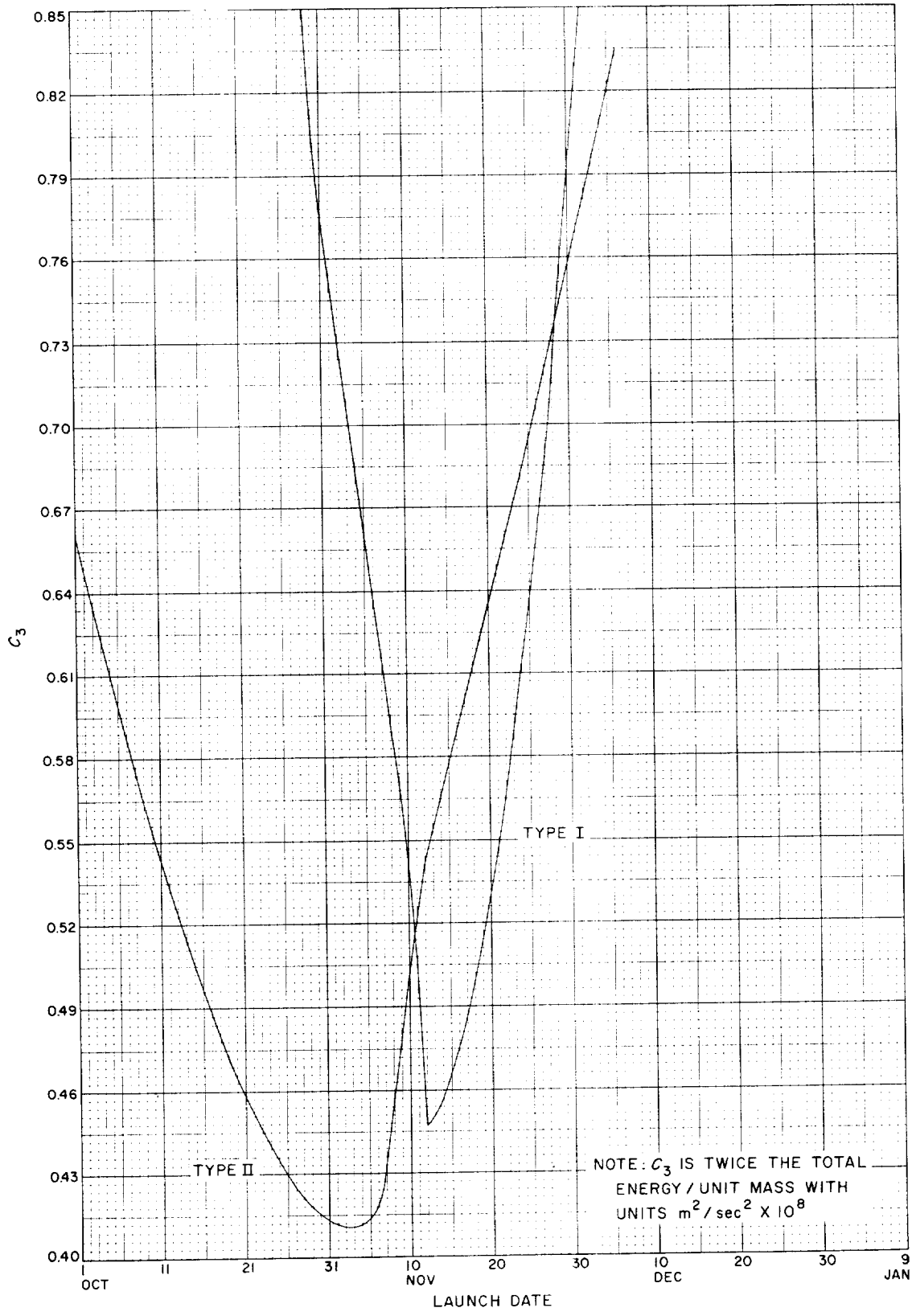

Fig. 5–1. Mercury 1968: Minimum injection energy vs launch date

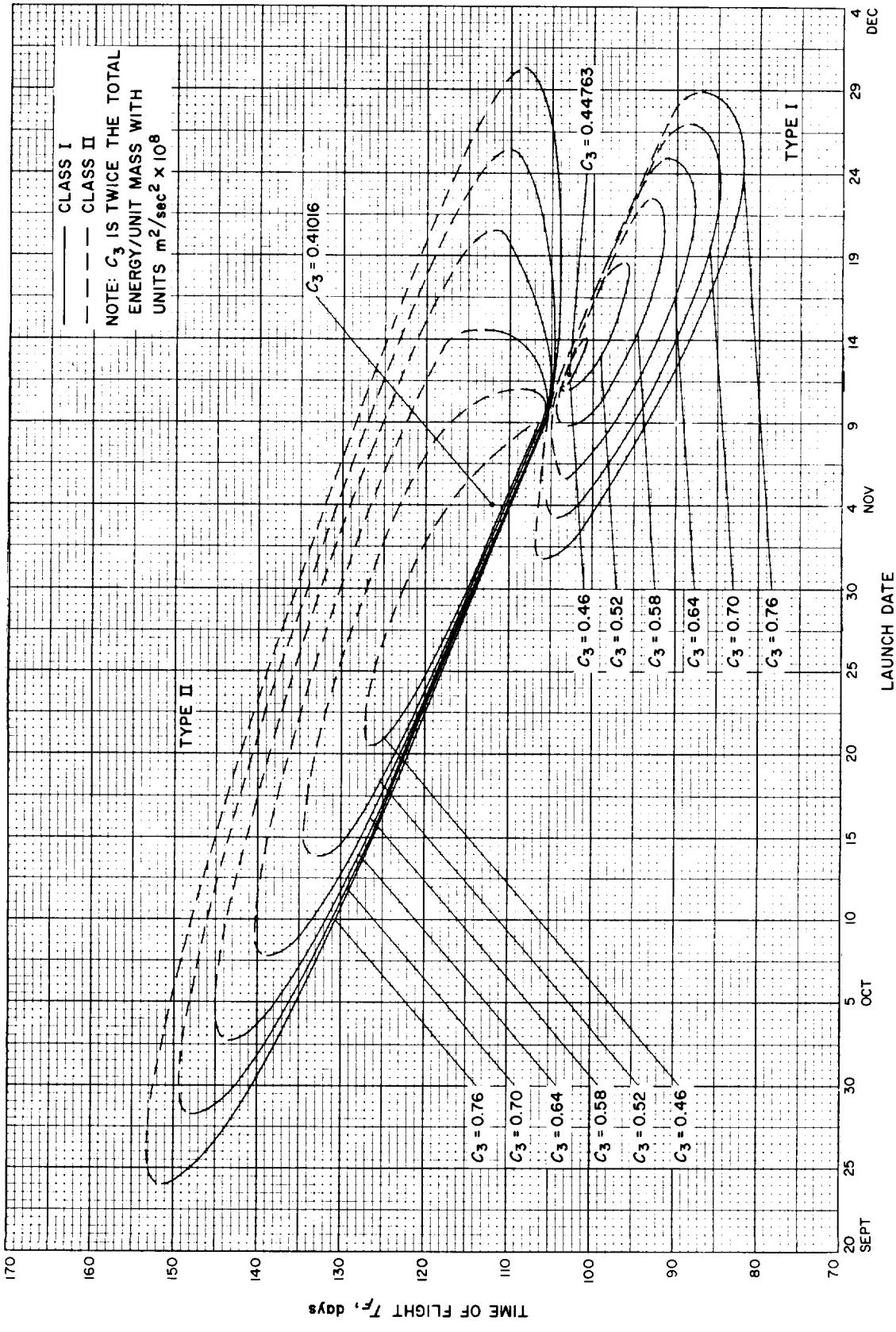

Fig. 5-2. Mercury 1968: Time of flight vs launch date

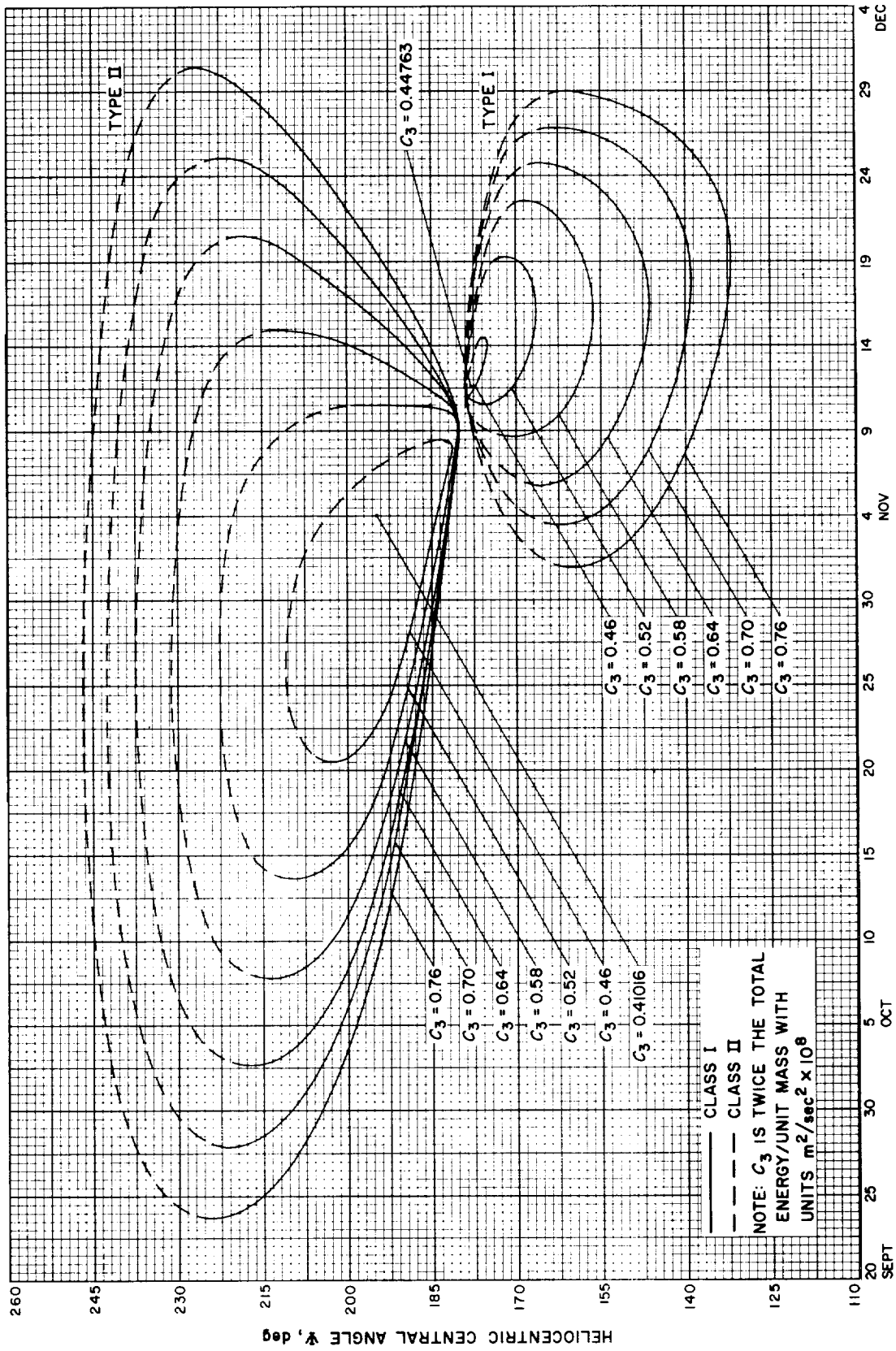

Fig. 5–3. Mercury 1968: Heliocentric central angle vs launch date

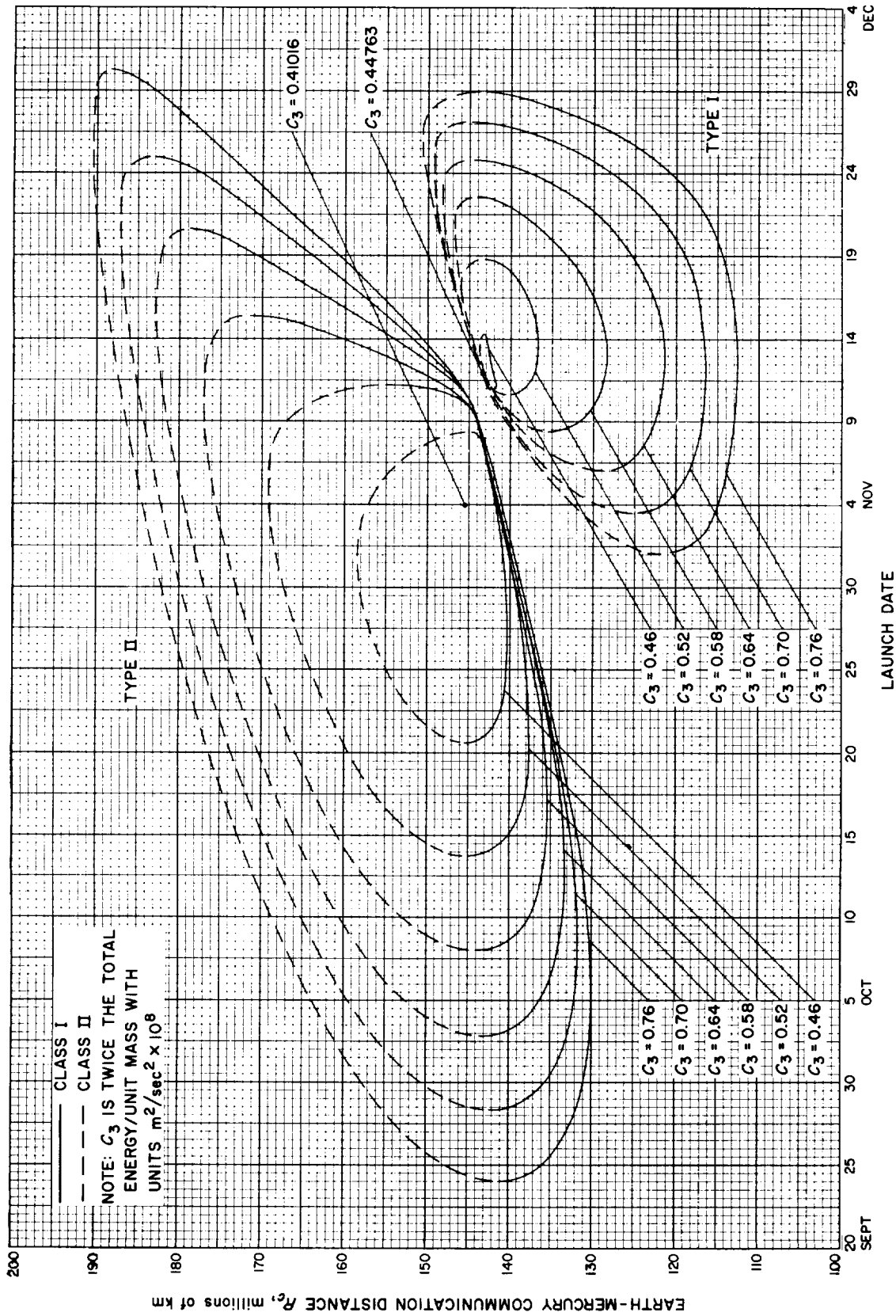

Fig. 5–4. Mercury 1968: Earth–Mercury communication distance vs launch date

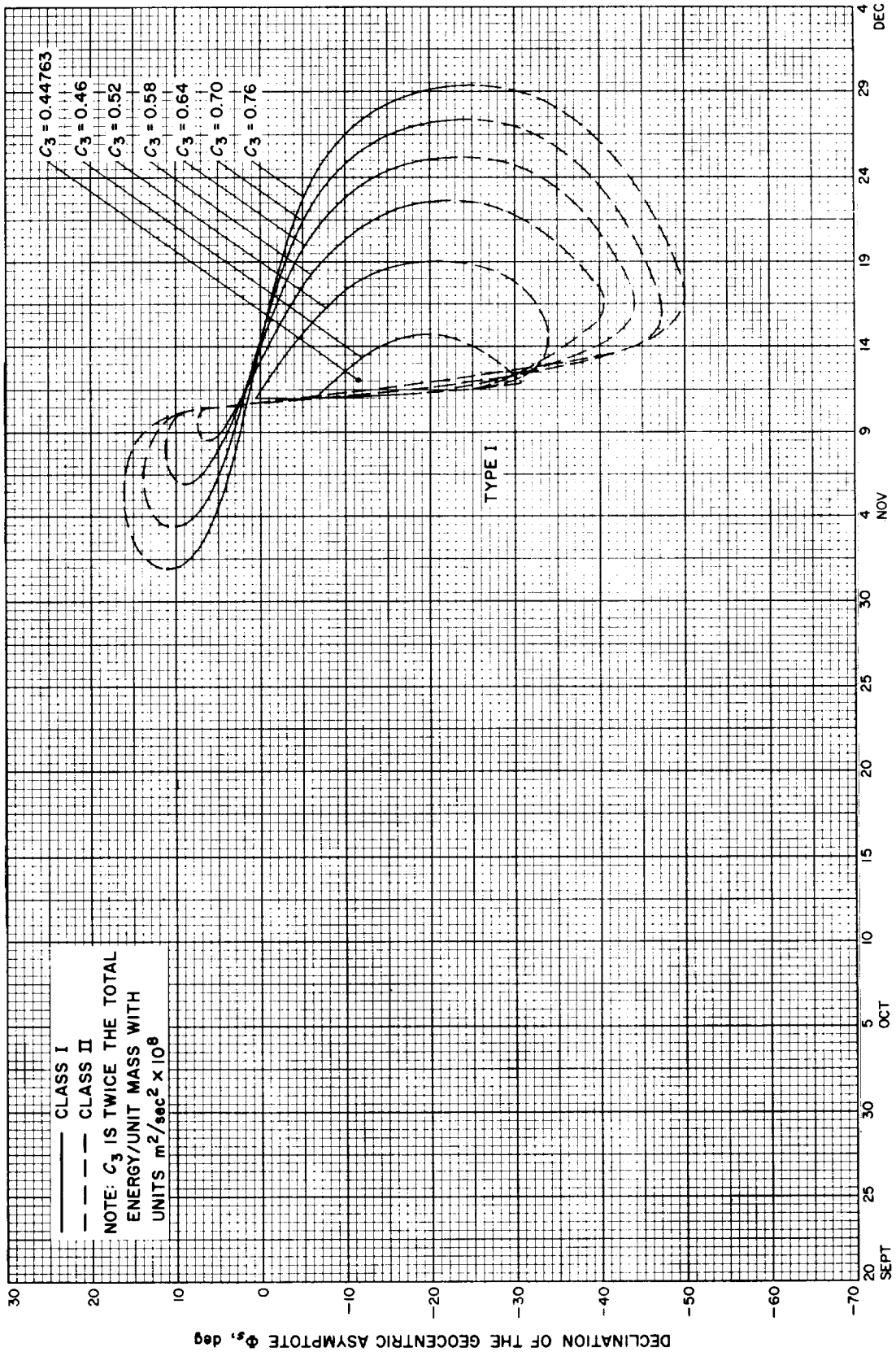

Fig. 5–5(I). Mercury 1968: Declination of the geocentric asymptote vs launch date, Type I

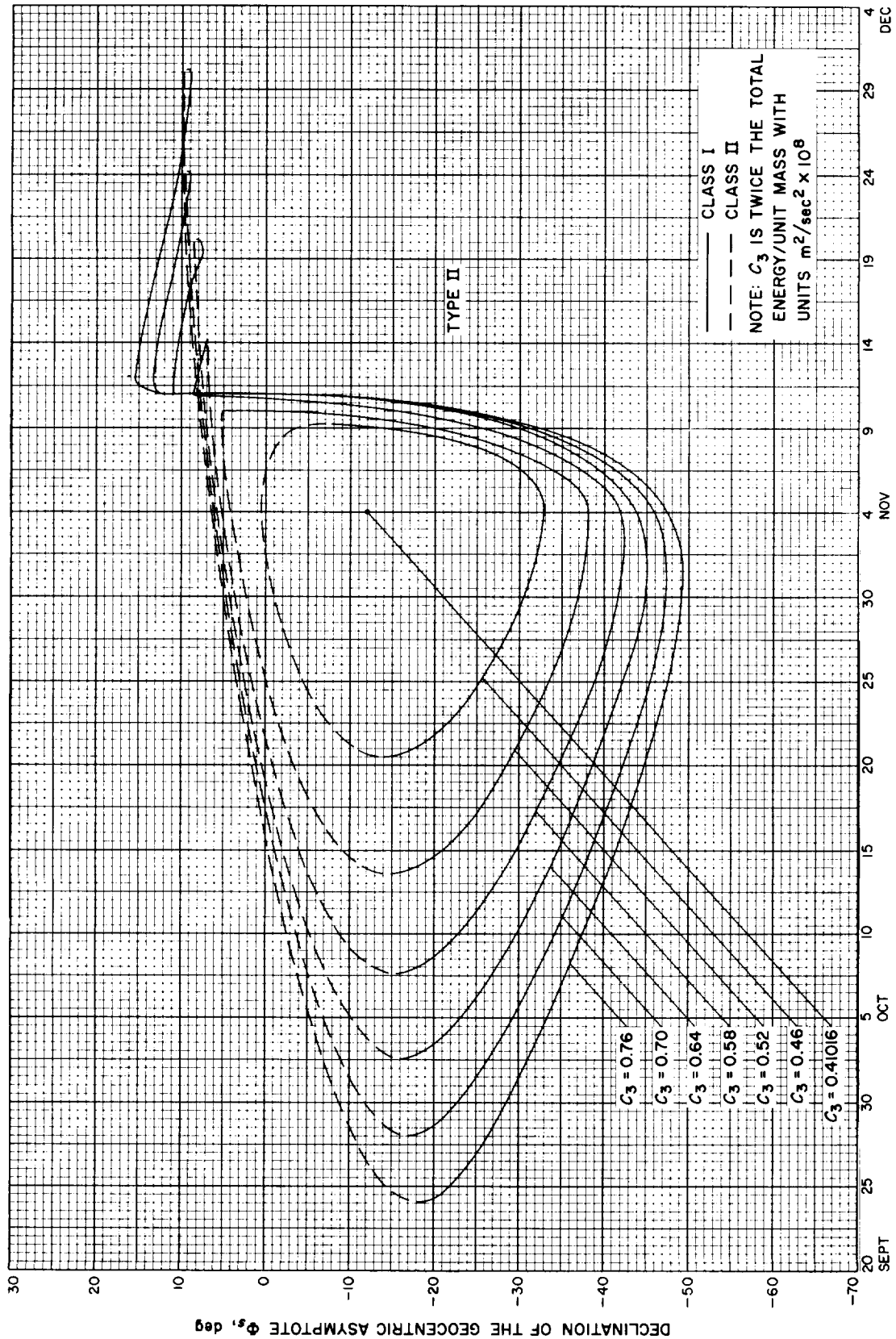

Fig. 5-5(II). Mercury 1968: Declination of the geocentric asymptote vs launch date, Type II

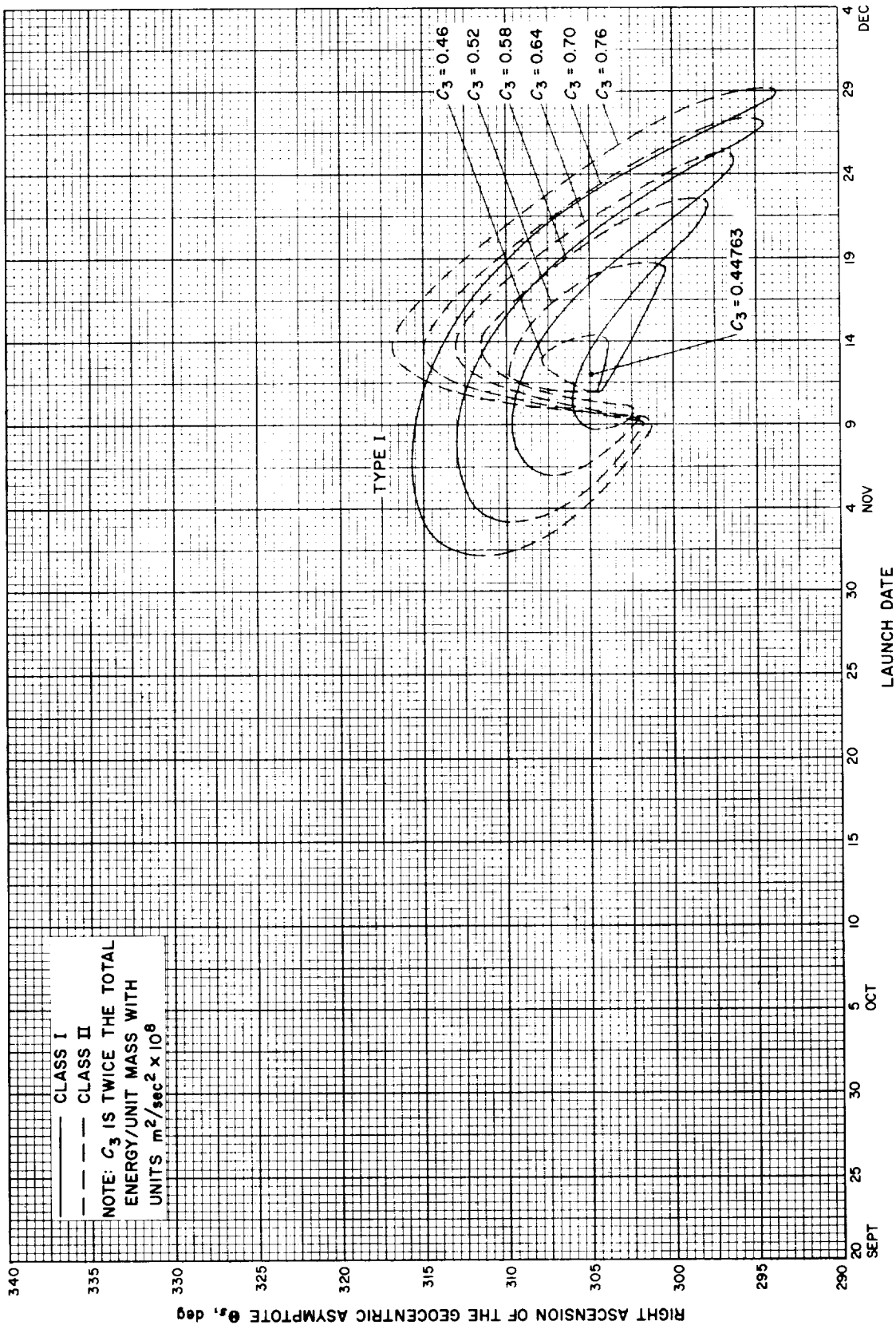

Fig. 5-6(I). Mercury 1968: Right ascension of the geocentric asymptote vs launch date, Type I

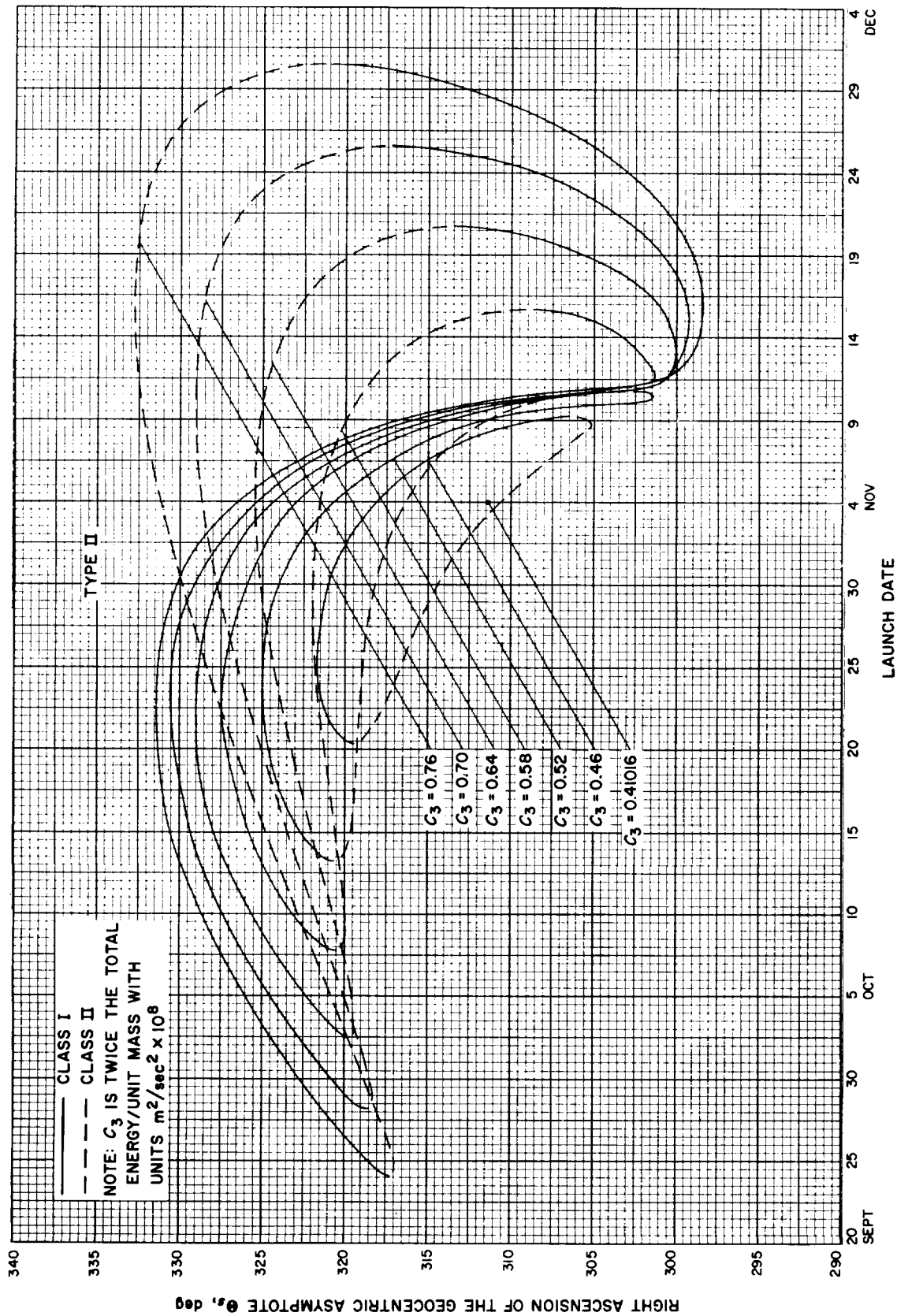

Fig. 5–6(II). Mercury 1968: Right ascension of the geocentric asymptote vs launch date, Type II

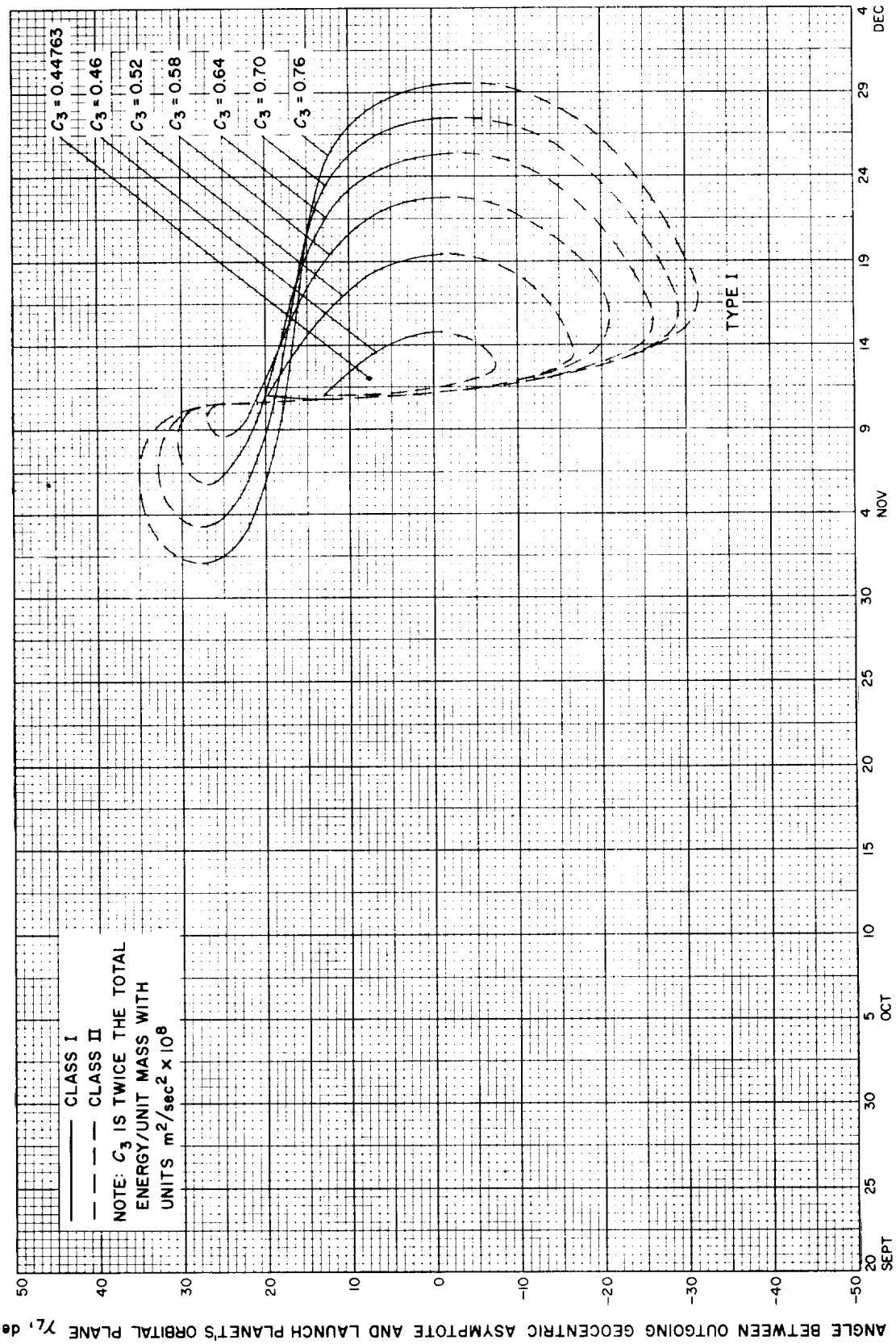

Fig. 5-7(I). Mercury 1968: Angle between outgoing geocentric asymptote and launch planet's orbital plane vs launch date, Type I

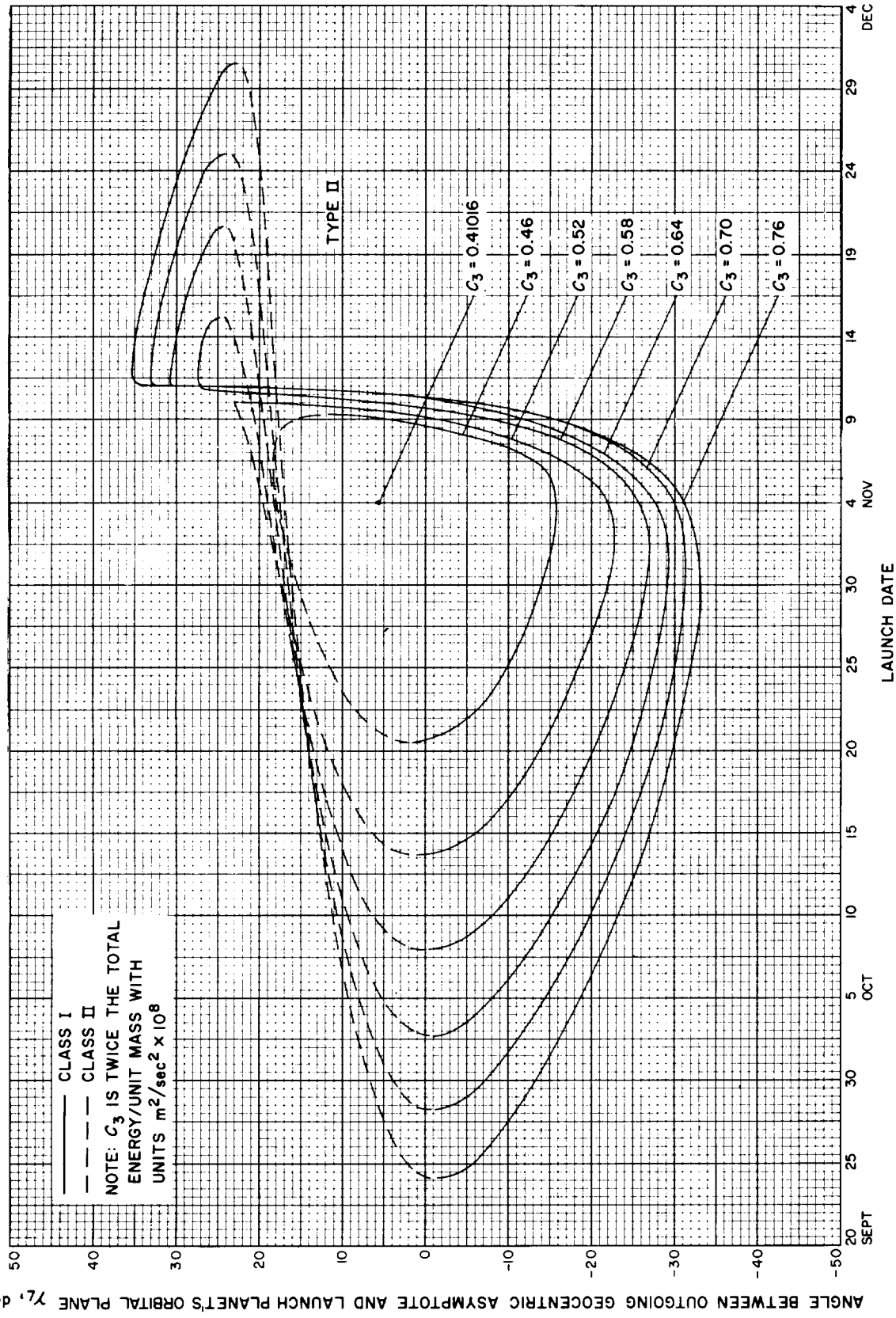

Fig. 5-7(III). Mercury 1968: Angle between outgoing geocentric asymptote and launch planet's orbital plane vs launch date, Type II

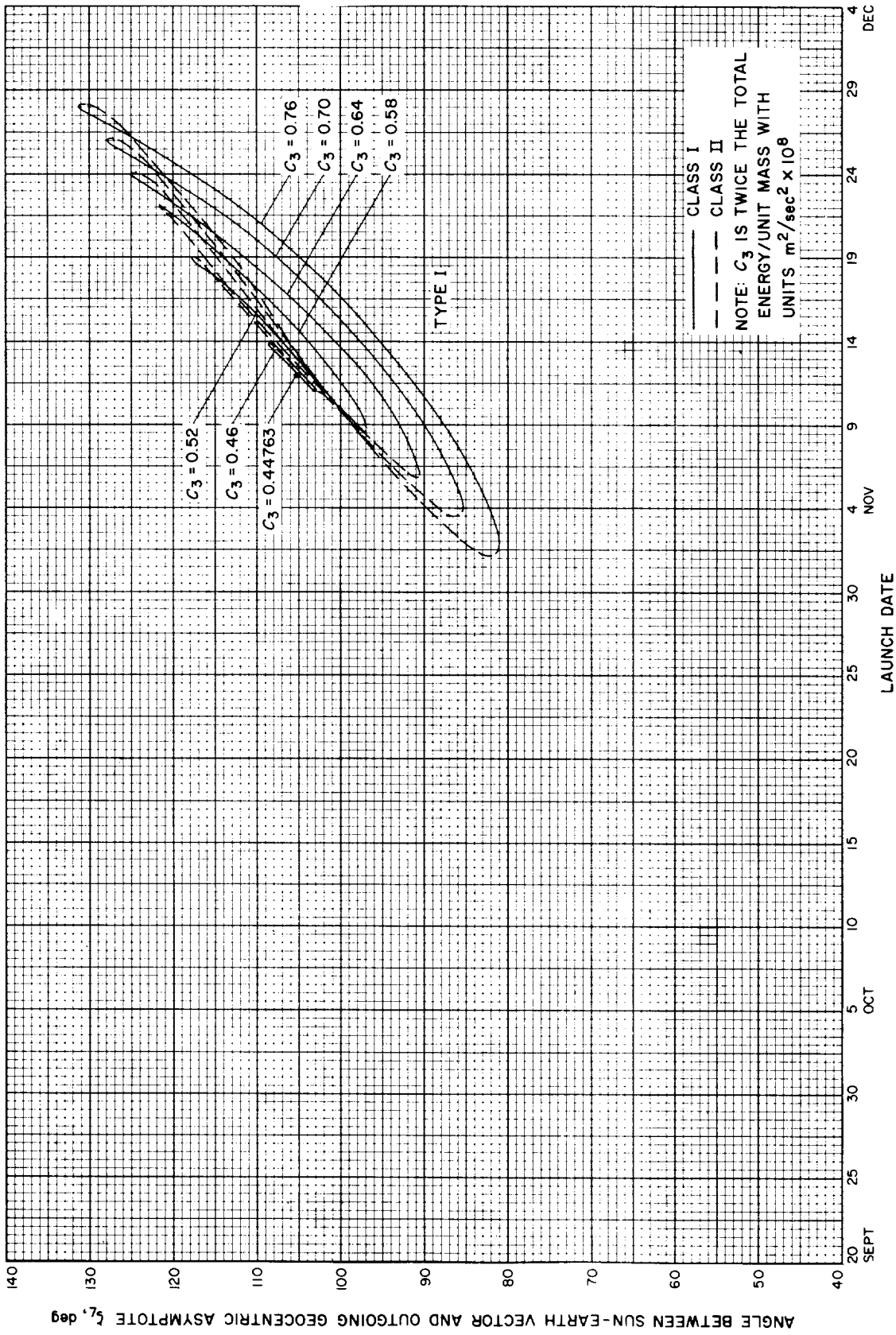

Fig. 5–8(I). Mercury 1968: Angle between Sun–Earth vector and outgoing geocentric asymptote vs launch date, Type I

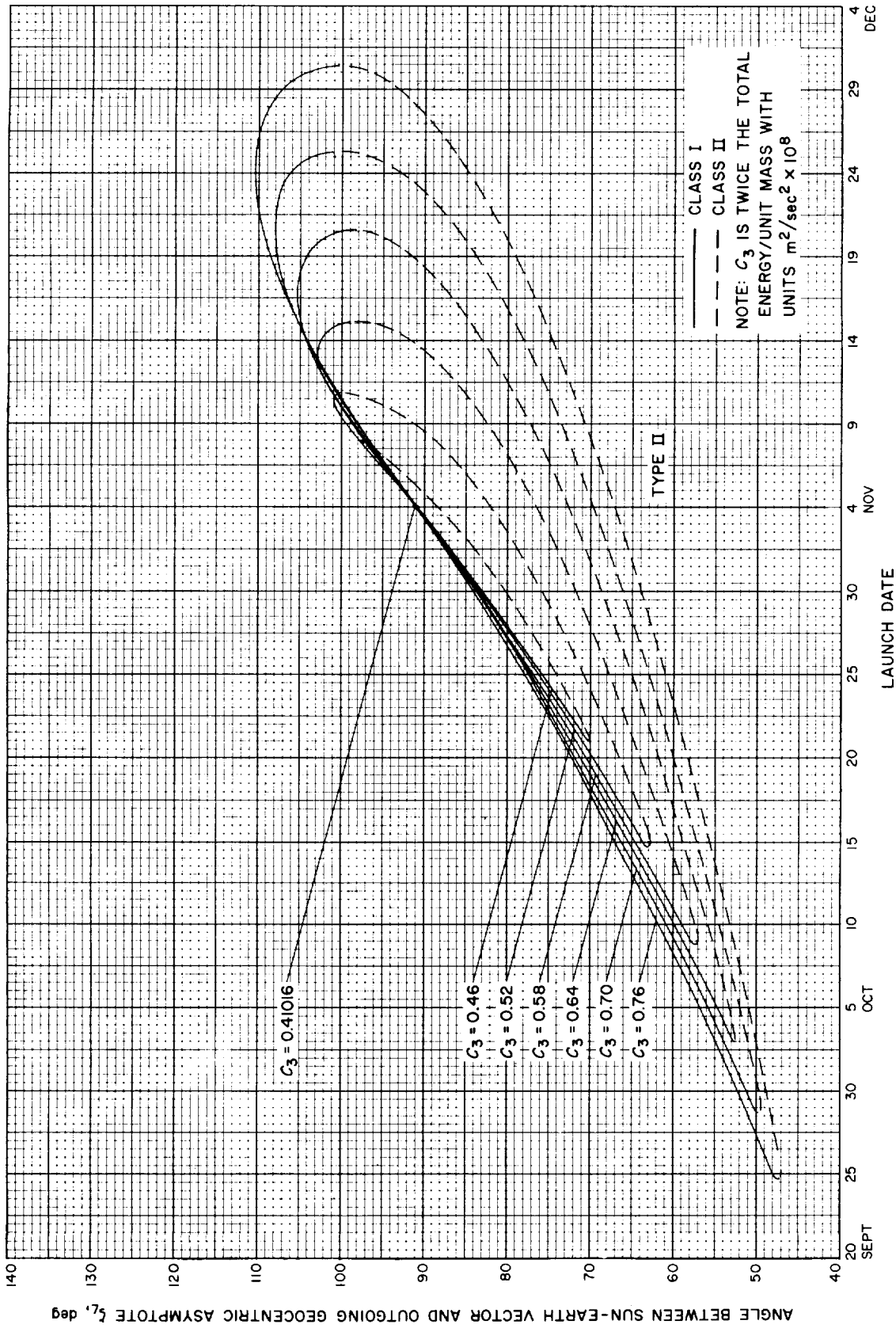

Fig. 5-8(II). Mercury 1968: Angle between Sun–Earth vector and outgoing geocentric asymptote vs launch date, Type II

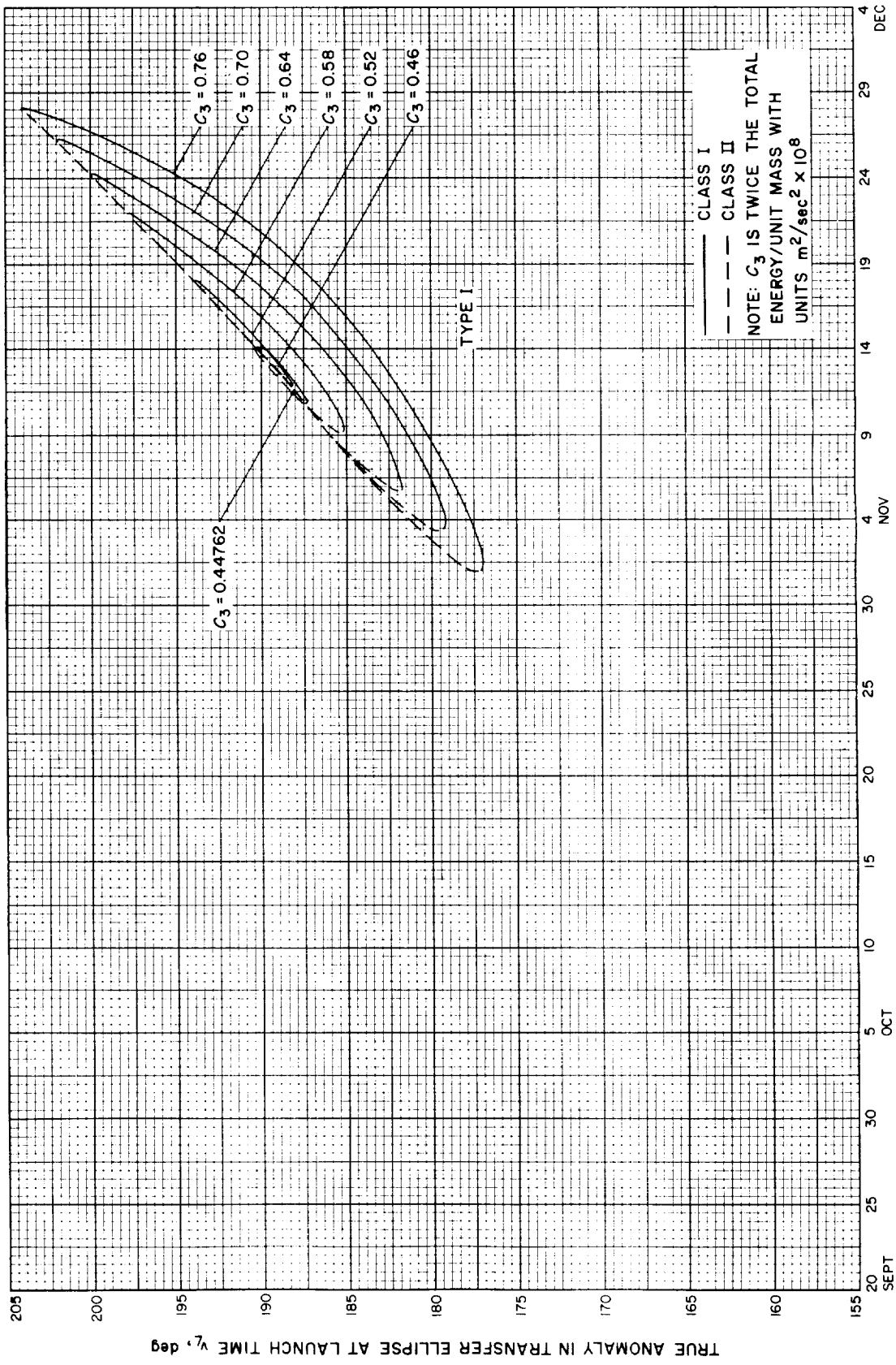

Fig. 5-9(I). Mercury 1968: True anomaly in transfer ellipse at launch time vs launch date, Type I

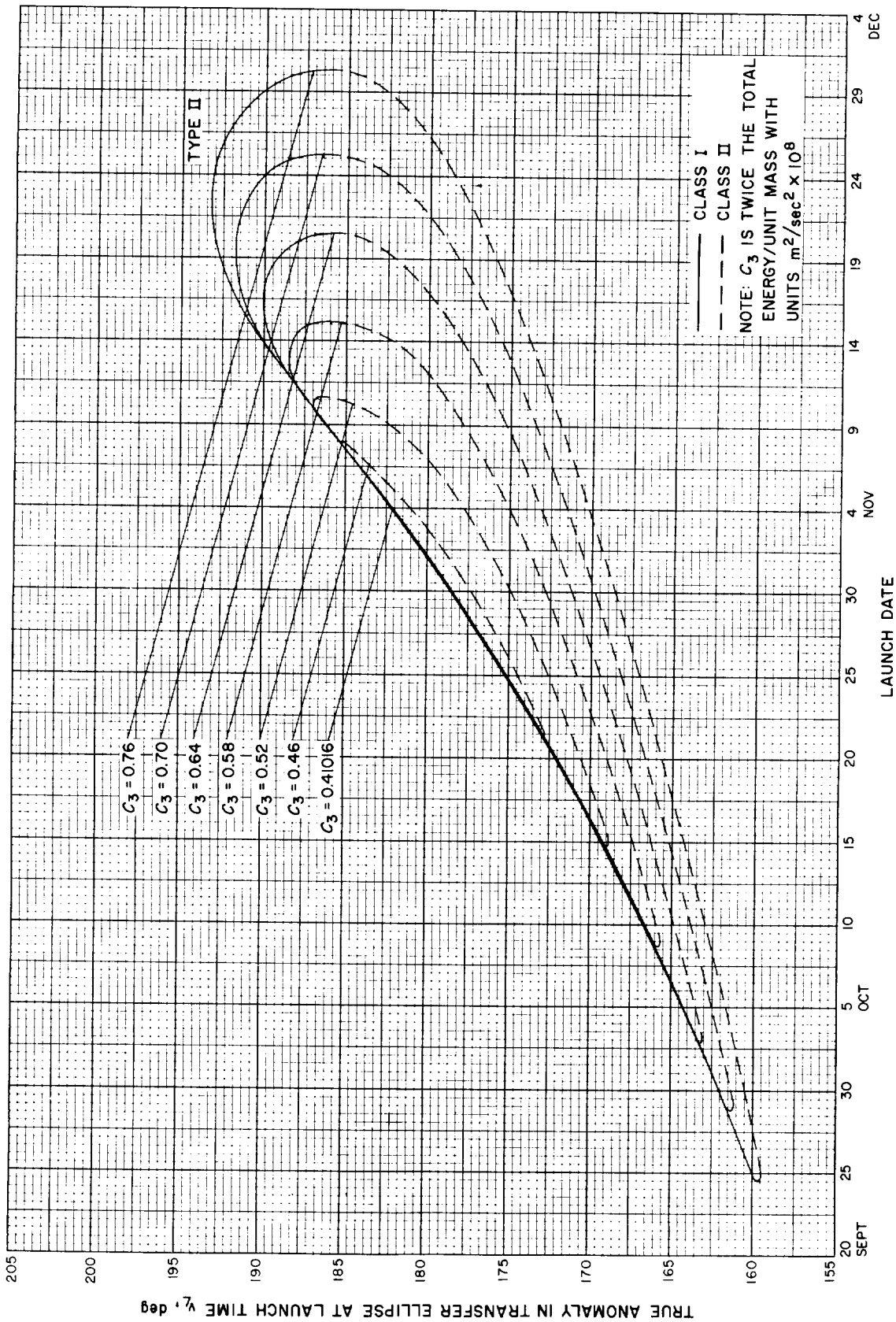

Fig. 5-9(II). Mercury 1968: True anomaly in transfer ellipse at launch time vs launch date, Type II

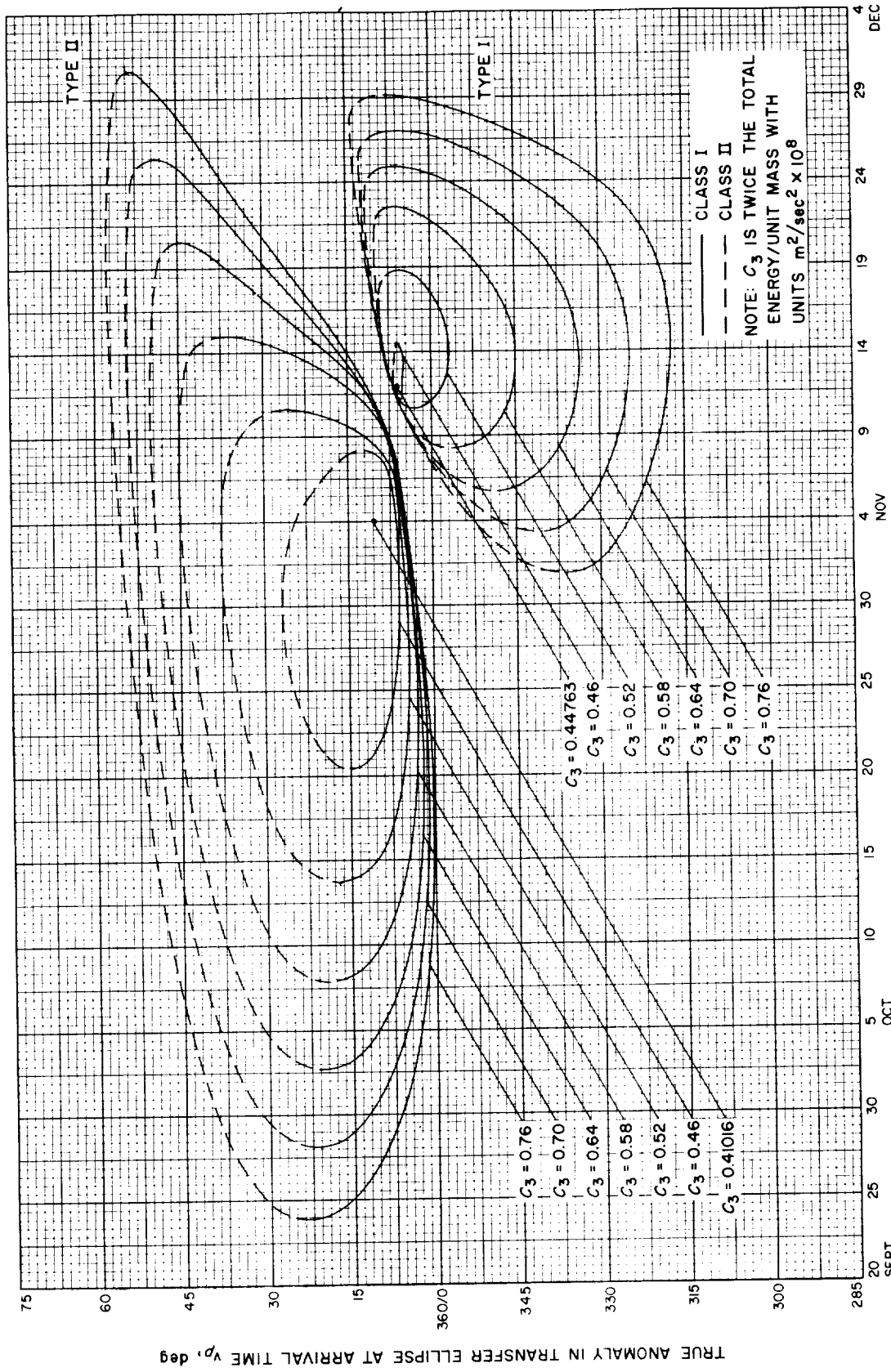

Fig. 5–10. Mercury 1968: True anomaly in transfer ellipse at launch time vs launch date

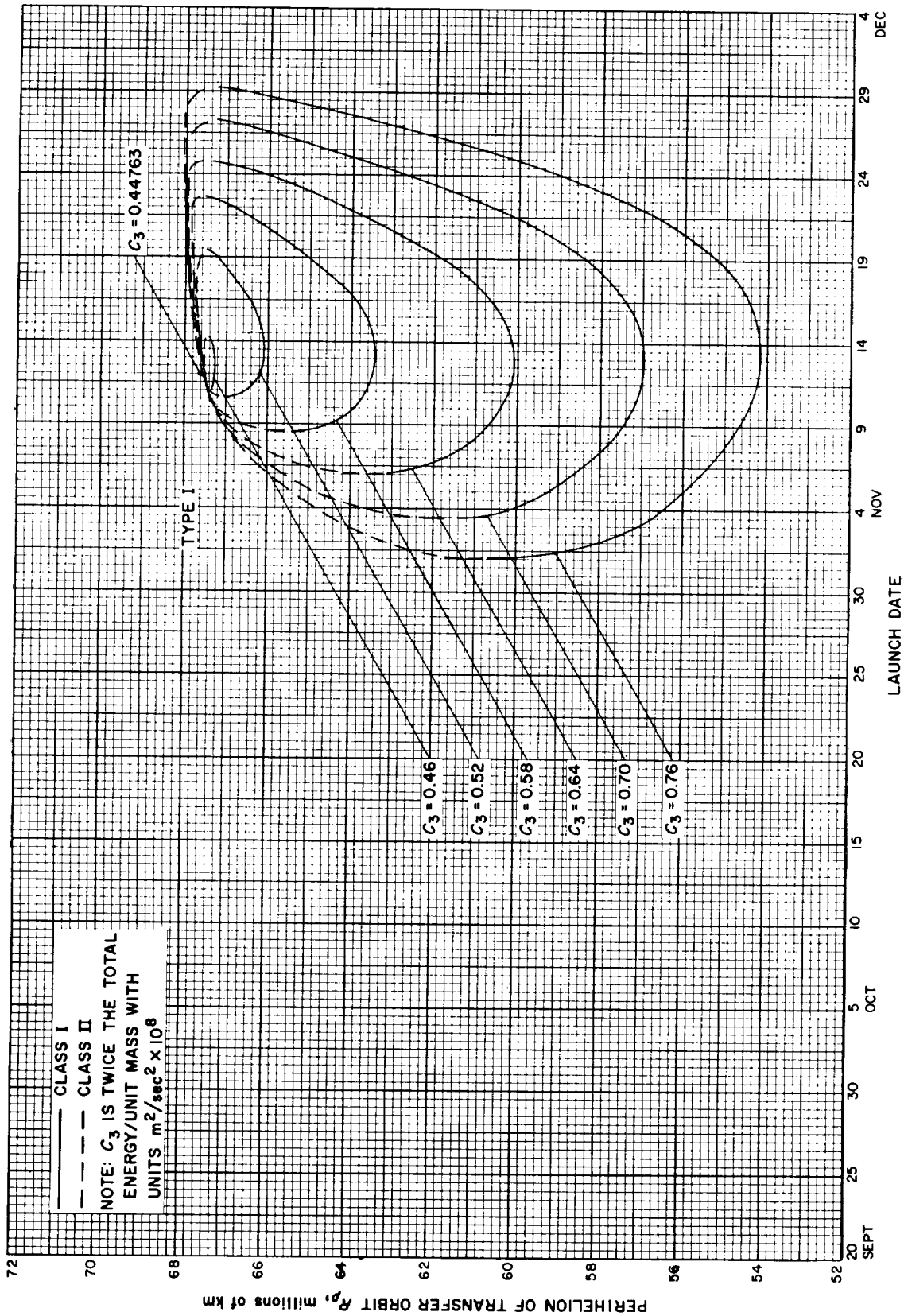

Fig. 5-11(I). Mercury 1968: Perihelion of transfer orbit vs launch date, Type I

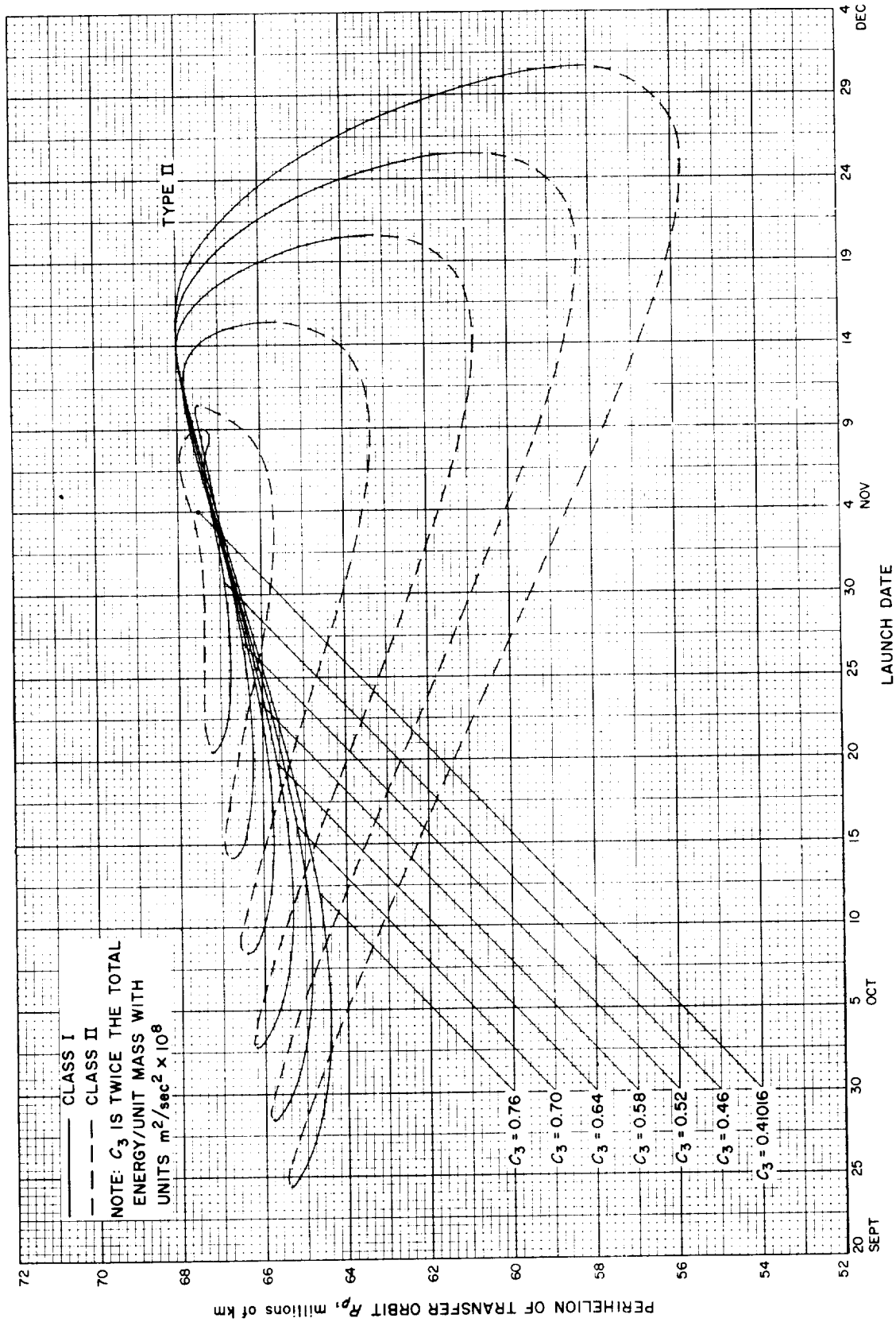

Fig. 5-11(II). Mercury 1968: Perihelion of transfer orbit vs launch date, Type II

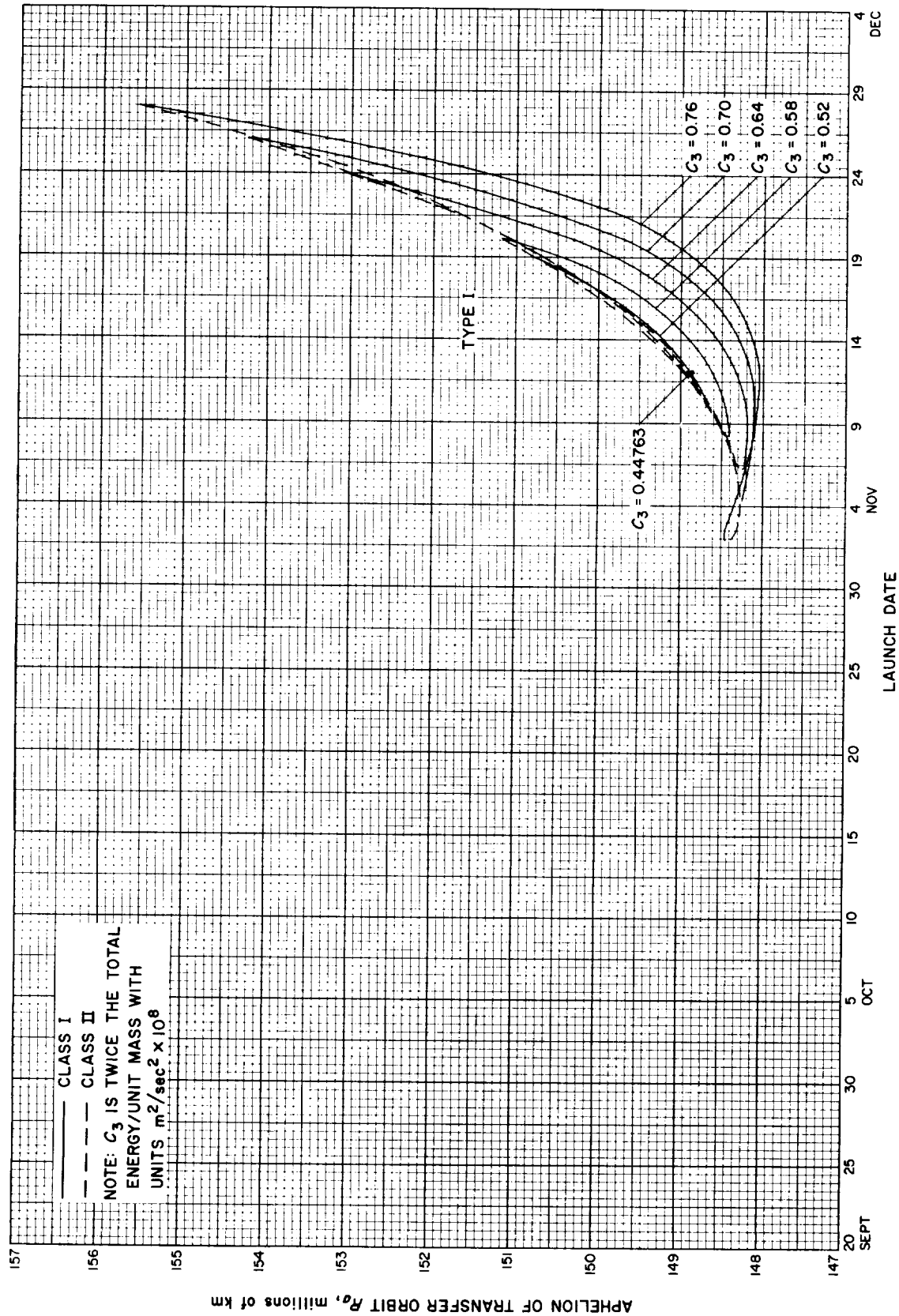

Fig. 5–12(I). Mercury 1968: Aphelion of transfer orbit vs launch date, Type I

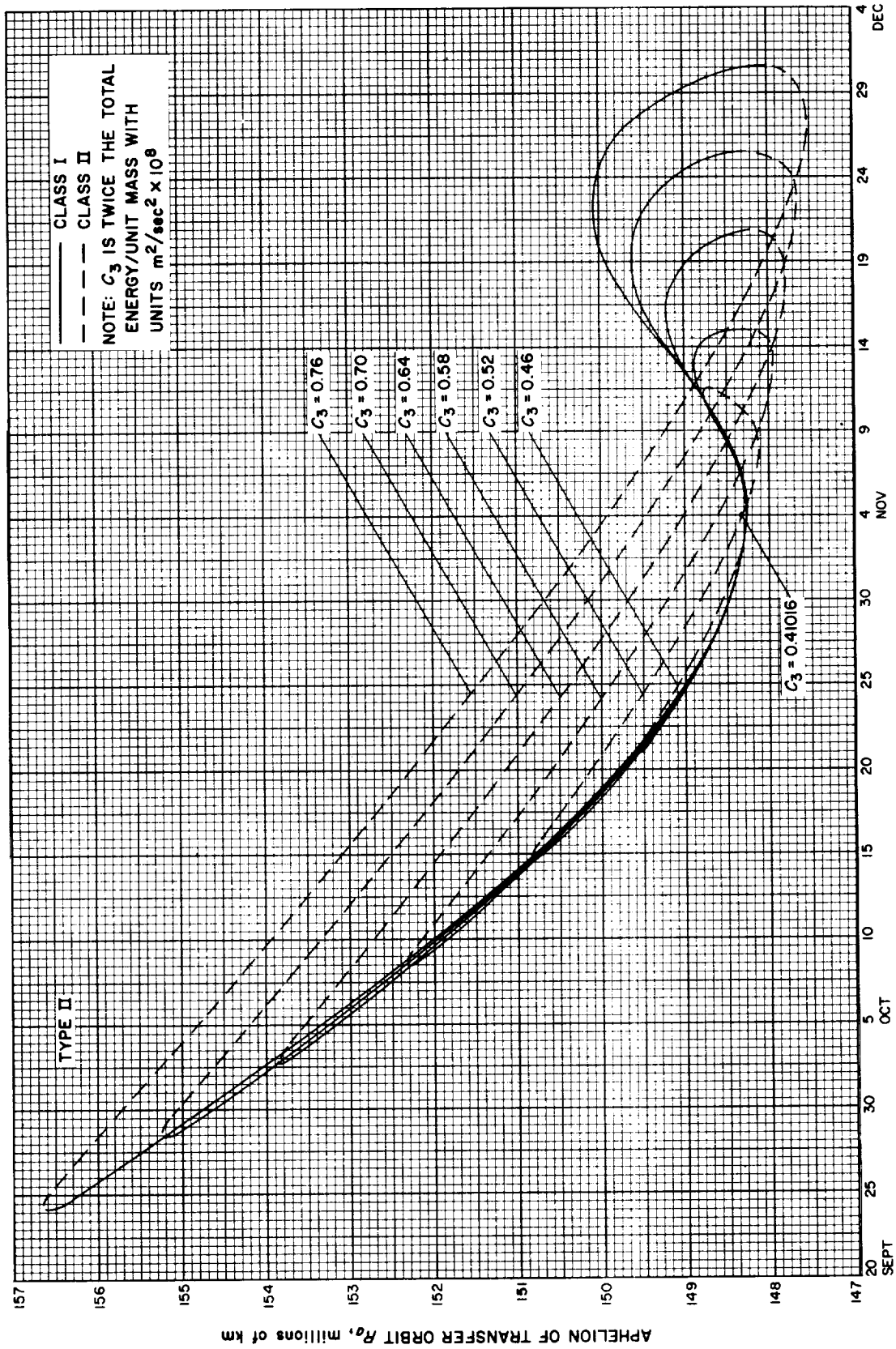

Fig. 5-12(III). Mercury 1968: Aphelion of transfer orbit vs launch date, Type II

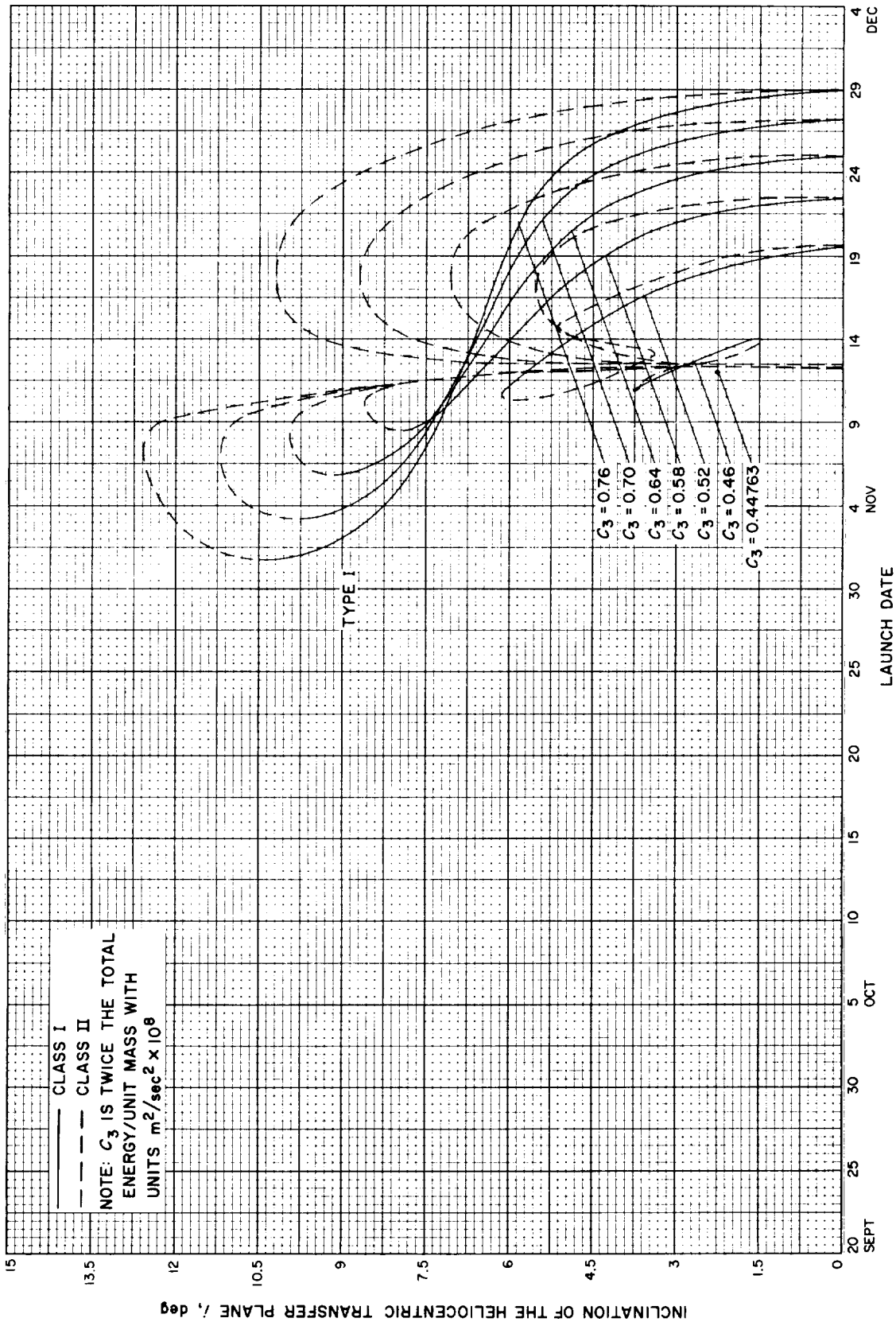

Fig. 5-13(I). Mercury 1968: Inclination of the heliocentric transfer plane vs launch date, Type I

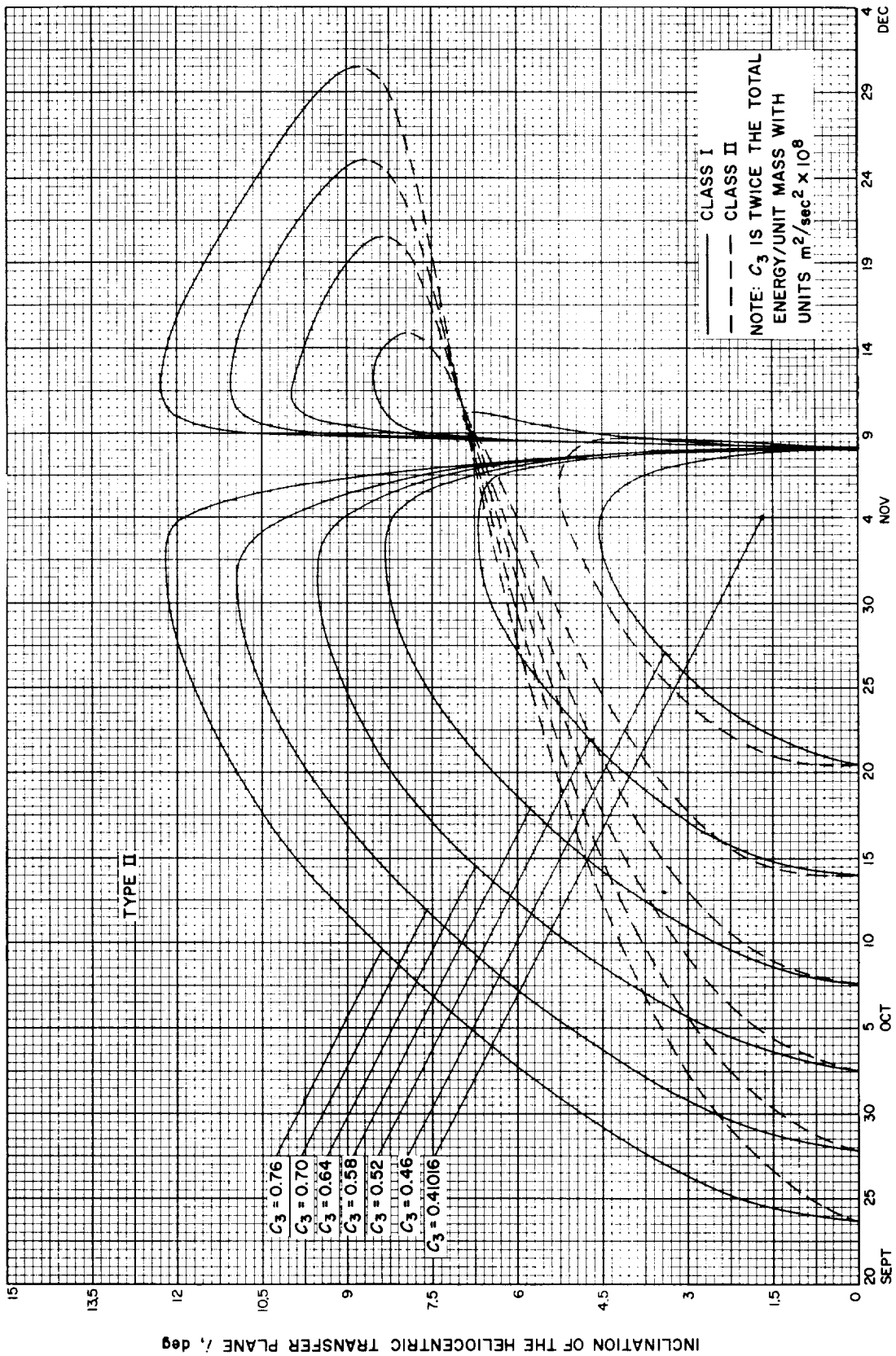

Fig. 5-13(II). Mercury 1968: Inclination of the heliocentric transfer plane vs launch date, Type II

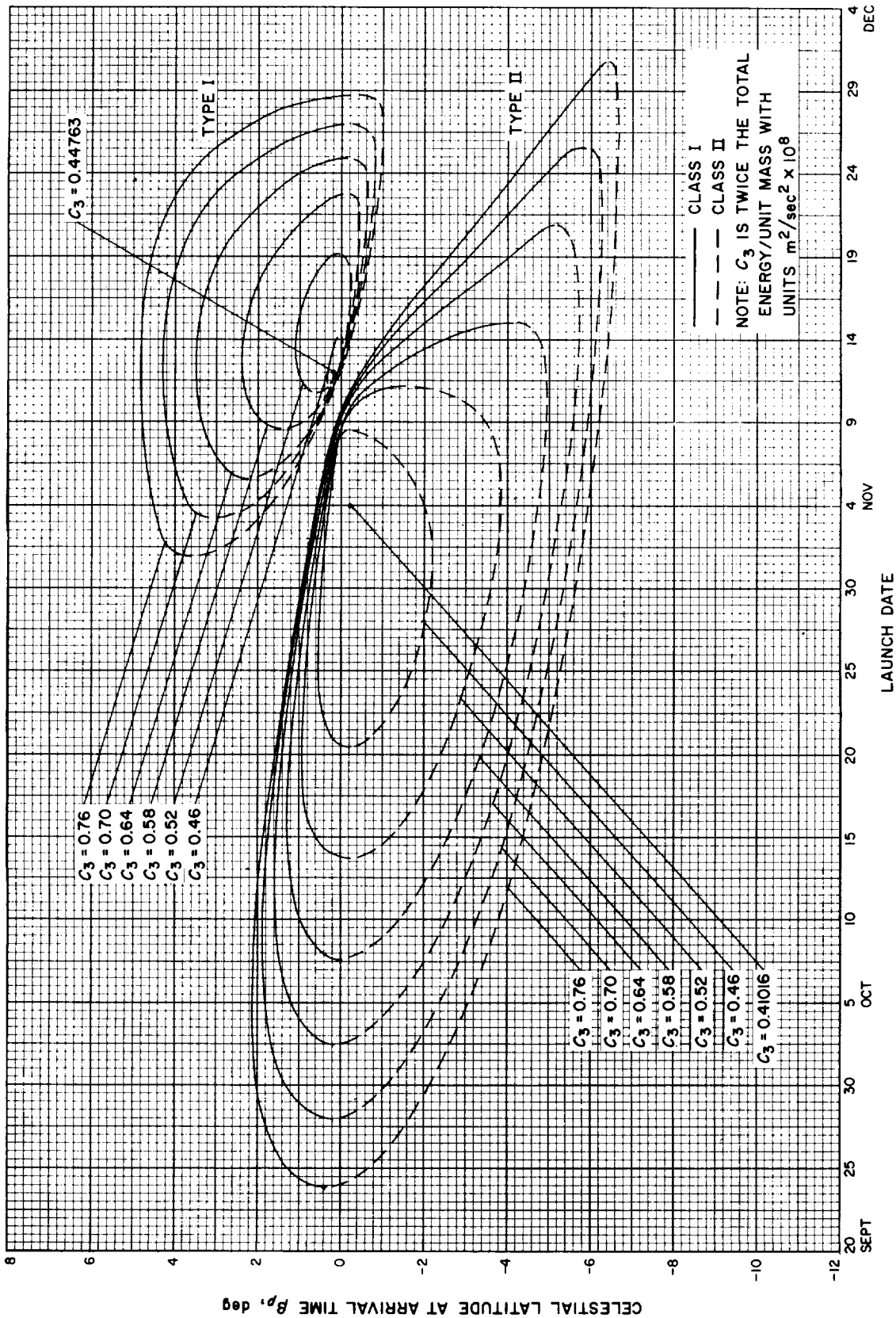

Fig. 5-14. Mercury 1968: Celestial latitude at arrival time vs launch date

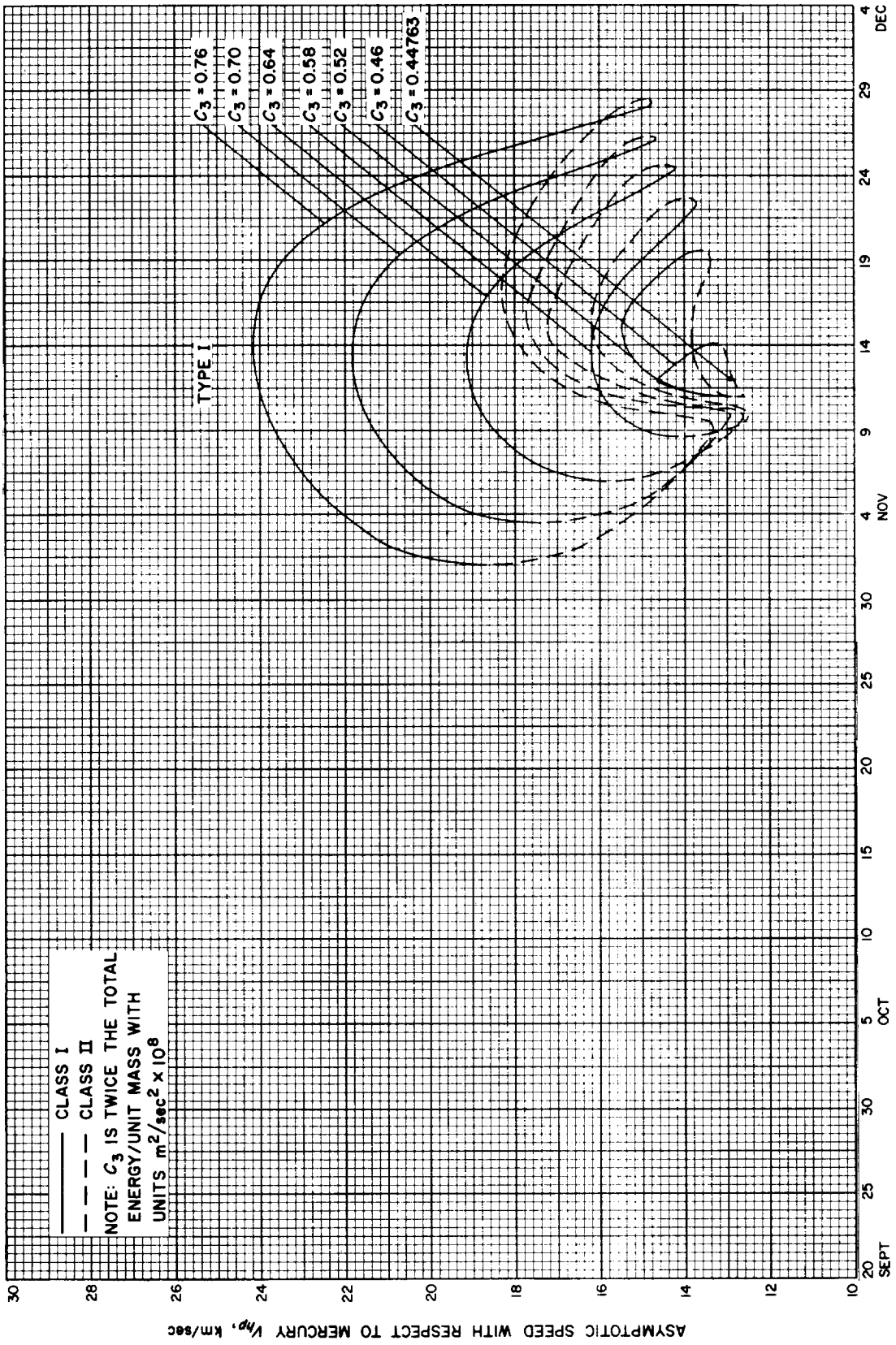

Fig. 5-15(I). Mercury 1968: Asymptotic speed with respect to Mercury vs launch date, Type I

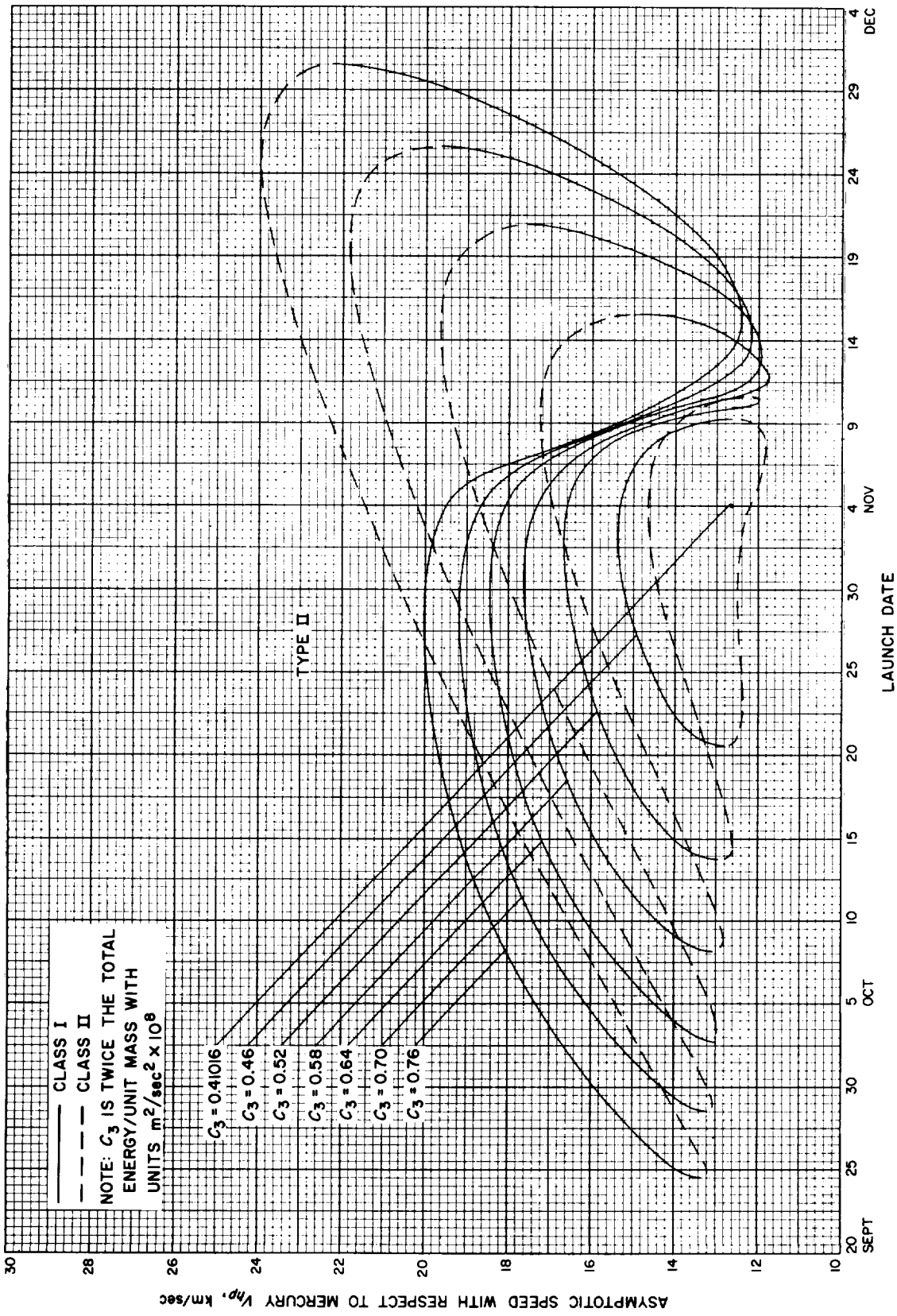

Fig. 5–15(II). Mercury 1968: Asymptotic speed with respect to Mercury vs launch date, Type II

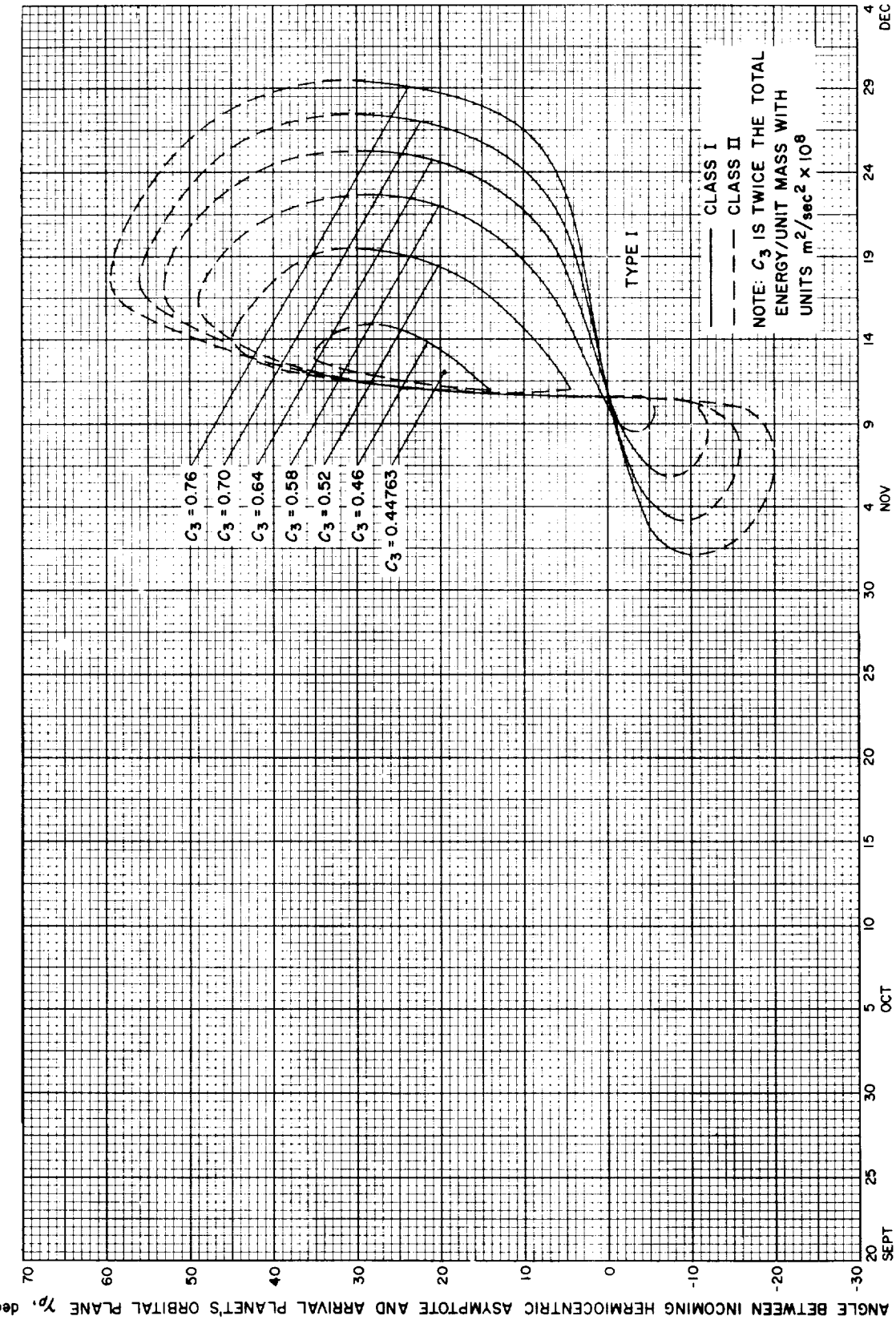

Fig. 5–16(I). Mercury 1968: Angle between the incoming hermiocentric asymptote and arrival planet's orbital plane vs launch date, Type I

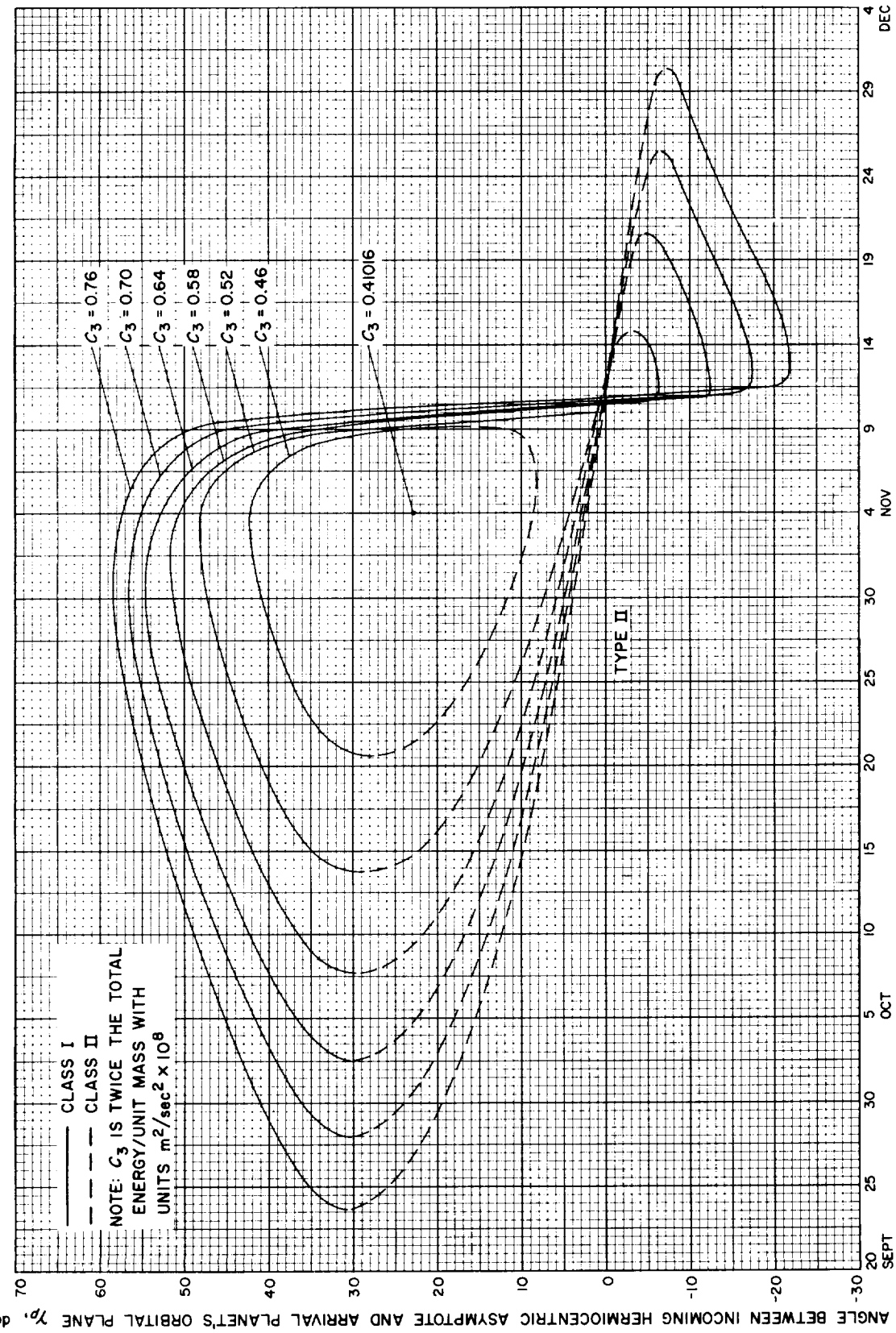

Fig. 5-16(II). Mercury 1968: Angle between the incoming hermiocentric asymptote and arrival planet's orbital plane vs launch date, Type II

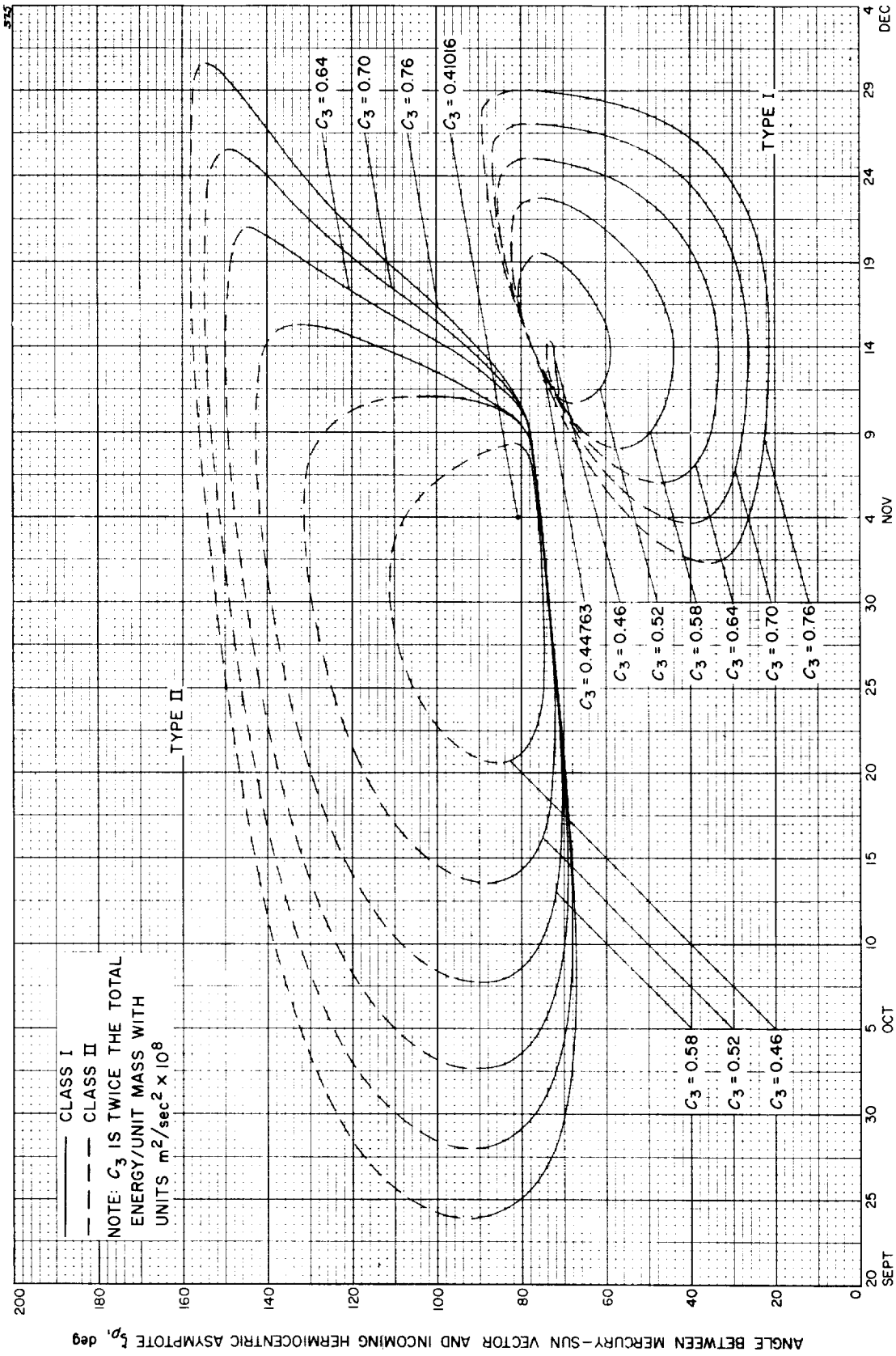

Fig. 5-17. Mercury 1968: Angle between Mercury–Sun vector and incoming hermiocentric asymptote vs launch date, Type I

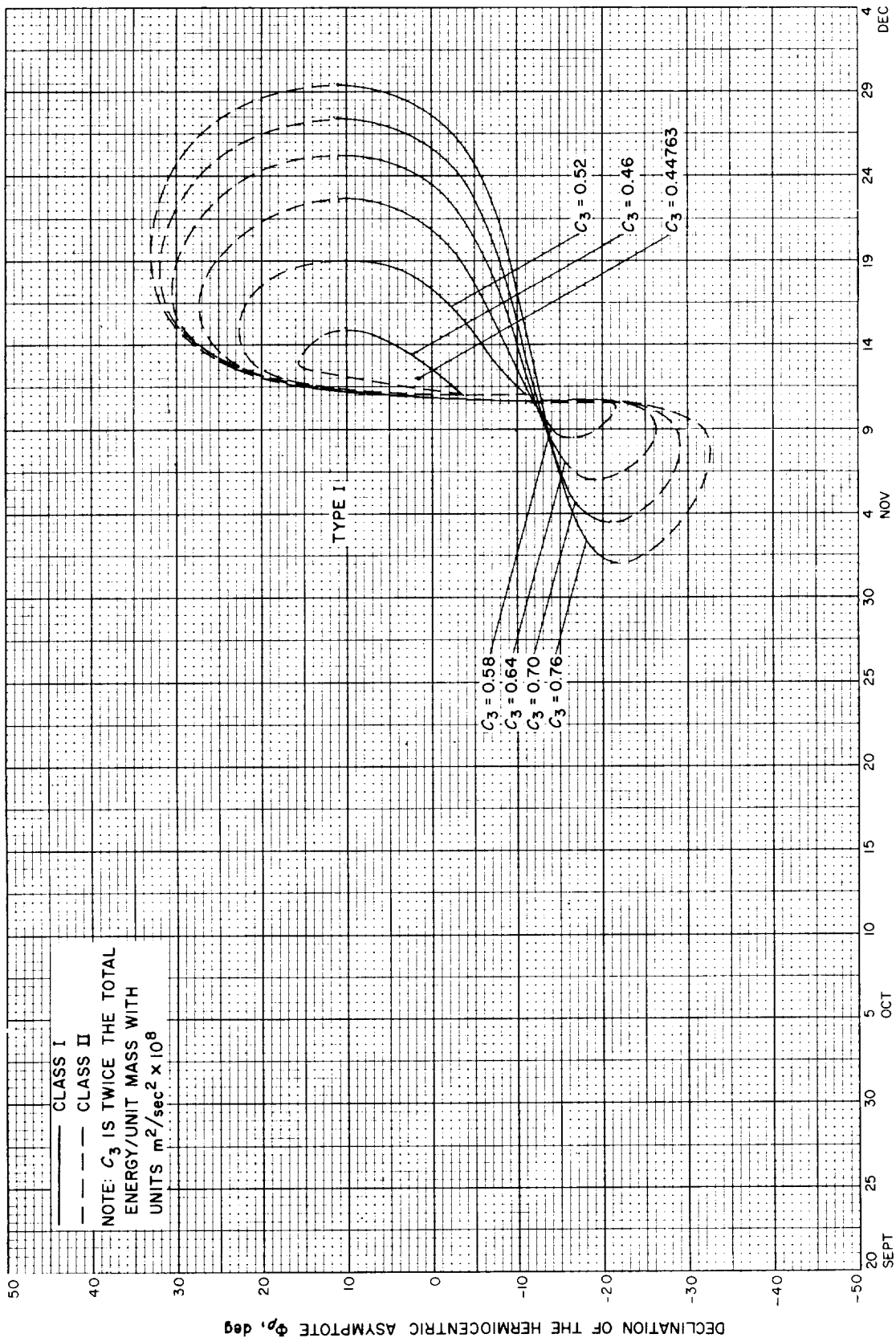

Fig. 5-18(I). Mercury 1968: Declination of the hermiocentric asymptote vs launch date, Type I

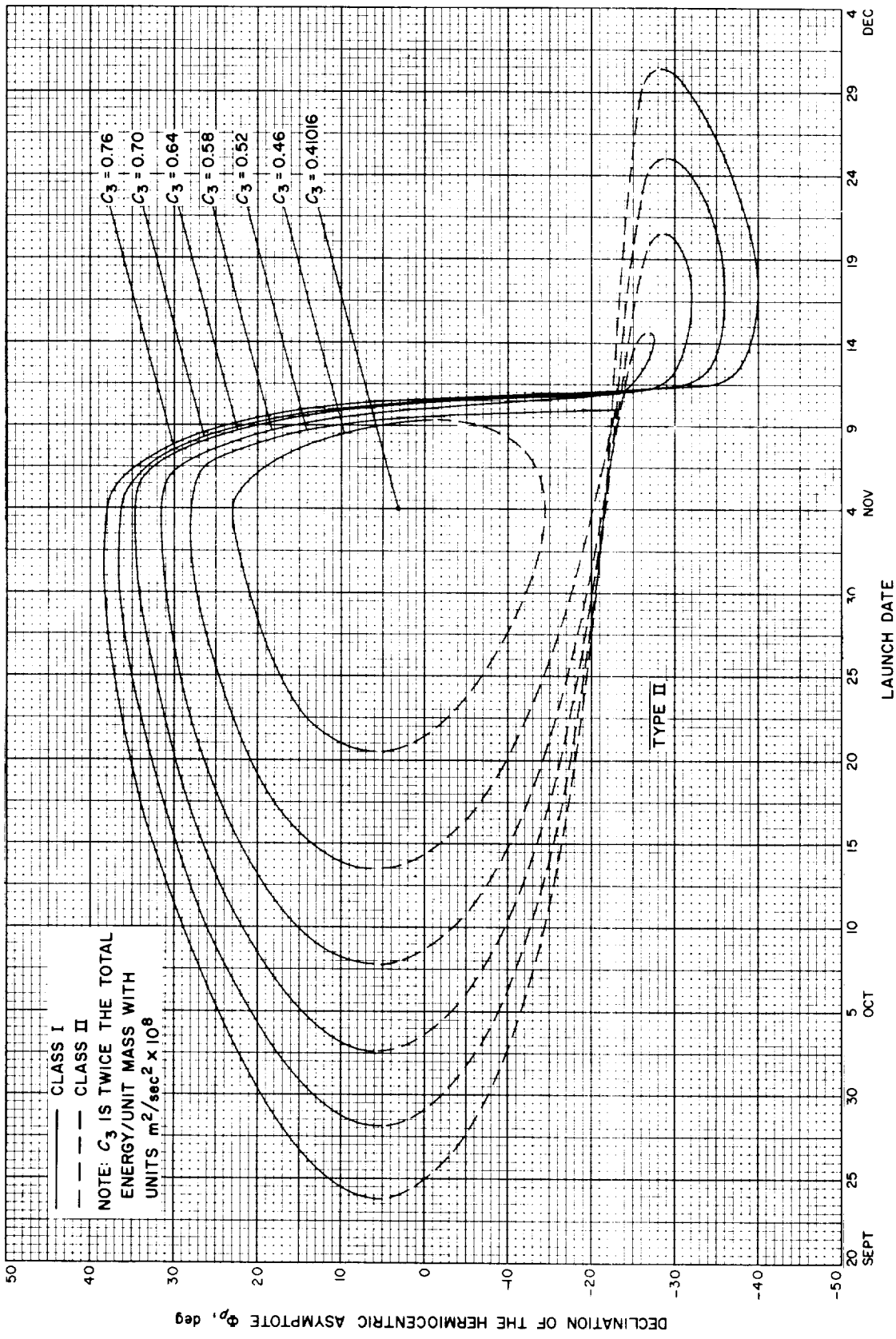

Fig. 5-18(II). Mercury 1968: Declination of the hermiocentric asymptote vs launch date, Type II

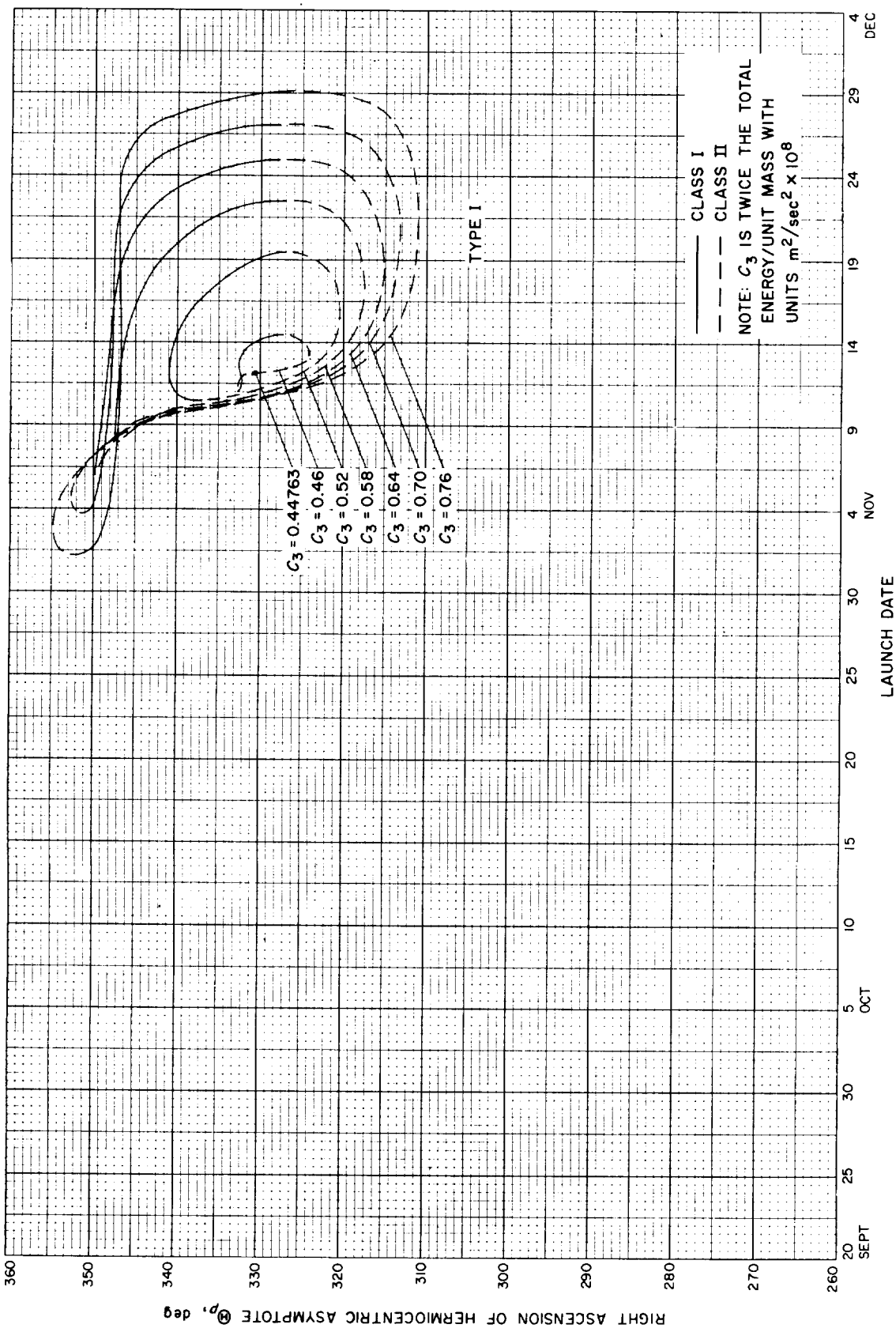

Fig. 5-19(l). Mercury 1968: Right ascension of the hermiocentric asymptote vs launch date, Type I

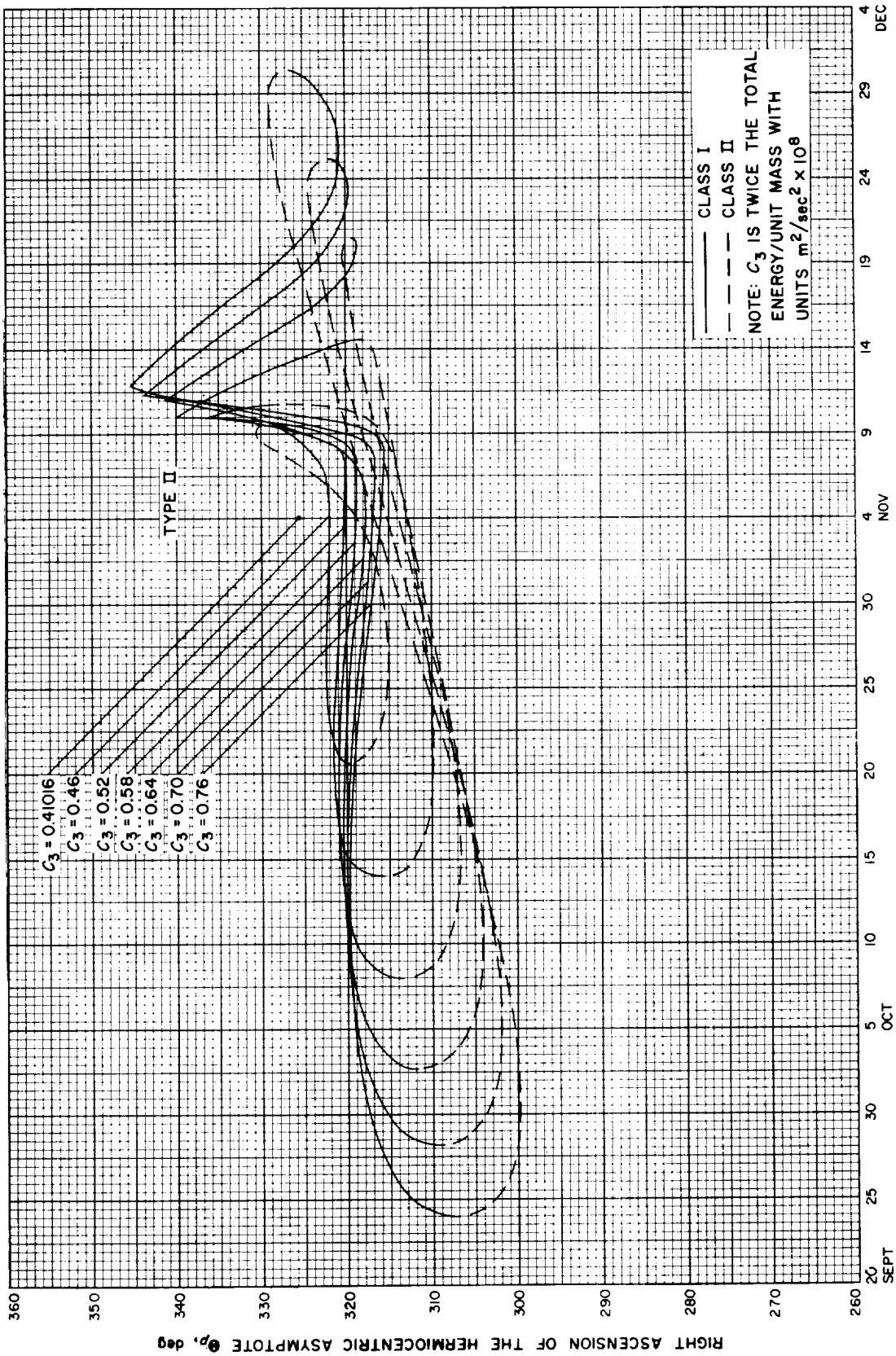

Fig. 5-19(II). Mercury 1968: Right ascension of the hermiocentric asymptote vs launch date, Type II

VI. JUPITER 1968–69: TRAJECTORY PARAMETER GRAPHS

Figure

6–1. Jupiter 68–69: Minimum injection energy vs launch date

6–2. Jupiter 68–69: Time of flight vs launch date

6–3. Jupiter 68–69: Heliocentric central angle vs launch date

6–4(I). Jupiter 68–69: Earth–Jupiter communication distance vs launch date, Type I

6–4(II). Jupiter 68–69: Earth–Jupiter communication distance vs launch date, Type II

6–5(I). Jupiter 68–69: Declination of the geocentric asymptote vs launch date, Type I

6–5(II). Jupiter 68–69: Declination of the geocentric asymptote vs launch date, Type II

6–6(I). Jupiter 68–69: Right ascension of the geocentric asymptote vs launch date, Type I

6–6(II). Jupiter 68–69: Right ascension of the geocentric asymptote vs launch date, Type II

6–7(I). Jupiter 68–69: Angle between the outgoing geocentric asymptote and launch planet's orbital plane vs launch date, Type I

6–7(II). Jupiter 68–69: Angle between the outgoing geocentric asymptote and launch planet's orbital plane vs launch date, Type II

6–8(I). Jupiter 68–69: Angle between Sun–Earth vector and the outgoing geocentric asymptote vs launch date, Type I

6–8(II). Jupiter 68–69: Angle between Sun–Earth vector and the outgoing geocentric asymptote vs launch date, Type II

6–9(I). Jupiter 68–69: True anomaly in transfer ellipse at launch time vs launch date, Type I

6–9(II). Jupiter 68–69: True anomaly in transfer ellipse at launch time vs launch date, Type II

6–10. Jupiter 68–69: True anomaly in transfer ellipse at arrival time vs launch date

6–11(I). Jupiter 68–69: Perihelion of transfer orbit vs launch date, Type I

6–11(II). Jupiter 68–69: Perihelion of transfer orbit vs launch date, Type II

6–12(I). Jupiter 68–69: Aphelion of transfer orbit vs launch date, Type I

VI. JUPITER 1968-69: TRAJECTORY PARAMETER GRAPHS (Cont'd)

Figure

6–12(II). Jupiter 68–69: Aphelion of transfer orbit vs launch date, Type II

6–13(I). Jupiter 68–69: Inclination of the heliocentric transfer plane vs launch date, Type I

6–13(II). Jupiter 68–69: Inclination of the heliocentric transfer plane vs launch date, Type II

6–14. Jupiter 68–69: Celestial latitude at arrival time vs launch date

6–15(I). Jupiter 68–69: Asymptotic speed with respect to Jupiter vs launch date, Type I

6–15(II). Jupiter 68–69: Asymptotic speed with respect to Jupiter vs launch date, Type II

6–16. Jupiter 68–69: Angle between incoming zeocentric asymptote and arrival planet's orbital plane vs launch date

6–17. Jupiter 68–69: Angle between Jupiter–Sun vector and incoming zeocentric asymptote vs launch date

6–18(I). Jupiter 68–69: Declination of the zeocentric asymptote vs launch date, Type I

6–18(II). Jupiter 68–69: Declination of the zeocentric asymptote vs launch date, Type II

6–19(I). Jupiter 68–69: Right ascension of zeocentric asymptote vs launch date, Type I

6–19(II). Jupiter 68–69: Right ascension of zeocentric asymptote vs launch date, Type II

6–20(I). Jupiter 68–69: Angle between Planet–Earth vector and incoming asymptote vs launch date, Type I

6–20(II). Jupiter 68–69: Angle between Planet–Earth vector and incoming asymptote vs launch date, Type II

6–21(I). Jupiter 68–69: Angle between the planet–Canopus vector and incoming asymptote vs launch date, Type I

6–21(II). Jupiter 68–69: Angle between the planet–Canopus vector and incoming asymptote vs launch date, Type II

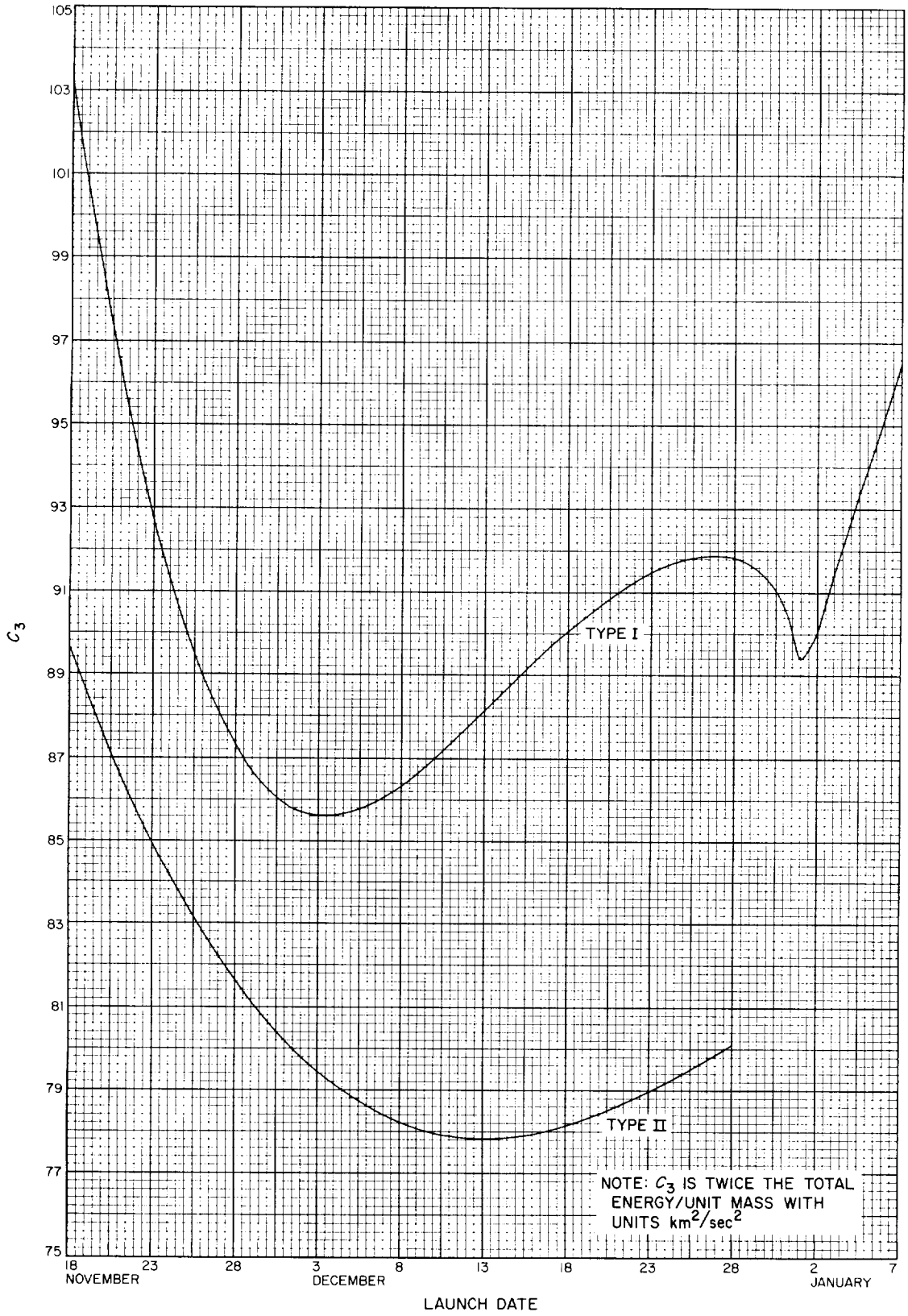

Fig. 6–1. Jupiter 68–69: Minimum injection energy vs launch date

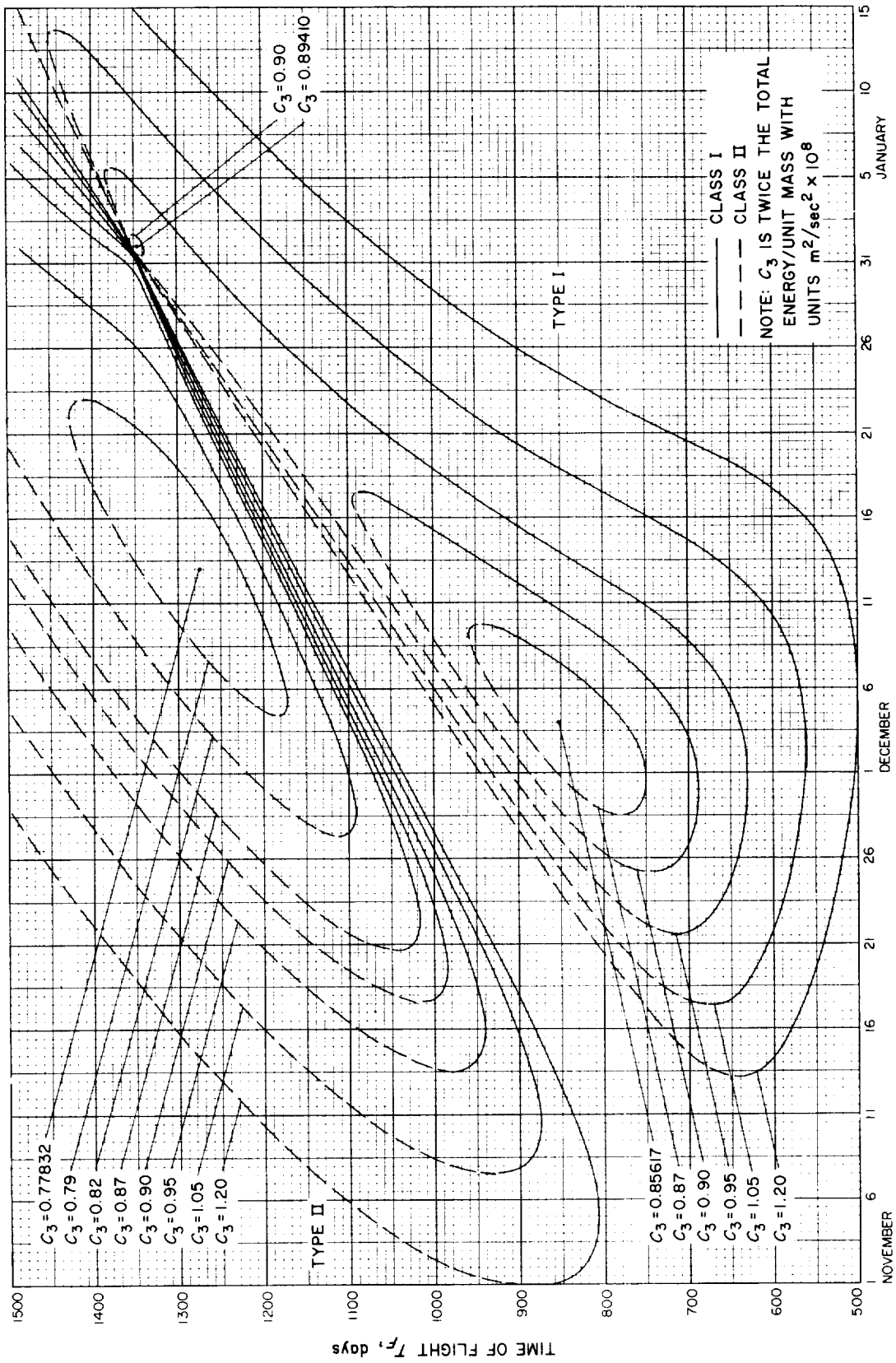

Fig. 6–2. Jupiter 68–69: Time of flight vs launch date

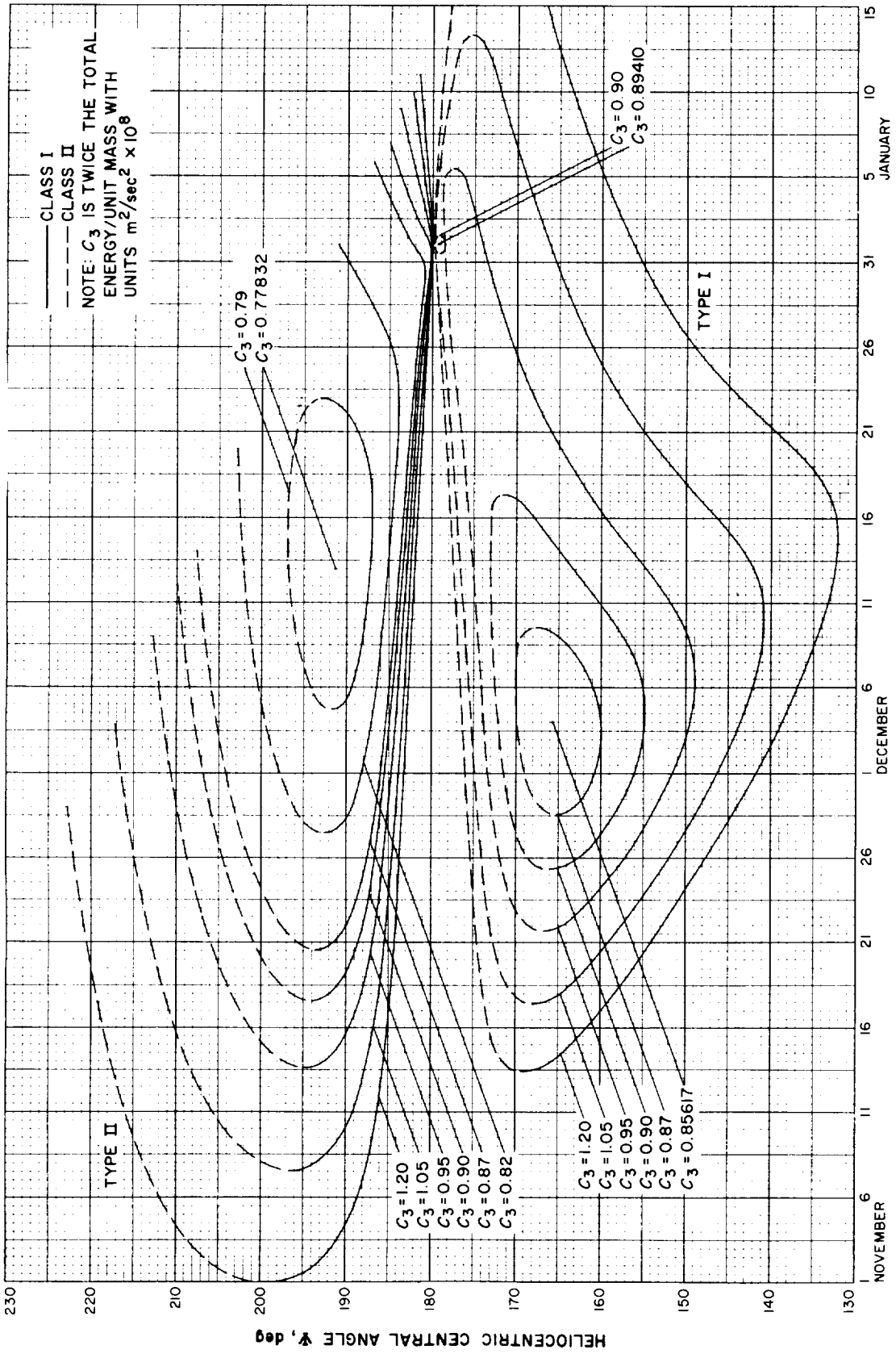

Fig. 6–3. Jupiter 68–69: Heliocentric central angle vs launch date

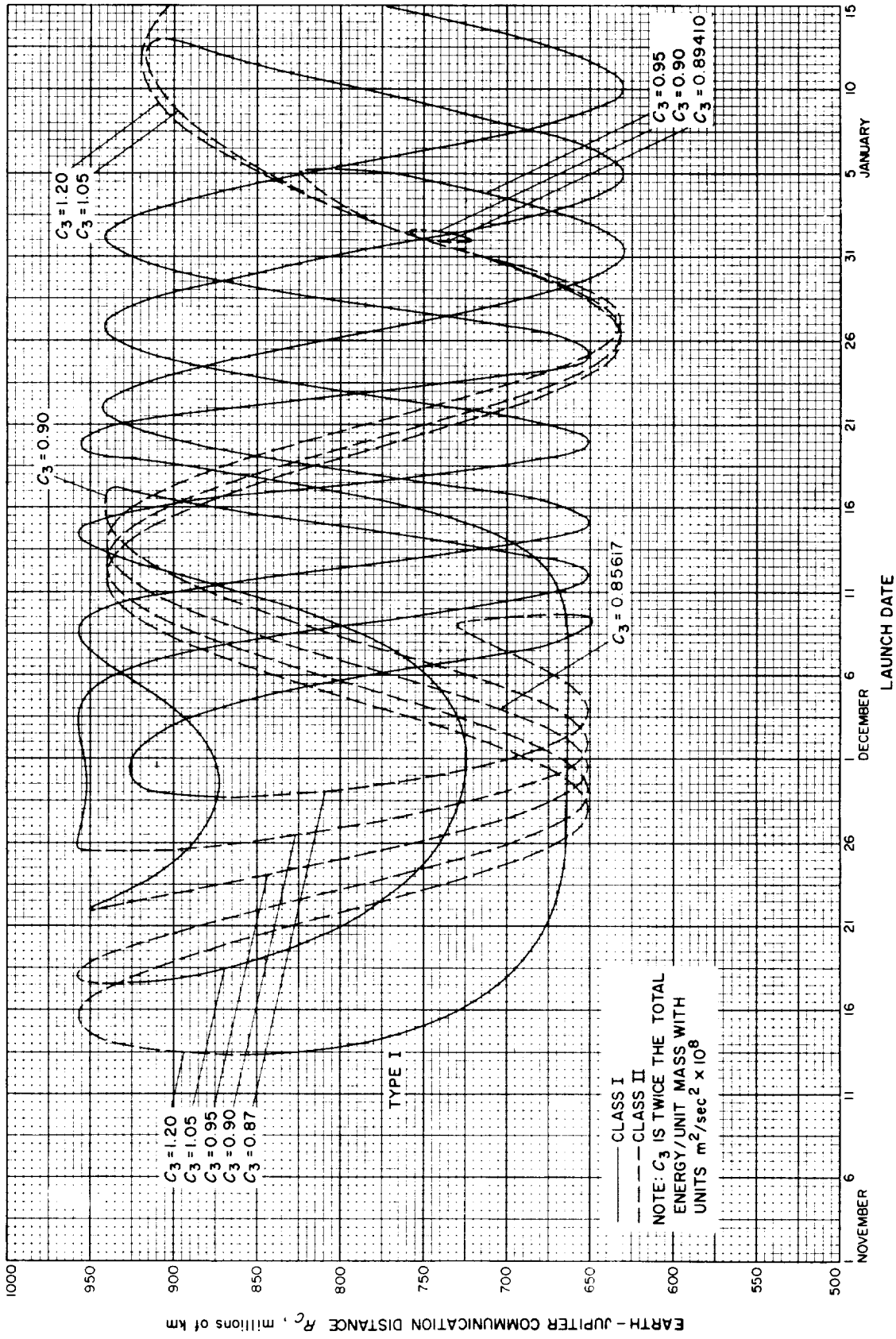

Fig. 6-4(I). Jupiter 68–69: Earth–Jupiter communication distance vs launch date, Type I

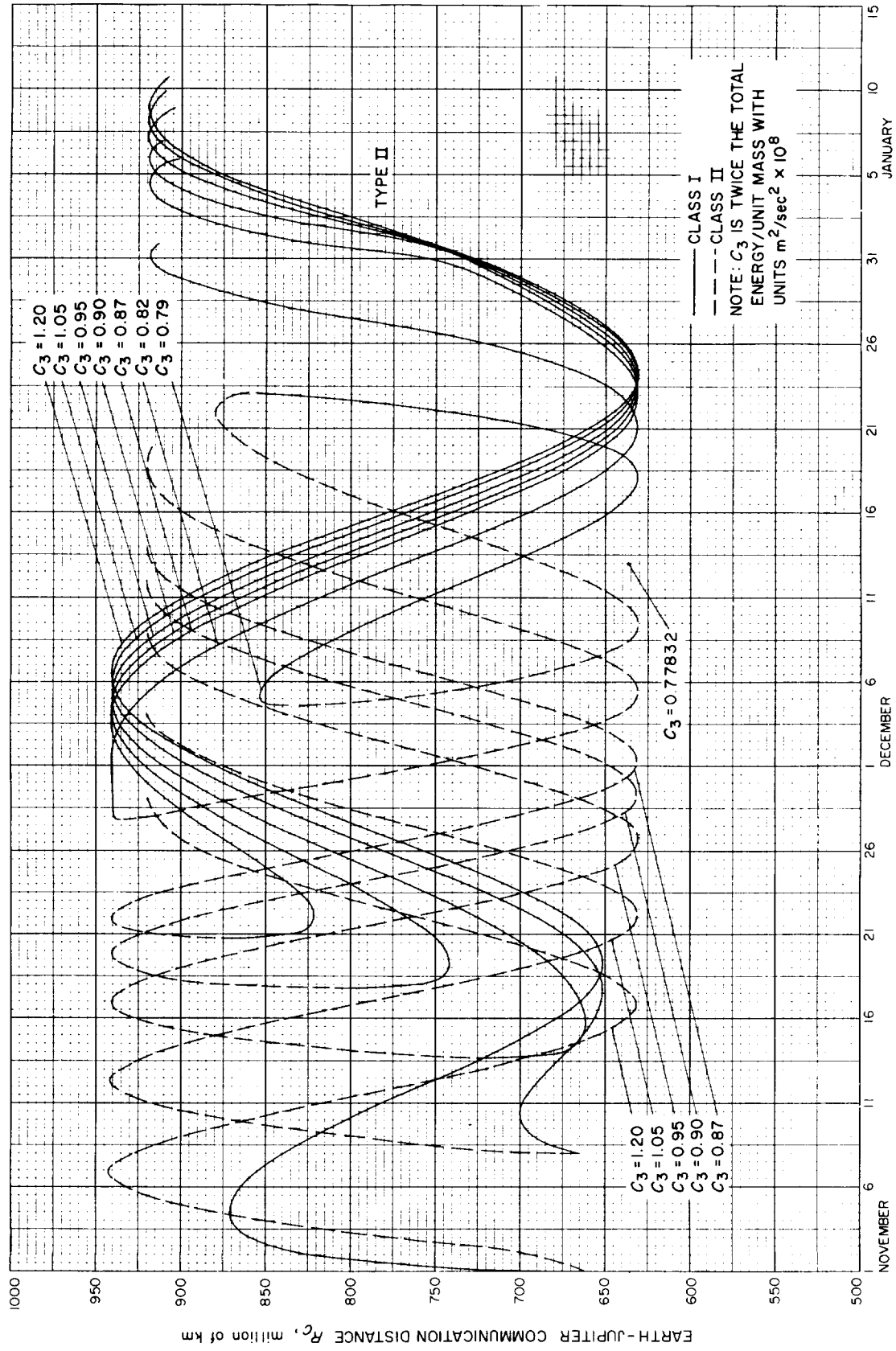

Fig. 6-4(II). Jupiter 68–69: Earth–Jupiter communication distance vs launch date, Type II

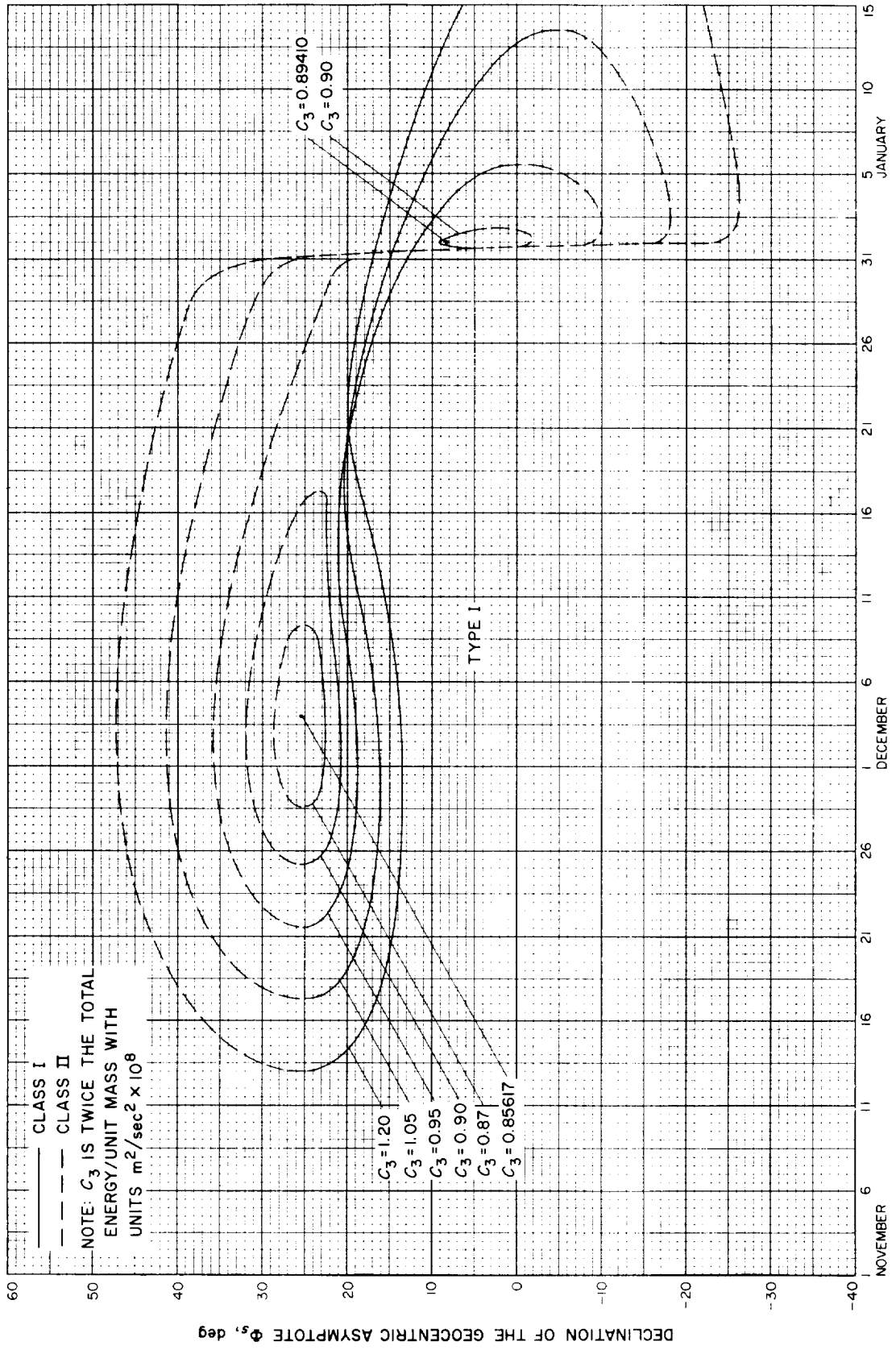

Fig. 6-5(I). Jupiter 68–69: Declination of the geocentric asymptote vs launch date, Type I

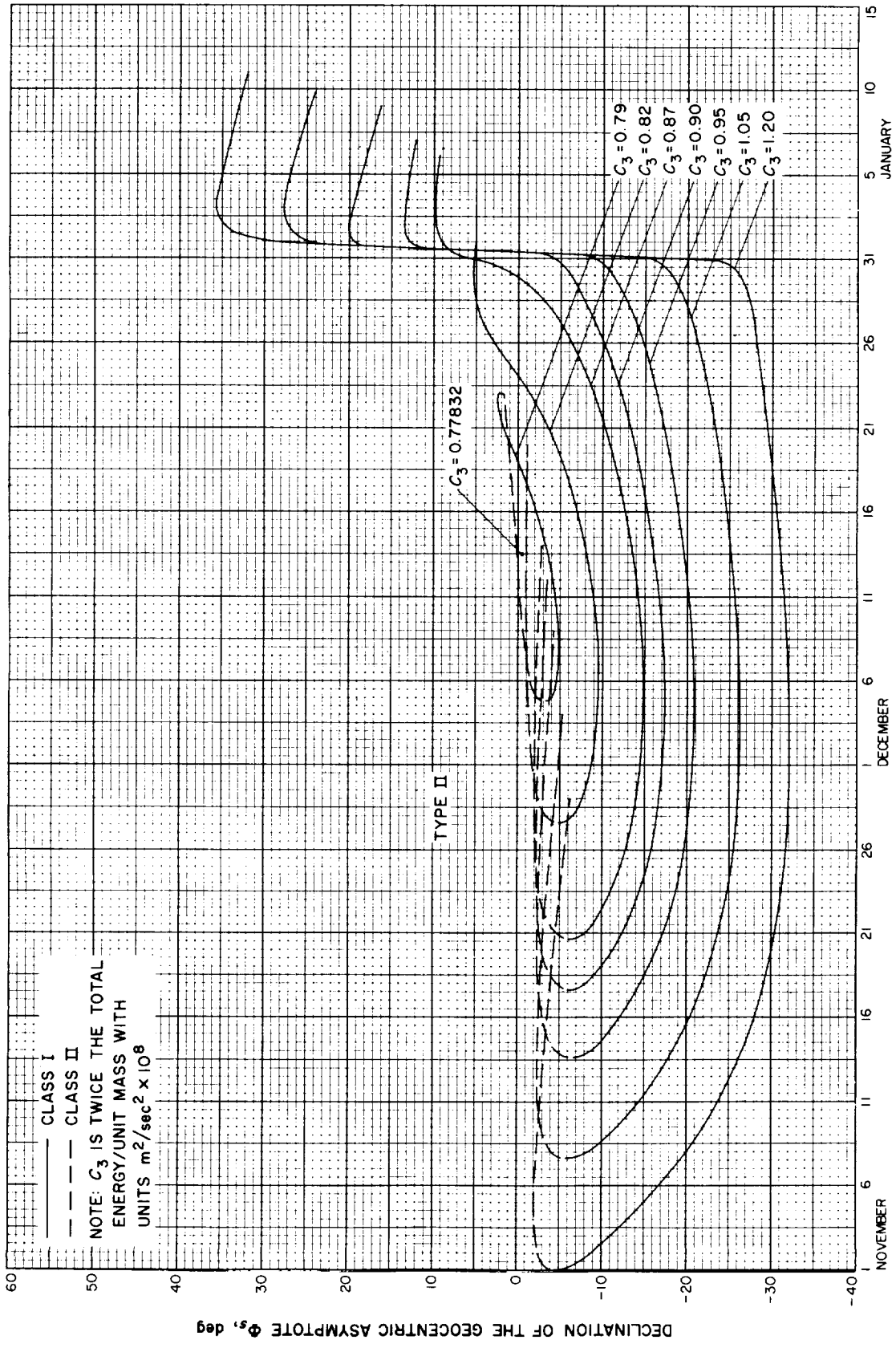

Fig. 6-5(III). Jupiter 68–69: Declination of the geocentric asymptote vs launch date, Type II

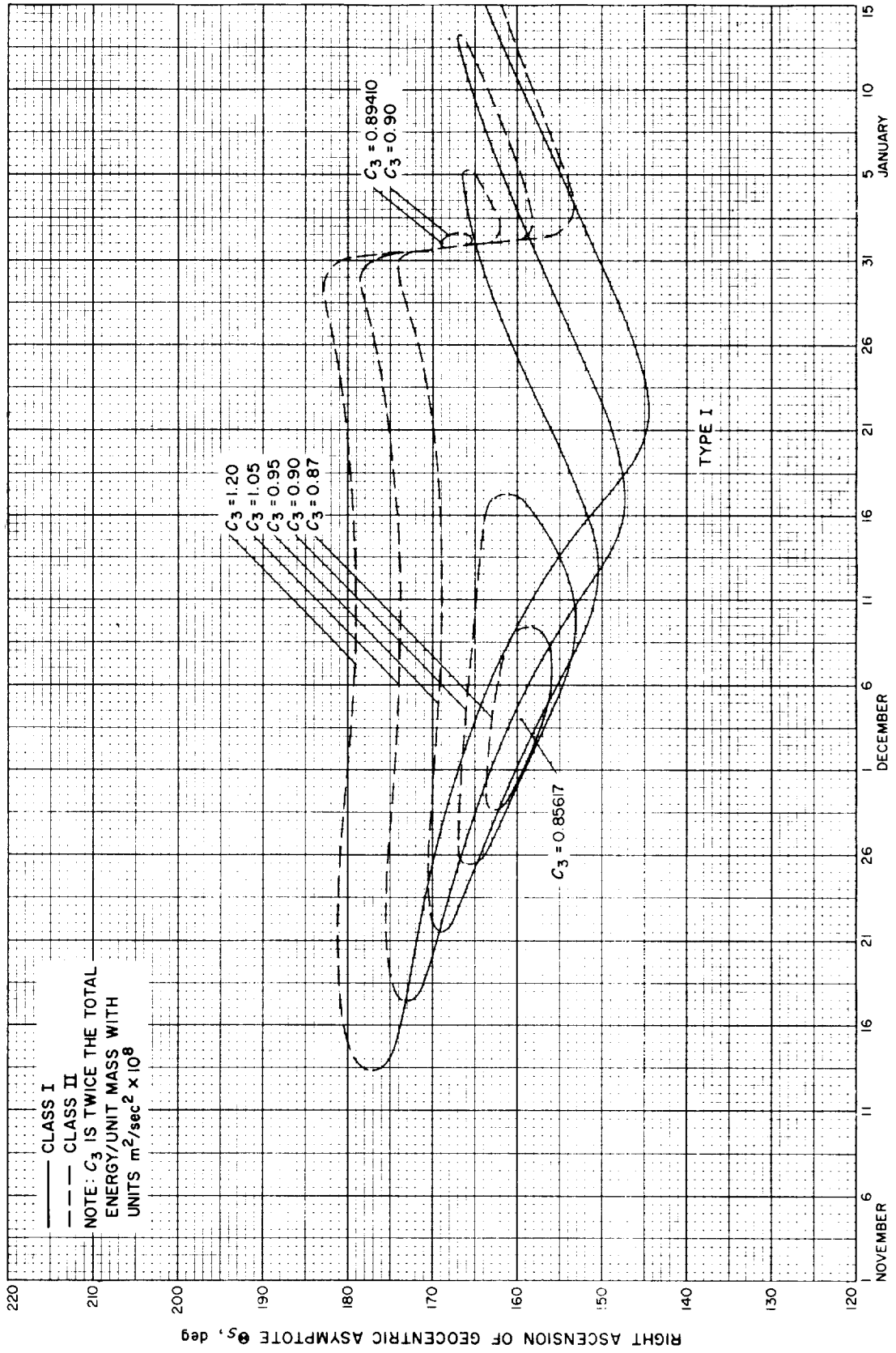

Fig. 6–6(I). Jupiter 68–69: Right ascension of the geocentric asymptote vs launch date, Type I

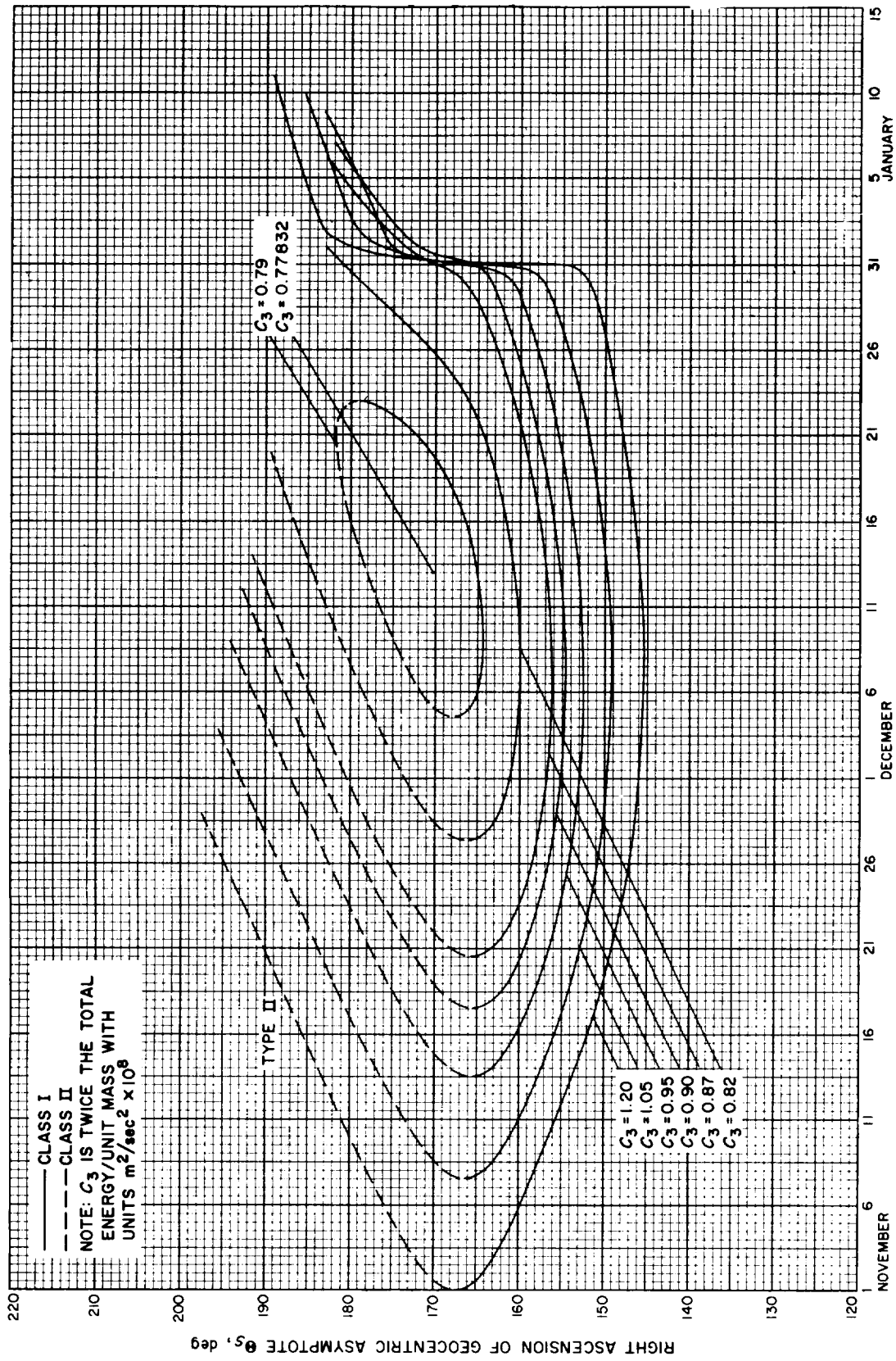

Fig. 6-6(II). Jupiter 68-69: Right ascension of the geocentric asymptote vs launch date, Type II

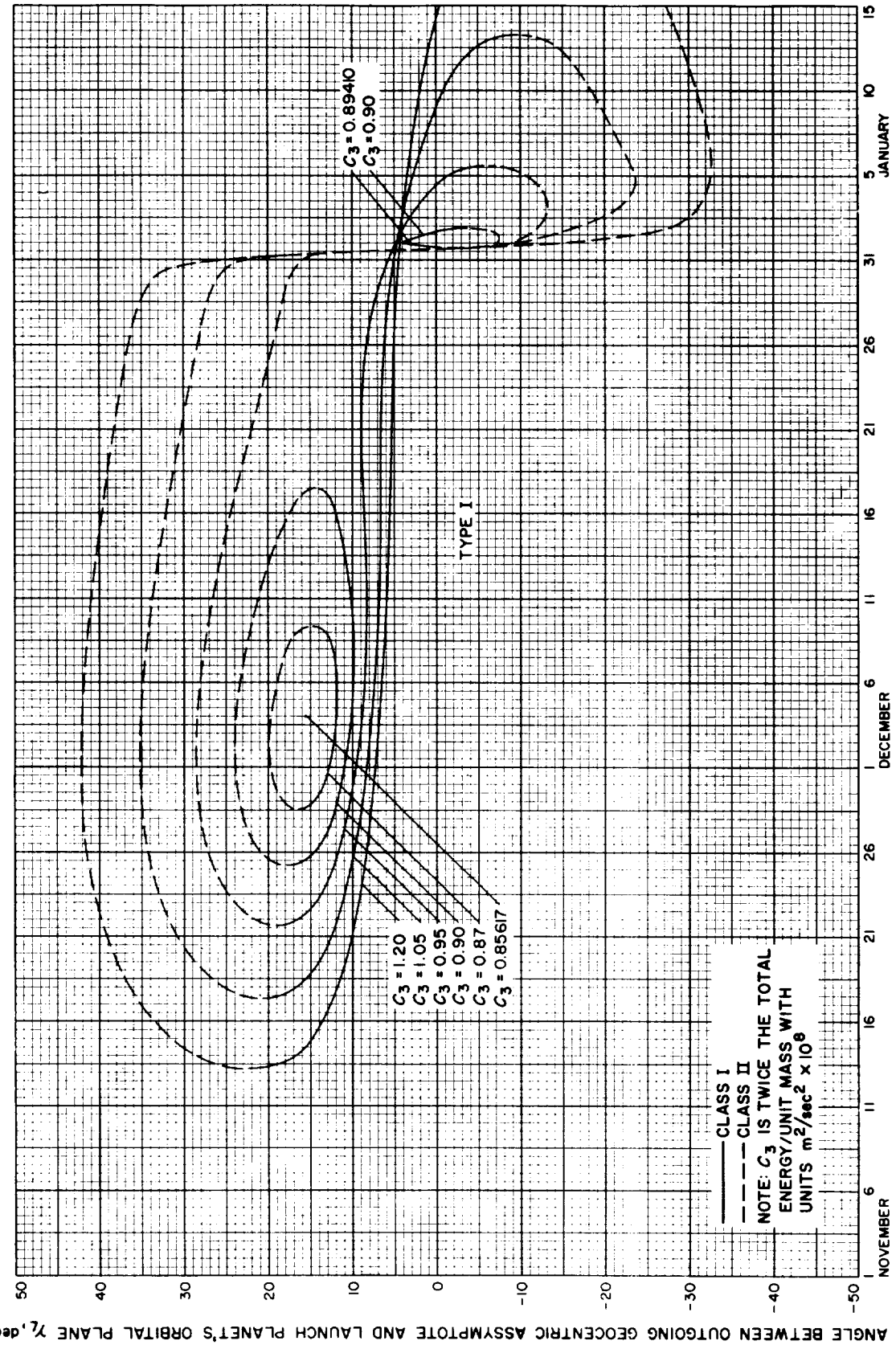

Fig. 6-7(I). Jupiter 68-69: Angle between the outgoing geocentric asymptote and launch planet's orbital plane vs launch date, Type I

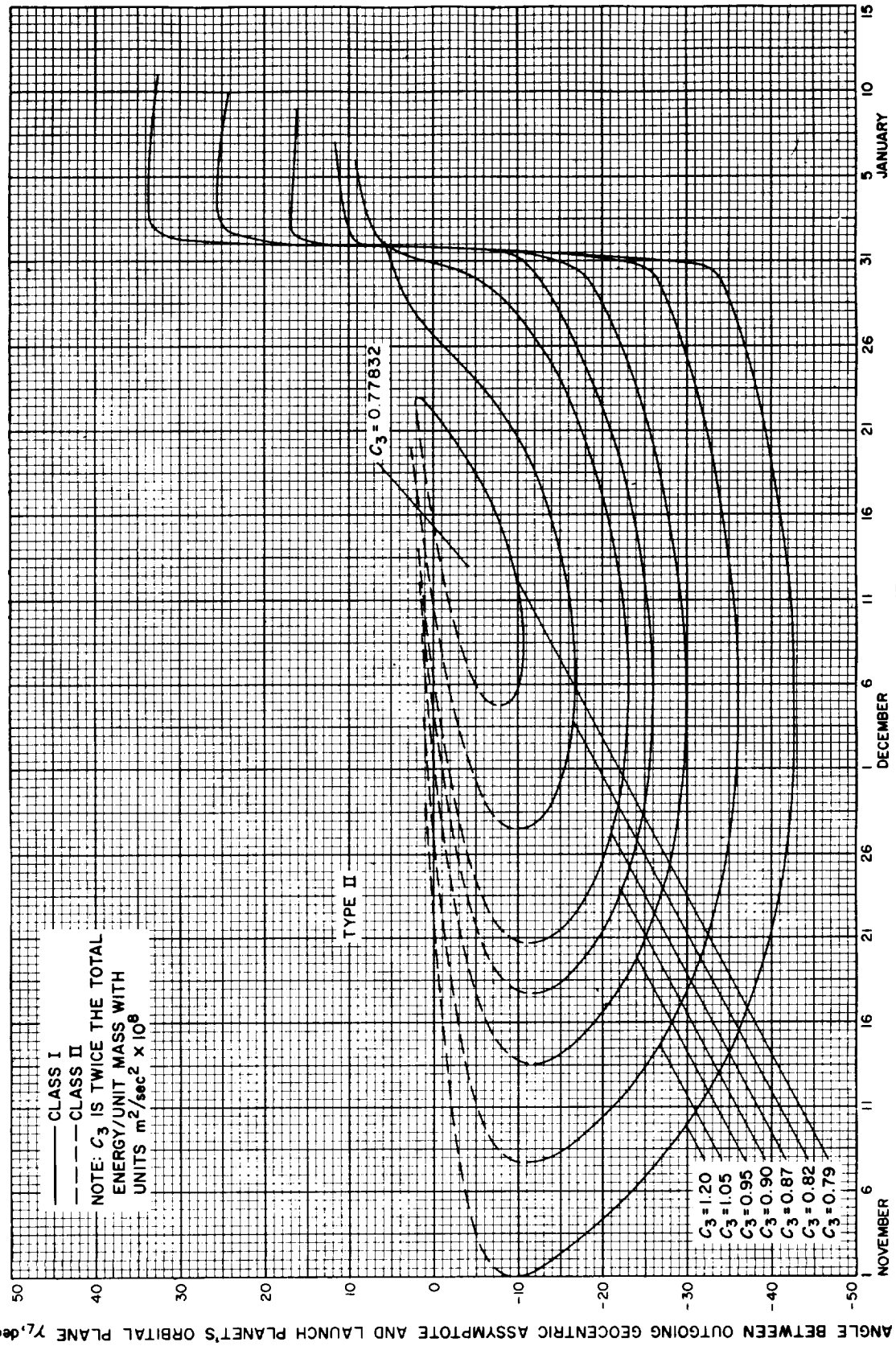

Fig. 6-7(II). Jupiter 68–69: Angle between the outgoing geocentric asymptote and launch planet's orbital plane vs launch date, Type II

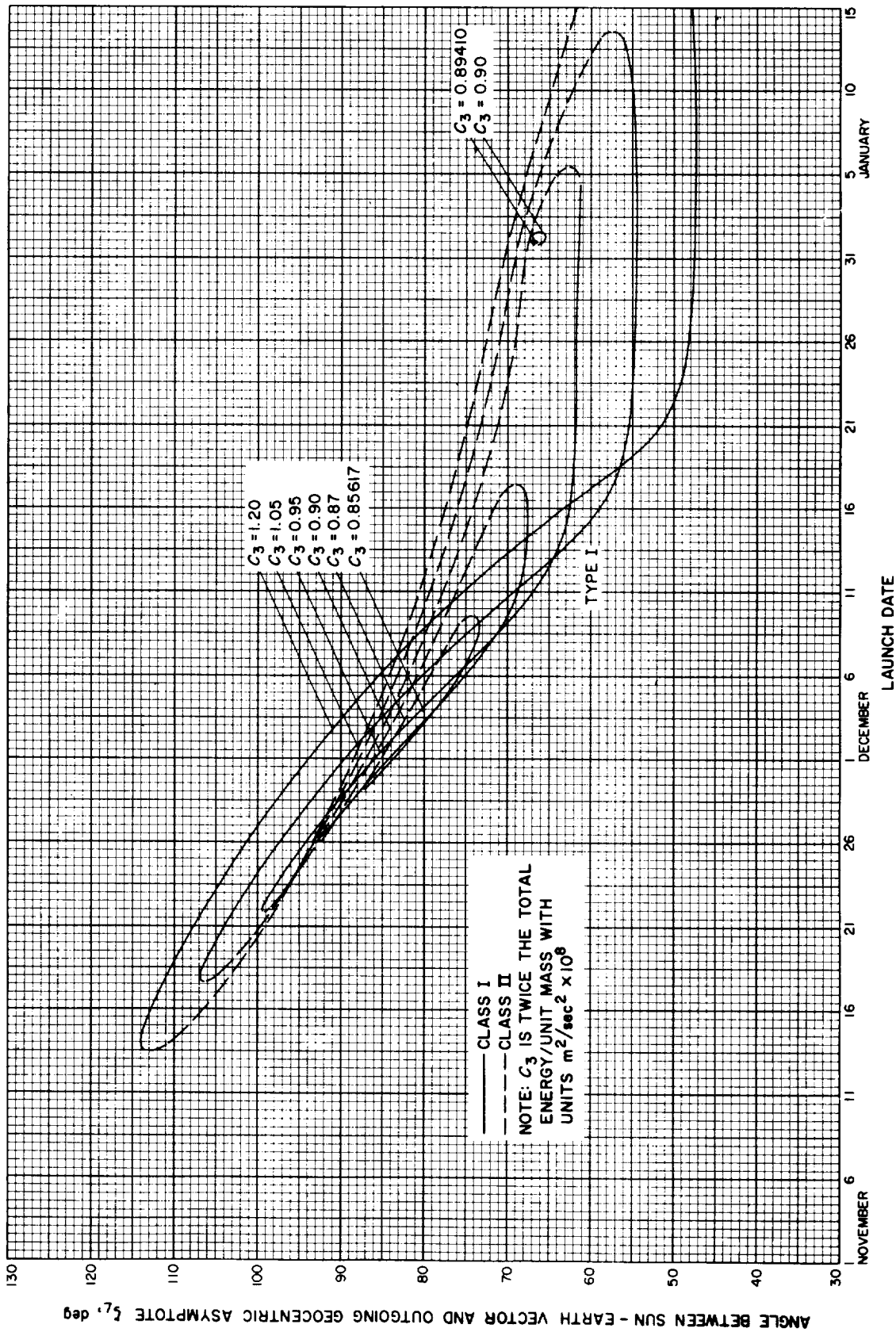

Fig. 6–8(I). Jupiter 68–69: Angle between Sun–Earth vector and the outgoing geocentric asymptote vs launch date, Type I

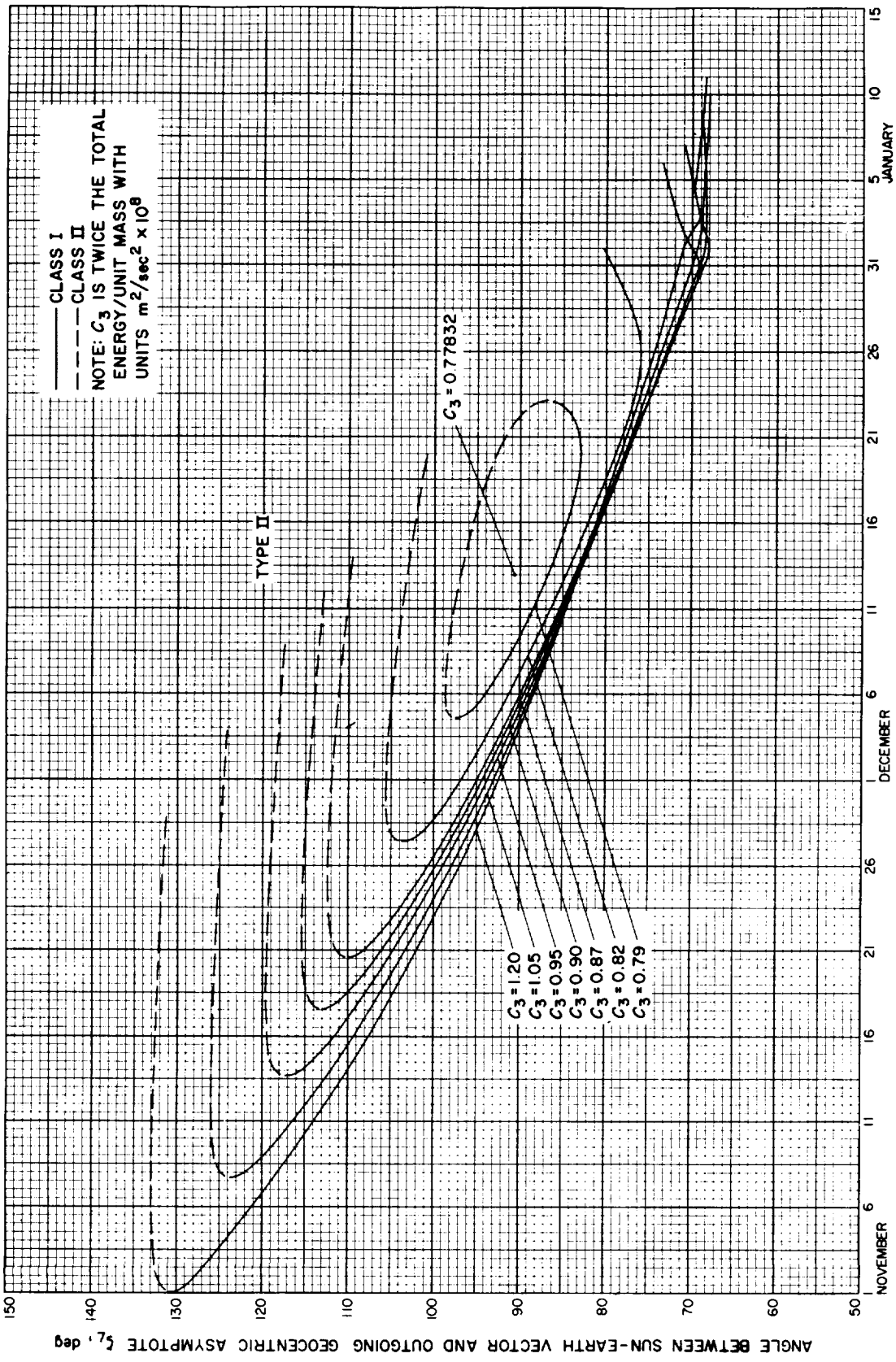

Fig. 6-8(II). Jupiter 68–69: Angle between Sun–Earth vector and the outgoing geocentric asymptote vs launch date, Type II

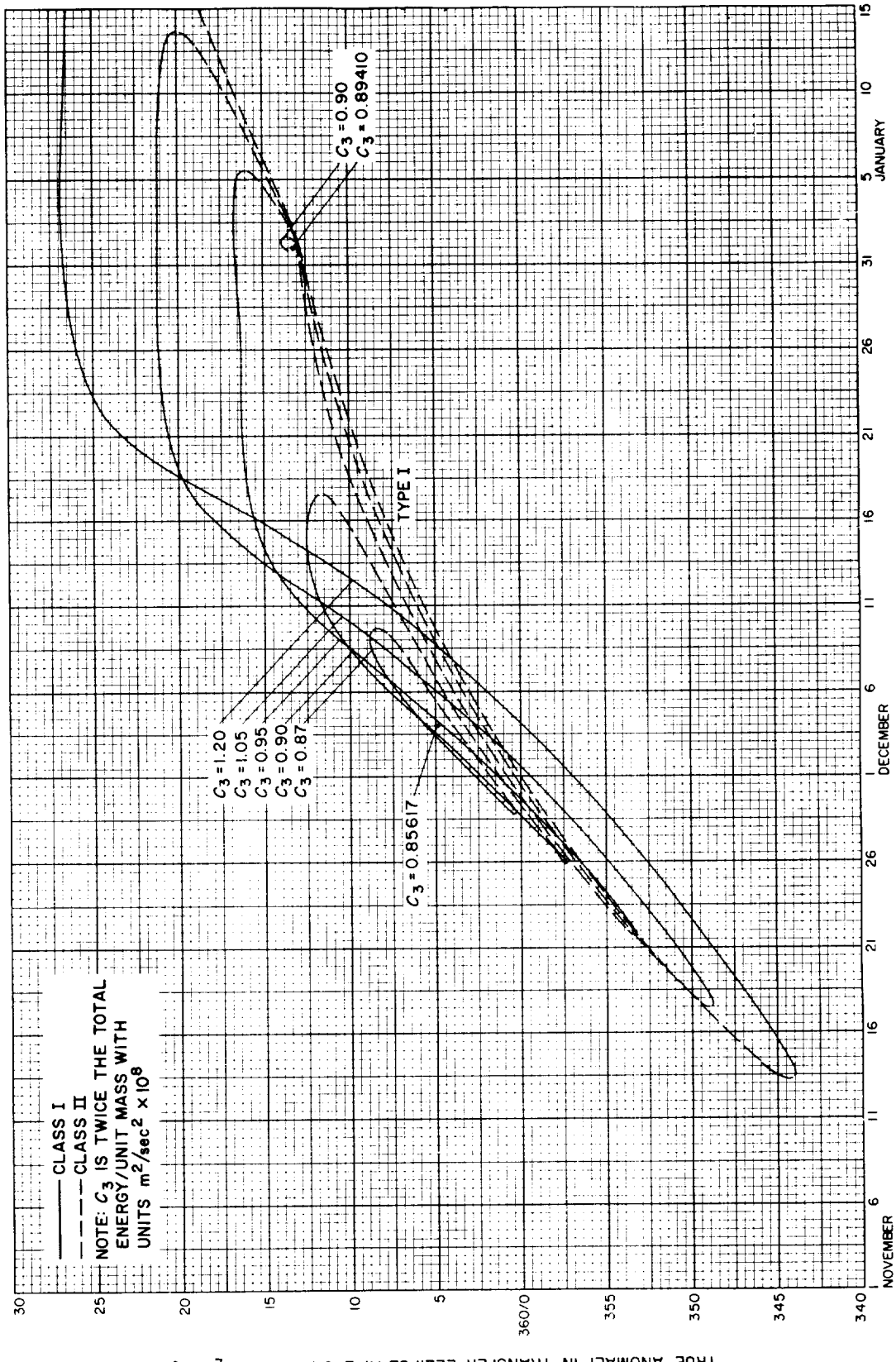

Fig. 6-9(I). Jupiter 68–69: True anomaly in transfer ellipse at launch time vs launch date, Type I

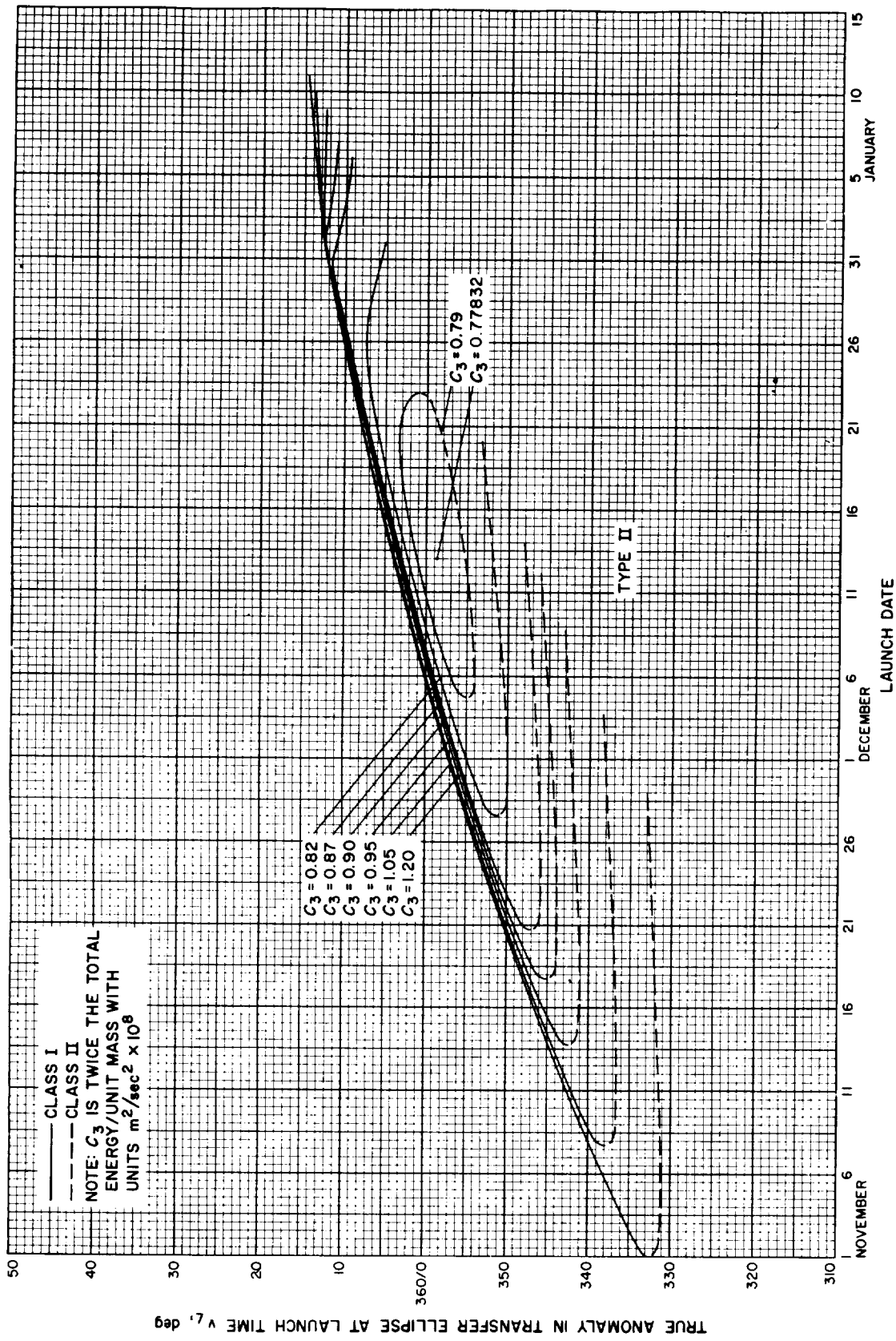

Fig. 6-9(II). Jupiter 68–69: True anomaly in transfer ellipse at launch time vs launch date, Type II

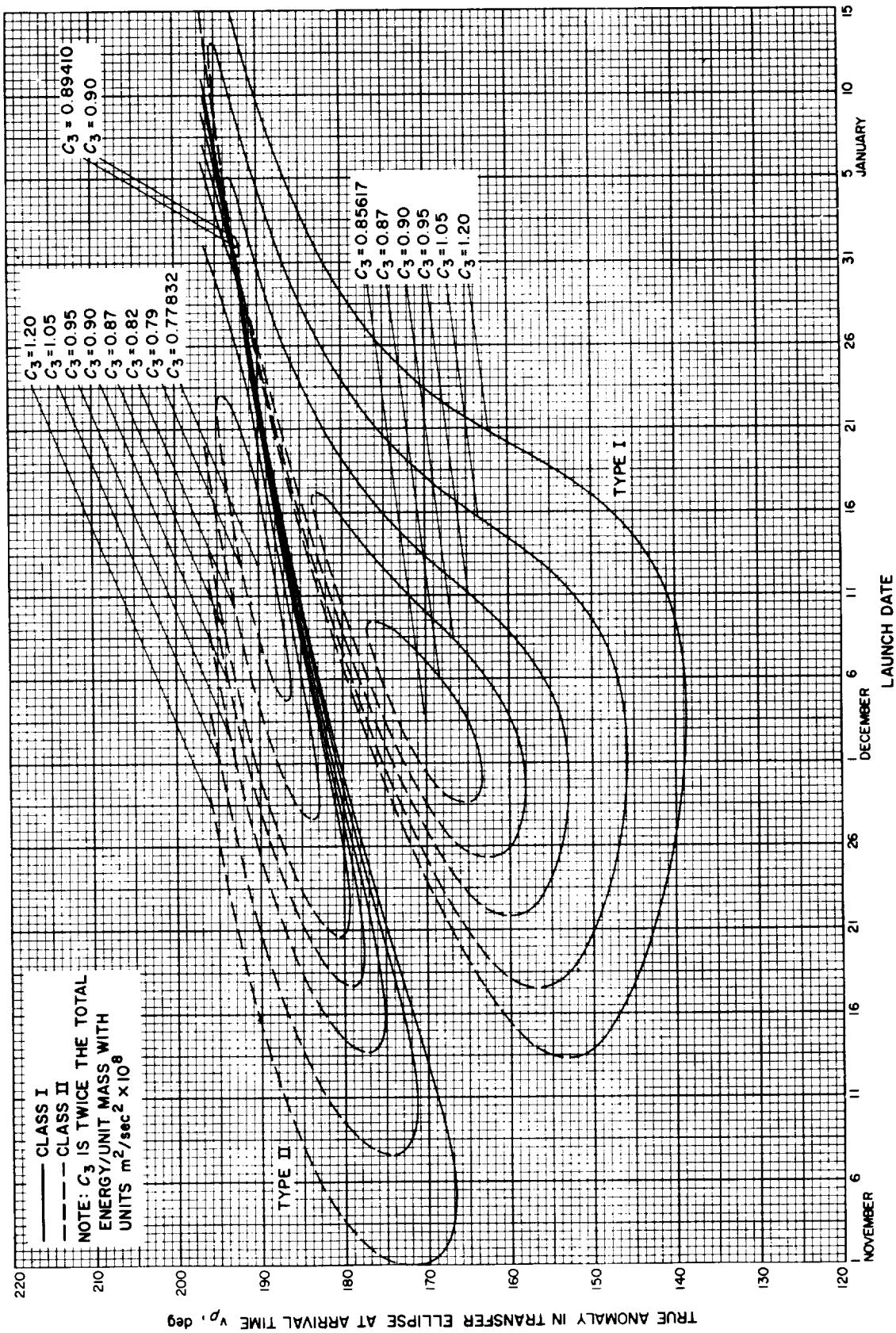

Fig. 6-10. Jupiter 68-69: True anomaly in transfer ellipse at arrival time vs launch date

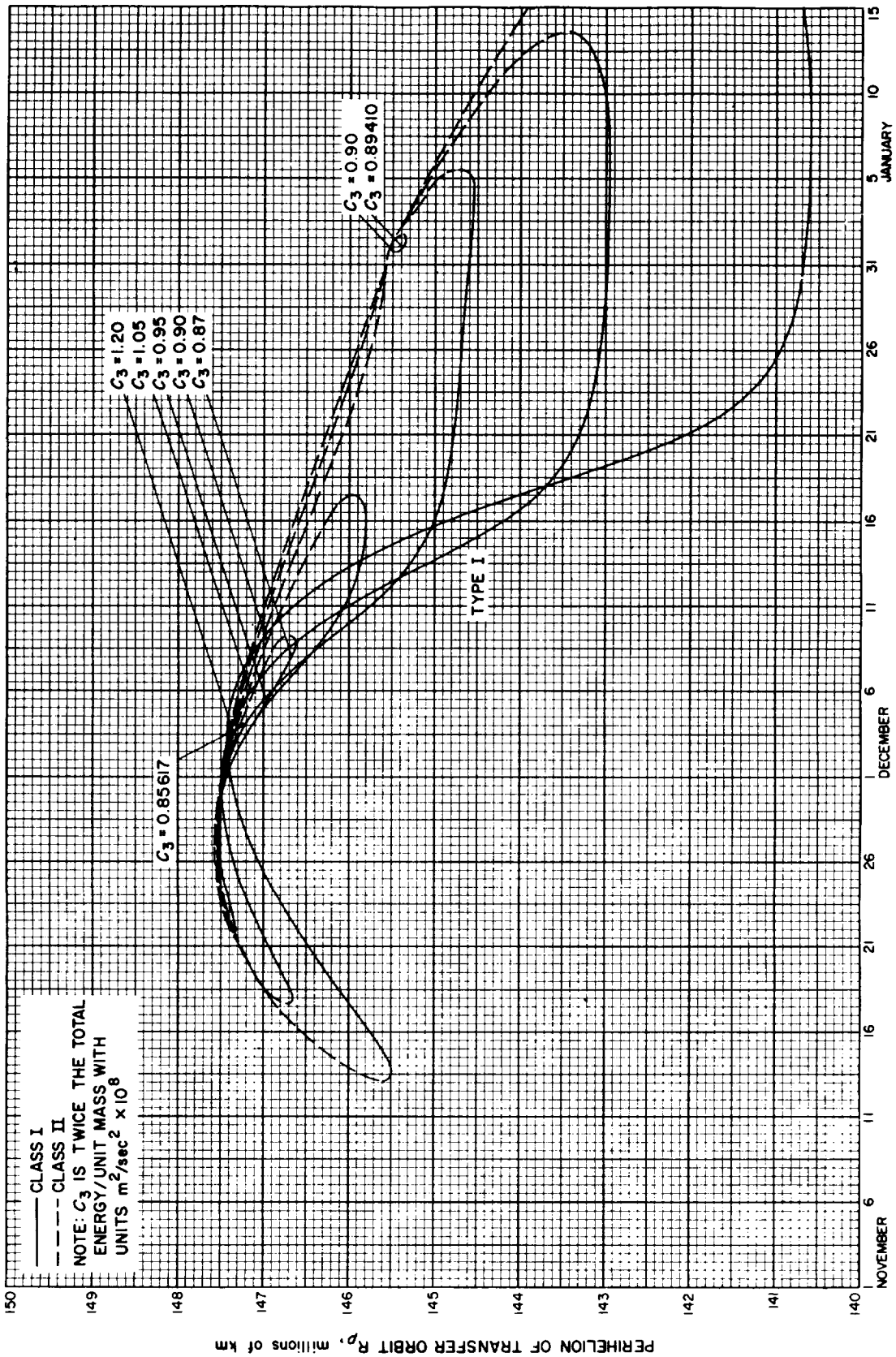

Fig. 6-11(I). Jupiter 68–69: Perihelion of transfer orbit vs launch date, Type I

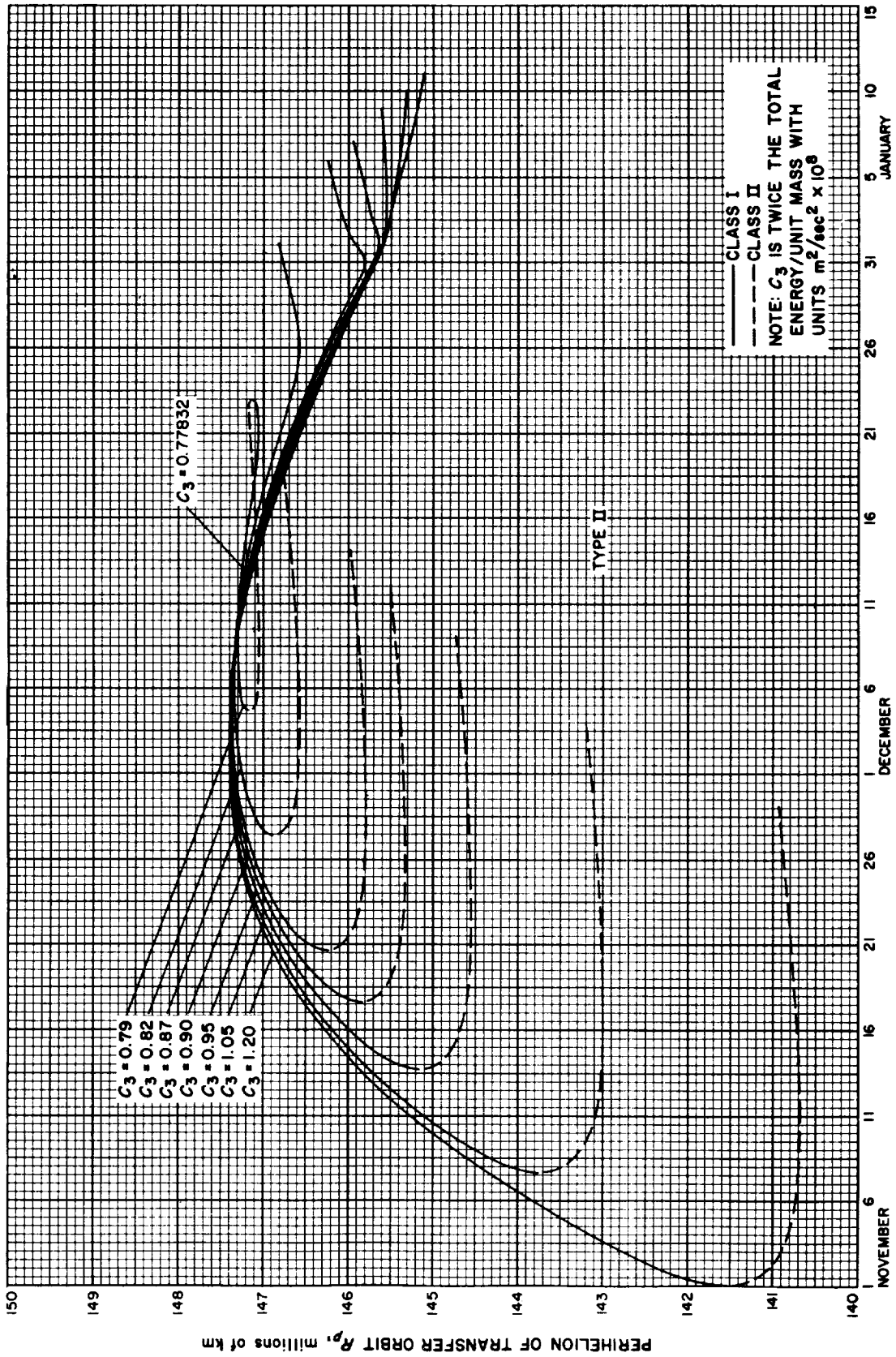

Fig. 6-11(II). Jupiter 68–69: Perihelion of transfer orbit vs launch date, Type II

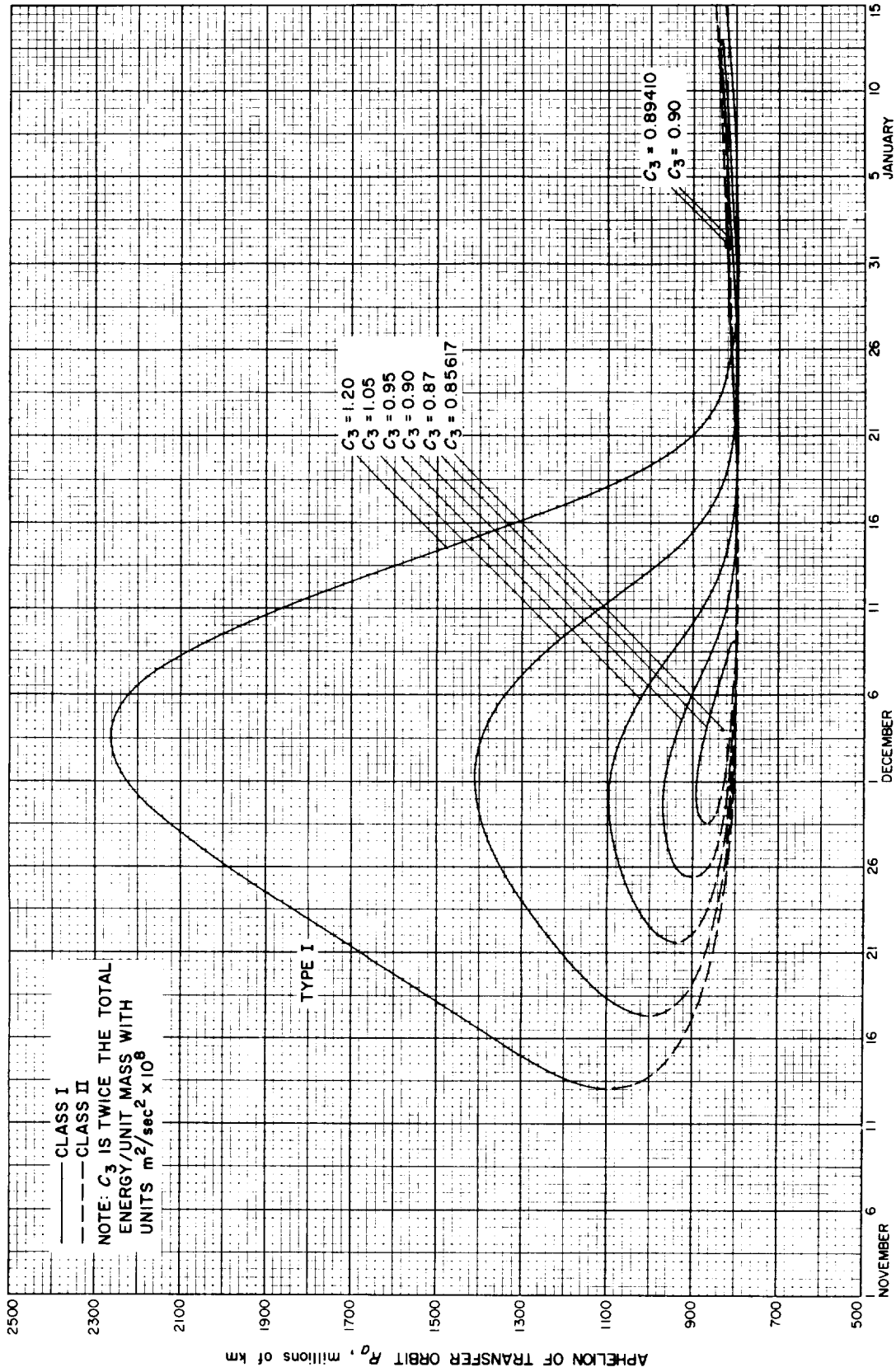

Fig. 6-12(I). Jupiter 68–69: Aphelion of transfer orbit vs launch date, Type I

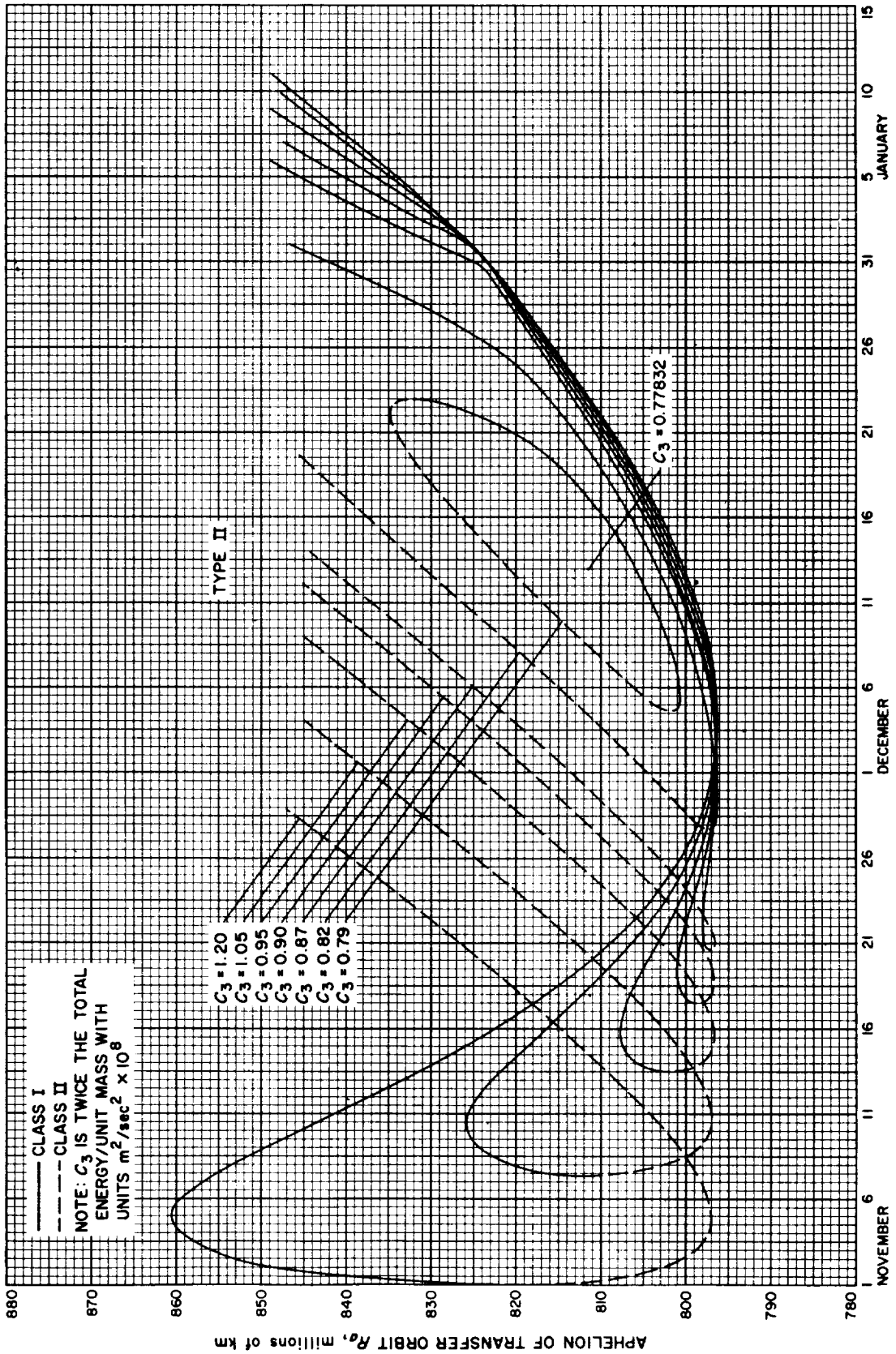

Fig. 6–12(II). Jupiter 68–69: Aphelion of transfer orbit vs launch date, Type II

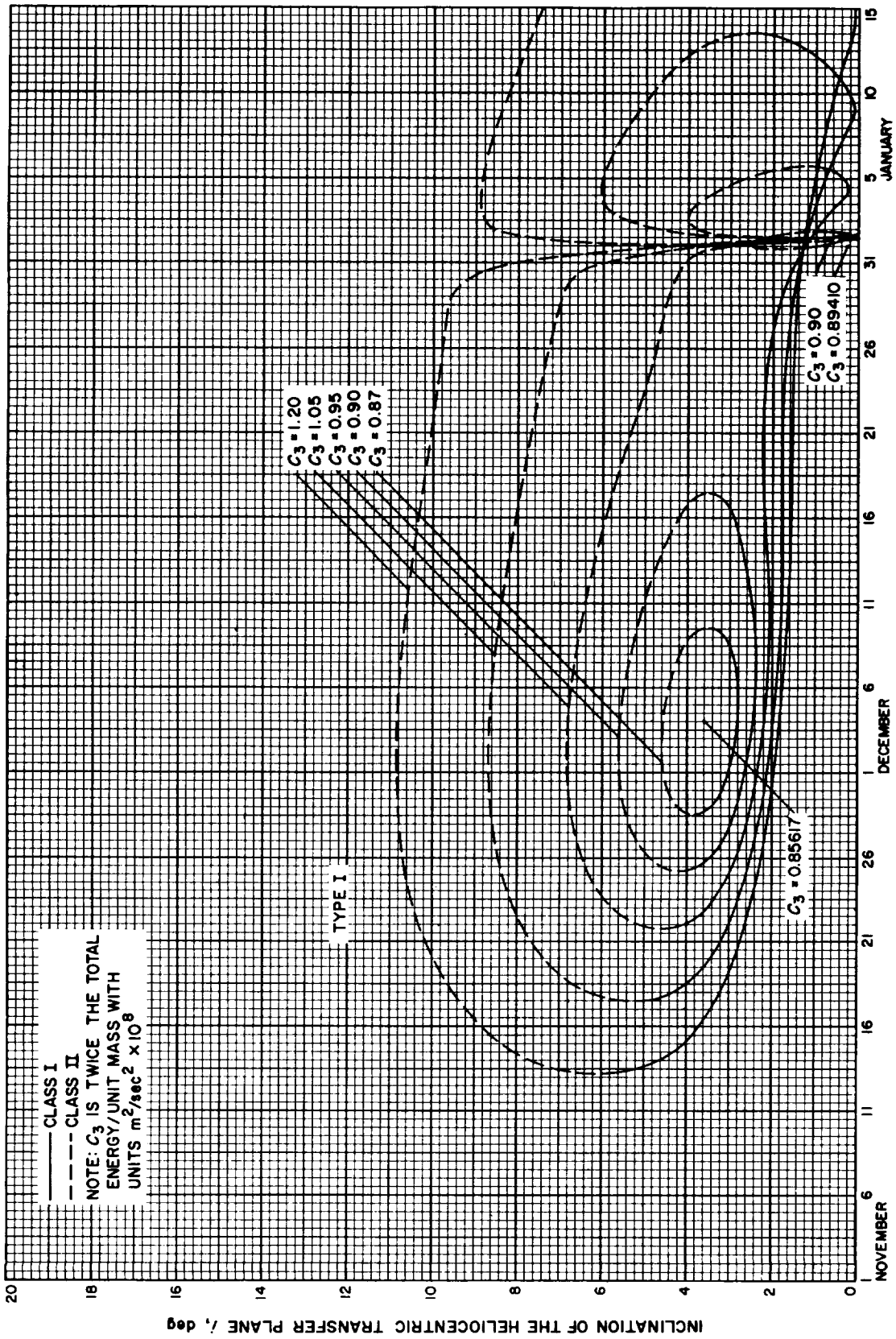

Fig. 6–13(I). Jupiter 68–69: Inclination of the heliocentric transfer plane vs launch date, Type I

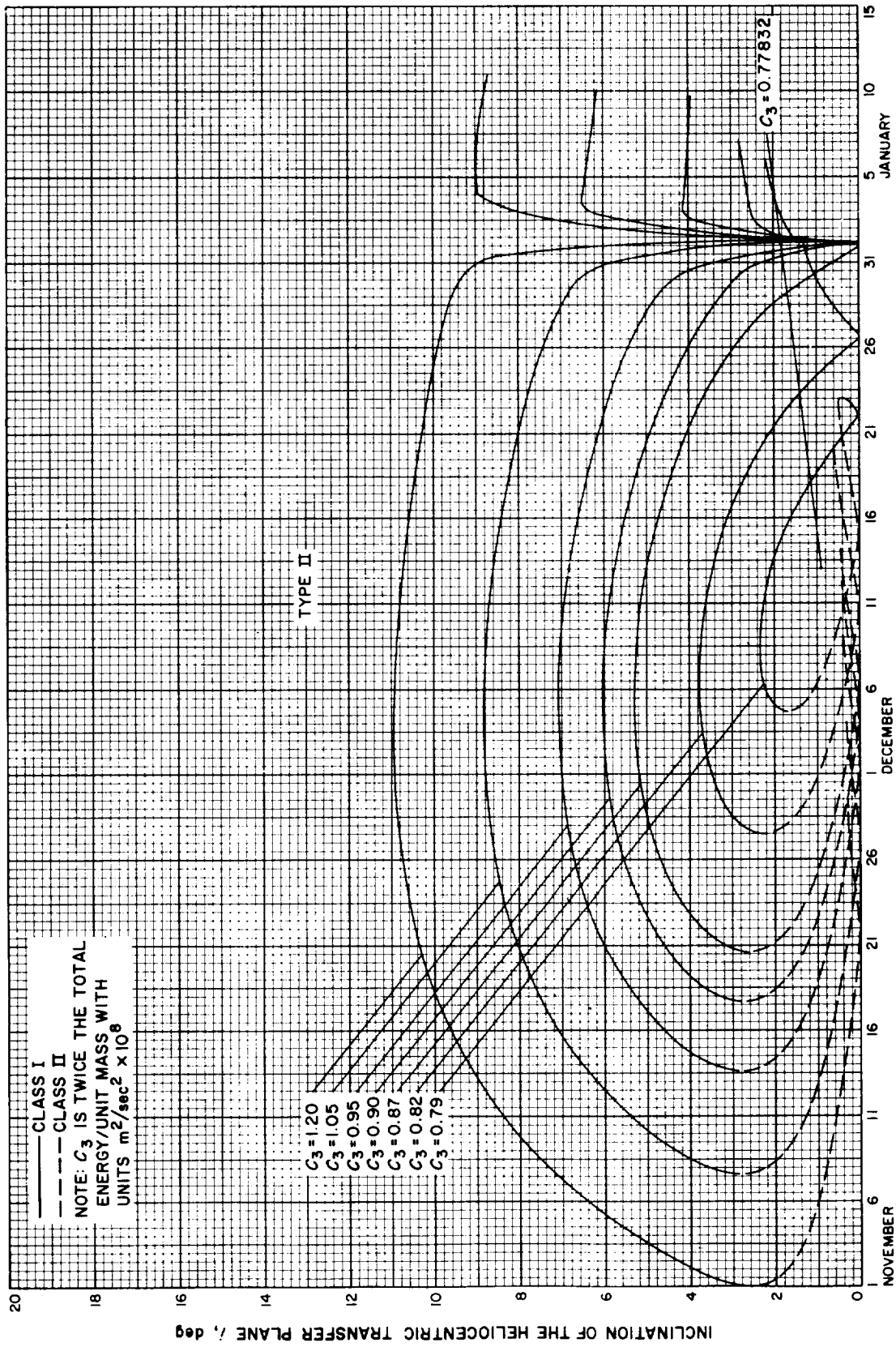

Fig. 6-13(II). Jupiter 68–69: Inclination of the heliocentric transfer plane vs launch date, Type II

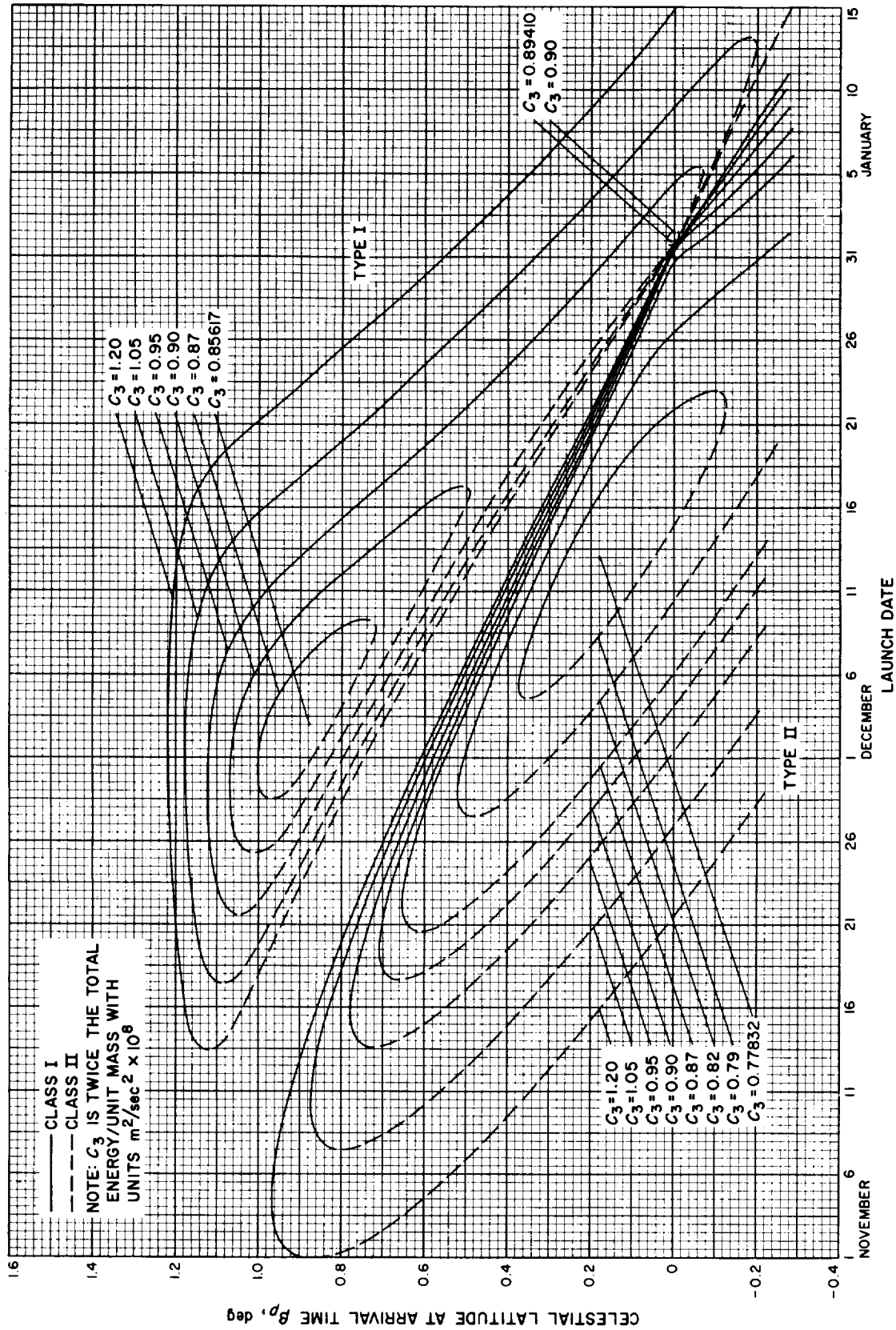

Fig. 6-14. Jupiter 68–69: Celestial latitude at arrival time vs launch date

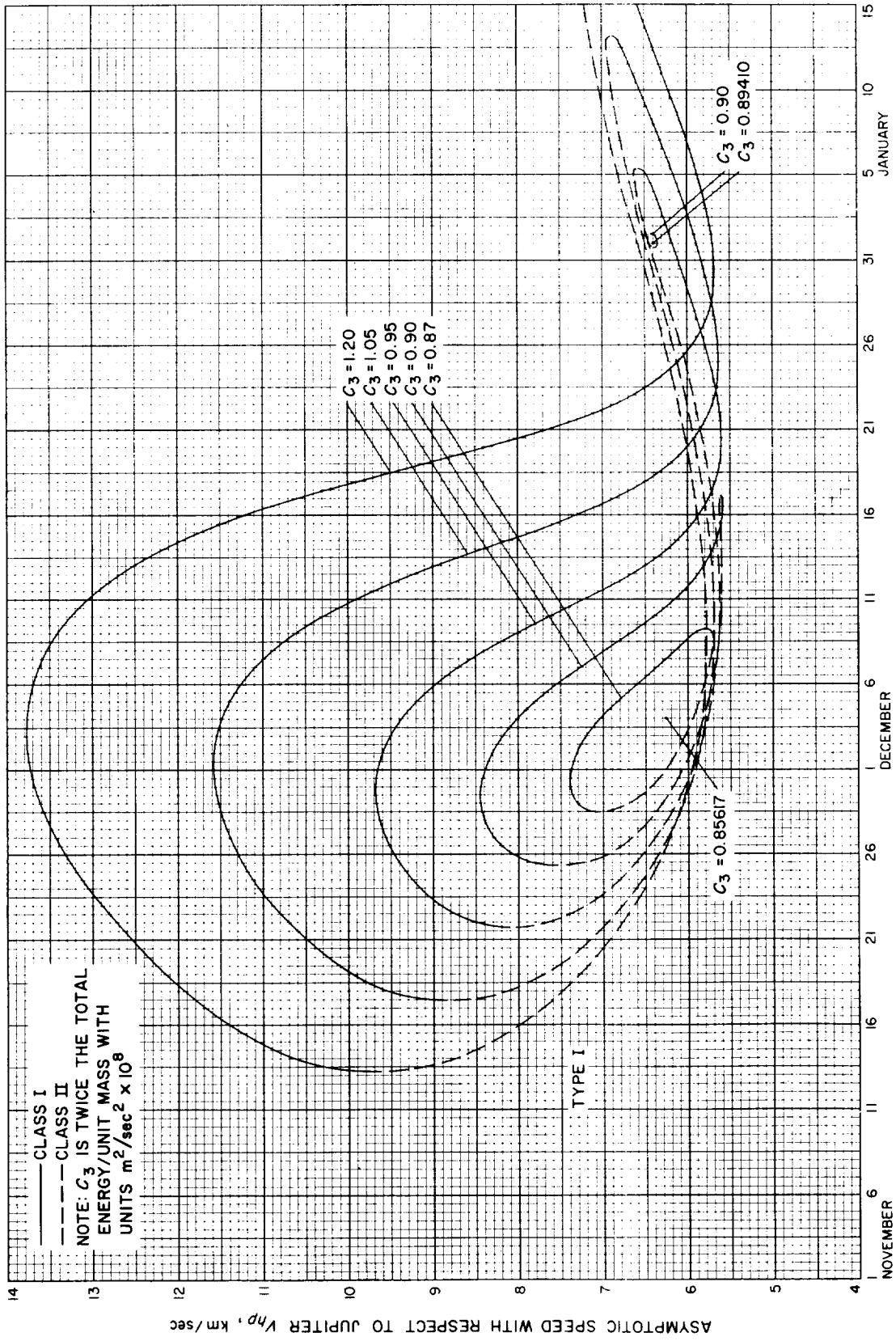

Fig. 6–15(I). Jupiter 68–69: Asymptotic speed with respect to Jupiter vs launch date, Type I

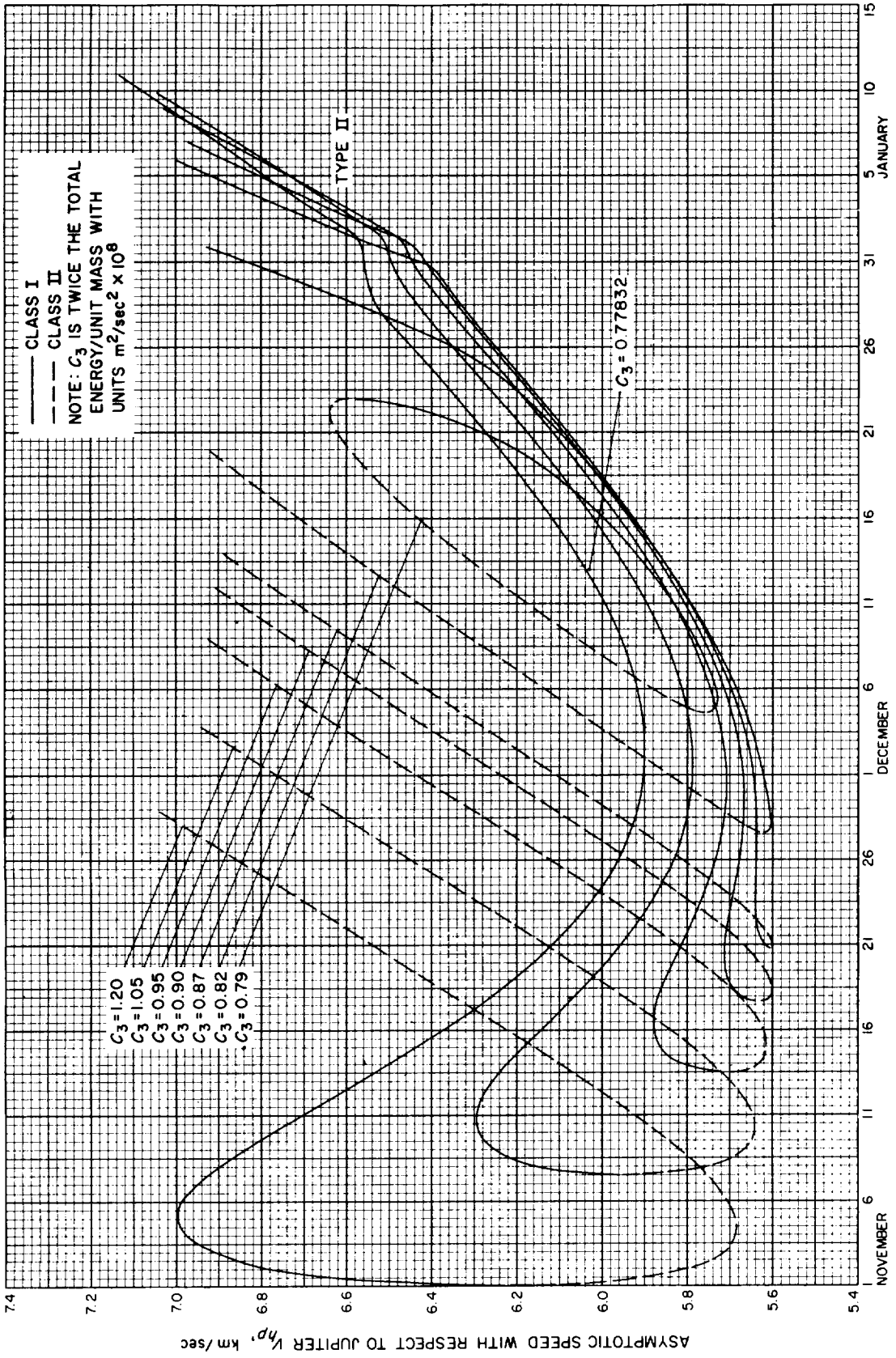

Fig. 6-15(II). Jupiter 68–69: Asymptotic speed with respect to Jupiter vs launch date, Type II

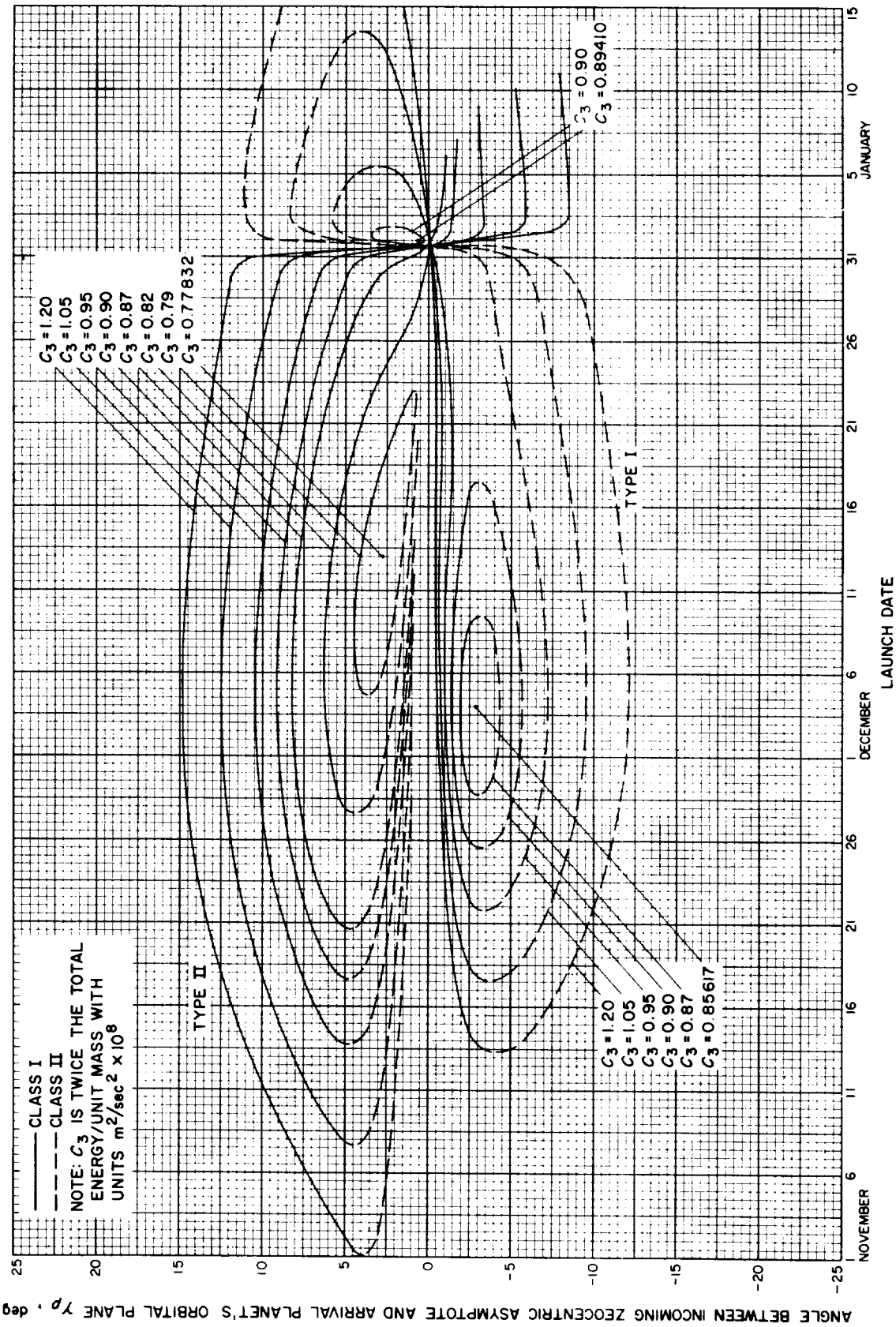

Fig. 6–16. Jupiter 68–69: Angle between incoming zeocentric asymptote and arrival planet's orbital plane vs launch date

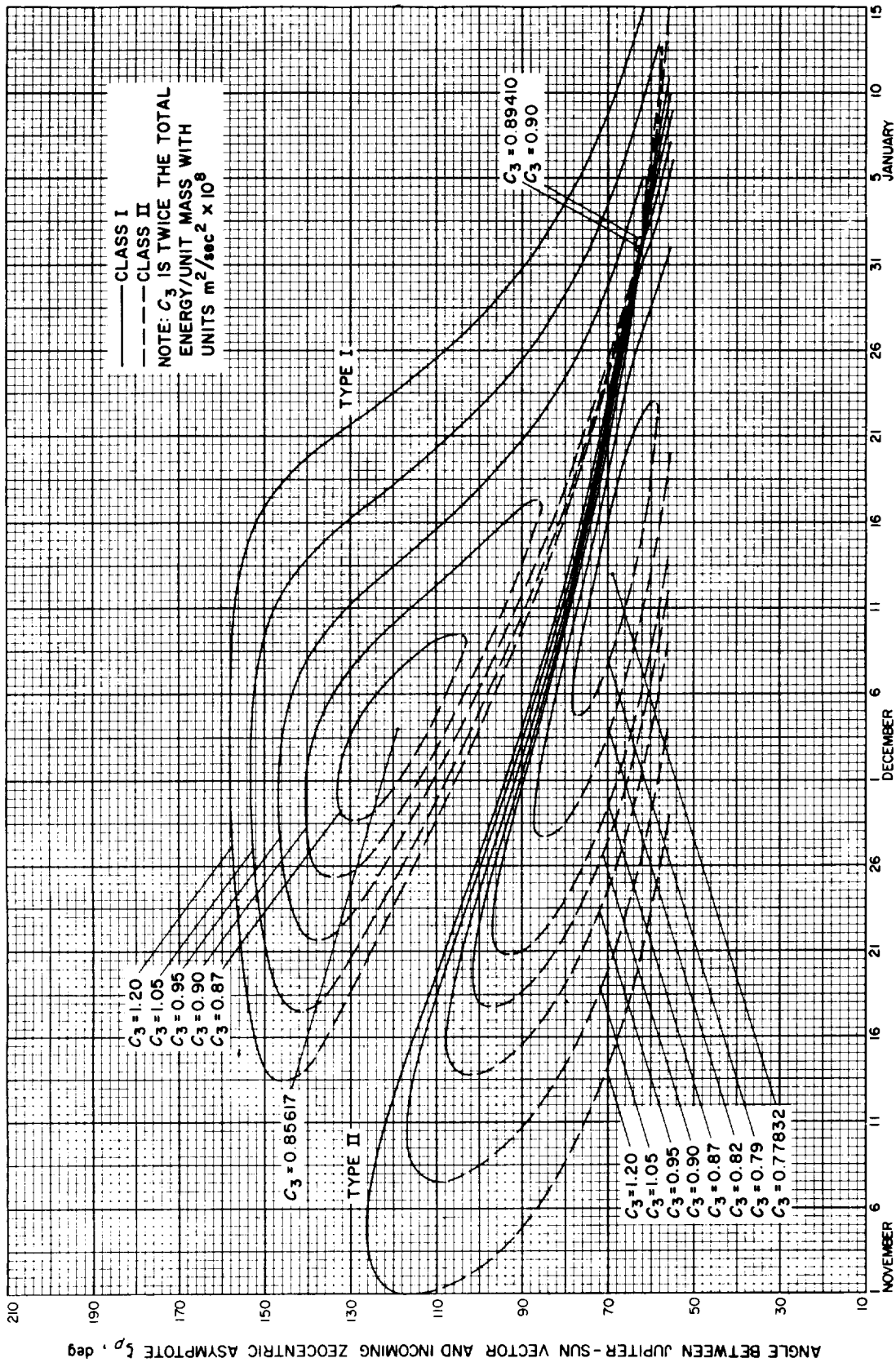

Fig. 6–17. Jupiter 68–69: Angle between Jupiter–Sun vector and incoming zeocentric asymptote vs launch date

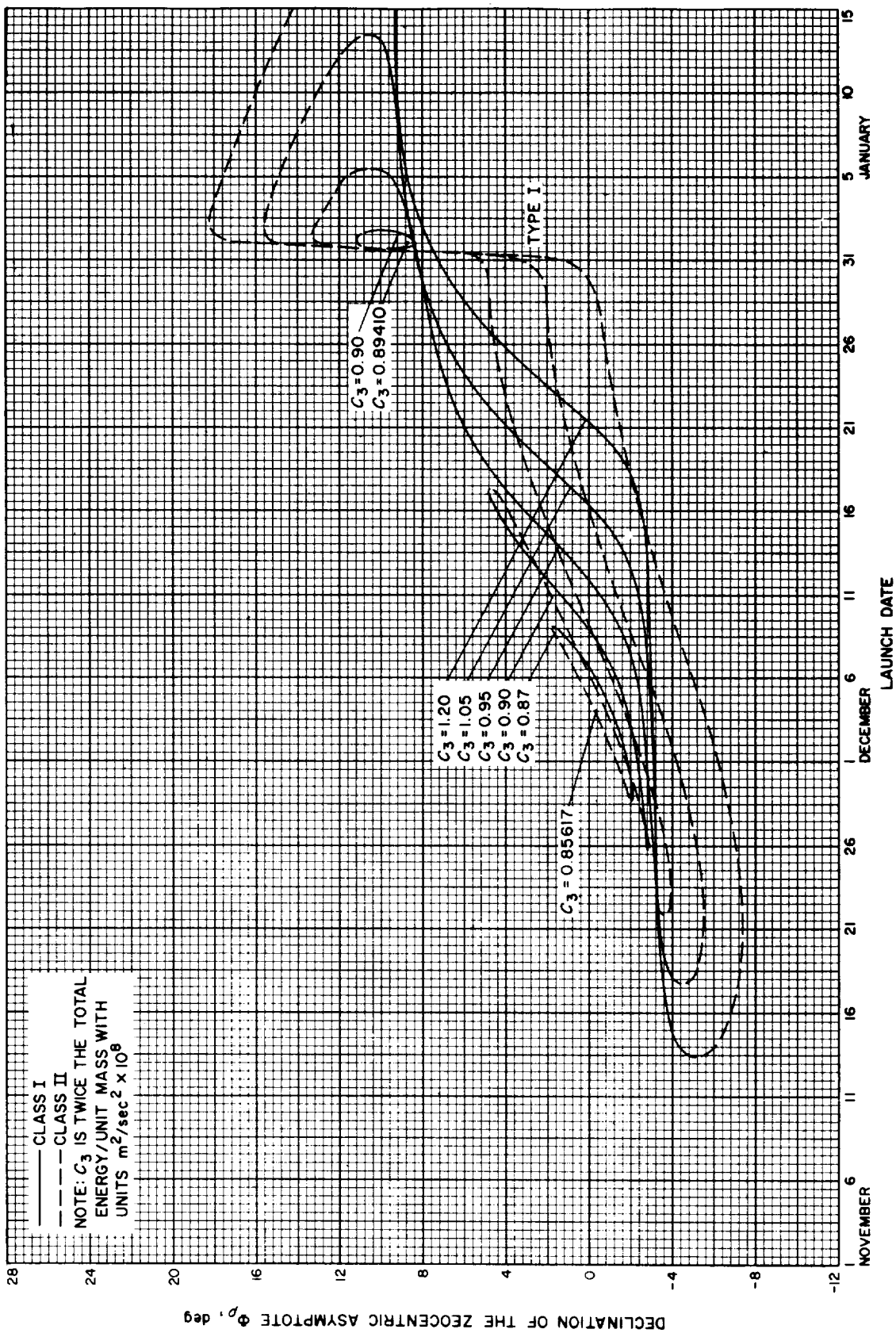

Fig. 6-18(I). Jupiter 68–69: Declination of the zeocentric asymptote vs launch date, Type I

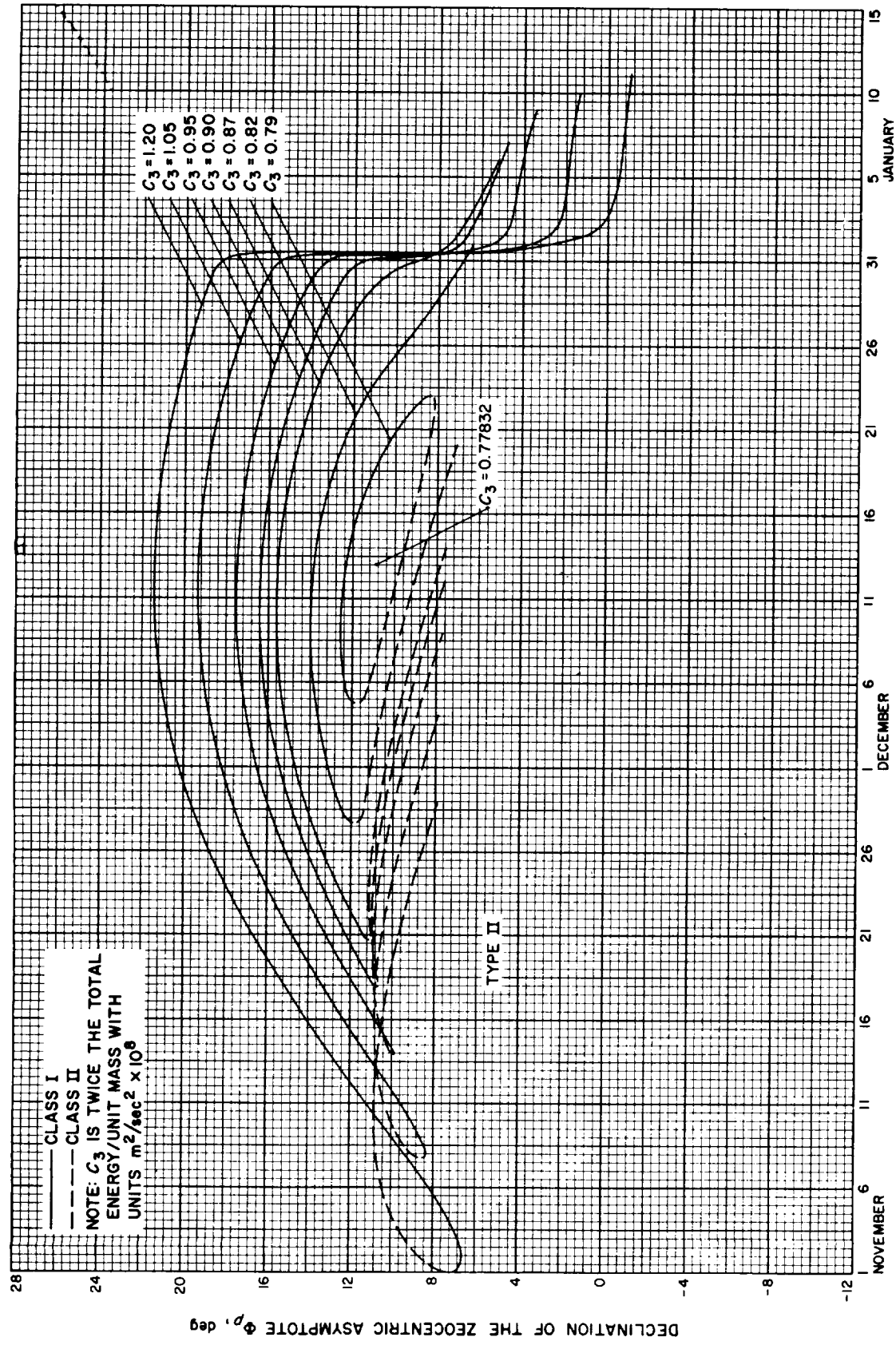

Fig. 6-18(II). Jupiter 68-69: Declination of the zeocentric asymptote vs launch date, Type II

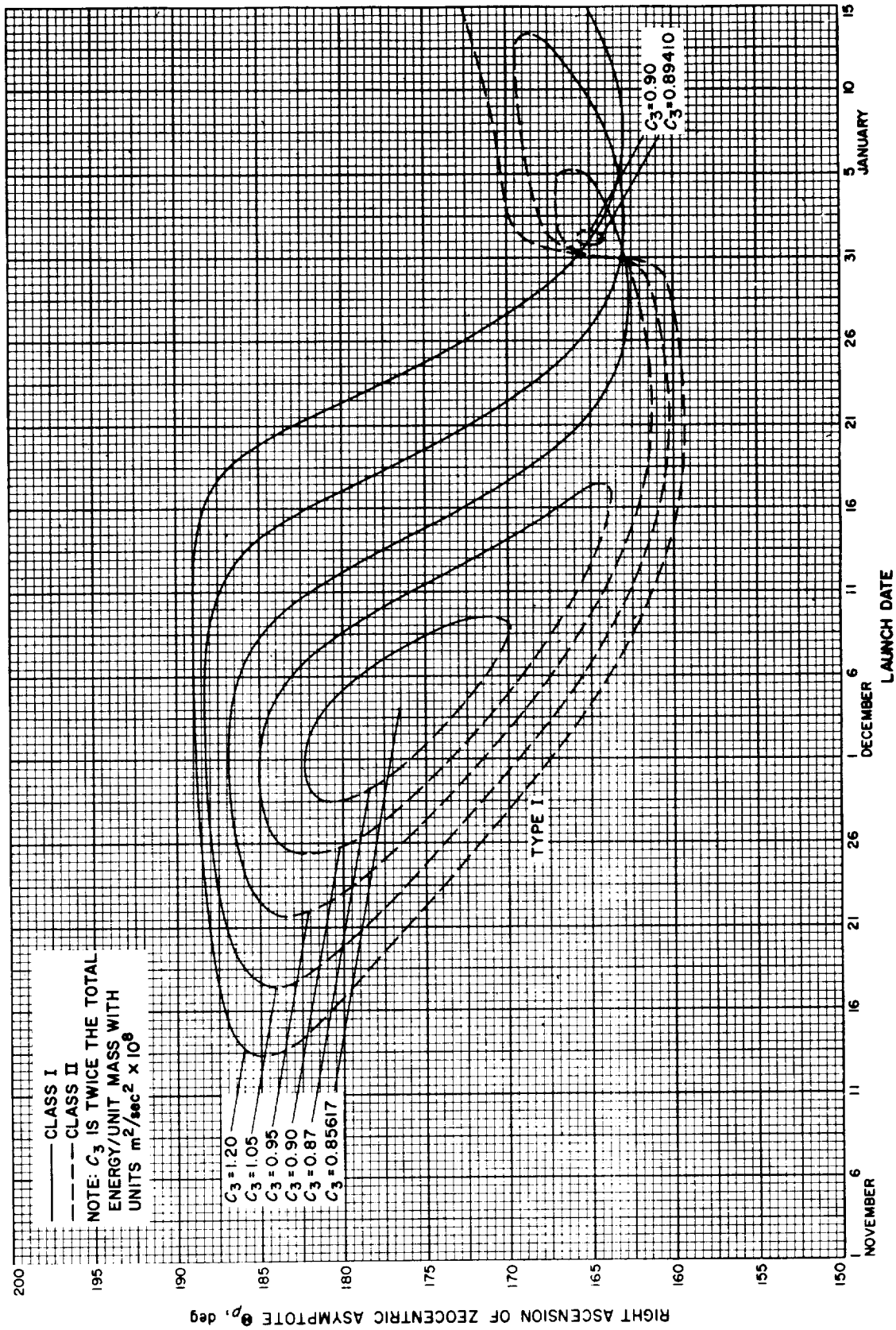

Fig. 6–19(I). Jupiter 68–69: Right ascension of zeocentric asymptote vs launch date, Type I

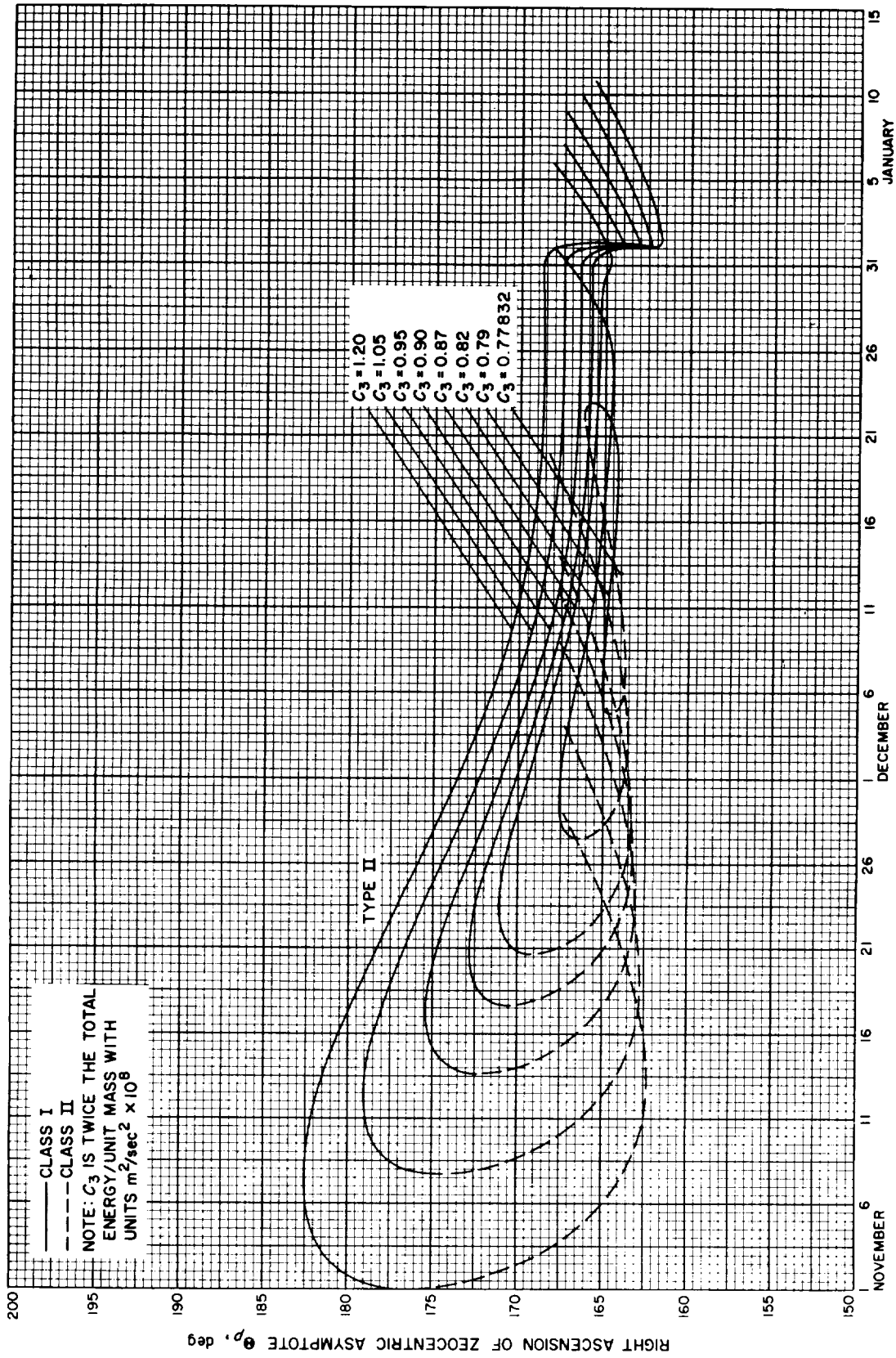

Fig. 6–19(II). Jupiter 68–69: Right ascension of zeocentric asymptote vs launch date, Type II

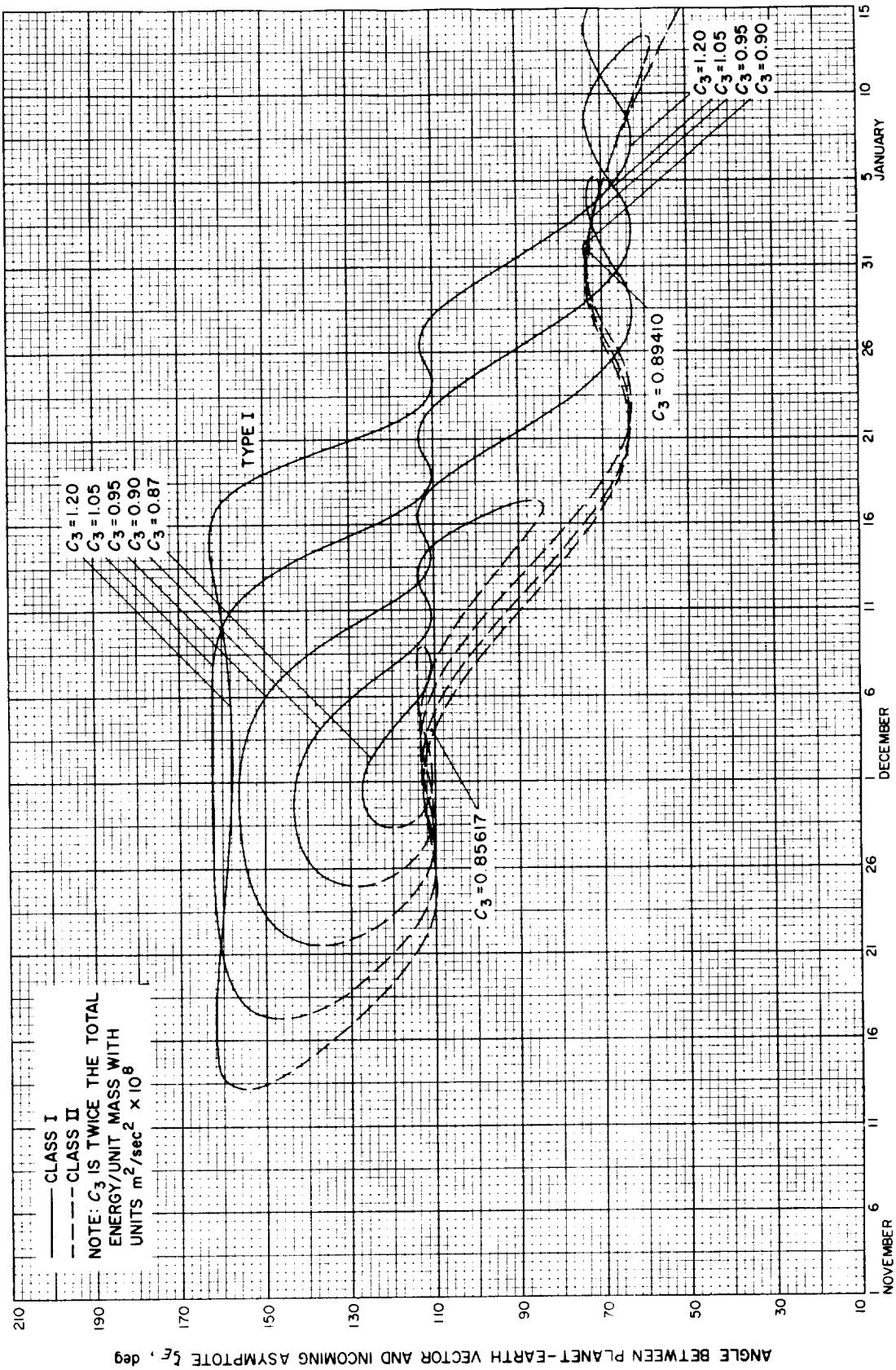

Fig. 6-20(I). Jupiter 68–69: Angle between Planet–Earth vector and incoming asymptote vs launch date, Type I

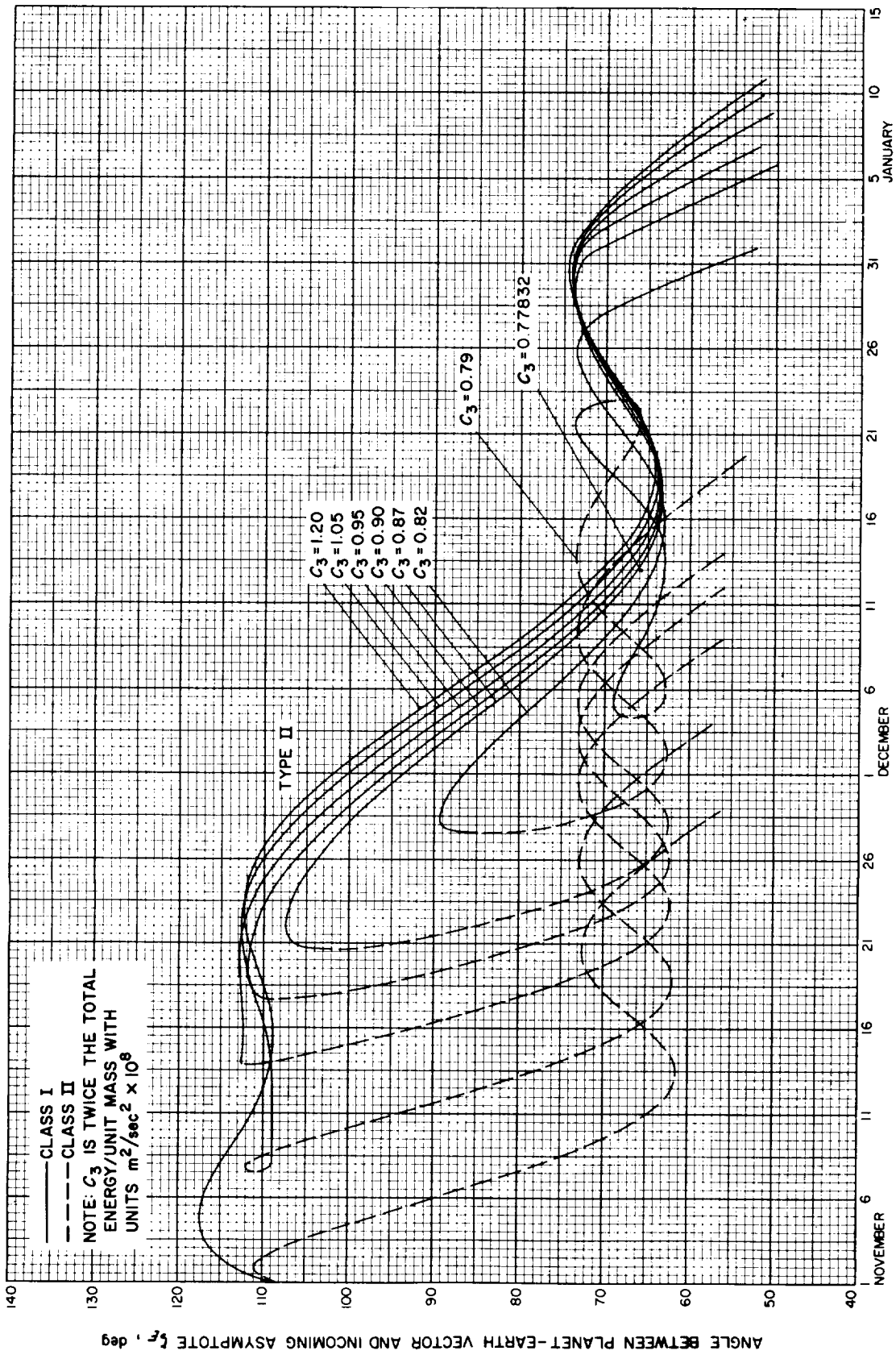

Fig. 6-20(II). Jupiter 68–69: Angle between Planet–Earth vector and incoming asymptote vs launch date, Type II

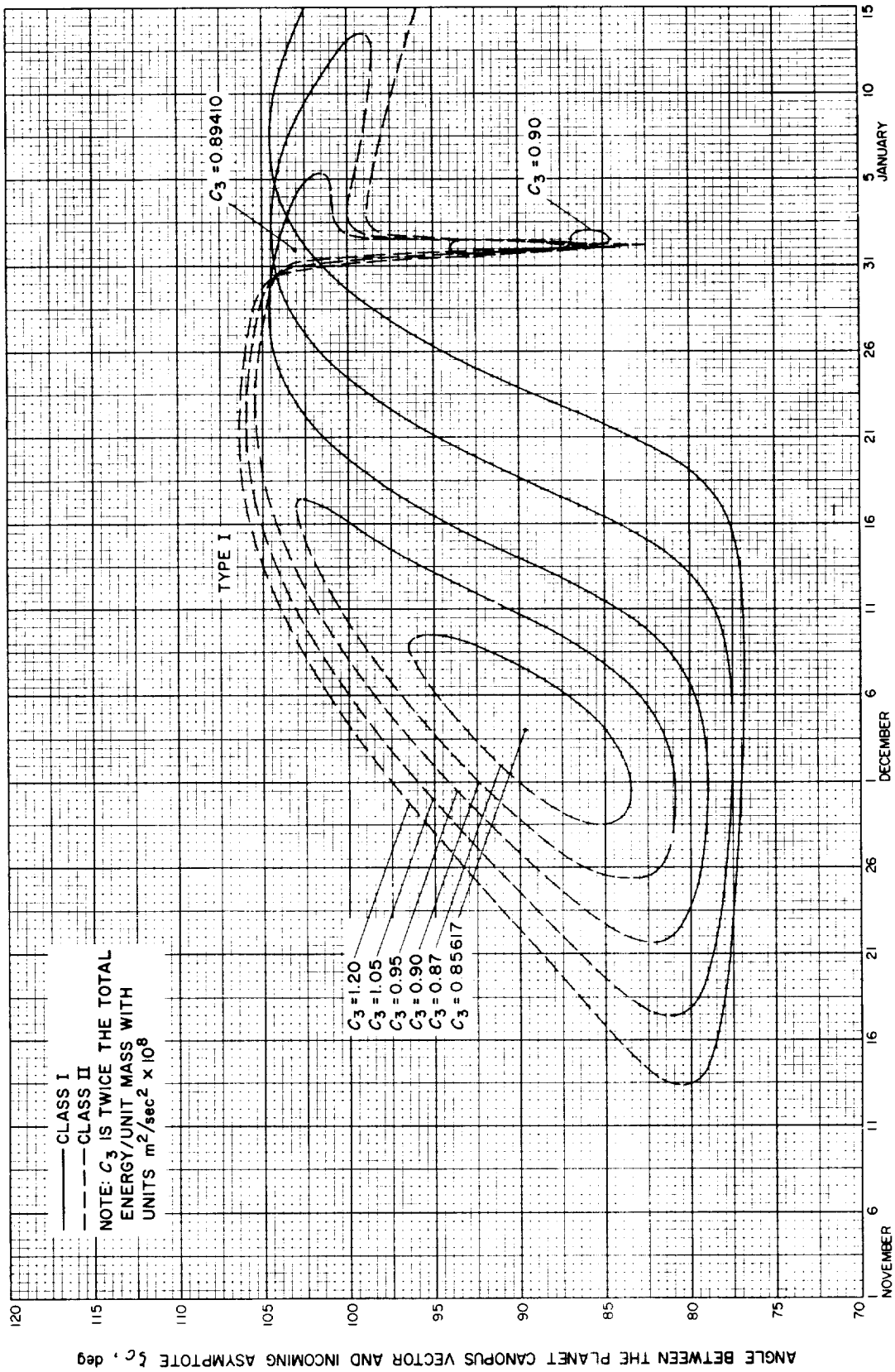

Fig. 6-21(I). Jupiter 68–69: Angle between the planet–Canopus vector and incoming asymptote vs launch date, Type I

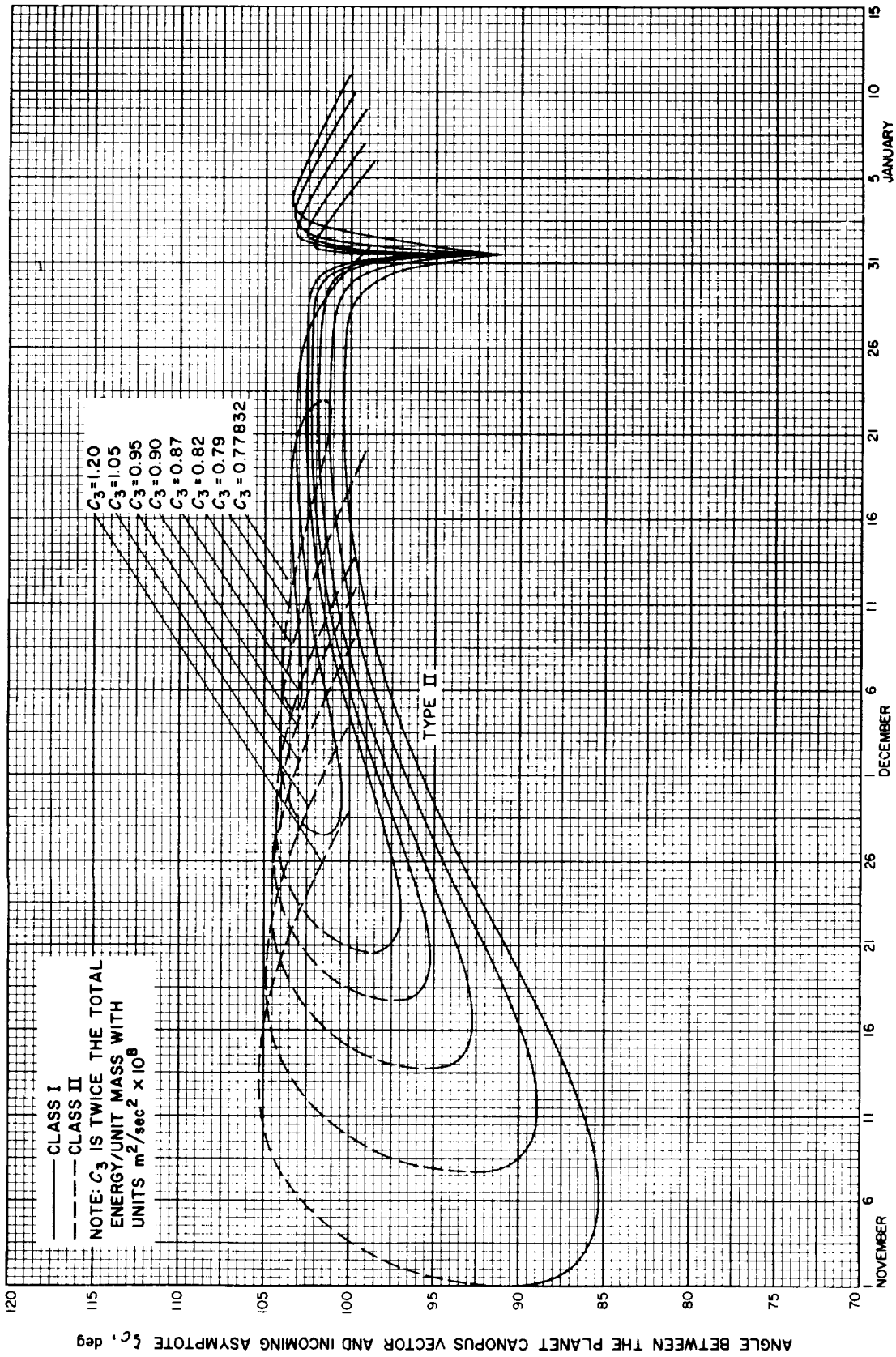

Fig. 6-21(II). Jupiter 68–69: Angle between the planet–Canopus vector and incoming asymptote vs launch date, Type II

VII. JUPITER 1969–70: TRAJECTORY PARAMETER GRAPHS

Figure

7–1. Jupiter 69–70: Minimum injection energy vs launch date

7–2. Jupiter 69–70: Time of flight vs launch date

7–3. Jupiter 69–70: Heliocentric central angle vs launch date

7–4(I). Jupiter 69–70: Earth–Jupiter communication distance vs launch date, Type I

7–4(II). Jupiter 69–70: Earth–Jupiter communication distance vs launch date, Type II

7–5(I). Jupiter 69–70: Declination of the geocentric asymptote vs launch date, Type I

7–5(II). Jupiter 69–70: Declination of the geocentric asymptote vs launch date, Type II

7–6(I). Jupiter 69–70: Right ascension of the geocentric asymptote vs launch date, Type I

7–6(II). Jupiter 69–70: Right ascension of the geocentric asymptote vs launch date, Type II

7–7(I). Jupiter 69–70: Angle between outgoing geocentric asymptote and launch planet's orbital plane vs launch date, Type I

7–7(II). Jupiter 69–70: Angle between outgoing geocentric asymptote and launch planet's orbital plane vs launch date, Type II

7–8. Jupiter 69–70: Angle between Sun–Earth vector and outgoing geocentric asymptote vs launch date

7–9. Jupiter 69–70: True anomaly in transfer ellipse at launch time vs launch date

7–10. Jupiter 69–70: True anomaly in transfer ellipse at arrival time vs launch date

7–11(I). Jupiter 69–70: Perihelion of transfer orbit vs launch date, Type I

7–11(II). Jupiter 69–70: Perihelion of transfer orbit vs launch date, Type II

7–12(I). Jupiter 69–70: Aphelion of transfer orbit vs launch date, Type I

7–12(II). Jupiter 69–70: Aphelion of transfer orbit vs launch date, Type II

7–13(I). Jupiter 69–70: Inclination of the heliocentric transfer plane vs launch date, Type I

7–13(II). Jupiter 69–70: Inclination of the heliocentric transfer plane vs launch date, Type II

VII. JUPITER 1969–70: TRAJECTORY PARAMETER GRAPHS (Cont'd)

Figure

7–14. Jupiter 69–70: Celestial latitude at arrival time vs launch date

7–15(I). Jupiter 69–70: Asymptotic speed with respect to Jupiter vs launch date, Type I

7–15(II). Jupiter 69–70: Asymptotic speed with respect to Jupiter vs launch date, Type II

7–16(I). Jupiter 69–70: Angle between incoming zeocentric asymptote and arrival planet's orbital plane vs launch date, Type I

7–16(II). Jupiter 69–70: Angle between incoming zeocentric asymptote and arrival planet's orbital plane vs launch date, Type II

7–17. Jupiter 69–70: Angle between Jupiter–Sun vector and incoming zeocentric asymptote vs launch date

7–18(I). Jupiter 69–70: Declination of the zeocentric asymptote vs launch date, Type I

7–18(II). Jupiter 69–70: Declination of the zeocentric asymptote vs launch date, Type II

7–19(I). Jupiter 69–70: Right ascension of the zeocentric asymptote vs launch date, Type I

7–19(II). Jupiter 69–70: Right ascension of the zeocentric asymptote vs launch date, Type II

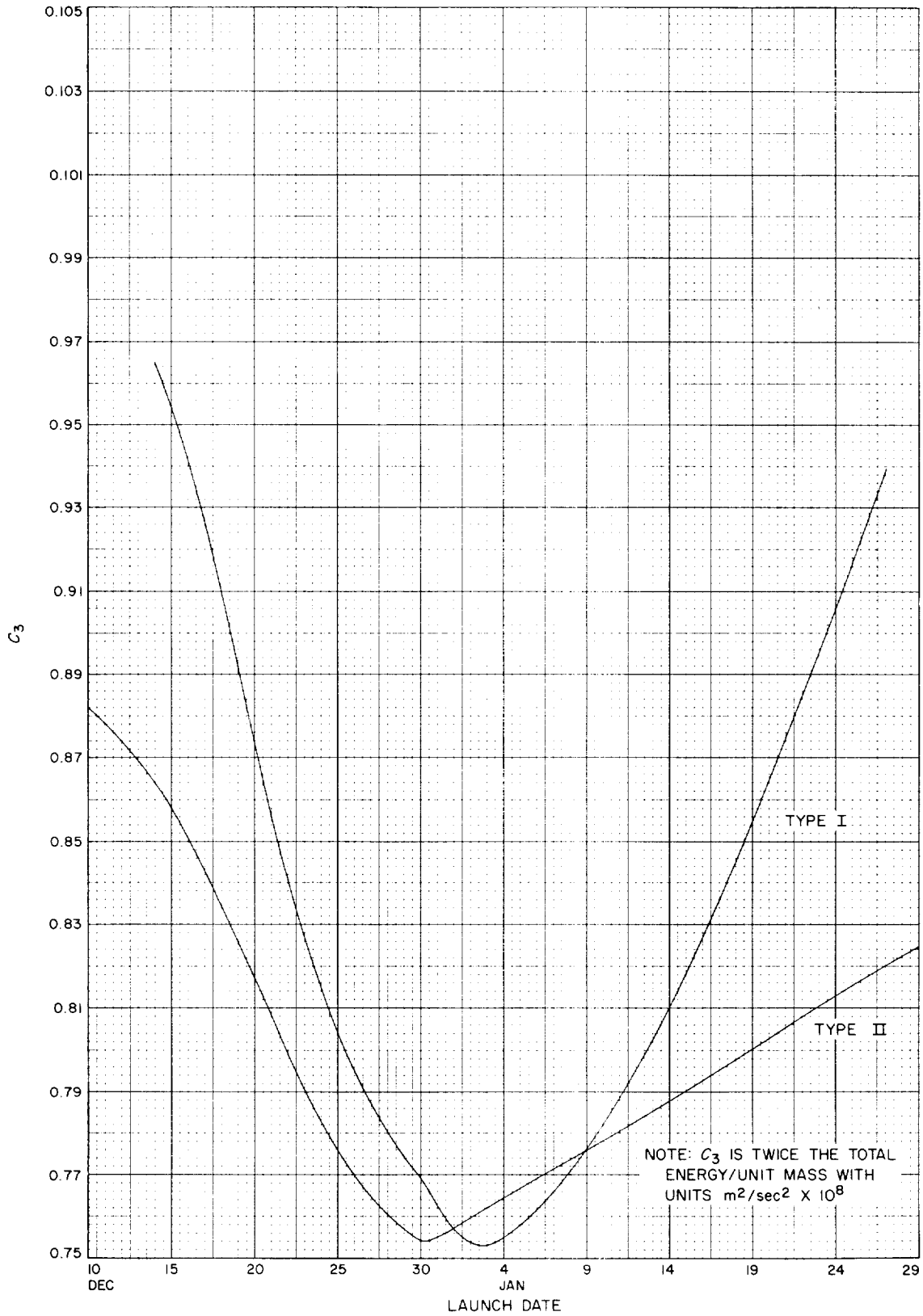

Fig. 7–1. Jupiter 69–79: Minimum injection energy vs launch date

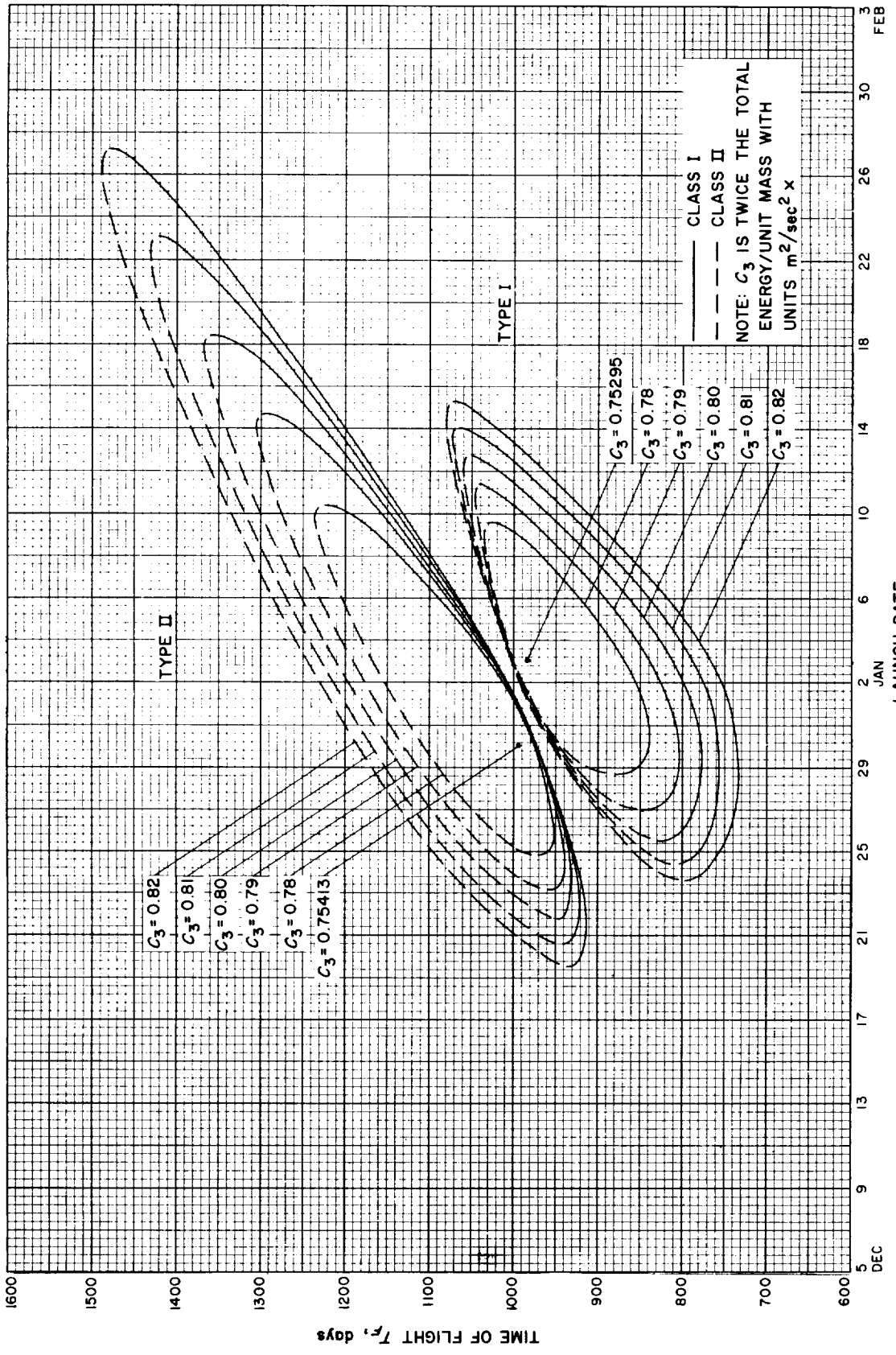

Fig. 7-2. Jupiter 69–79: Time of flight vs launch date

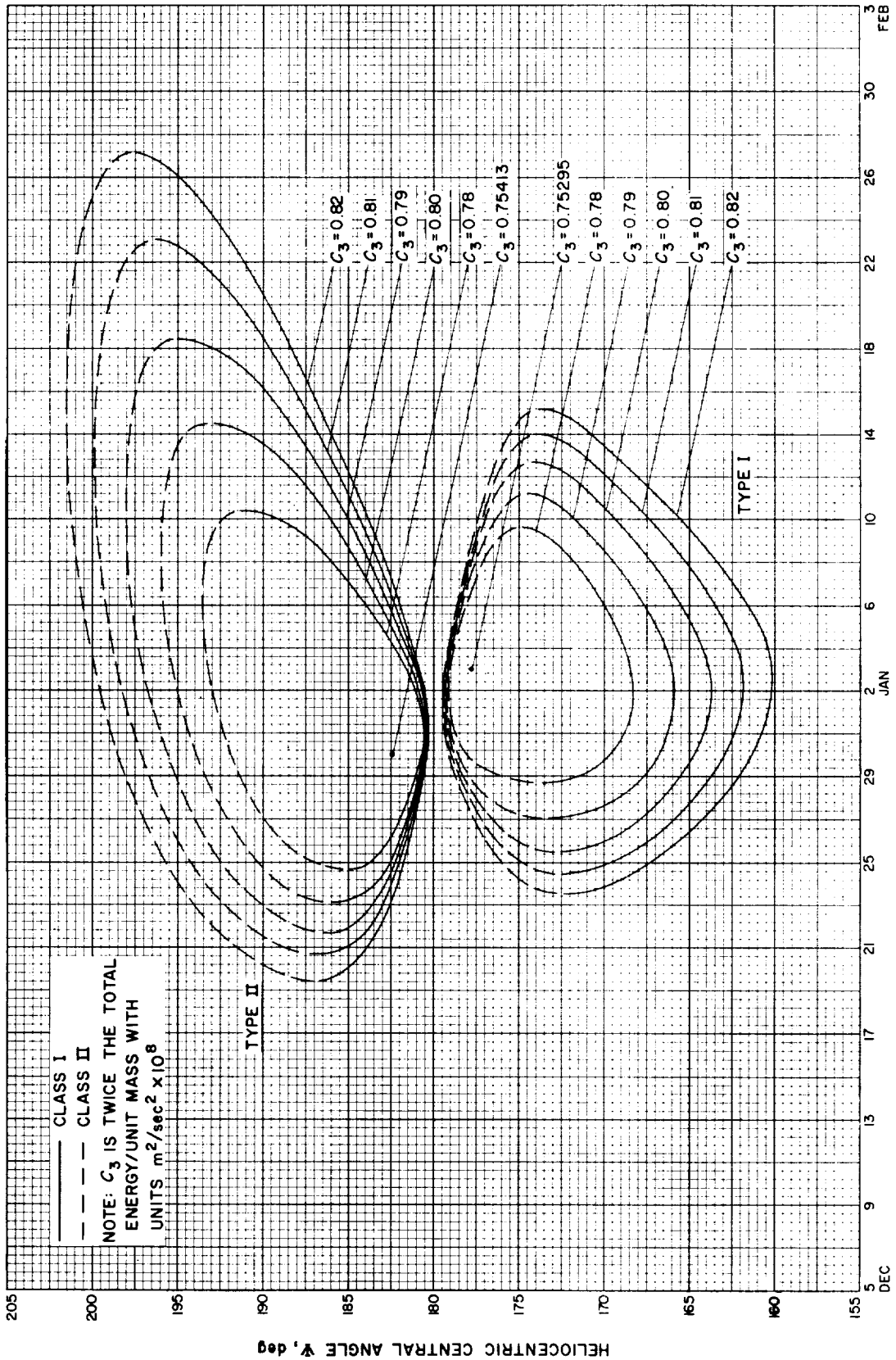

Fig. 7–3. Jupiter 69–70: Heliocentric central angle vs launch date

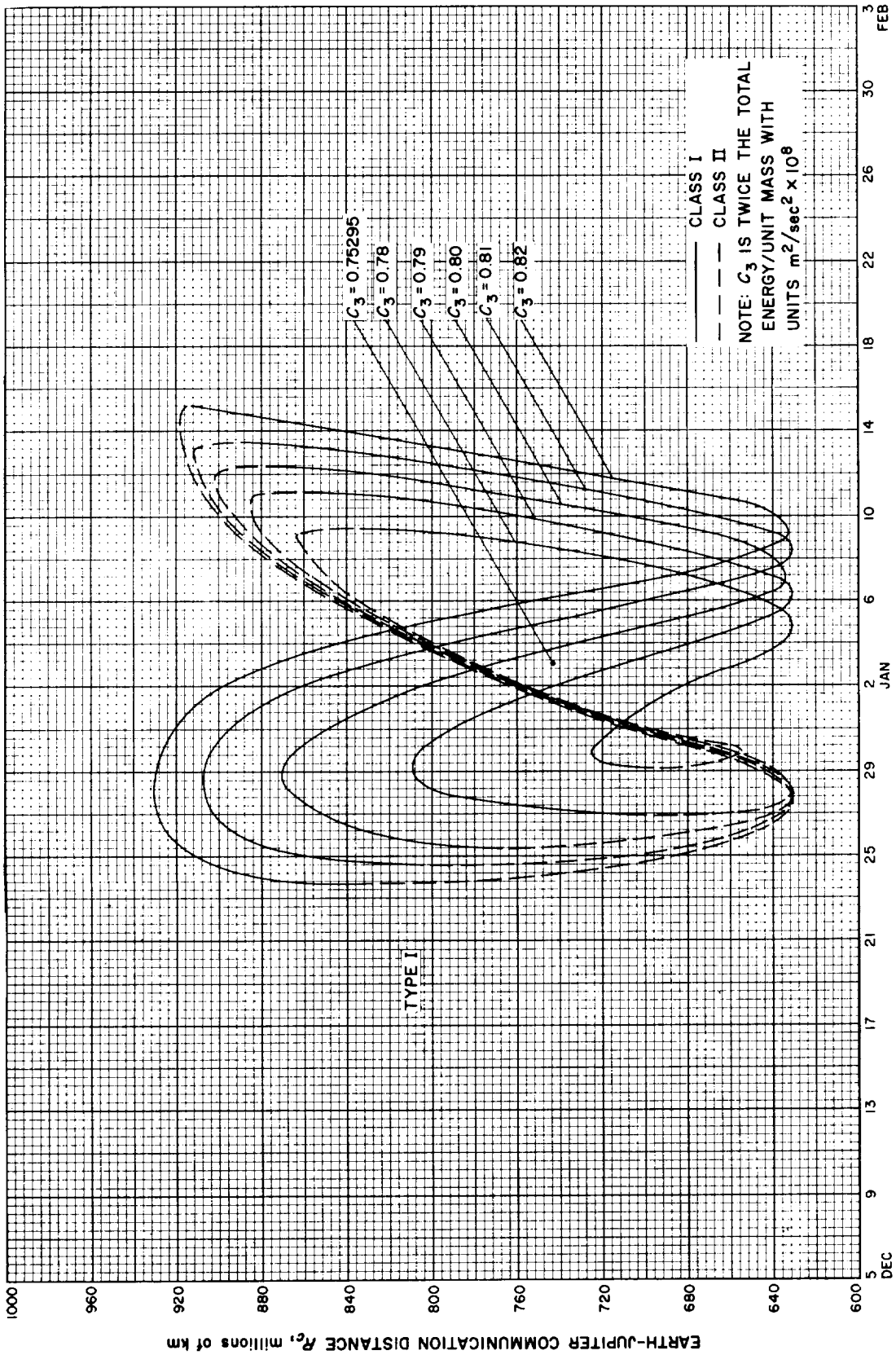

Fig. 7-4(I). Jupiter 69–70: Earth–Jupiter communication distance vs launch date, Type I

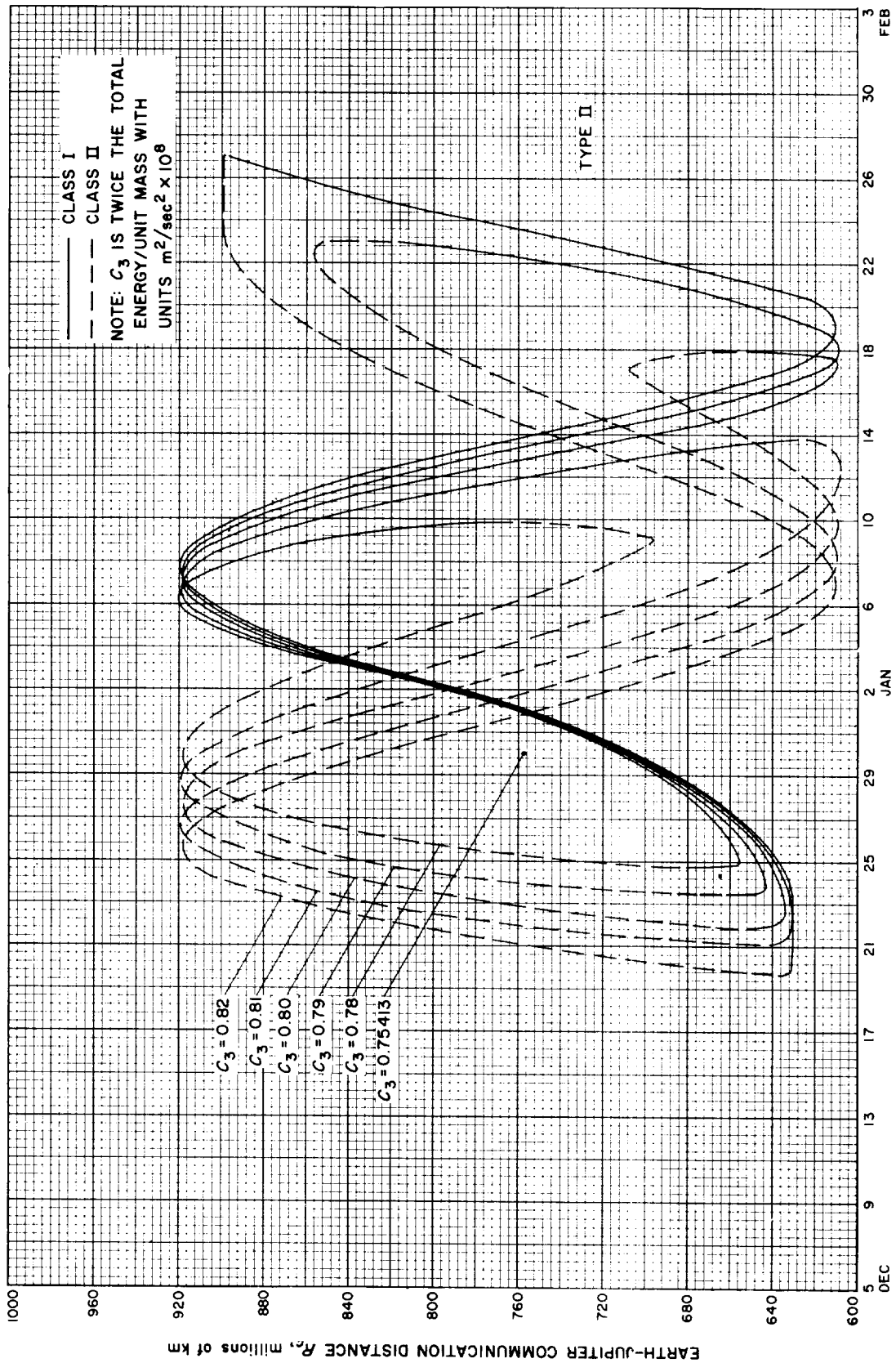

Fig. 7–4(II). Jupiter 69–70: Earth–Jupiter communication distance vs launch date, Type II

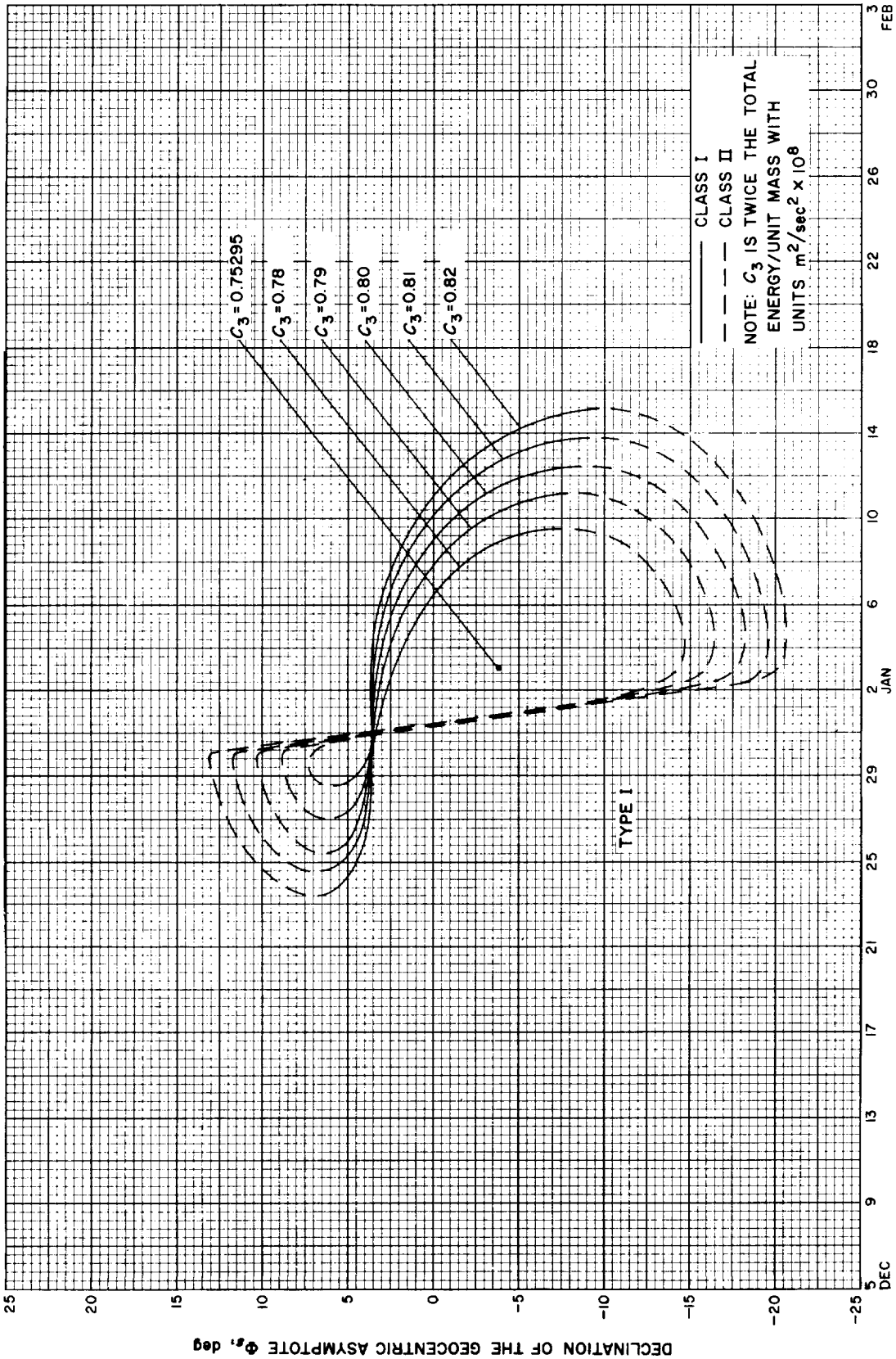

Fig. 7-5(I). Jupiter 69-70: Declination of the geocentric asymptote vs launch date, Type I

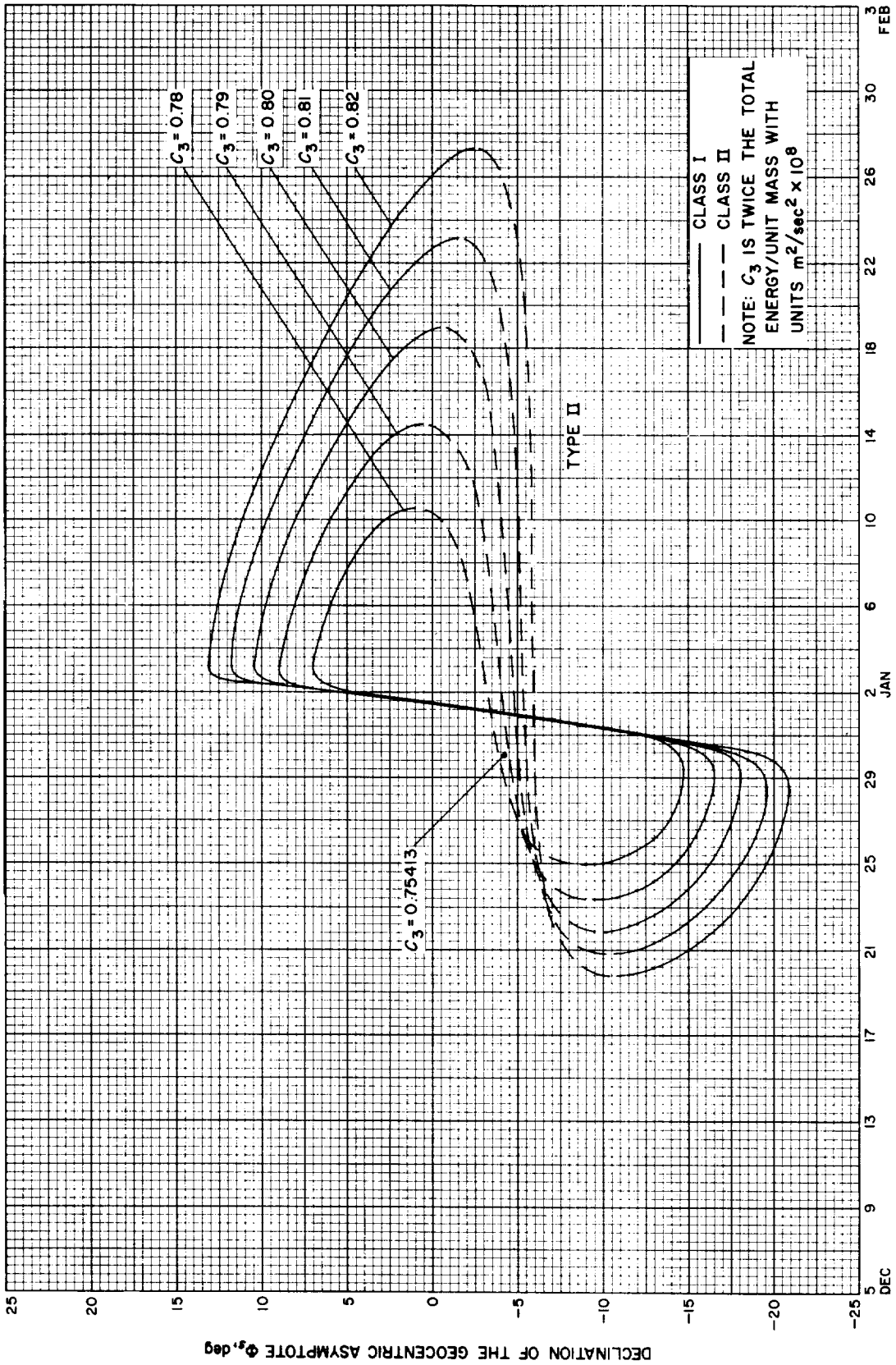

Fig. 7–5(II). Jupiter 69–70: Declination of the geocentric asymptote vs launch date, Type II

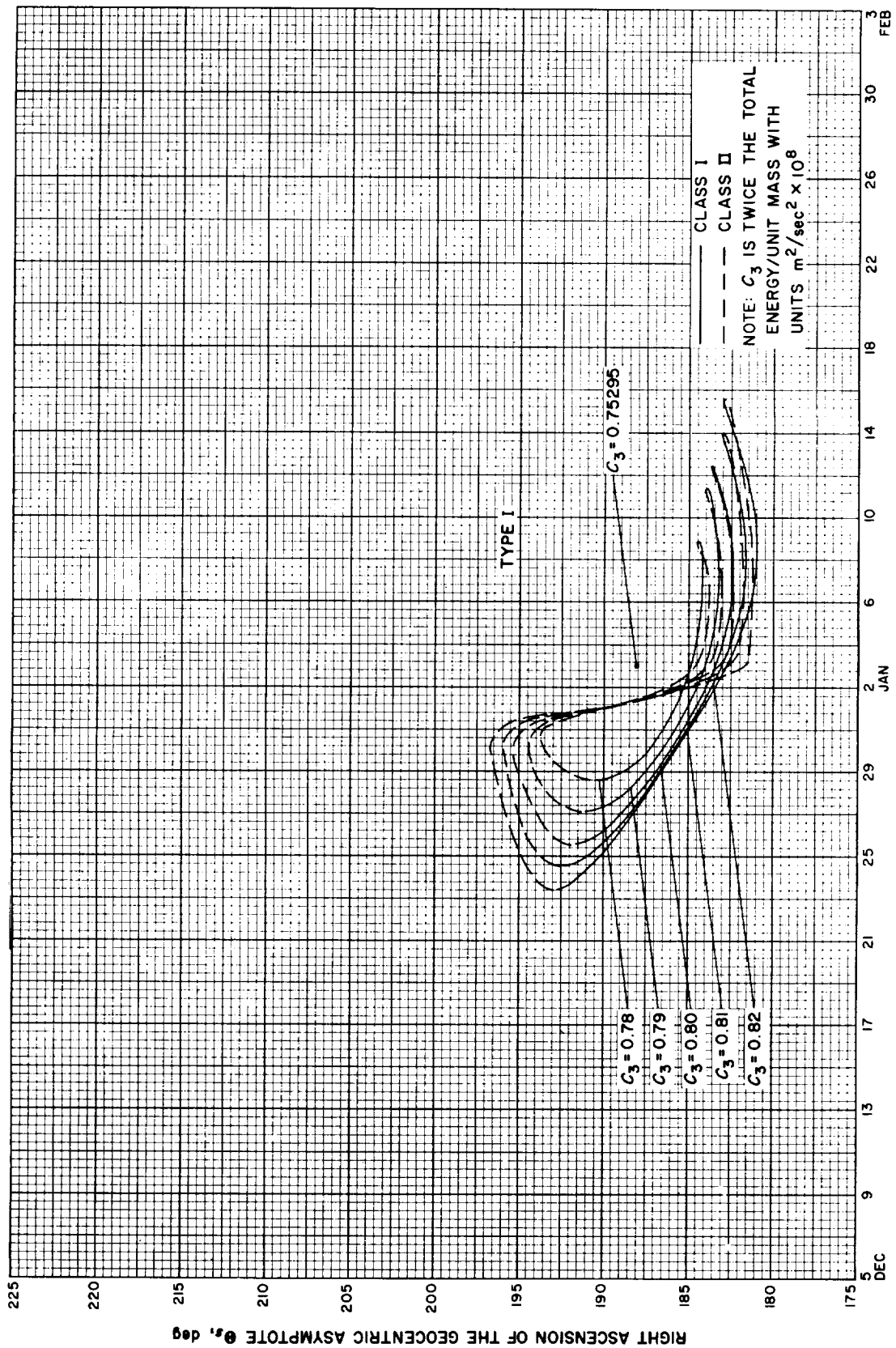

Fig. 7–6(I). Jupiter 69–70: Right ascension of the geocentric asymptote vs launch date, Type I

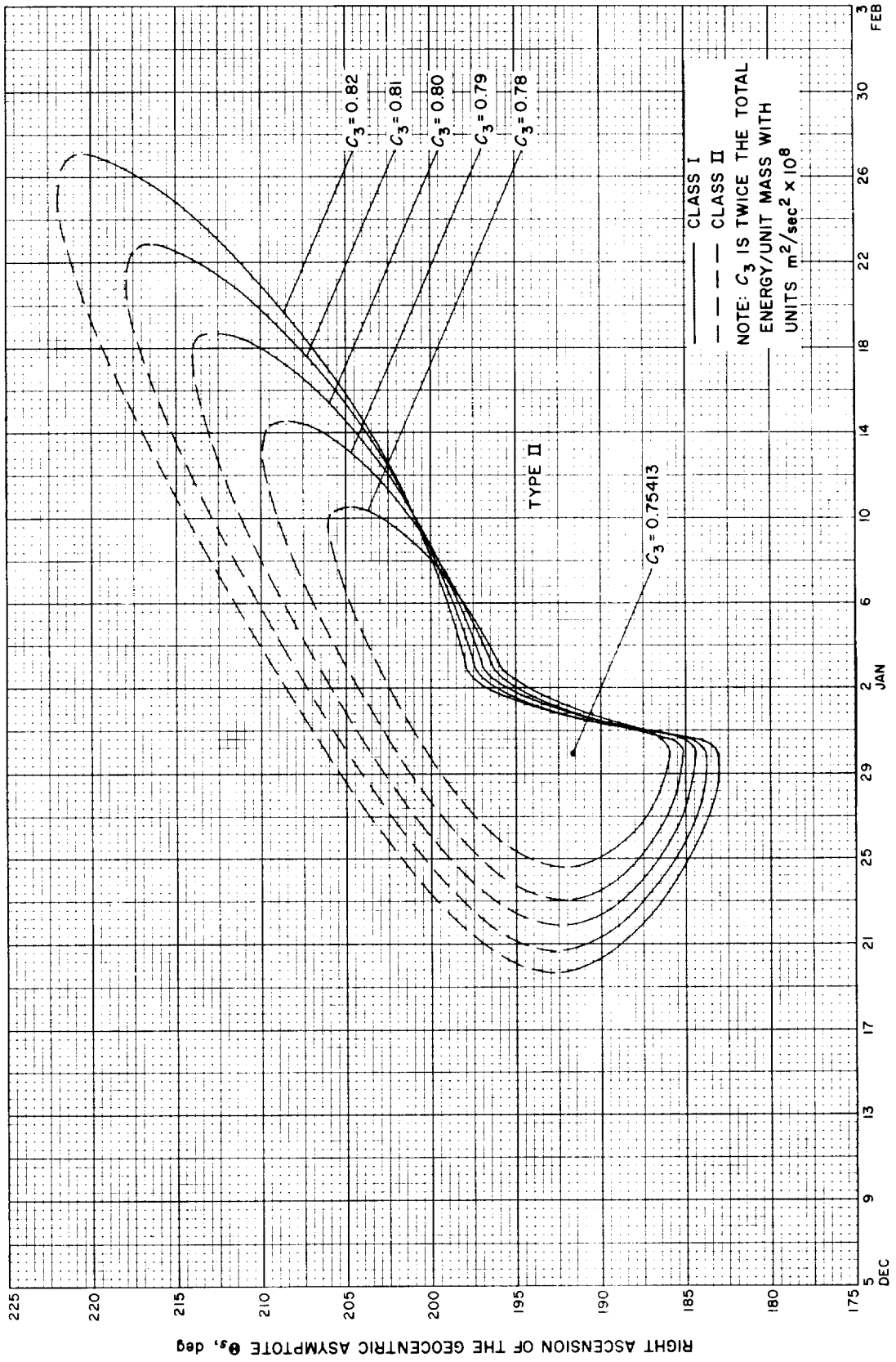

Fig. 7-6(II). Jupiter 69-70: Right ascension of the geocentric asymptote vs launch date, Type II

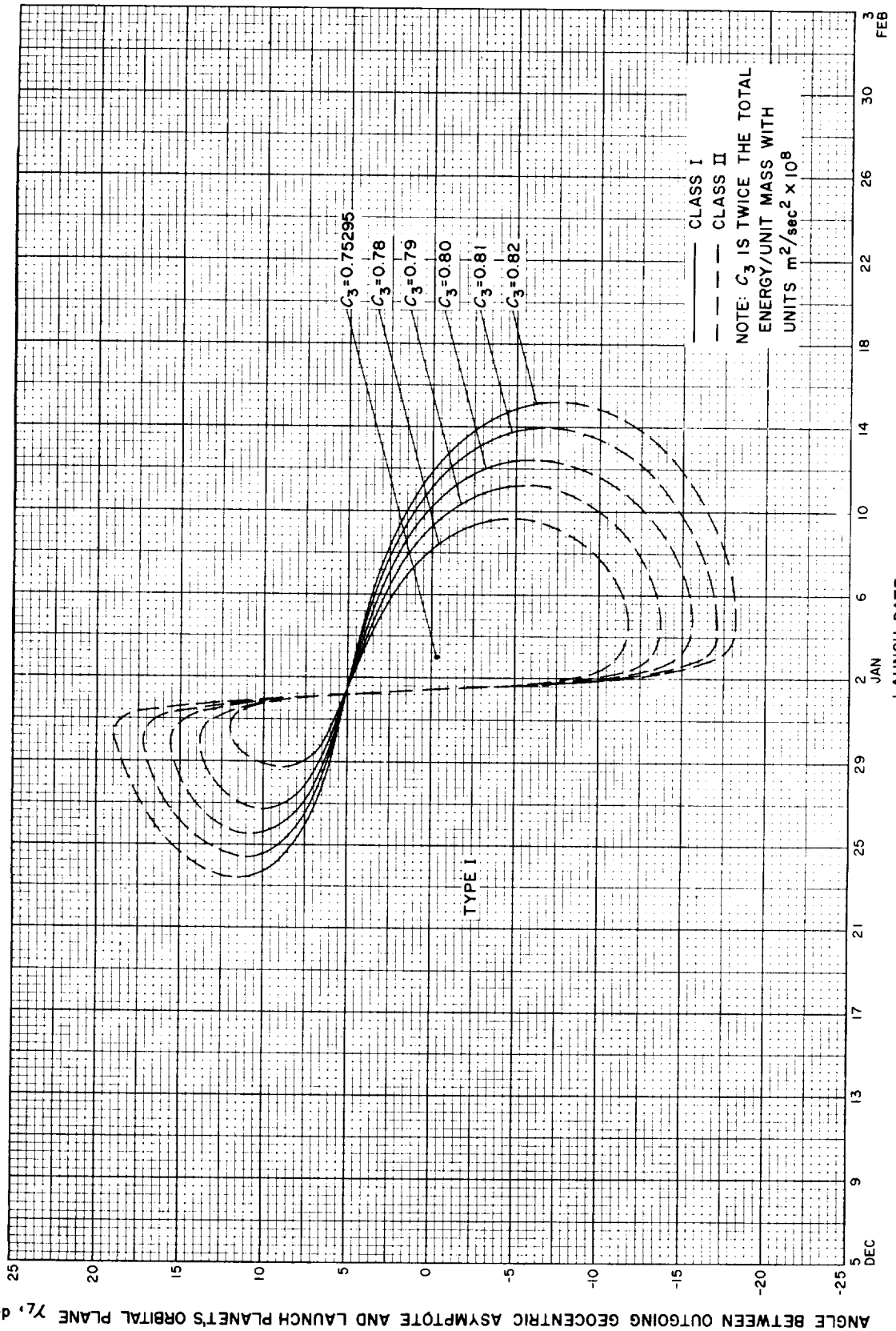

Fig. 7-7(I). Jupiter 69–70: Angle between outgoing geocentric asymptote and launch planet's orbital plane vs launch date, Type I

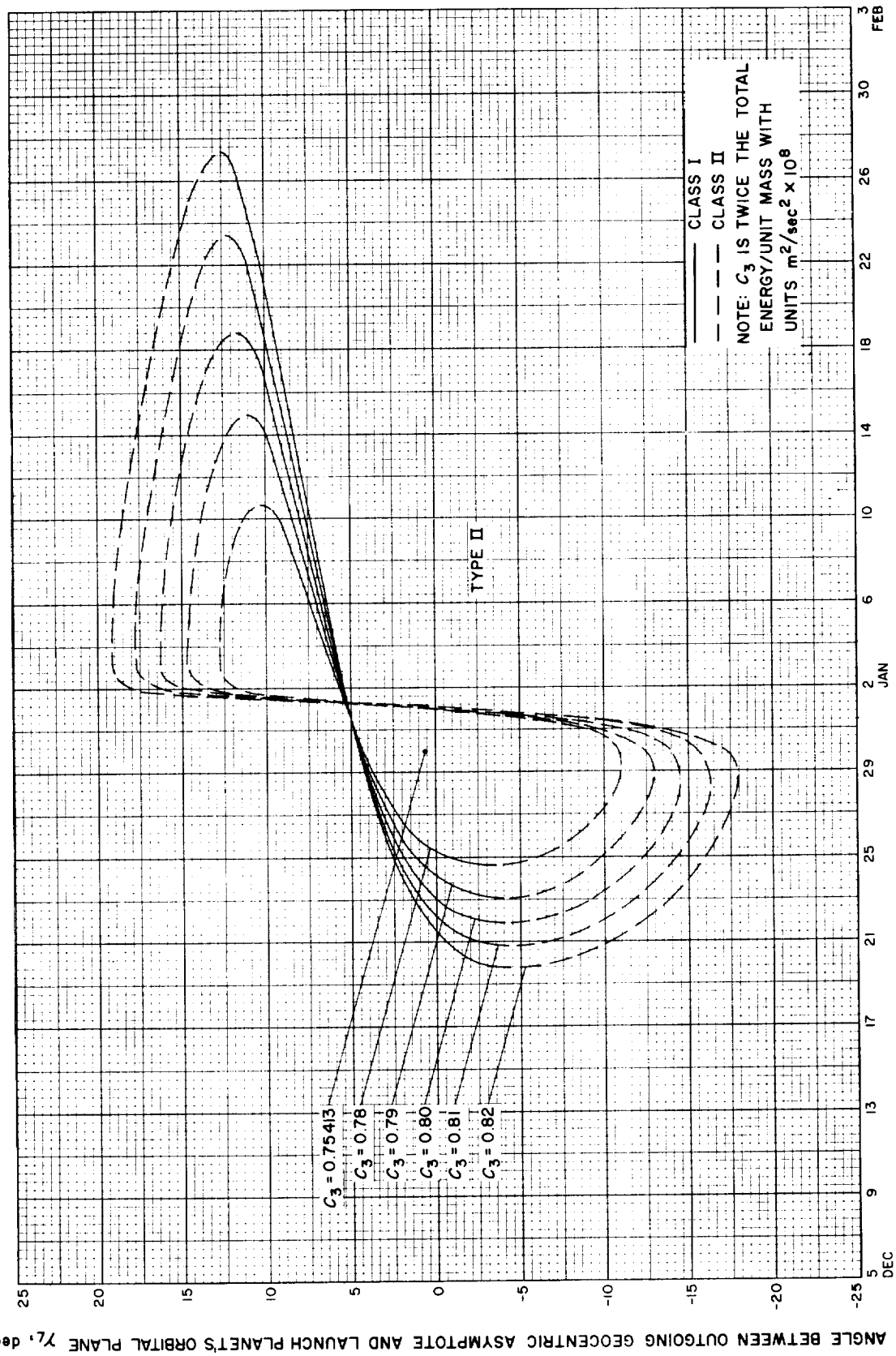

Fig. 7–7(II). Jupiter 69–70: Angle between outgoing geocentric asymptote and launch planet's orbital plane vs launch date, Type II

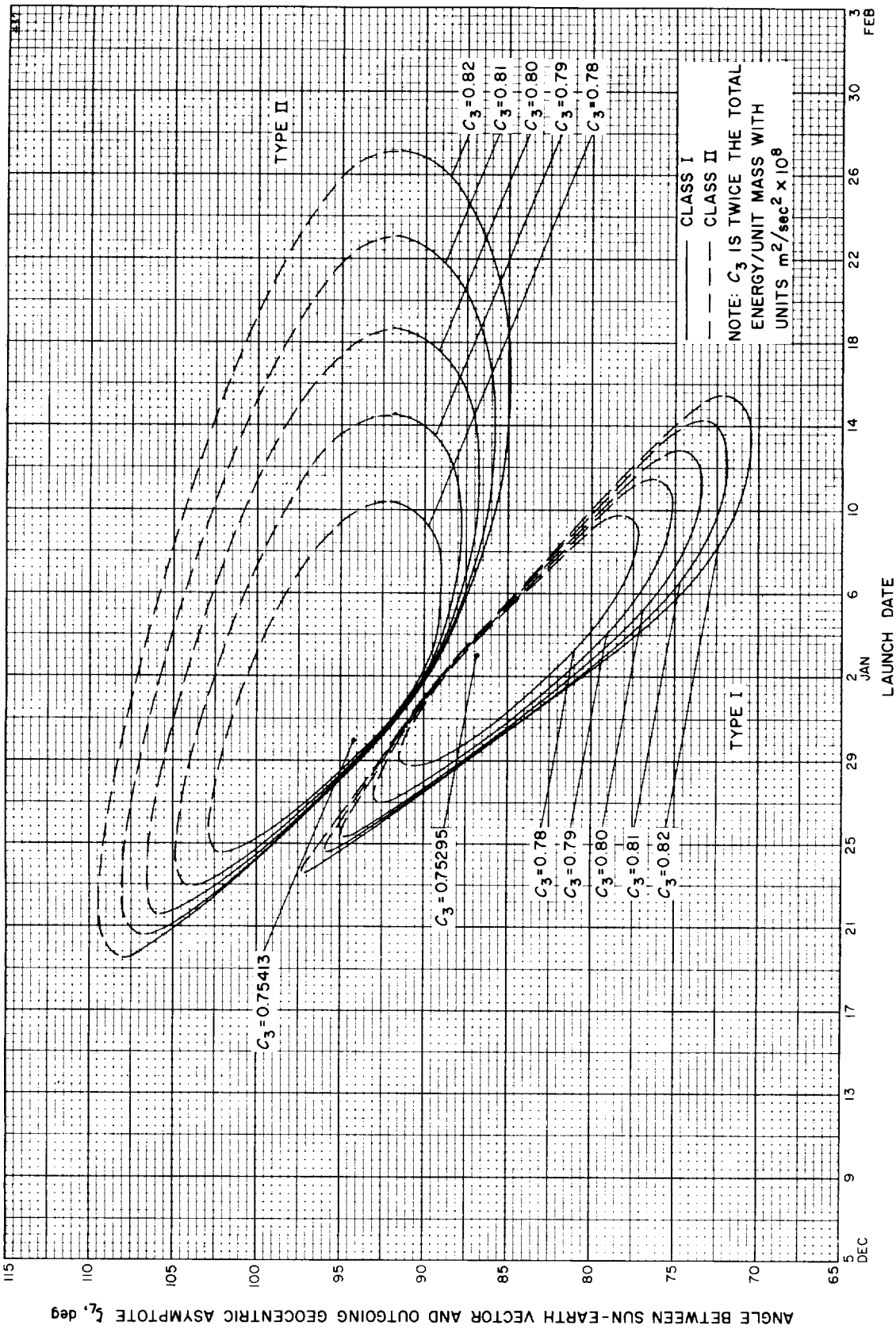

Fig. 7-8. Jupiter 69-70: Angle between Sun-Earth vector and outgoing geocentric asymptote vs launch date

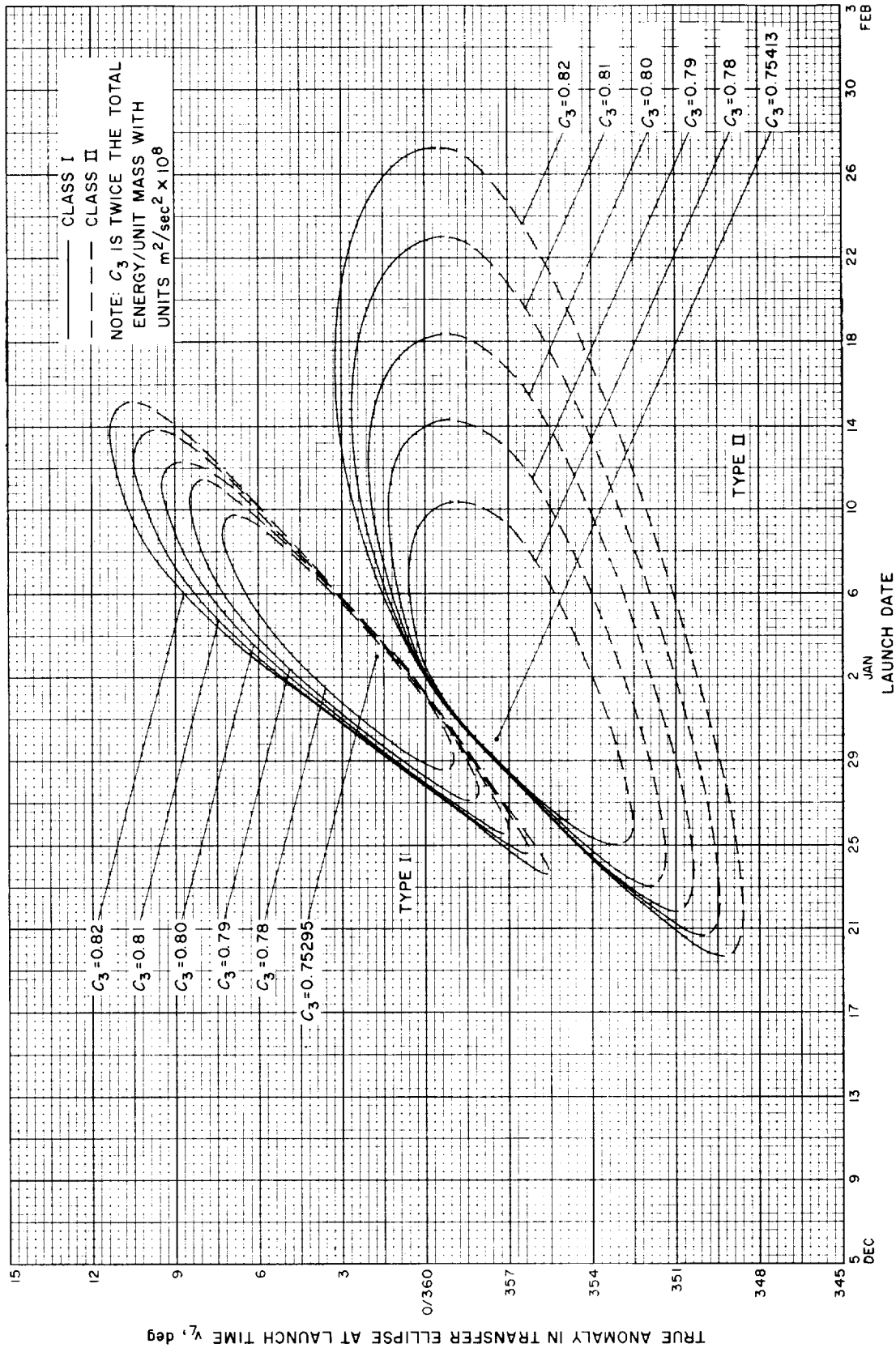

Fig. 7–9. Jupiter 69–70: True anomaly in transfer ellipse at launch time vs launch date

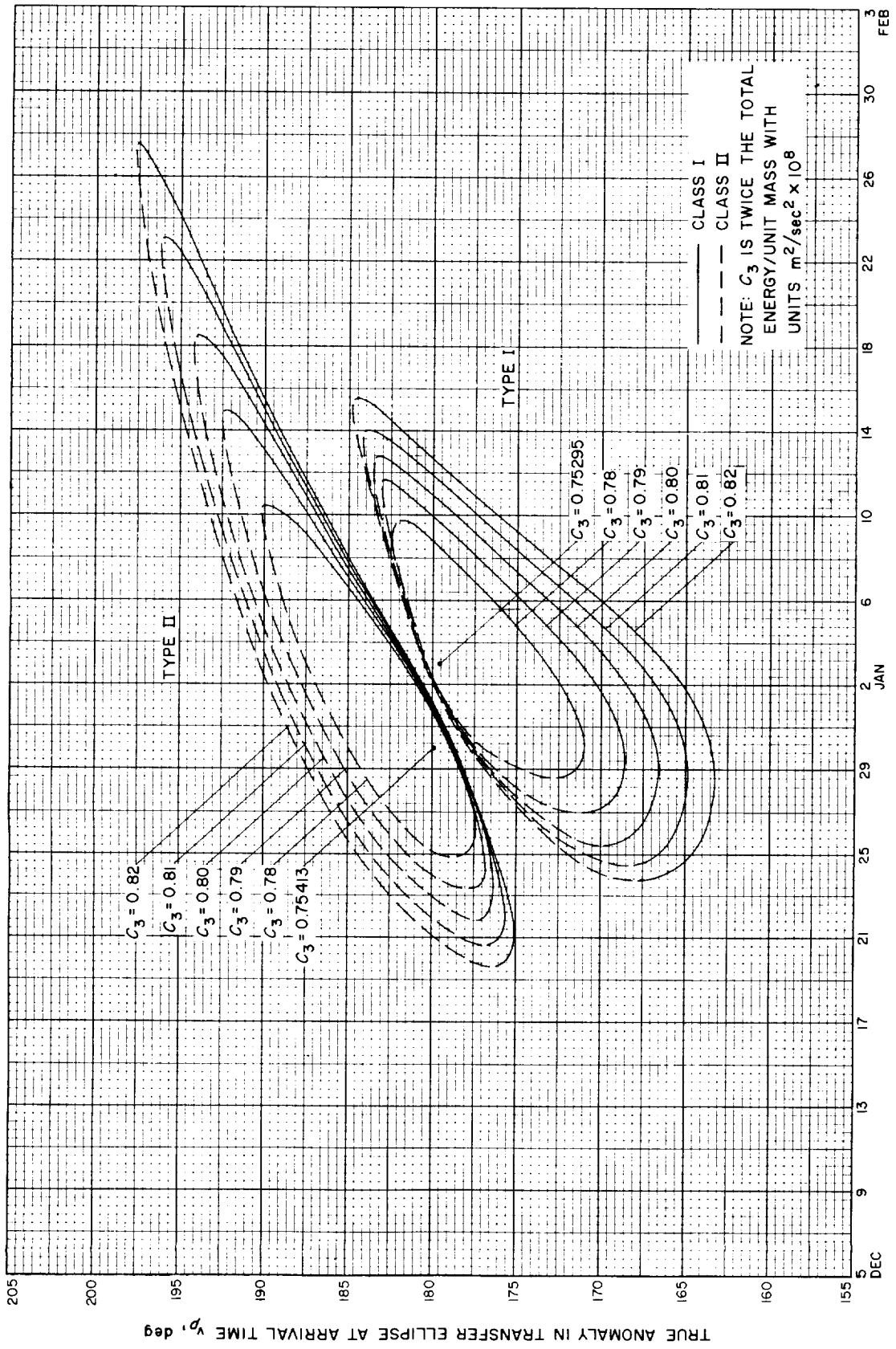

Fig. 7–10. Jupiter 69–70: True anomaly in transfer ellipse at arrival time vs launch date

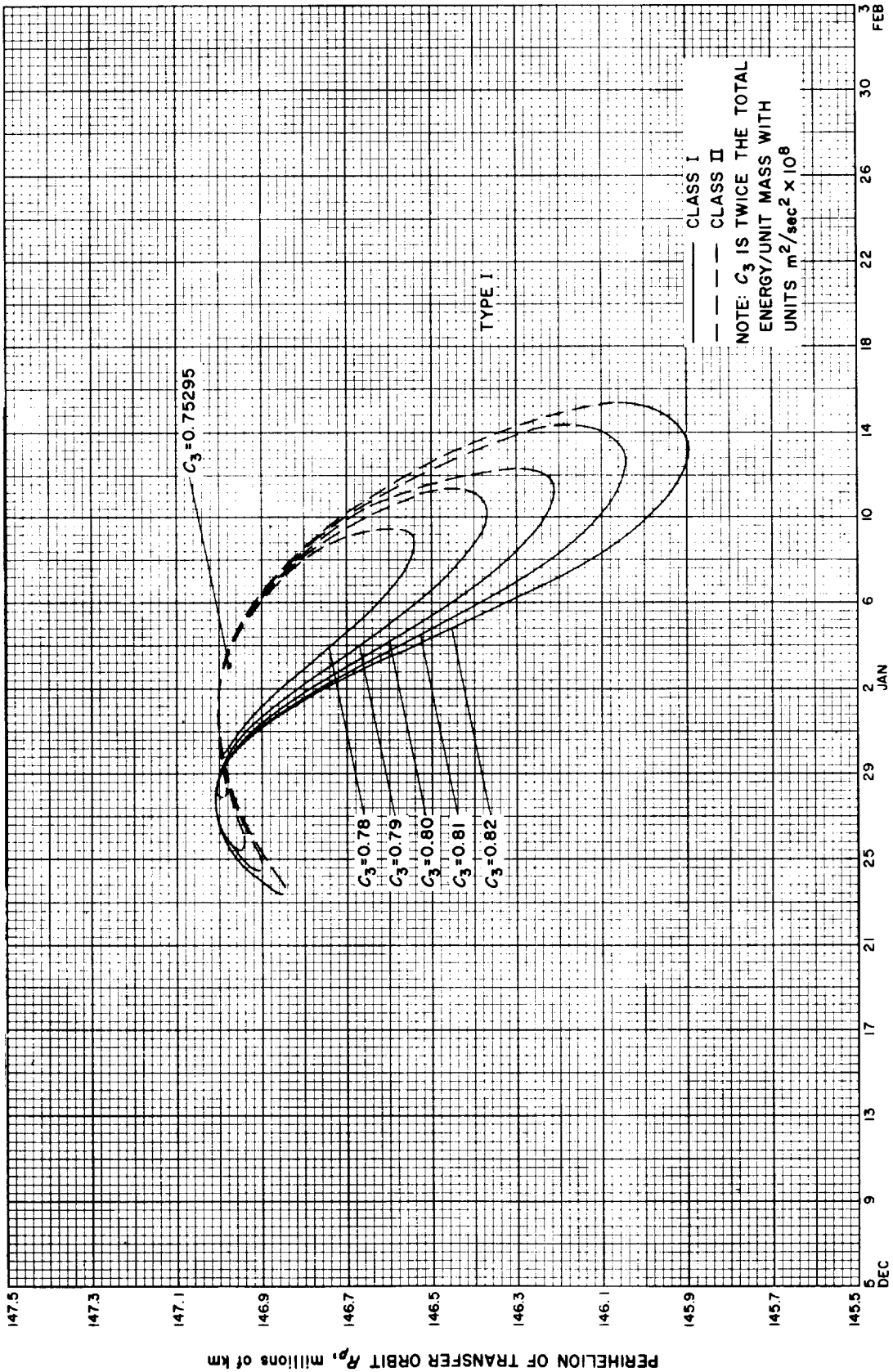

Fig. 7-1111. Jupiter 69–70: Perihelion of transfer orbit vs launch date, Type I

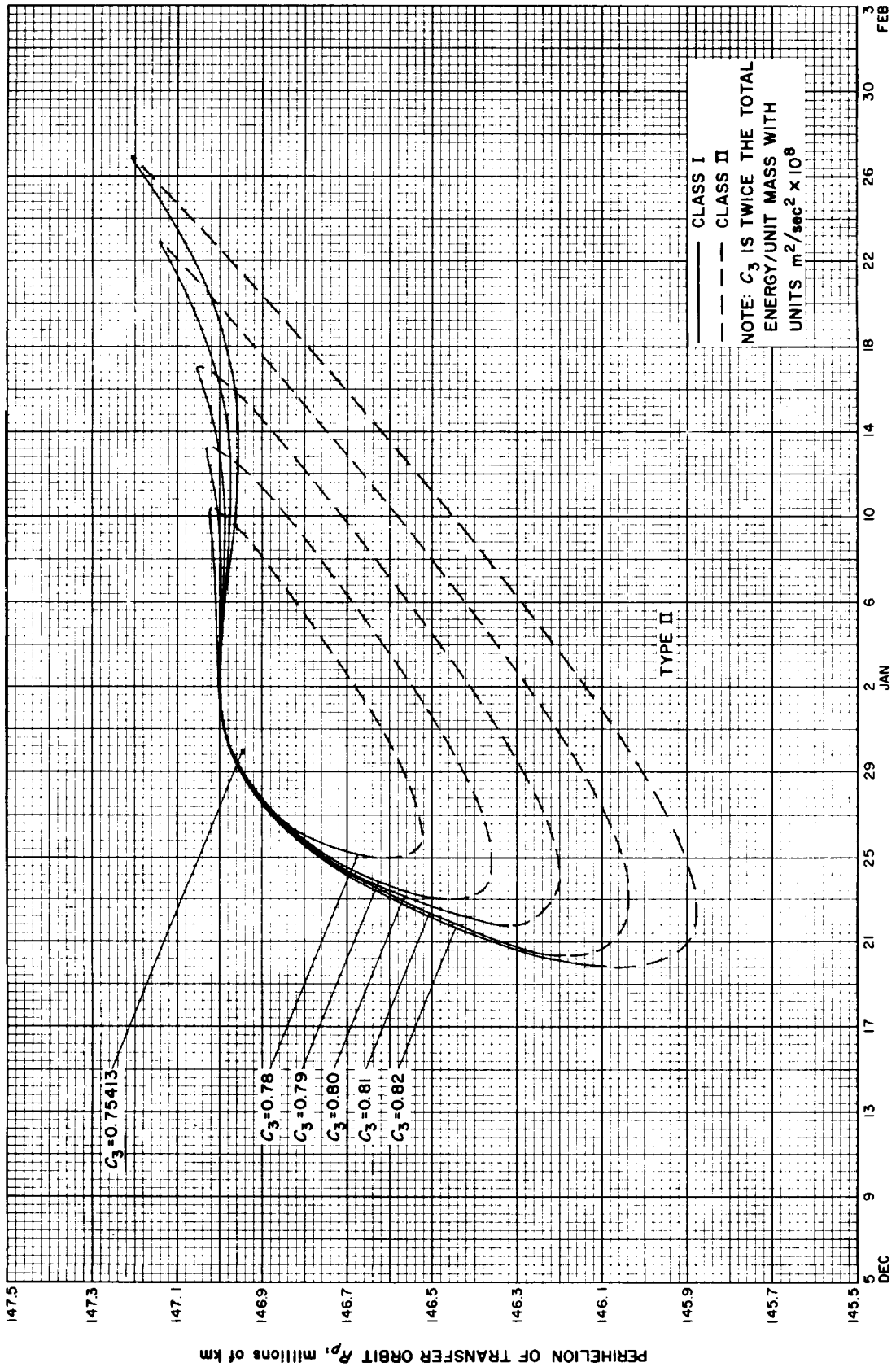

Fig. 7-11(II). Jupiter 69-70: Perihelion of transfer orbit vs launch date, Type II

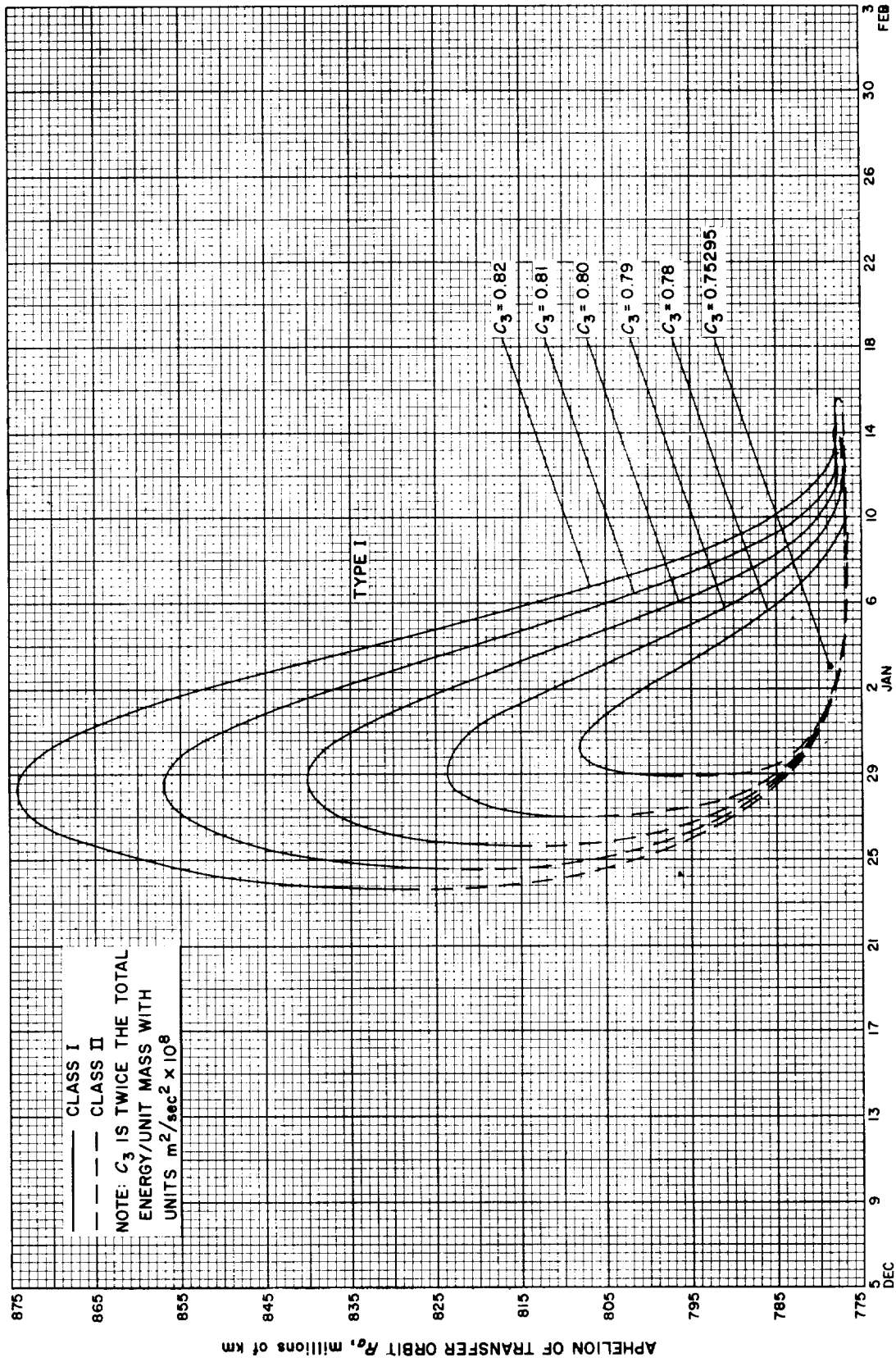

Fig. 7-12(I). Jupiter 69–70: Aphelion of transfer orbit vs launch date, Type I

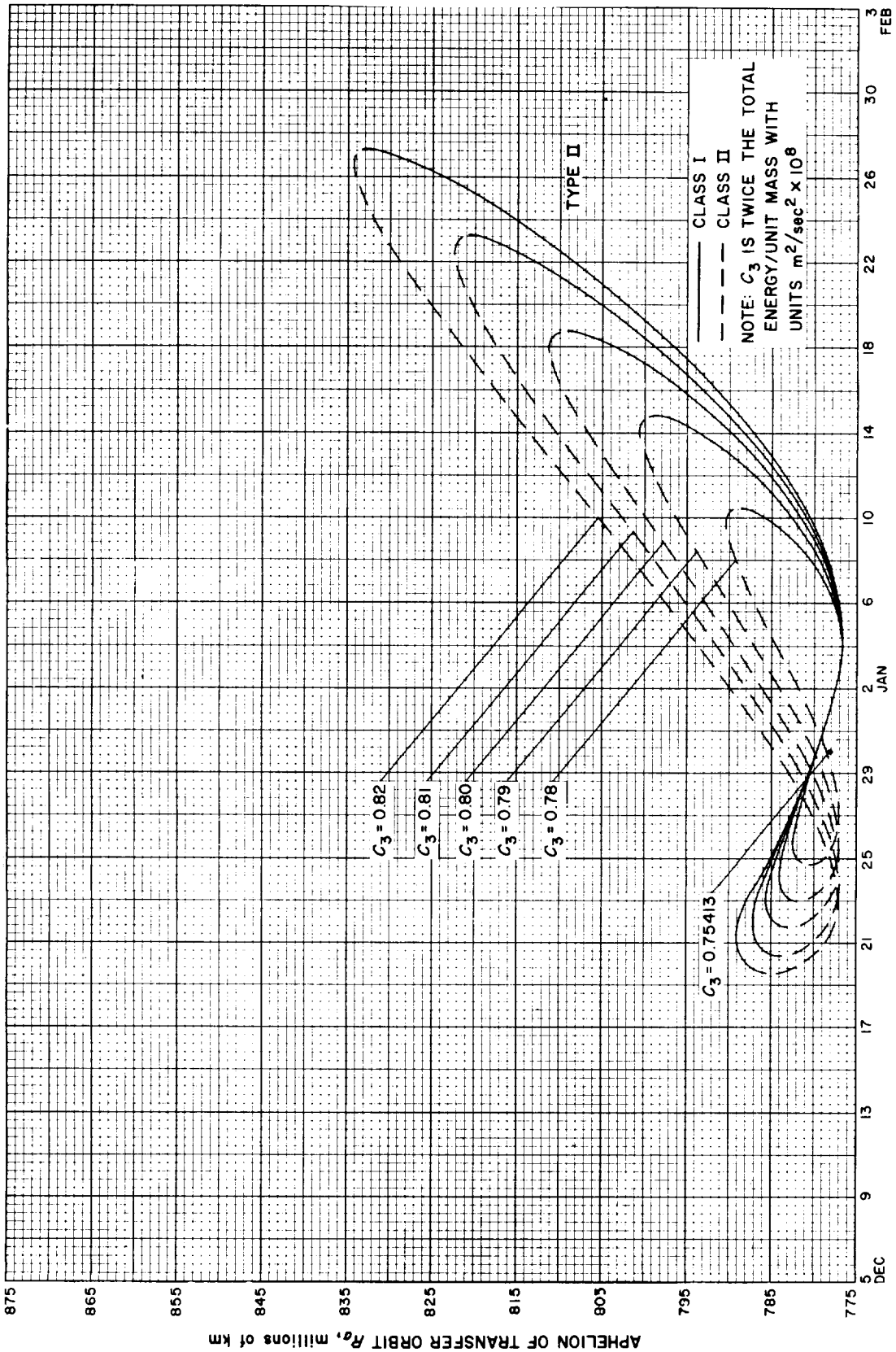

Fig. 7–12(III). Jupiter 69–70: Aphelion of transfer orbit vs launch date, Type II

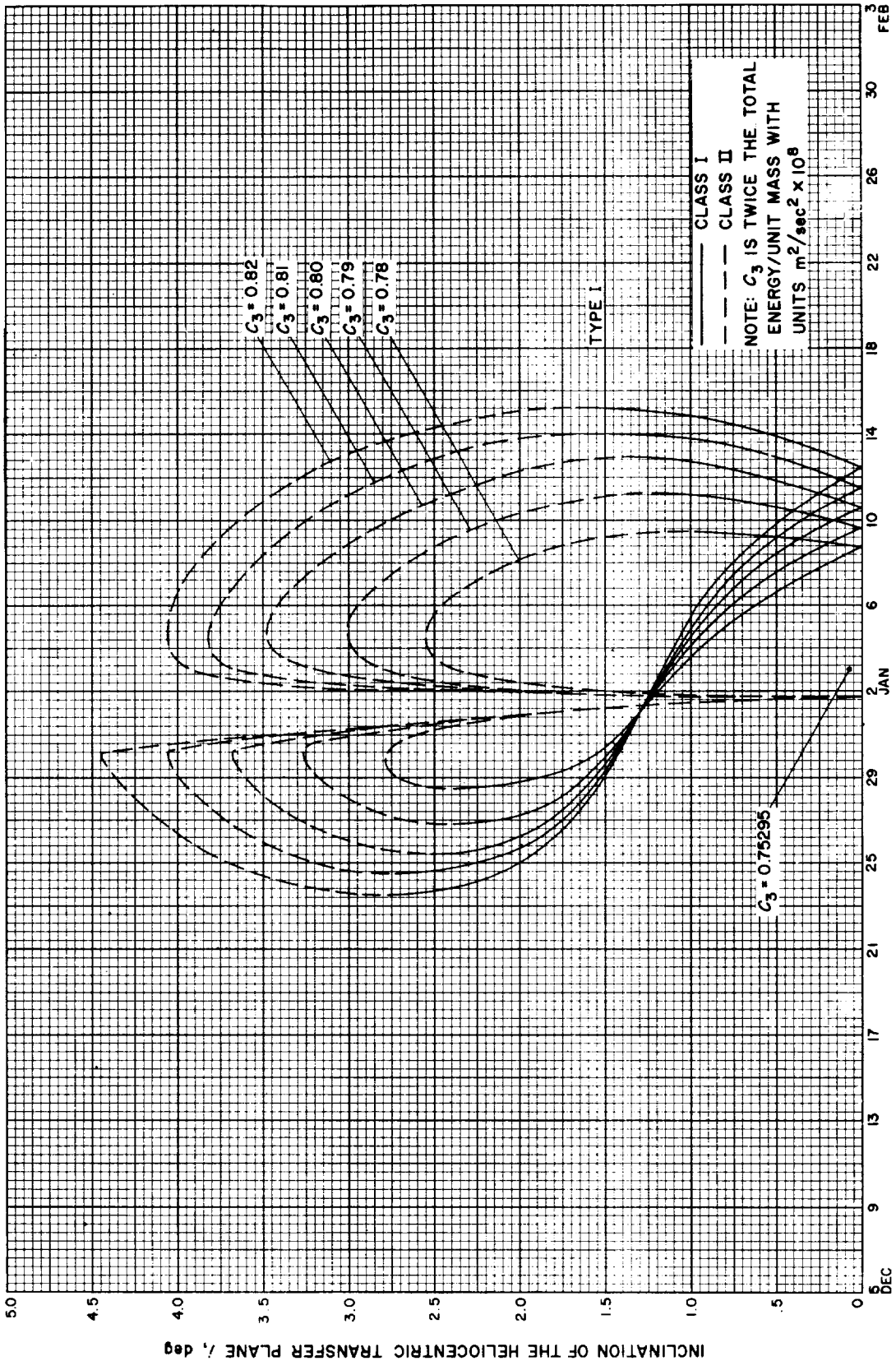

Fig. 7-13(I). Jupiter 69-70: Inclination of the heliocentric transfer plane vs launch date, Type I

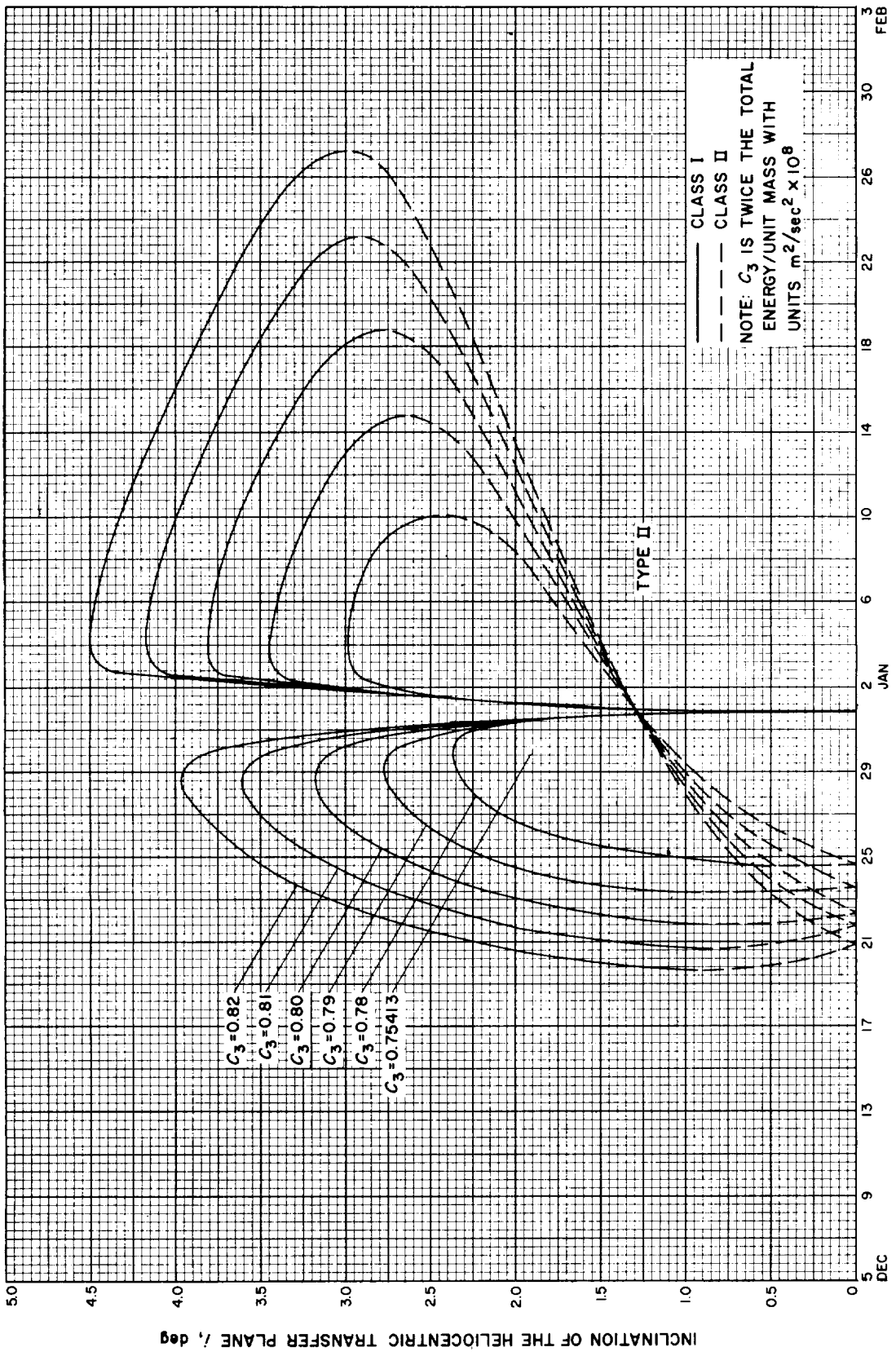

Fig. 7-13(II). Jupiter 69-70: Inclination of the heliocentric transfer plane vs launch date, Type II

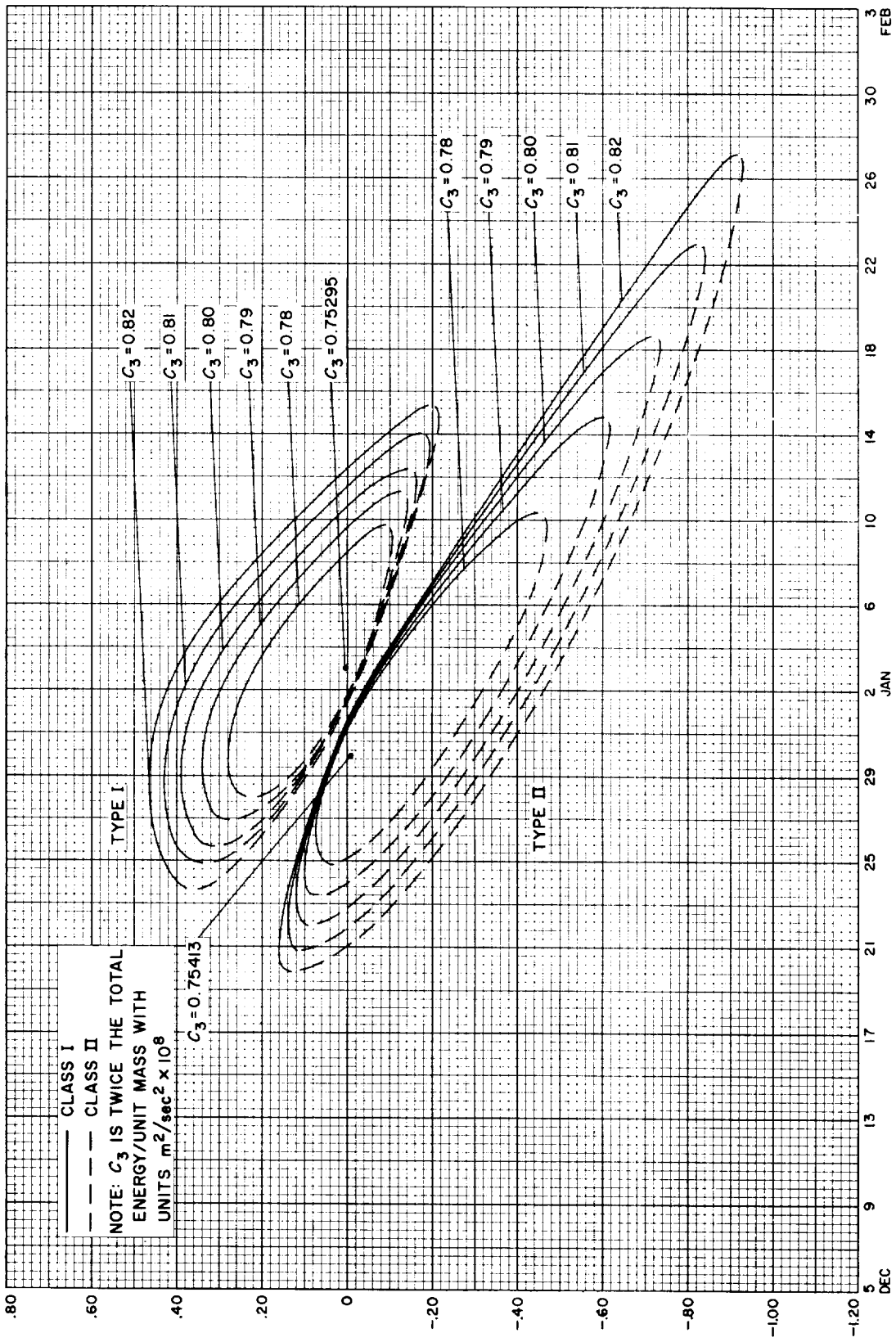

Fig. 7-14. Jupiter 69–70: Celestial latitude at arrival time vs launch date

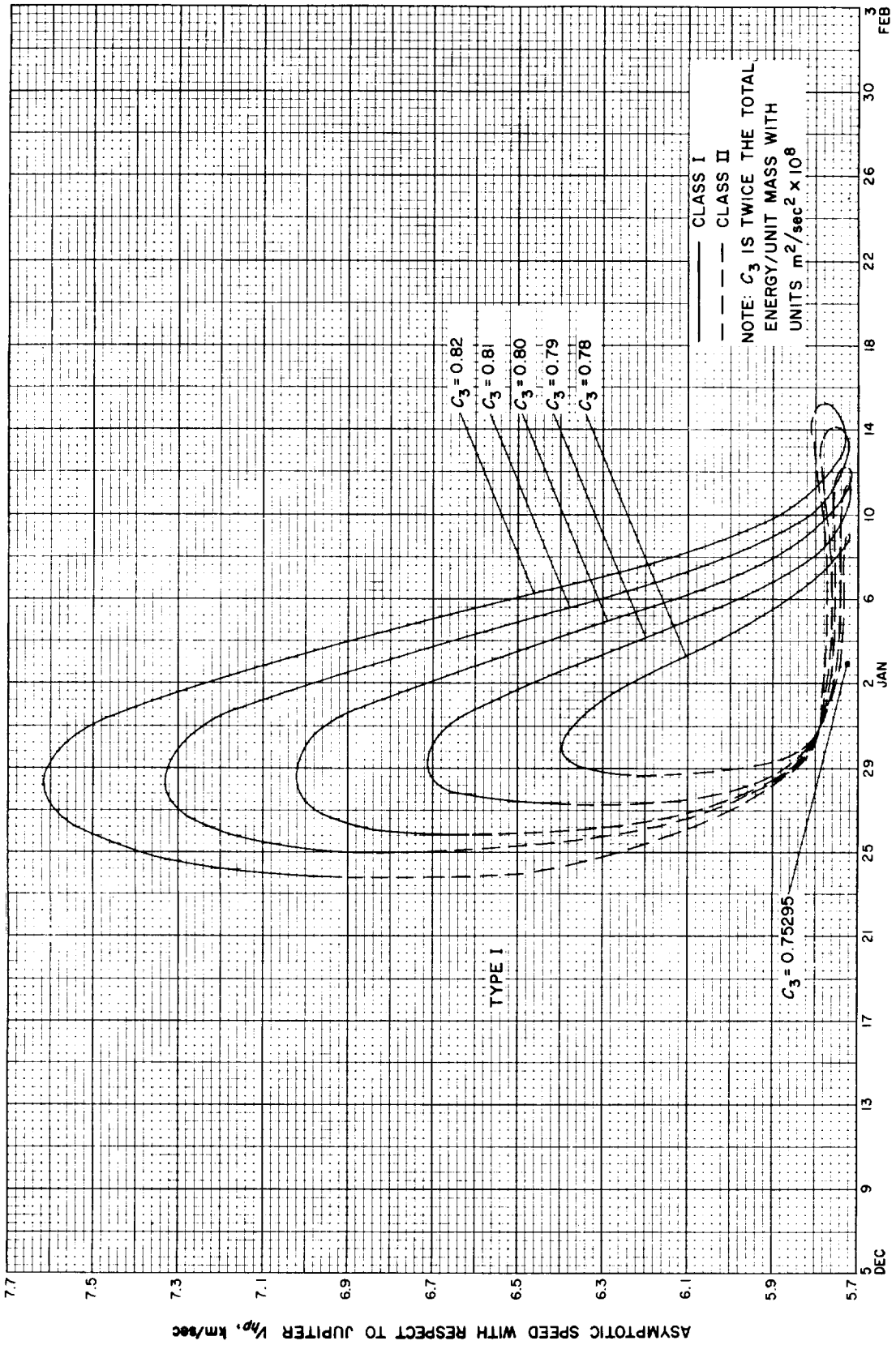

Fig. 7-15(I). Jupiter 69-70: Asymptotic speed with respect to Jupiter vs launch date, Type I

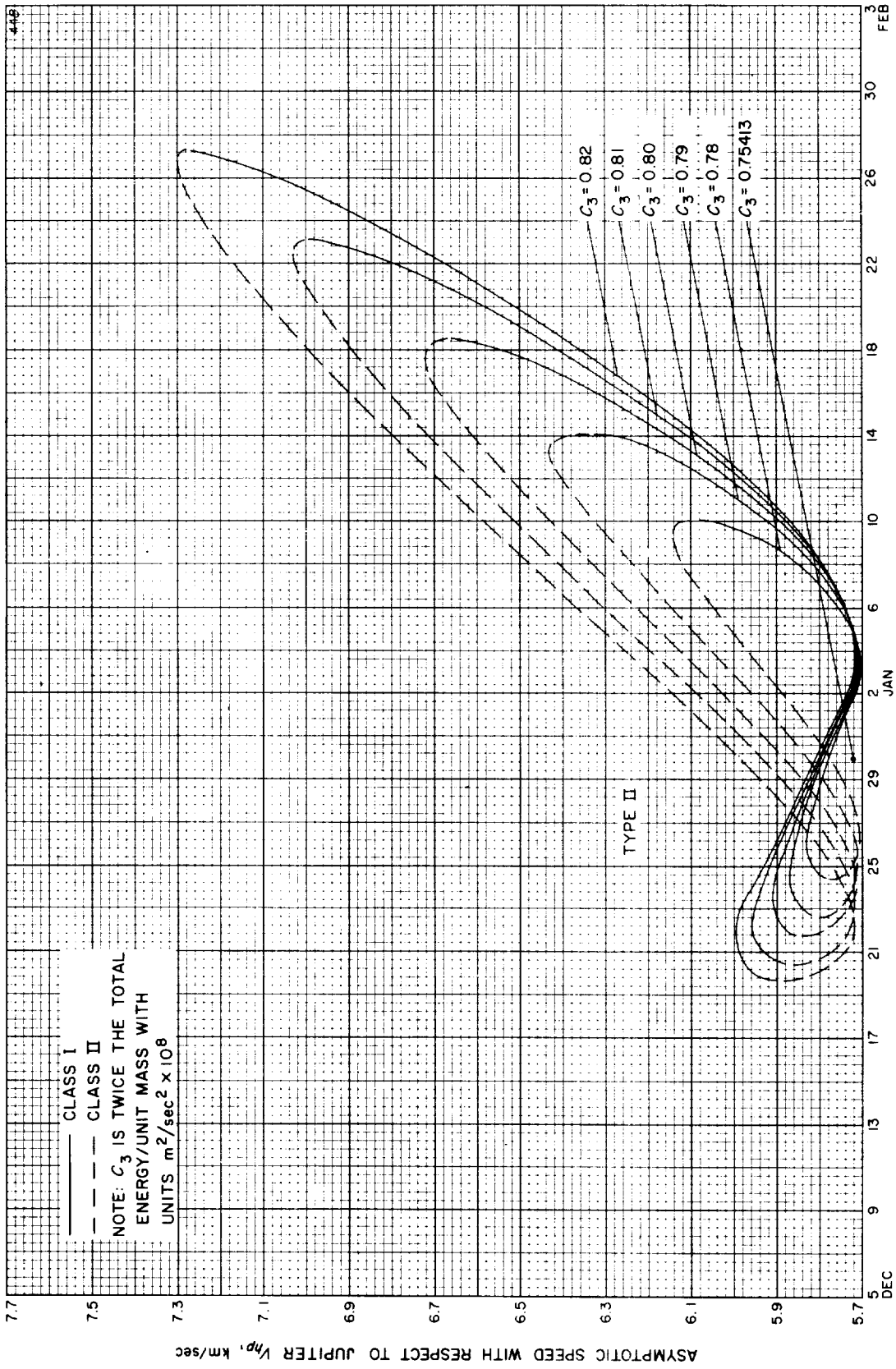

Fig. 7-15(II). Jupiter 69–70: Asymptotic speed with respect to Jupiter vs launch date, Type II

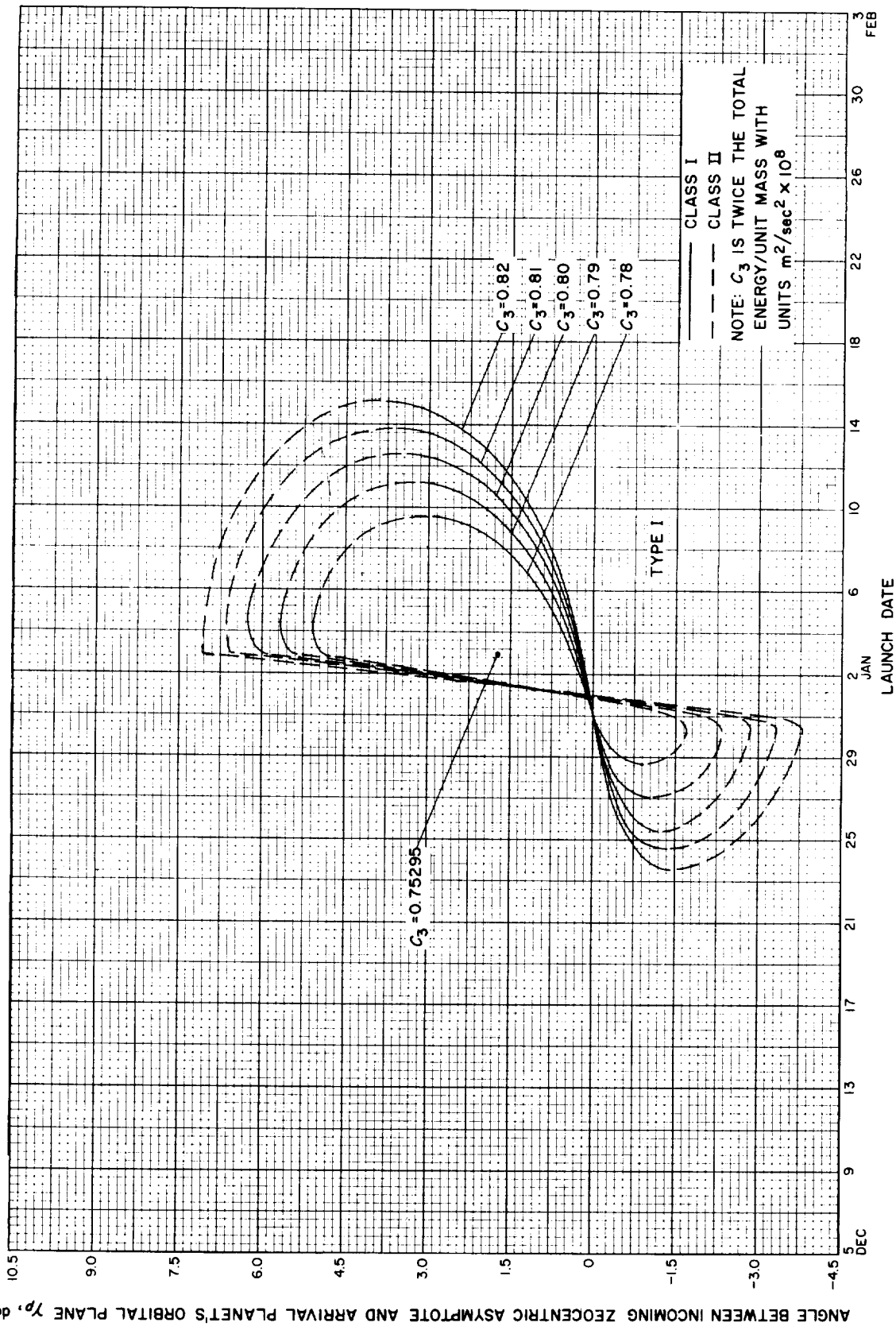

Fig. 7-16(I). Jupiter 69-70: Angle between incoming zeocentric asymptote and arrival planet's orbital plane vs launch date, Type I

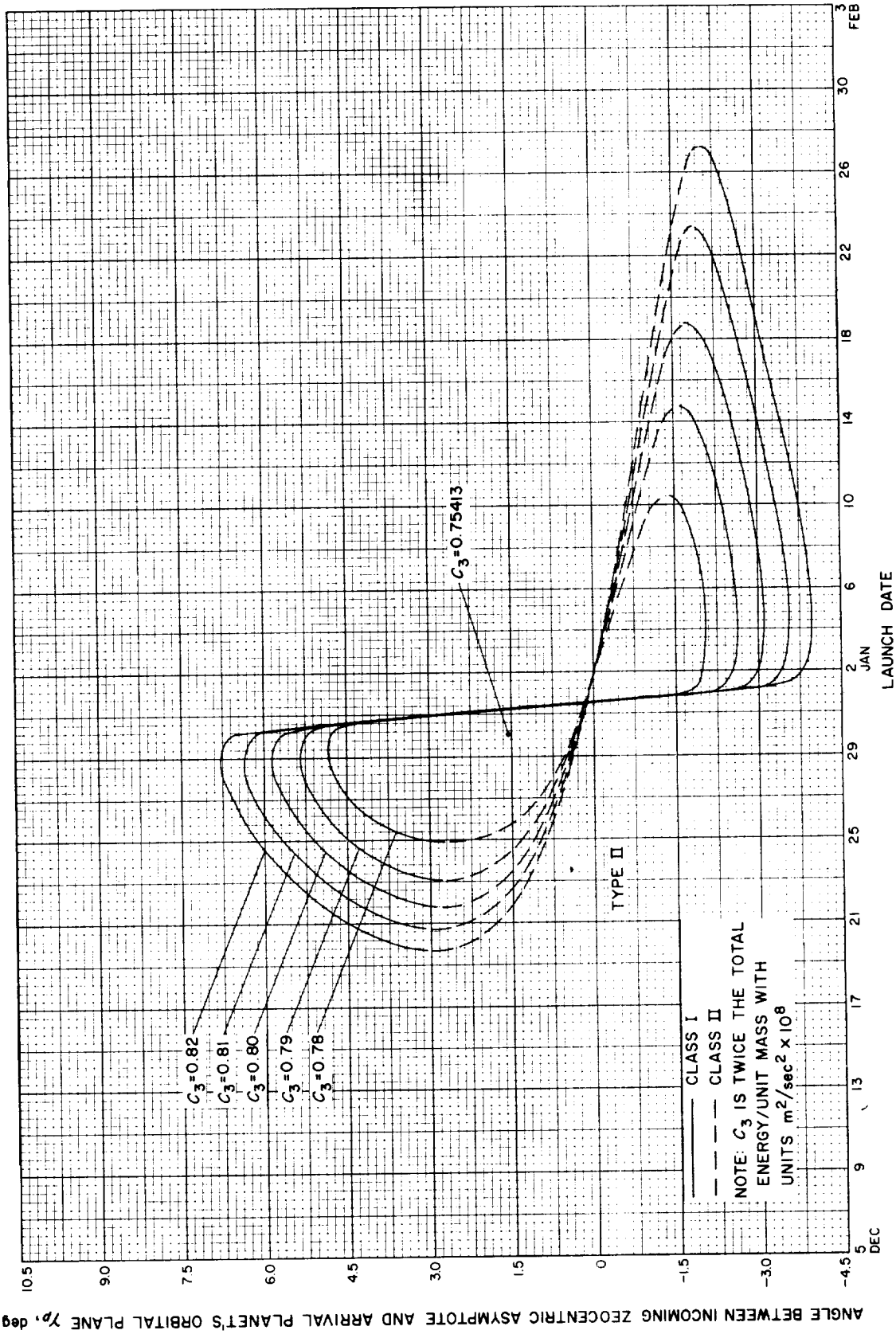

Fig. 7-16(II). Jupiter 69-70: Angle between incoming zeocentric asymptote and arrival planet's orbital plane vs launch date, Type II

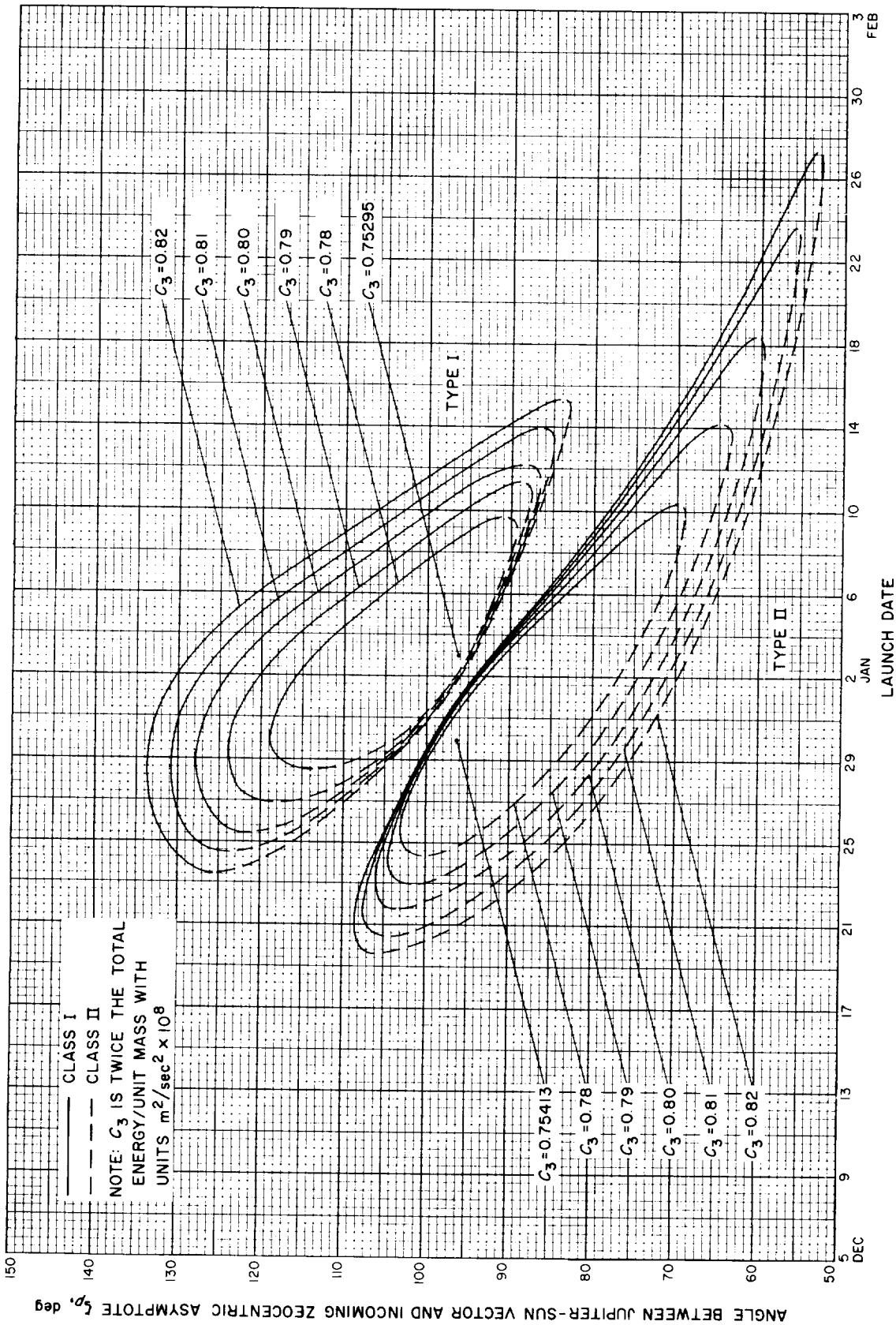

Fig. 7-17. Jupiter 69-70: Angle between Jupiter-Sun vector and incoming zeocentric asymptote vs launch date

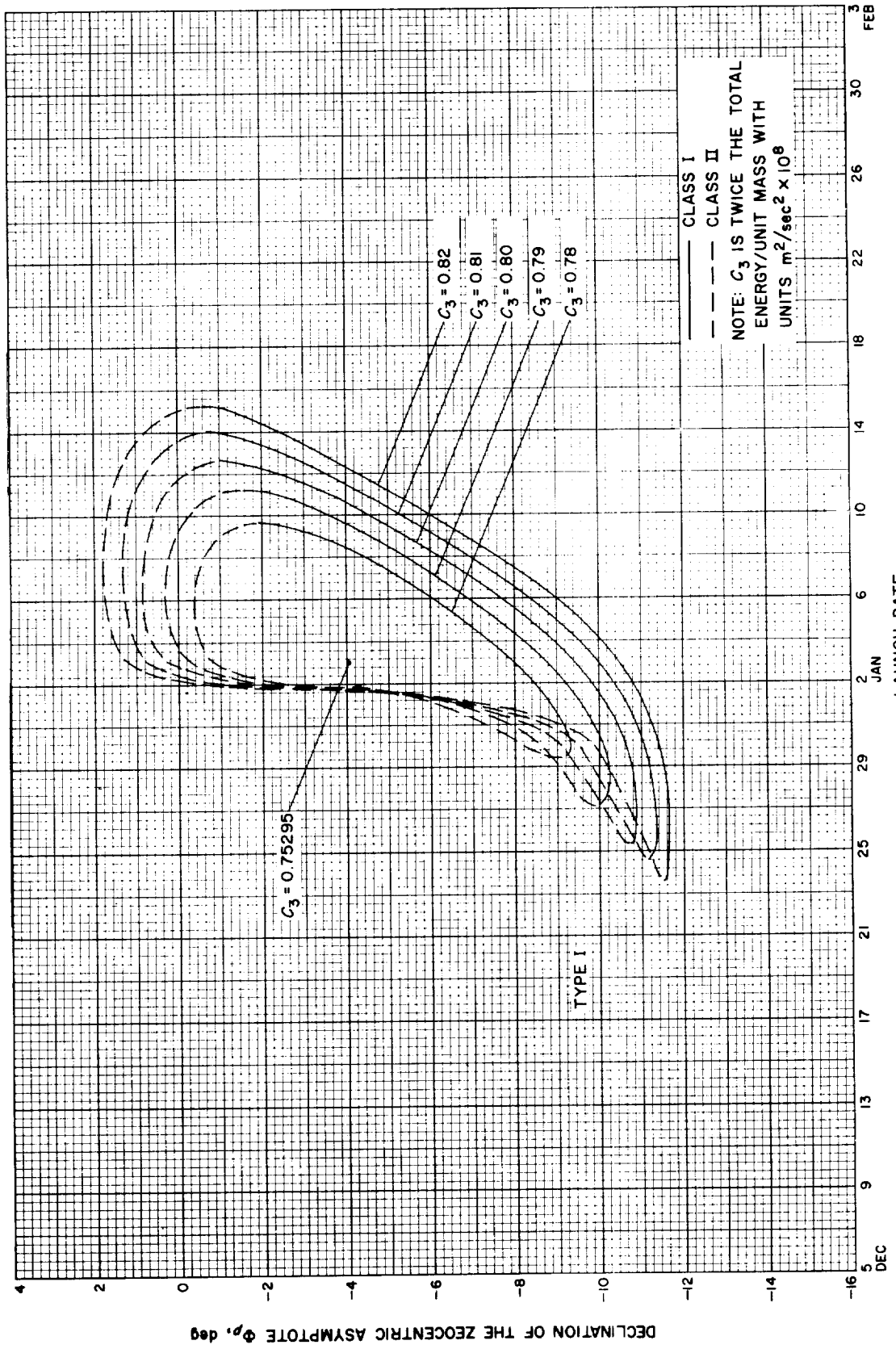

Fig. 7-18(I). Jupiter 69–70: Declination of the zeocentric asymptote vs launch date, Type I

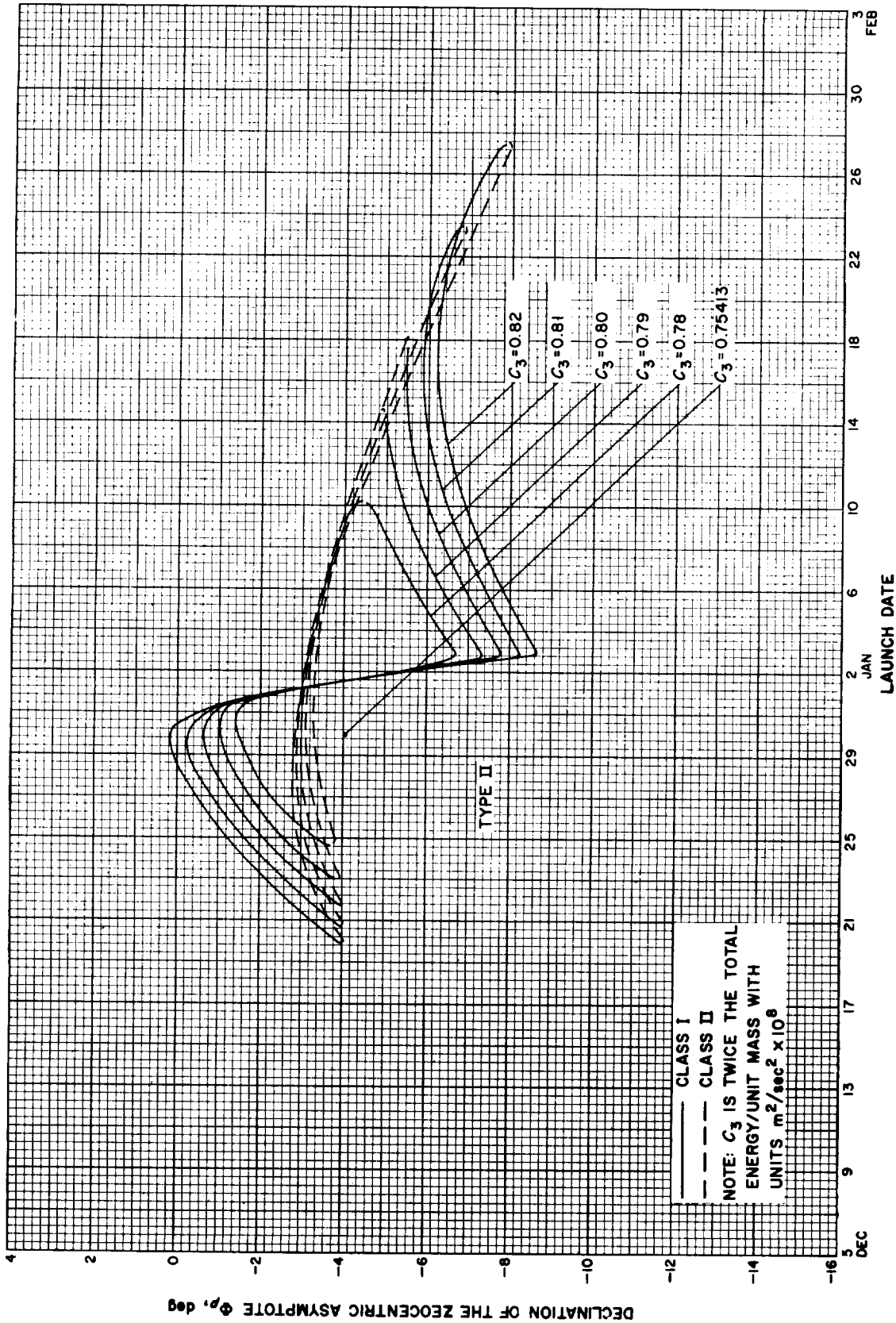

Fig. 7-18(II). Jupiter 69–70: Declination of the zeocentric asymptote vs launch date, Type II

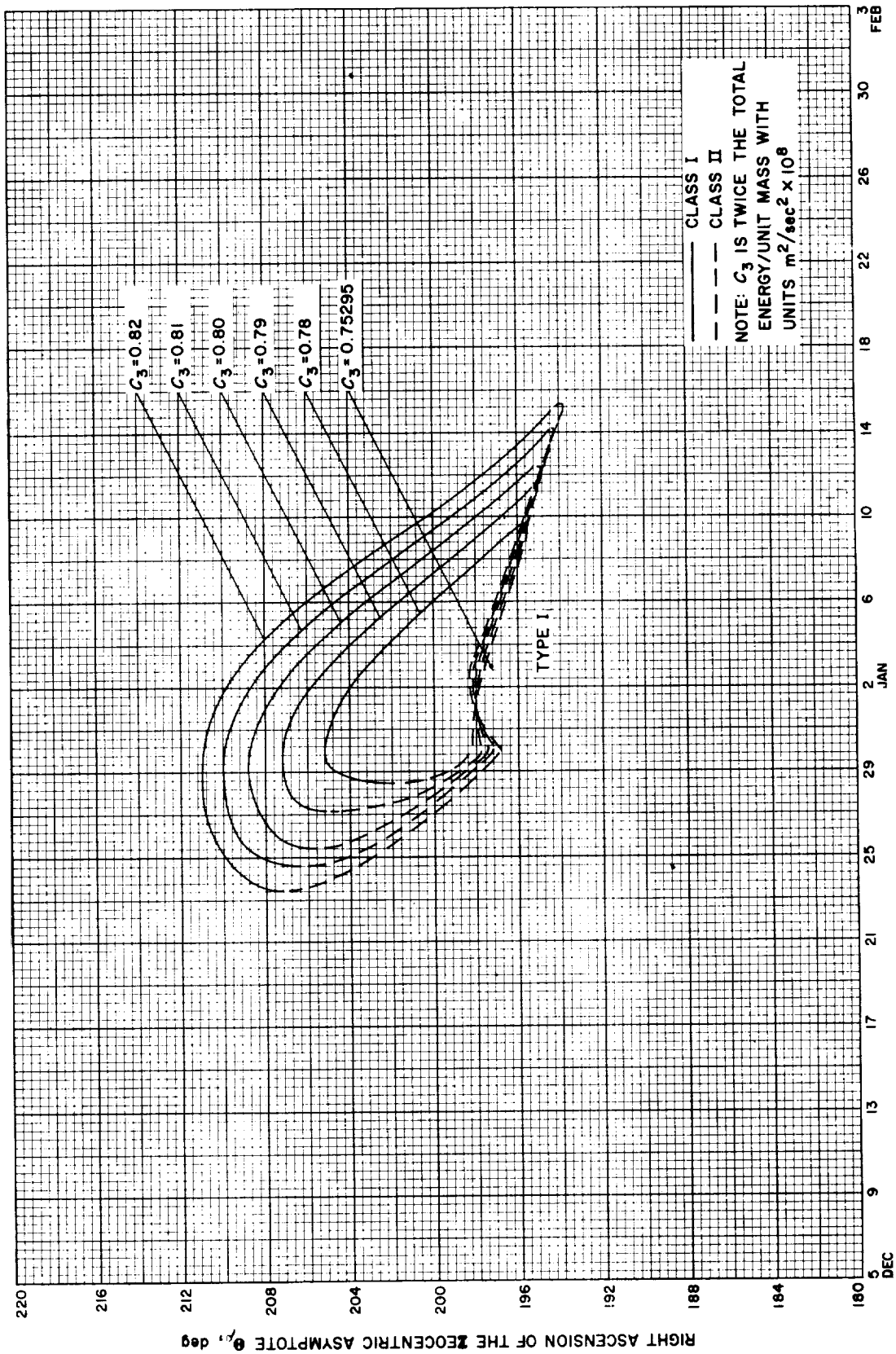

Fig. 7-19(I). Jupiter 69-70: Right ascension of the zeocentric asymptote vs launch date, Type I

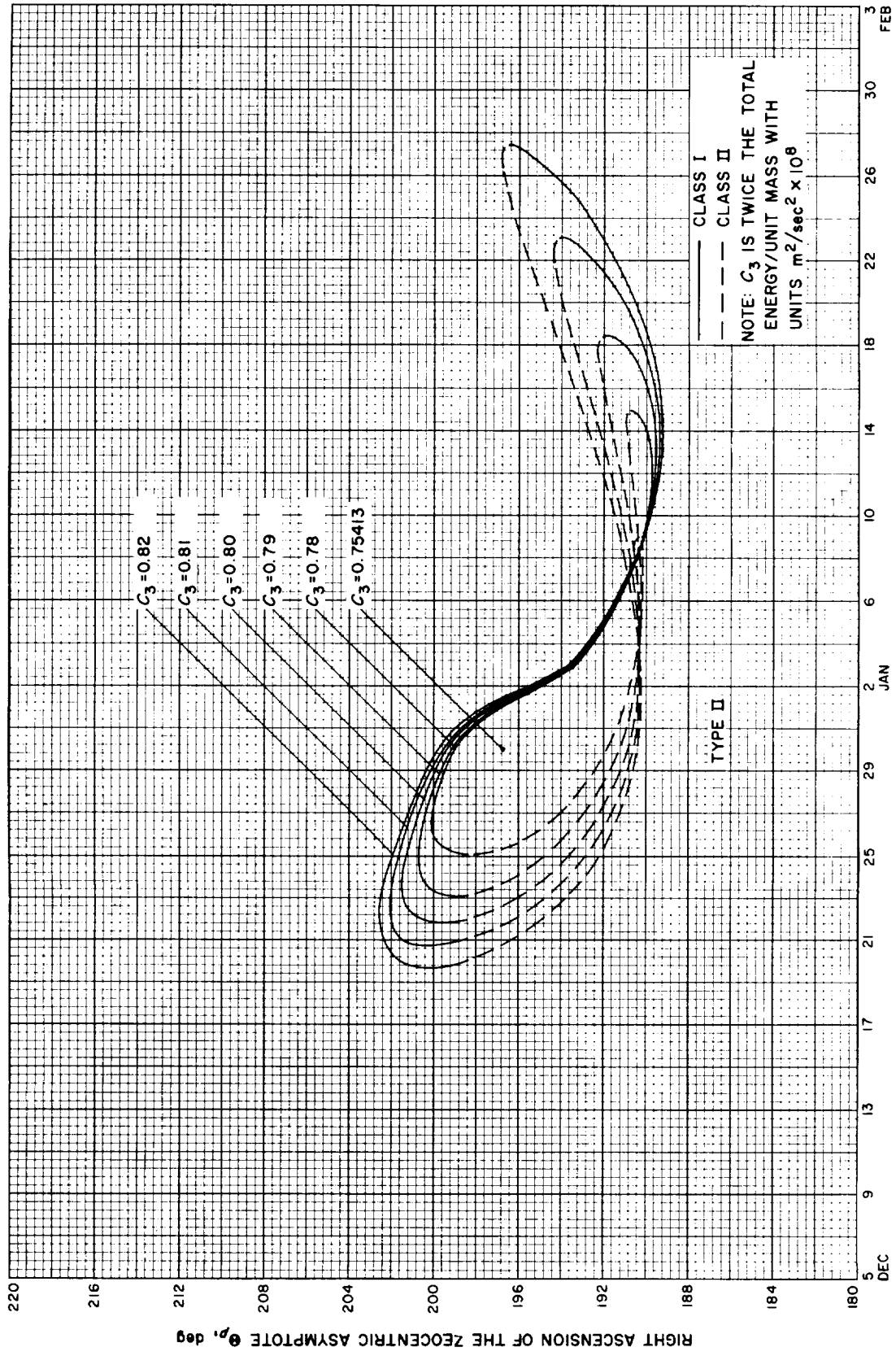

Fig. 7–19(II). Jupiter 69–70: Right ascension of the zeocentric asymptote vs launch date, Type II

VIII. JUPITER 1970–71: TRAJECTORY PARAMETER GRAPHS

Figure

8–1. Jupiter 70–71: Minimum injection energy vs launch date

8–2. Jupiter 70–71: Time of flight vs launch date

8–3. Jupiter 70–71: Heliocentric central angle vs launch date

8–4(I). Jupiter 70–71: Earth–Jupiter communication distance vs launch date, Type I

8–4(II). Jupiter 70–71: Earth–Jupiter communication distance vs launch date, Type II

8–5(I). Jupiter 70–71: Declination of the geocentric asymptote vs launch date, Type I

8–5(II). Jupiter 70–71: Declination of the geocentric asymptote vs launch date, Type II

8–6. Jupiter 70–71: Right ascension of the geocentric asymptote vs launch date

8–7. Jupiter 70–71: Angle between outgoing geocentric asymptote and launch planet's orbital plane vs launch date

8–8(I). Jupiter 70–71: Angle between Sun–Earth vector and outgoing geocentric asymptote vs launch date, Type I

8–8(II). Jupiter 70–71: Angle between Sun–Earth vector and outgoing geocentric asymptote vs launch date, Type II

8–9(I). Jupiter 70–71: True anomaly in transfer ellipse at launch time vs launch date, Type I

8–9(II). Jupiter 70–71: True anomaly in transfer ellipse at launch time vs launch date, Type II

8–10. Jupiter 70–71: True anomaly in transfer ellipse at arrival time vs launch date

8–11(I). Jupiter 70–71: Perihelion of transfer orbit vs launch date, Type I

8–11(II). Jupiter 70–71: Perihelion of transfer orbit vs launch date, Type II

8–12(I). Jupiter 70–71: Aphelion of transfer orbit vs launch date, Type I

8–12(II). Jupiter 70–71: Aphelion of transfer orbit vs launch date, Type II

8–13(I). Jupiter 70–71: Inclination of the heliocentric transfer plane vs launch date, Type I

8–13(II). Jupiter 70–71: Inclination of the heliocentric transfer plane vs launch date, Type II

VIII. JUPITER 1970–71: TRAJECTORY PARAMETER GRAPHS (Cont'd)

Figure

8–14. Jupiter 70–71: Celestial latitude at arrival time vs launch date

8–15(I). Jupiter 70–71: Asymptotic speed with respect to Jupiter vs launch date, Type I

8–15(II). Jupiter 70–71: Asymptotic speed with respect to Jupiter vs launch date, Type II

8–16. Jupiter 70–71: Angle between incoming zeocentric asymptote and arrival planet's orbital plane vs launch date

8–17. Jupiter 70–71: Angle between Jupiter–Sun vector and incoming zeocentric asymptote vs launch date

8–18(I). Jupiter 70–71: Declination of zeocentric asymptote vs launch date, Type I

8–18(II). Jupiter 70–71: Declination of zeocentric asymptote vs launch date, Type II

8–19(I). Jupiter 70–71: Right ascension of zeocentric asymptote vs launch date, Type I

8–19(II). Jupiter 70–71: Right ascension of zeocentric asymptote vs launch date, Type II

8–20(I). Jupiter 70–71: Angle between planet–Earth vector and incoming asymptote vs launch date, Type I

8–20(II). Jupiter 70–71: Angle between planet–Earth vector and incoming asymptote vs launch date, Type II

8–21(I). Jupiter 70–71: Angle between planet–Canopus vector and incoming asymptote vs launch date, Type I

8–21(II). Jupiter 70–71: Angle between planet–Canopus vector and incoming asymptote vs launch date, Type II

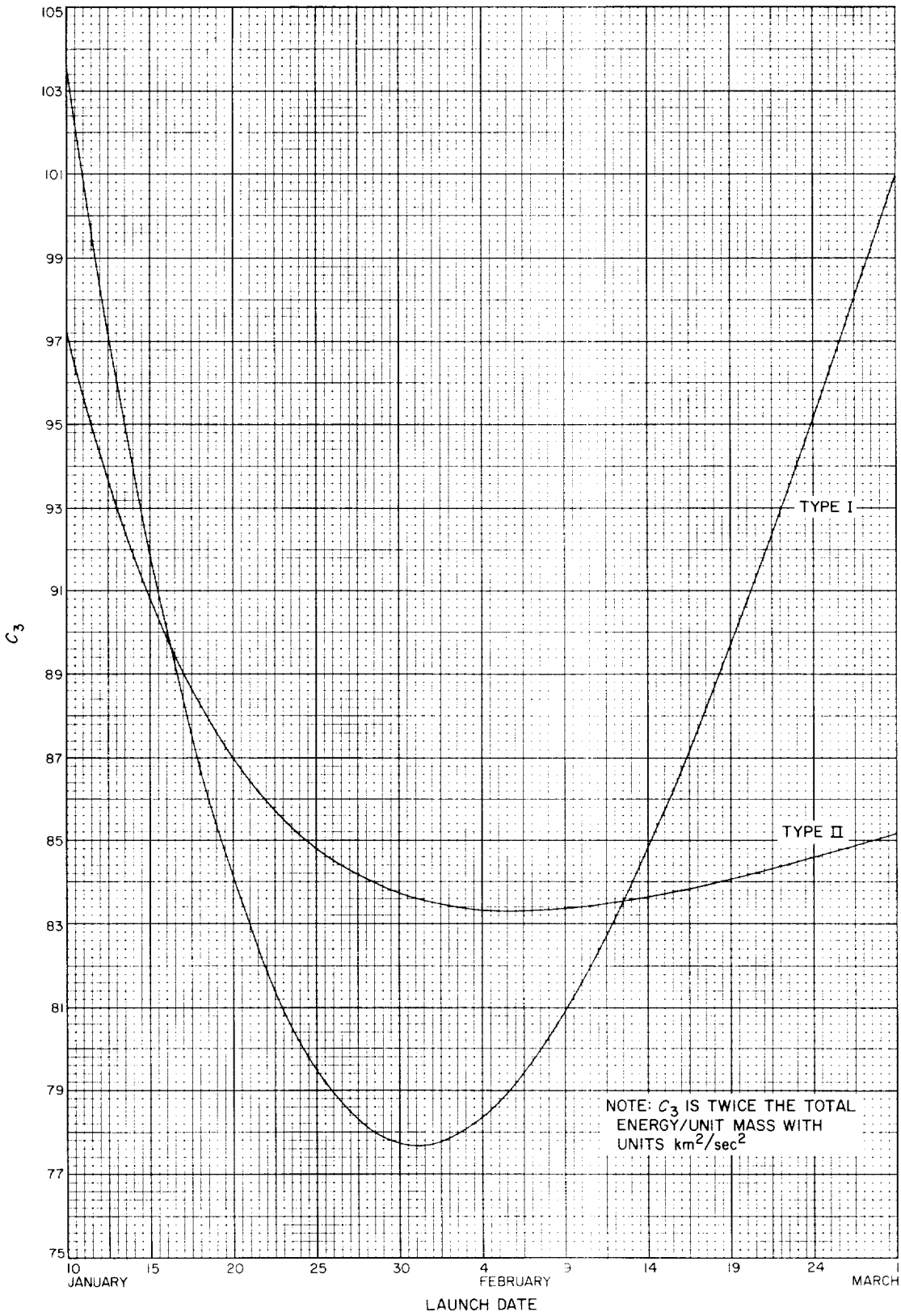

Fig. 8–1. Jupiter 70–71: Minimum injection energy vs launch date

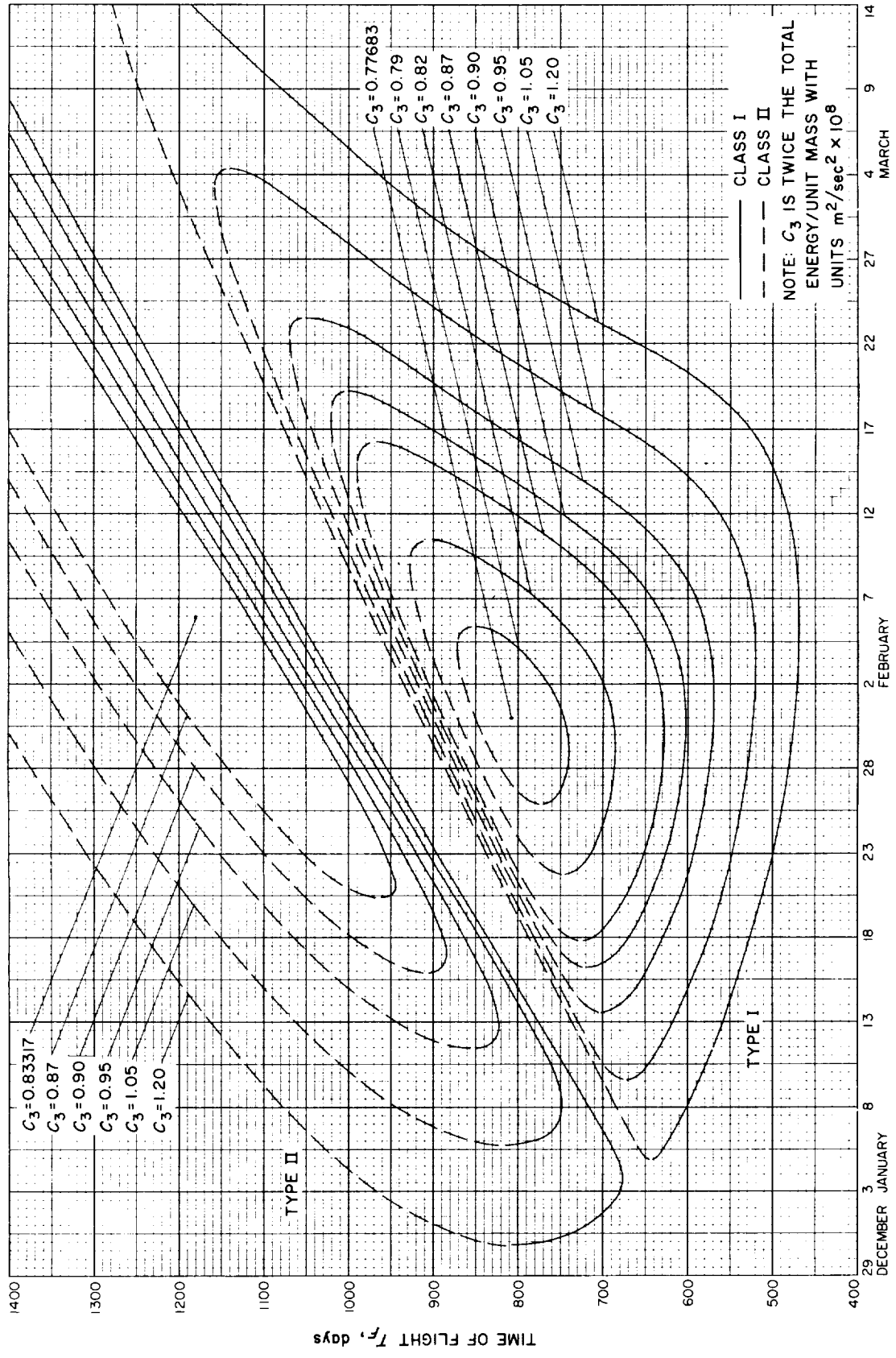

Fig. 8-2. Jupiter 70–71: Time of flight vs launch date

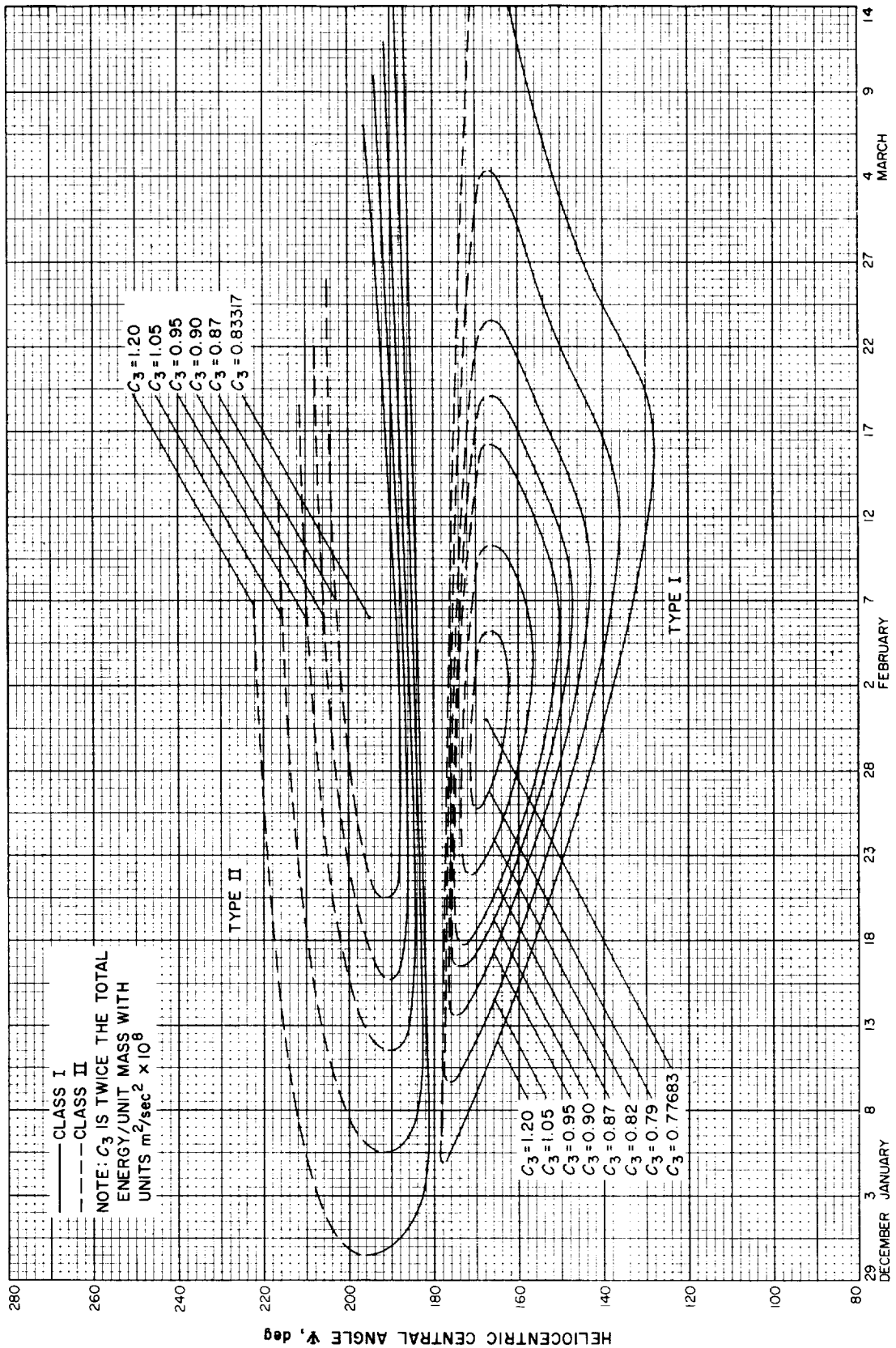

Fig. 8–3. Jupiter 70–71: Heliocentric central angle vs launch date

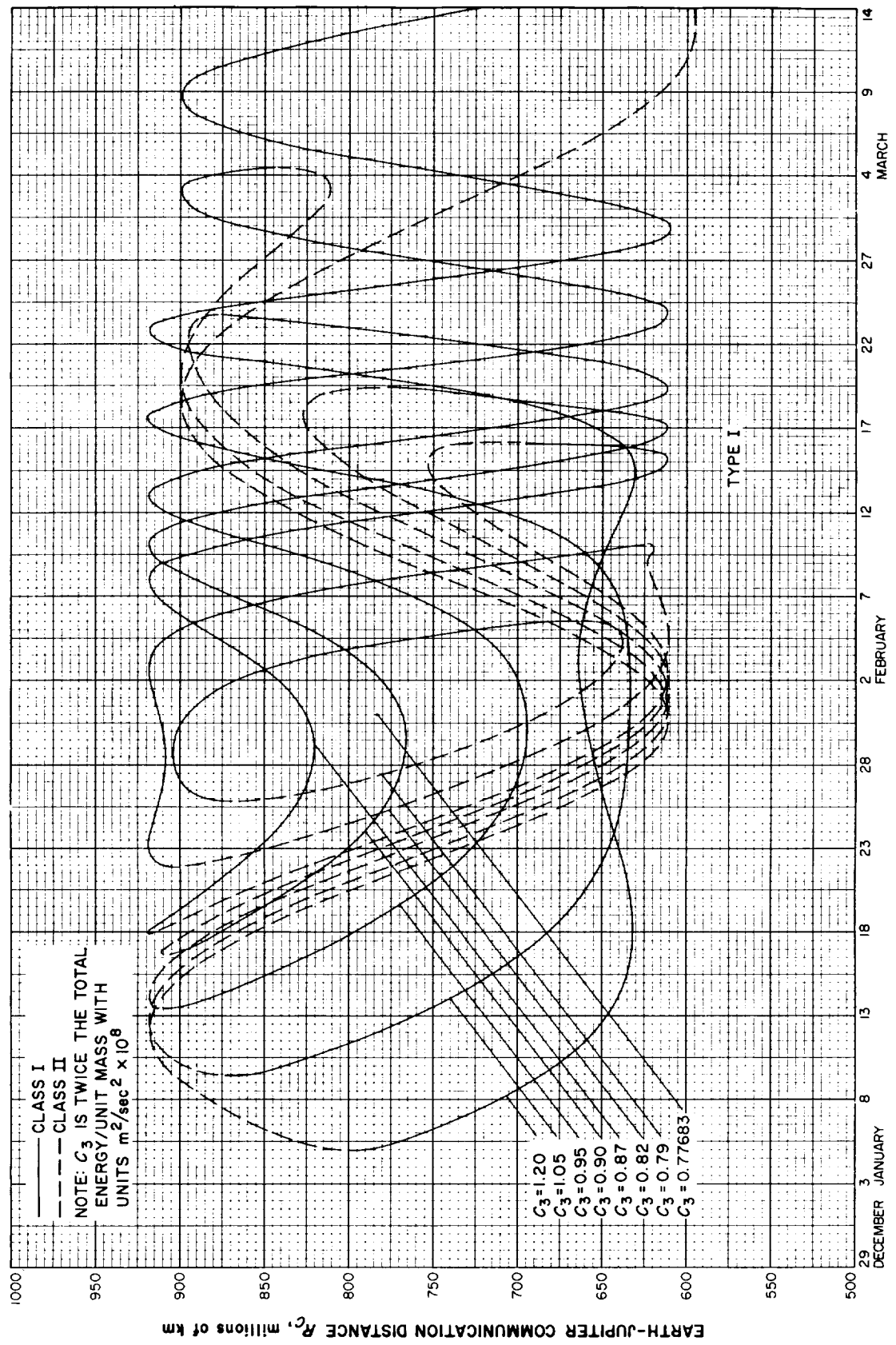

Fig. 8-4(I). Jupiter 70–71: Earth–Jupiter communication distance vs launch date, Type I

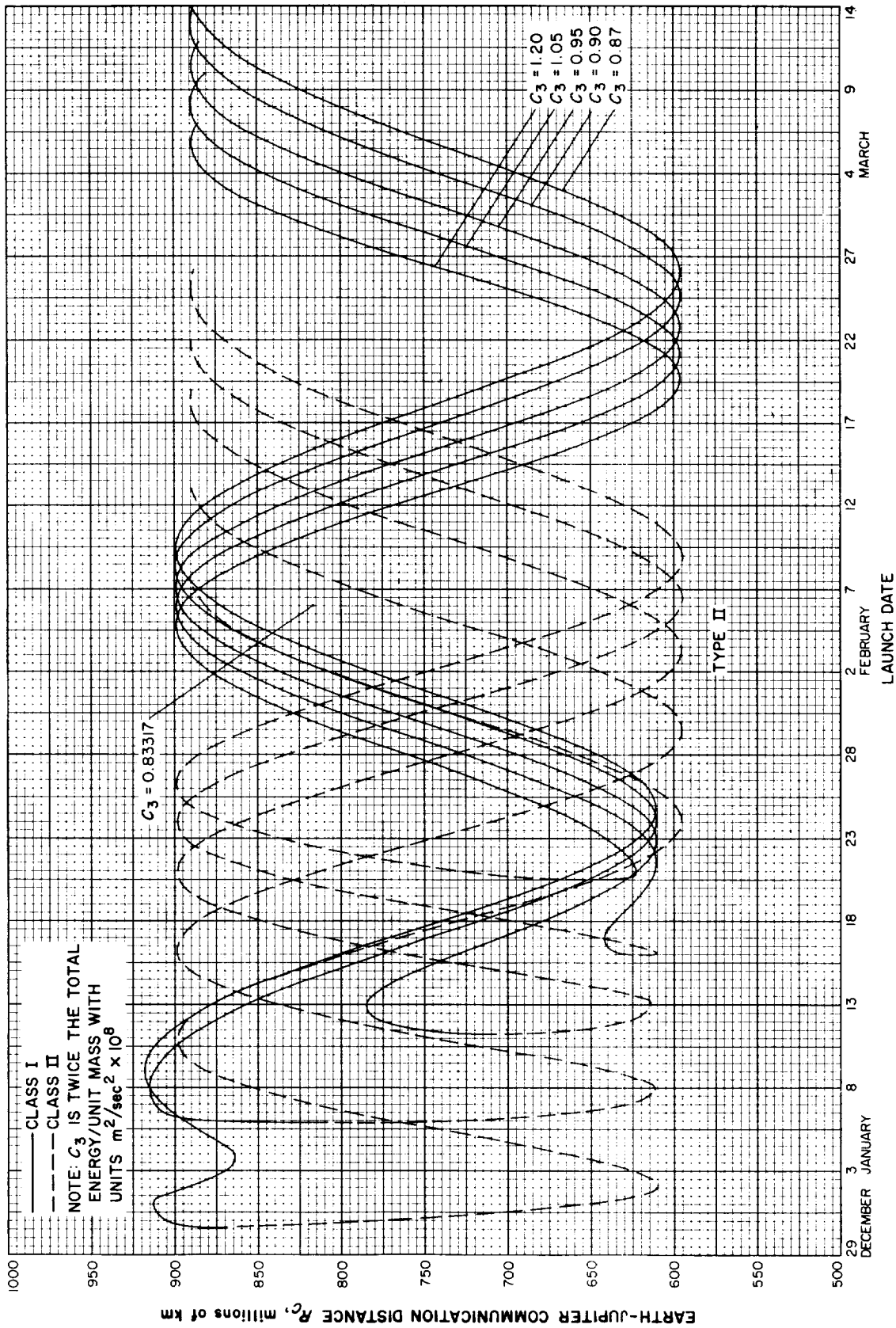

Fig. 8–4(II). Jupiter 70–71: Earth–Jupiter communication distance vs launch date, Type II

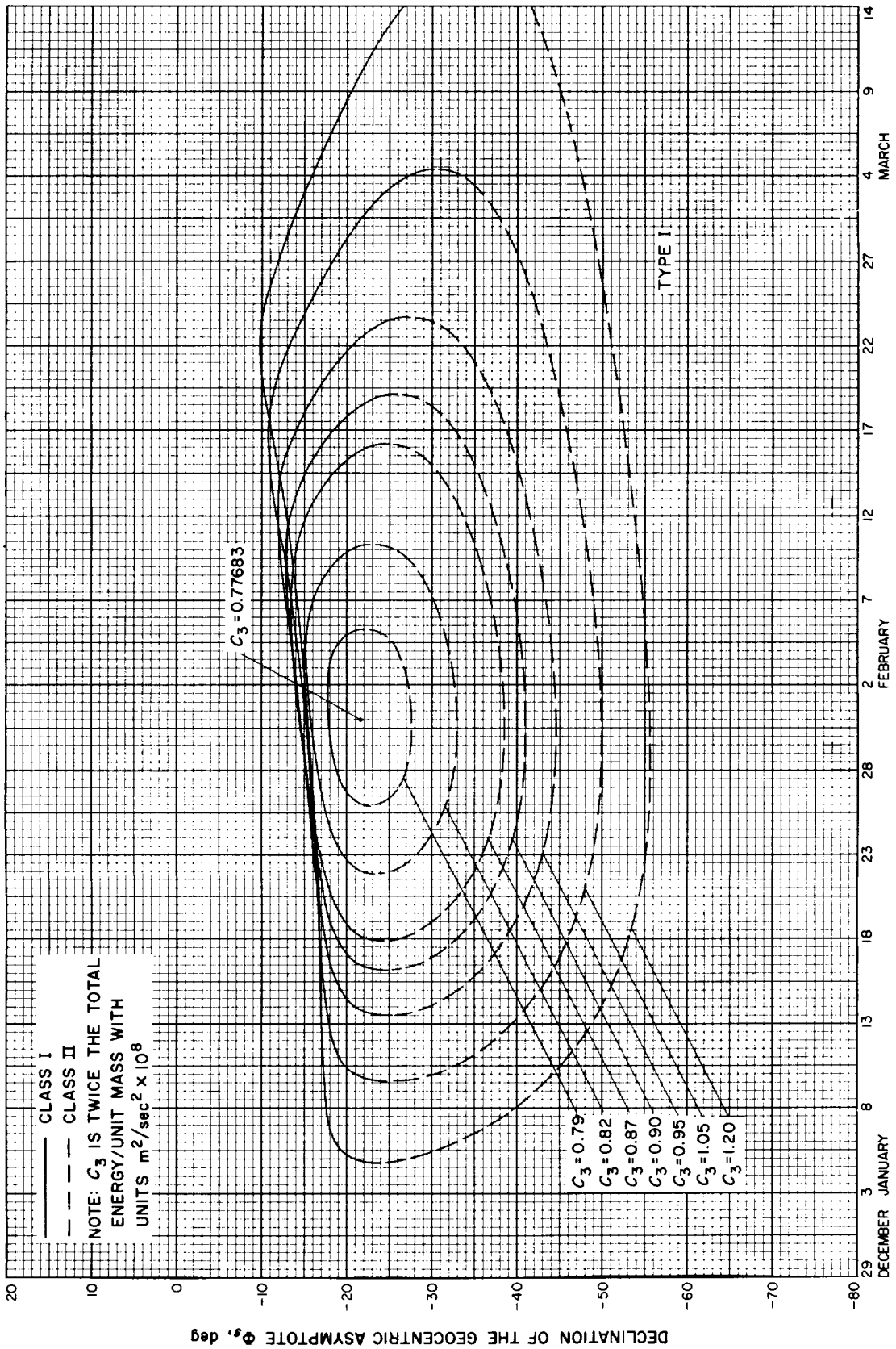

Fig. 8-5(I). Jupiter 70–71: Declination of the geocentric asymptote vs launch date, Type I

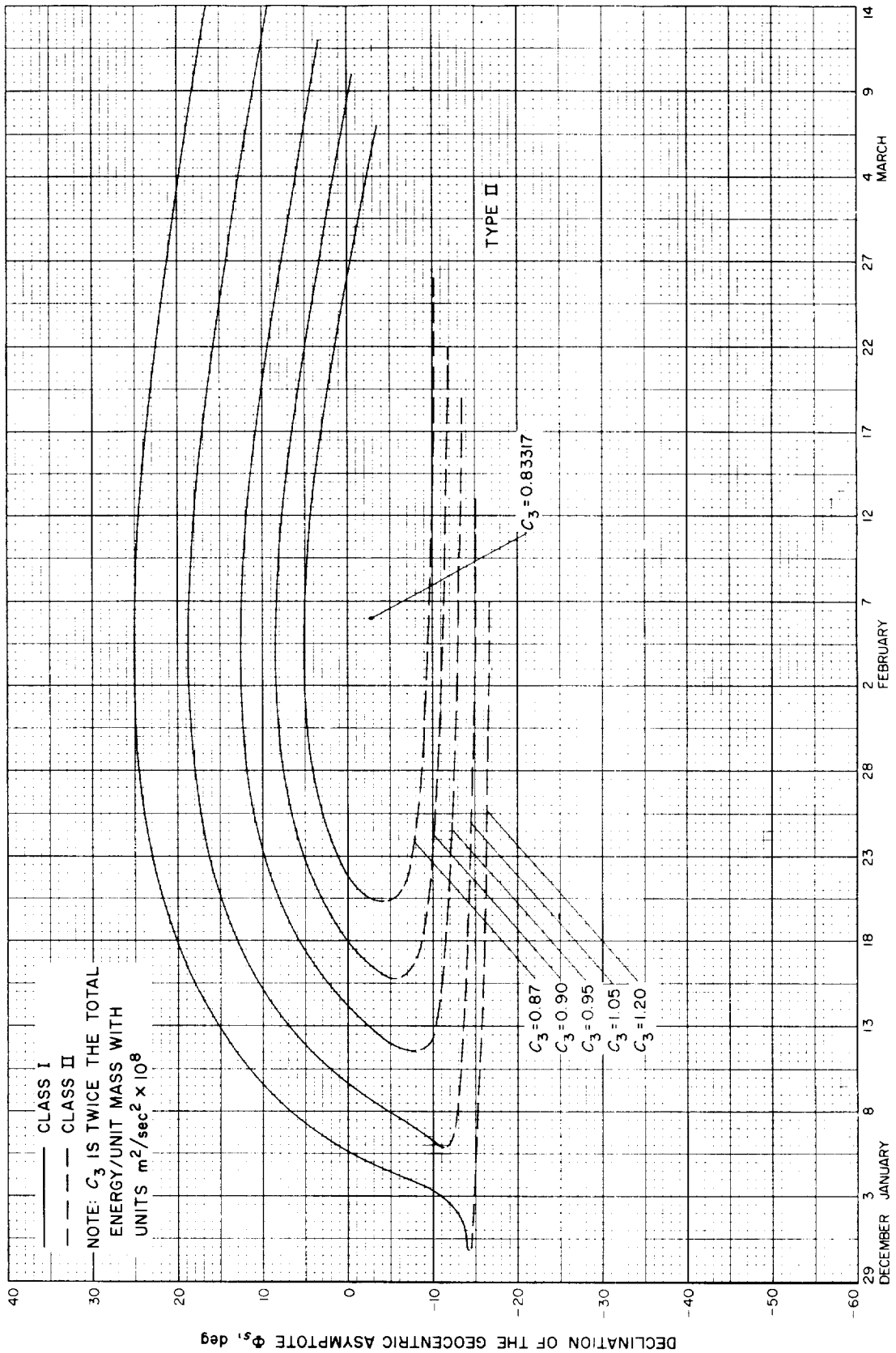

Fig. 8-5(II). Jupiter 70–71: Declination of the geocentric asymptote vs launch date, Type II

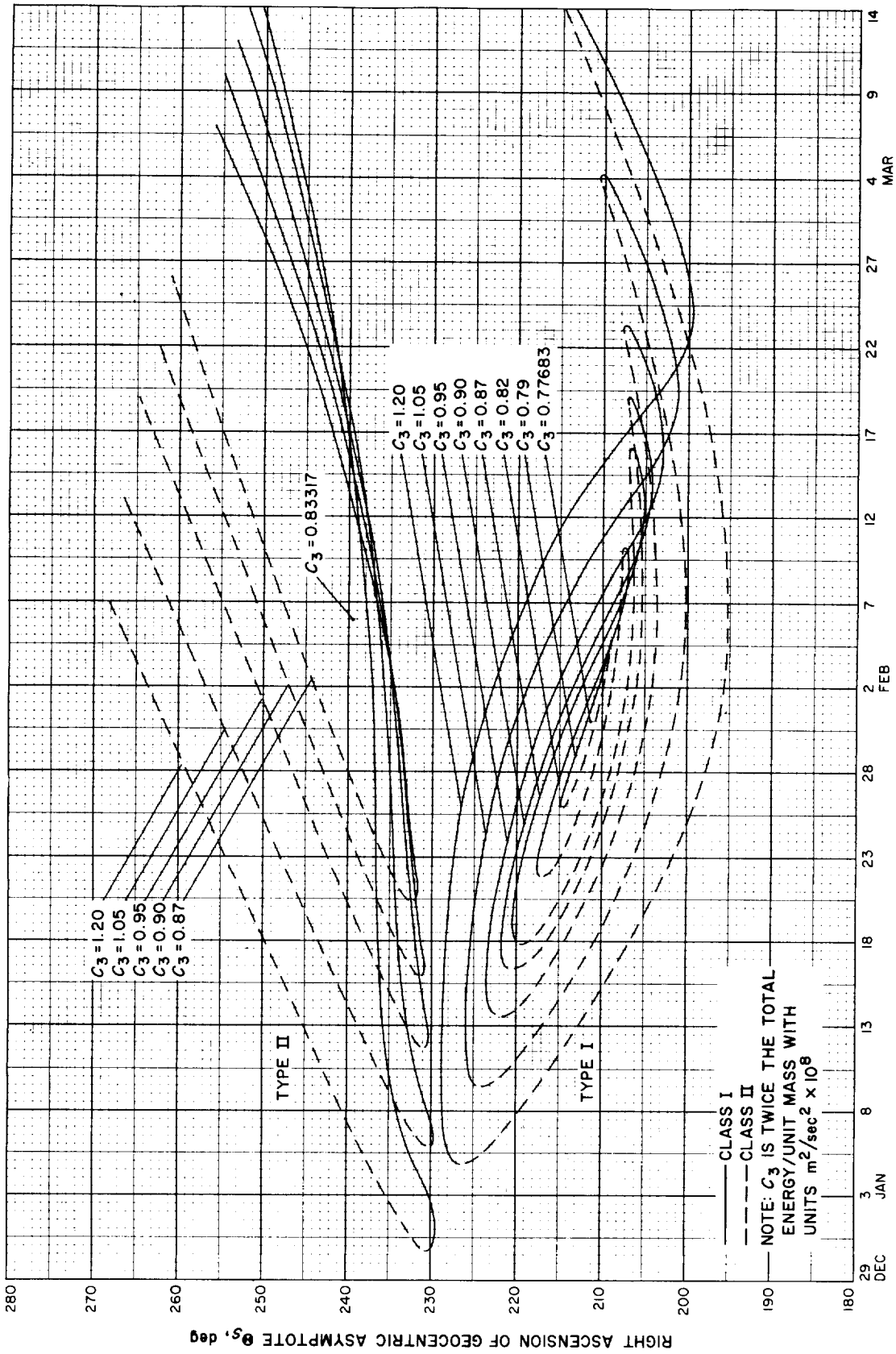

Fig. 8–6. Jupiter 70–71: Right ascension of the geocentric asymptote vs launch date

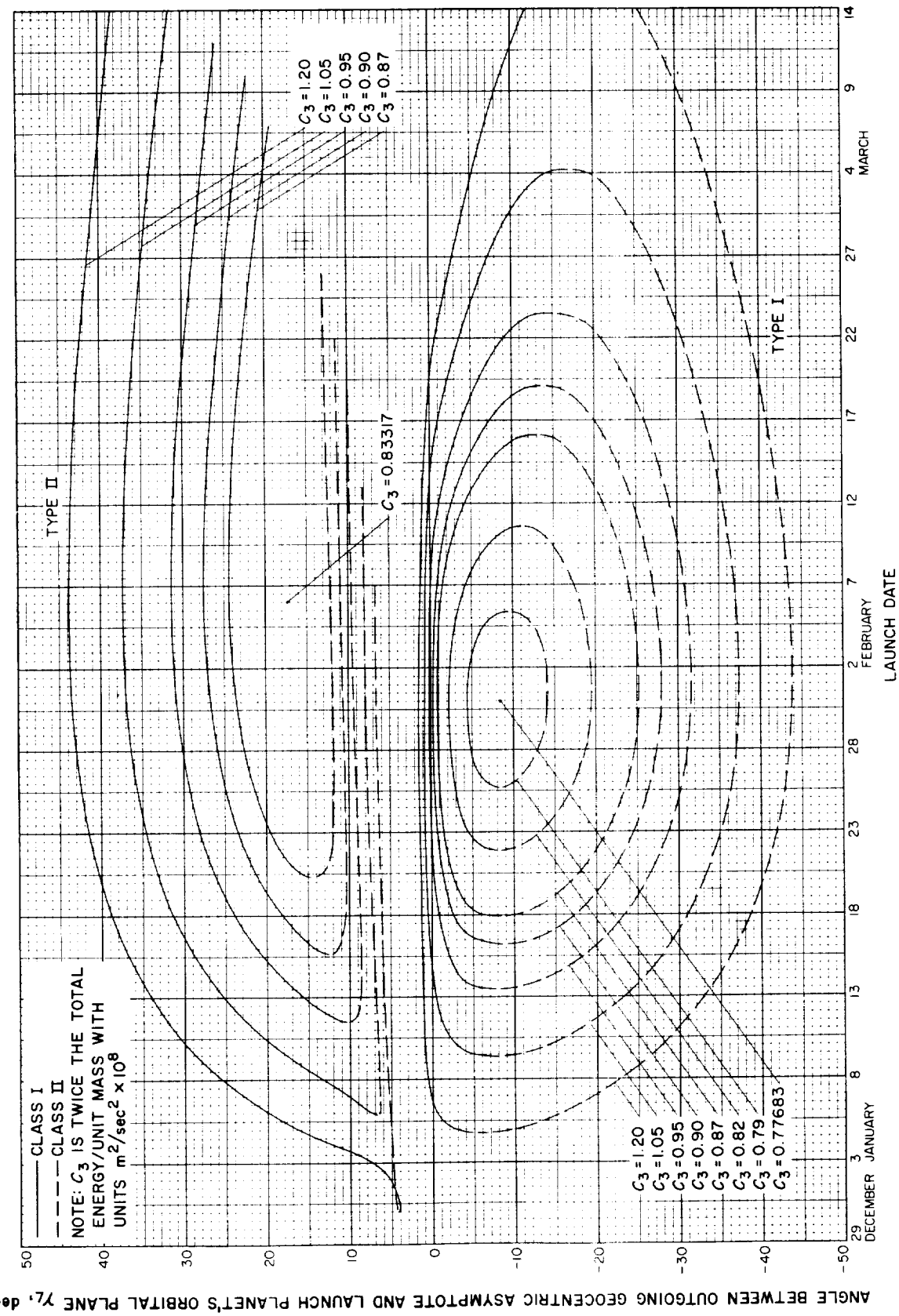

Fig. 8-7. Jupiter 70–71: Angle between outgoing geocentric asymptote and launch planet's orbital plane vs launch date

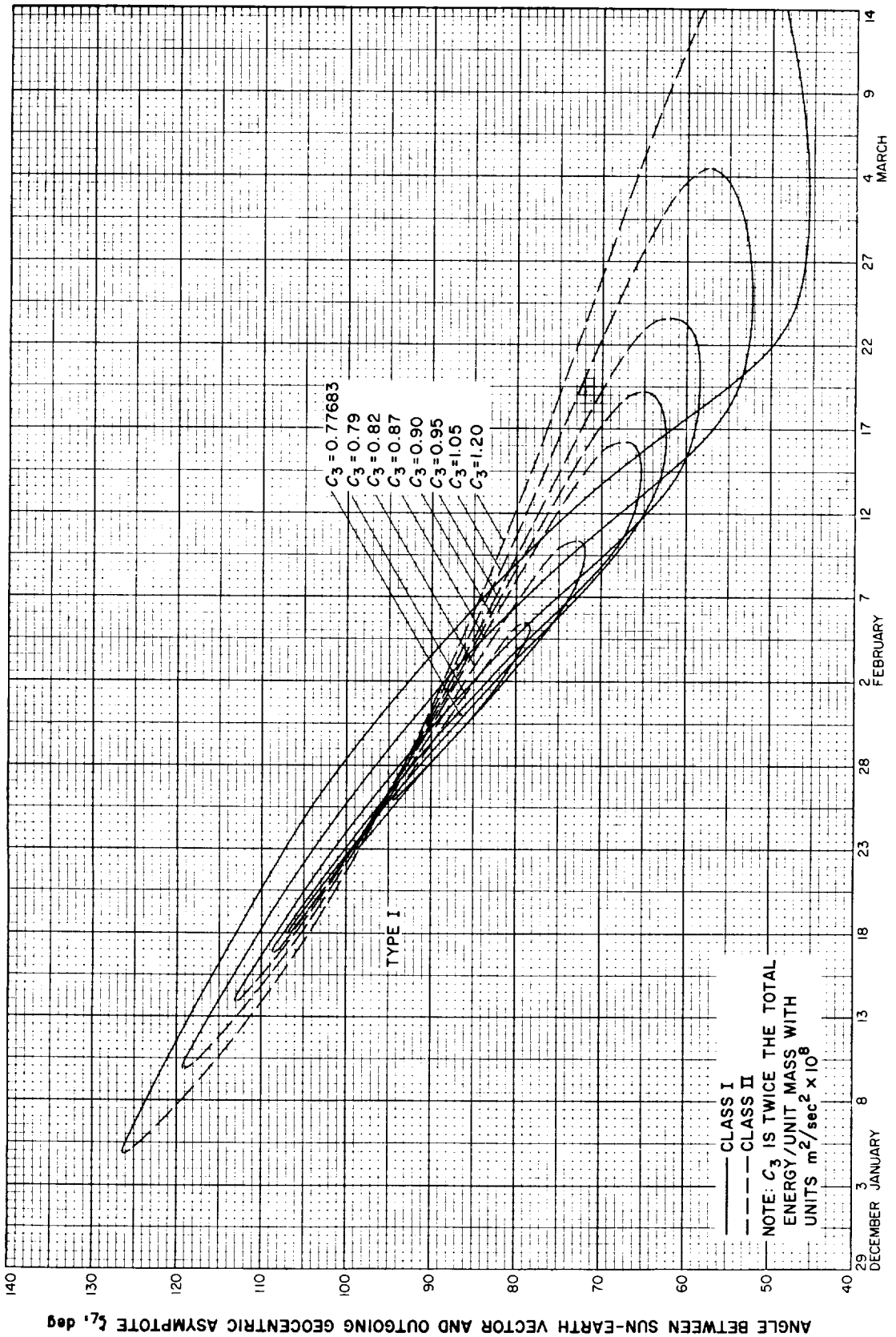

Fig. 8-8(1). Jupiter 70–71: Angle between Sun–Earth vector and outgoing geocentric asymptote vs launch date, Type I

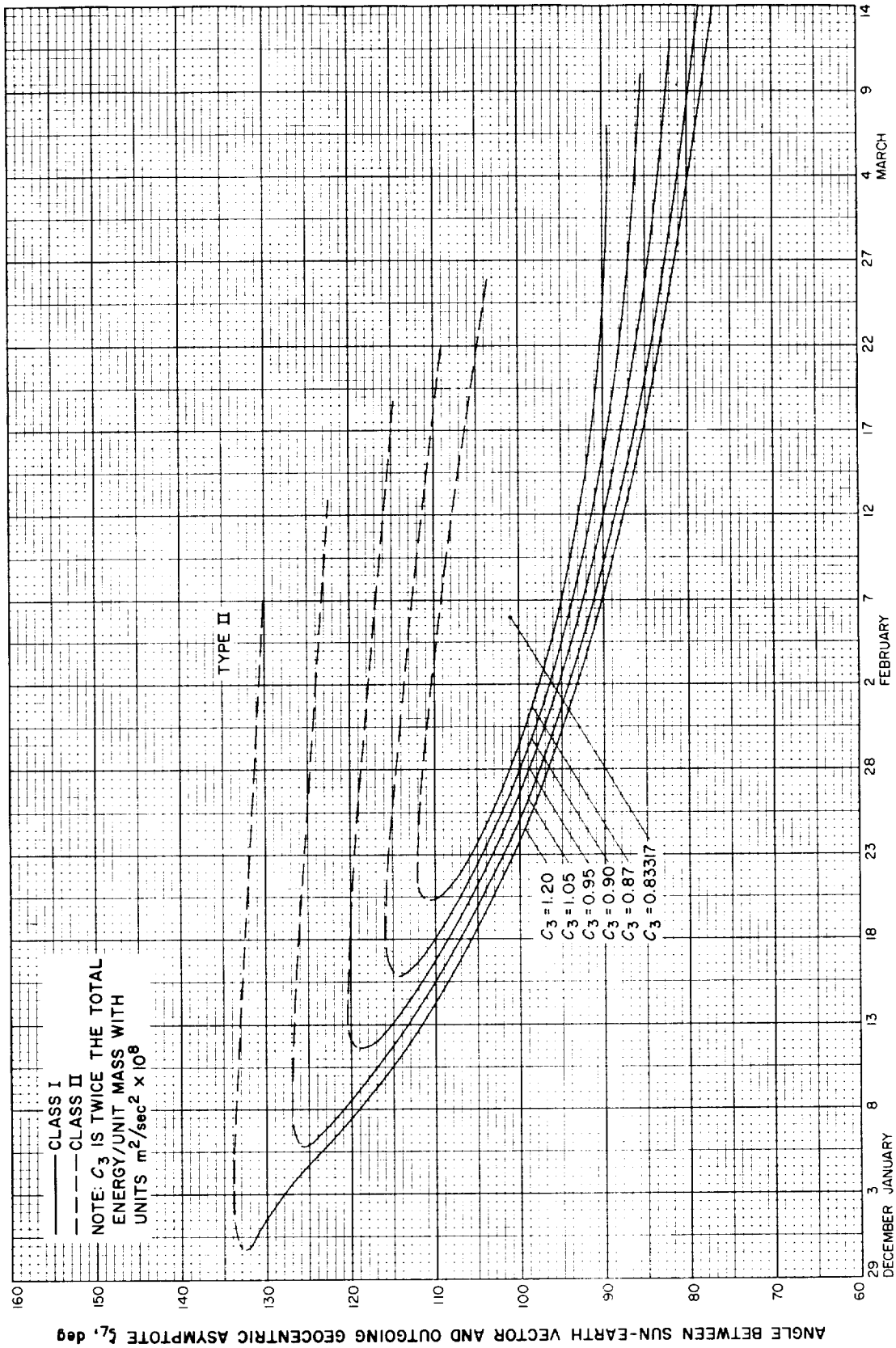

Fig. 8-8(II). Jupiter 70–71: Angle between Sun–Earth vector and outgoing geocentric asymptote vs launch date, Type II

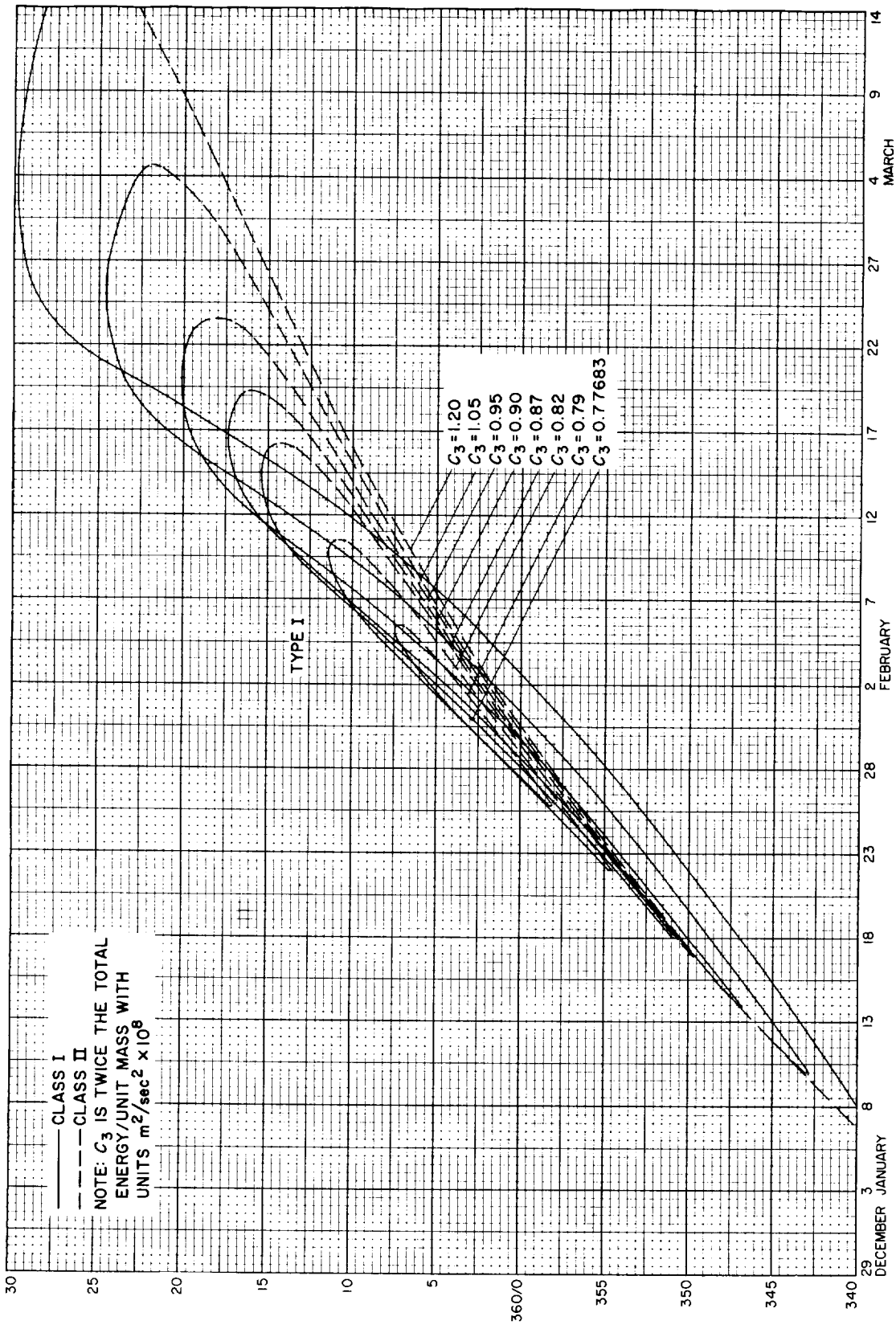

Fig. 8-9(I). Jupiter 70–71: True anomaly in transfer ellipse at launch time vs launch date, Type I

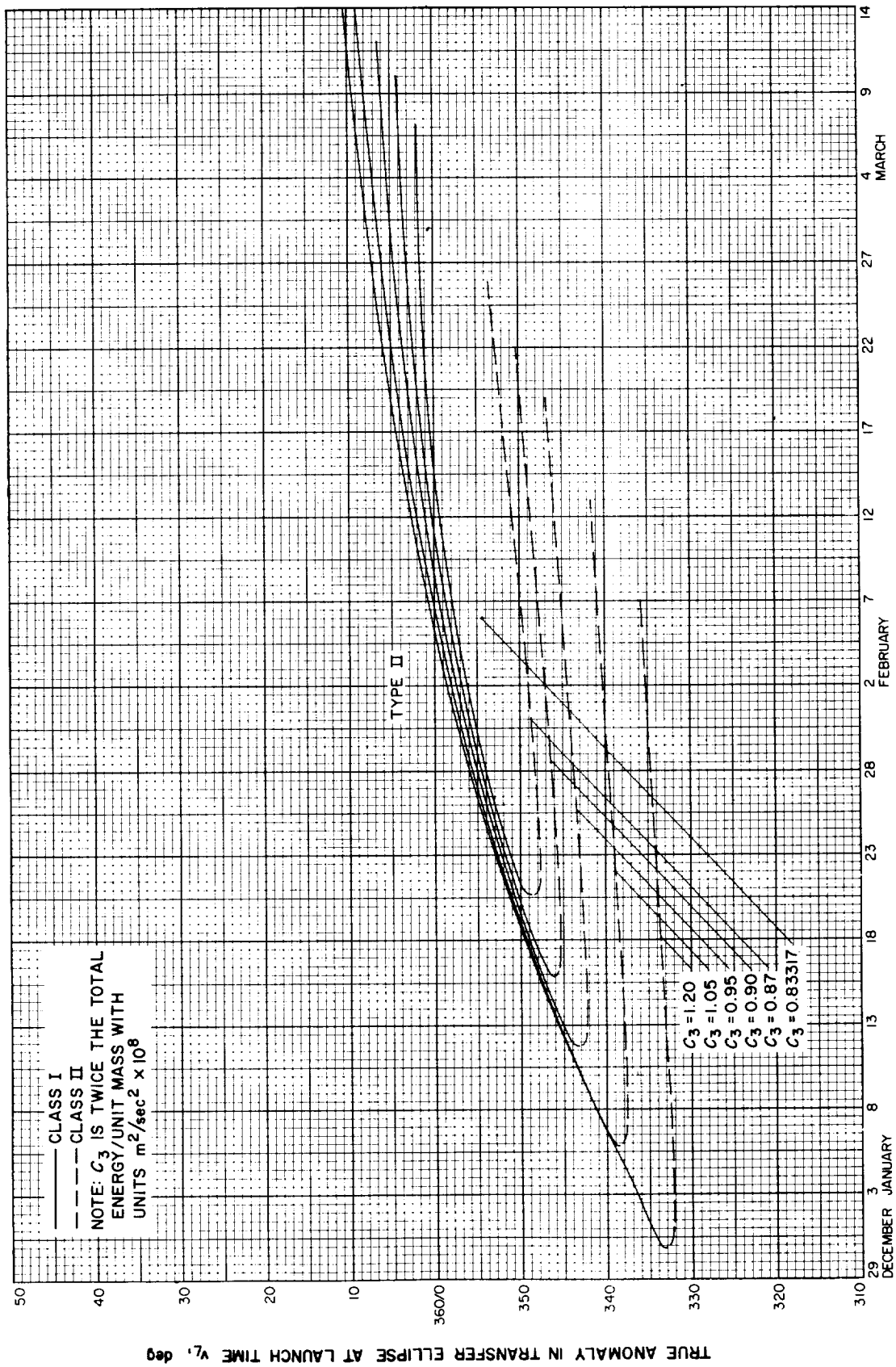

Fig. 8-9(II). Jupiter 70–71: True anomaly in transfer ellipse at launch time vs launch date, Type II

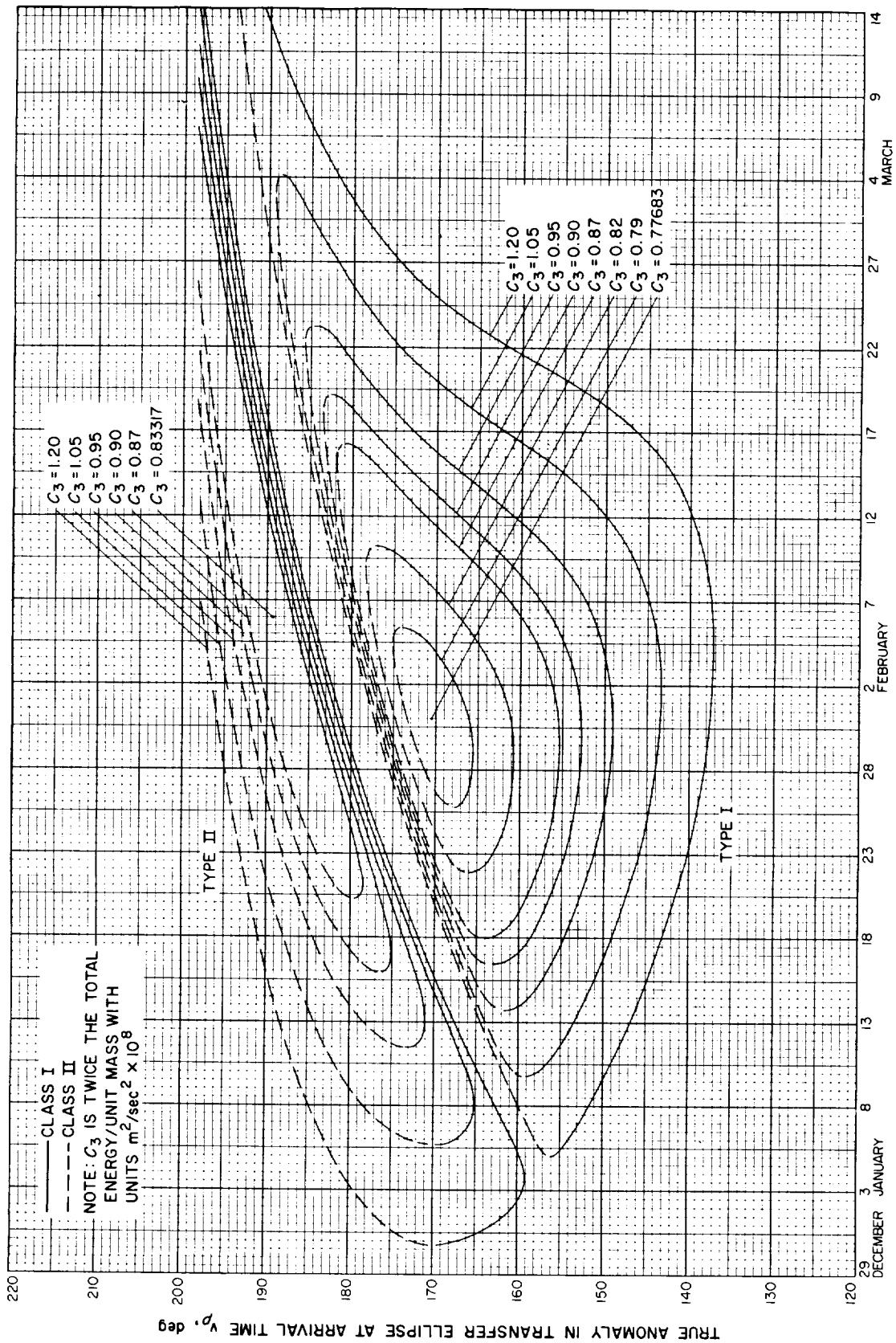

Fig. 8–10. Jupiter 70–71: True anomaly in transfer ellipse at arrival time vs launch date

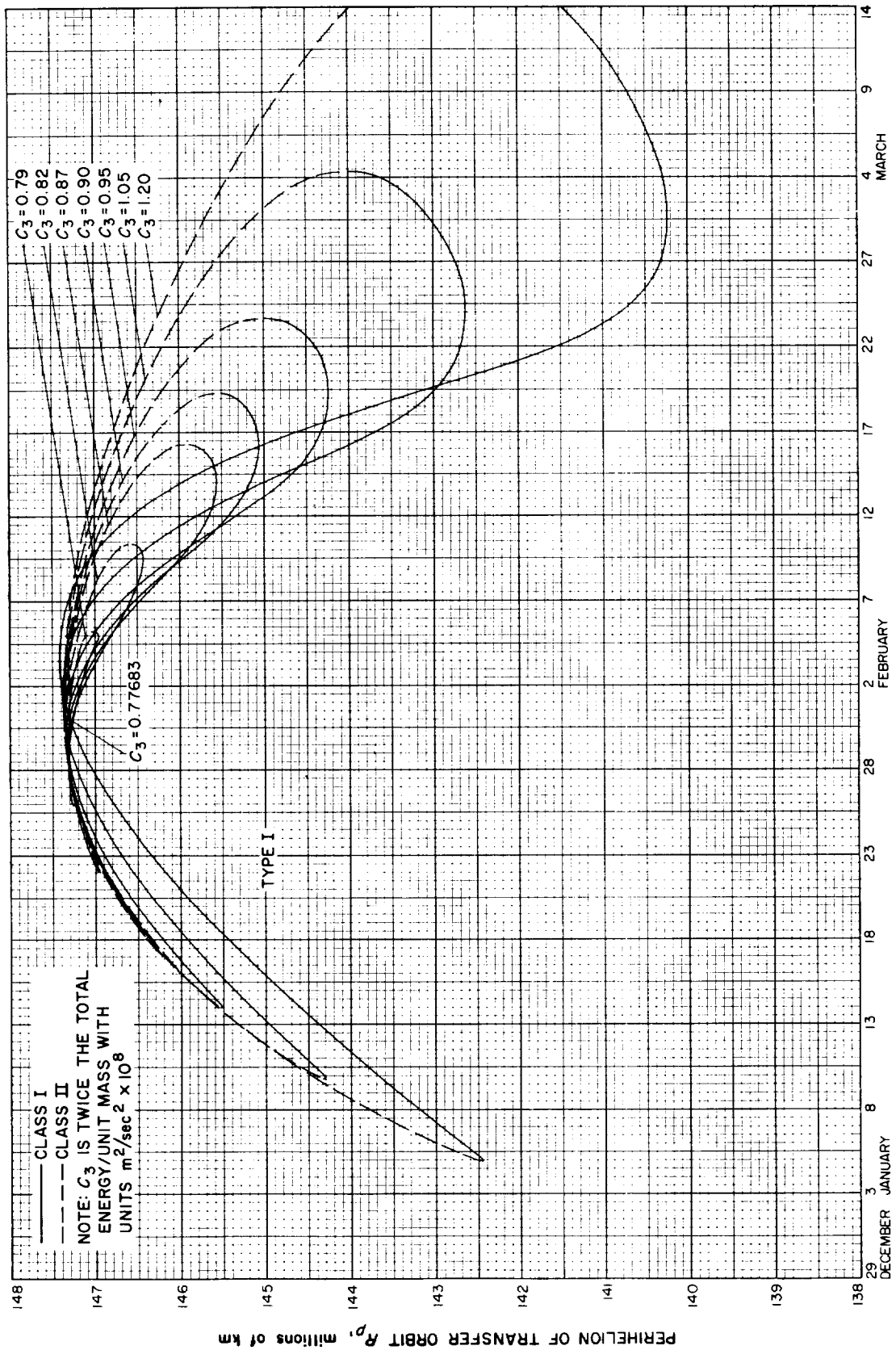

Fig. 8-11(I). Jupiter 70–71: Perihelion of transfer orbit vs launch date, Type I

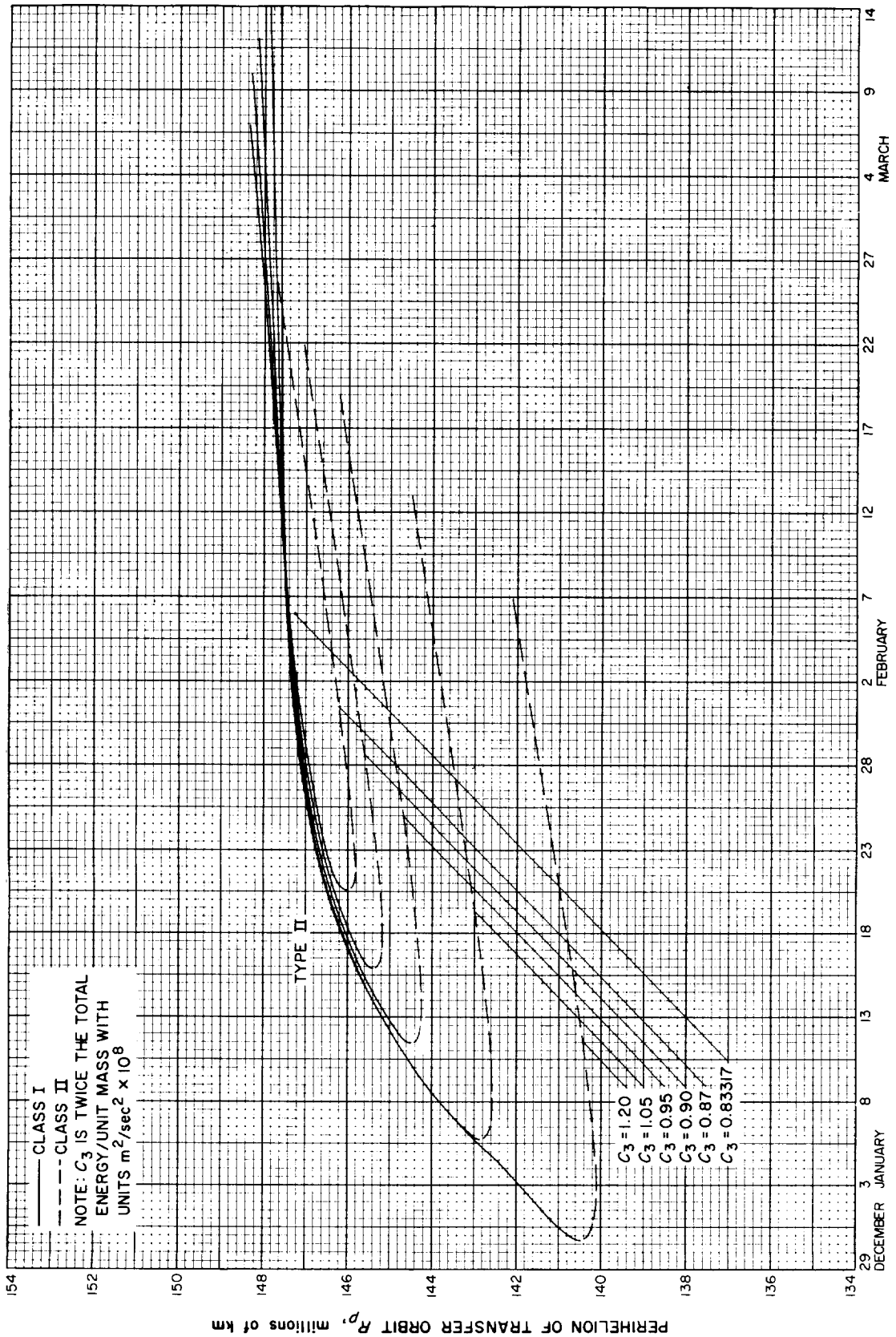

Fig. 8-11(II). Jupiter 70–71: Perihelion of transfer orbit vs launch date, Type II

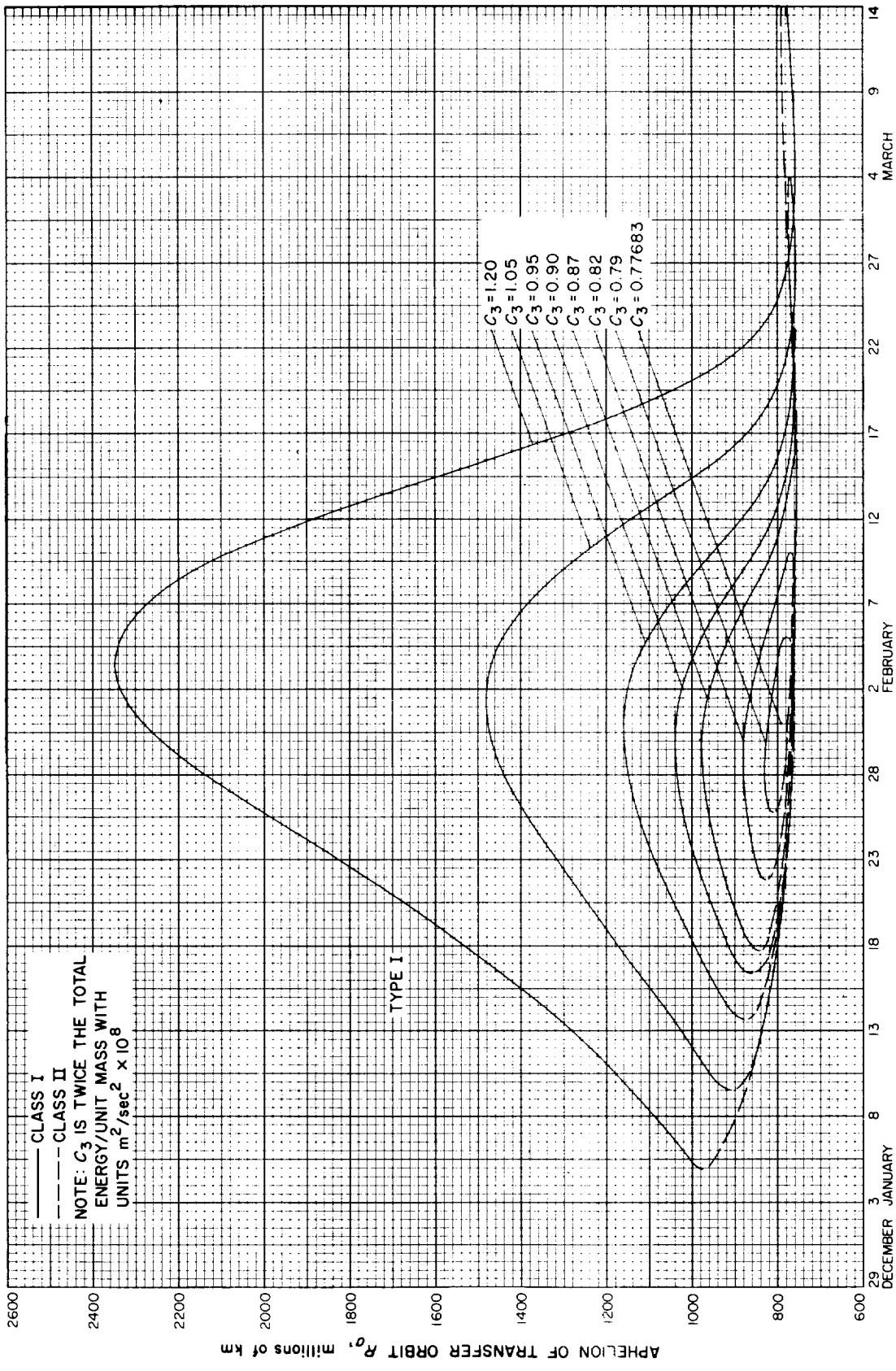

Fig. 8-12(I). Jupiter 70–71: Aphelion of transfer orbit vs launch date, Type I

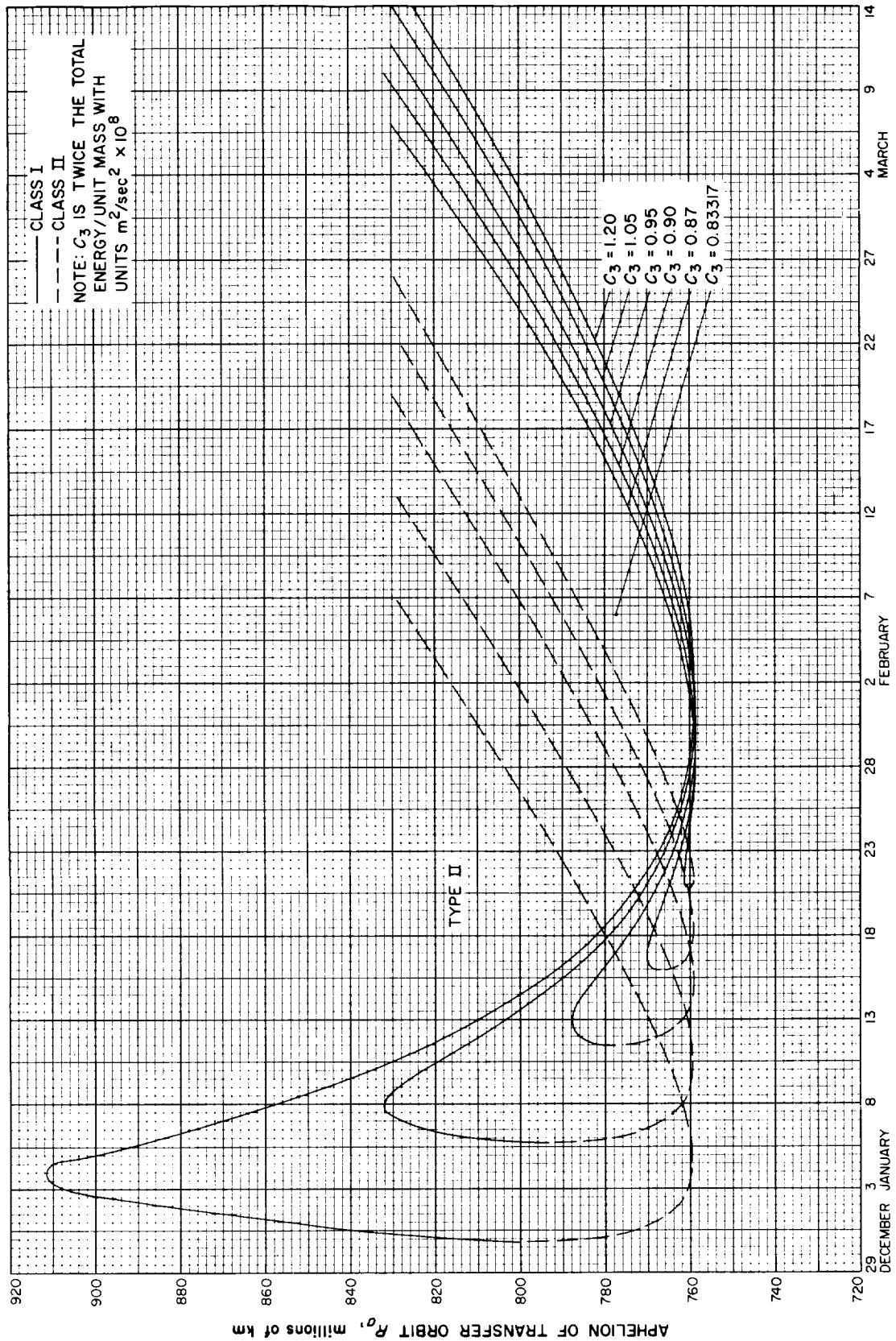

Fig. 8-12(II). Jupiter 70–71: Aphelion of transfer orbit vs launch date, Type II

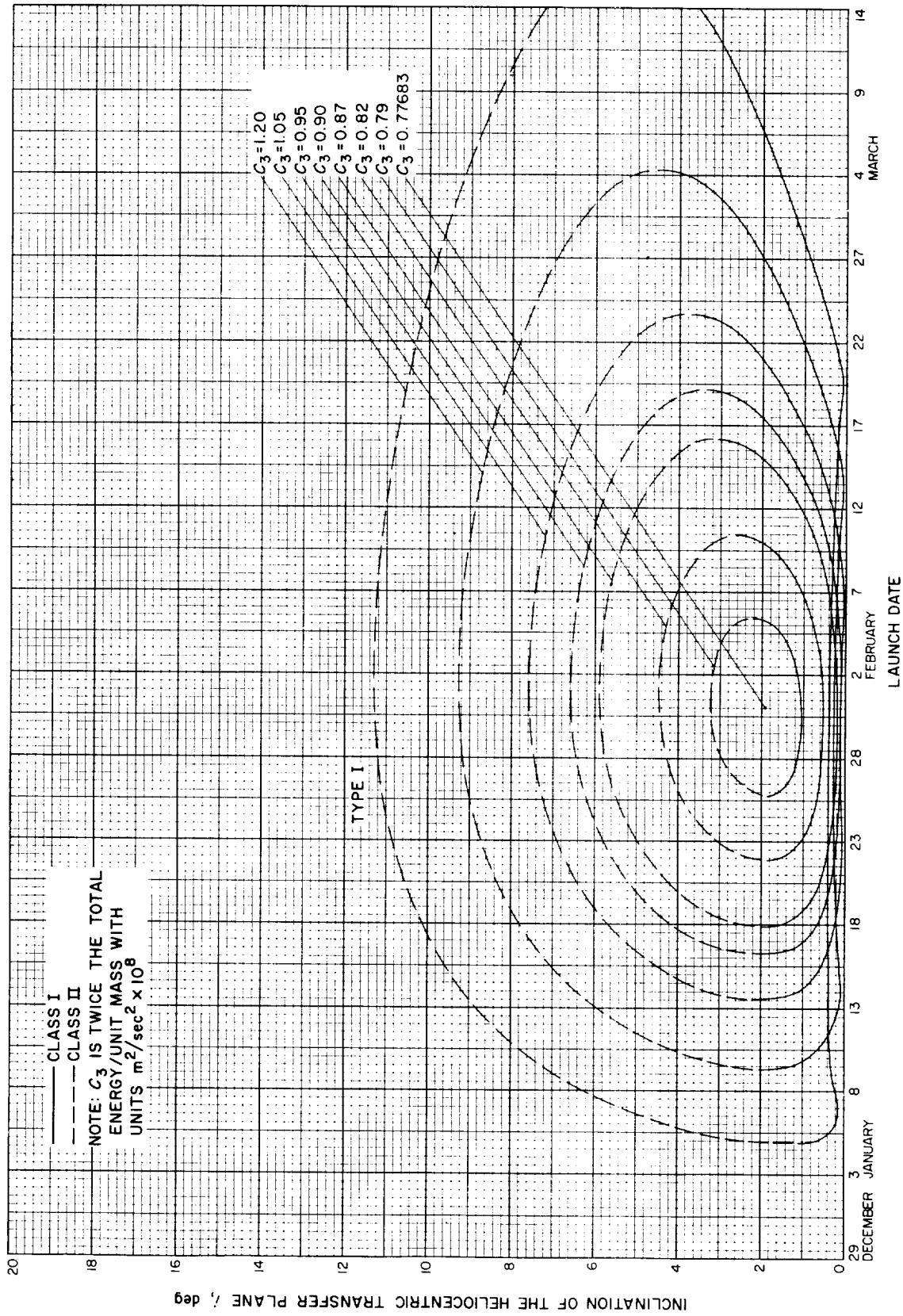

Fig. 8-13(I). Jupiter 70-71: Inclination of the heliocentric transfer plane vs launch date, Type I

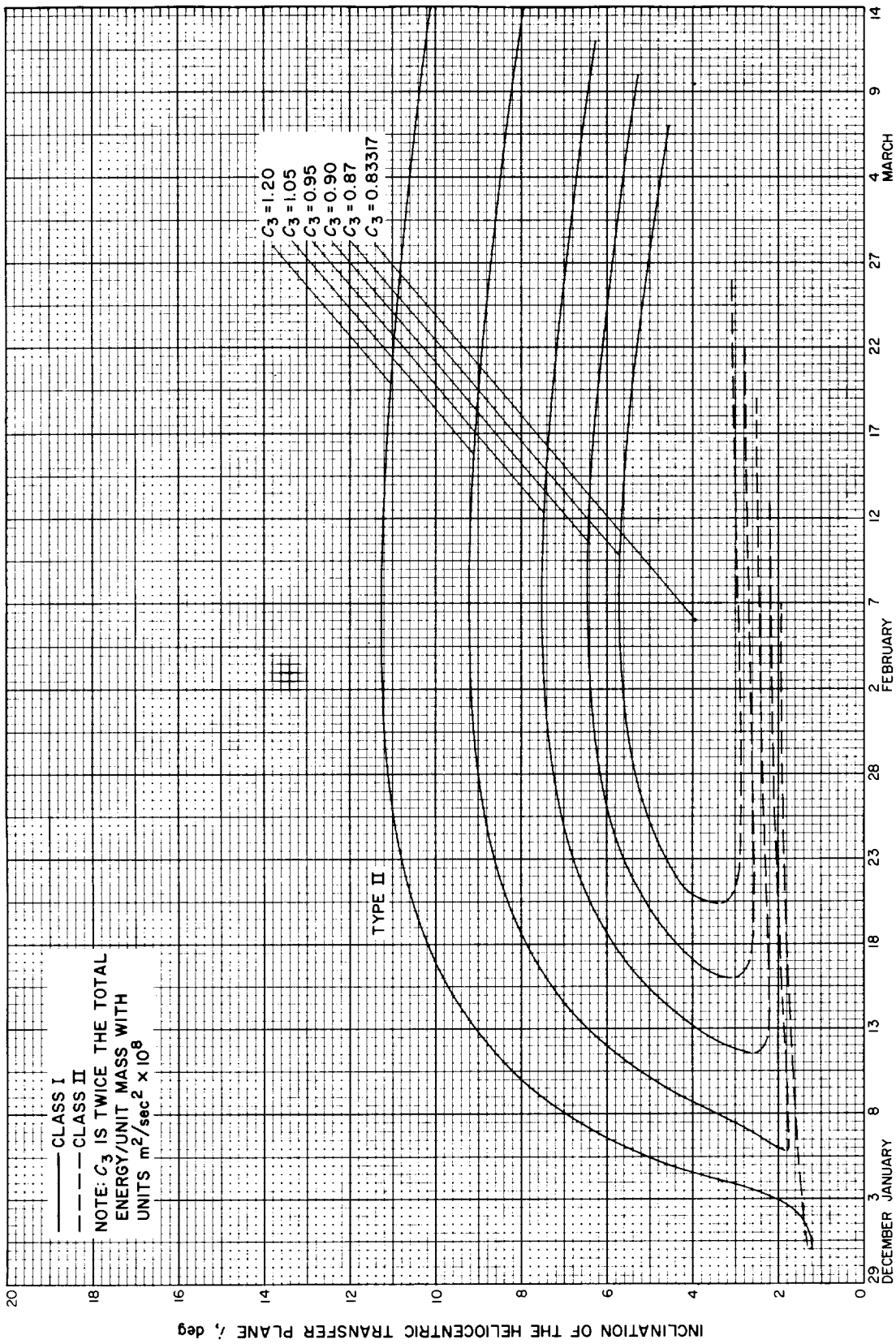

Fig. 8-13(II). Jupiter 70–71: Inclination of the heliocentric transfer plane vs launch date, Type II

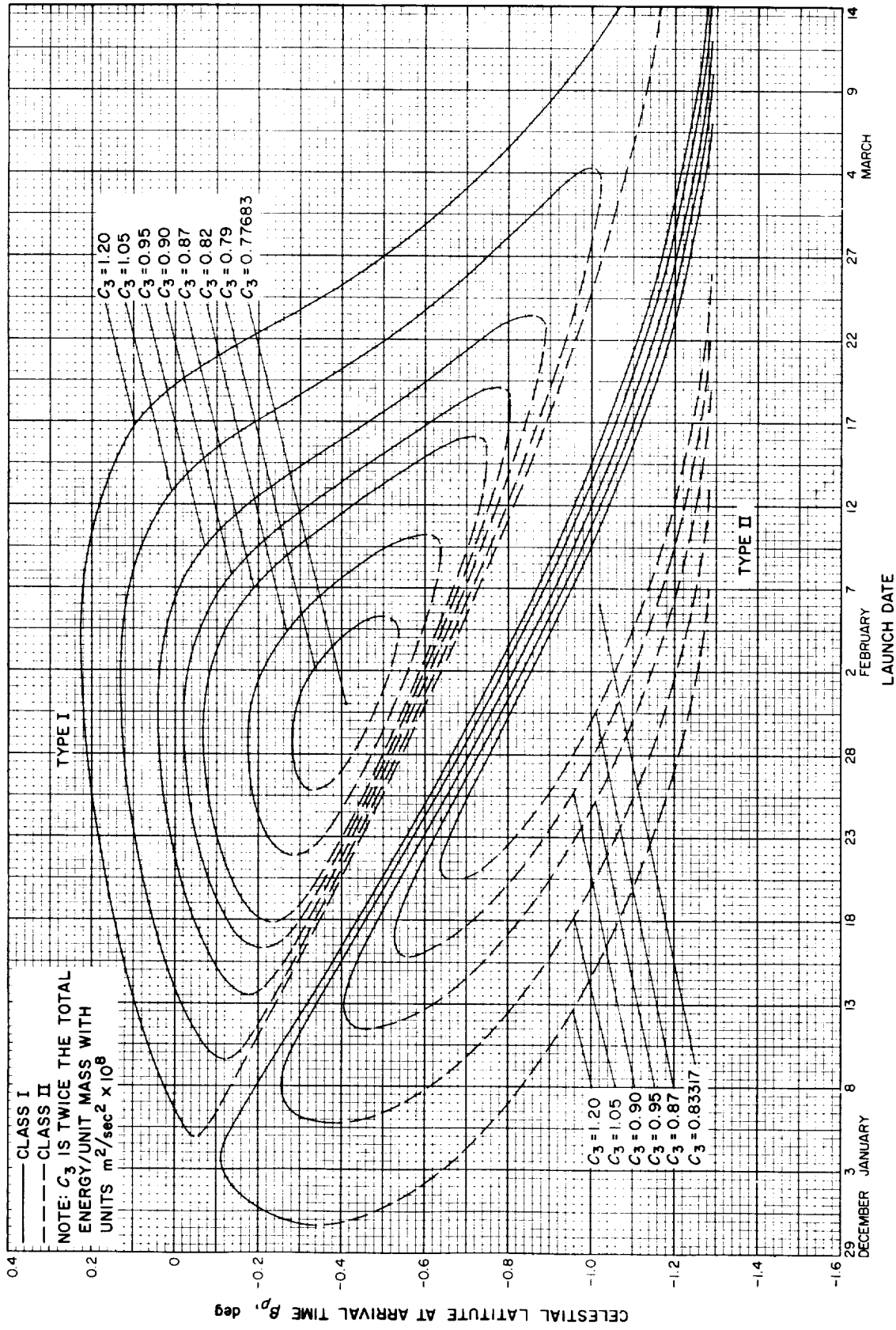

Fig. 8–14. Jupiter 70–71: Celestial latitude at arrival time vs launch date

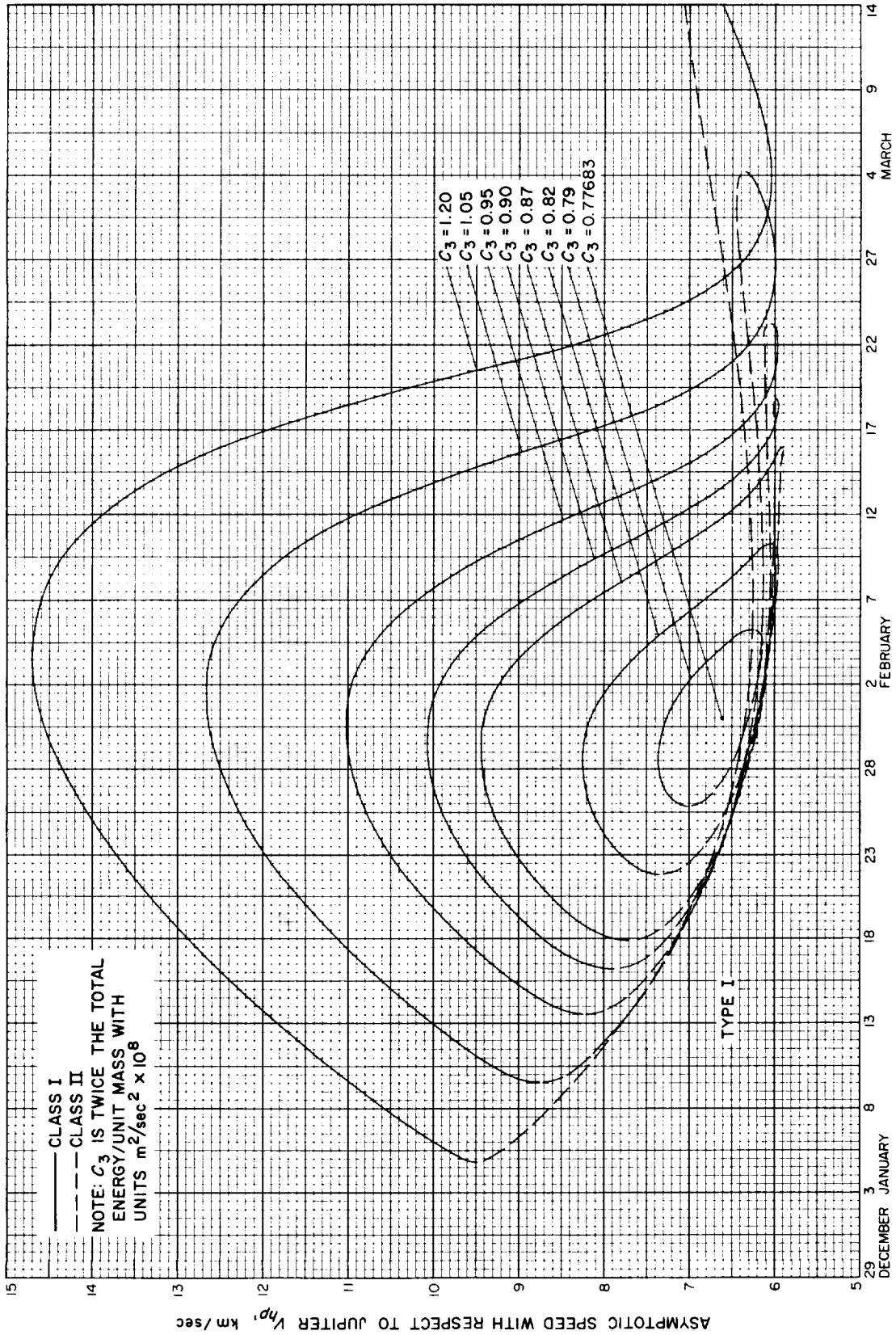

Fig. 8-15(I). Jupiter 70–71: Asymptotic speed with respect to Jupiter vs launch date, Type I

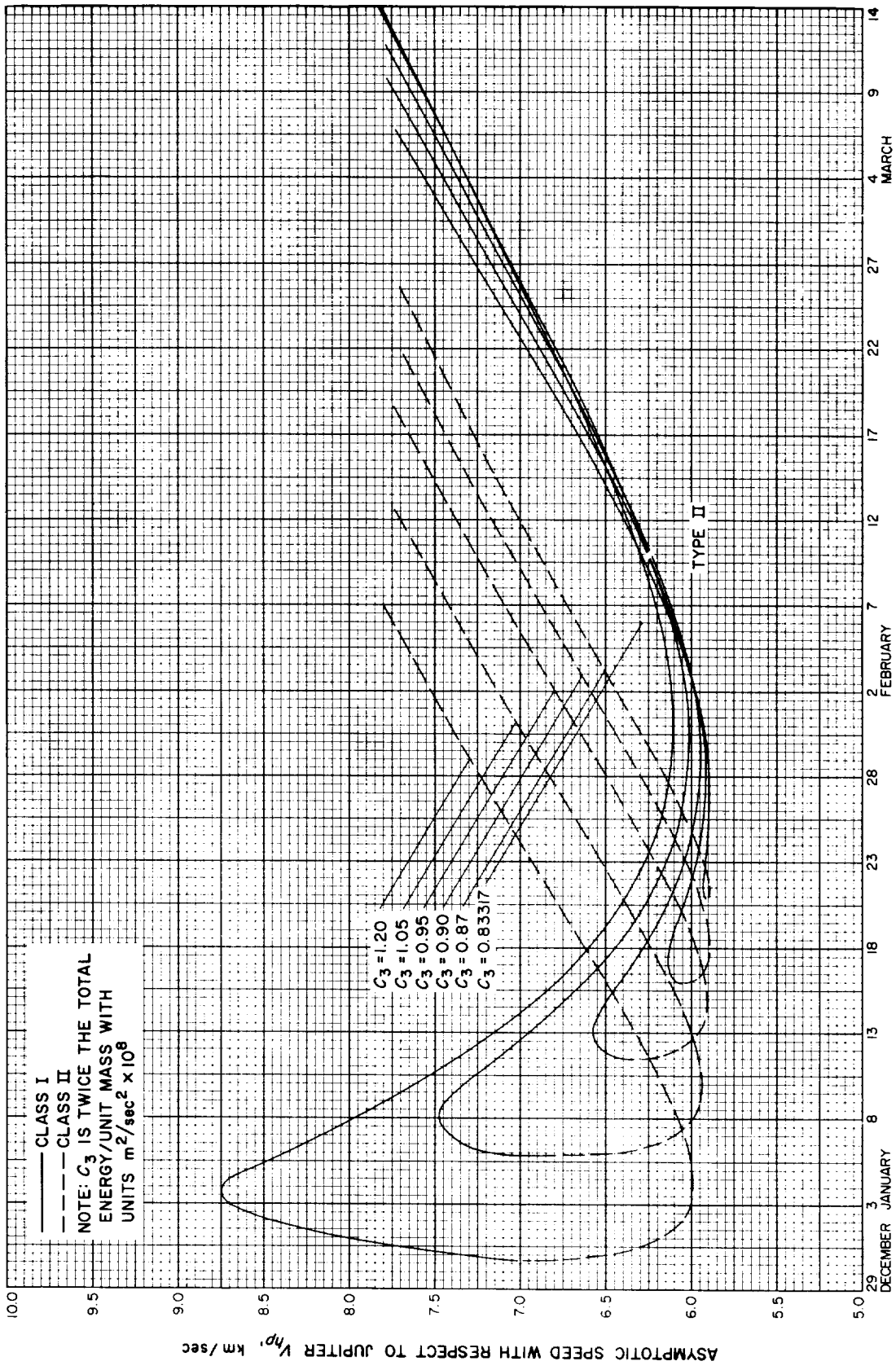

Fig. 8-15(II). Jupiter 70–71: Asymptotic speed with respect to Jupiter vs launch date, Type II

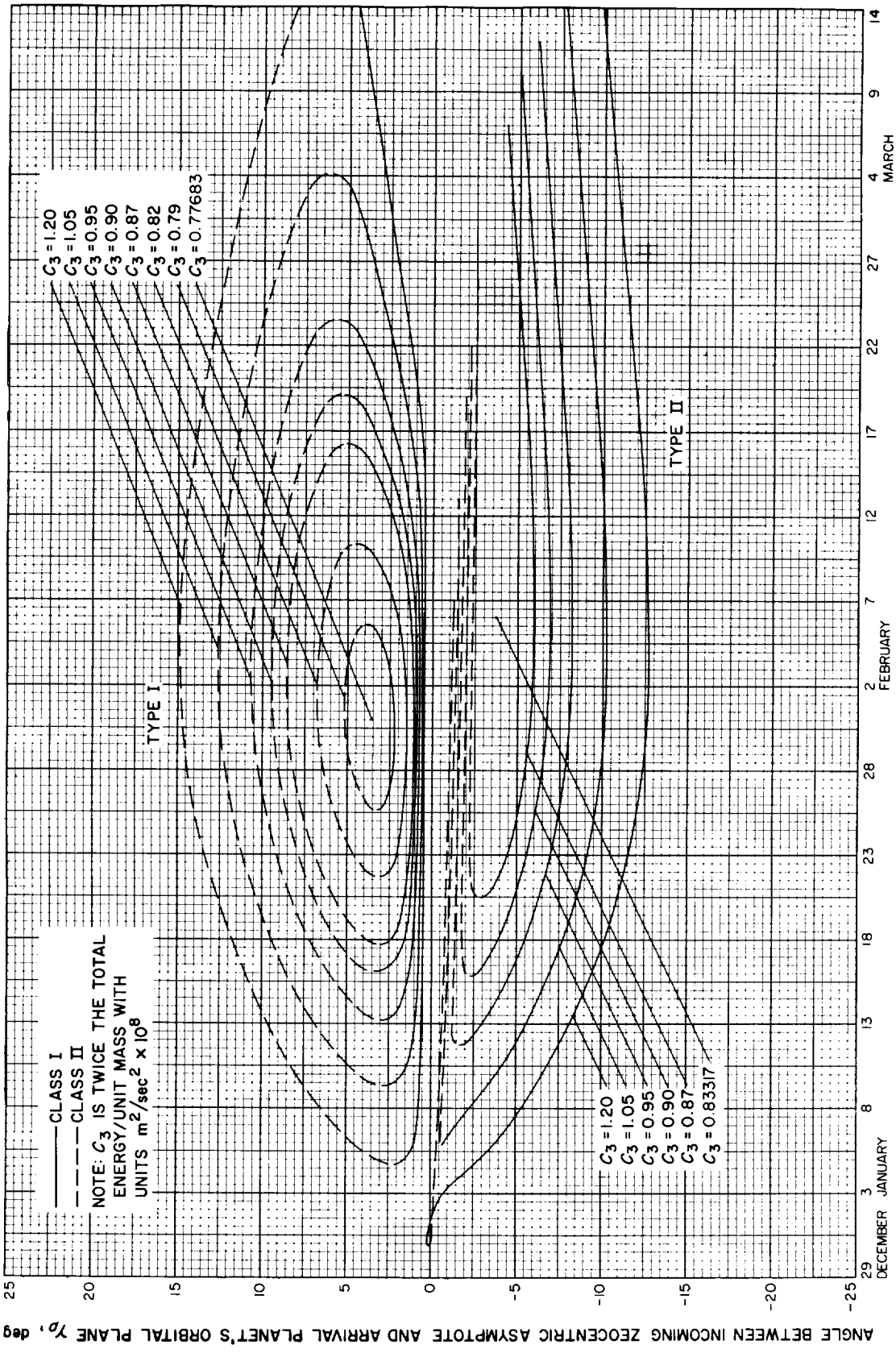

Fig. 8–16. Jupiter 70–71: Angle between incoming zeocentric asymptote and arrival planet's orbital plane vs launch date

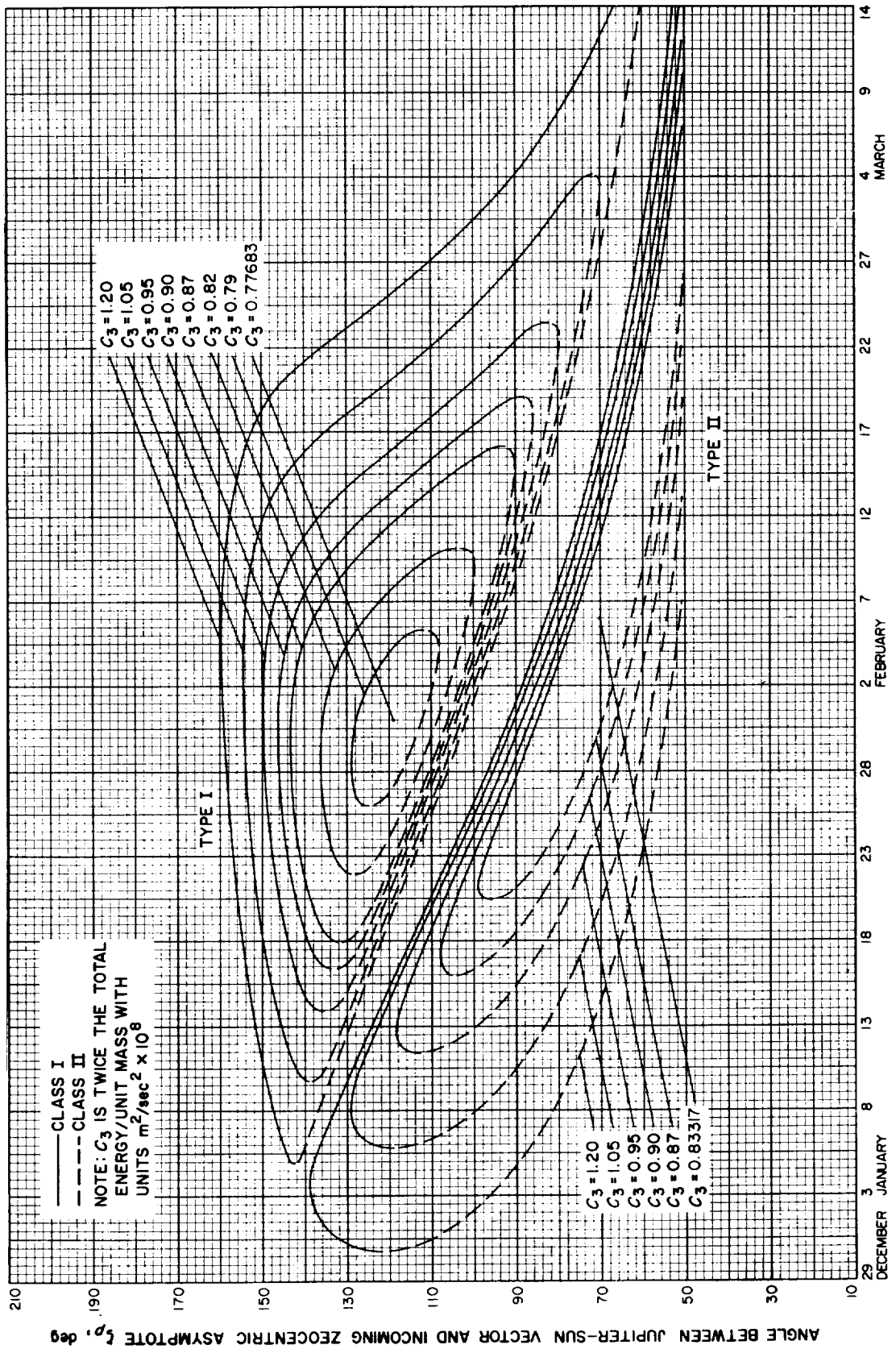

Fig. 8-17. Jupiter 70–71: Angle between Jupiter–Sun vector and incoming zeocentric asymptote vs launch date

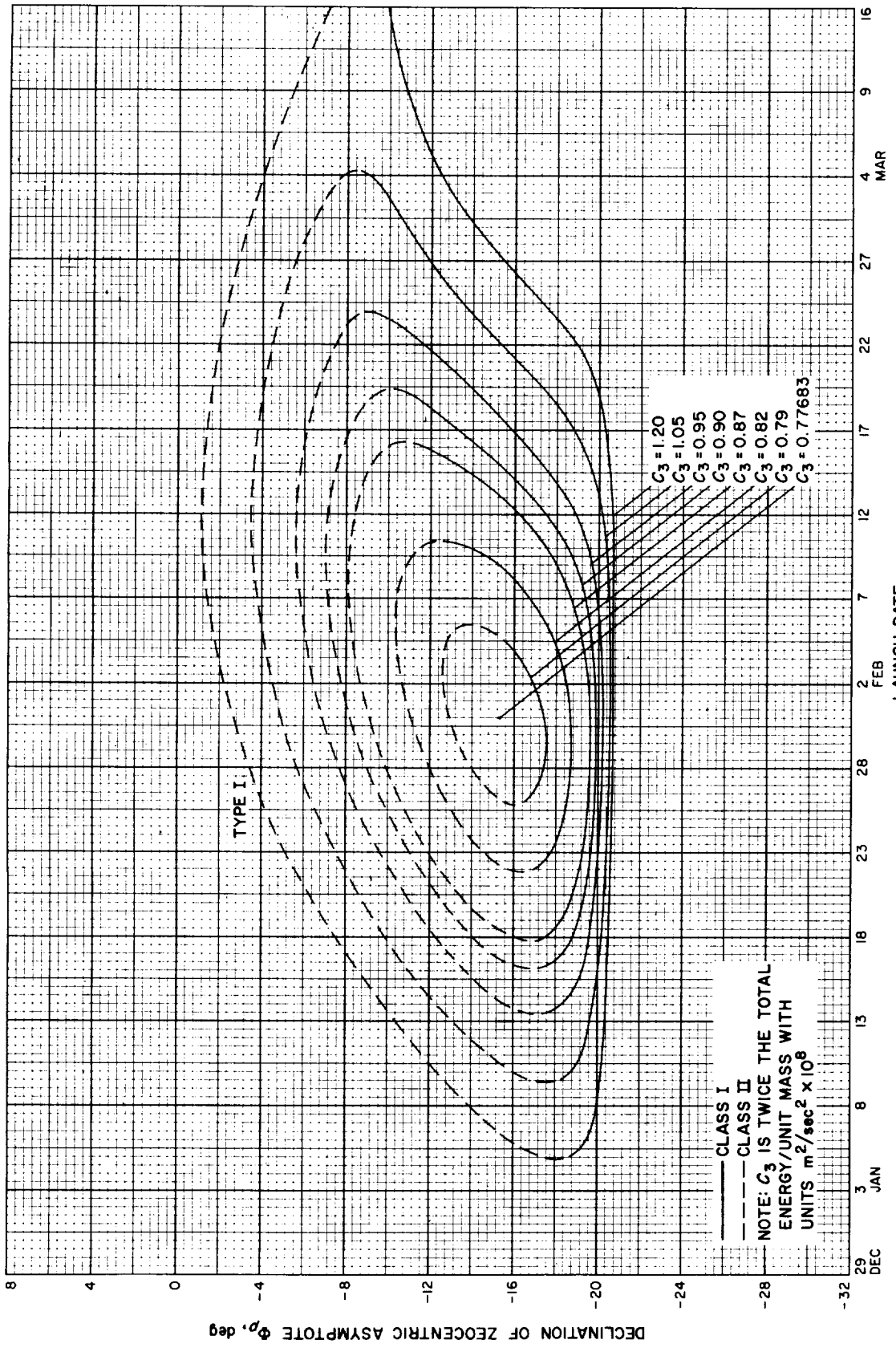

Fig. 8-18(I). Jupiter 70-71: Declination of zeocentric asymptote vs launch date, Type I

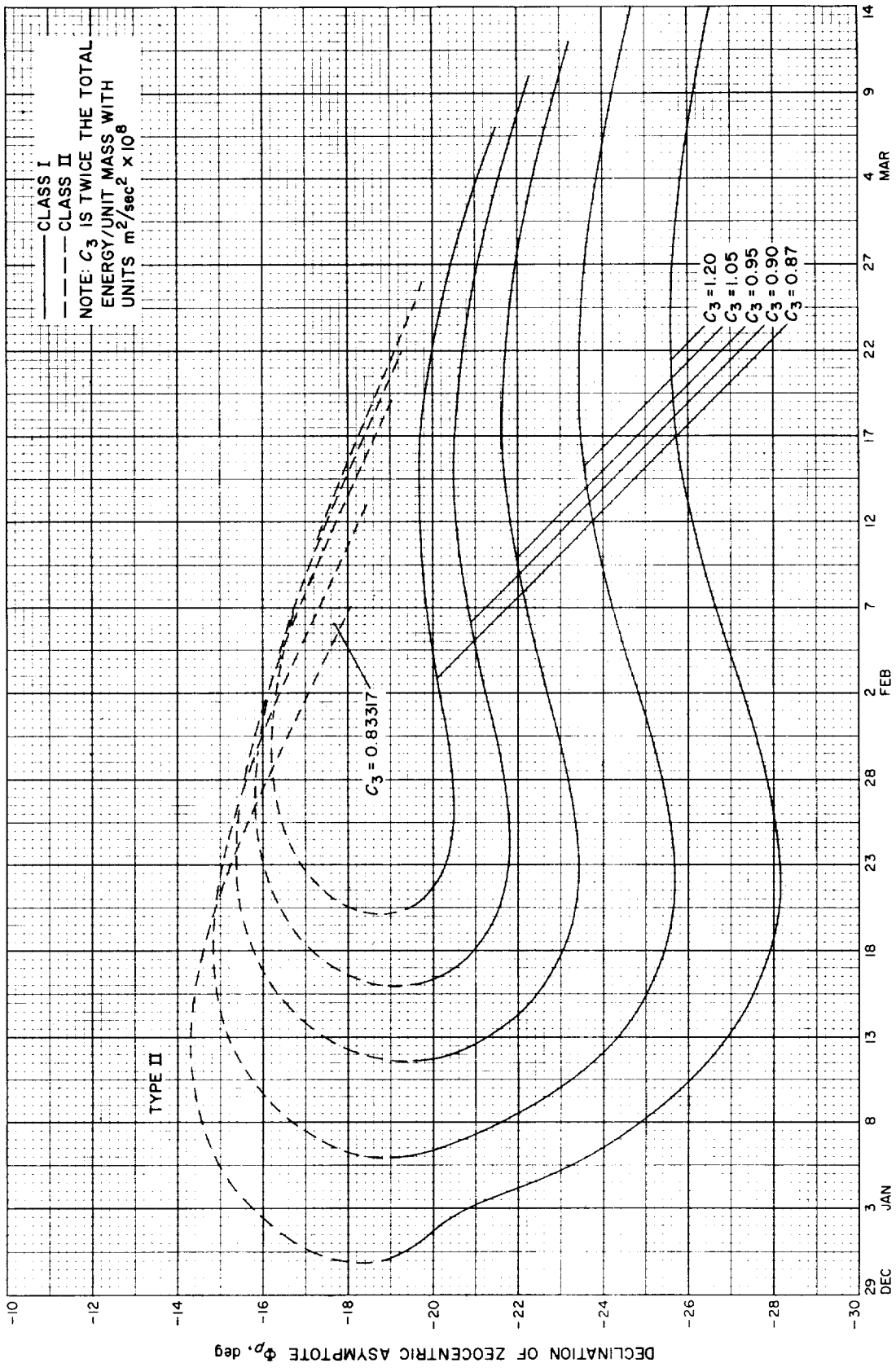

Fig. 8-18(II). Jupiter 70-71: Declination of zeocentric asymptote vs launch date, Type II

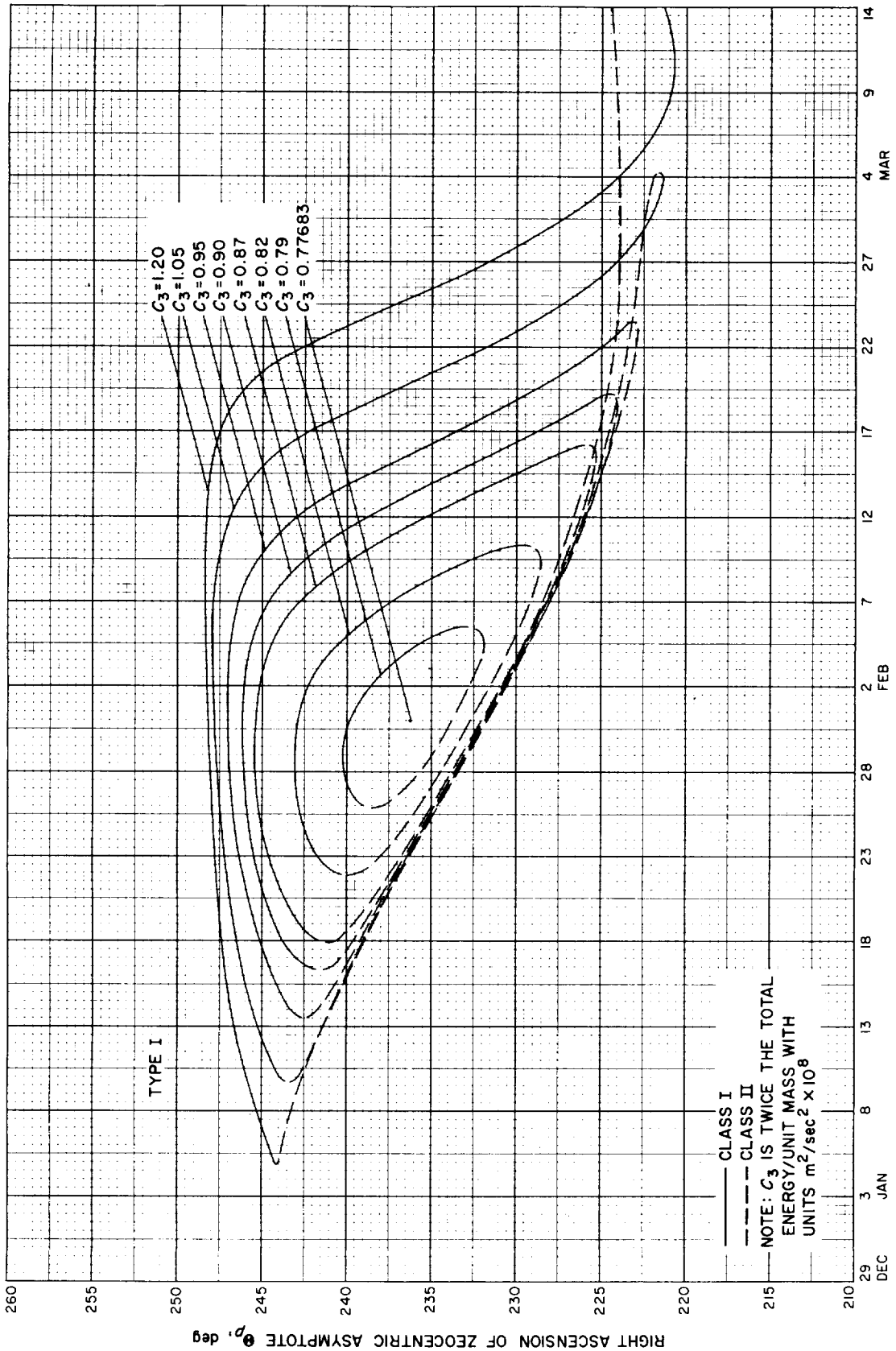

Fig. 8–19(I). Jupiter 70–71: Right ascension of zeocentric asymptote vs launch date, Type I

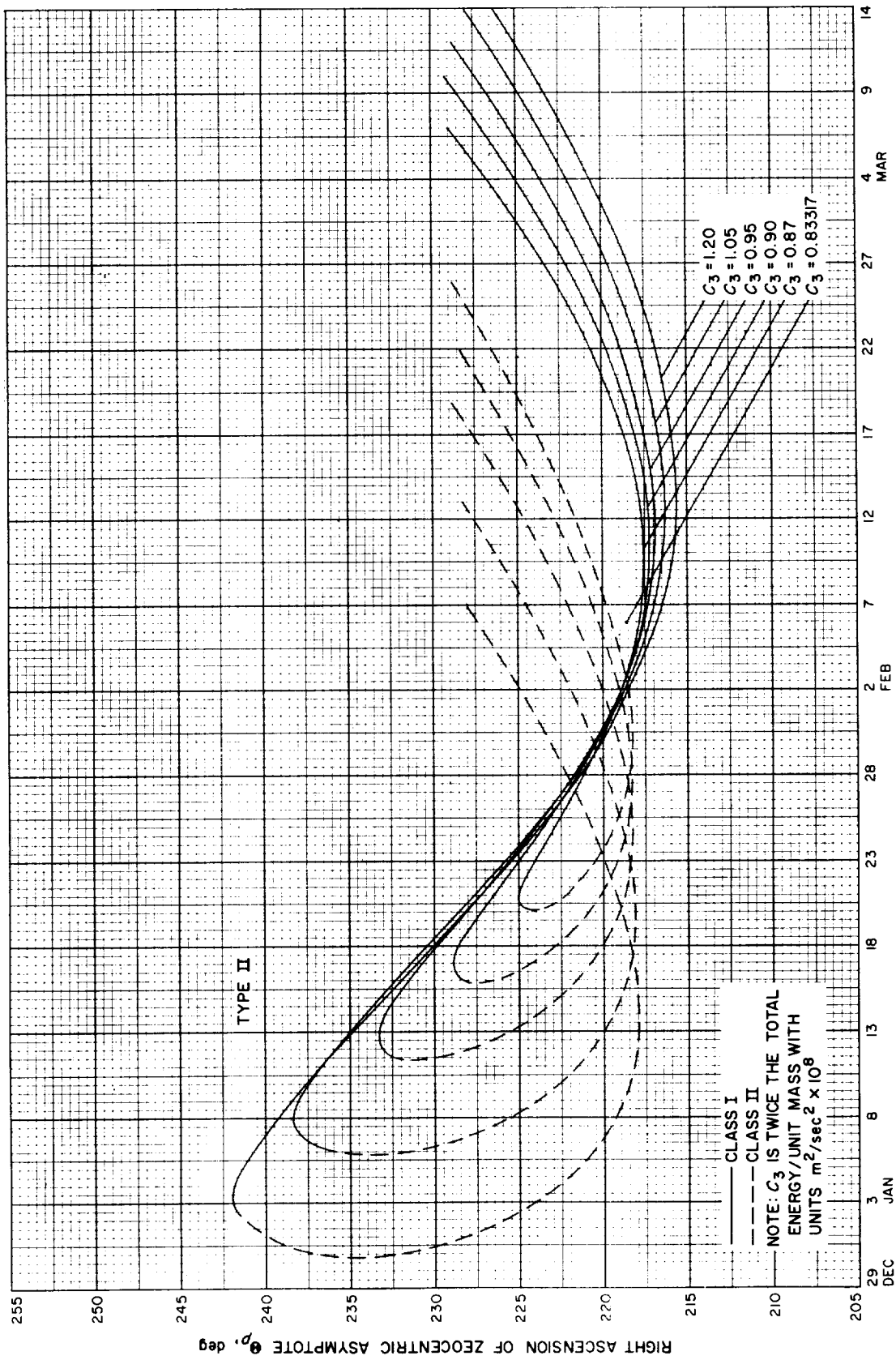

Fig. 8-19(II). Jupiter 70-71: Right ascension of zeocentric asymptote vs launch date, Type II

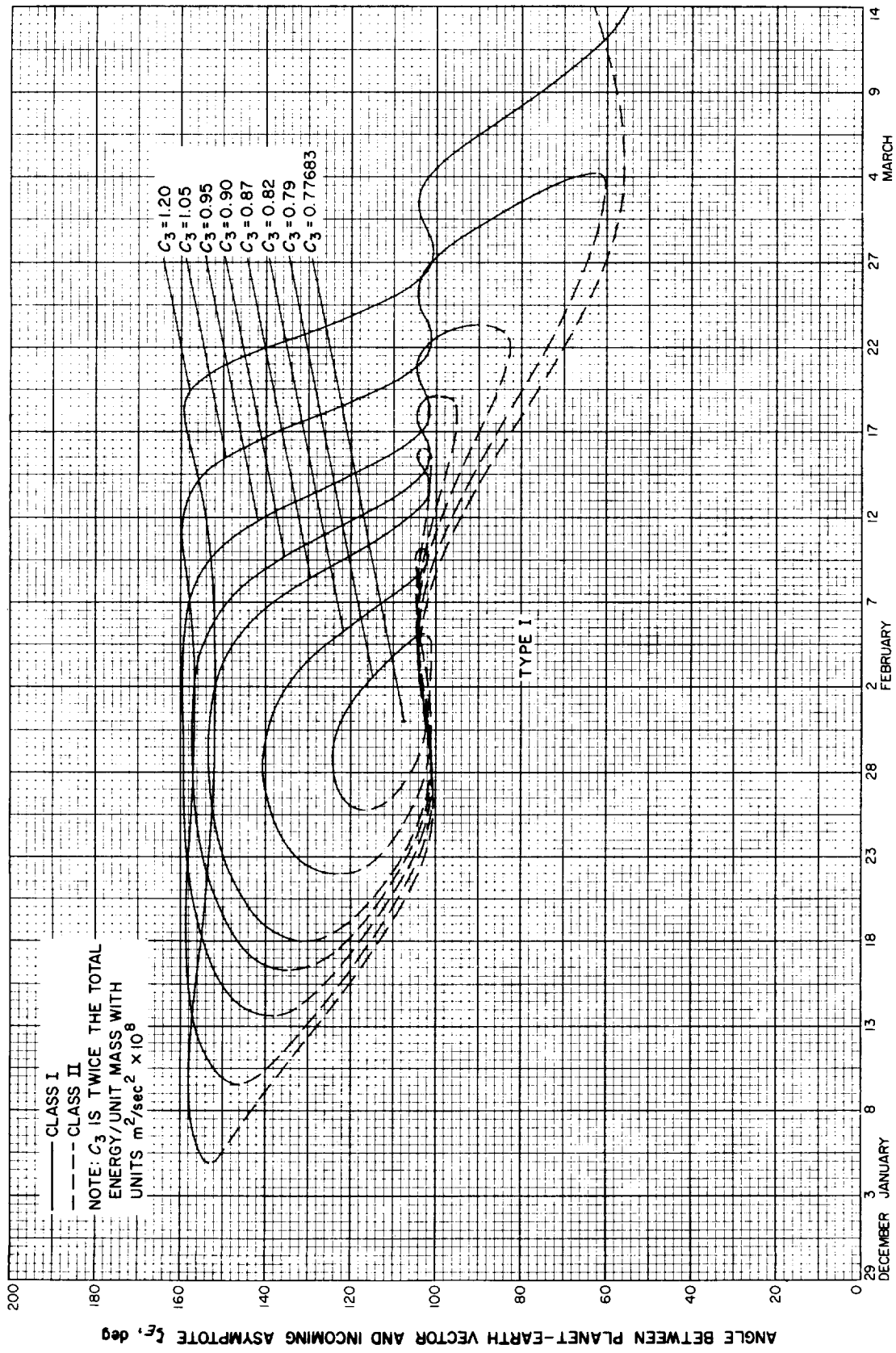

Fig. 8-20(I). Jupiter 70–71: Angle between planet–Earth vector and incoming asymptote vs launch date, Type I

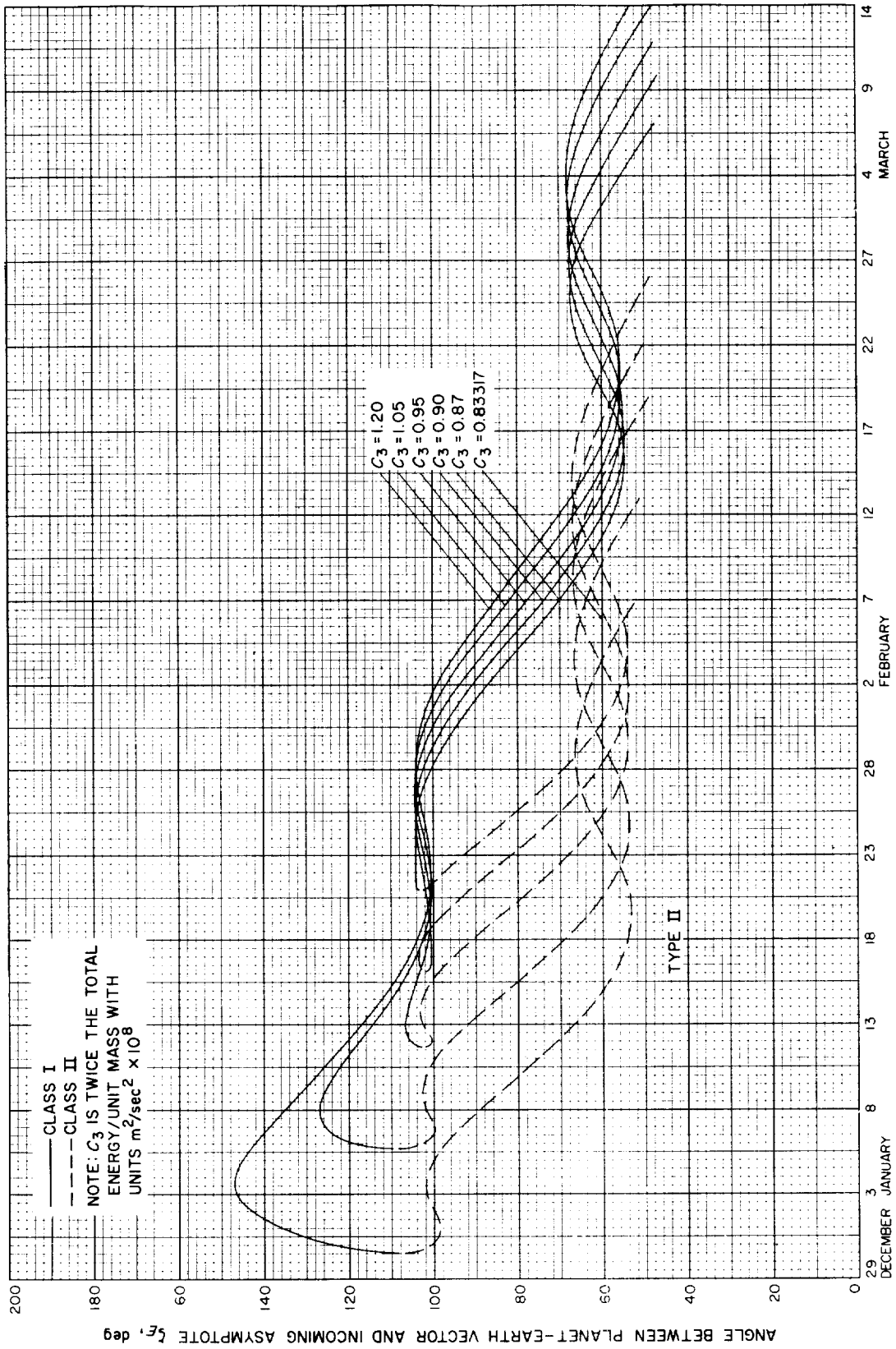

Fig. 8-20(II). Jupiter 70–71: Angle between planet–Earth vector and incoming asymptote vs launch date, Type II

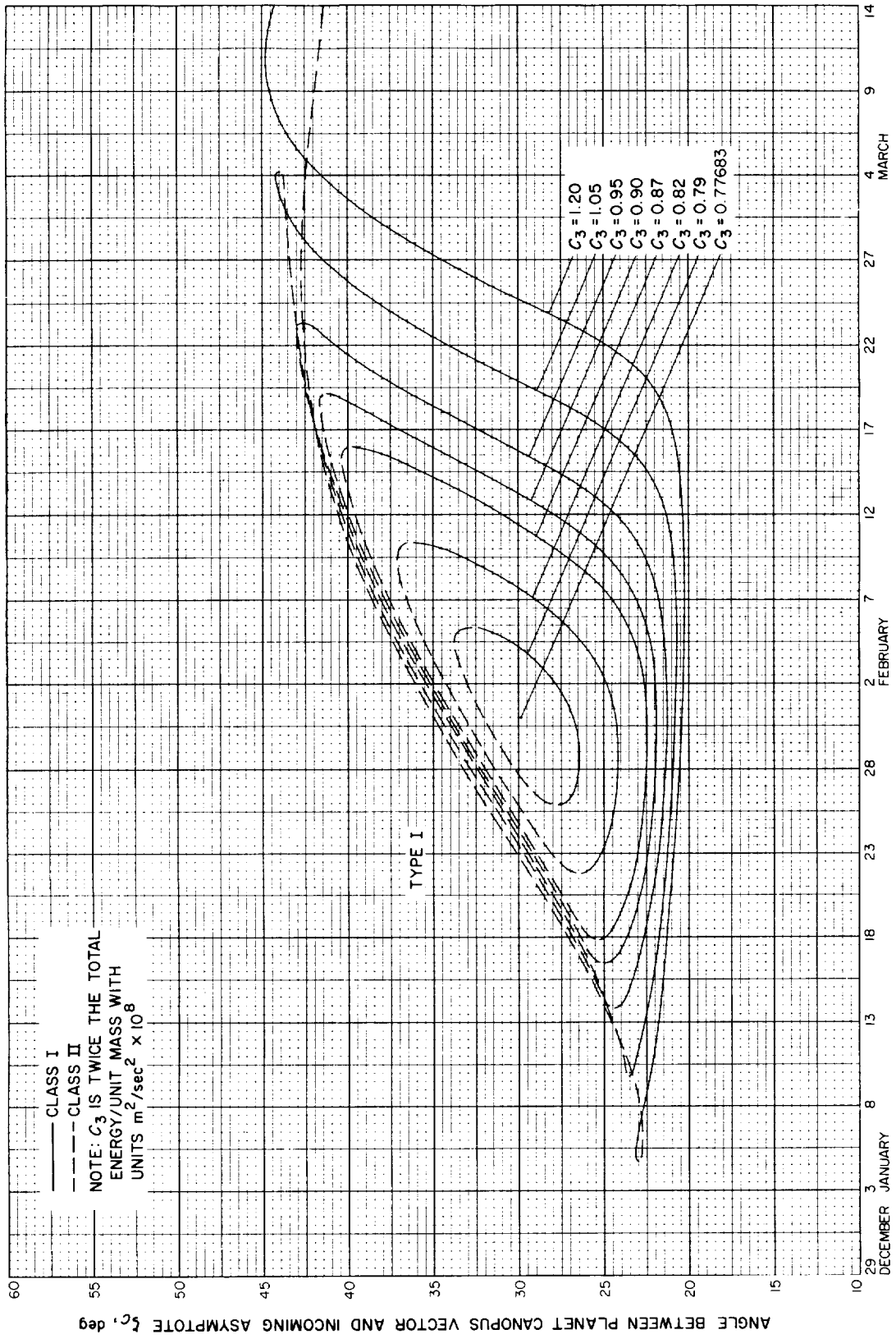

Fig. 8-21(1). Jupiter 70–71: Angle between planet–Canopus vector and incoming asymptote vs launch date, Type I

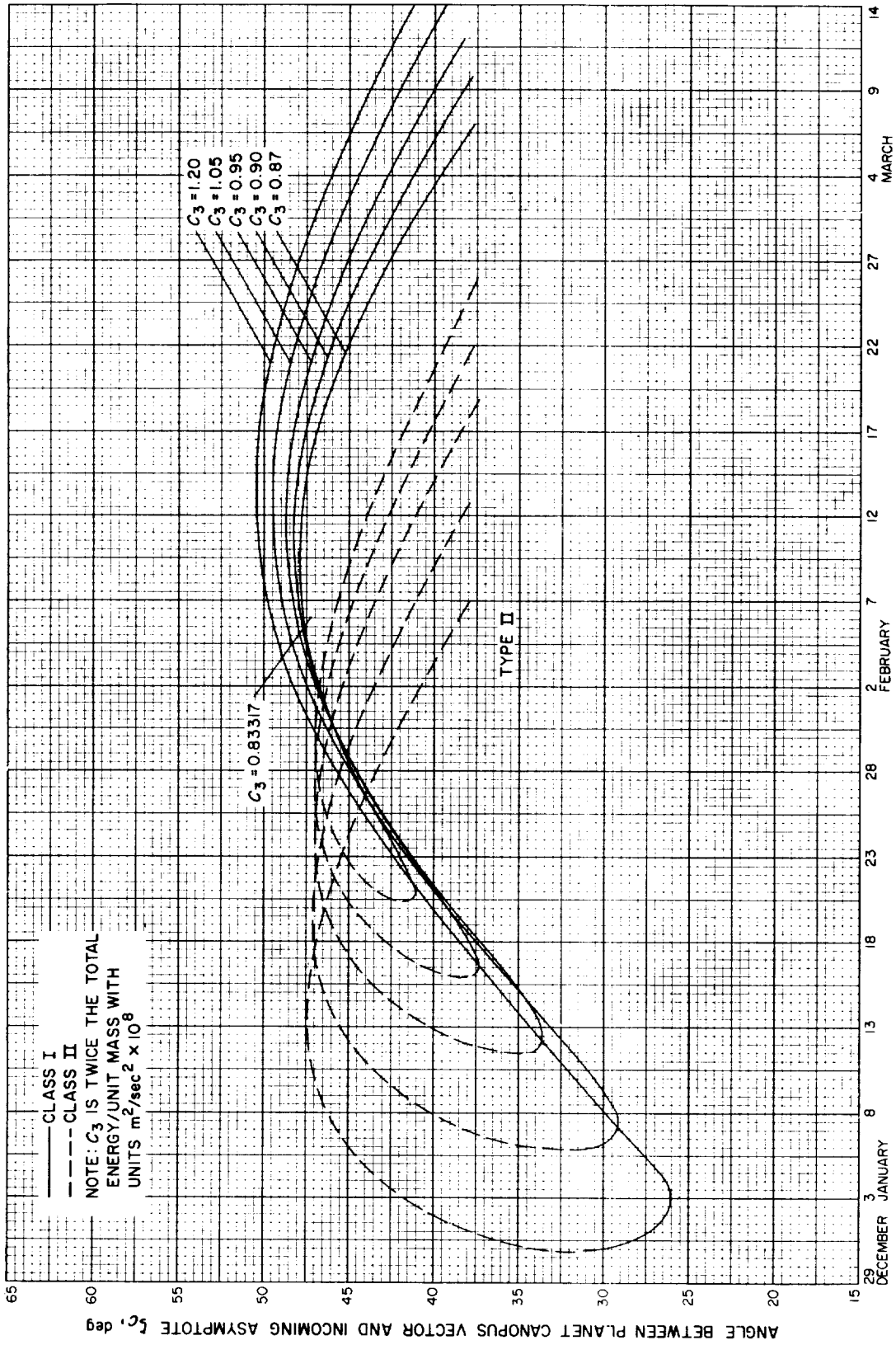

Fig. 8-21(II). Jupiter 70–71: Angle between planet–Canopus vector and incoming asymptote vs launch date, Type II

IX. JUPITER 1972: TRAJECTORY PARAMETER GRAPHS

Figure

9–1. Jupiter 1972: Minimum injection energy vs launch date

9–2. Jupiter 1972: Time of flight vs launch date

9–3. Jupiter 1972: Heliocentric central angle vs launch date

9–4(I). Jupiter 1972: Earth–Jupiter communication distance vs launch date, Type I

9–4(II). Jupiter 1972: Earth–Jupiter communication distance vs launch date, Type II

9–5. Jupiter 1972: Declination of the geocentric asymptote vs launch date

9–6. Jupiter 1972: Right ascension of geocentric asymptote vs launch date

9–7. Jupiter 1972: Angle between outgoing geocentric asymptote and launch planet's orbital plane vs launch date

9–8(I). Jupiter 1972: Angle between Sun–Earth vector and outgoing geocentric asymptote vs launch date, Type I

9–8(II). Jupiter 1972: Angle between Sun–Earth vector and outgoing geocentric asymptote vs launch date, Type II

9–9(I). Jupiter 1972: True anomaly in transfer ellipse at launch time vs launch date, Type I

9–9(II). Jupiter 1972: True anomaly in transfer ellipse at launch time vs launch date, Type II

9–10. Jupiter 1972: True anomaly in transfer ellipse at arrival time vs launch date

9–11(I). Jupiter 1972: Perihelion of transfer orbit vs launch date, Type I

9–11(II). Jupiter 1972: Perihelion of transfer orbit vs launch date, Type II

9–12(I). Jupiter 1972: Aphelion of transfer orbit vs launch date, Type I

9–12(II). Jupiter 1972: Aphelion of transfer orbit vs launch date, Type II

9–13(I). Jupiter 1972: Inclination of the heliocentric transfer plane vs launch date, Type I

9–13(II). Jupiter 1972: Inclination of the heliocentric transfer plane vs launch date, Type II

9–14(I). Jupiter 1972: Celestial latitude at arrival time vs launch date, Type I

9–14(II). Jupiter 1972: Celestial latitude at arrival time vs launch date, Type II

IX. JUPITER 1972: TRAJECTORY PARAMETER GRAPHS (Cont'd)

Figure

9–15(I). Jupiter 1972: Asymptotic speed with respect to Jupiter vs launch date, Type I

9–15(II). Jupiter 1972: Asymptotic speed with respect to Jupiter vs launch date, Type II

9–16. Jupiter 1972: Angle between incoming zeocentric asymptote and arrival planet's orbital plane vs launch date

9–17. Jupiter 1972: Angle between Jupiter–Sun vector and incoming zeocentric asymptote vs launch date

9–18. Jupiter 1972: Declination of zeocentric asymptote vs launch date

9–19(I). Jupiter 1972: Right ascension of zeocentric asymptote vs launch date, Type I

9–19(II). Jupiter 1972: Right ascension of zeocentric asymptote vs launch date, Type II

9–20(I). Jupiter 1972: Angle between planet–Earth vector and incoming asymptote vs launch date, Type I

9–20(II). Jupiter 1972: Angle between planet–Earth vector and incoming asymptote vs launch date, Type II

9–21(I). Jupiter 1972: Angle between planet–Canopus vector and incoming asymptote vs launch date, Type I

9–21(II). Jupiter 1972: Angle between planet–Canopus vector and incoming asymptote vs launch date, Type II

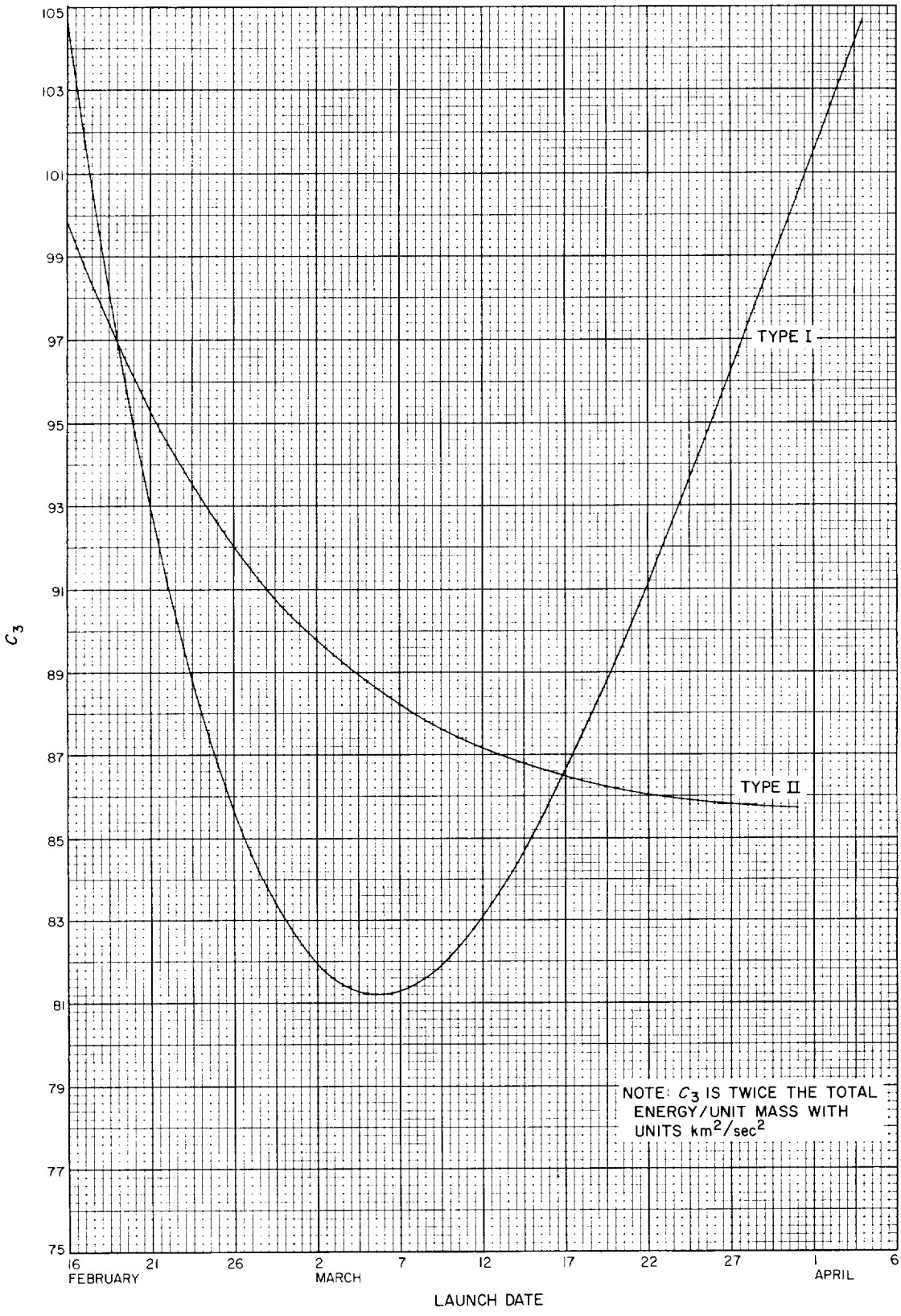

Fig. 9–1. Jupiter 1972: Minimum injection energy vs launch date

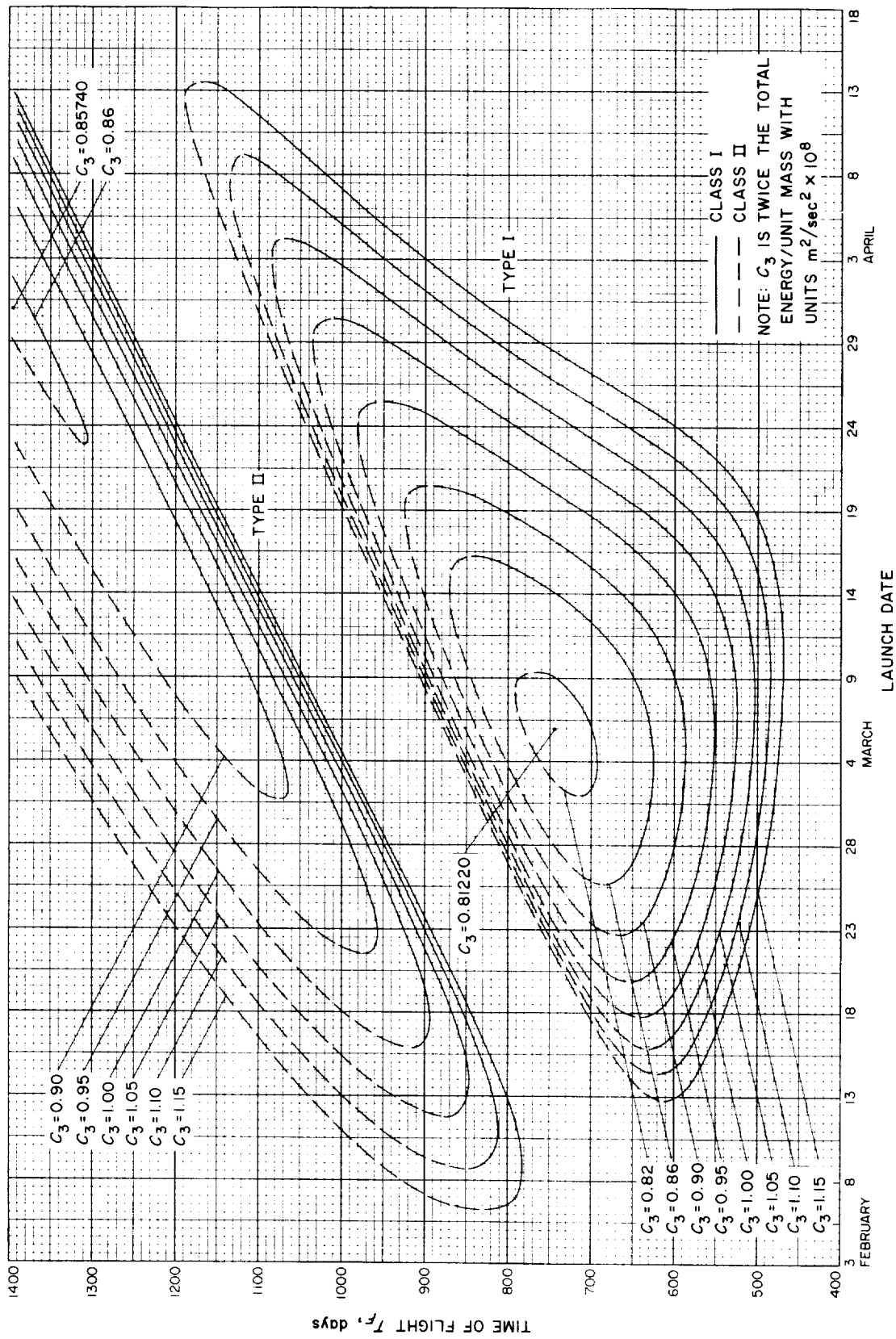

Fig. 9–2. Jupiter 1972: Time of flight vs launch date

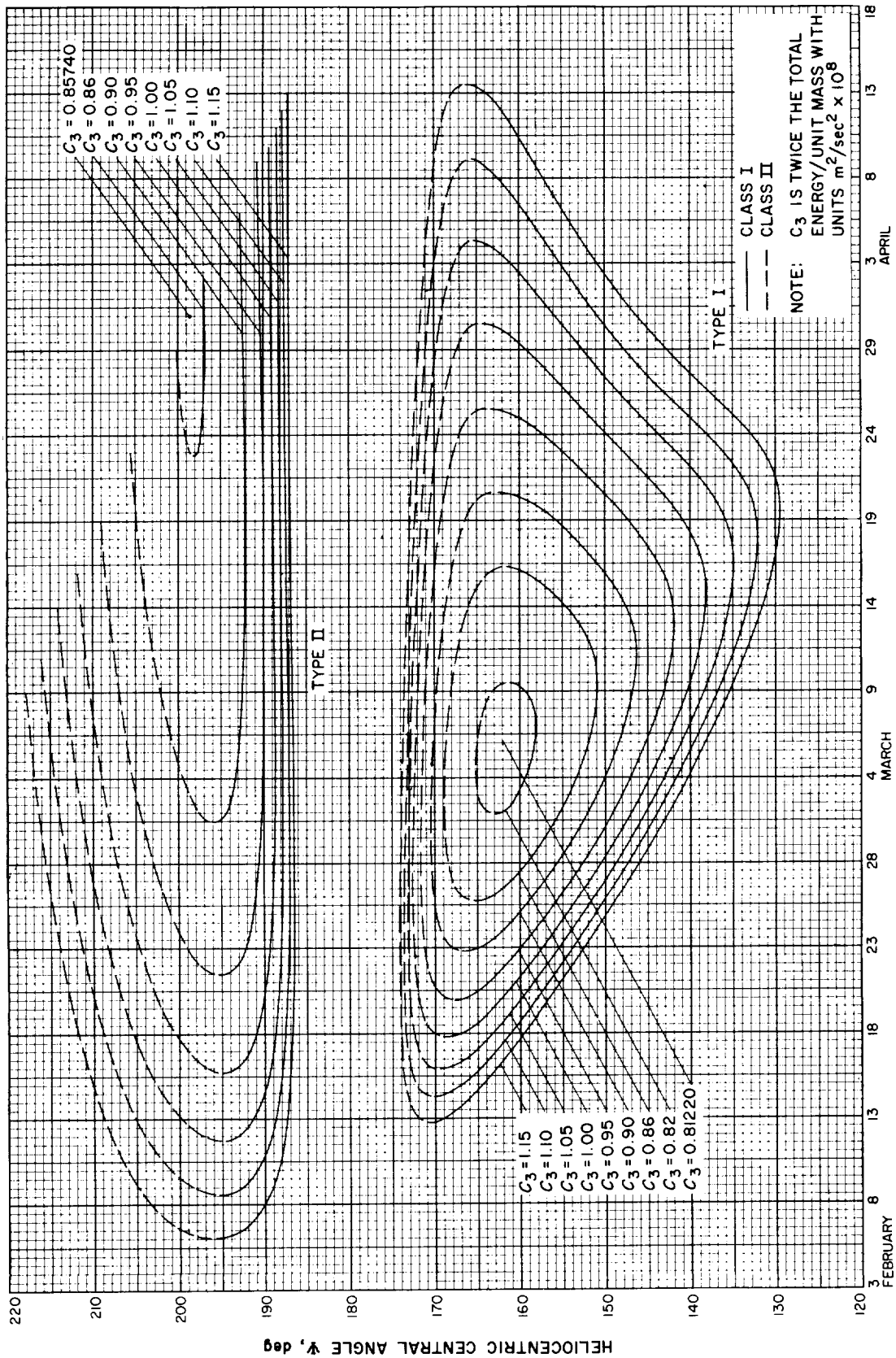

Fig. 9–3. Jupiter 1972: Heliocentric central angle vs launch date

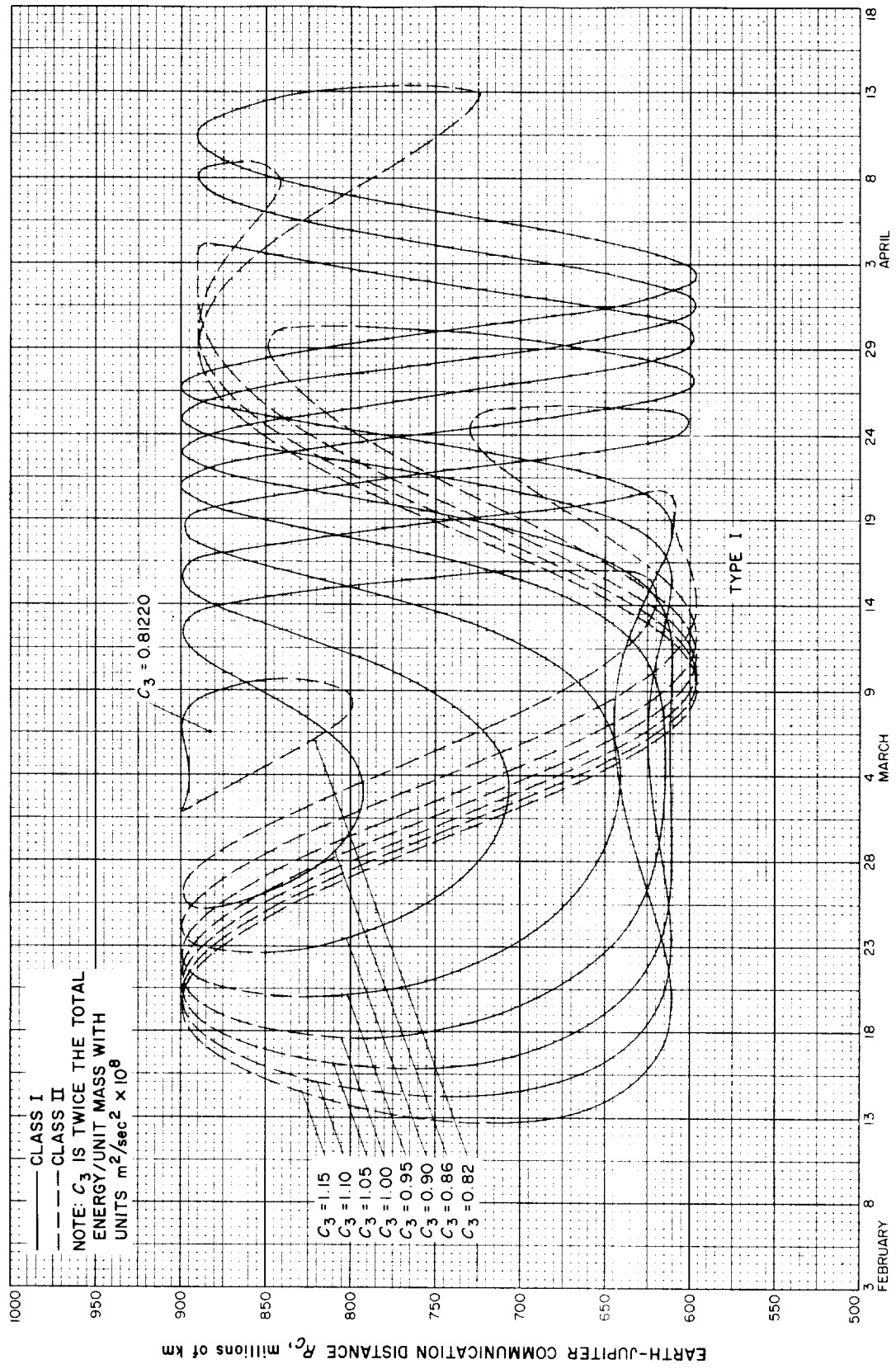

Fig. 9-4(I). Jupiter 1972: Earth–Jupiter communication distance vs launch date, Type I

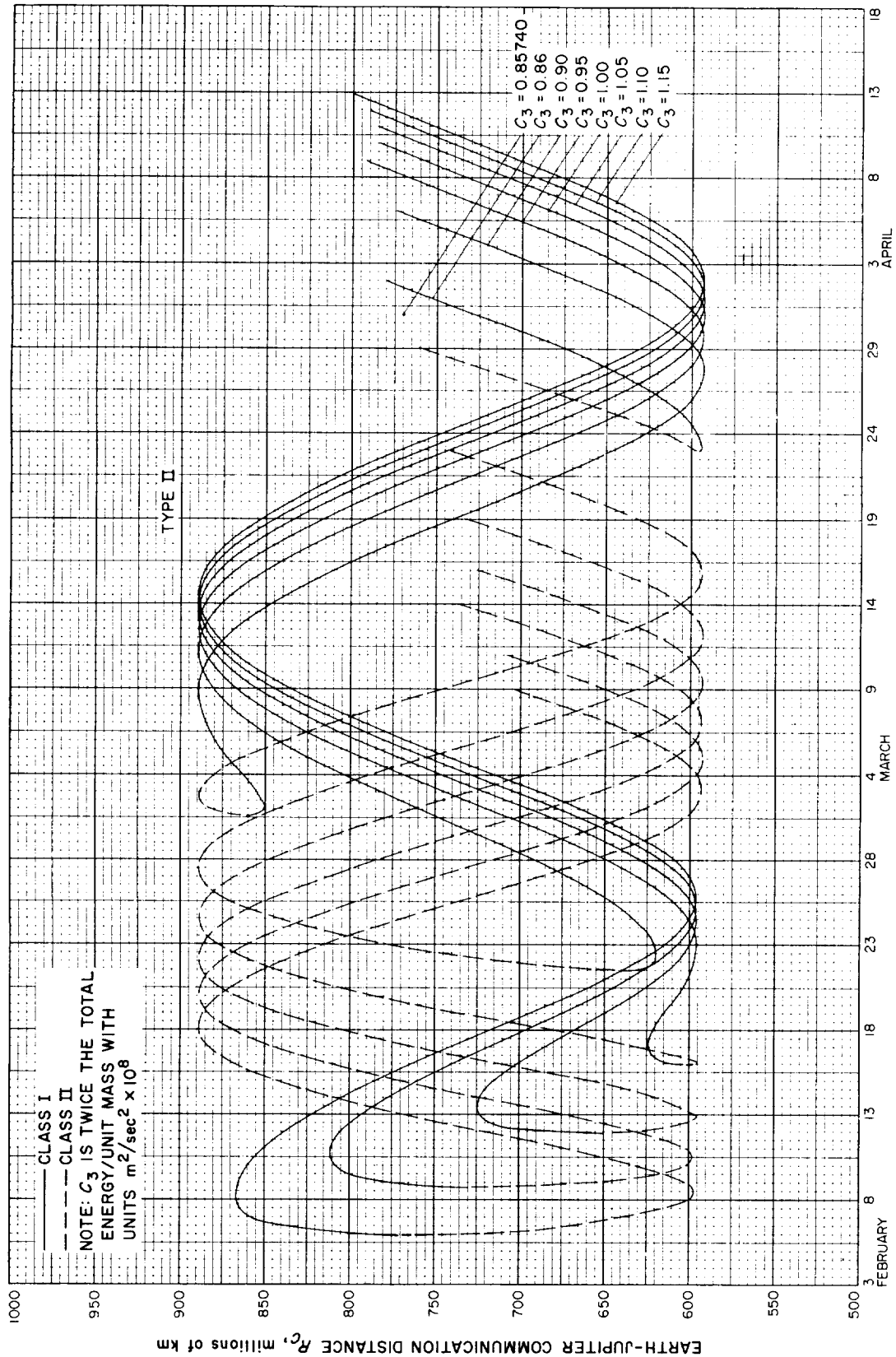

Fig. 9-4(II). Jupiter 1972: Earth–Jupiter communication distance vs launch date, Type II

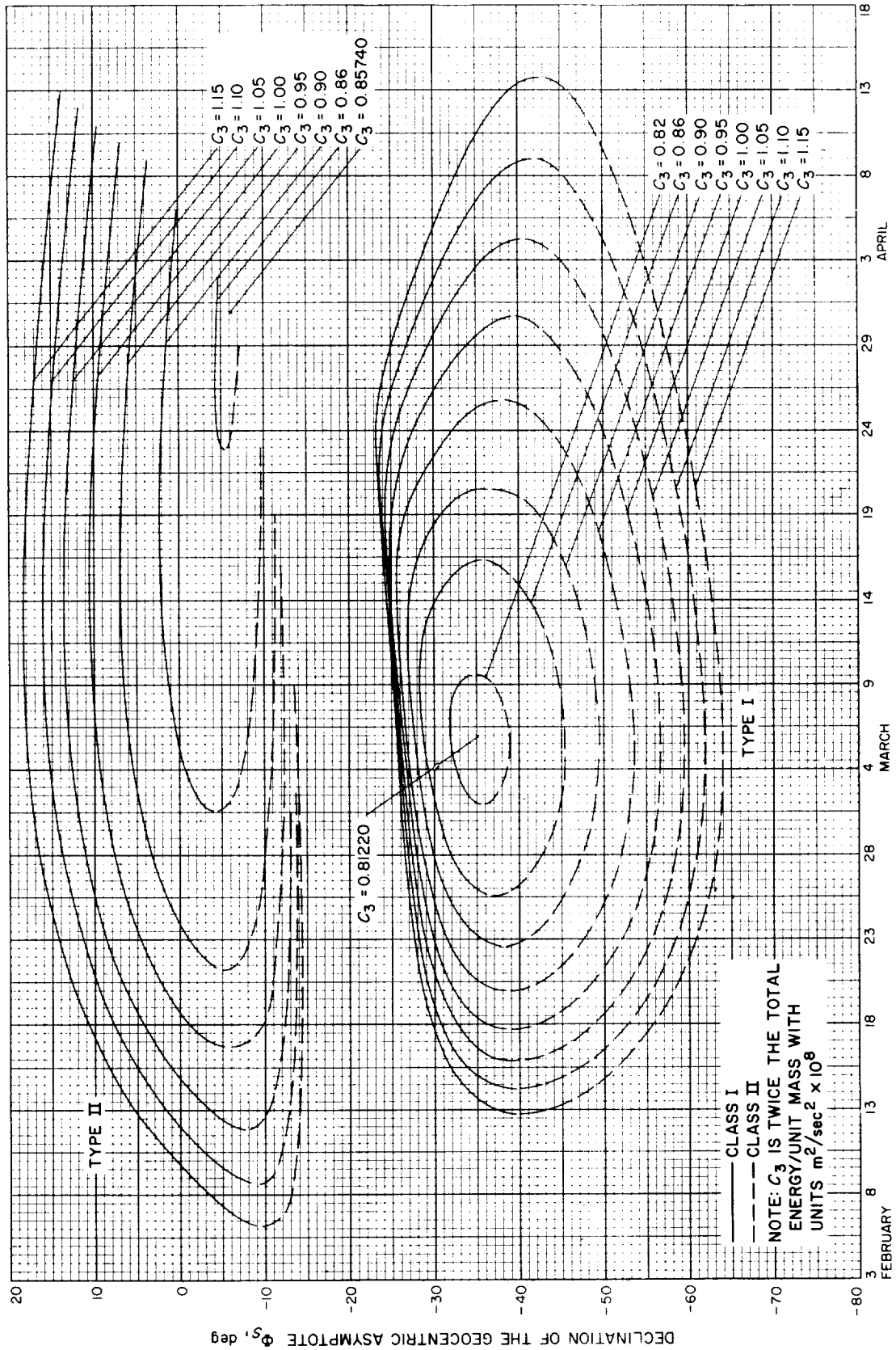

Fig. 9-5. Jupiter 1972: Declination of the geocentric asymptote vs launch date

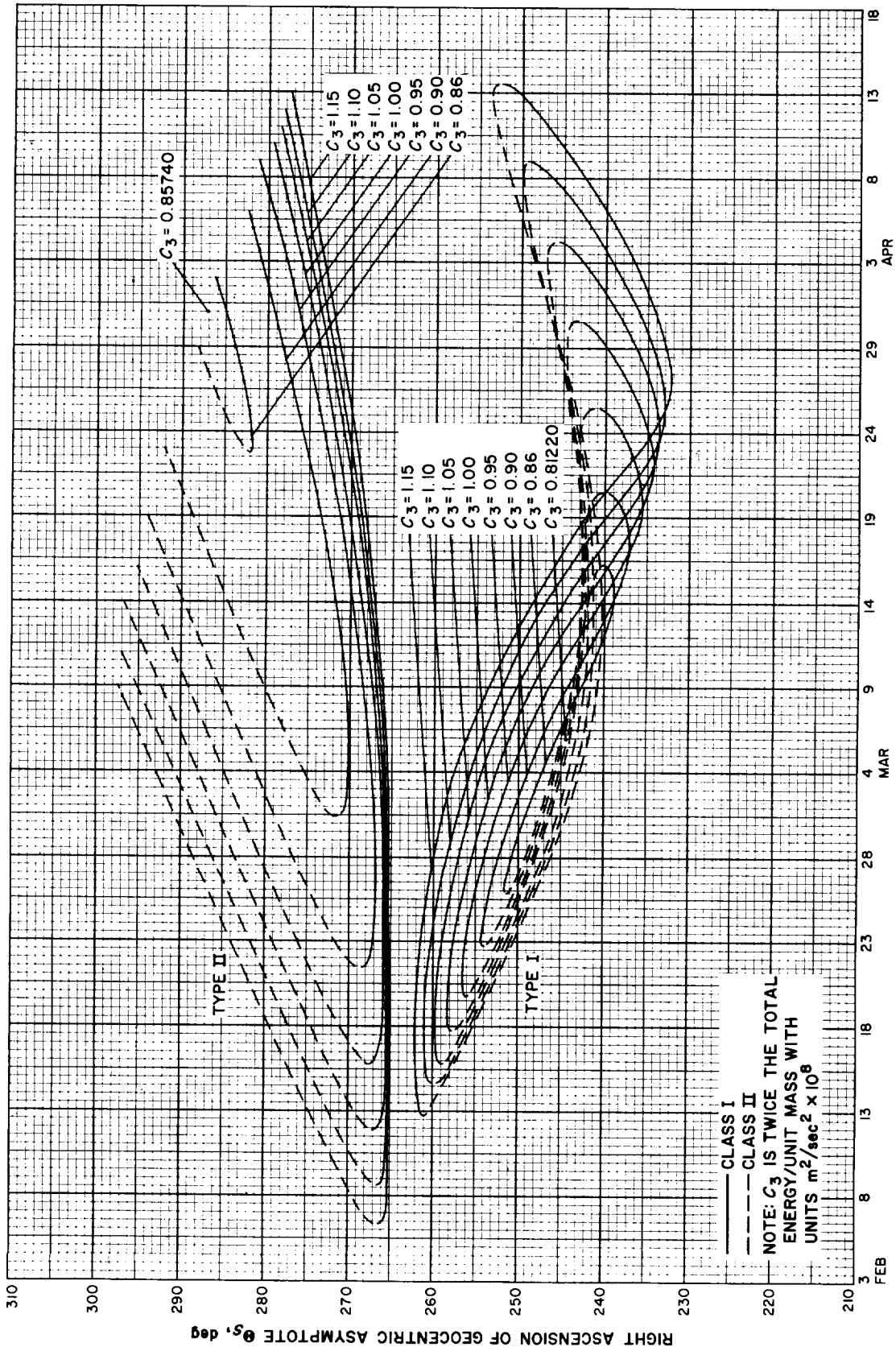

Fig. 9-6. Jupiter 1972: Right ascension of geocentric asymptote vs launch date

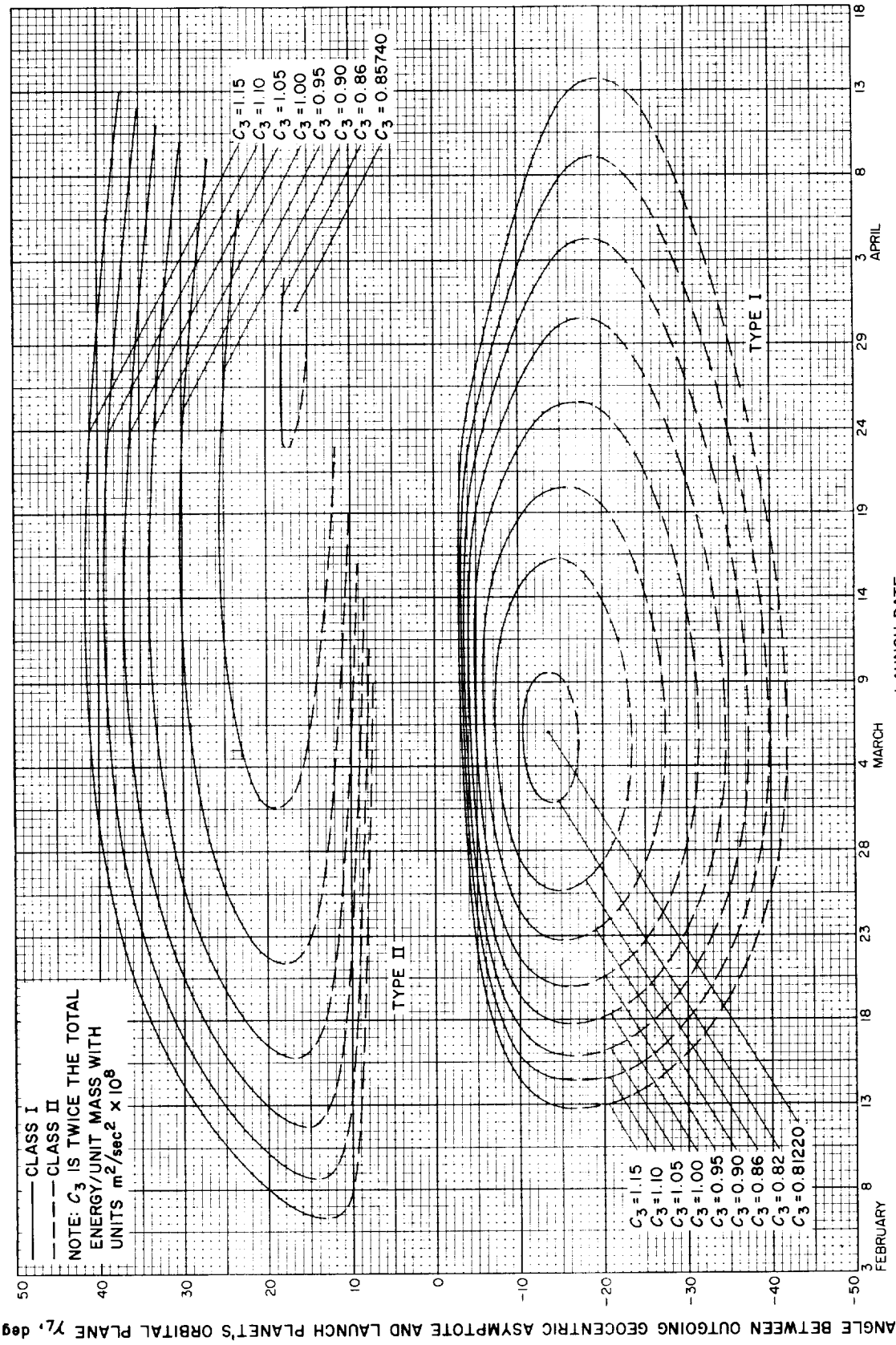

Fig. 9-7. Jupiter 1972: Angle between outgoing geocentric asymptote and launch planet's orbital plane vs launch date

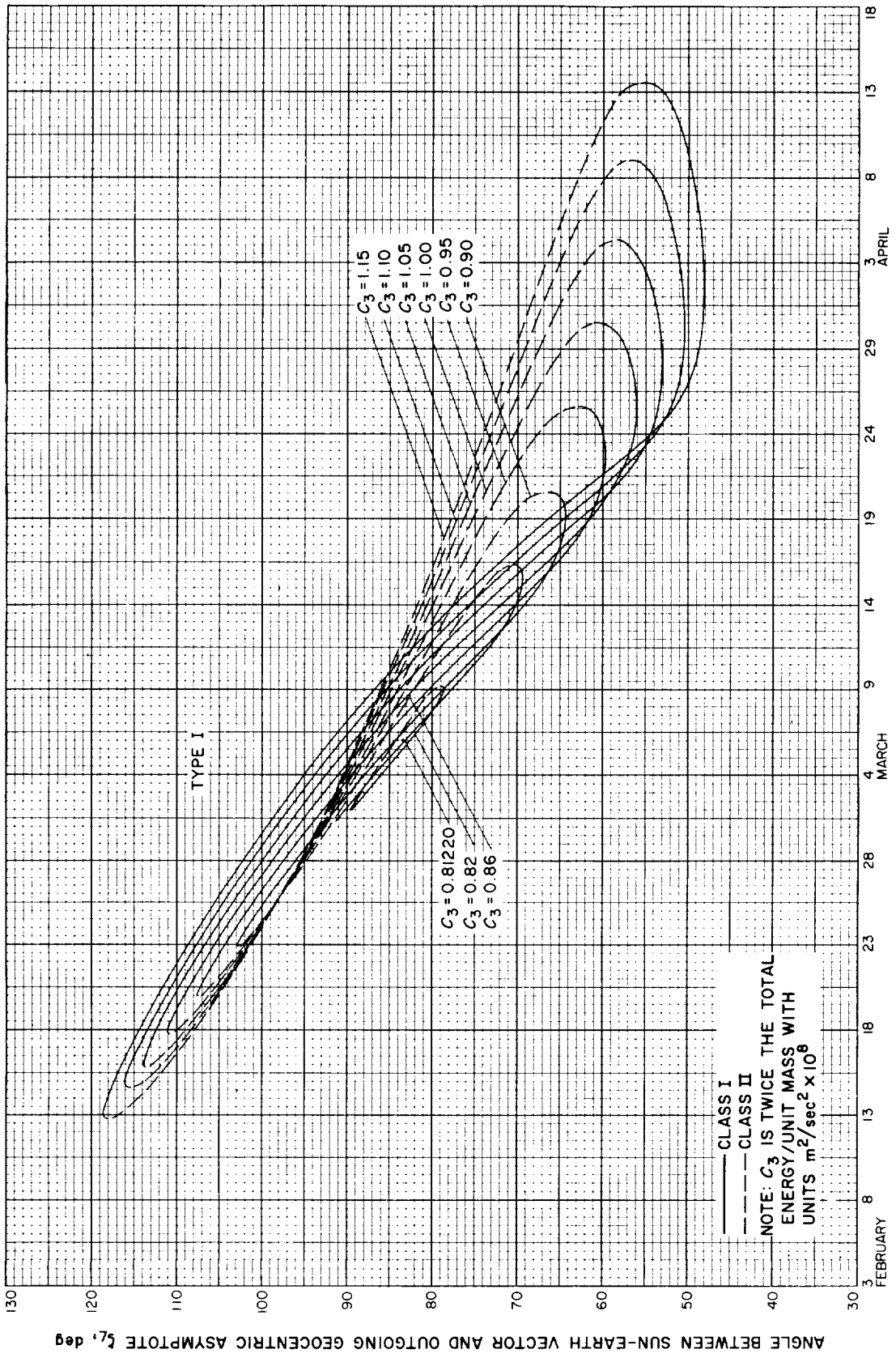

Fig. 9-8(I). Jupiter 1972: Angle between Sun–Earth vector and outgoing geocentric asymptote vs launch date, Type I

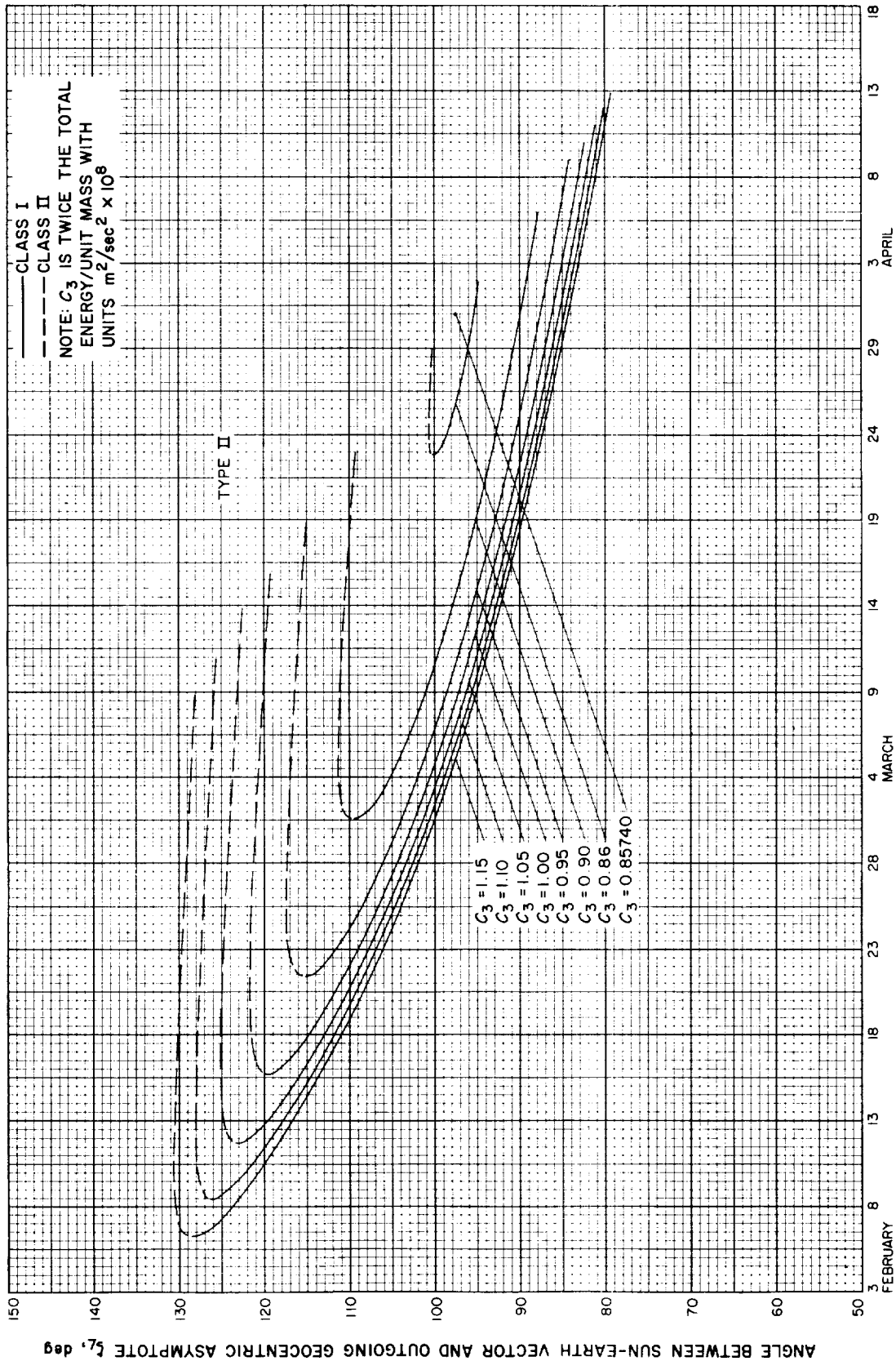

Fig. 9-8(II). Jupiter 1972: Angle between Sun–Earth vector and outgoing geocentric asymptote vs launch date, Type II

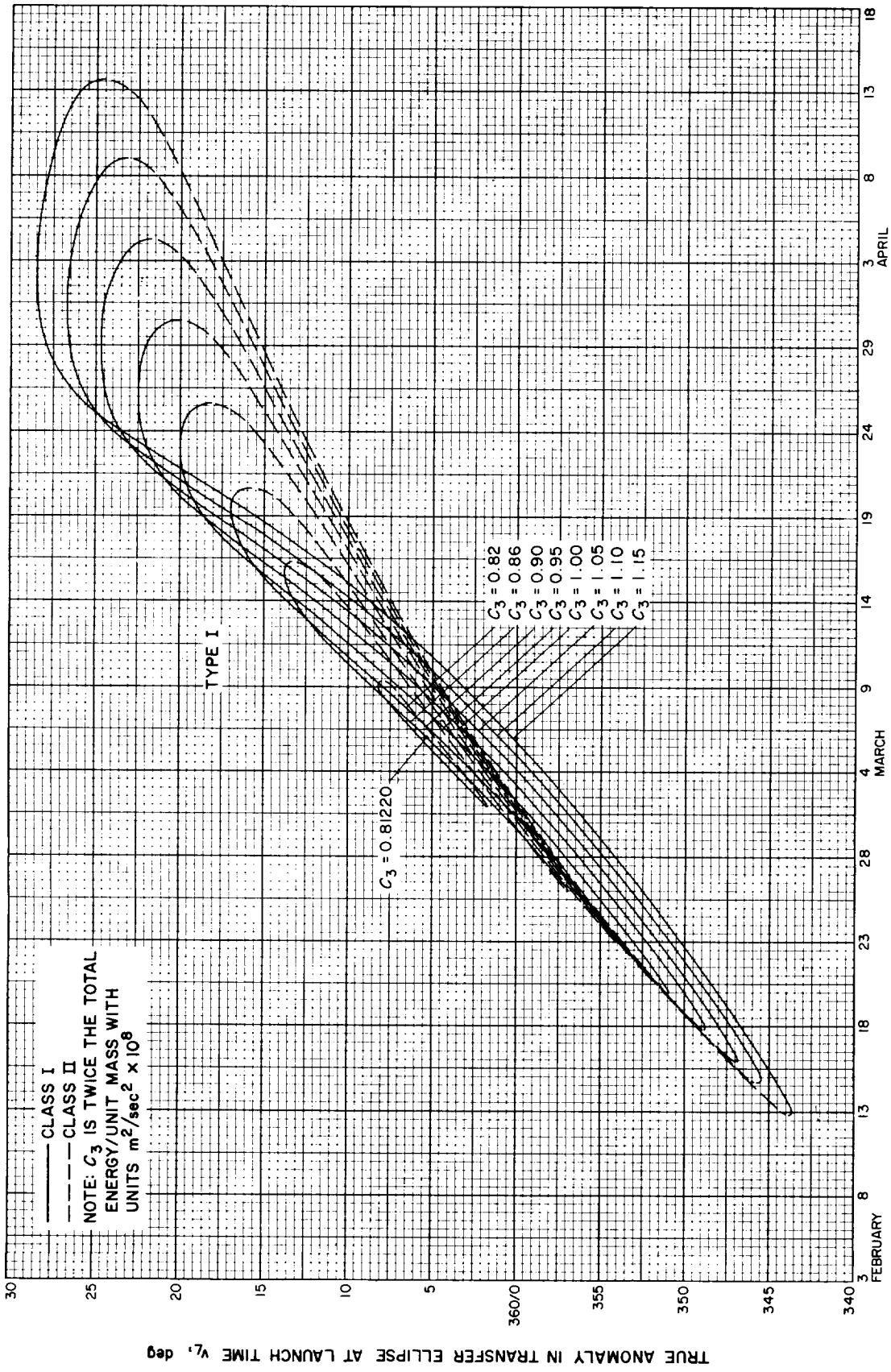

Fig. 9-9(1). Jupiter 1972: True anomaly in transfer ellipse at launch time vs launch date, Type I

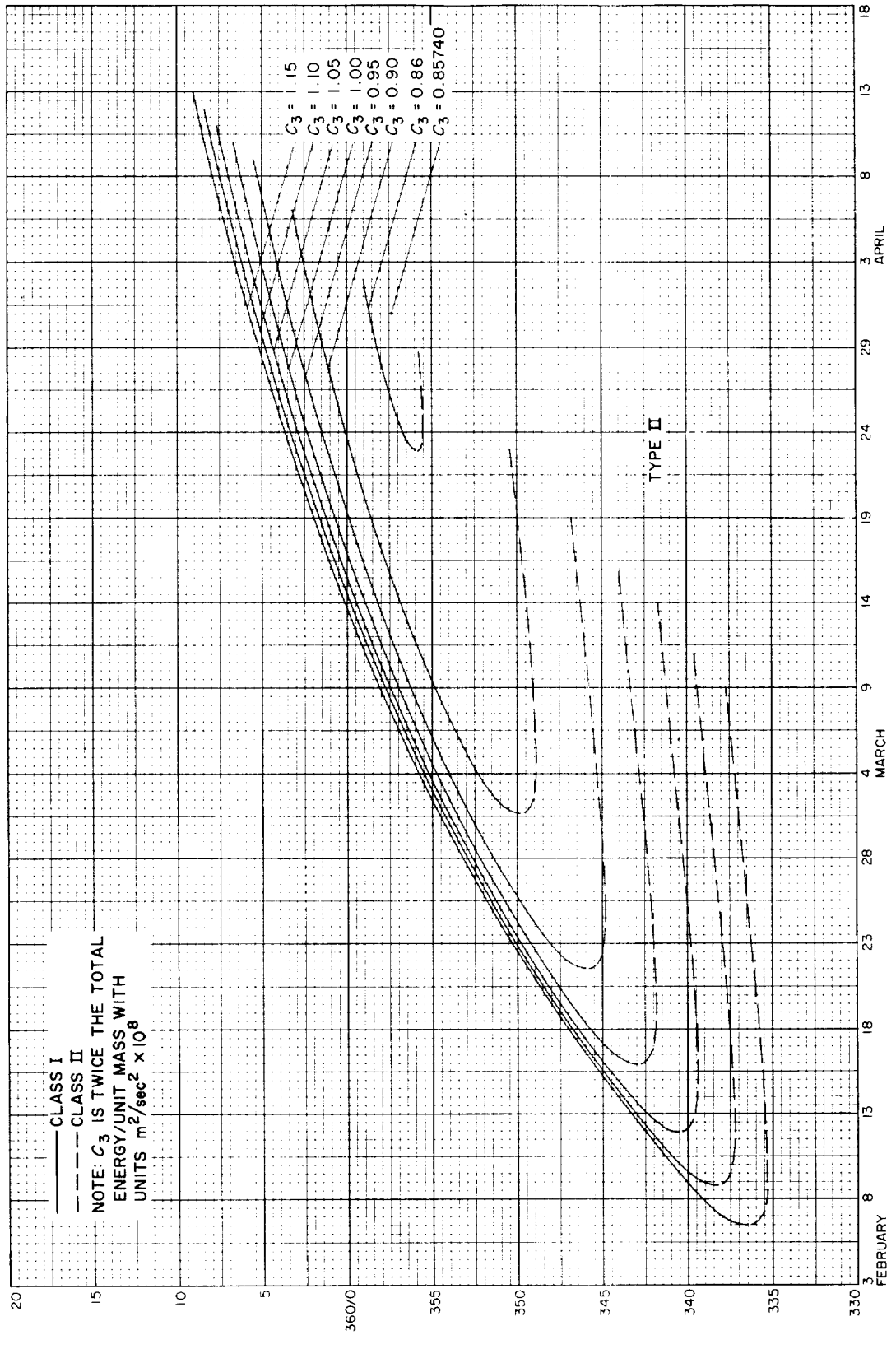

Fig. 9-9(III). Jupiter 1972: True anomaly in transfer ellipse at launch time vs launch date, Type II

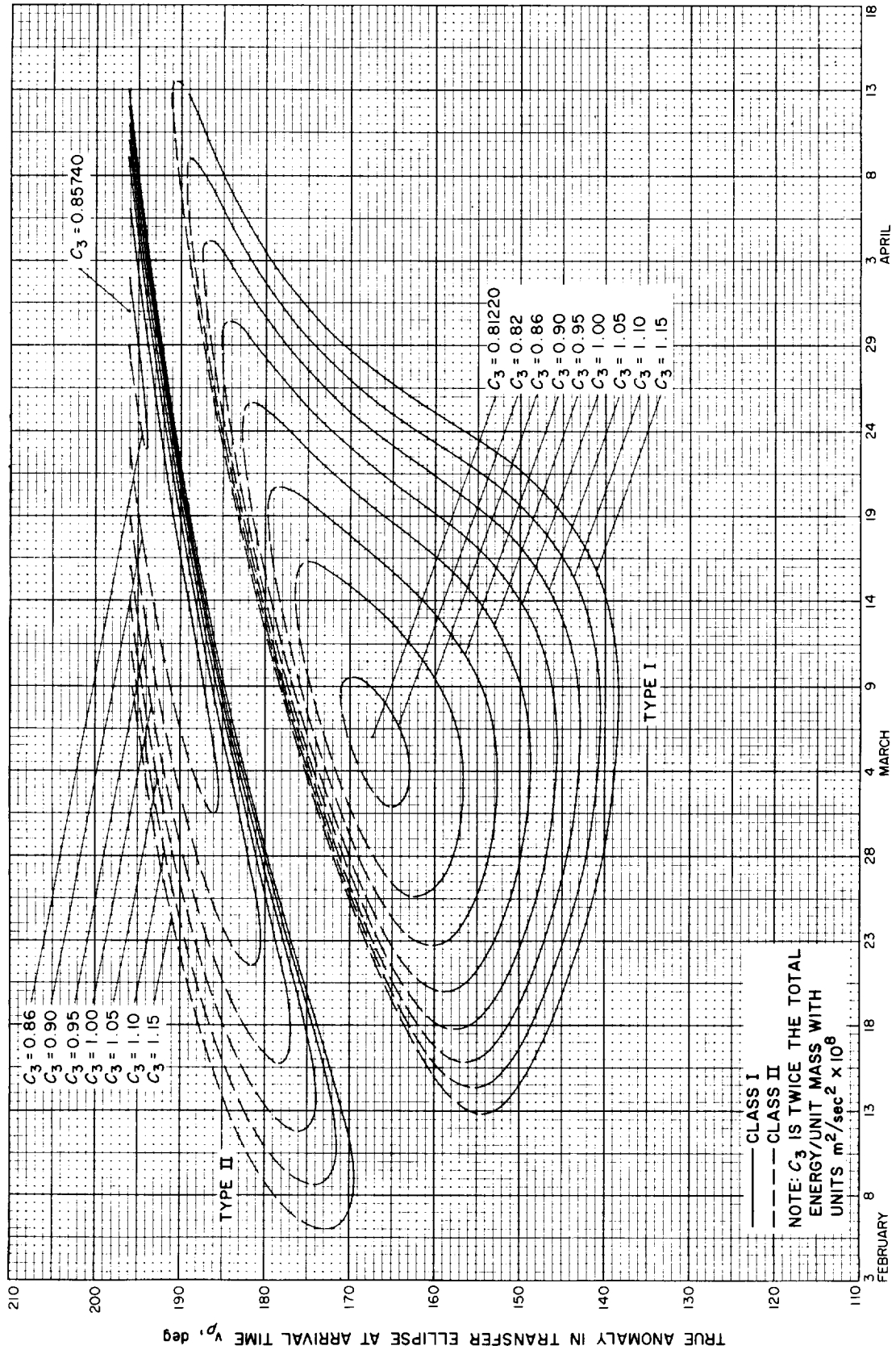

Fig. 9–10. Jupiter 1972: True anomaly in transfer ellipse at arrival time vs launch date

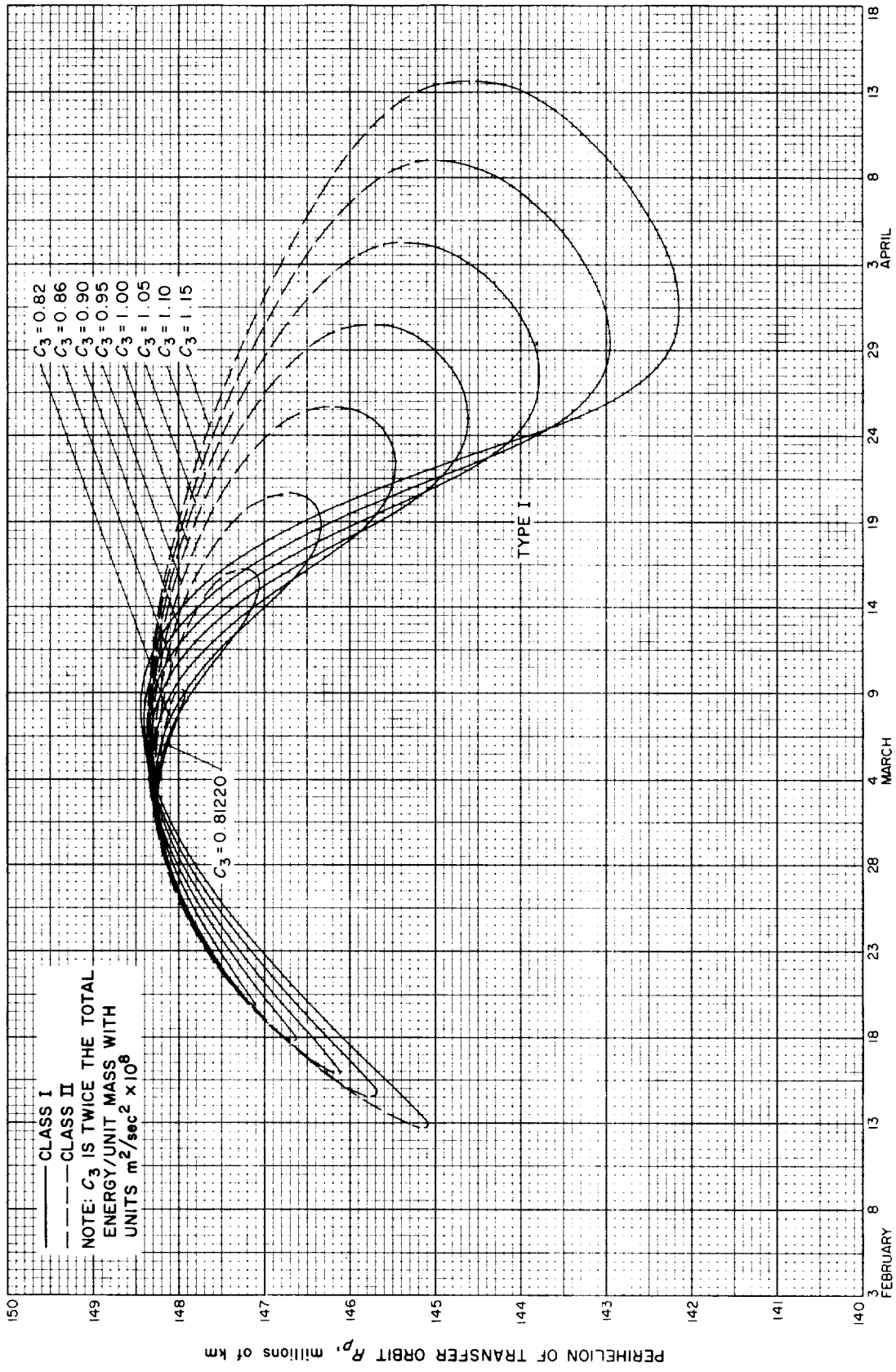

Fig. 9–11(I). Jupiter 1972: Perihelion of transfer orbit vs launch date, Type I

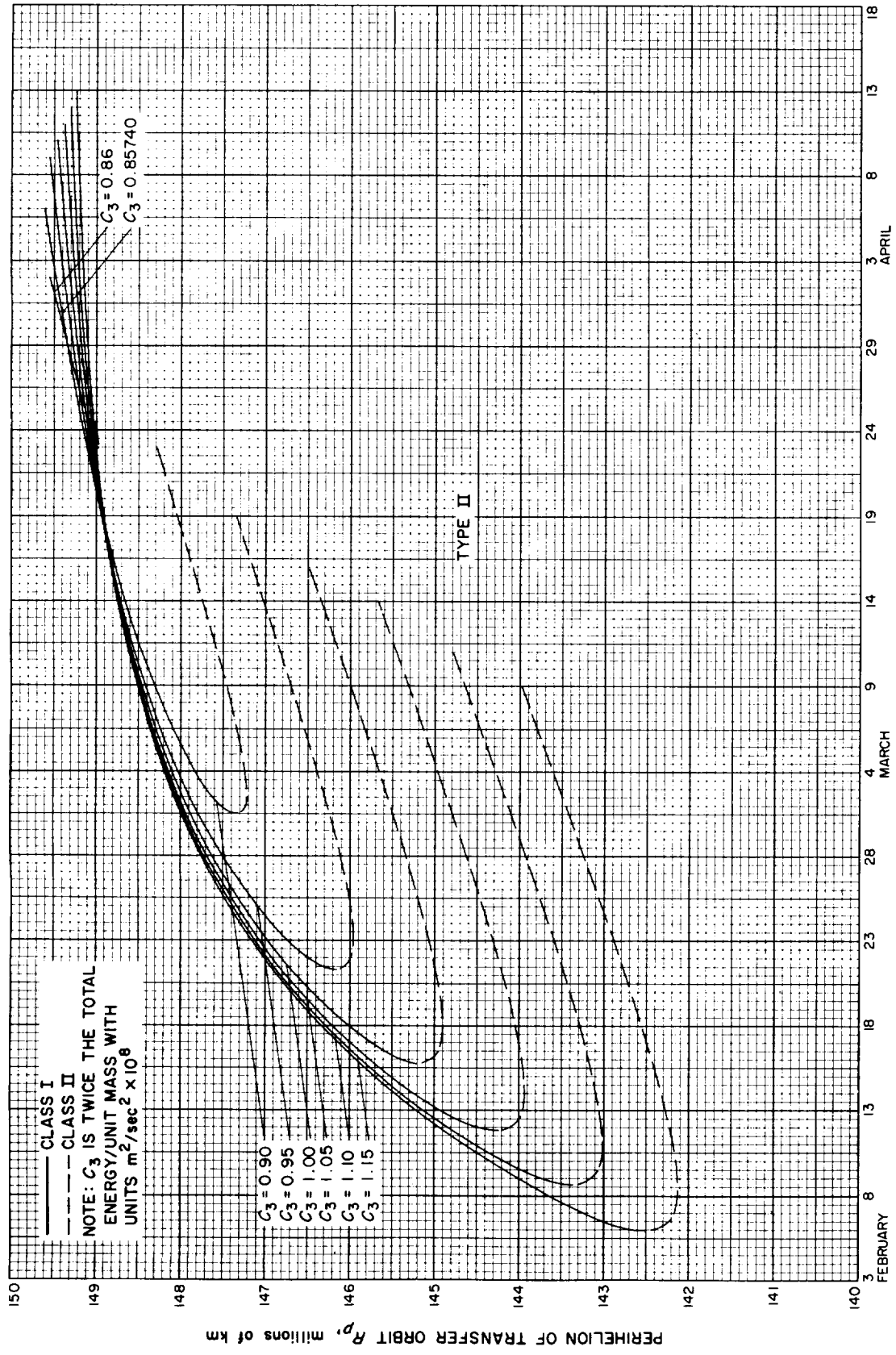

Fig. 9–11(II). Jupiter 1972: Perihelion of transfer orbit vs launch date, Type II

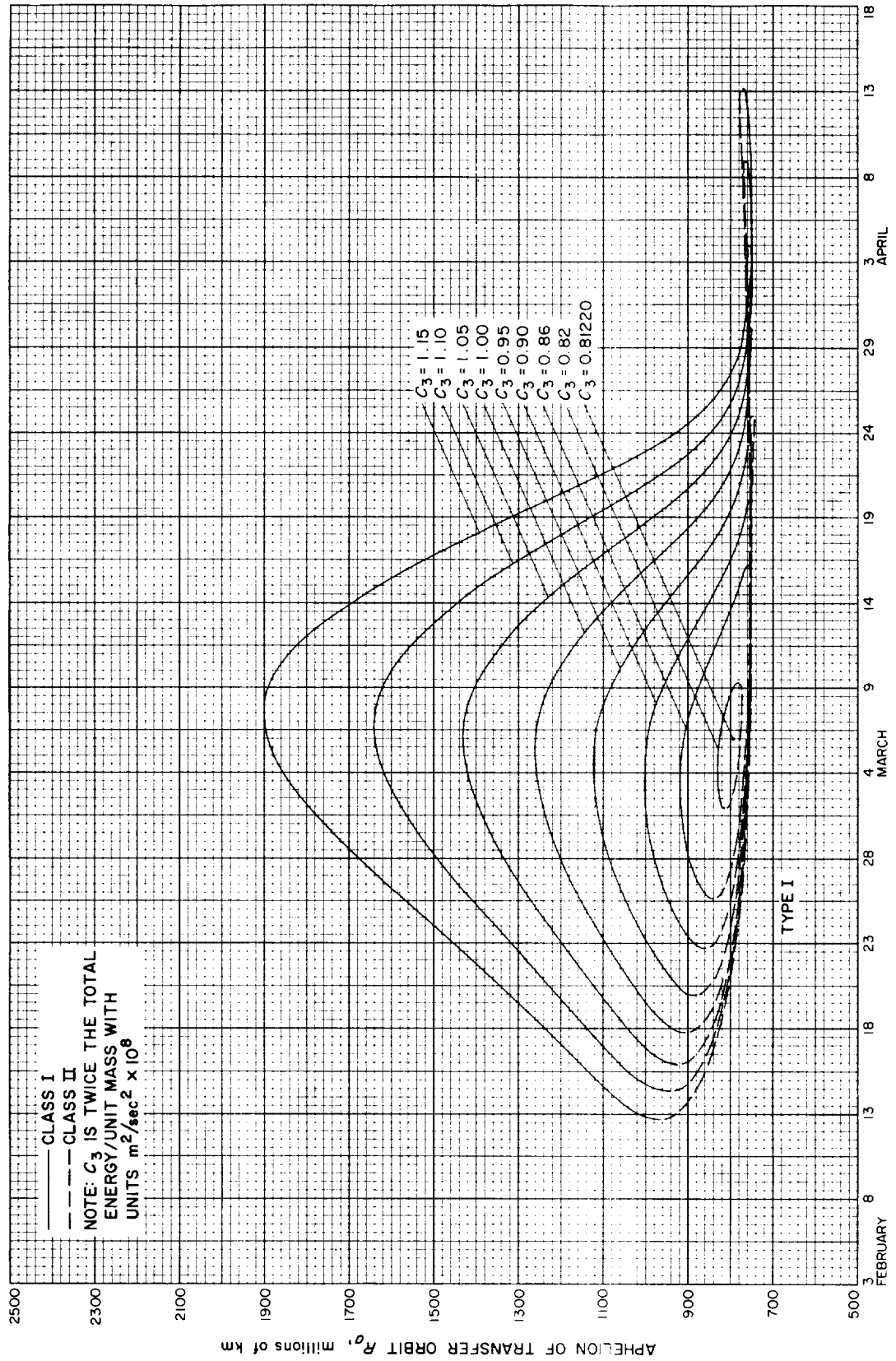

Fig. 9–12(I). Jupiter 1972: Aphelion of transfer orbit vs launch date, Type I

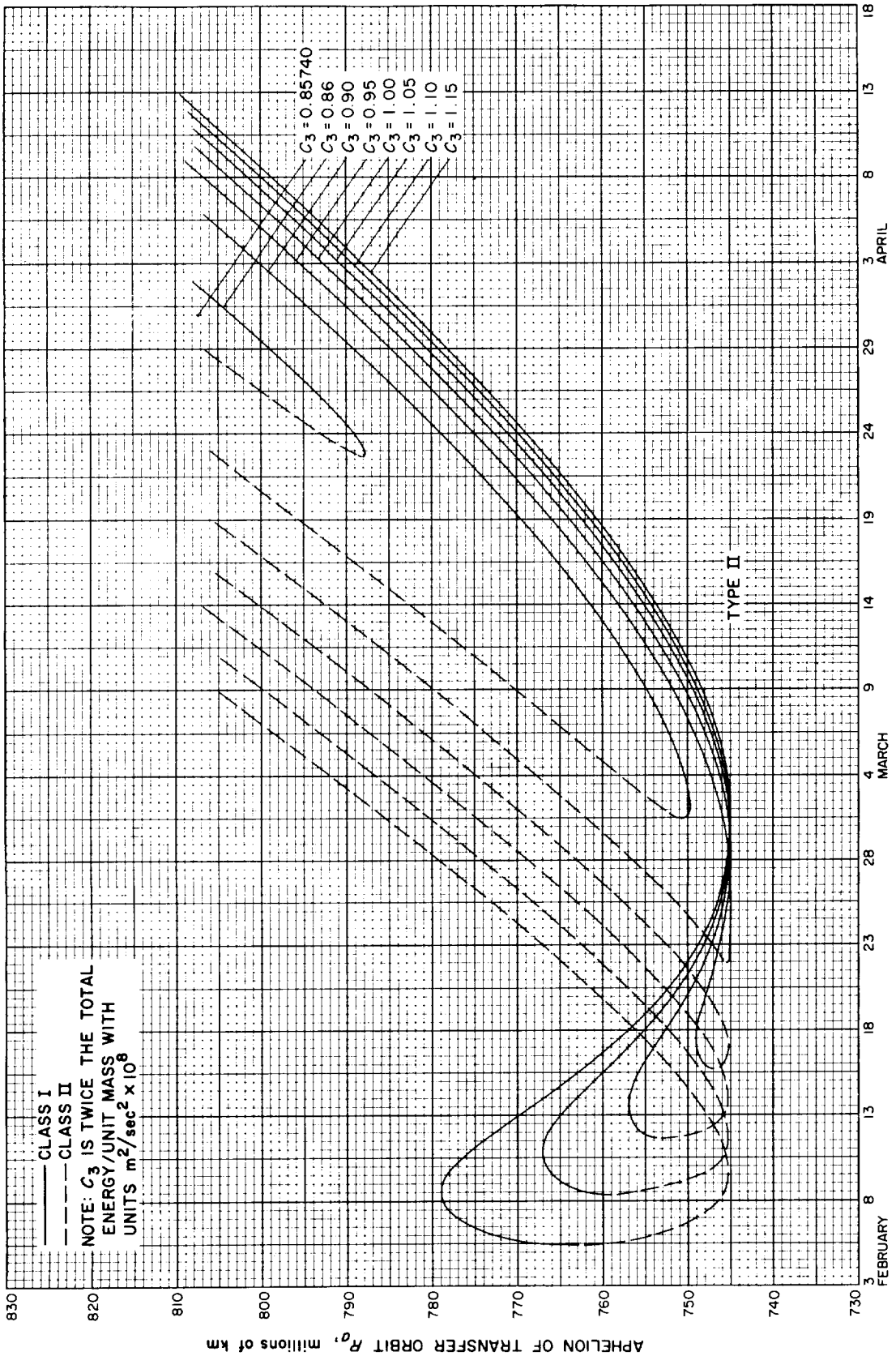

Fig. 9-12(II). Jupiter 1972: Aphelion of transfer orbit vs launch date, Type II

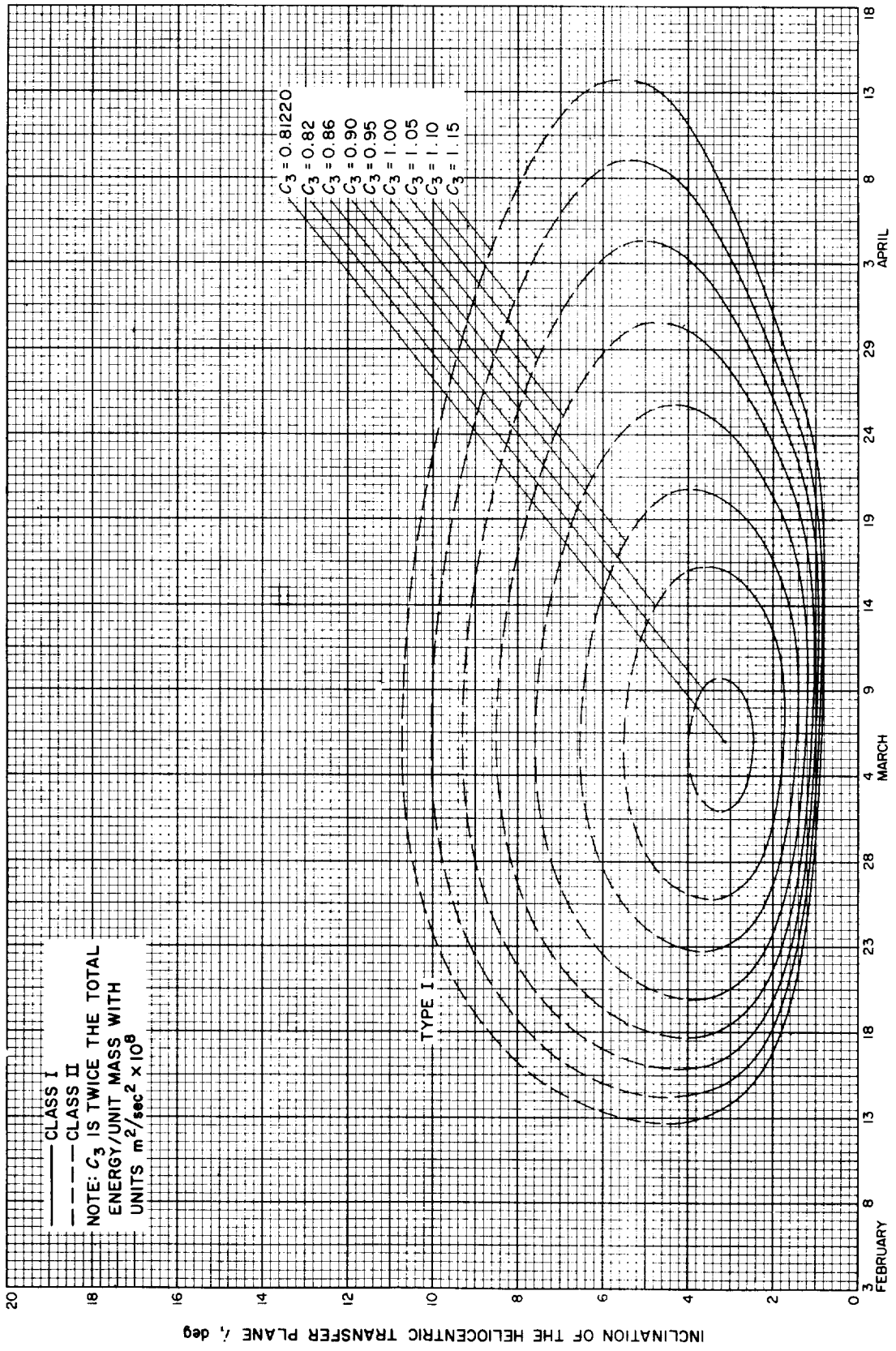

Fig. 9–13(I). Jupiter 1972: Inclination of the heliocentric transfer plane vs launch date, Type I

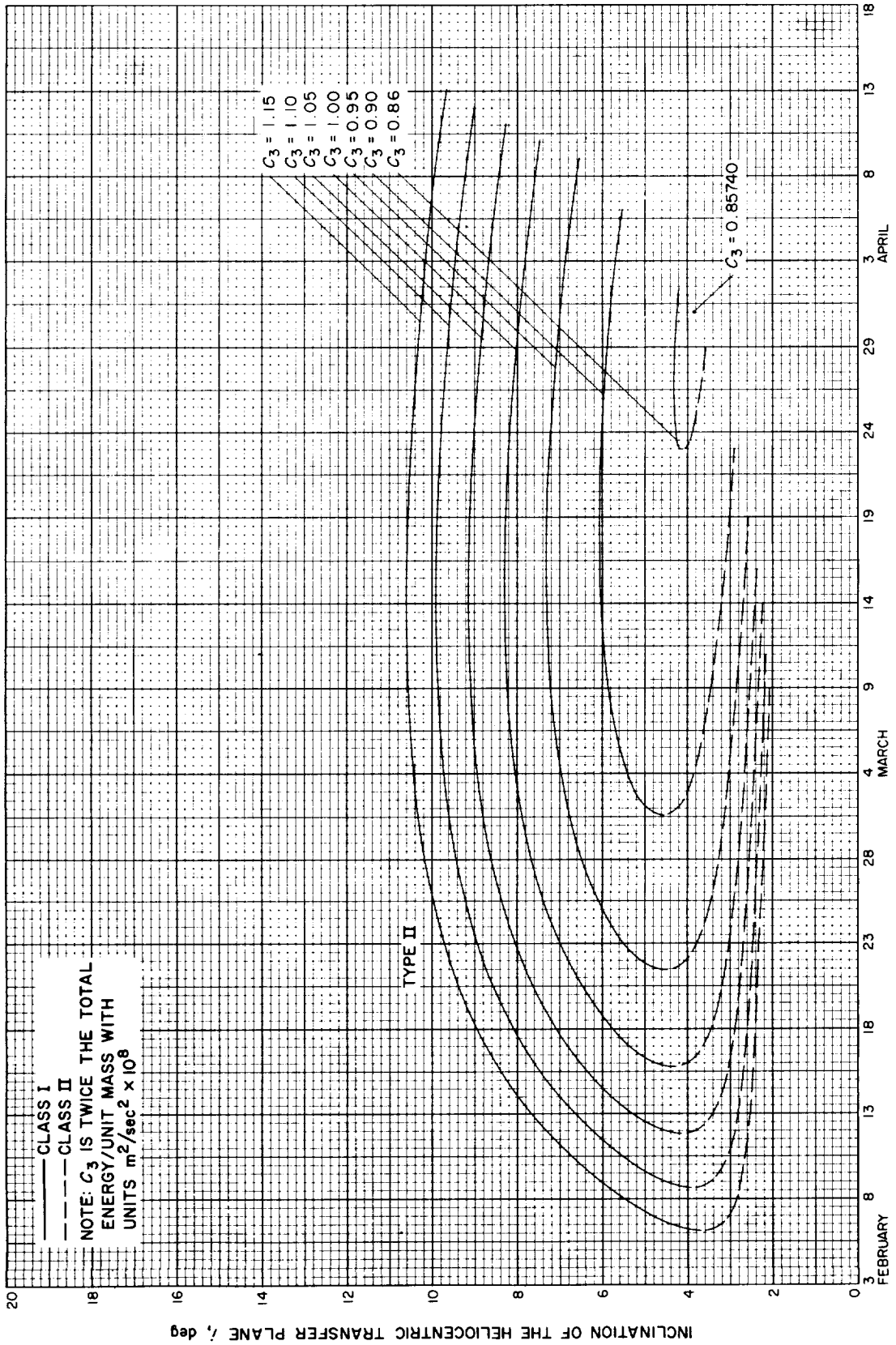

Fig. 9-13(II). Jupiter 1972: Inclination of the heliocentric transfer plane vs launch date, Type II

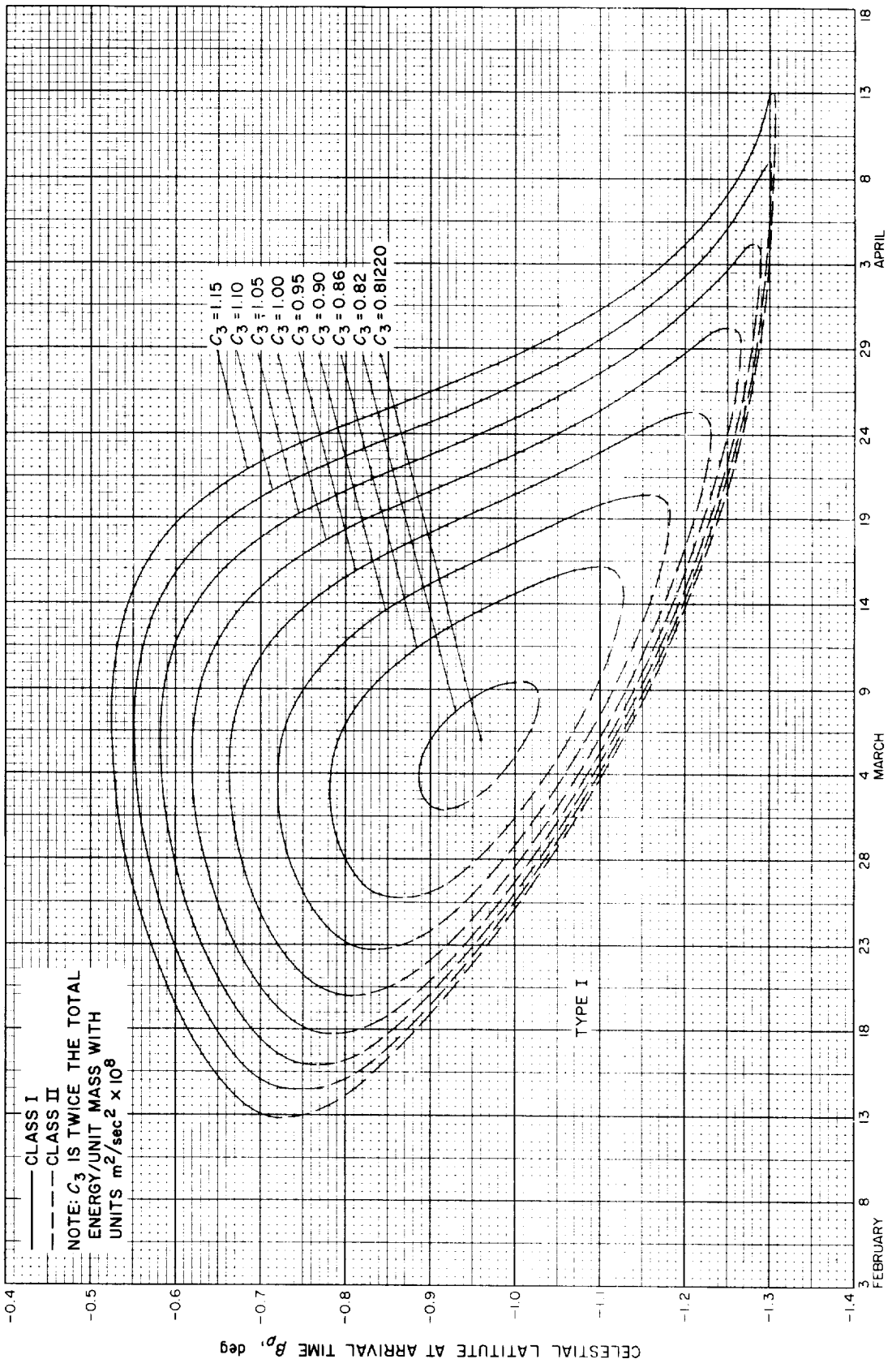

Fig. 9-14(I). Jupiter 1972: Celestial latitude at arrival time vs launch date, Type I

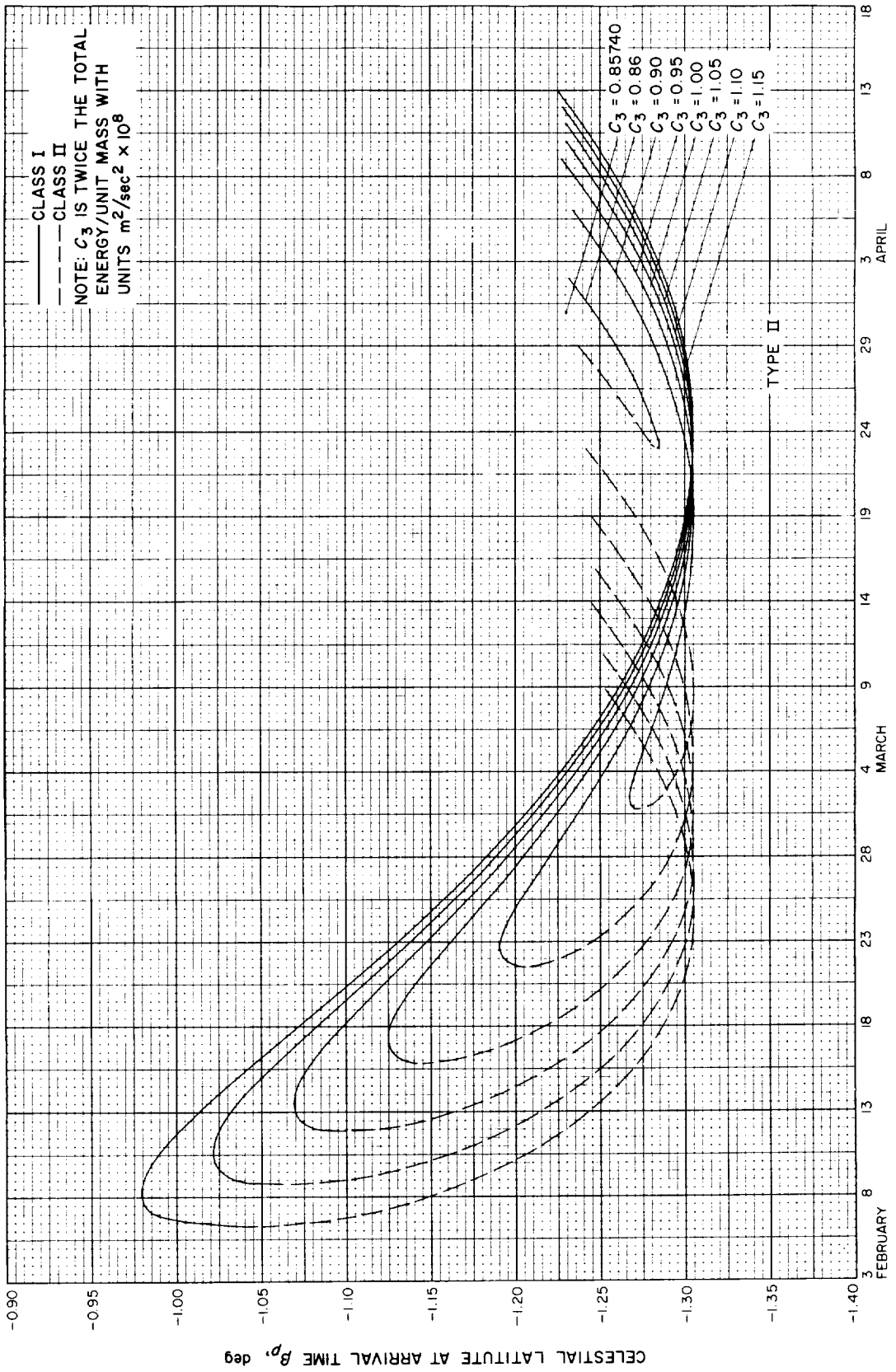

Fig. 9–14(III). Jupiter 1972: Celestial latitude at arrival time vs launch date, Type II

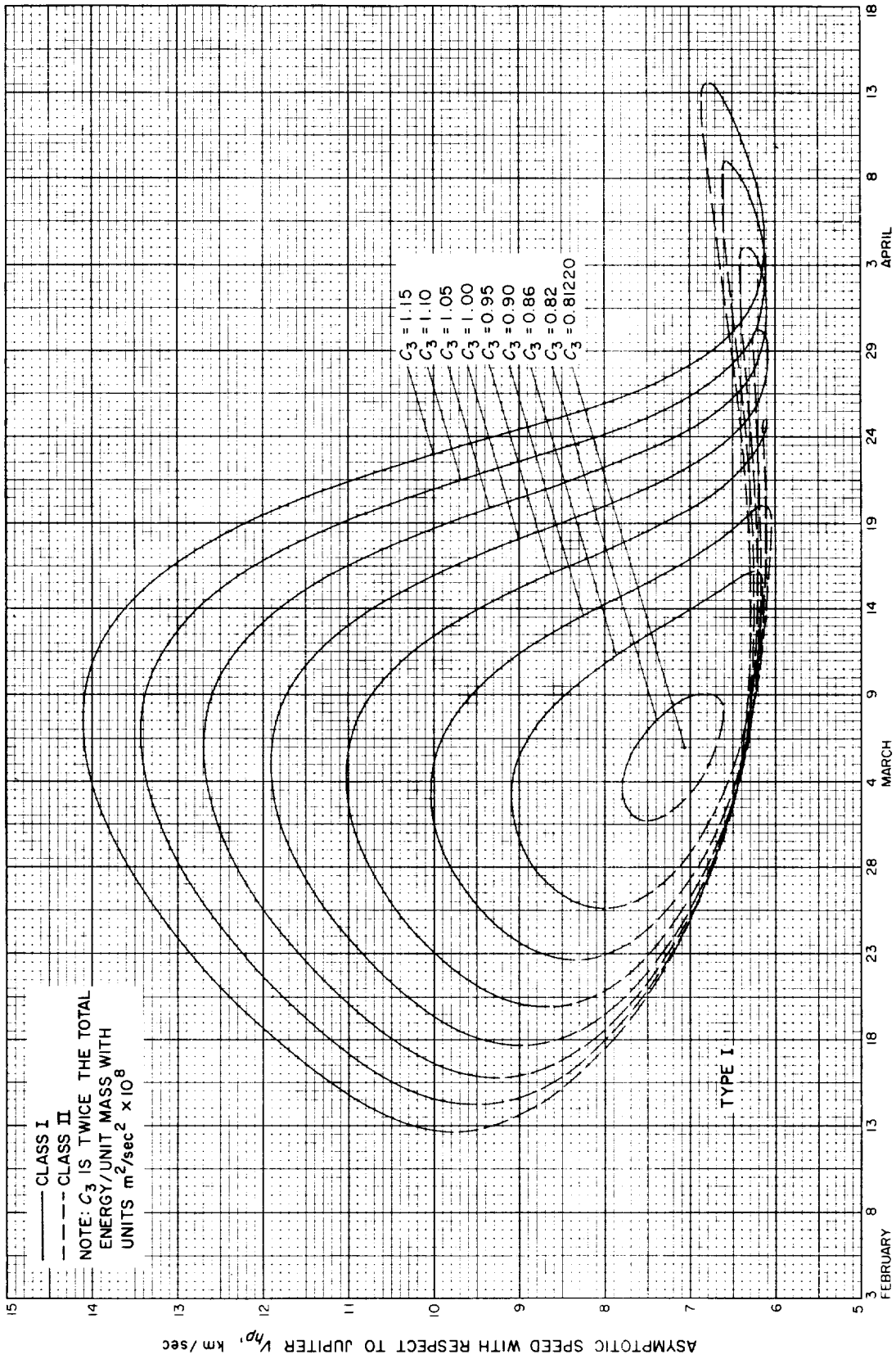

Fig. 9-15(I). Jupiter 1972: Asymptotic speed with respect to Jupiter vs launch date, Type I

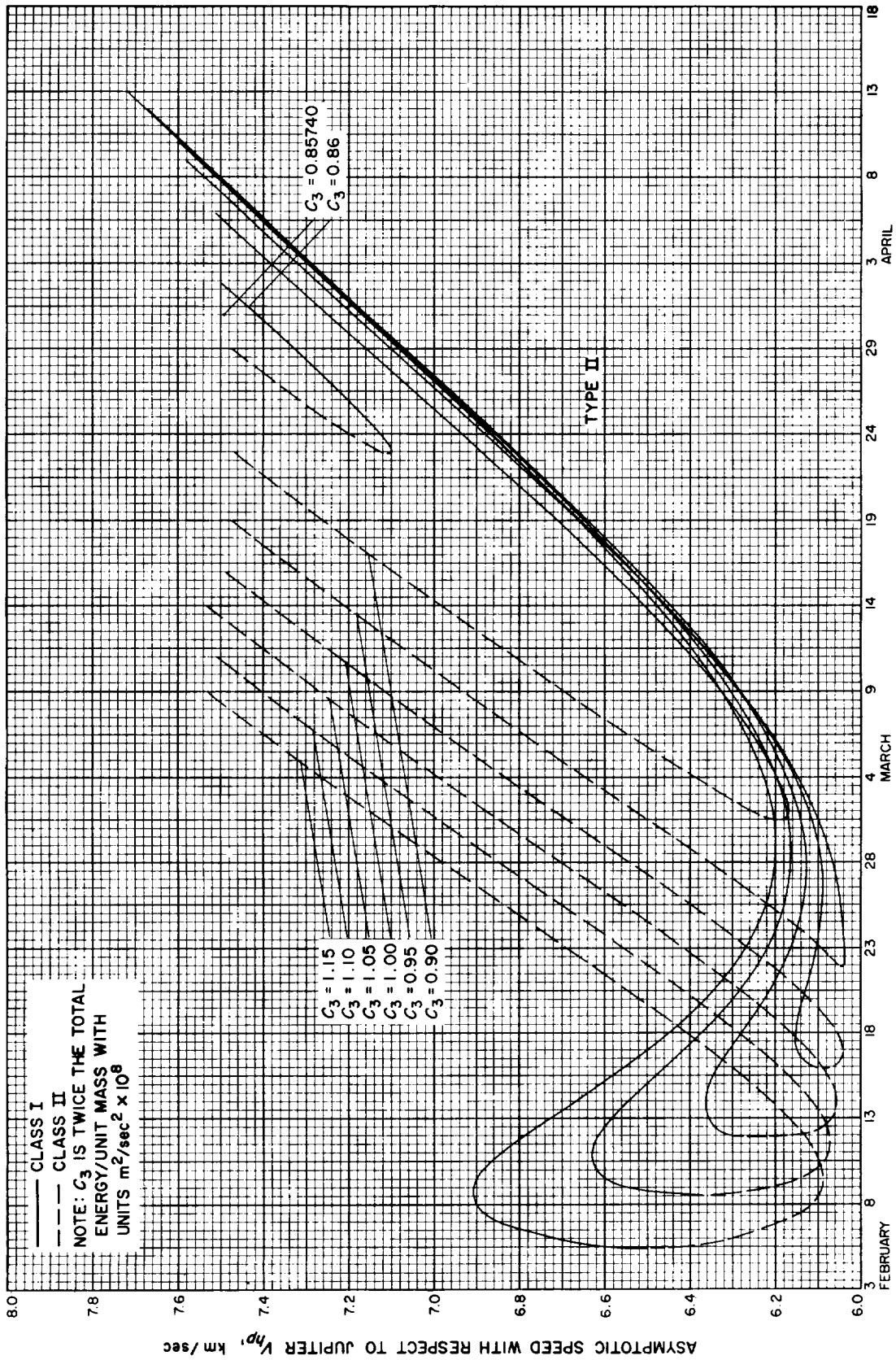

Fig. 9-15(II). Jupiter 1972: Asymptotic speed with respect to Jupiter vs launch date, Type II

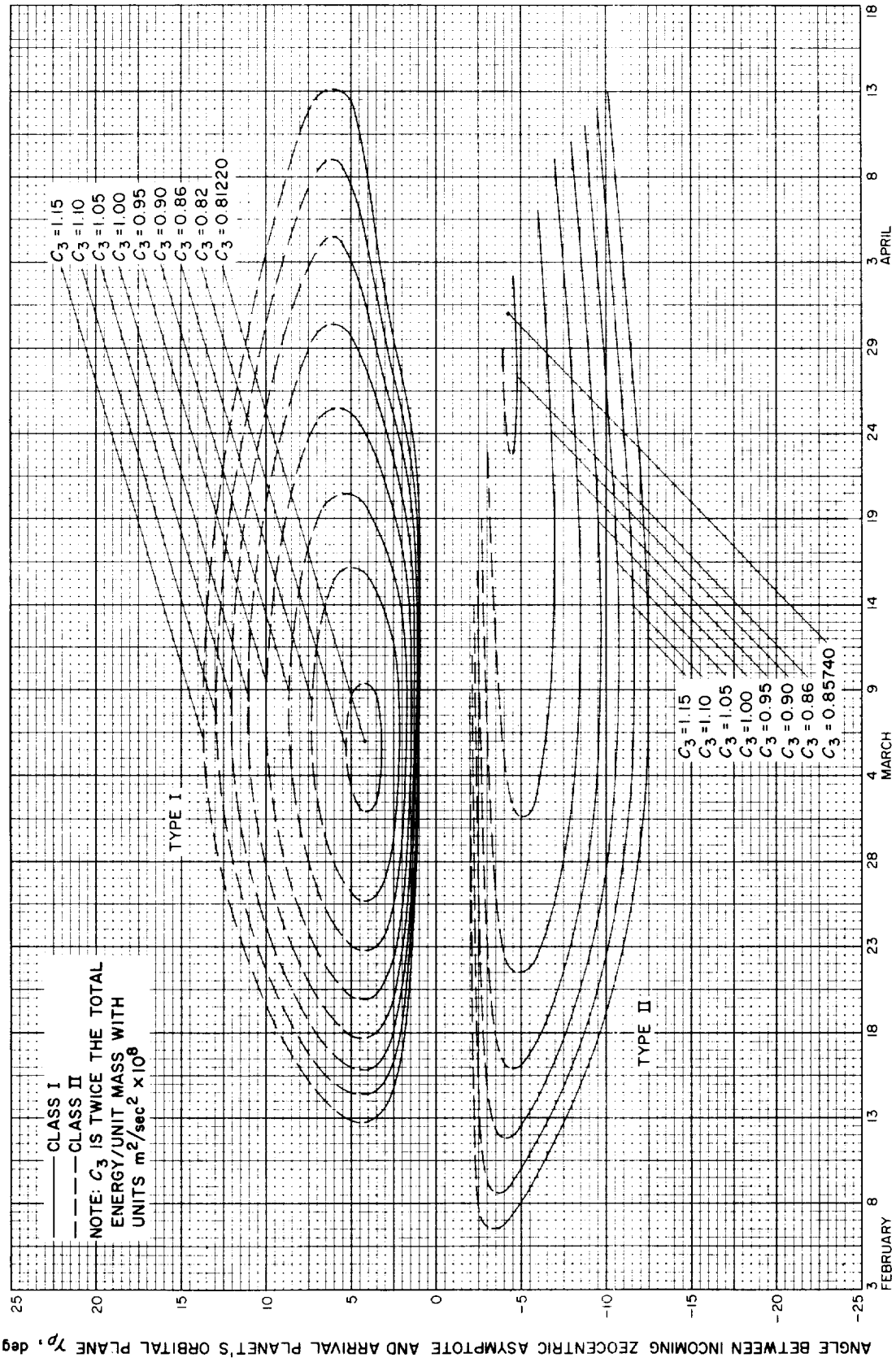

Fig. 9–16. Jupiter 1972: Angle between incoming zeocentric asymptote and arrival planet's orbital plane vs launch date

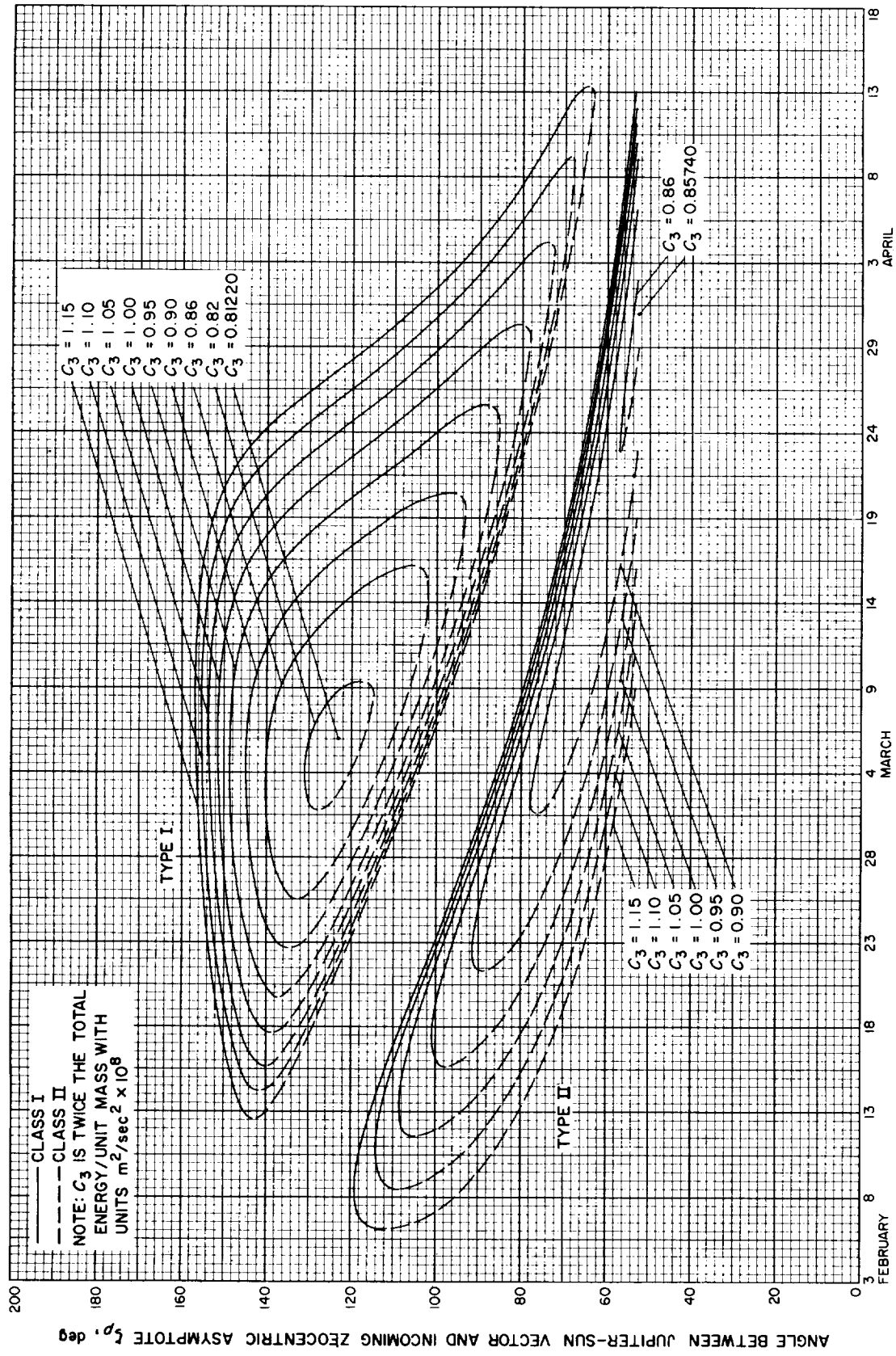

Fig. 9–17. Jupiter 1972: Angle between Jupiter–Sun vector and incoming zeocentric asymptote vs launch date

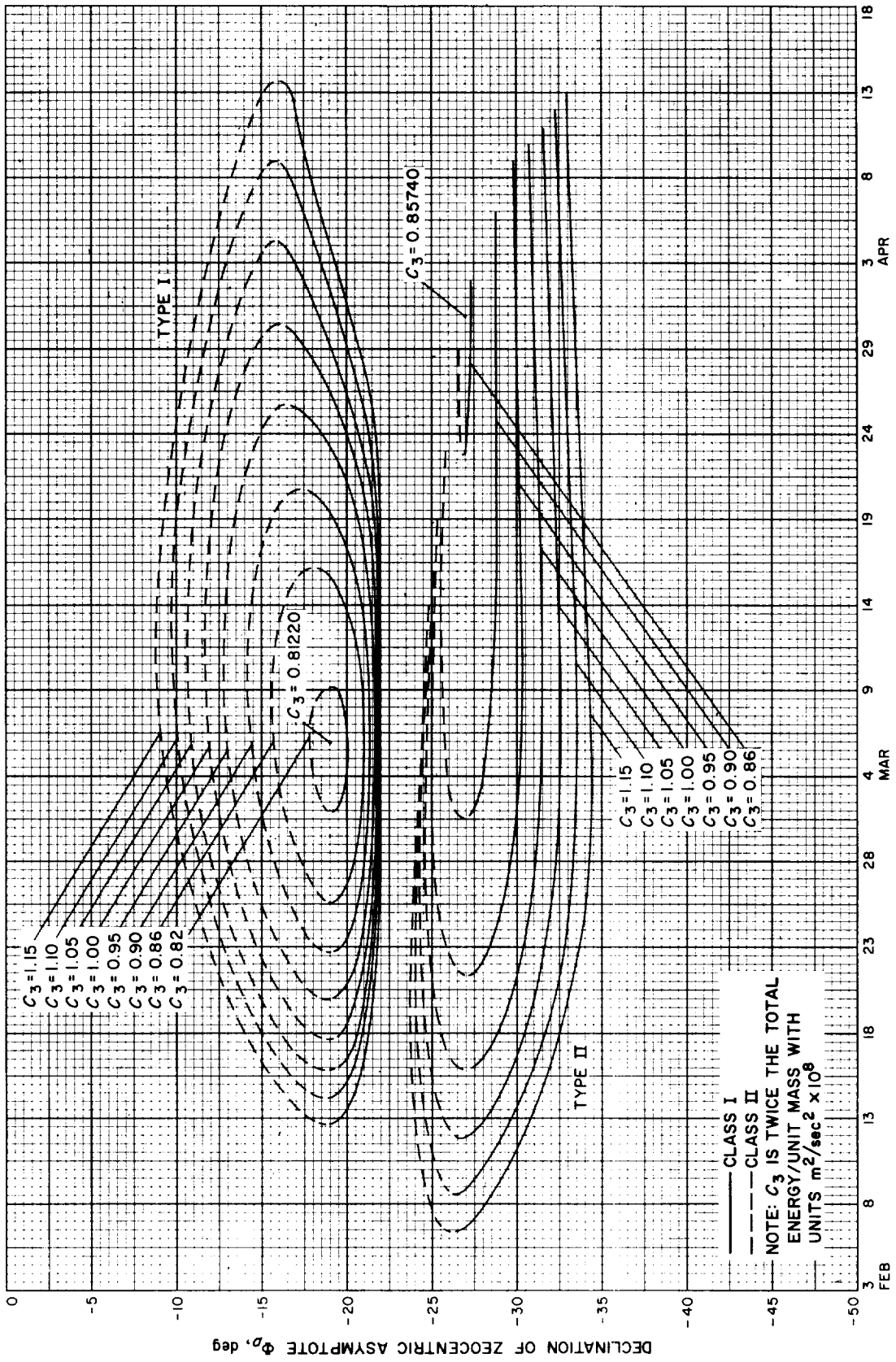

Fig. 9–18. Jupiter 1972: Declination of zeocentric asymptote vs launch date

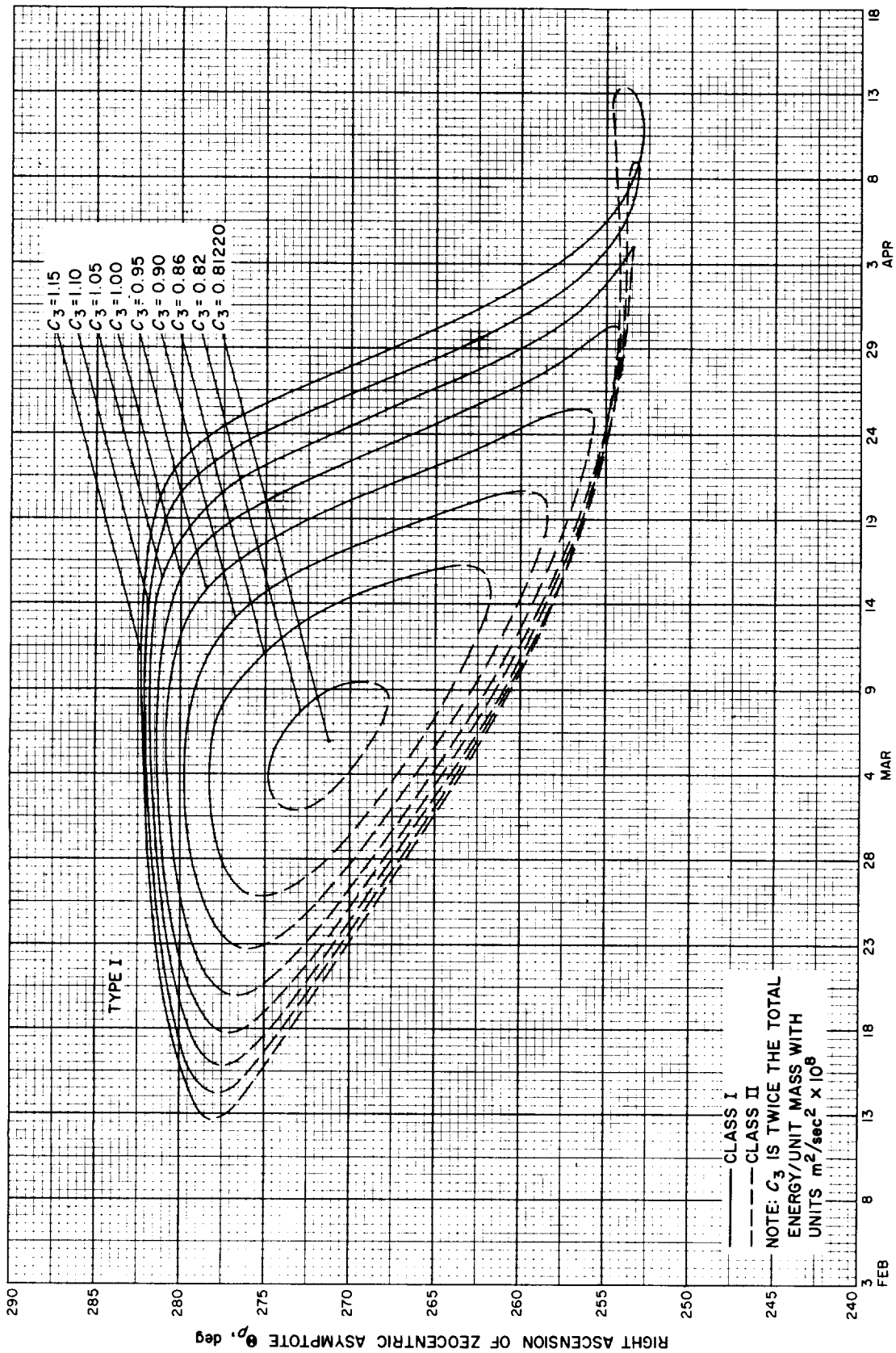

Fig. 9-19(I). Jupiter 1972: Right ascension of zeocentric asymptote vs launch date, Type I

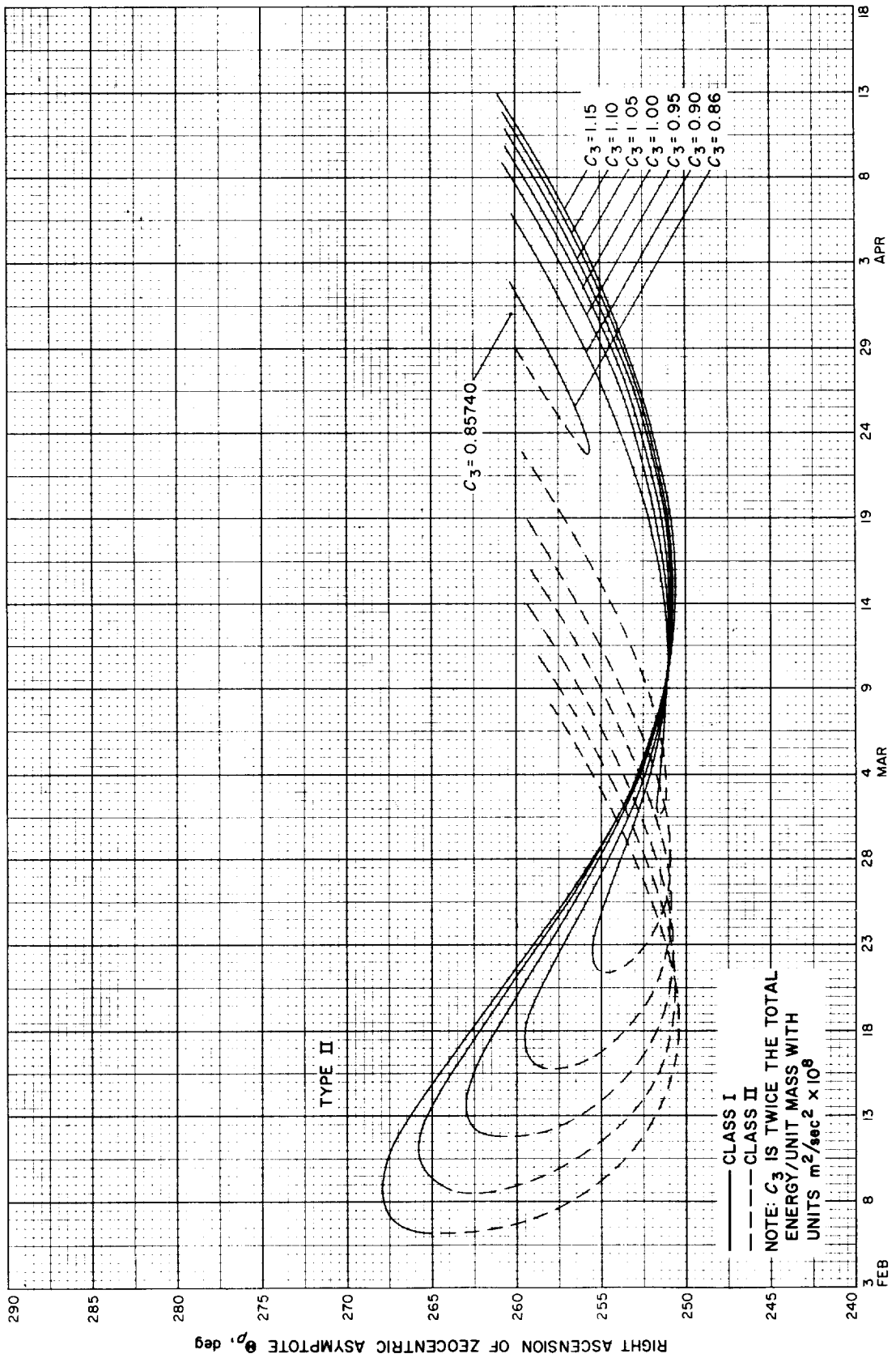

Fig. 9–19(II). Jupiter 1972: Right ascension of zeocentric asymptote vs launch date, Type II

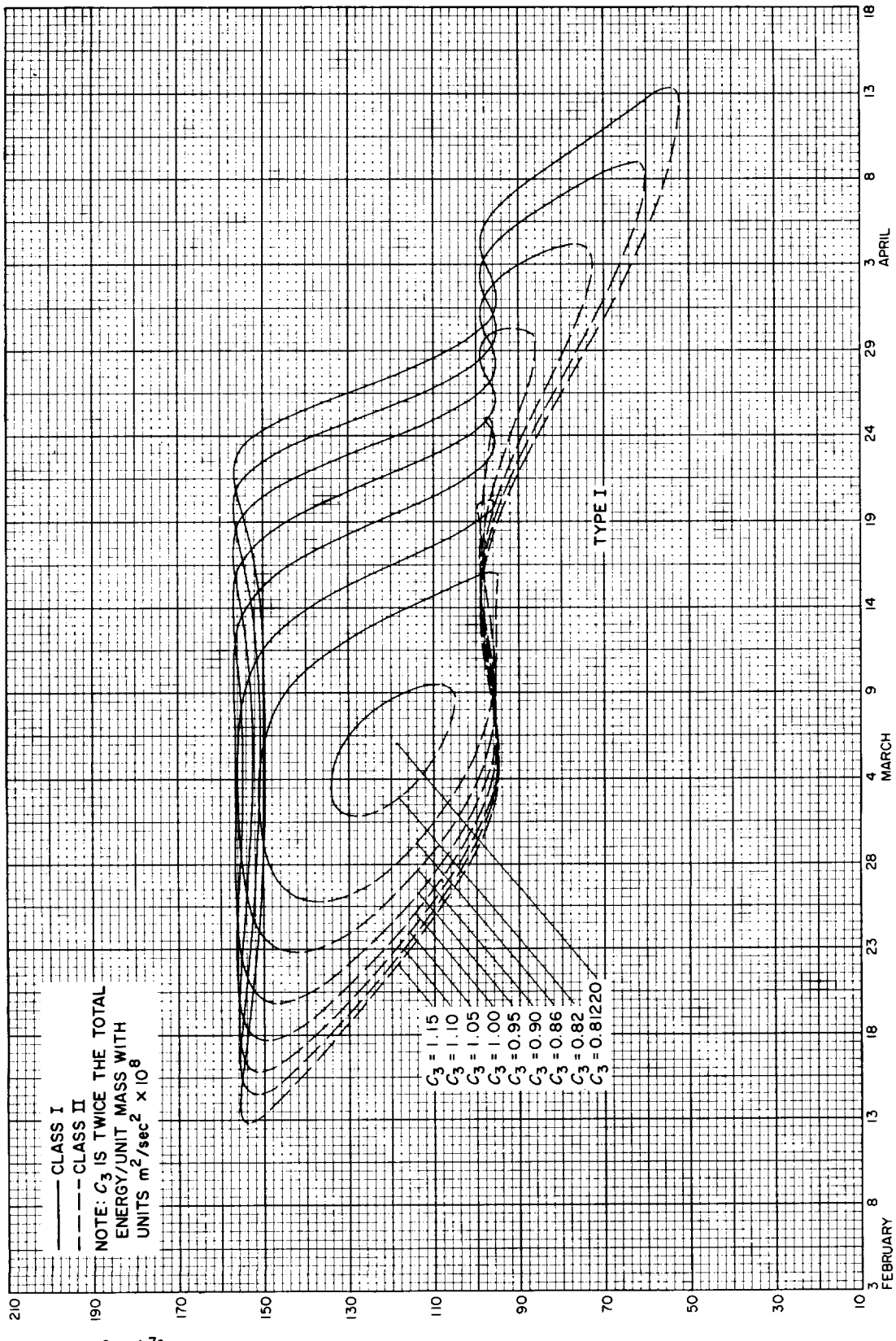

Fig. 9–20(I). Jupiter 1972: Angle between planet–Earth vector and incoming asymptote vs launch date, Type I

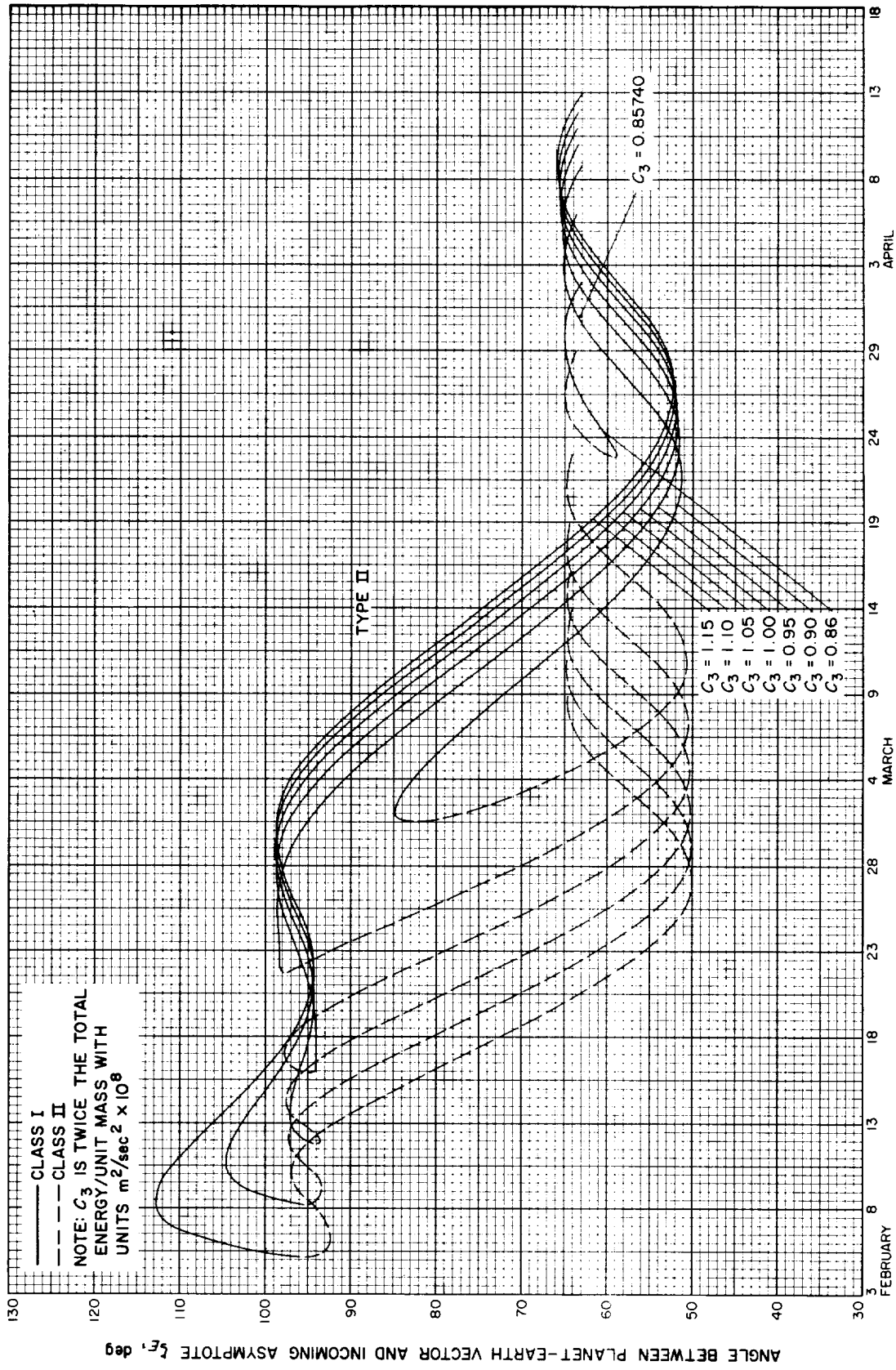

Fig. 9-20(II). Jupiter 1972: Angle between planet–Earth vector and incoming asymptote vs launch date, Type II

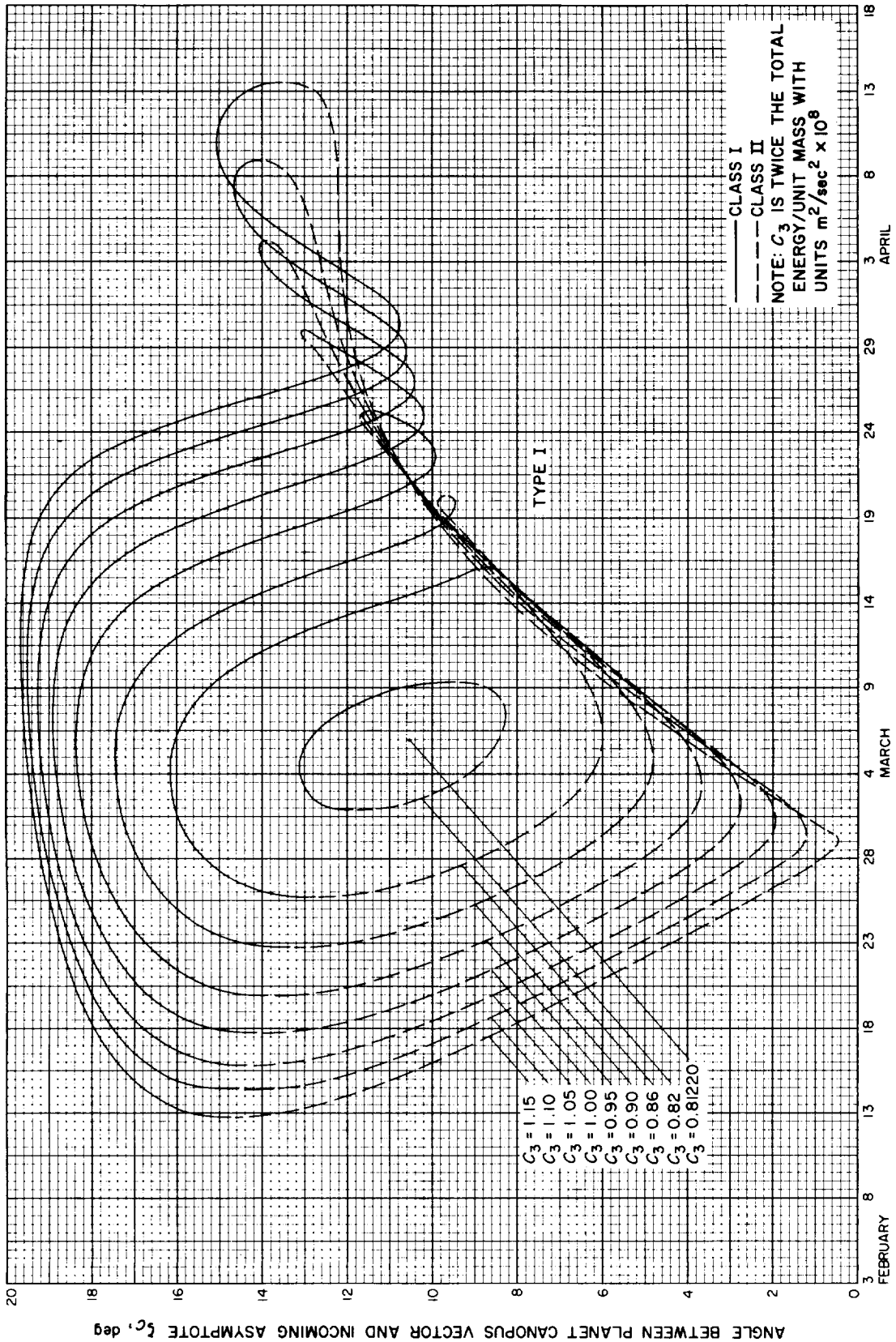

Fig. 9-21(I). Jupiter 1972: Angle between planet–Canopus vector and incoming asymptote vs launch date, Type I

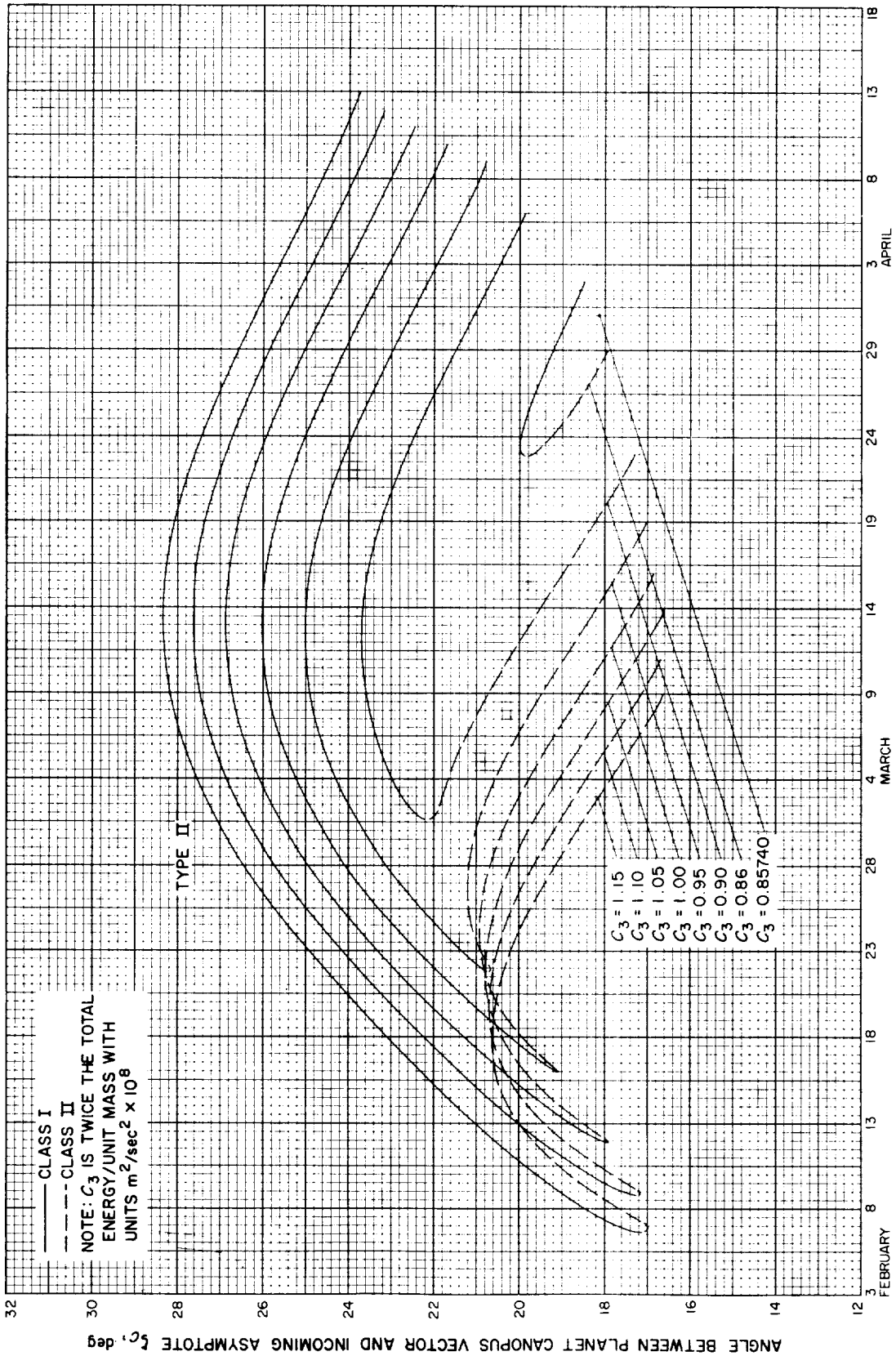

Fig. 9-21(II). Jupiter 1972: Angle between planet–Canopus vector and incoming asymptote vs launch date, Type II

X. JUPITER 1973: TRAJECTORY PARAMETER GRAPHS

Figure

10–1. Jupiter 1973: Minimum injection energy vs launch date

10–2(I). Jupiter 1973: Time of flight vs launch date, Type I

10–2(II). Jupiter 1973: Time of flight vs launch date, Type II

10–3. Jupiter 1973: Heliocentric central angle vs launch date

10–4(I). Jupiter 1973: Earth–Jupiter communication distance vs launch date, Type I

10–4(II). Jupiter 1973: Earth–Jupiter communication distance vs launch date, Type II

10–5(I). Jupiter 1973: Declination of geocentric asymptote vs launch date, Type I

10–5(II). Jupiter 1973: Declination of geocentric asymptote vs launch date, Type II

10–6(I). Jupiter 1973: Right ascension of geocentric asymptote vs launch date, Type I

10–6(II). Jupiter 1973: Right ascension of geocentric asymptote vs launch date, Type II

10–7. Jupiter 1973: Angle between outgoing geocentric asymptote and launch planet's orbital plane vs launch date

10–8(I). Jupiter 1973: Angle between Sun–Earth vector and outgoing geocentric asymptote vs launch date, Type I

10–8(II). Jupiter 1973: Angle between Sun–Earth vector and outgoing geocentric asymptote vs launch date, Type II

10–9(I). Jupiter 1973: True anomaly in transfer ellipse at launch time vs launch date, Type I

10–9(II). Jupiter 1973: True anomaly in transfer ellipse at launch time vs launch date, Type II

10–10. Jupiter 1973: True anomaly in transfer ellipse at arrival time vs launch date

10–11(I). Jupiter 1973: Perihelion of transfer orbit vs launch date, Type I

10–11(II). Jupiter 1973: Perihelion of transfer orbit vs launch date, Type II

10–12(I). Jupiter 1973: Aphelion of transfer orbit vs launch date, Type I

10–12(II). Jupiter 1973: Aphelion of transfer orbit vs launch date, Type II

X. JUPITER 1973: TRAJECTORY PARAMETER GRAPHS (Cont'd)

Figure

10–13(I). Jupiter 1973: Inclination of the heliocentric transfer plane vs launch date, Type I

10–13(II). Jupiter 1973: Inclination of the heliocentric transfer plane vs launch date, Type II

10–14(I). Jupiter 1973: Celestial latitude at arrival time vs launch date, Type I

10–14(II). Jupiter 1973: Celestial latitude at arrival time vs launch date, Type II

10–15(I). Jupiter 1973: Asymptotic speed with respect to Jupiter vs launch date, Type I

10–15(II). Jupiter 1973: Asymptotic speed with respect to Jupiter vs launch date, Type II

10–16. Jupiter 1973: Angle between incoming zeocentric asymptote and arrival planet's orbital plane vs launch date

10–17. Jupiter 1973: Angle between Jupiter–Sun vector and incoming zeocentric asymptote vs launch date

10–18. Jupiter 1973: Declination of zeocentric asymptote vs launch date

10–19(I). Jupiter 1973: Right ascension of zeocentric asymptote vs launch date, Type I

10–19(II). Jupiter 1973: Right ascension of zeocentric asymptote vs launch date, Type II

10–20(I). Jupiter 1973: Angle between planet–Earth vector and incoming asymptote vs launch date, Type I

10–20(II). Jupiter 1973: Angle between planet–Earth vector and incoming asymptote vs launch date, Type II

10–21(I). Jupiter 1973: Angle between planet–Canopus vector and incoming asymptote vs launch date, Type I

10–21(II). Jupiter 1973: Angle between planet–Canopus vector and incoming asymptote vs launch date, Type II

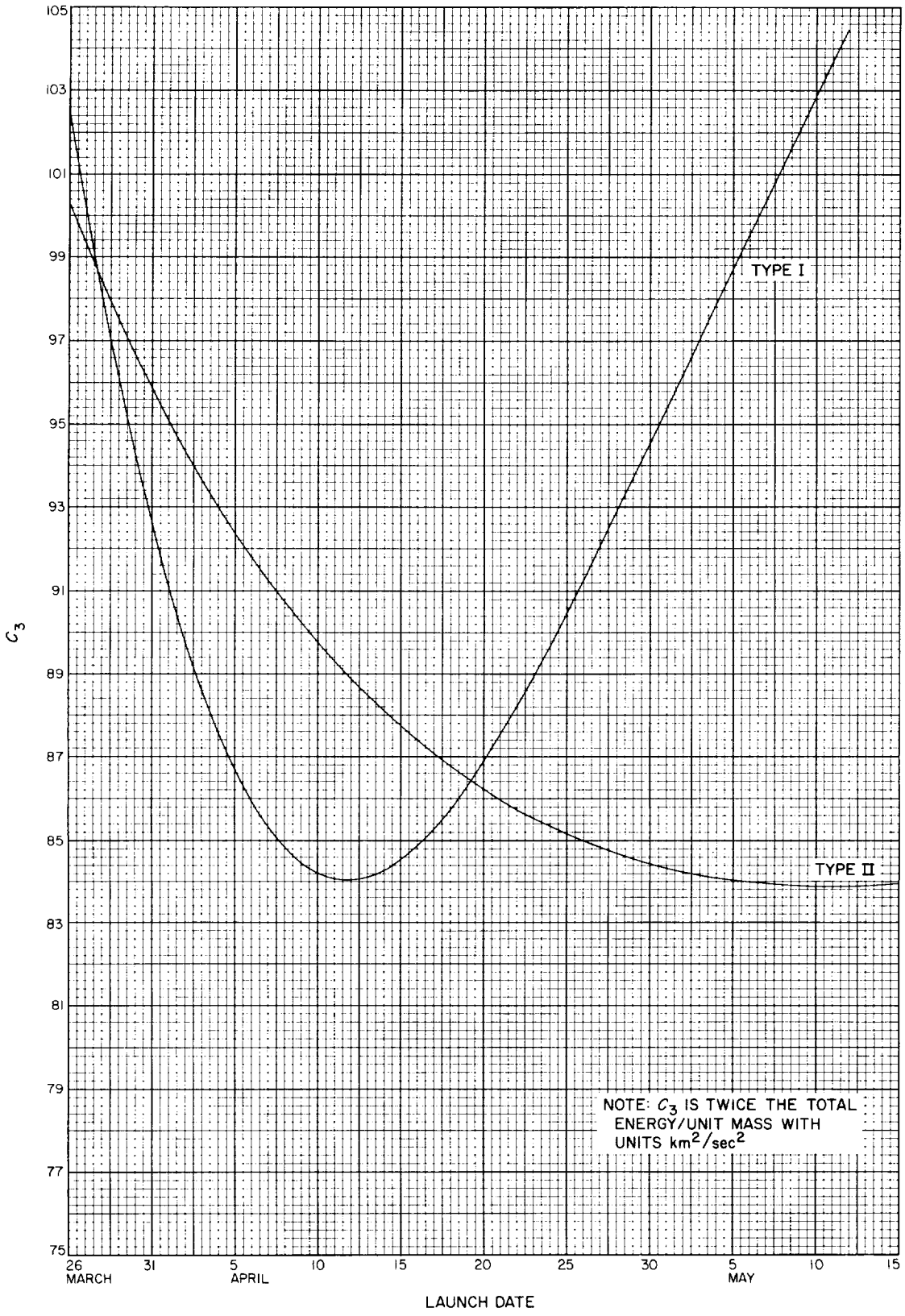

Fig. 10–1. Jupiter 1973: Minimum injection energy vs launch date

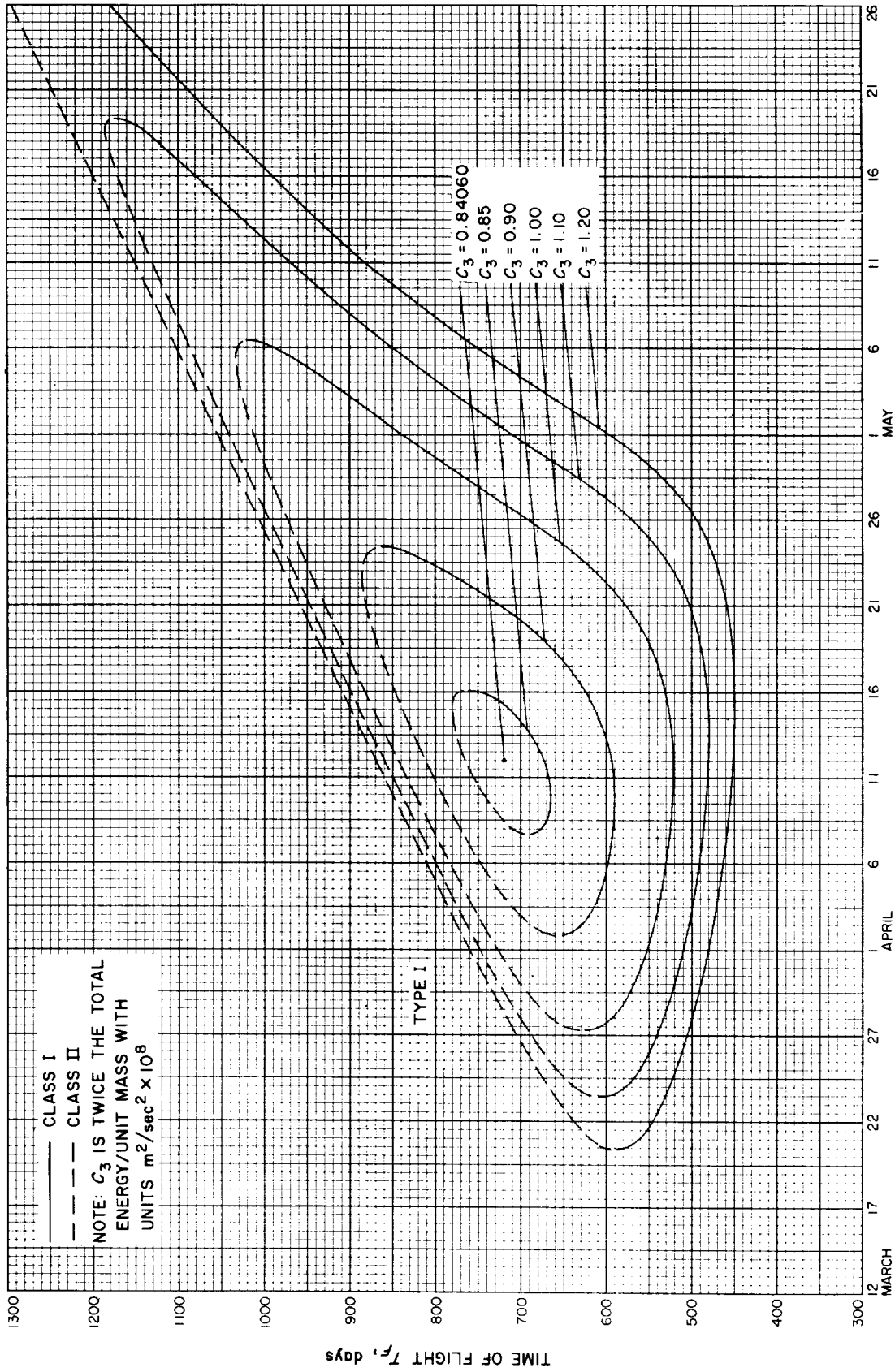

Fig. 10-2(II). Jupiter 1973: Time of flight vs launch date, Type I

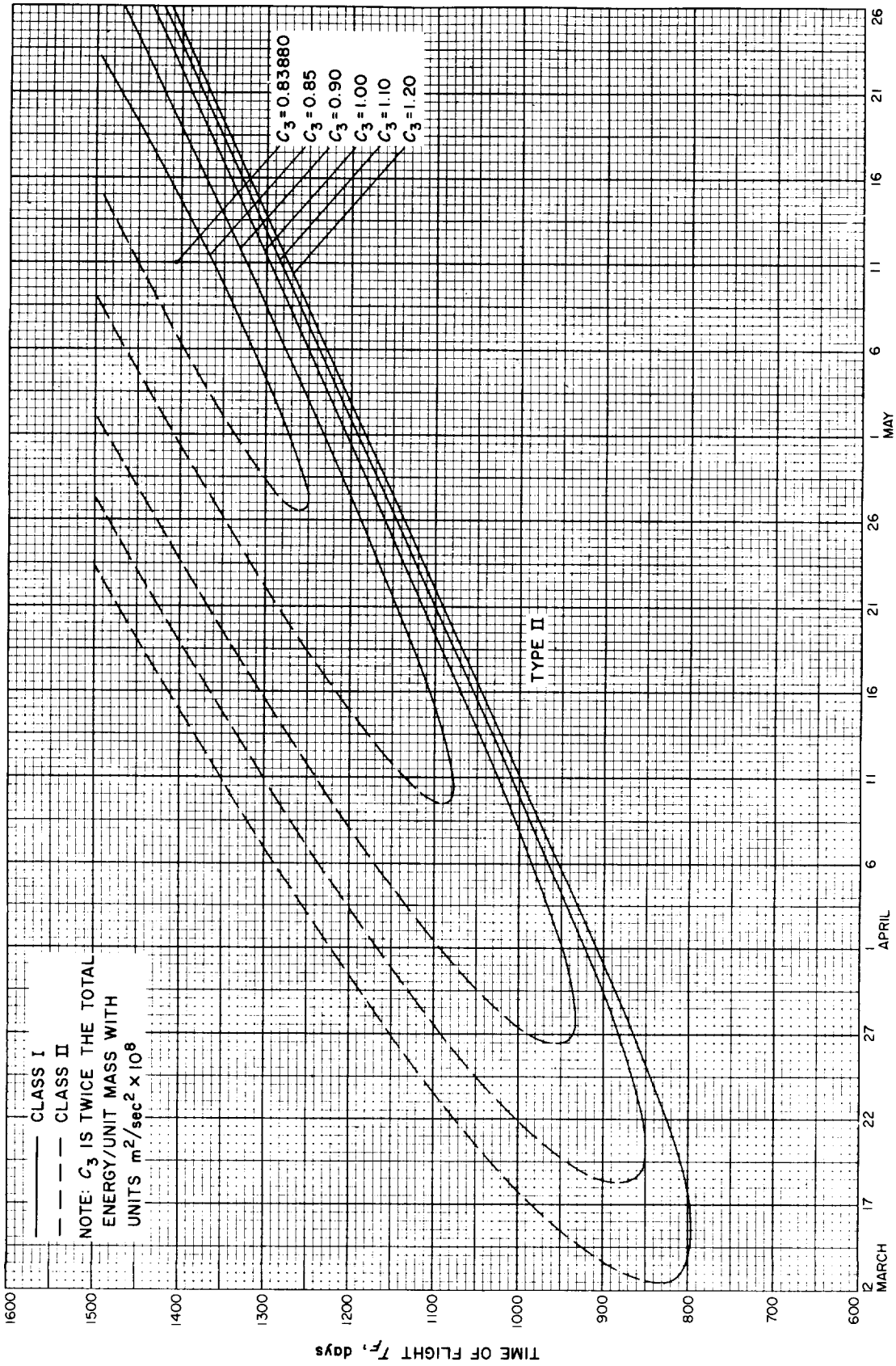

Fig. 10–2(III). Jupiter 1973: Time of flight vs launch date, Type II

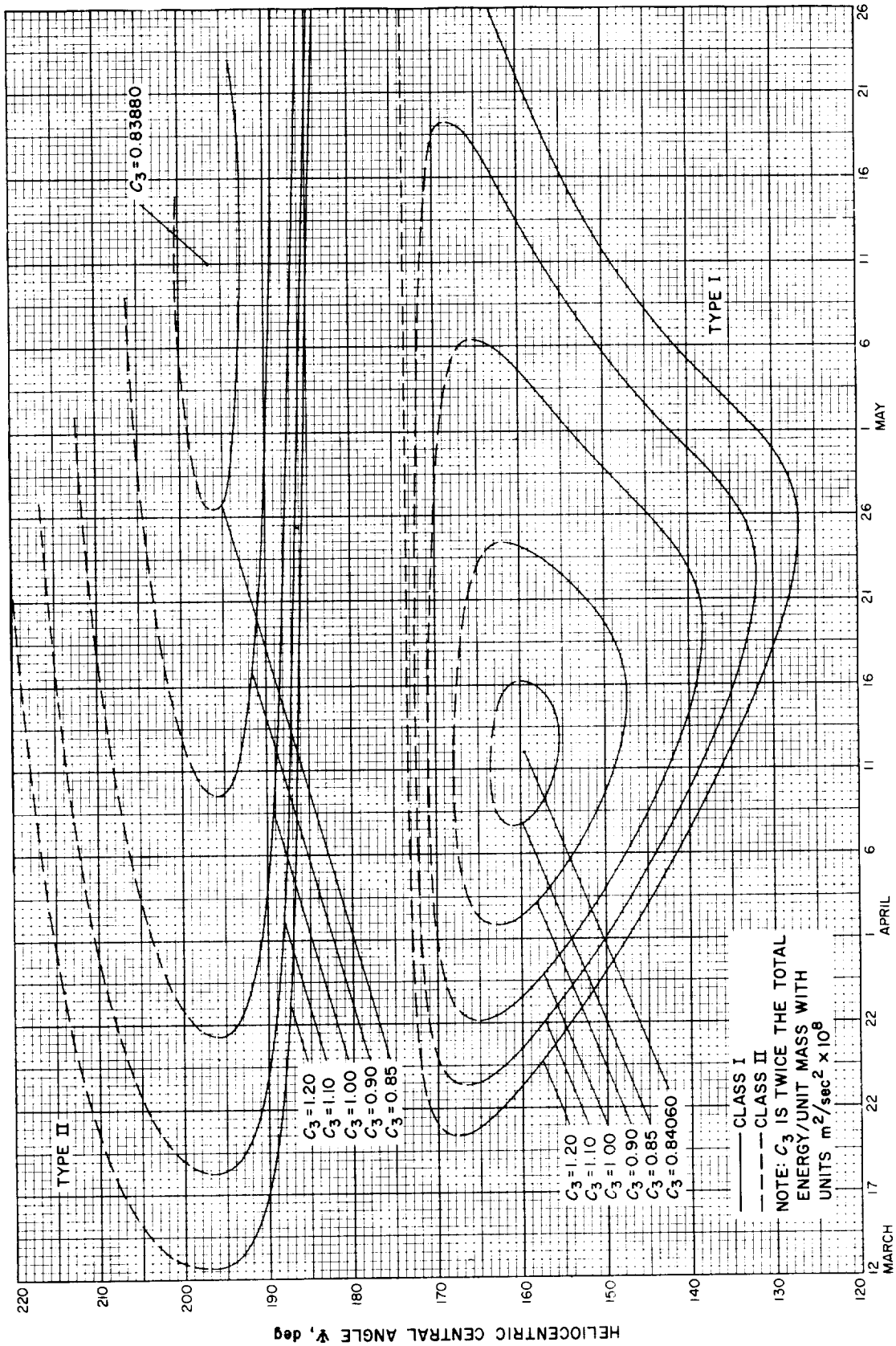

Fig. 10–3. Jupiter 1973: Heliocentric central angle vs launch date

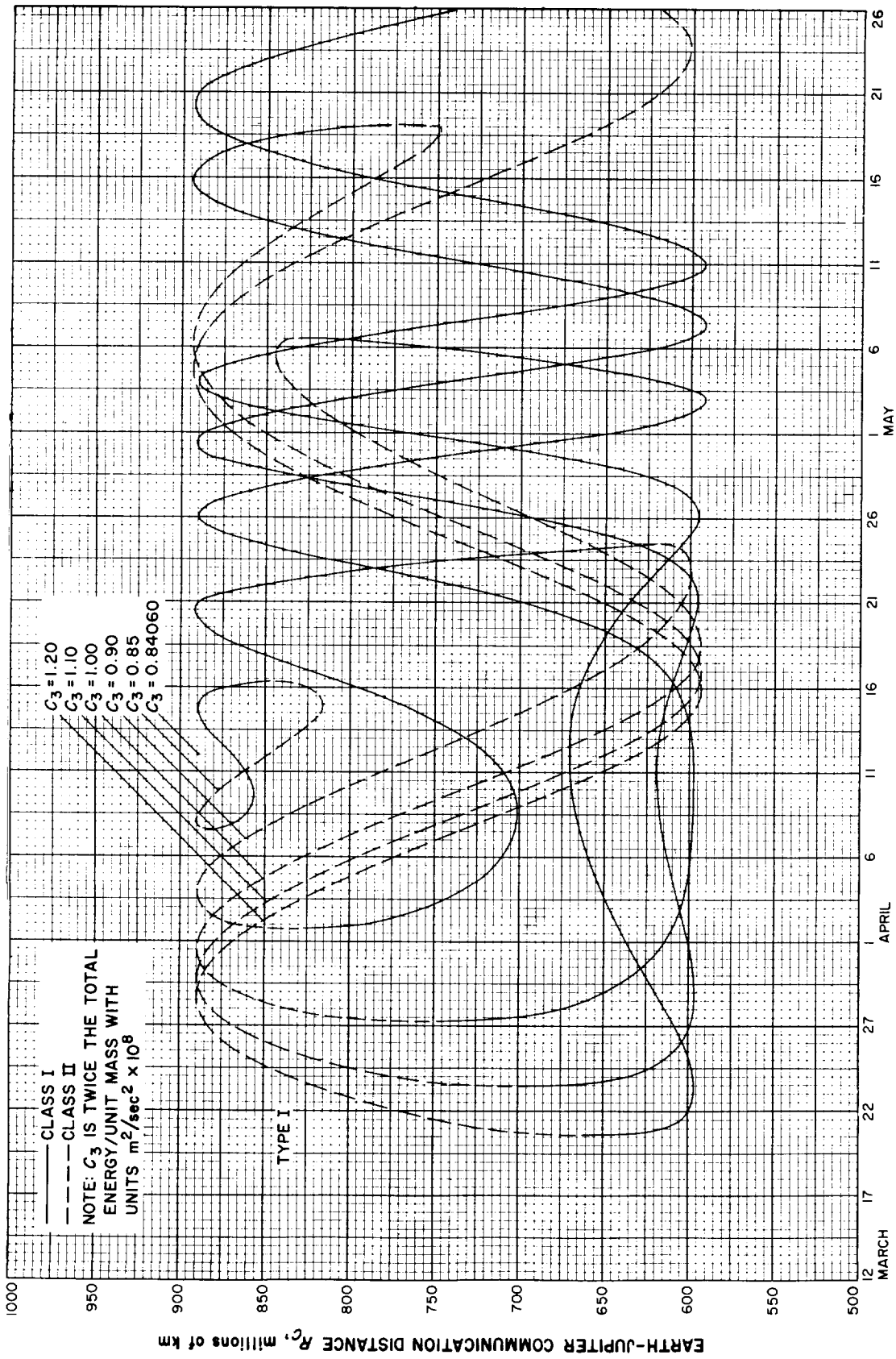

Fig. 10-4(I). Jupiter 1973: Earth–Jupiter communication distance vs launch date, Type I

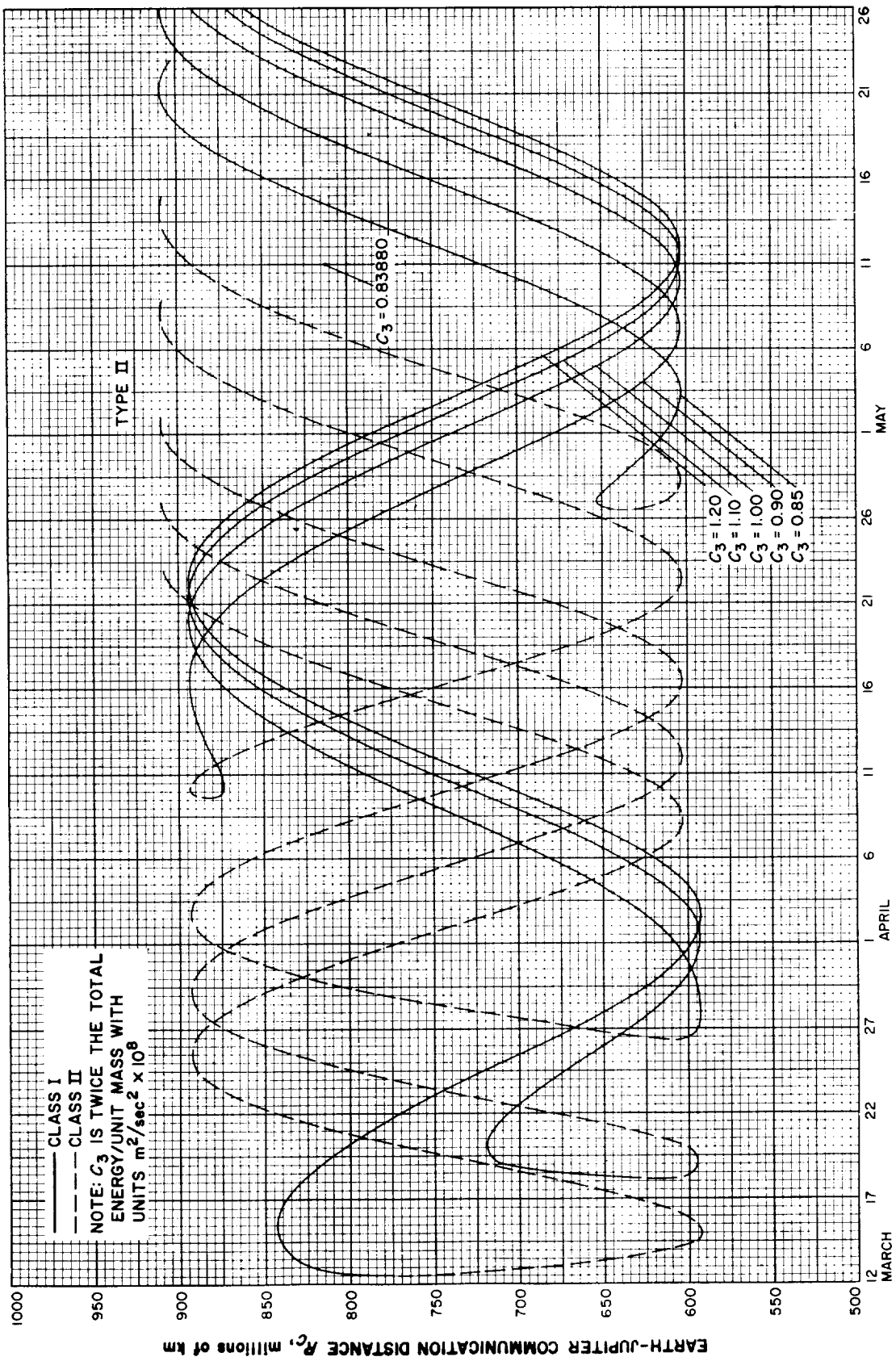

Fig. 10–4(II). Jupiter 1973: Earth–Jupiter communication distance vs launch date, Type II

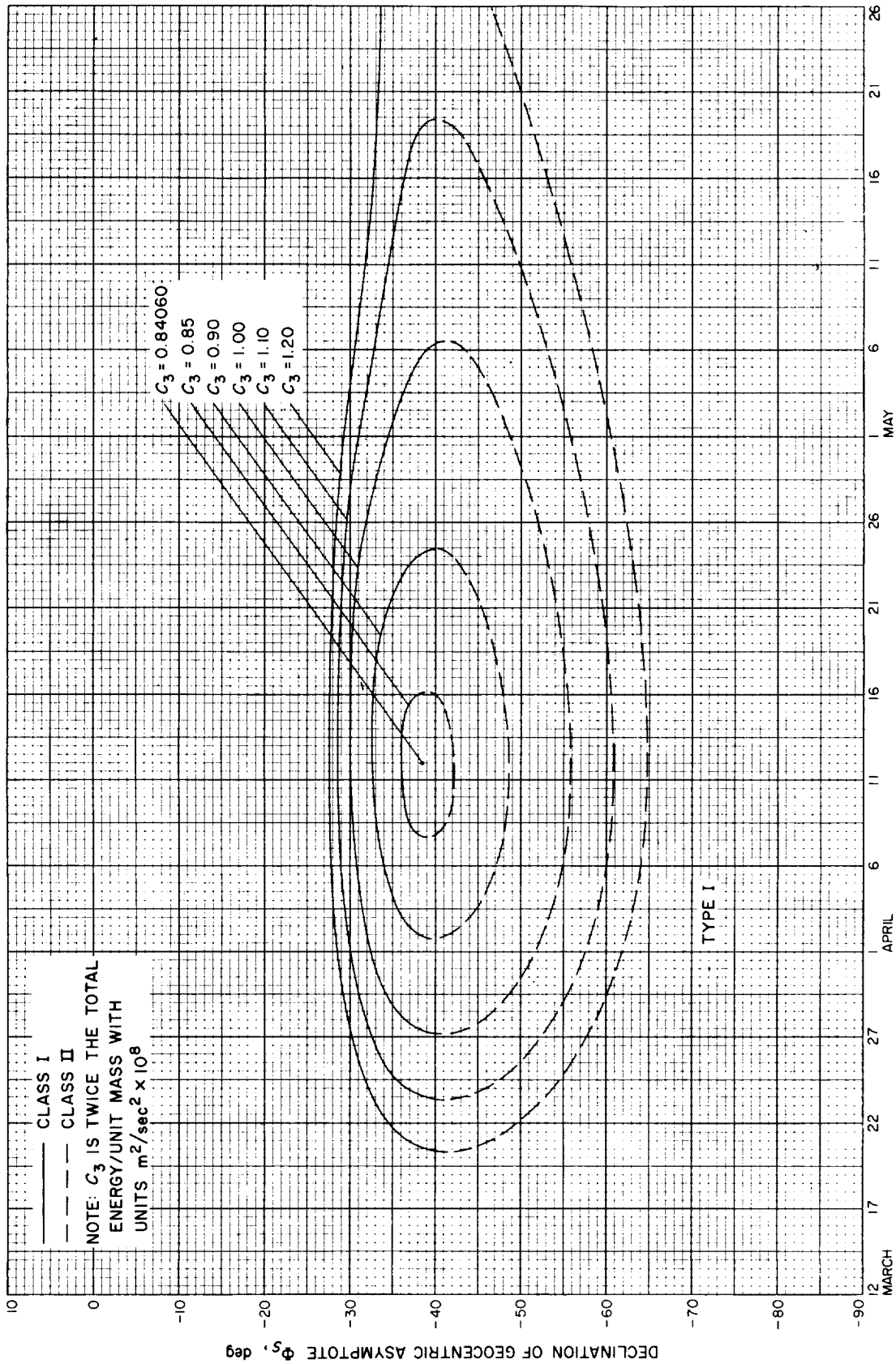

Fig. 10–5(I). Jupiter 1973: Declination of geocentric asymptote vs launch date, Type I

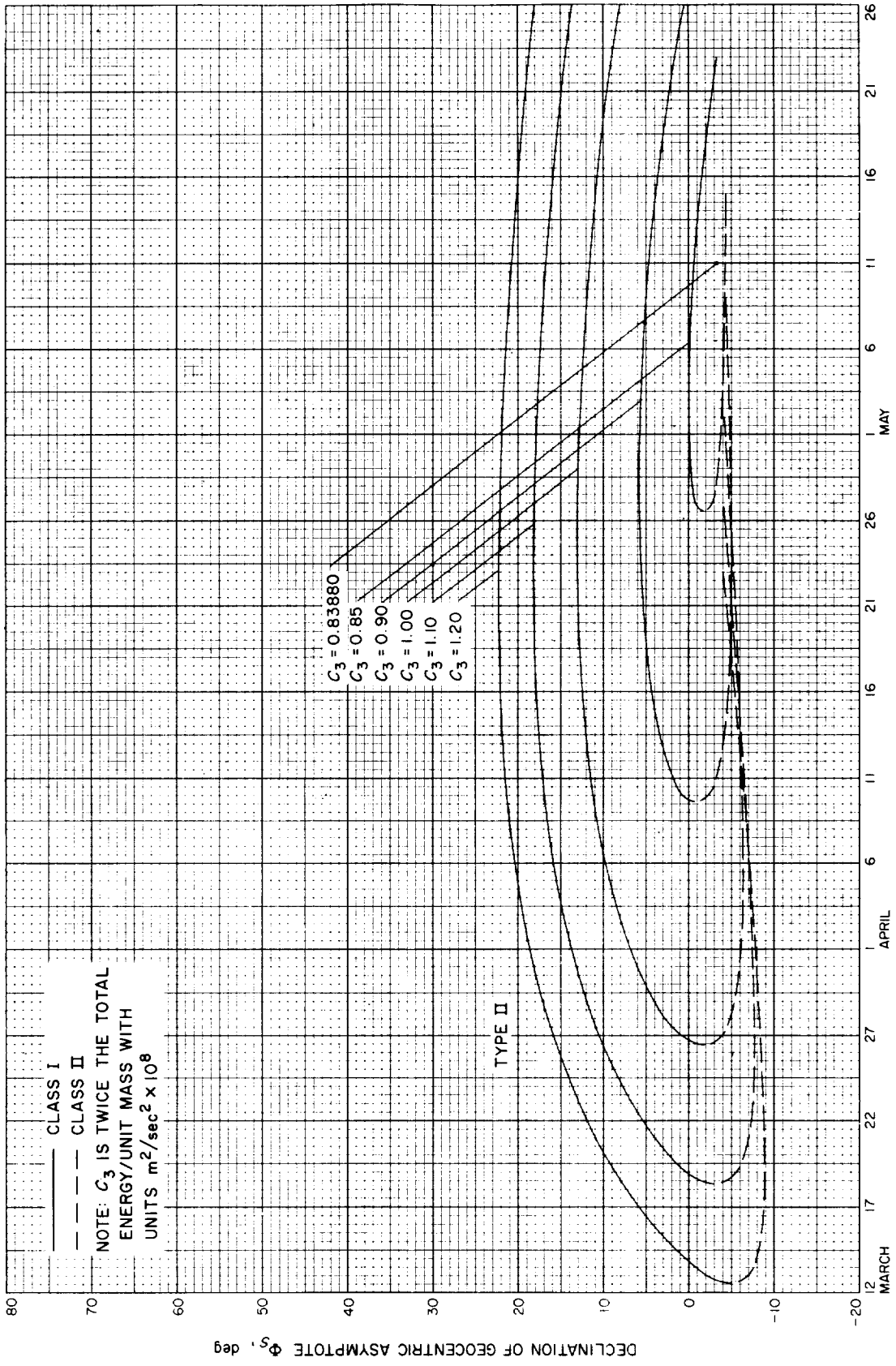

Fig. 10–5(II). Jupiter 1973: Declination of geocentric asymptote vs launch date, Type II

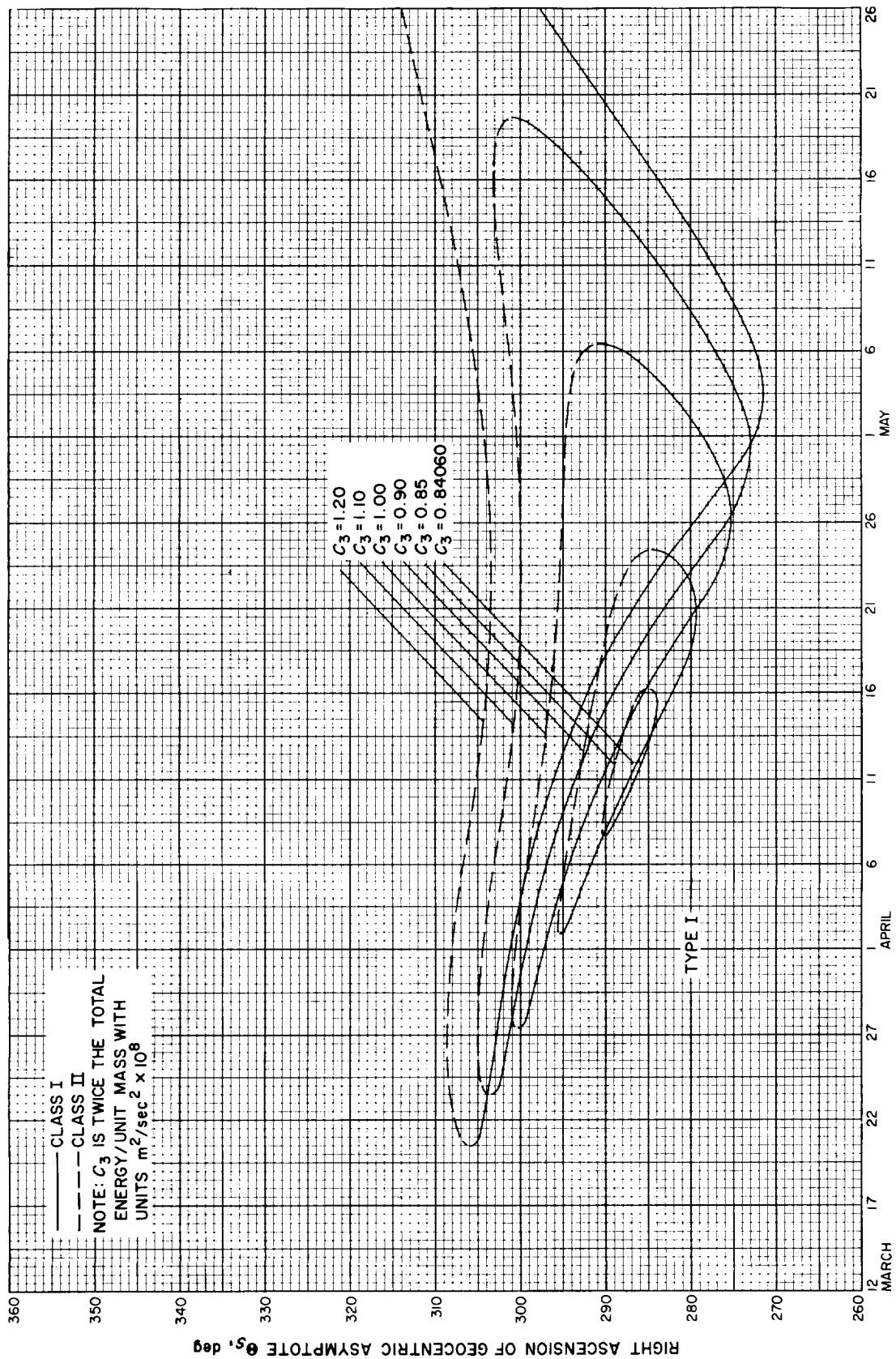

Fig. 10–6(I). Jupiter 1973: Right ascension of geocentric asymptote vs launch date, Type I

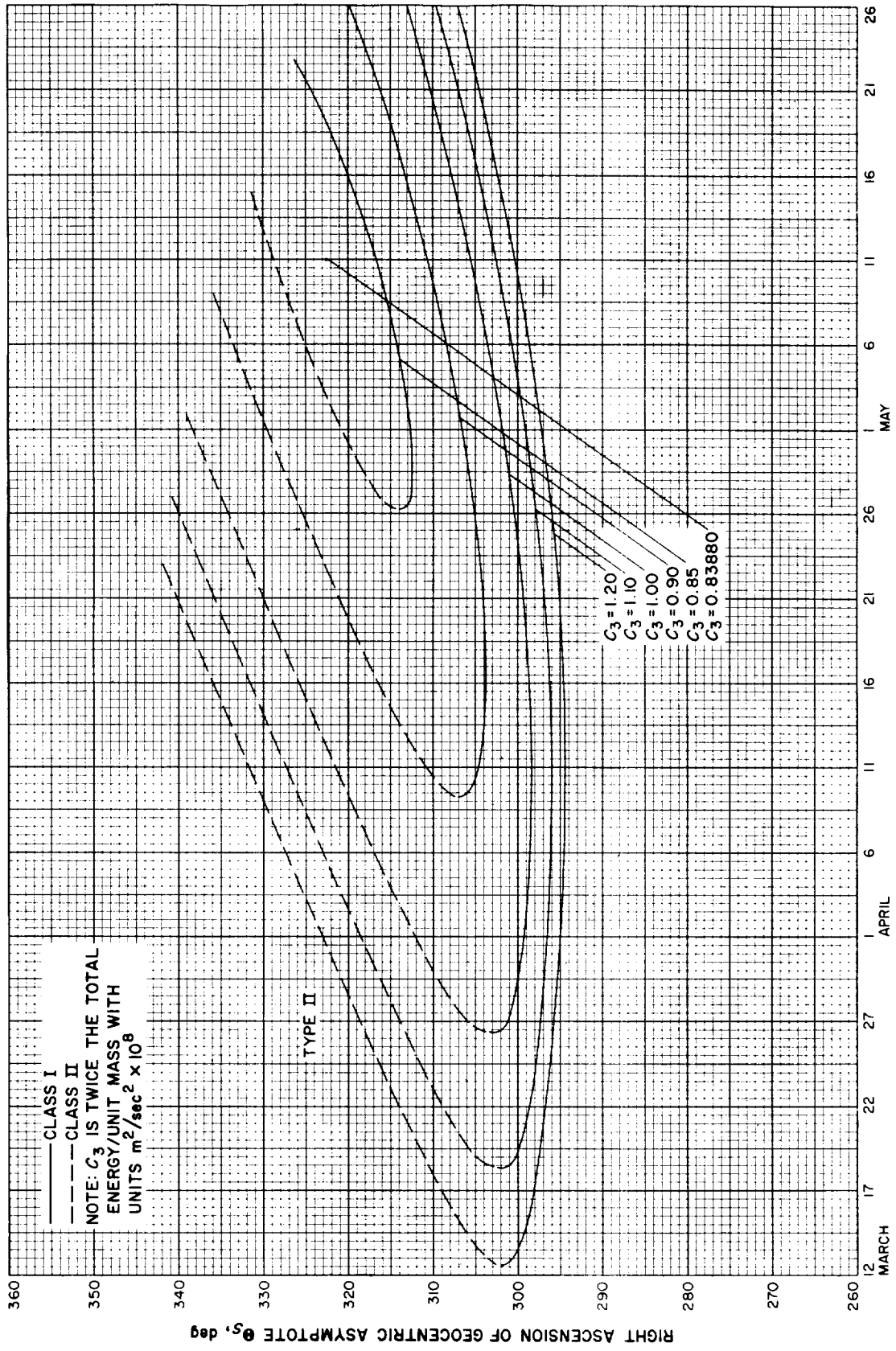

Fig. 10–6(II). Jupiter 1973: Right ascension of geocentric asymptote vs launch date, Type II

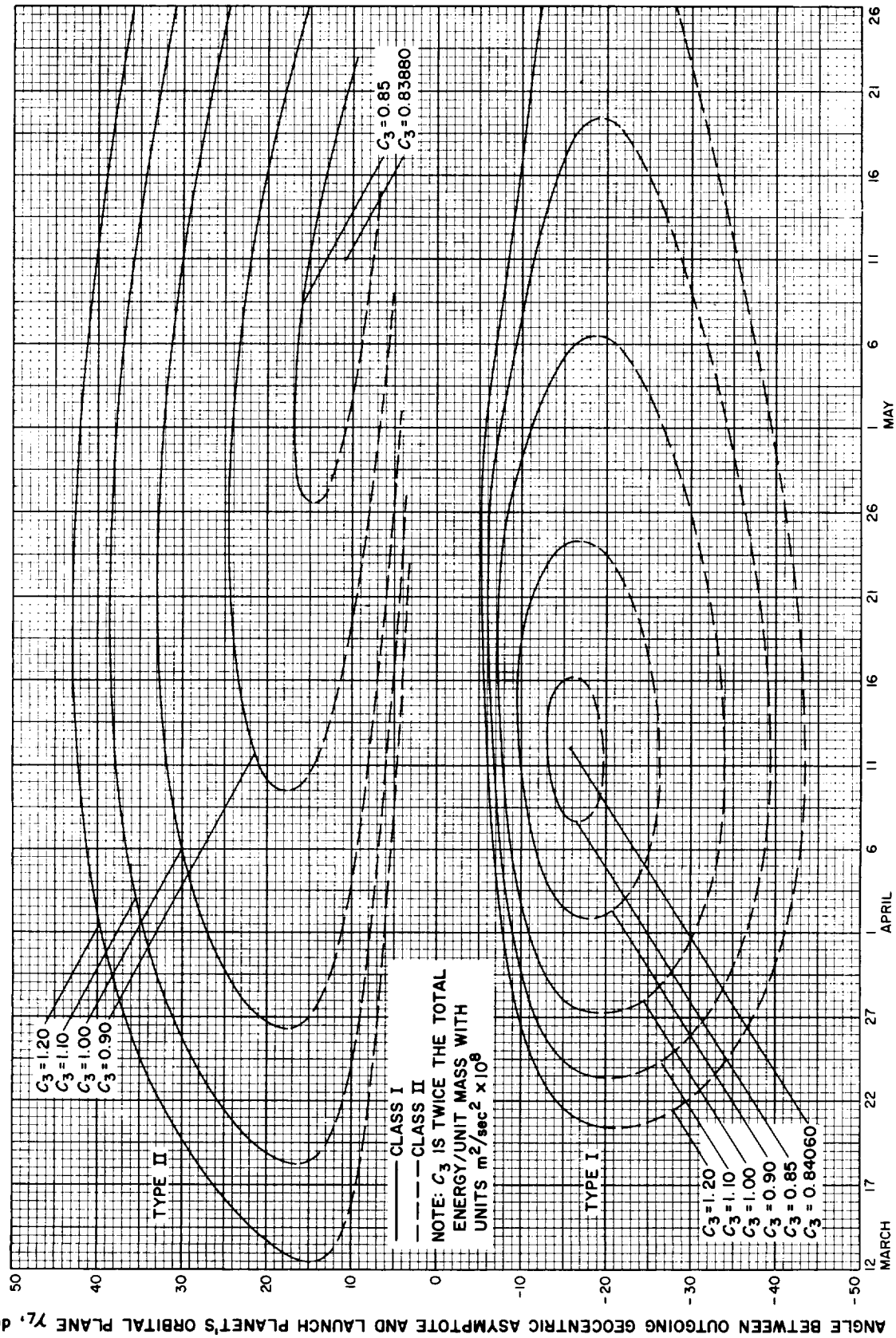

Fig. 10–7. Jupiter 1973: Angle between outgoing geocentric asymptote and launch planet's orbital plane vs launch date

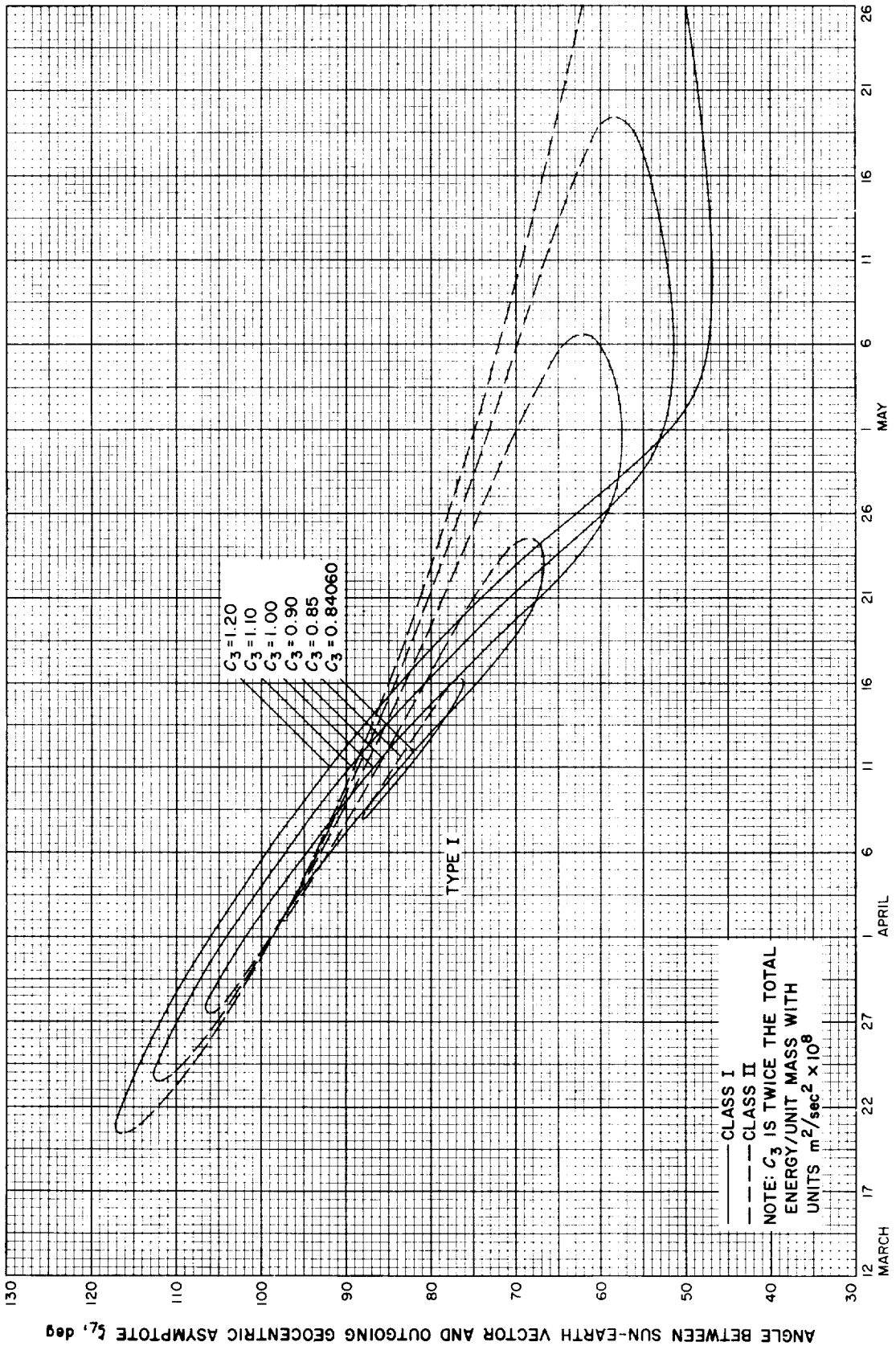

Fig. 10-8(I). Jupiter 1973: Angle between Sun–Earth vector and outgoing geocentric asymptote vs launch date, Type I

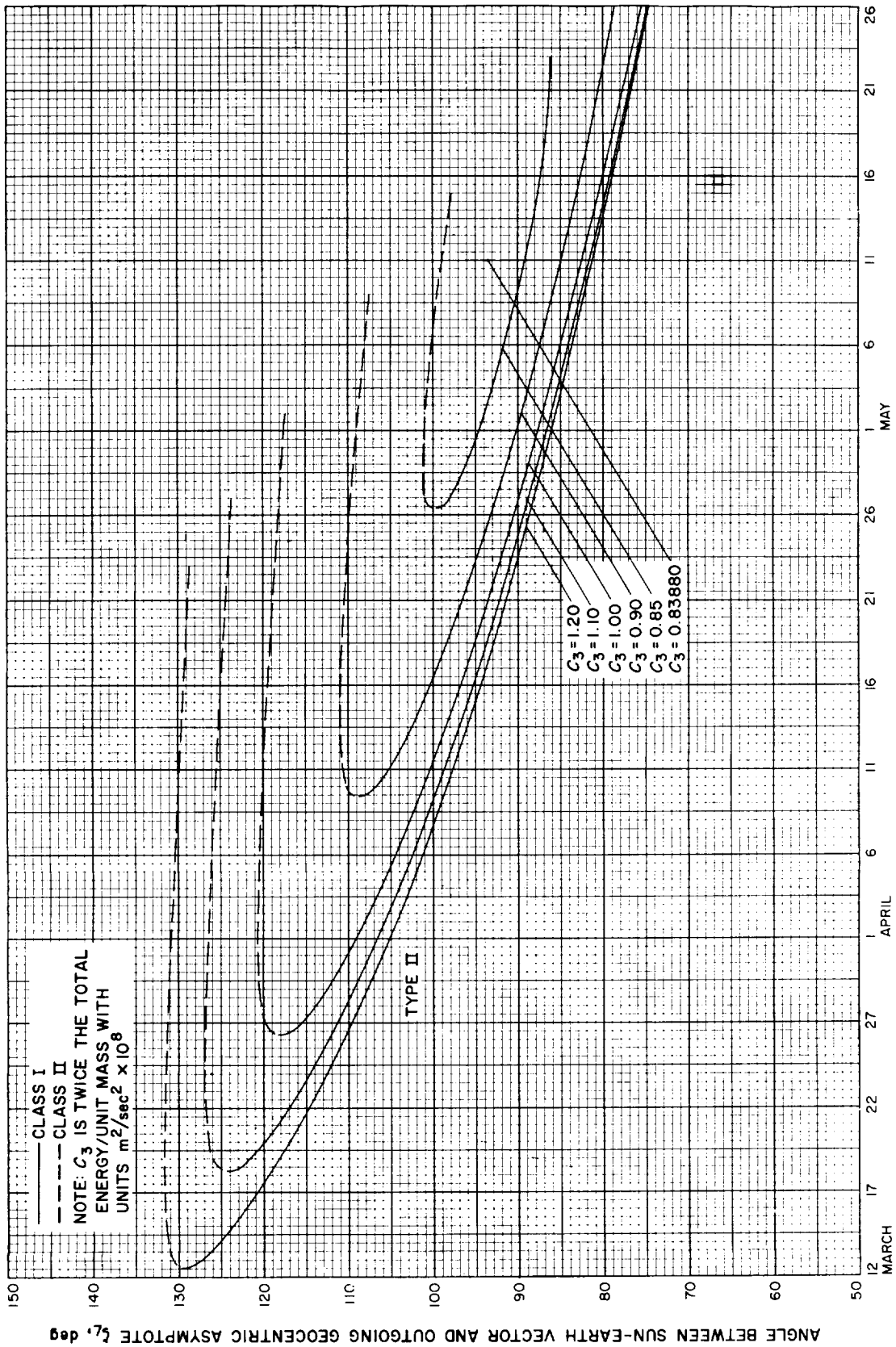

Fig. 10-8(III). Jupiter 1973: Angle between Sun–Earth vector and outgoing geocentric asymptote vs launch date, Type II

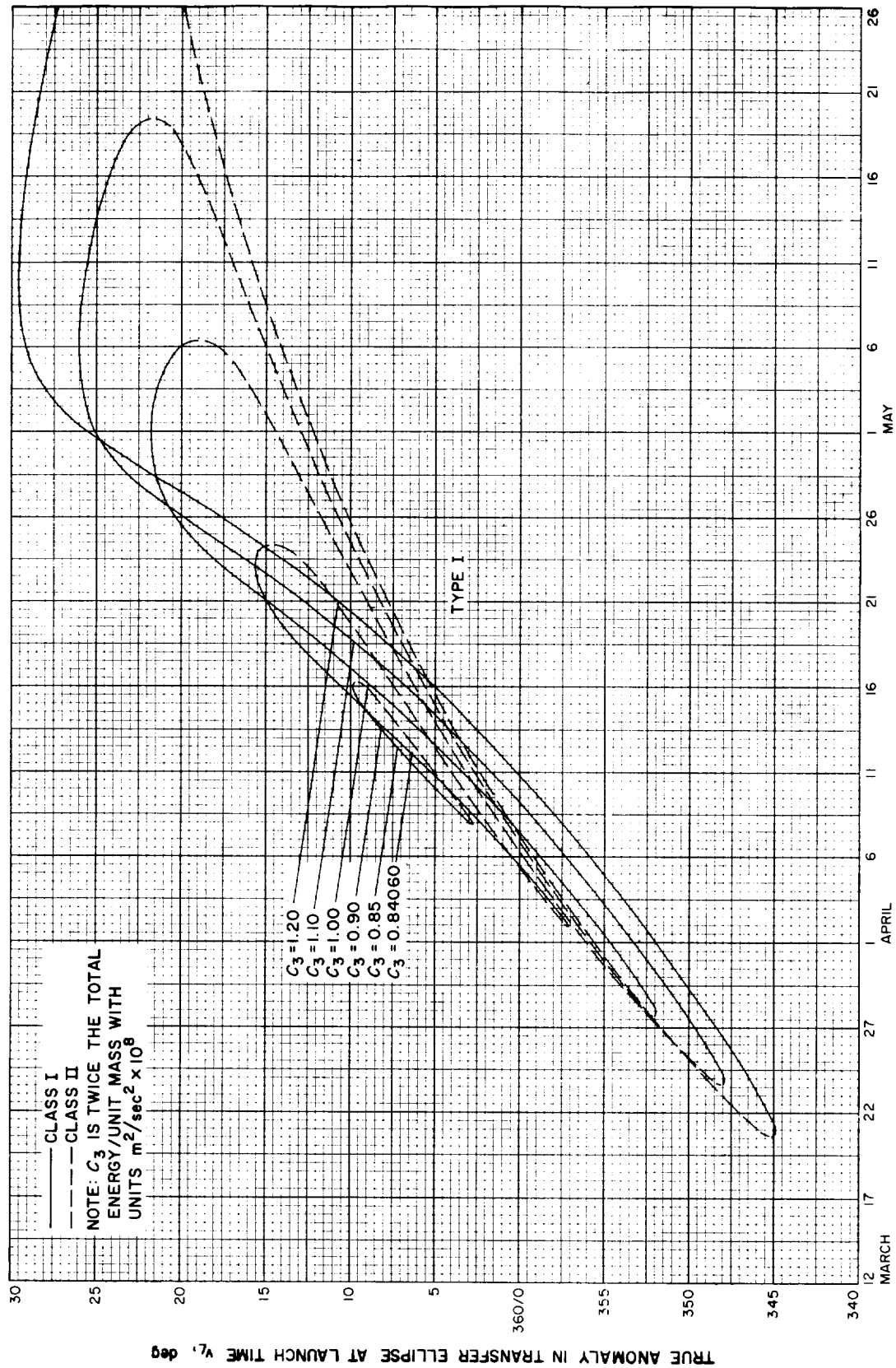

Fig. 10–9(1). Jupiter 1973: True anomaly in transfer ellipse at launch time vs launch date, Type I

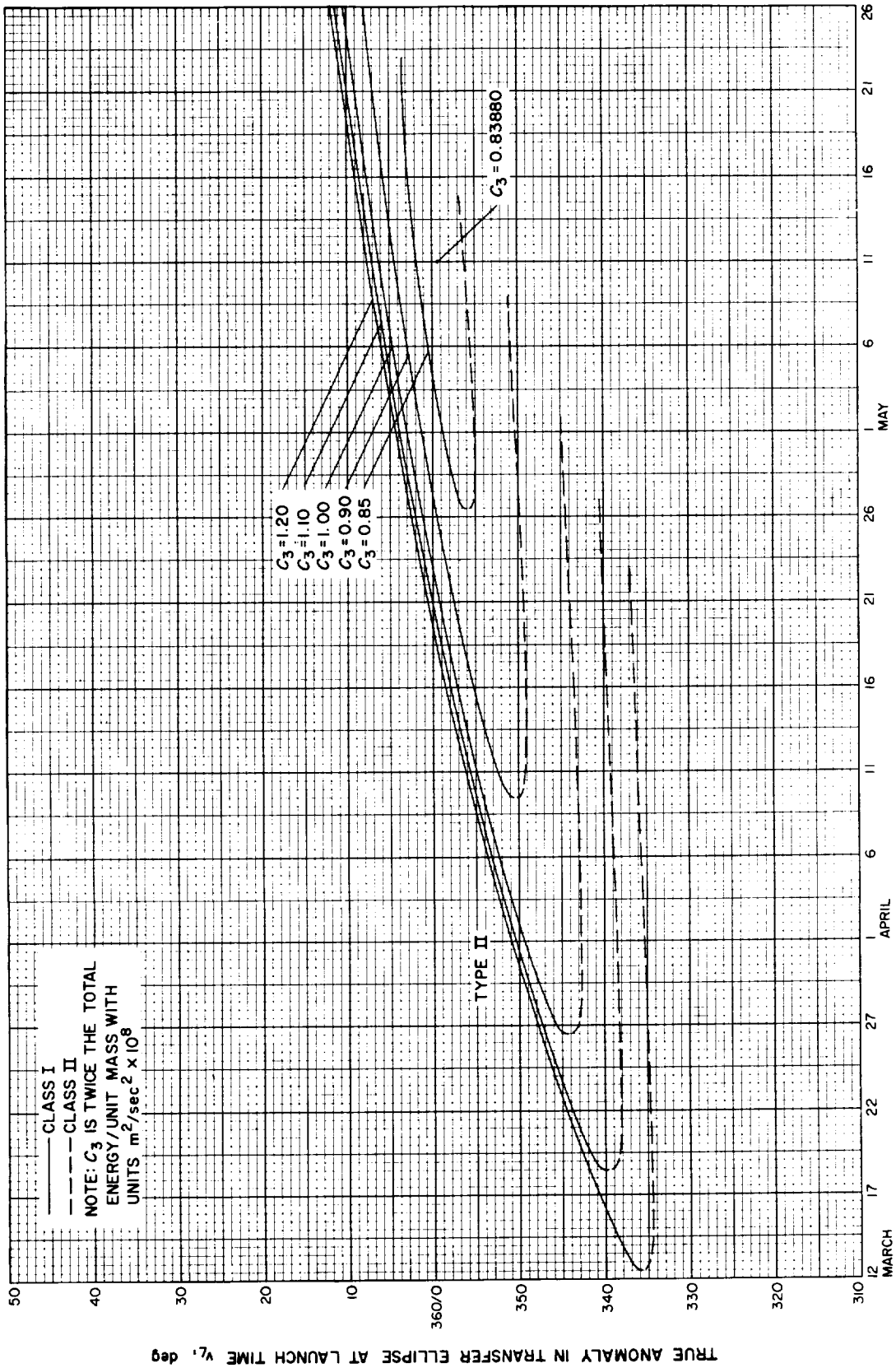

Fig. 10–9(II). Jupiter 1973: True anomaly in transfer ellipse at launch time vs launch date, Type II

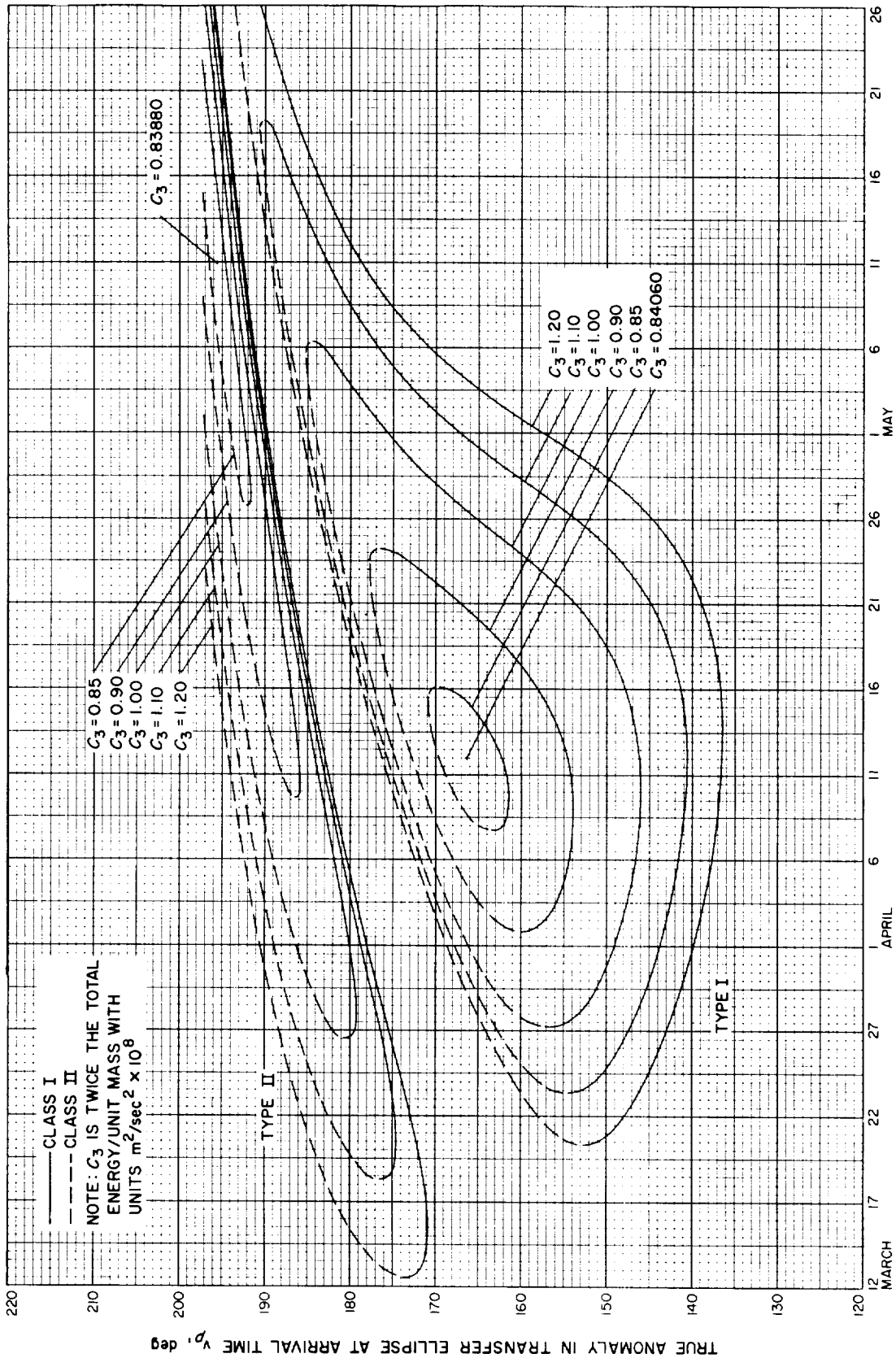

Fig. 10–10. Jupiter 1973: True anomaly in transfer ellipse at arrival time vs launch date

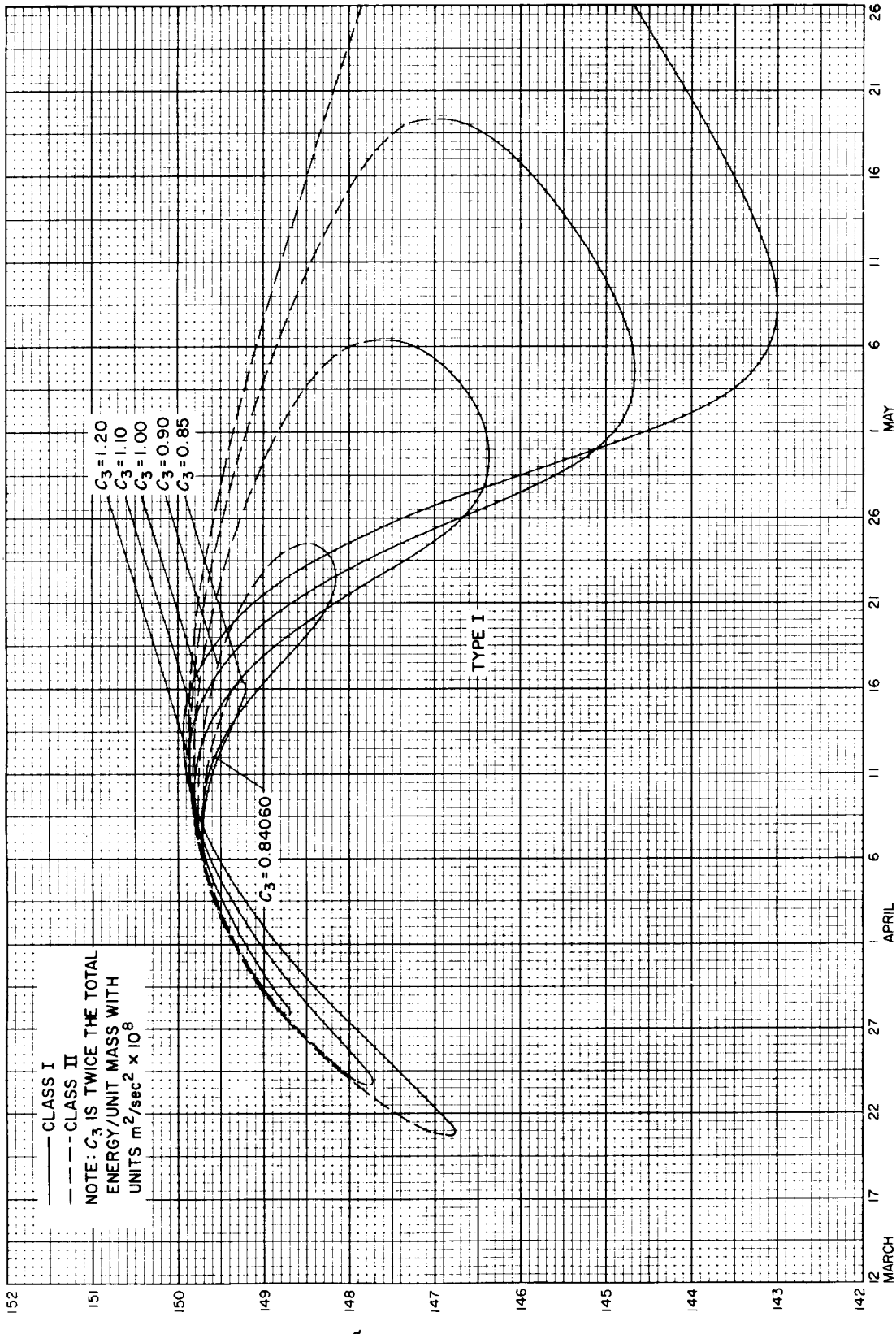

Fig. 10-11(I). Jupiter 1973: Perihelion of transfer orbit vs launch date, Type I

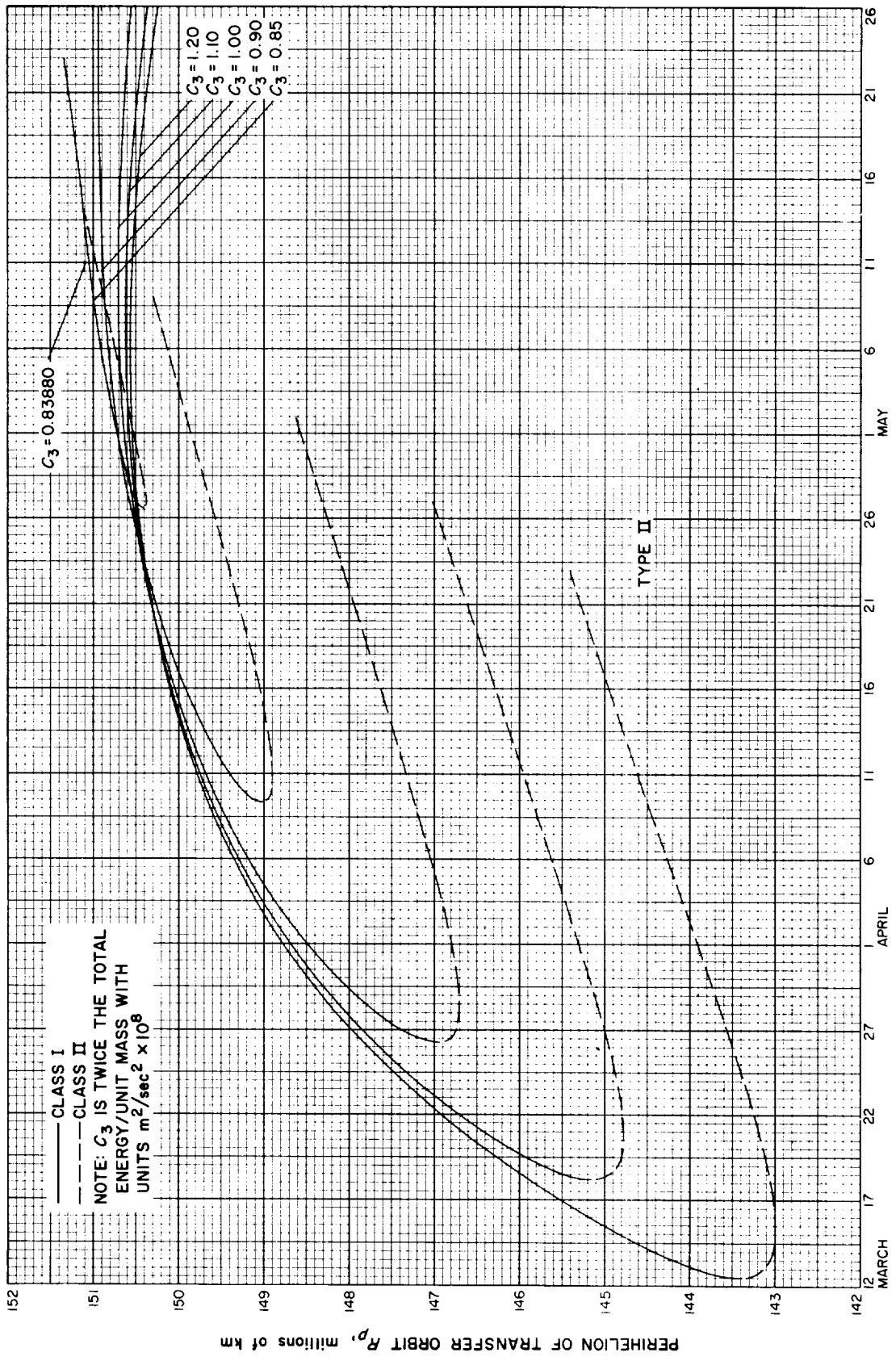

Fig. 10–11(II). Jupiter 1973: Perihelion of transfer orbit vs launch date, Type II

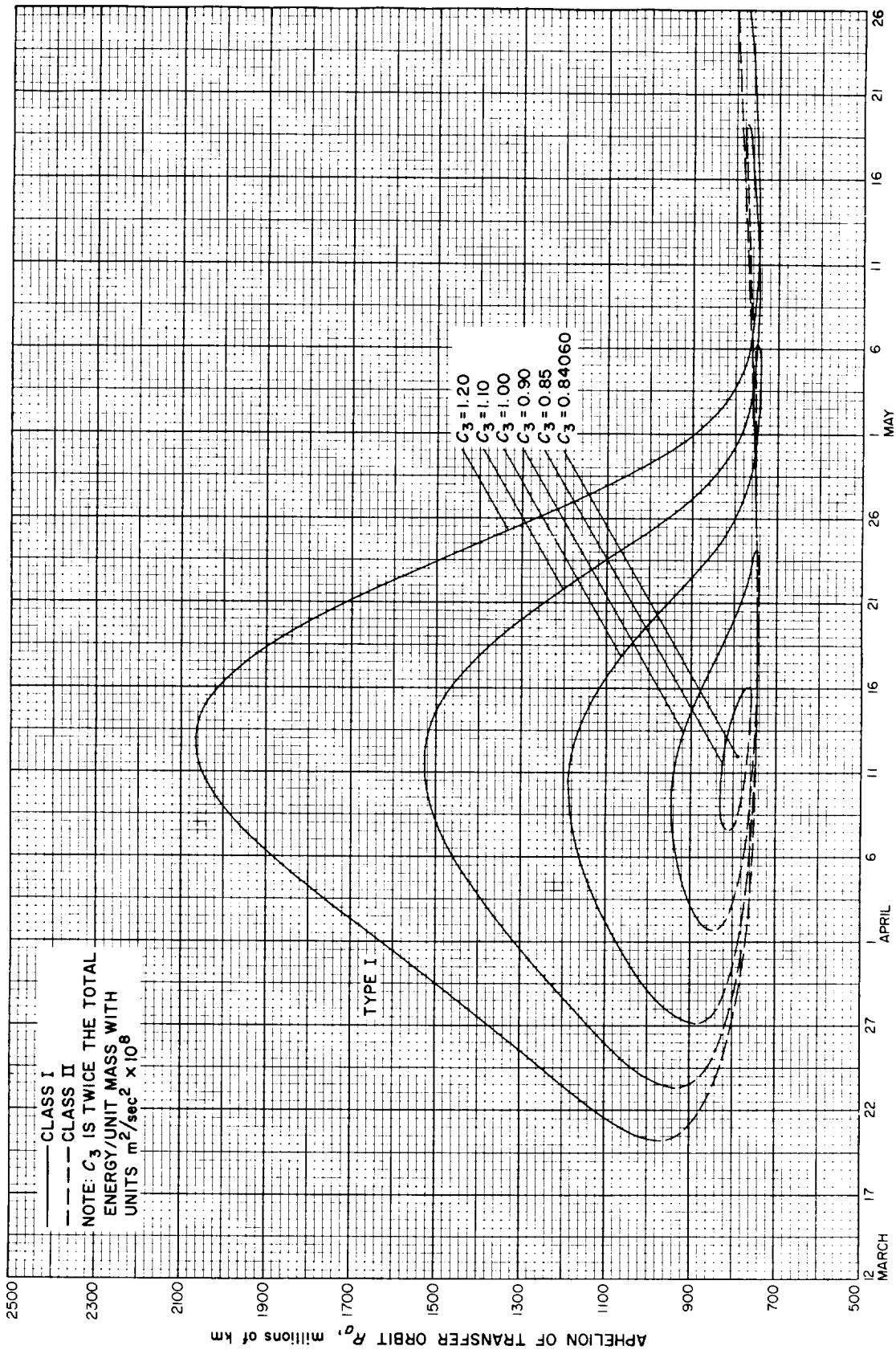

Fig. 10–12(I). Jupiter 1973: Aphelion of transfer orbit vs launch date, Type I

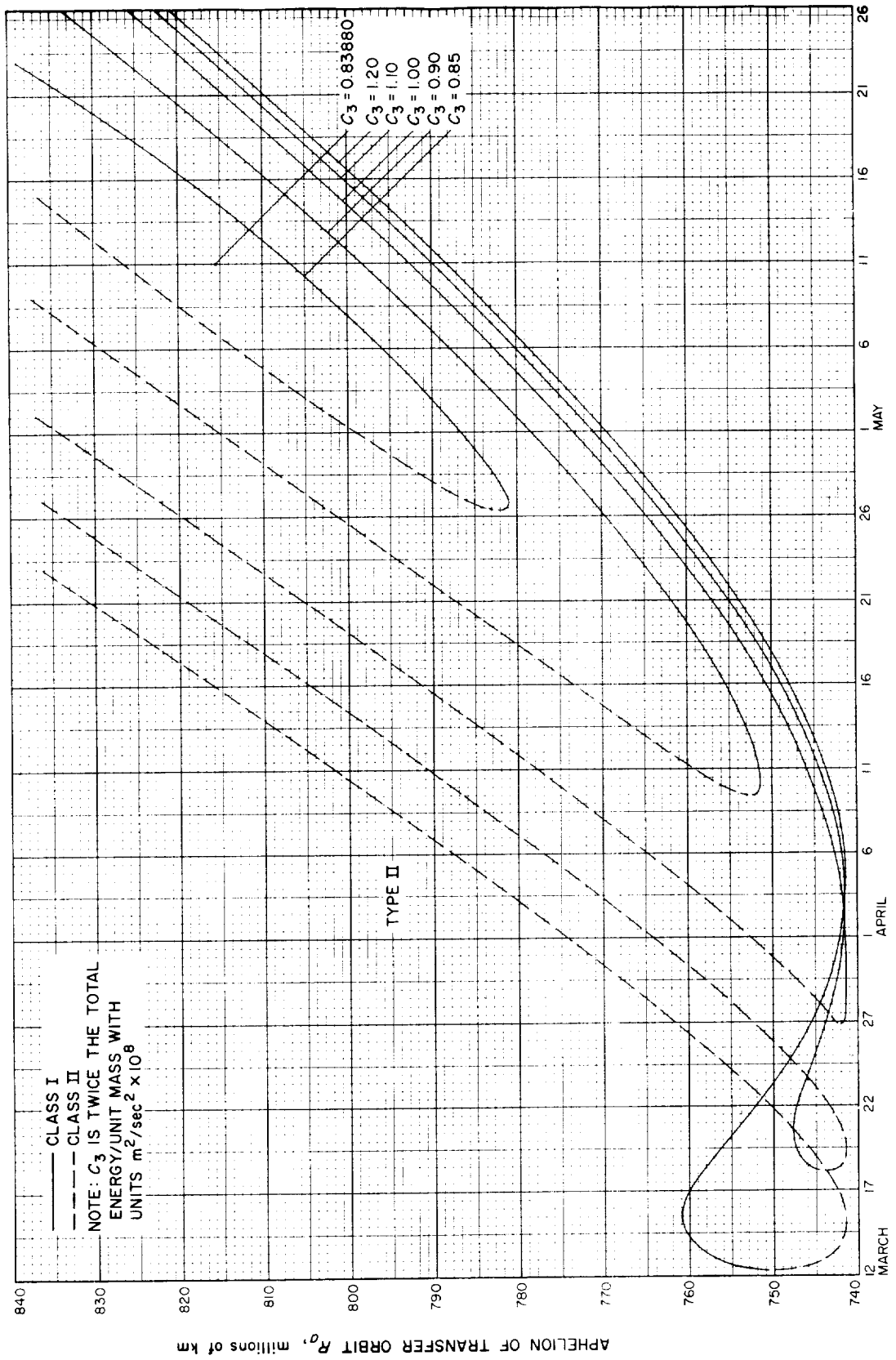

Fig. 10-12(II). Jupiter 1973: Aphelion of transfer orbit vs launch date, Type II

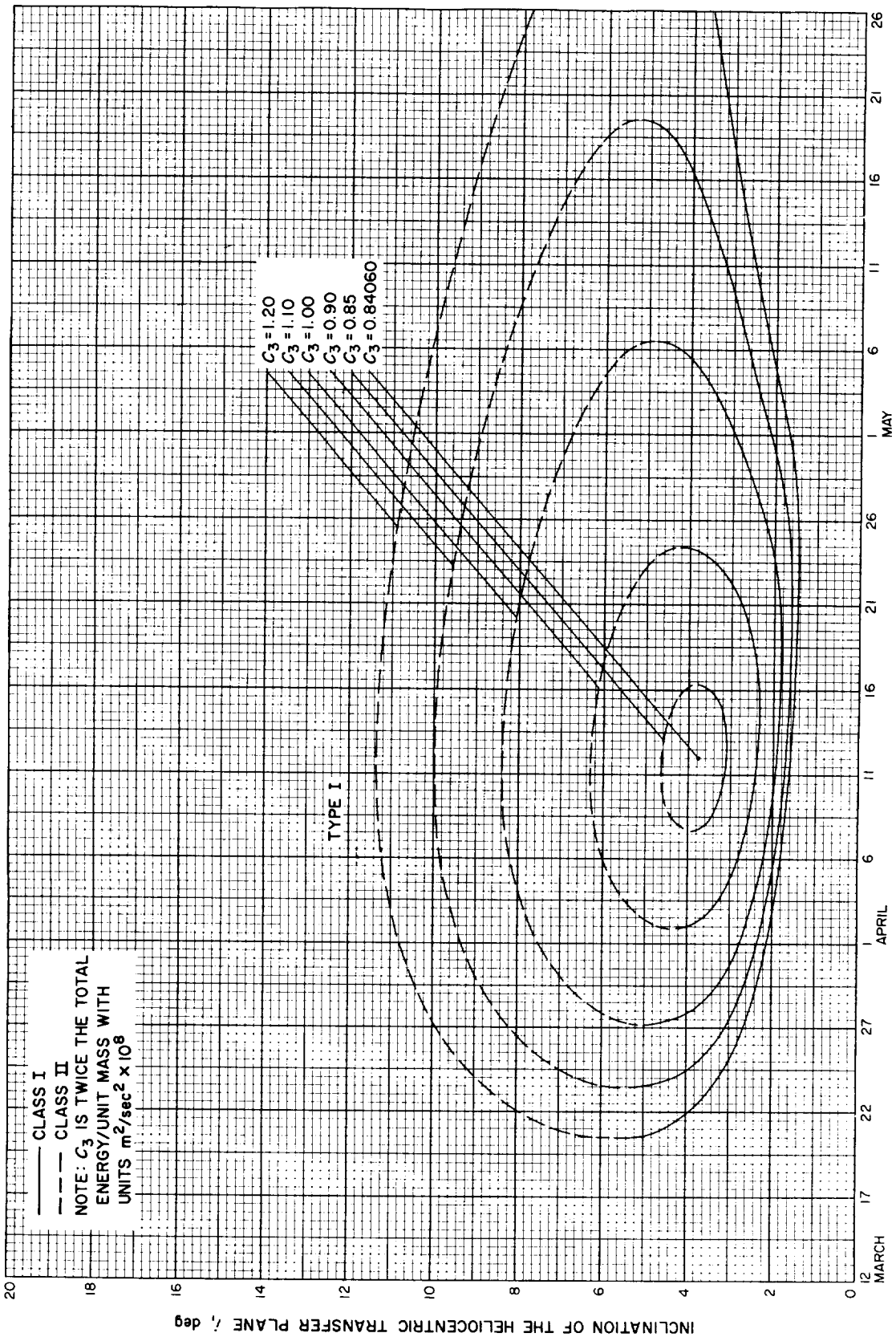

Fig. 10-13(I). Jupiter 1973: Inclination of the heliocentric transfer plane vs launch date, Type I

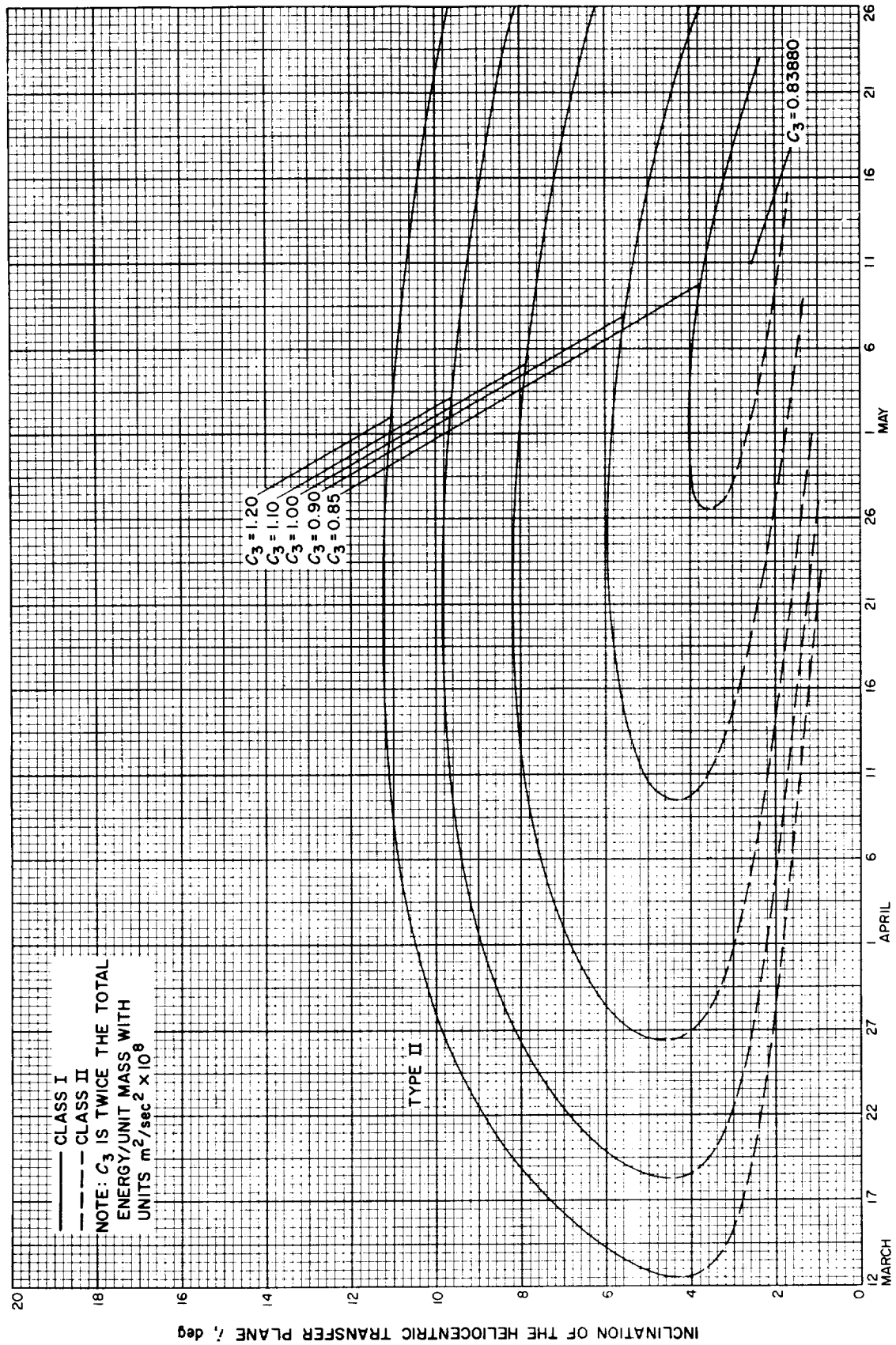

Fig. 10–13(II). Jupiter 1973: Inclination of the heliocentric transfer plane vs launch date, Type II

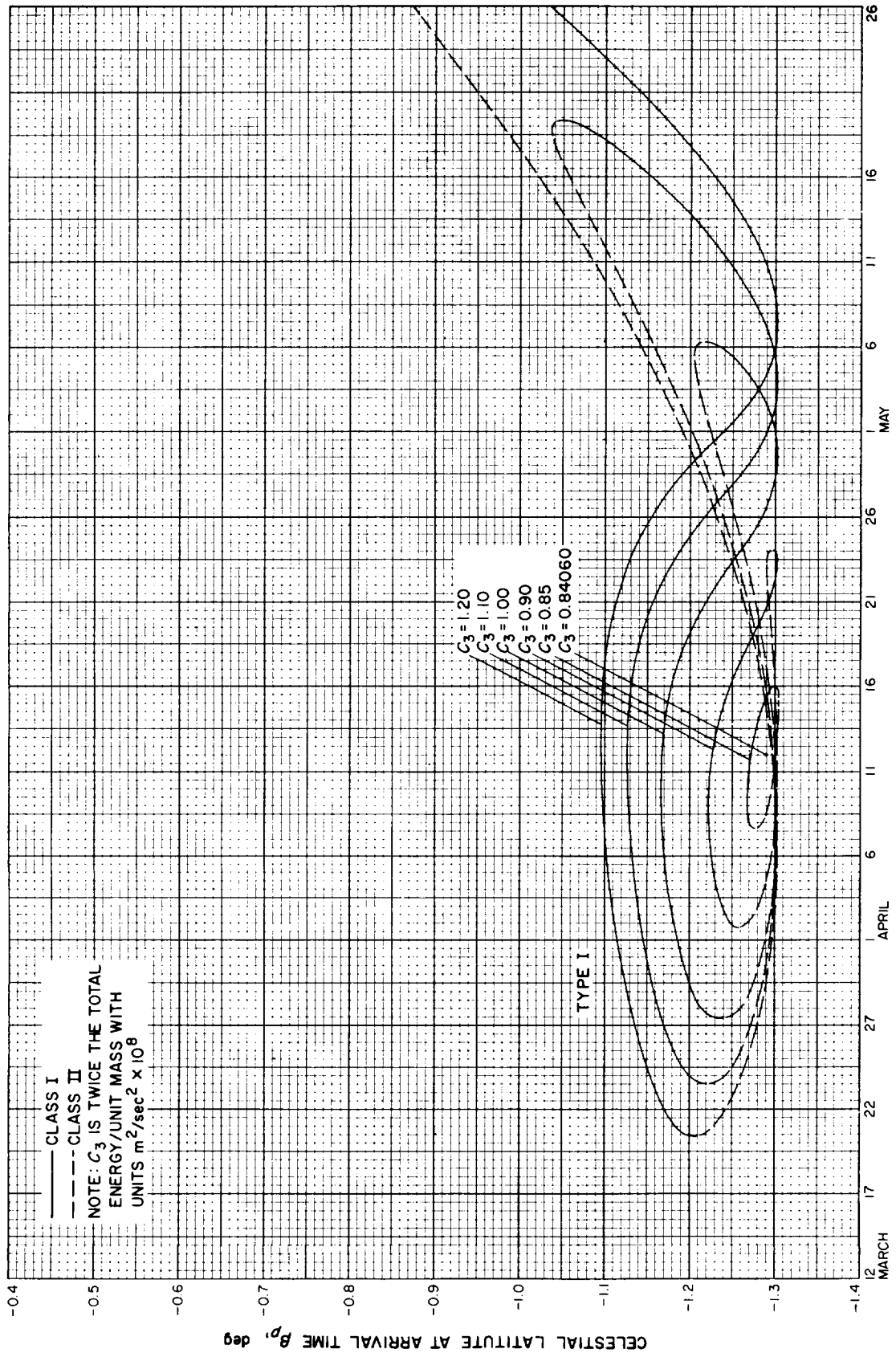

Fig. 10–14(I). Jupiter 1973: Celestial latitude at arrival time vs launch date, Type I

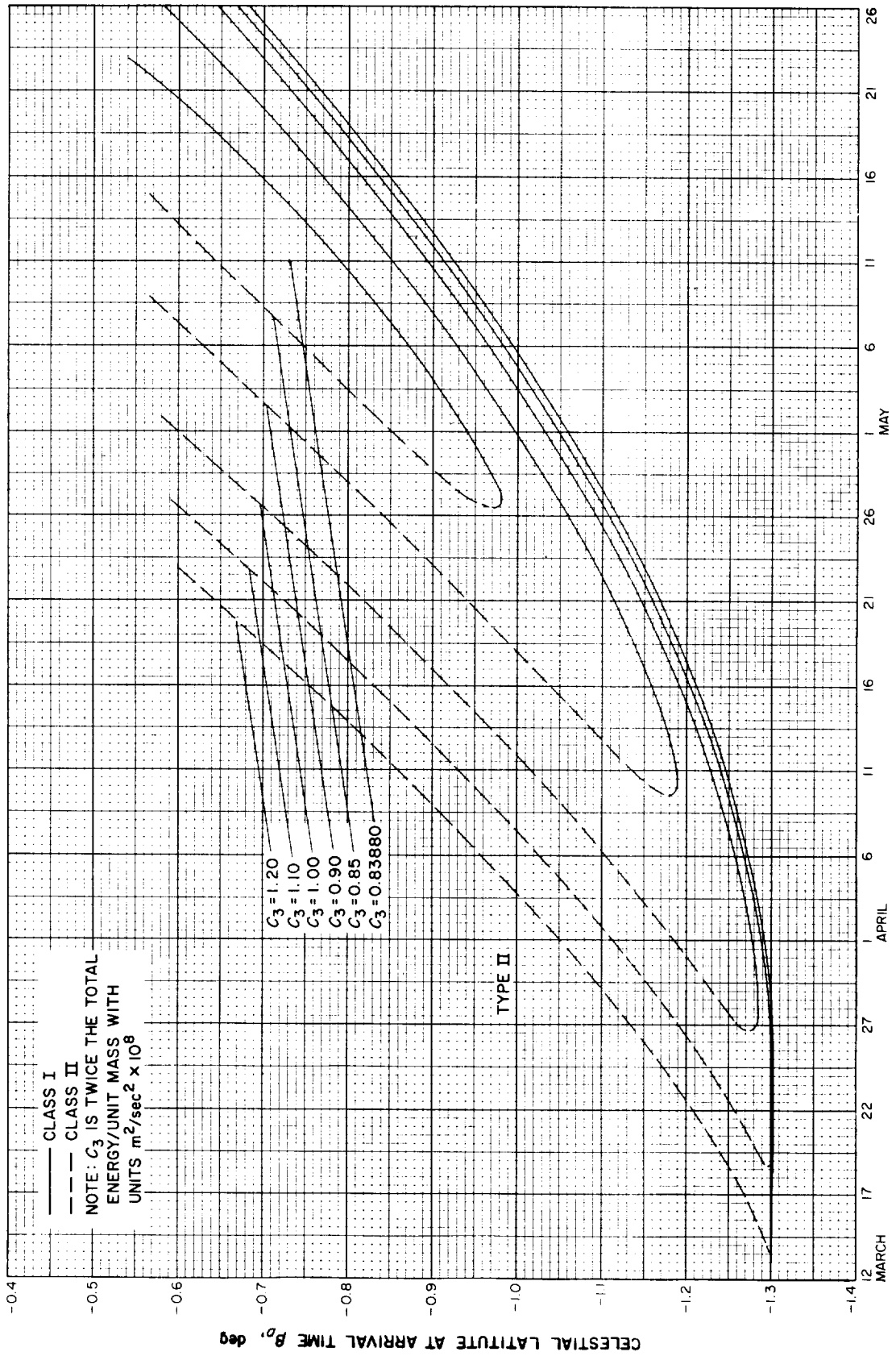

Fig. 10–14(II). Jupiter 1973: Celestial latitude at arrival time vs launch date, Type II

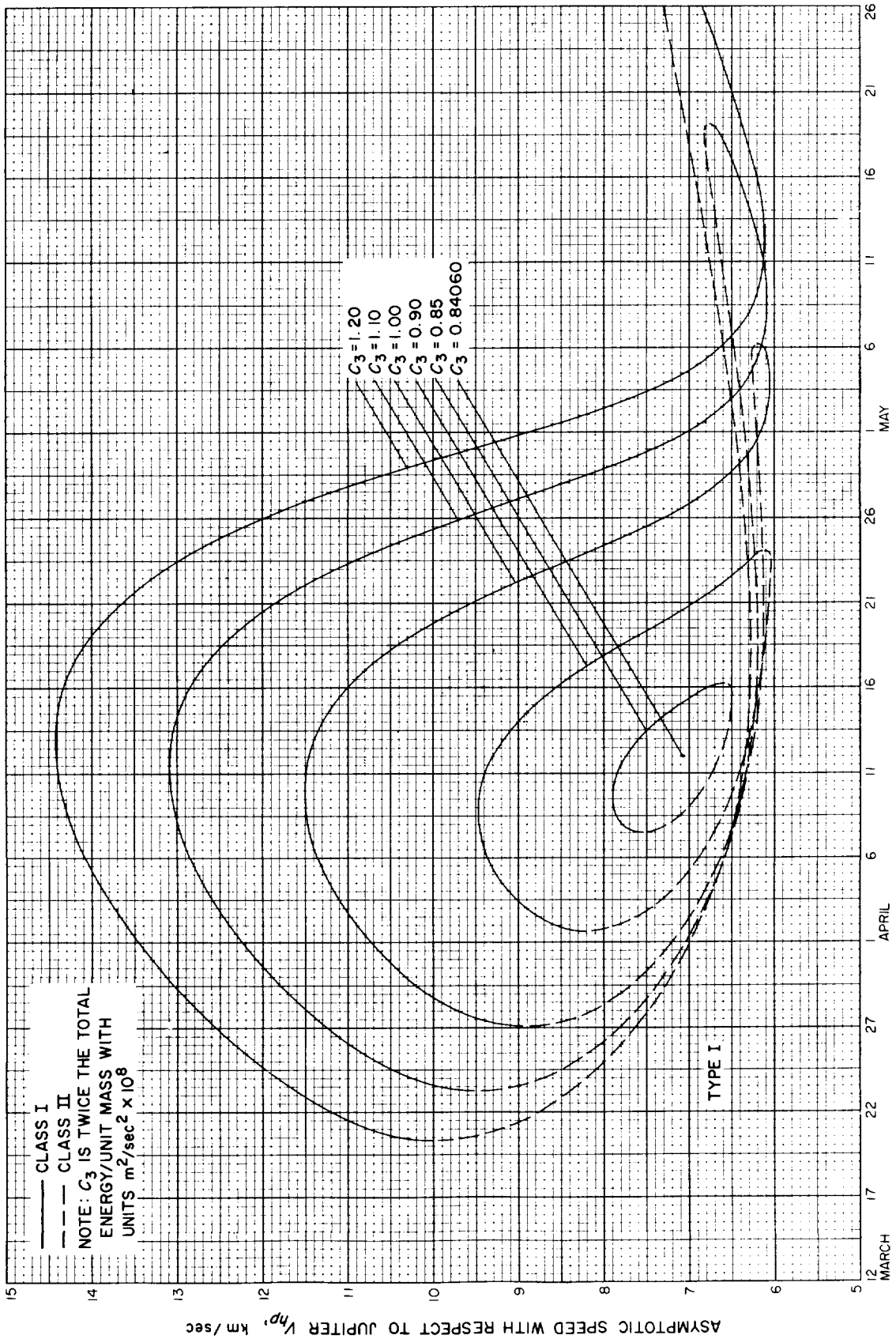

Fig. 10–15(I). Jupiter 1973: Asymptotic speed with respect to Jupiter vs launch date, Type I

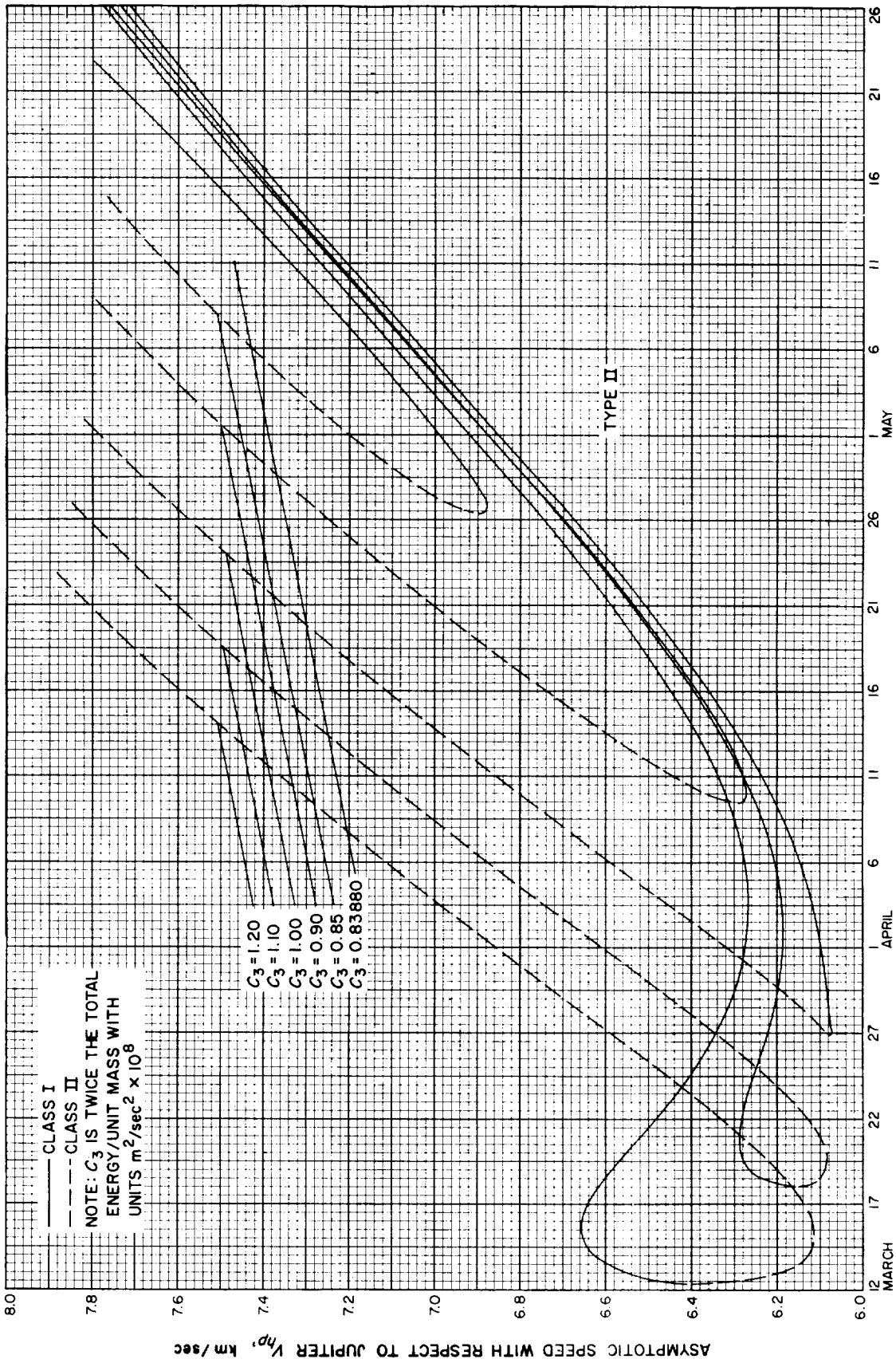

Fig. 10–15(II). Jupiter 1973: Asymptotic speed with respect to Jupiter vs launch date, Type II

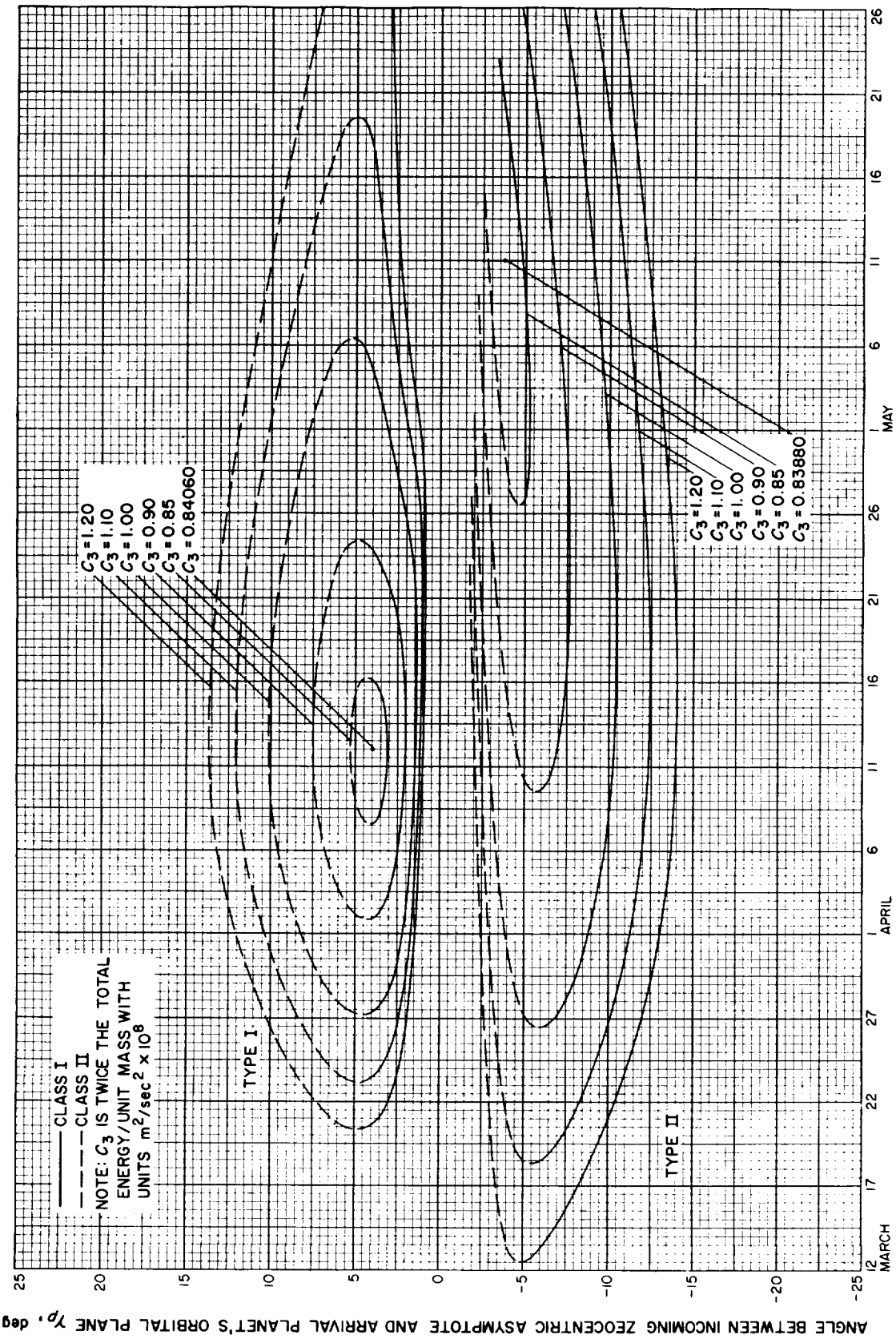

Fig. 10–16. Jupiter 1973: Angle between incoming zeocentric asymptote and arrival planet's orbital plane vs launch date

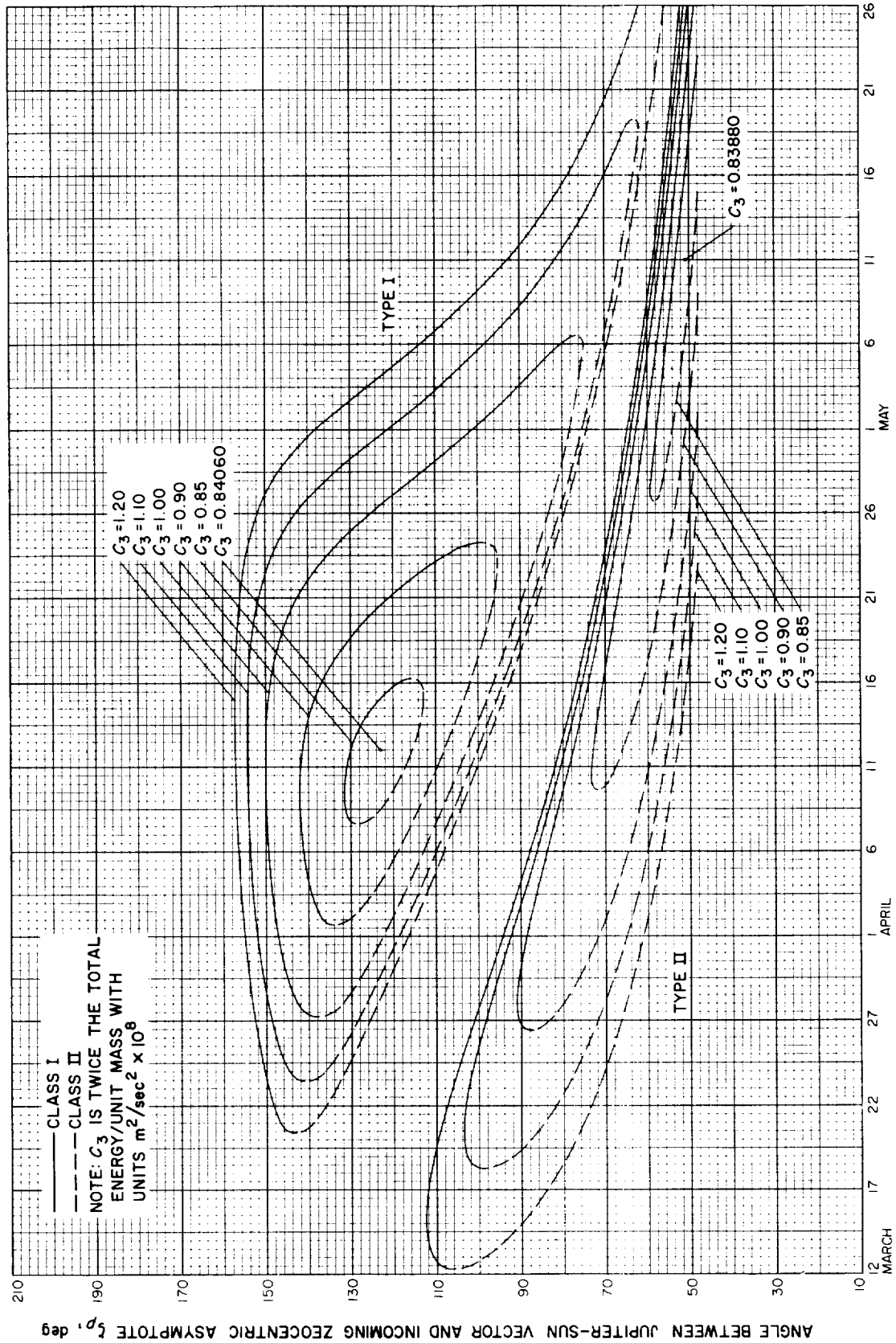

Fig. 10–17. Jupiter 1973: Angle between Jupiter–Sun vector and incoming zeocentric asymptote vs launch date

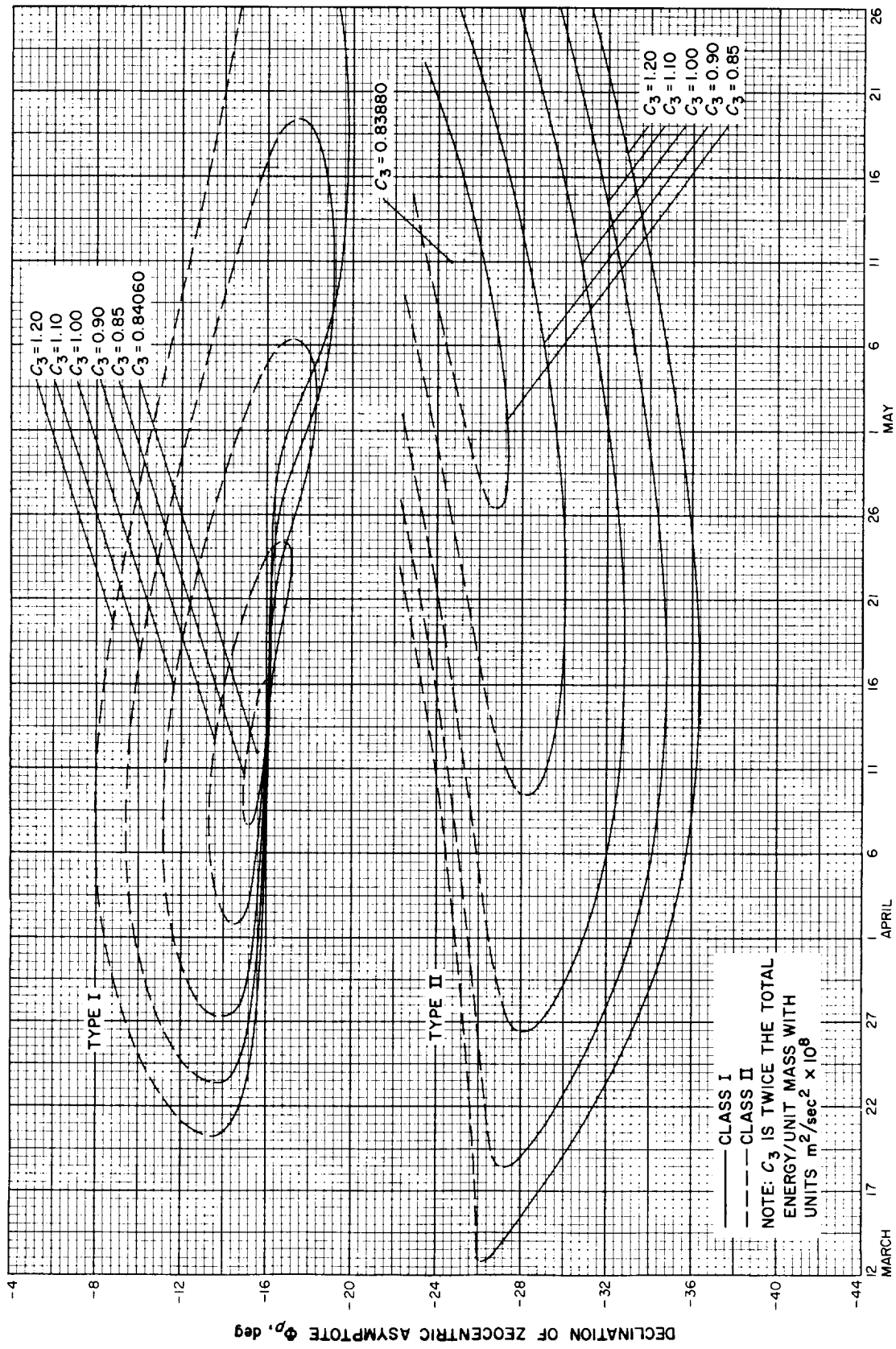

Fig. 10–18. Jupiter 1973: Declination of zeocentric asymptote vs launch date

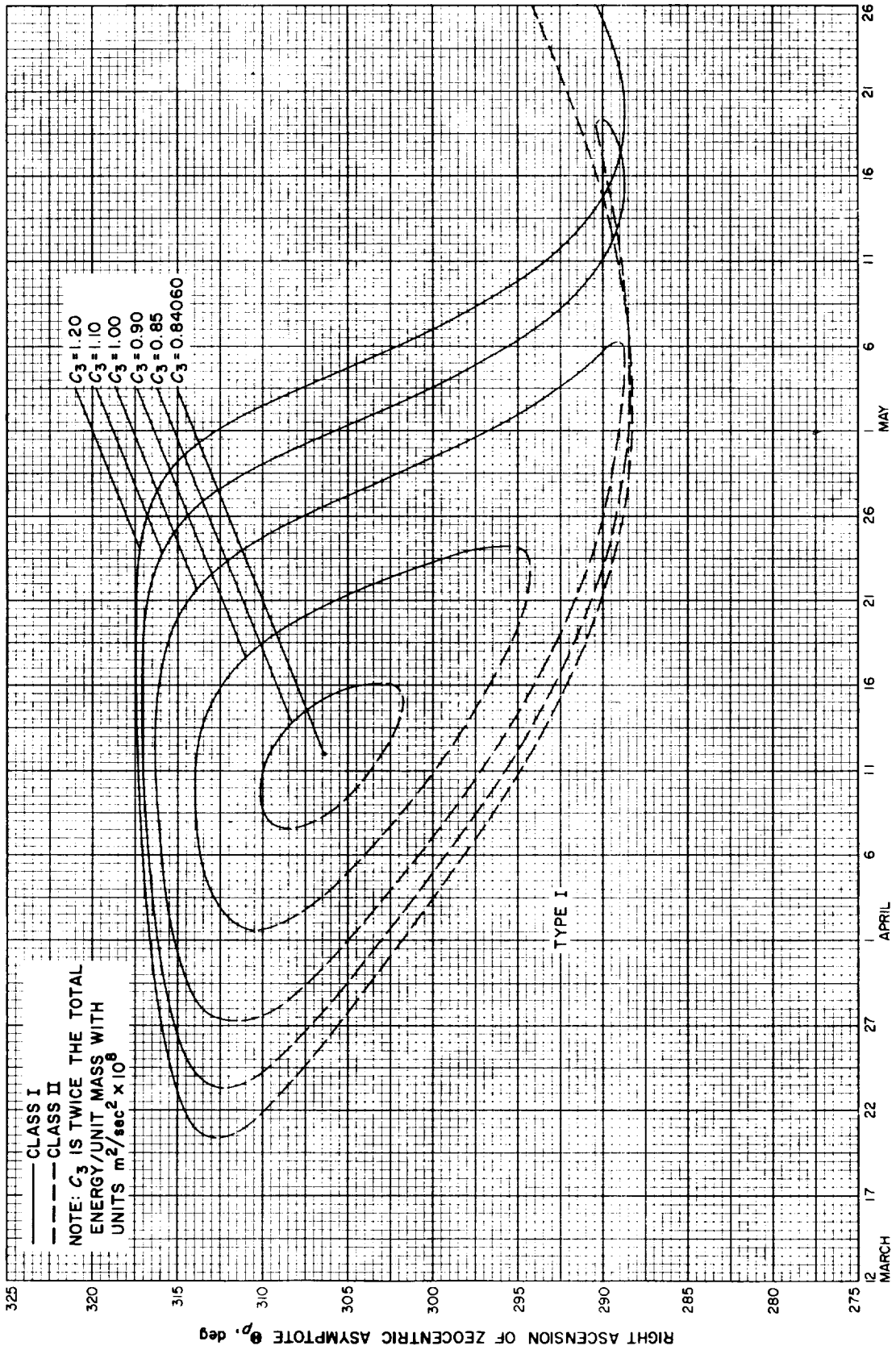

Fig. 10-19(I). Jupiter 1973: Right ascension of zeocentric asymptote vs launch date, Type I

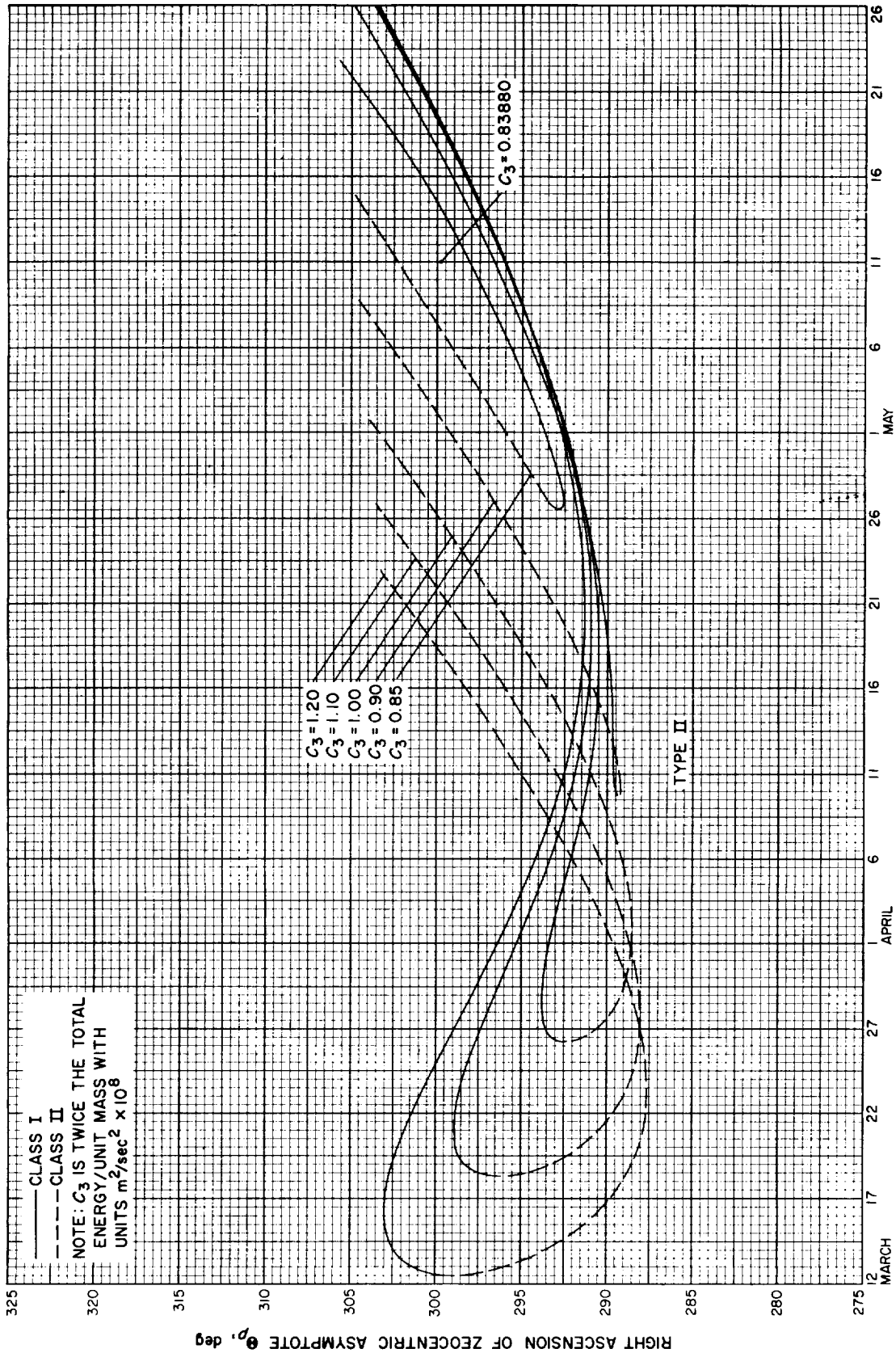

Fig. 10–19(II). Jupiter 1973: Right ascension of zeocentric asymptote vs launch date, Type II

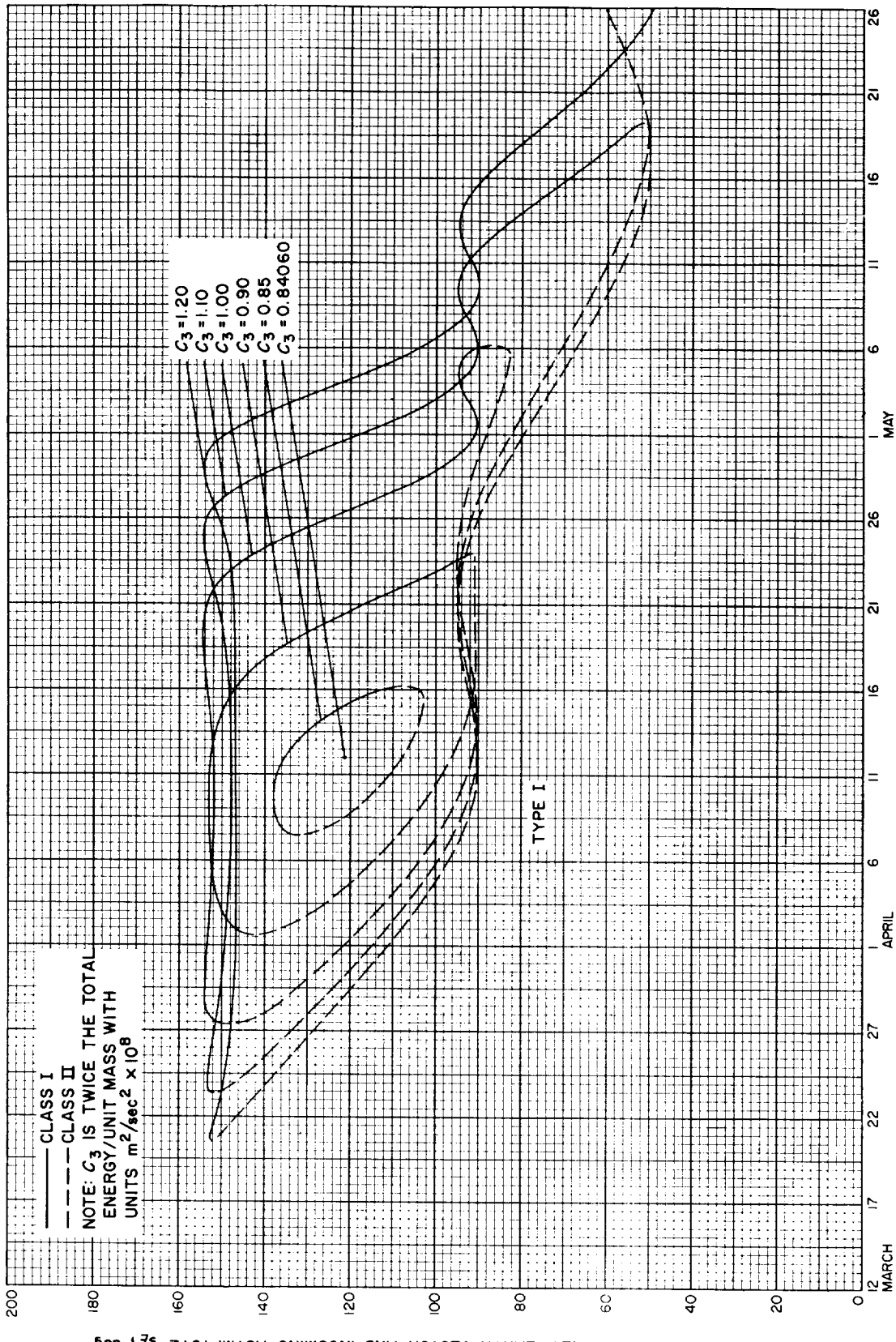

Fig. 10–20(I). Jupiter 1973: Angle between planet–Earth vector and incoming asymptote vs launch date, Type I

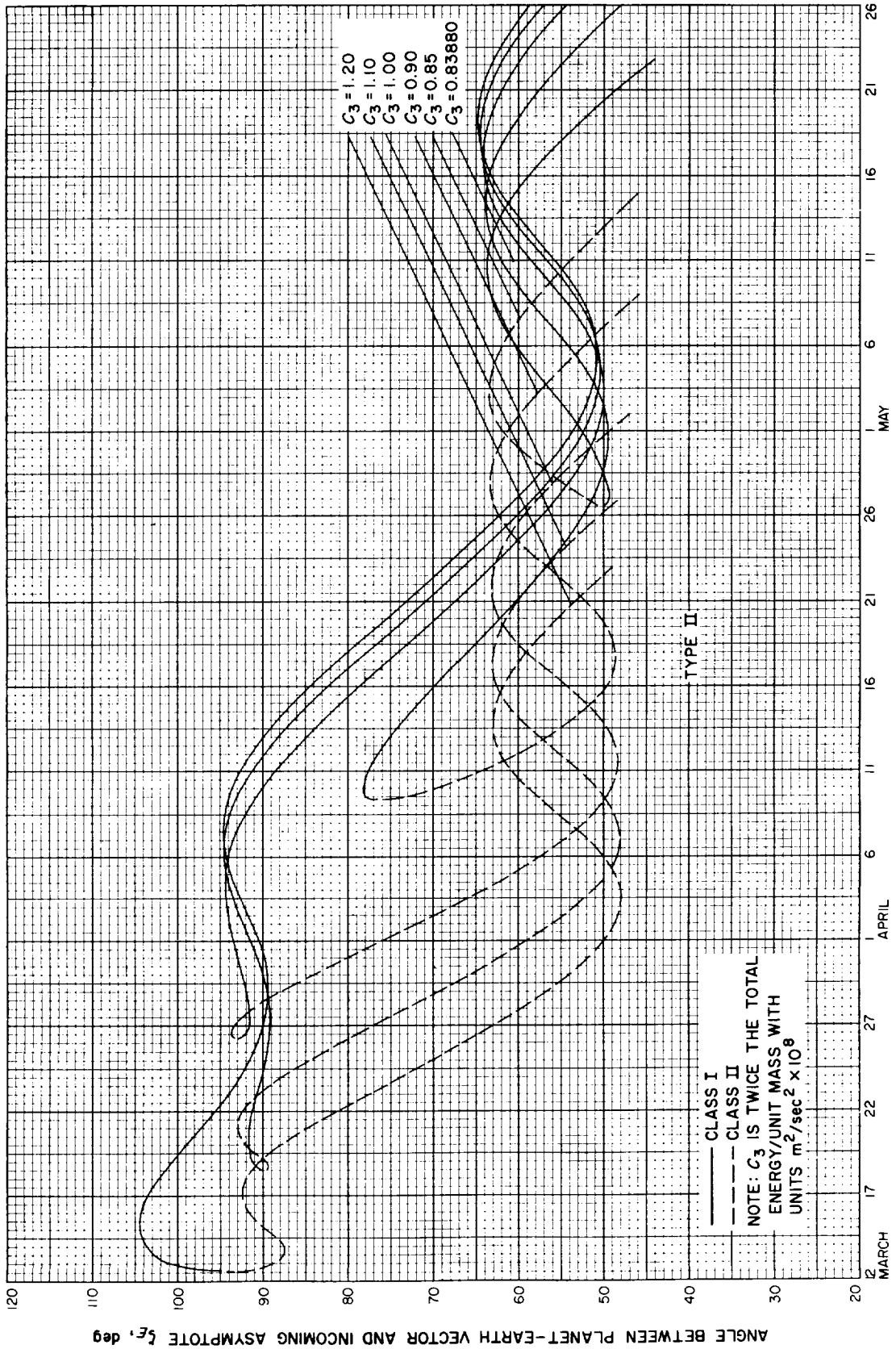

Fig. 10–20(II). Jupiter 1973: Angle between planet–Earth vector and incoming asymptote vs launch date, Type II

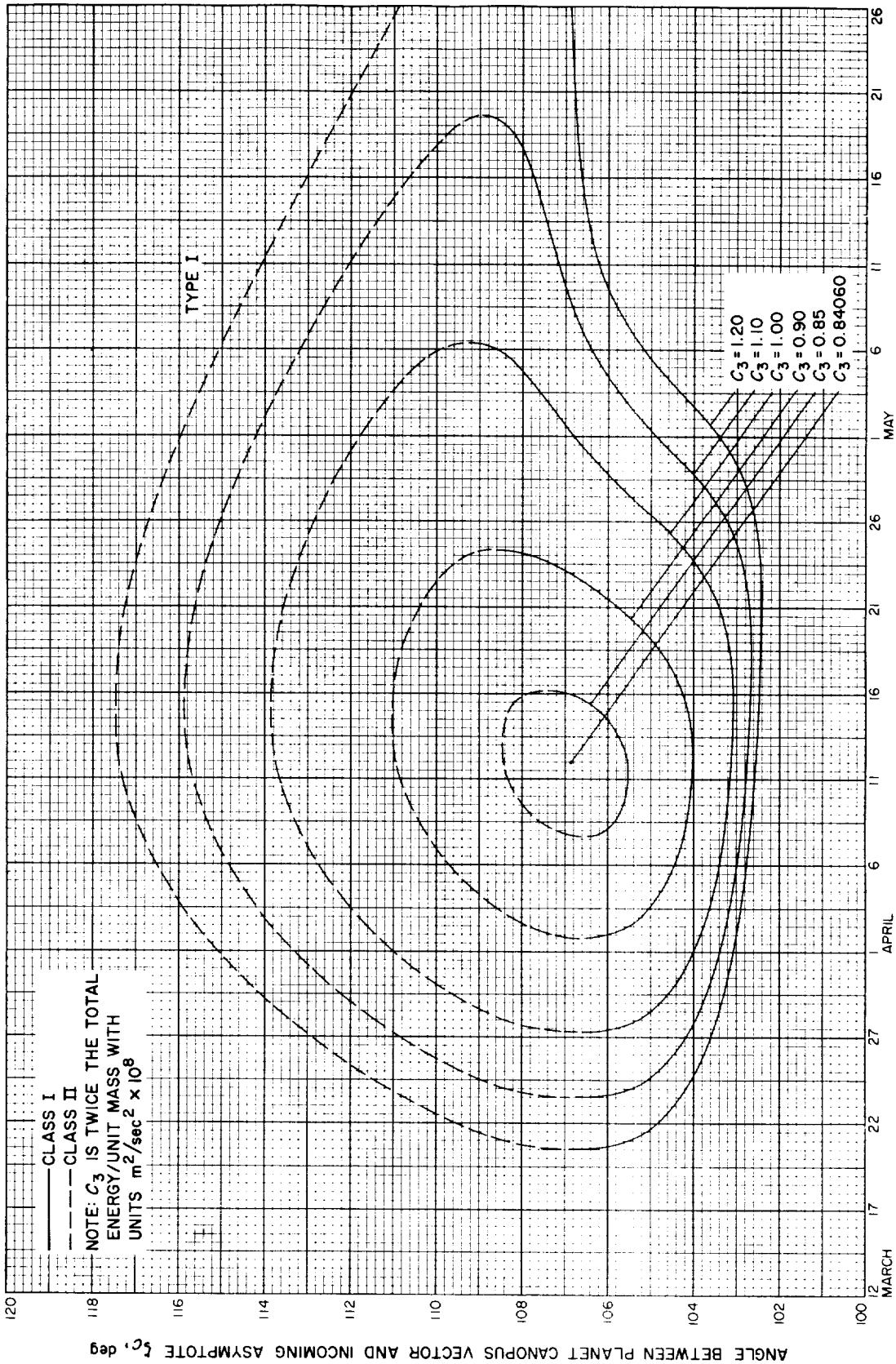

Fig. 10-21(I). Jupiter 1973: Angle between planet–Canopus vector and incoming asymptote vs launch date, Type I

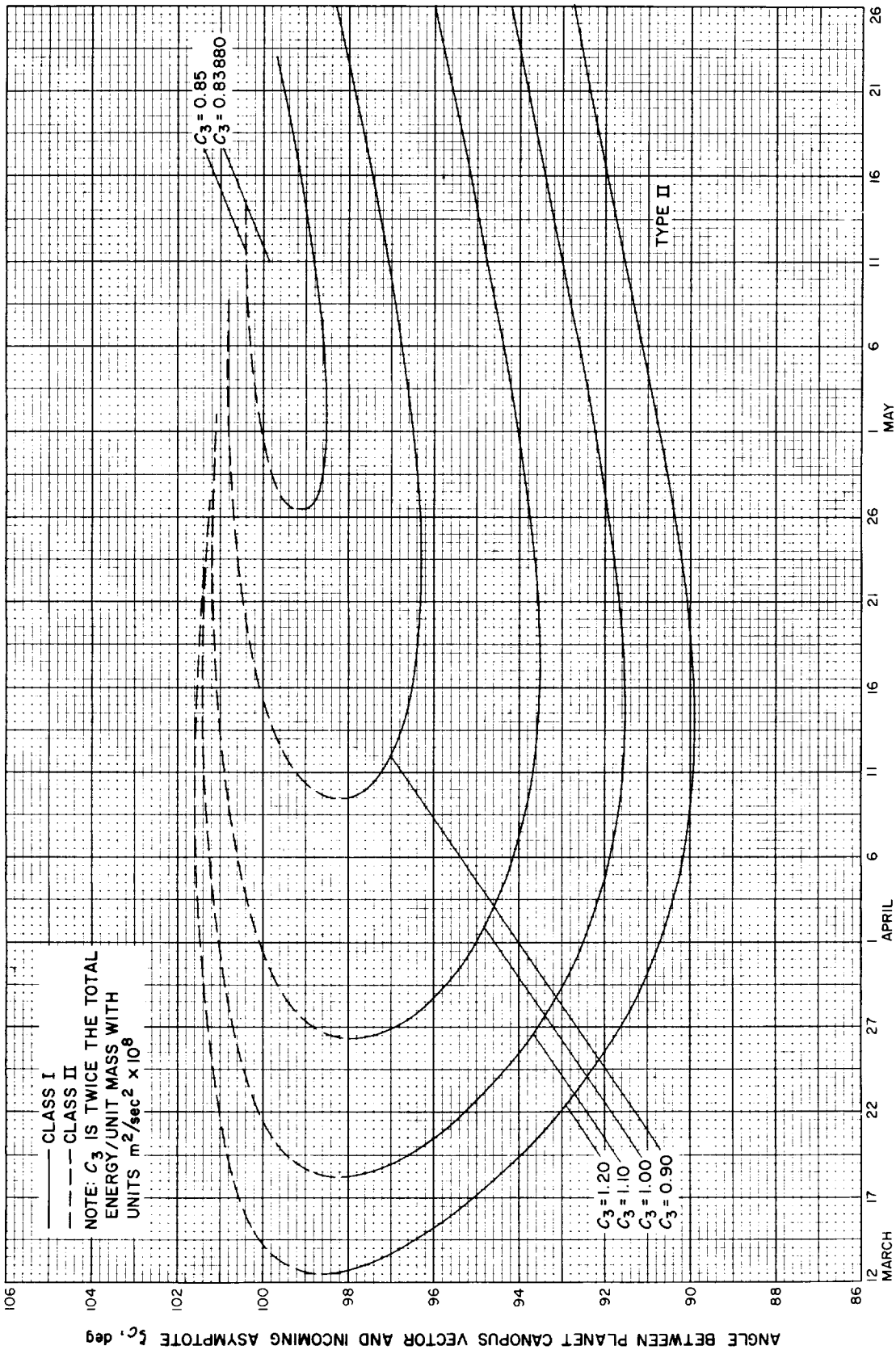

Fig. 10-21(II). Jupiter 1973: Angle between planet–Canopus vector and incoming asymptote vs launch date, Type II

NOMENCLATURE

C_3	*vis viva* energy (injection energy of escape hyperbola)
i	inclination of heliocentric transfer orbit, deg
R_a	aphelion of transfer orbit, millions of km
R_C	Earth–Mercury (or –Jupiter) communication distance, millions of km
R_p	perihelion of transfer orbit, millions of km
T_F	time of flight, days
v_L	true anomaly in transfer ellipse at launch time, deg
v_p	true anomaly in transfer ellipse at arrival time, deg
V_{hp}	asymptotic speed (or hyperbolic-excess speed) with respect to Mercury (or Jupiter), km/sec
β_p	celestial latitude of Mercury (or Jupiter) at arrival time, deg
γ_L	angle between outgoing geocentric asymptote and launch planet's orbital plane, deg (also defined as celestial latitude of outgoing asymptote)
γ_p	angle between incoming hermiocentric[b] or zeocentric[c] asymptote and arrival planet's orbital plane, deg
ζ_L	angle between Sun–Earth vector and outgoing geocentric asymptote, deg (also defined as Earth–probe–Sun angle)
ζ_p	angle between Mercury–Sun (or Jupiter–Sun) vector and incoming hermiocentric (or zeocentric) asymptote, deg (also defined as Sun–probe–target angle)
Θ_p	right ascension of hermiocentric (or zeocentric) asymptote, deg
Θ_S	right ascension of geocentric asymptote, deg
Φ_p	declination of hermiocentric (or zeocentric) asymptote, deg
Φ_S	declination of geocentric asymptote, deg
Ψ	heliocentric central angle, deg

[a] This table of Nomenclature presents only the notation used in the graphs of Sections IV to X. All other terms are defined at point of first mention in Sections I to III.

[b] Hermiocentric refers to Mercury.

[c] Zeocentric refers to Jupiter.

REFERENCES

1. Battin, R. H., "The Determination of Round-Trip Planetary Reconnaissance Trajectories," *Journal of the Aero/Space Sciences*, Vol. 26, No. 9, September 1959.
2. Clarke, V. C., Jr., *Design of Lunar and Interplanetary Ascent Trajectories*, Technical Report No. 32-30, Rev. 1, Jet Propulsion Laboratory, Pasadena, March 15, 1962.
3. Holdbridge, D. B., *Space Trajectories Program for the IBM Computer*, Technical Report No. 32-223, Rev. 1, Jet Propulsion Laboratory, Pasadena, September 1, 1962.
4. *The American Ephemeris and Nautical Almanac for the year 1960*, p. 498, U. S. Government Printing Office, Washington.
5. Allen, C. W., *Astrophysical Quantities*, The Athlone Press, University of London, London, 1955.
6. Cutting, E., and Sturms, F. M., "Trajectory Analysis of a 1970 Mission to Mercury via a Close Encounter with Venus," AIAA Paper 60-90, *AIAA 2nd Annual Aerospace Sciences Meeting*, New York, New York, January 25-27, 1965.
7. Baker, A. B., "Approximate Payload Capabilities of Boosters for Planetary Missions," *Journal of Spacecraft and Rockets*, Vol. 1, No. 4, p. 439, 1964, RCA, Princeton, New Jersey.
8. Clarke, V. C., Jr., Bollman, W. E., Roth, R. Y., and Scholey, W. J.,*Design Parameters for Ballistic Interplanetary Trajectories, Part I. One-way Transfers to Mars and Venus*, Technical Report No. 32-77, Jet Propulsion Laboratory, Pasadena, California, January 16, 1963.
9. W. E. Bollman, *One-way Type-II Transfers to Mars*, Addendum 1 to Ref. 8, Jet Propulsion Laboratory, Pasadena, California (to be published).

ACKNOWLEDGMENT

The authors wish to acknowledge the valuable assistance of M. Beckwith, who carried out the production of the computations and automatic plotting of the graphs.